

TABLE OF CONTENT

ISBN 978-5-00015-013-9

INTRODUCTION PROGRAM COMMITTEE

PROGRAM

overview PROGRAM
scientific PROGRAM

ABSTRACTS

INFORMATION

ADDRESS
METRO MAP
REGISTRATION AND INFORMATION DESK
SCIENTIFIC SESSIONS
POSTER SESSIONS
SOCIAL PROGRAM
INTERNET ACCESS AND WiFi
LUNCH POINTS

NOTEBOOK

Москва
ИКИ РАН
2016

THE SEVENTH MOSCOW SOLAR SYSTEM SYMPOSIUM 7M-S³

SPACE RESEARCH INSTITUTE
MOSCOW, RUSSIA
October 10-14, 2016

Starting from 2010, the Space Research Institute holds annual international symposia on Solar system exploration. Main topics of these symposia include wide range of problems related to formation and evolution of Solar system, planetary systems of other stars; exploration of Solar system planets, their moons, small bodies; interplanetary environment, astrobiology problems. Experimental planetary studies, science instruments and preparation for space missions are also considered at these symposia.

Special session dedicated to the memory of Robert W. Farquhar, a pioneer of mission design is planned for discussion of problems connected with interplanetary flight dynamics including trajectory optimization and motion control.

The Seventh Moscow international Solar System Symposium (7M-S³) will be held from October 10 till 14, 2016.

Subject matter of this symposium will cover many problems of the Solar system science with the central topic "Moon and Mars exploration". This topic relates to scientific problems of several projects which are under development in Russia: "Luna-Glob", "Luna-Resource" and two joint Roscosmos-ESA missions to Mars: "ExoMars 2016", which was launched on March 14, 2016, and "ExoMars 2020".

THE FOLLOWING SESSIONS WILL BE HELD DURING THE SYMPOSIUM:

- OPENING SESSION
- Session MARS
- Session MOON
- Session VENUS
- Session DUST AND DUSTY PLASMA IN SPACE
- Session ASTROBIOLOGY, LABORATORY SIMULATIONS AND ANALOG ENVIRONMENTS
- Session SMALL BODIES
- Session DEDICATED TO THE MEMORY OF ROBERT W. FARQUHAR
- Session INTERSTELLAR FLIGHTS: NEW INITIATIVE
- Session FUTURE MISSIONS AND NEW TECHNIQUES

Space Research Institute holds this symposium with participation of the following organizations:

- RUSSIAN ACADEMY OF SCIENCES
- RUSSIAN FOUNDATION FOR BASIC RESEARCH
- VERNADSKY INSTITUTE OF GEOCHEMISTRY AND ANALYTICAL CHEMISTRY
- EARTH PHYSICS INSTITUTE
- KELDYSH INSTITUTE OF APPLIED MATHEMATICS
- RADIO ELECTRONICS INSTITUTE
- STERNBERG ASTRONOMICAL INSTITUTE, MOSCOW STATE UNIVERSITY.

symposium website: <http://ms2016.cosmos.ru>
contact email address: ms2016@cosmos.ru

Мероприятие проводится при финансовой поддержке Российской академии наук и Российского фонда фундаментальных исследований, Проект № 16-02-20754

PROGRAM COMMITTEE

chair:

acad. **Zelenyi L.M.** IKI RAS

members:

Bazilevskiy A.T. GEOHI RAS

Bibring J.-P. IAS, CNRS, France

Borovin G.K. Keldysh AMI

Chicarro A. ESTEC

Dunham D. KinetX Aerospace, Inc

Duxbury T. George Mason University

Eismont N.A. IKI RAS

Head III J. Brown University

Korablev O.I. IKI RAS

Kostitsyn Y.A. GEOHI RAS

Marov M.Ya. GEOHI RAS

Martynov M.B. Lavochkin Association

Mitrofanov I.G. IKI RAS

Owen T. Hawaii University

Rodin A.V. IKI RAS

Shevchenko V.V. GAISH MSU

Smirnov V.M. IRE RAS

Svedhem H. ESTEC

Vaisberg O.L. IKI RAS

Vorobyova E.A. MSU

Witasse O. ESTEC

Wu Ji China

Zharkov V.N. IFZ RAS

Zakharov A.V. IKI RAS

Zasova L.V. IKI RAS

secretary:

Roste O. IKI RAS, ms3@iki.rssi.ru

overview 7M-S³ program

THE SEVENTH MOSCOW SOLAR SYSTEM SYMPOSIUM (7M-S³)

IKI RAS, 10-14 OCTOBER 2016

	10 october	11 october	12 october	13 october	14 october
10.00	OPENING SESSION				session 7 DEDICATED TO THE MEMORY OF ROBERT W. FARQUHAR
10.20					
10.40					
11.00					
11.20	session 1. MARS	session 2. MOON	session 2. MOON: MAPPING IN LUNA-26	session 4. DUST AND DUSTY PLASMA IN SPACE	session 8. INTERSTELLAR FLIGHTS: NEW INITIATIVE
11.40					
12.00					
12.20					
12.40	session 1. MARS	session 2. MOON	session 3. VENUS	session 5. ASTROBIOLOGY	session 9. FUTURE MISSIONS AND NEW TECHNIQUES
13.00					
14.00					
14.20					
14.40	session 1. MARS	session 2. MOON	session 3. VENUS	session 6. SMALL BODIES	session 9. FUTURE MISSIONS AND NEW TECHNIQUES
15.00					
15.20					
15.40					
16.00	session 1. MARS	session 2. MOON	session 3. VENUS	session 6. SMALL BODIES	session 9. FUTURE MISSIONS AND NEW TECHNIQUES
16.20					
16.40					
17.00					
17.20	session 1. MARS	session 2. MOON	session 3. VENUS	session 6. SMALL BODIES	session 9. FUTURE MISSIONS AND NEW TECHNIQUES
17.40					
18.00					
18.20					
18.40	POSTER SESSION WELCOME PARTY	SOCIAL EVENTS IN MOSCOW	POSTER SESSION	CONCERT	SOCIAL EVENTS IN MOSCOW
19.00					
19.20			SOCIAL EVENTS IN MOSCOW	RECEPTION	
19.40					
20.00	POSTER SESSION WELCOME PARTY	SOCIAL EVENTS IN MOSCOW			SOCIAL EVENTS IN MOSCOW

7M-S³ SCIENTIFIC PROGRAM

monday, 10 october 2016			
OPENING SESSION			10.00-11.40
convener: Lev ZELENYI			
7MS3-OS-01	Lev ZELENYI	Milestones of the Russian Space Science Program for the Decade 2016-2025	10.00-10.30
7MS3-OS-02	James GREEN	NASA's Planetary Science Missions Present and Future Plans	10.30-11.00
7MS3-OS-03	ROSCOSMOS presentation		11.00-11.40
coffee-break			11.40-12.00
session 1. MARS			12.00-18.00
conveners: James HEAD, Oleg KORABLEV			
7MS3-MS-01	Valery SHEMATOVICH et al	Electron precipitation at Mars: effect of crustal magnetic field	12.00-12.20
7MS3-MS-02	Eduard DUBININ et al	Ion fluxes and their routes at Mars. Mars Express and MAVEN observations	12.20-12.40
7MS3-MS-03	Mikhail VERIGIN and Galina KOTOVA	Oxygen loss from Mars: Earlier PHOBOS 2, recent MAVEN observations, and how to measure oxygen loss by in-situ ion measurements	12.40-13.00
lunch			13.00-14.00
7MS3-MS-04	Vladimir KRASNOPOLSKY	IRTF/CSHELL Observations of the CO Dayglow at 4.7 μm , CO Mixing Ratio, and HDO/H ₂ O on Mars	14.00-14.20
7MS3-MS-05	Anna FEDOROVA et al	Observations of water vapor in the Martian middle atmosphere on Mars-Express	14.20-14.40
7MS3-MS-06	James HEAD	Mars climate history: A geological perspective	14.40-15.00
7MS3-MS-07	Maxim LITVAK et al	Global and local trends in observation of subsurface water in Gale crater from DAN/MSL data	15.00-15.20
7MS3-MS-08	Jordanka SEMKOVA et al	Dosimetry investigations onboard ExoMars missions. Results from radiation measurements during ExoMars 2016 TGO cruise to Mars	15.20-15.40
7MS3-MS-09	Jose Luis VAZQUEZ-POLETTI et al	Martian Computing Clouds: A Two Use Case Study	15.40-16.00
coffee-break			16.00-16.20
7MS3-MS-10	James HEAD et al	Mars human science exploration and resource utilization: The dichotomy boundary Deuteronilus Mensae exploration zone	16.20-16.40
7MS3-MS-11	Sierra KAUFMAN et al	Aluminum Phyllosilicates: Implications for Past Climate History of Mars	16.40-17.00
7MS3-MS-12	Adeene DENTON and James HEAD	Fretted terrain origins and the problems of Arabia Terra, with a focus on stratigraphic and temporal relationships	17.00-17.20
7MS3-MS-13	Thomas DUXBURY	Precision cartographic map of the ExoMars Schiaparelli landing site on Mars derived from Mars Reconnaissance Orbiter Context Camera images	17.20-17.40
7MS3-MS-14	Vladimir GUBENKO et al	Parameters of saturated internal gravity waves identified in the Martian atmosphere from an analysis of Mars Global Surveyor radio occultation data	17.40-18.00
POSTER SESSION (all sessions)			18.00-19.00

tuesday, 11 october 2016			
session 2. MOON			10.00-18.00
conveners: Igor MITROFANOV, Maxim LITVAK			
7MS3-MN-01	Anton SANIN et al	Lunar neutrons, as signatures of water	10.00-10.20
7MS3-MN-02	Timothy McCLANAHAN et al	High concentration of hydrogen-bearing volatiles at the base of poleward-facing slopes in the Moon's large southern permanently shadowed regions	10.20-10.40
7MS3-MN-03	Daniela ROMMEL et al	Petrological mapping of regions in the South Pole-Aitken Basin	10.40-11.00
7MS3-MN-04	Mikhail KRESLAVSKY et al	Degradation of small craters in lunar highlands	11.00-11.20
7MS3-MN-05	Ekaterina KRONROD et al	Cold and hot models of the lunar mantle	11.20-11.40
coffee-break			11.40-12.00
7MS3-MN-06	John KELLER and N. PETRO	Recent results of the Lunar Reconnaissance Orbiter mission	12.00-12.20
7MS3-MN-07	Boris IVANOV	Small lunar craters size-frequency distribution: degradation and widening	12.20-12.40
7MS3-MN-08	Lionel WILSON and James HEAD	Three-stage eruption sequence in lunar shield volcanoes and the production of magmatic foam	12.40-13.00
lunch			13.00-14.00
7MS3-MN-09	Igor MITROFANOV	Status of Luna-25 landing site selection	14.00-14.20
7MS3-MN-10	Jessica FLAHAUT et al	Candidate landing sites for the Luna-Glob mission	14.20-14.40
7MS3-MN-11	Mikhail IVANOV et al	Geological characterization of the three most promising landing sites for the Luna-Glob mission	14.40-15.00
7MS3-MN-12	Sergey FILIMONOV and Sergey AKSENOV	Heat radiation impact modeling on the spacecraft located on Moon polar regions	15.00-15.20
7MS3-MN-13	Vladimir ERMAKOV and D. TUFANOV	Computer simulation of lunar surface sputtering for Luna-Resource mission	15.20-15.40
7MS3-MN-14	James CARPENTER et al	Robotic precursors to human explorers: ESA lunar mission activities and studies	15.40-16.00
coffee-break			16.00-16.20
7MS3-MN-15	Maria ZAKHAROVA and Evgeny SLYUTA	The multi-scale mapping of Mons Rumker area for designing lunar rover's route purpose	16.20-16.40
7MS3-MN-16	Jürgen OBERST and P. GLÄSER	Lunar Polar Illumination and Implications for Future Landing Sites	16.40-17.00
7MS3-MN-17	Dmitry MOISEENKO et al	Scientific objectives and parameters of ARIES-L instrument qualification model for Luna-Glob mission	17.00-17.20
7MS3-MN-18	Alexander GUSEV et al	Tidal-librational dissipative dynamics of the Moon and radio/laser beacons VLBI/LRR/LLR technologies for ChangE-5/6, Luna-25/26/27, ILOM missions	17.20-17.40
7MS3-MN-19	Maxim LITVAK et al	Instrumentation for polar regolith analysis of Luna-25 and Luna-27 spacecraft	17.40-18.00

wednesday, 12 october 2016			
session 2. MOON. SCIENCE AND PLANNING OF LUNAR SURFACE MAPPING IN LUNA-26 PROJECT			10.00-13.00
conveners: Anatoly PETRUKOVICH, Ivan POLYANSKIY			
7MS3-MN-20	Anatoli PETRUKOVICH et al	Russian Lunar orbiter mission	10.00-10.20
7MS3-MN-21	Vladimir SMIRNOV et al	Radar complex in the "Luna-Resource" project	10.20-10.40
7MS3-MN-22	Anton SANIN et al	LGNS instrument for Luna-26 mission	10.40-11.00
7MS3-MN-23	Ivan Polyanskiy et al	LSTK - lunar stereo topographic camera for "Luna-Resource-1» orbital mission	11.00-11.20
7MS3-MN-24	Mikhail KRESLAVSKY et al	Advanced global topographic mapping of the Moon: An important objective of upcoming lunar orbital missions	11.20-11.40
Coffee-break			11.40-12.00
7MS3-MN-25	Maria ZAKHAROVA and Evgeny SLYUTA	Challenges of the 3D Moon surface mapping	12.00-12.20
7MS3-MN-26	Anatoly ZUBAREV et al	Priorities for imaging for lunar orbital missions considering further photogrammetric processing	12.20-12.40
7MS3-MN-27	Anatoly ZUBAREV et al	The effect of image compression on DTM quality	12.40-13.00
lunch			13.00-14.00
session 3. VENUS			14.00-18.00
convener: Ludmila ZASOVA			
7MS3-VN-01	Vladimir KRASNOPOLSKY	Nitrogen Isotope Ratios in the Solar System and Its Evolution on Titan	14.00-14.20
7MS3-VN-02	Vladimir KRASNOPOLSKY	On the iron chloride aerosol in the clouds of Venus	14.20-14.40
7MS3-VN-03	Sanjay LIMAYE	Ultraviolet Absorber in the Clouds of Venus	14.40-15.00
7MS3-VN-04	Denis BELAYEV et al	Sulphur bearing species at the night side of Venus' upper mesosphere	15.00-15.20
7MS3-VN-05	Alexandr PAVELIEV et al	Venera 9, 10 and Venera 15, 16 bistatic radar results: the Venus surface and lower atmosphere	15.20-15.40
7MS3-VN-06	Eugenia GUSEVA	Topographic characteristics of rift zones on Venus	15.40-16.00
coffee-break			16.00-16.20
7MS3-VN-07	Chikako HIROSE et al	The Japanese Venus orbiter AKATSUKI and its initial scientific results	16.20-16.40
7MS3-VN-08	Ludmila ZASOVA et al	JSDT :Scientific goals and architecture of the mission Venera-D	16.40-17.00
7MS3-VN-09	Mikhail IVANOV et al	The landing potential of terrains on the surface of Venus: prognosis for the Venera-D mission	17.00-17.20
7MS3-VN-10	Tibor KREMIC et al	Venera-D: Technology Implications	17.20-17.40
7MS3-VN-11	Greg LEE et al	Venus Atmospheric Maneuverable Platform (VAMP)- Air Vehicle Concept and Entry CONOPs	17.40-18.00
POSTER SESSION (all sessions)			18.00-19.00

thursday, 13 october 2016			
session 4. DUST AND DUSTY PLASMA IN SPACE			10.00-13.00
conveners: Alexander ZAKHAROV, Mihaly HORANYI			
7MS3-DP-01	Sergey POPEL and Lev ZELENYI	Dusty plasmas in the solar system: recent developments, advances, and unsolved problems	10.00-10.20
7MS3-DP-02	Oleg PETROV et al	Coulomb "Explosion" of Dust Cluster under Microgravity	10.20-10.40
7MS3-DP-03	Mihaly HORANYI et al	The lunar dust environment: the effects of impacts and near-surface plasmas	10.40-11.00
7MS3-DP-04	Nikolay BORISOV et al	The role of the inner radiation belt in dust grains lofting from the Jupiter's moons Thebe and Amalthea	11.00-11.20
7MS3-DP-05	Tatiana SALNIKOVA et al	On the probabilistic model of the Kordylewski cosmic dust clouds	11.20-11.40
coffee-break			11.40-12.00
7MS3-DP-06	Fabrice CIPRIANI et al	Simulation of the dusty plasma environment of 65803 Didymos for the Asteroid Impact Mission (AIM)	12.00-12.20
7MS3-DP-07	Andrey DIVIN et al	Three dimensional kinetic Particle-in-Cell simulation of the 67P environment	12.20-12.40
7MS3-DP-08	Iliia KUZNETSOV et al	Lunar dusty plasma and spacecraft instruments interaction: SPIS-Dust simulation	12.40-13.00
lunch			13.00-14.00
session 5. ASTROBIOLOGY, LABORATORY SIMULATIONS AND ANALOG ENVIRONMENTS			14.00-16.00
convener: Elena VOROBYOVA			
7MS3-AB-01	Nikita DEMIDOV	Where to look for life on Mars – the view from cryobiosphere of Earth	14.00-14.15
7MS3-AB-02	Mojdeh DALIR SHARAMI and Saleheh EBADIRAD	Martian evolution and habitability: From the planet formation to the Possibility of DNA and RNA synthesis on the planet Mars	14.15-14.30
7MS3-AB-03	Georgi MANAGADZE	The Actual Problems of Astrobiology: From emergence and search till detection and identification of life	14.30-14.45
7MS3-AB-04	Maxim ZAITSEV et al	An estimate of a qualitative composition of «exogenous» planetary surface organics by the study of model impact-induced transformation of carbonaceous meteorites	14.45-15.00
7MS3-AB-05	Sergei IPATOV and Mikhail MAROV	Delivery of water and planetesimals from the feeding zone of Jupiter and Saturn to forming terrestrial planets	15.00-15.15
7MS3-AB-06	Vladimir BUSAREV	Where should we look for relics of an extinct primitive life?	15.15-15.30
7MS3-AB-07	Oleg KOTSYURBENKO	Microbial community of the upper soil layer of Negev desert as the model microbial system for astrobiological experiments in the planned mission Phobos-Grunt 2	15.30-15.45
7MS3-AB-08	Natalia KHAMIDULLINA et al	The planetary protection requirements fulfillment during the launch campaign of the ExoMars-2016 mission	15.45-16.00
coffee-break			16.00-16.20

session 6. SMALL BODIES**convener: Alexander BASILEVSKY****16.20-18.00**

7MS3-SB-01	Sergey EFIMOV and Vladislav SIDORENKO	Intermittency in dynamics of resonant Kuiper belt objects	16.20-16.35
7MS3-SB-02	Evgenij ZUBKO et al	Why comets reveal various positive polarization?	16.35-16.50
7MS3-SB-03	Peter WURZ et al	Chemical composition of the semi-volatile grains of comet 67P/Churyumov-Gerasimenko	16.50-17.05
7MS3-SB-04	Yuri SKOROV et al	The microphysical properties of the dust particles on 67P/CG nucleus from the MIRO data	17.05-17.20
7MS3-SB-05	Sergey KRASILNIKOV et al	Pinnacles on the 67P/Churyumov-Gerasimenko comet nucleus	17.20-17.35
7MS3-SB-06	Alexander BASILEVSKY et al	Graininess of the material of the comet 67P nucleus as deduced from analysis of the Rosetta NavCam, Osiris and ROLIS images	17.35-17.50
7MS3-SB-07	Lev ZELENYI and Leonid KSAFOMALITY	Does regional surface morphology of comets 67P/CG and 1P/Halley carry any traces of their origin in low velocity collisions?	17.50-18.00

friday, 14 october 2016			
session 7. SESSION DEDICATED TO THE MEMORY OF ROBERT W. FARQUHAR			10.00-11.00
convener: Natan EISMONT			
7MS3-RF-01	David DUNHAM et al	Robert Farquhar's Ideas for Human Exploration of Space	10.00-10.20
7MS3-RF-02	David DUNHAM	Robert Farquhar's Impressive Space Exploration Legacy	10.20-10.40
7MS3-RF-03	Atila PORO	Grazing Asteroid Occultation	10.40-11.00
session 8. INTERSTELLAR FLIGHTS: NEW INITIATIVE			11.00-13.00
convener: Lev ZELENYI			
7MS3-IF-01	Simon WORDEN	The Breakthrough Initiatives - The Search for Life in the Universe and Mankind's First Interstellar Voyage	11.00-11.40
coffee-break			11.40-12.00
7MS3-IF-02	Louis FRIEDMAN et al	A Mission to the Solar Gravity Lens Focus	12.00-12.20
7MS3-IF-03	Vyacheslav TURYSHEV et al	Direct Multipixel Imaging of an exo-Earth with a Solar Gravitational Lens Telescope	12.20-12.40
7MS3-IF-04	Helen POPOVA et al	On the stability of nanocraft orientation while illuminated by intense laser beam	12.40-13.00
lunch			13.00-14.00
session 9. FUTURE MISSIONS AND NEW TECHNIQUES			14.00-18.00
conveners: Oleg KORABLEV, Thomas DUXBURY			
7MS3-FM-01	Dmitri SKULACHEV	PAT-M Radiometer Onboard the ExoMars-2020 Lander. Calibration Procedure and Possibility of Martian Atmosphere Temperature Measurements During a Dust Storm	14.00-14.20
7MS3-FM-02	Sergey ASEEV et al	Gas-analytical chromatography system for mission "ExoMars 2020"	14.20-14.40
7MS3-FM-03	Thomas DUXBURY et al	Mars Express OMEGA and HRSC: important datasets for MMX planning, site selection and operations	14.40-15.00
7MS3-FM-04	Adeene DENTON et al	Tectonic history of Enceladus's South Polar Terrain and its ties to the formation of the tiger stripe fractures	15.00-15.20
7MS3-FM-05	Anton BUTENKO and Sergey AKSENOV	Investigation of possibility of using melting probes for exploration of icy satellites	15.20-15.40
7MS3-FM-06	Pavel KLIMOV et al	The development of reflective optical systems based on nanocomposite structures for space research	15.40-16.00
Coffee-break			16.00-16.20

7MS3-FM-07	Mikhail MISHCHENKO	Active remote sensing of planetary atmospheres and surfaces	16.20-16.40
7MS3-FM-08	Kirill ZAKHARCHENKO et al	Radiation monitor based on diamond detectors for long-term space missions	16.40-17.00
7MS3-FM-09	Iliia KUZNETSOV et al	Dust Analyzer developing for Russian Lunar lander mission	17.00-17.20
7MS3-FM-10	Alexander TAVROV and Leonid KSAFOMALITY	On unusual properties of the KIC 8462852 satellites (KEPLER mission heritage)	17.20-17.40
7MS3-FM-11	Markiyan CHUBEY et al	Orbital Stellar Stereoscopic Observatory Project: motivations and autonomous navigation in the heliocentric transfer and operational orbits	17.40-18.00

POSTER SESSION

10 october 18.00-19.00

12 october 18.00-19.00

MARS		
7MS3-PS-01	Anna FEDOROVA et al	Long-term O2 nightglow observations on Mars by SPICAM/MEx
7MS3-PS-02	Ekaterina GRISHAKINA	Cryological mapping of Mars
7MS3-PS-03	Ashley HORAN and James HEAD	Late Noachian Icy Highlands Climate Model: Exploring the possibility of transient melting and fluvial/lacustrine activity through peak temperatures
7MS3-PS-04	Erica JAWIN and James HEAD	Global patterns of paraglacial activity in the martian mid-latitudes
7MS3-PS-05	David WEISS and James HEAD	Hellas Basin Floor, Mars: Is the Honeycomb Terrain Formed by Salt or Ice Diapirism?
7MS3-PS-06	M. Pilar VELASCO et al	Modelization and simulations of the atmospheric dust dynamic through Fractional Calculus
7MS3-PS-07	Sergey VOROPAEV	Phobos evolution under the tidal action of Mars
7MS3-PS-08	Alexey BATOV et al	Static stresses estimates in Mars with an elastic mantle
7MS3-PS-09	Vladimir ZHARKOV and Tamara GUDKOVA	On the model structure of the gravity field of Mars
7MS3-PS-10	Alexander KOSOV et al	GARS instrument - an imitator of Exomars-2016 TGO transmitter
MOON		
7MS3-PS-11	Vladislav TRET'AYKOV	Scientific program of Luna-25 and Luna-27 landers
7MS3-PS-12	James HEAD et al	Ina pit crater: Origin as a drained summit lava lake and magmatic foam extrusions modified by seismic sieving
7MS3-PS-13	James CASSANELLI and James HEAD	Did the Orientale Impact Melt Sheet Undergo Large-Scale Igneous Differentiation by Crystal Settling?
7MS3-PS-14	Sierra KAUFMAN et al	Mineral associations in enstatite chondrites: possible insights into minerals on Mercury
7MS3-PS-15	Ariel DEUTSCH et al	Constraining the ages of ice deposits at Mercury's north polar region: implications for water-ice delivery mechanisms
7MS3-PS-16	Victor KRONROD et al	Lunar crustal porosity, thermal conductivity and uranium concentration in the crust and mantle
7MS3-PS-17	Evgeny SLYUTA et al	Preliminary data on age of Mons Rumker region
7MS3-PS-18	Evgeny SLYUTA	Project «Lunar Robot-Geologist»: concept, scientific problems, scientific equipment, technical configuration
7MS3-PS-19	Vladislav MAKOVCHUK et al	Experimental research of thermal sensors using control samples of lunar soil imitators
7MS3-PS-20	Ekaterina GRISHAKINA et al	Imitators of the lunar soil for large-scale field experimental research
7MS3-PS-21	Svetlana Pugacheva et al	The natural resources of the Lunar Procellarum KREEP Terrane
7MS3-PS-22	Svetlana PUGACHEVA et al	On the possibility of the existence of deposits of volatiles compounds in the area northwest of the Boguslawsky crater

7MS3-PS-23	Yangxiaoyi LU and Vladislav SHEVCHENKO	Relation between magnetic field and dust distribution on the lunar surface
7MS3-PS-24	Tamara GUDKOVA et al	Cutoff frequency – momentum scaling law for impacts inverted from Apollo seismic data
7MS3-PS-25	Alexandra HEFFELS et al	New Velocity-Depth Profiles from Re-Evaluation of Apollo 17 Lunar Seismic Profiling Experiment
7MS3-PS-26	Arne GRUMPE et al	Illumination dependent behavior of the lunar 3 μ m absorption band depth in the lunar crater Dryden
7MS3-PS-27	Jan DECA et al	Solar Wind Interaction with Lunar Magnetic Anomalies: Reiner Gamma
7MS3-PS-28	Mikhail SINITSYN	Analysis of epithermal neutron flux from Bouguer anomalies
7MS3-PS-29	Parya ABOUHAMZEH	Studying Moon's edge with occultation methods
7MS3-PS-30	Oleg KHÄVROSHKIN and V. TSYPLAKOV	Moon as a Giant Detector for Neutrino Streams from Pulsars
7MS3-PS-31	Gennady KOCHEMASOV	The Moon and Phobos: specific responses of two satellites moving off and nearer their respective planets
7MS3-PS-32	Gennady KOCHEMASOV	Galactic trace on the lunar surface: intercrossing short wave folding in the Mare Imbrium
7MS3-PS-33	Arthur ZAGIDULLIN et al	Theory rotational of the Moon in the framework of the "main problem"
7MS3-PS-34	Michael SHPEKIN et al	Orbital images of high resolution and their role in the study of the matter state in lunar craters

MOON. SCIENCE AND PLANNING OF LUNAR SURFACE MAPPING IN LUNA-26 PROJECT

7MS3-PS-35	Alexander KOKHANOV et al	Integral automated GIS-algorithm for complex analysis of planetary surface and landing site characterization
7MS3-PS-36	Natalia KOZLOVA et al	Lunar rover localization method using joint processing of original surface images with artificially modelled ones
7MS3-PS-37	Andrei GAROV et al	Unified approach to building software for operational planning of Lunar surface imaging and providing broad access to resulted images using 3D web-GIS

VENUS

7MS3-PS-38	Mikhail LUGININ et al	Analysis of upper haze of Venus from Venus Express SPICAV-IR data
7MS3-PS-39	Dmitry GORINOV and Ludmila ZASOVA	Oxygen nightside airglow on Venus in relation to atmospheric dynamics based on VIRTIS-M observations
7MS3-PS-40	Michael BONDARENKO and Anatoly GAVRIK	On Possible GW Origin Of "Meteoric" Layers in Venesian Ionosphere
7MS3-PS-41	Samaneh SHAMYATI	Mercury-Sun distance from the Transit of Mercury
7MS3-PS-42	Daria EVDOKIMOVA et al	Studying of cloud variations using night observations data of SPICAV IR in 2016-2011
7MS3-PS-43	Alexey EKONOMOV et al	Superrotation study in the atmosphere of Venus by means of balloon probes.
7MS3-PS-44	Igor KHATUNTSEV et al	Winds in the middle cloud deck from the near-IR imaging by the Venus Monitoring Camera onboard Venus Express
7MS3-PS-45	Marina PATSAEVA and Igor KHATUNTSEV	Influence of Venus topography on variations of zonal and meridional winds according to measurements in UV and near-IR channels of VMC/Venus Express

DUST AND DUSTY PLASMA IN SPACE

- 7MS3-PS-46 **Sergey POPEL et al** Adiabatic trapping of electrons and localized wave structures in lunar dusty plasmas and Earth's mesosphere
- 7MS3-PS-47 **Sergey POPEL and T. MOROZOVA** Waves in the region of interaction between Earth's magnetosphere and lunar dusty plasma
- 7MS3-PS-48 **Yulia IZVEKOVA and Sergey POPEL** Dust vortex motions in the atmospheres of Earth and Mars

ASTROBIOLOGY, LABORATORY SIMULATIONS AND ANALOG ENVIRONMENTS

- 7MS3-PS-49 **Elena VOROBYOVA et al** Life in the Alien Environments: Simulation of the Physical Parameters of Extraterrestrial Habitats on the Earth Analog Environments
- 7MS3-PS-50 **Anna DUNAEVA et al** Physical and thermal conditions for existence of liquid water oceans within icy satellites Callisto and Titan
- 7MS3-PS-51 **Jessica FLAHAUT et al** Remote sensing and in situ mineralogic survey of the Chilean salars: An analog to Mars evaporate deposits?
- 7MS3-PS-52 **Victor TEJFEL et al** Jupiter: new confirmations of the ammonia absorption depression at low northern latitudes
- 7MS3-PS-53 **Nataliya ZUBKO et al** Light scattering by chemically heterogeneous planetary regolith
- 7MS3-PS-54 **Vladimir CHEPTSOV et al** Influence of Gamma Irradiation in Simulated Martian Conditions on Catalase Activity and Reactivity of Exometabolites of *Kocuria rosea* and *Arthrobacter* polychromogenes
- 7MS3-PS-55 **Vladimir CHEPTSOV et al** Limits of Resistance of Soil Microbial Communities to Impact of Gamma Radiation
- 7MS3-PS-56 **Iliia KUZNETSOV and E. LISIN** Ground-Based Dusty Exosphere simulation chamber for the developing and calibration of Lunar Lander instruments
- 7MS3-PS-57 **Ilya DIGEL et al** Neural Network Based Simulations for Autonomous Exploration of the Ocean Floor by Robotic Systems
- 7MS3-PS-58 **Ilya DIGEL et al** Differential Optical Detection of "Black Smokers" Sulfur Compounds Using Self-Organizing Maps
- 7MS3-PS-59 **Tatiana BORISOVA et al** Enhancement of inorganic Martian dust simulants with carbon component and its effects on key characteristics of glutamatergic neurotransmission
- 7MS3-PS-60 **Margarita KRUCHKOVA et al** Can the Fungal Communities of the Earth Deserts Survive in Simulated Martian Conditions?
- 7MS3-PS-61 **S. SHASHKOVSKIY et al** Surface decontamination of "Exomars-2020" martian landing module elements by pulsed UV irradiation

SMALL BODIES

- 7MS3-PS-62 **Yuri SKOROV et al** A model of short-lived outbursts on the 67P/CG from fractured terrains in the Anukhet region

FUTURE MISSIONS AND NEW TECHNIQUES

- 7MS3-PS-63 **Anatoly MANUKIN et al** High-sensitivity three-axis seismic accelerometer for measurements at the spacecraft and the planets of solar system
- 7MS3-PS-64 **Yuri OZOROVICH et al** Scientific aspects and opportunities of the "Robotic Space Mission to Europa": Space systems application and technology for space mission to Europa (Enceladus) - Jupiter's and Saturn's ice moons

7MS3-PS-65	Vladimir GROMOV and A.KOSOV	The Ranging Accuracy of the Radioscience Experiment with the Radio-Beacon Transponder in Comparison with Laser Ranging
7MS3-PS-66	Yaroslav ILYUSHIN et al	Development of complex methods for regional atmospheric monitoring based on space-borne and ground-based registration of navigational signals
7MS3-PS-67	Gennady KOCHEMASOV	Wave modulation in planetology: a new way of planetary thinking
7MS3-PS-68	Azariy BARÉNBAUM	On the modern state of Comparative Planetology
7MS3-PS-69	Vladimir GUBENKO et al	Geographical distributions of an internal gravity wave activity in the Earth's polar atmosphere for different seasons revealed by radio occultation FORMOSAT-3/COSMIC data

MILESTONES OF THE RUSSIAN SPACE SCIENCE PROGRAM FOR THE DECADE 2016-2025

L. Zelenyi^{1,2}

¹Russian Academy of Sciences, Space Council

²Space Research Institute of Russian Academy of Sciences (IKI RAS),

117997, 84/32 Profsoyuznaya str., Moscow, Russia

Contact: iki@cosmos.ru

The Federal Space Program for 2016-2025 among different space activities includes space projects in several space science fields. According to this program the main targets in planetary exploration are Mars and the Moon.

The ExoMars Program is a joint project between the European Space Agency (ESA) and Roscosmos. The project consists of two missions with launches in 2016 and 2020. The scientific objectives of ExoMars are: to search for signs of past and present life on Mars; to investigate the water/geochemical environment as a function of depth in the shallow subsurface; to study Martian atmospheric trace gases and their sources; to characterize the surface environment.

There is a preliminary agreement between Roscosmos and ESA on the continuations of joint cooperation after the ExoMars Program in exploration of the Martian moons - Phobos and Deimos. Their study cover three major topics related to (1) origin of planetary satellites, (2) small bodies, and (3) Mars (formation and evolution of Mars; Mars ejecta at the satellites). Most of the above questions require the sample return from the Martian moon, while some could be also answered by *in situ* experiments. The recovery of the science goals of a mission to the Martian moons and the delivery of the samples of Phobos to Earth remain of highest priority for Russian scientific community. This recovery mission named Boomerang was postponed following the ExoMars and is considered for launch in 2024. The Phobos Sample Return mission has to be an important step in Mars exploration and a direct precursor of Mars Sample Return.

Moon is the nearest designation in the way of the humans into the solar system. There are three main reasons for humans to explore the Moon: (1) Moon is the natural land for the future observatories for astronomy, physics and chemistry, (2) Moon obtains natural resources and environment, which could be useful for future development of the industrial civilization, and (3) Moon allows to create and to test the space transportation systems for further exploration of Mars, and beyond. Having these reasons in mind, one may predict that space nations will re-start the process of human exploration of the Moon in the next decade of this century, after the first heroic steps on the lunar surface in 1969 – 1972 by the Apollo's men. The best lunar sites for future human outpost on the Moon are thought to be at poles, because the polar location provides the best conditions for illumination (and solar power) together with the accessible resources of lunar volatiles (with the most useful one, water). We plan to perform the sequence of robotic lunar missions, which goal will be investigations and exploration of the lunar poles. The objectives of these missions shall address to the following tasks: a) to determine the best sites for location of the future space station with the most favorable conditions both for the science investigations and for the creation of the station infrastructure; b) to determine the local environment at lunar poles: dust, neutrals and plasma exosphere, radiation background at different phases of solar activity c) to study the composition of lunar polar regolith, in particular, the abundance of volatiles; to determine the main isotopic ratios of elements of lunar polar volatiles d) to perform the firsts technological experiments for lunar polar resources utilization (starting from extraction of oxygen, water and hydrogen); e) to create the first elements of the lunar base for energy provision and for radiation protection. The sequence of lunar robotic missions of the first stage includes Luna-Glob (2019), Luna-Resurs Orbiter (2020) and Luna-Resurs Lander (2021) and Luna-Grunt (2023-2024).

NASA'S PLANETARY SCIENCE MISSIONS PRESENT AND FUTURE PLANS

J.L. Green

¹NASA Planetary Science Division, 300 E St. SW, Washington, DC, USA

Contact: James.Green@nasa.gov

Planetary Science missions have revolutionized our understanding of the origin and evolution of the solar system. Planetary scientists are also enabling human space exploration by studying and characterizing planetary environments beyond Earth and identifying possible resources that will enable safe and effective human missions to destinations beyond low Earth orbit. Robotic explorers are gathering data to help us understand how the planets formed, what triggered different evolutionary paths among planets, what processes are active, and how the Earth formed, evolved, and became habitable. To search for evidence of life beyond Earth, we've used this data to map zones of habitability, studied the chemistry of unfamiliar worlds, and revealed the processes that lead to conditions necessary for life. In addition, we have significantly increased our ability to detect, track, catalog, and characterize near-Earth objects that may either pose hazards to Earth or provide destinations and resources for future exploration.

NASA's Planetary Science Division (PSD) and space agencies around the world are collaborating on an extensive array of missions exploring our solar system. NASA has always encouraged international participation on our missions both strategic (ie: Mars 2020) and competitive (ie: Discovery and New Frontiers) and other Space Agencies have reciprocated and invited NASA investigators to participate in their missions. Indeed, we are living in a golden age of discovery with a large number of operating missions ranging from orbiting Mercury to heading for Pluto and beyond.

I will present an overview of the current and possible future NASA planetary missions. The exploration of the Solar System is uniquely poised to bring planetary scientists, worldwide, together under the common theme of understanding the origin, evolution, and bodies of our solar neighborhood. In the past decade we have witnessed great examples of international partnerships that made various missions the success they are known for today. As Director of Planetary Science at NASA I will continue to seek cooperation with our strong international partners in support of planetary missions.

ELECTRON PRECIPITATION AT MARS: EFFECT OF CRUSTAL MAGNETIC FIELD

V.I. Shematovich¹, D.V. Bisikalo¹, J.-C. Gérard², B. Hubert²

¹*Institute of Astronomy RAS, 48 Pyatnitskaya str., Moscow 119017, Russian Federation*

²*Institute of Astrophysics and Geophysics of the University of Liège, Liège, Belgium*

Contact: shematov@inasan.ru

INTRODUCTION:

We have conducted simulations of the auroral precipitation at Mars using a Monte Carlo model (Shematovich et al., 2008), accounting for the crustal magnetic field and of a possible ambient constant field. The auroral emissions of the CO Cameron and CO₂⁺ FDB bands have also been computed. The analysis of the sensitivity of the calculations versus the control parameters of the model shows that the vertical dependence of the magnetic field and the energy of the precipitating electrons both influence the solution.

- 1) The ratio between the upward and downward energy fluxes computed at the top of the atmosphere is very sensitive to the presence of the magnetic field. Indeed, for the case without crustal magnetic field we have the flux ratio of 0.1, while inclusion of the crustal magnetic field drastically increases this ratio due to the effect of magnetic mirroring. For typical topology of the magnetic field the flux ratio at the top could be as large as 0.3, and even 0.6 for the case of moderate value of the crustal magnetic field.
- 2) The energy of the precipitating electrons is another important property of the auroral flux at the top of the model atmosphere. In the simulations without magnetic field the energy flux ratio is relatively low and drops from 29.8% to 10.8 % for initial energies increasing from 25 to 600 eV. The situation is quite different in the presence of a crustal magnetic field for which the computed upward energy fluxes are significantly higher than without B-field. They vary from 33% up to 44%.
- 3) The auroral column brightness computed assuming an isotropic precipitation is only weakly increased by the inclusion of the magnetic field, due to the competing effect of mirroring and field line concentration. In contrast, the auroral power is reduced by the presence of the magnetic field because a part of the precipitating energy is mirrored by CMF back to space.

Finally, this study shows that even a weak magnetic field could strongly change the effects of the high-energy electron precipitation in the planetary atmospheres such as energy deposition, ionization and excitation rates and etc. Therefore, even weak magnetic fields should be taken into account when the heating efficiency of the hydrogen- and water vapor atmospheres of the exoplanets are considered (Bisikalo and Shematovich, 2015).

ACKNOWLEDGMENTS:

This work is supported by the RFBR project No. 14-02-00838a and by the Basic Research Program of the Presidium of the Russian Academy of Sciences (Program 09).

REFERENCES

- Shematovich et al., J. Geophys. Res., 2008, 113, E02011.
Bisikalo and Shematovich, Astron. Rep., 2015, 59, 836.

ION FLUXES AND THEIR ROUTES AT MARS. MARS EXPRESS AND MAVEN OBSERVATIONS

**E. Dubinin¹, M. Fraenz¹, J. McFadden², D. Brain³, F. Eparvier³,
B.M. Jakosky³, S. Barabash⁴, O. Vaisberg⁵, L. Zelenyi⁵**

¹*Max-Planck-Institute for Solar System Research, Goettingen, Germany,*

²*Space Sciences Laboratory, U.C. Berkeley, Berkeley, CA, USA*

³*Laboratory for Atmospheric and Space Physics, Univ. of Colorado, Boulder, CO, USA*

⁴*Swedish Institute of Space Physics, Kiruna, Sweden*

⁵*Space Research Institute of Russian Academy of Sciences (IKI RAS)*

Profsoyuznaya Str, Moscow, Russia, 117997

Contact: dubinin@mps.mpg.de.

Recent observations by Mars Express and MAVEN spacecraft have shown that the Martian atmosphere/ionosphere is exposed to the impact of solar wind which results in losses of volatiles from Mars. This erosion is an important factor for the evolution of the Martian atmosphere and its water inventory. General features of the losses through different channels at Mars observed by Mars Express and MAVEN are discussed. There are several important plasma reservoirs with different mechanisms of plasma filling and ion energization. Among them is the boundary layer at the interface between the ionosphere and solar wind, trans-terminator flow in the ionosphere, plasma sheet, lobes, pickup ion plume. Dynamics of ions in these regions is different and strongly controlled by the solar wind, IMF and solar irradiance. To estimate the escape forced by the solar wind during the early Solar system conditions we need to know how the ionosphere of Mars and escape fluxes depend on variations in the strength of the external drivers, in particularly, of solar wind and solar EUV flux. We present multi-instrument observations of the influence of the solar irradiance on the Martian ionosphere and escape fluxes. We use data obtained by the ASPERA-3 and MARSIS experiments on Mars Express and by the STATIC instrument and EUV monitor on MAVEN. Observations by Mars Express supplemented by the EUV monitoring at Earth orbit and translated to Mars orbit provide us information about this dependence over more than 10 years whereas the measurements made by MAVEN provide us for the first time the opportunity to study these processes with simultaneous monitoring of the ionospheric variations, planetary ion fluxes and solar irradiance. It is shown that fluxes of planetary ions through the different channels respond differently on the EUV variations. The most significant effect on the ion scavenging with increase of the solar irradiance is observed for low energy ions extracted from the ionosphere while the fluxes in the pickup ion plume are almost insensitive to the EUV variations.

OXYGEN LOSS FROM MARS: EARLIER PHOBOS 2, RECENT MAVEN OBSERVATIONS, AND HOW TO MEASURE OXYGEN LOSS BY IN-SITU ION MEASUREMENTS

M.I. Verigin, G.A. Kotova

Space Research Institute of Russian Academy of Sciences (IKI RAS),
117997, 84/32 Profsoyuznaya str., Moscow, Russia

Contact: verigin@iki.rssi.ru

INTRODUCTION:

The process of oxygen non thermal loss from Mars is well known for many decades (see, e.g., [1, 2]). About 64% of O atoms, originating at exobase due to dissociative recombination of O_2^+ ions, have sufficient energy to escape planetary gravity and to produce hot oxygen corona. O atoms are finally ionized and the resulting O^+ ions are swept away by the solar wind. O^+ ions in the vicinity of Mars were revealed in 1989 by mass-spectrometric plasma measurements onboard PHOBOS 2 orbiter [3, 4]. Earlier MARS 5 ion measurements [5, 6] had no mass-spectrometric possibilities and could not pretend for detection of Martian heavy ions, however, these measurements were interpreted in that manner. Specific behavior of the measurements was explained by the presence of protons only [7] though the authors of the data disagreed [8] and are still in disagreement [9] with the explanation proposed.

In-situ PHOBOS 2 measurements as well as subsequent ion measurements by MEX orbiter (see, e.g., [10]) provide possibility to evaluate a part of the planetary oxygen lost in the close vicinity of the planet at heights less than several thousands of km from Mars. Similar restrictions are usual in a large number of papers modeling loss of ions of Martian origin. On the other hand, the specific scale of Martian hot oxygen corona is several millions of km, and it is at these distances most of the oxygen of planetary origin is ionized and picked up by the solar wind [11]. The mass loading of solar wind flow by O^+ ions results in solar wind deceleration up to ~ 100 km/s upstream of the planetary bow shock, thus providing possibility to evaluate upper limit of hot oxygen corona density [11, 12].

First direct observations of O atoms of Martian corona started just in 2014 onboard MAVEN orbiter by IUVS experiment [13]. In the present talk these initial observations will be compared with the results of PHOBOS 2 coronal density deductions. Possibility of direct in-situ measurements of Martian ion losses via oxygen corona will also be discussed.

DATA ANALYSIS:

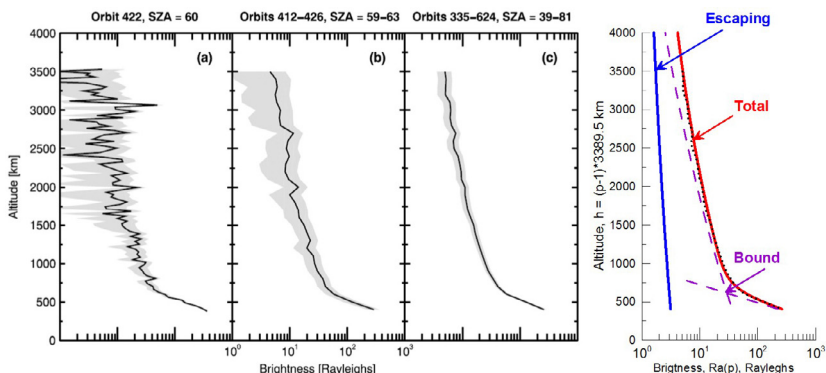


Fig. 1. a,b,c presents altitude brightness profiles of Martian coronal oxygen taken from [13], with 3σ uncertainties in gray. We scanned Figure 1c data, approximating the dayside global average profile (points in Figure 1d), and fitted it by the simple relation (1) that describes escaping (second term) and bounded parts (first and third terms) of total coronal oxygen brightness profile:

$$Ra(p) = a \cdot e^{(1.2-p)/h} + b/p + c/p^4, \quad (1)$$

where p is IUVS impact parameter in planetary radii, $a \approx 15.4$, $b \approx 3.5$, $c \approx 57$

and $h \approx 0.03$. Then using inverse Abel transform one may evaluate the oxygen corona number density n_o as a function of planetocentric radius r :

$$n_o(r) = -\frac{10^6}{\pi g} \cdot \int_r^\infty \frac{dRa(p)}{dp} \cdot \frac{dp}{\sqrt{p^2 - r^2}} \approx 163 \cdot \left(a \sqrt{\frac{\pi}{2rh}} e^{(1.2-p)/h} + \frac{b}{r^2} + \frac{3c\pi}{2r^5} \right), \quad (2)$$

with a factor $g \approx 5.76 \times 10^{-6} \text{ s}^{-1}$ appropriate for the oxygen line 1304 Å at time when the data were collected [13]. Planetocentric distance r and scaleheight h are in planetary radii in the above relations.

Oxygen number density as deduced from relation (2) is plotted by heavy blue line in Figure 2a. This density is compared with upper limit of the weighted oxygen and hydrogen number densities, evaluated in [12] using solar wind pre shock deceleration (heavy red line):

$$n_o(r) + n_H(r) \frac{m_H \tau_O}{m_O \tau_H} \approx \frac{2700}{r^2} \cdot \left(1 + \frac{15.4}{r^3} \right), \quad (3)$$

where m_H , m_O and τ_H , τ_O are hydrogen and oxygen masses and ionization timescales, respectively. Dashed red line in Figure 3a is ~ 0.7 of relation (3) that represents $n_o(r)$ addendum only [12]. It is easy to observe good correspondence of MAVEN IUVS results with previous deductions from TAUS experiment aboard PHOBOS 2 Martian orbiter. The correspondence is even better if one take into account higher solar activity (twice sunspot number) during PHOBOS 2 observations as compared with MAVEN observational period (Figure 3b).

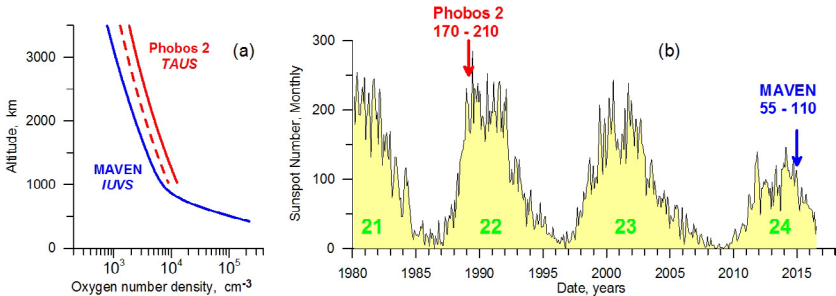


Fig. 2. O density profiles from IUVS and TAUS observations (a) and solar activity variations in 21-24 Solar cycles (b).

DISCUSSION AND POSSIBILITY OF MARTIAN OXYGEN LOSS RATE MEASUREMENTS BY IN-SITU ION INSTRUMENT:

In order to deduce oxygen loss rate from both approaches we should reliably determine radial distribution of escaping part of corona up to several millions of km. Present UV instruments doubtfully can measure oxygen density profile above several thousands of km both from its sensitivity and orbital limitations. At 4000 km height escaping O constitutes minor part of oxygen corona (see Fig. 1d). On the other hand, by specially designed ion spectrometer we can measure picked-up O⁺ ions very far from Mars. At such distances, originating from corona picked up ions have complicated, anisotropic, ring/bi-shell velocity distributions. The instrument for measurements of these ions must have energy range above 60 keV, must have sharp energy and fine angular resolutions and must have

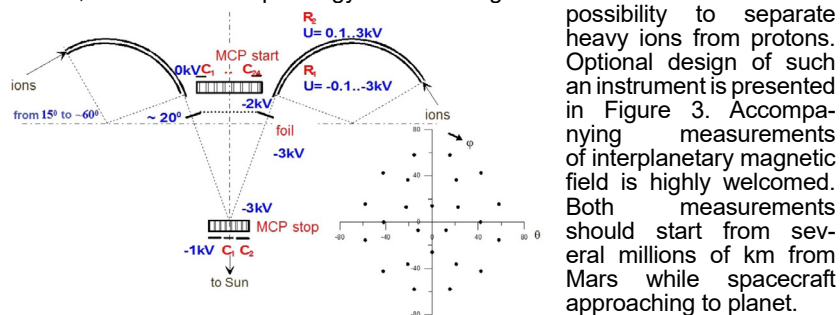


Fig. 3. Optional design of ion spectrometer for measuring oxygen loss by Mars.

possibility to separate heavy ions from protons. Optional design of such an instrument is presented in Figure 3. Accompanying measurements of interplanetary magnetic field is highly welcomed. Both measurements should start from several millions of km from Mars while spacecraft approaching to planet.

ACKNOWLEDGMENTS:

The paper is partially supported by the program P7 of RAS.

REFERENCES:

1. McElroy, M.B., Mars: An evolving atmosphere, *Science*, 175, 433, 1972.
2. Krasnopolsky V.A, *Photochemistry of the atmospheres of Mars and Venus*, Springer-Verlag, Berlin, 1986.
3. Rosenbauer, H., et al., *Nature*, 341, 612, 1989.
4. Lundin, R., et al., *Nature*, 341, 609, 1989.
5. Vaisberg, O.L., in: *Physics of Solar Planetary Environments*, 2, AGU publ., Boulder, Colorado, 854, 1976.
6. Vaisberg, O., and Smirnov V., *Adv. Space Res.*, 6, #1, 301, 1986.
7. Bezrukikh, V.V., Verigin, M.I., Shutte, N.M., *Kosmich. Issled.* 6, 583, 1978.
8. Vaisberg, O.L., and Smirnov, V.N., *Kosmich. Issled.* 16, 588, 1978.
9. Vaisberg O.L., *Planet. & Space Sci.*, 119, 69, 2015.
10. Dubinin, E., et al., *Space Sci. Rev.*, 126, 209, 2006.
11. Verigin, M.I., et al., *J. Geophys. Res.*, 96, #A11, 19315, 1991.
12. Kotova, G.A., et. al., *J. Geophys. Res.*, 102, #A2, 2165, 1997.
13. Deighan, J., et al., *Geophys. Res. Lett.*, 42, doi:10.1002/2015GL065487, 2015.

IRTF/CSHELL OBSERVATIONS OF THE CO DAYGLOW AT 4.7 μm , CO MIXING RATIO, AND HDO/H₂O ON MARS

V.A. Krasnopolsky

Catholic University of America, Department of Physics, 620 Michigan Avenue, N.E., Washington, DC 20064, USA
Contact: vlad.a.krasn@gmail.com

Here we will briefly discuss three sets of recent IRTF/CSHELL observations, whose results appeared superior to the similar spacecraft data.

The CO (2-1) and (1-0) dayglow at 4.7 μm was observed on Mars at the peak of northern summer ($L_s = 110^\circ$). There are six (2-1) and two (1-0) emission lines in the observed spectra. They are contaminated by the solar CO lines and some martian and telluric lines. Fitting by synthetic spectra results in intensities of the dayglow lines and reflectivities of Mars at 4.7 μm . The CO (1-0) dayglow is excited by absorption of sunlight at 4.7 μm ; the emission is optically thick with a non-LTE line distribution and peaks near 87 km. Mean intensity of the CO (1-0) dayglow is 1.7 MR with a weak limb darkening to 1.3 MR. This dayglow is poorly accessible for diagnostics of the martian atmosphere. The CO (2-1) dayglow is excited mostly by absorption of the sunlight by the CO (2-0) band at 2.35 μm . The dayglow is quenched by CO₂ and peaks at 50 km. Intensities of the observed six (2-1) lines result in rotational temperatures that should be equal to ambient temperatures at 50 km. These temperatures are retrieved from 50°S to 90°N and vary in the range of 140-170 K with a mean value of 153 K. The observed intensities of the CO (2-1) dayglow are corrected for airmass and the surface reflection and give vertical intensities that are equal to 2.1 MR at 20°N to 50°N decreasing to 1.5 MR at 90°N and 1 MR at 45°S. The dayglow intensities depend on CO mixing ratio at 50 km and solar zenith angle. Retrieved CO mixing ratios at 50 km gradually increase from 1100 ppm at 40°S to 1600 ppm at 70°N. This behavior is very different from that observed in the lowest scale height at the same season. This is the first observation of CO in the middle atmosphere of Mars. The CO (2-1) dayglow is a tool for remote sensing of temperature and CO at 50 km on Mars.

Our observations of variations of CO on Mars by means of the ground-based spatially-resolved high-resolution spectroscopy have been significantly improved using the ¹³CO lines near 4148 cm⁻¹ and the CO₂ lines near 4570 cm⁻¹. These lines are of optimal strength, of low sensitivity to variations of temperature, and covered by the ATMOS solar spectrum that makes it possible to use the synthetic spectra technique for retrieval of CO and CO₂ to get CO mixing ratios. The CO₂ line strengths from Toth et al. (2008) were also essential to improve accuracy of the results.

The ¹³CO/CO ratio of 1.023 times the terrestrial carbon isotope ratio was calculated using the known ¹³CO₂/CO₂ = 1.046 in the martian atmosphere, the photo-induced isotope fractionation in the CO₂ photolysis, and isotope fractionation in the reaction between CO and OH.

The observations were conducted at $L_s = 60, 89, 110,$ and 145° and covered the maximum of CO in the southern hemisphere during the northern summer. The CO mixing ratio was observed to be constant within 7% over latitudes

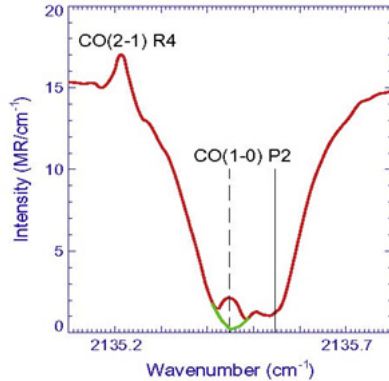


Fig. 1. The observed CO (1-0) P2 line includes the telluric line and Doppler-shifted Martian absorption and emission lines. The CO (2-1) R4 line is on the wing of this line.

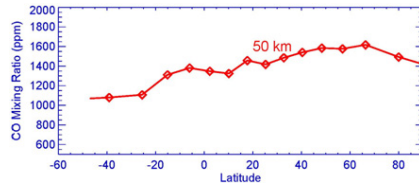


Fig. 2. Latitudinal variations of CO mixing ratio at 50 km at $L_s = 110^\circ$.

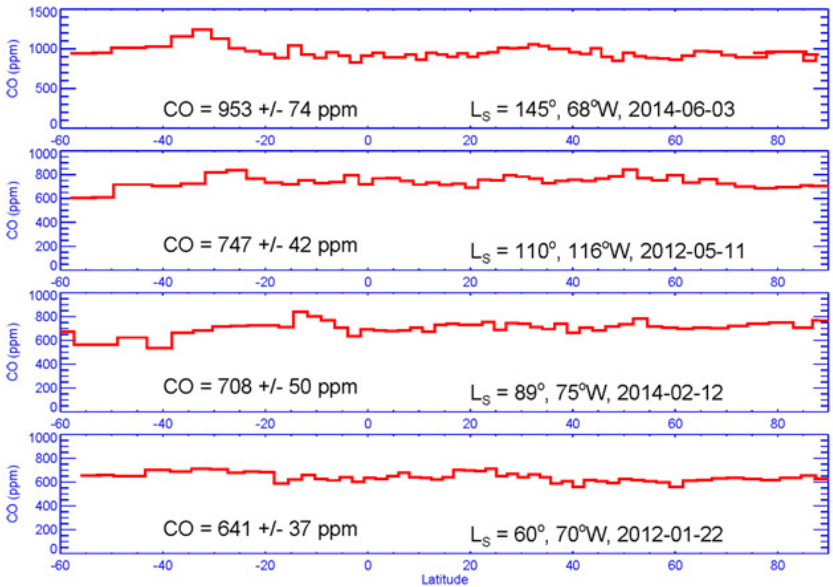


Fig. 3. Latitudinal variations of CO mixing ratio at four seasons.

from 55°S to 90°N, for each observed L_s period. Therefore our observations show that the enrichment of incondensable gases by condensation of CO_2 in the southern polar regions does not significantly extend to the middle and low latitudes. This behavior agrees with the Mars Climate Database (Lefevre and Forget 2009), whereas most other observations exhibit much larger latitudinal gradients and seasonal variations. Our measurements do not show the CO depletion at high northern latitudes predicted by MCD of $\sim 20\%$ at $L_s \approx 60\text{--}150^\circ$ and observed as much stronger by MRO/CRISM (Toigo et al. 2013). The retrieved global and annually mean CO abundance is equal to 700 ppm on Mars, which is also smaller than many recent results by a factor of ~ 1.4 .

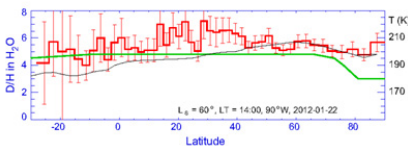


Fig. 4. Observed variation of D/H in H_2O are compared with the model predictions (green line) and temperature at half pressure level (black curve).

and 2994 cm^{-1} , respectively, cover six martian seasons in the period from 2007 to 2014. Infrared properties of water ice and dust are rather similar at these wavenumbers, and the HDO and H_2O line equivalent widths are comparable; therefore effects of aerosol absorption and scattering significantly cancel out in the HDO/ H_2O ratios. These ratios are rather constant in wide latitude ranges at four observing sessions, in accord with the GCM model by Montmessin et al. (2005). Results of two other sessions demonstrate significant deviations from the model predictions and strong correlation between HDO/ H_2O and temperature at $\sim 7\text{ km}$ above the surface with correlation coefficients of 0.9. The observed global-mean HDO/ H_2O ratio is 4.6 ± 0.7 times the terrestrial ratio, the ratio in vapor released by the north polar cap is 6.2 ± 1.4 , and the ratio in the north polar cap ice is 7.1 ± 1.6 . Updating the model of isotope fractionation in hydrogen escape by Krasnopolsky and Feldman (2001), 60 m of the global water layer was lost in the last 4 Byr and more than 1200 m could be lost by hydrodynamic escape of H_2 released in the reaction between water and iron. Variations of telluric D/H above Mauna Kea (Hawaii, elevation 4.2 km) are by-products of our observations; D/H varies from 0.4 to 0.9 in nine observations with a mean D/H = 0.67.

Ground-based spatially-resolved high-resolution spectroscopy is currently the only means to observe variations of the HDO/ H_2O ratio in the martian atmosphere. These observations are difficult because telluric water exceeds the martian water by two orders of magnitude even at the excellent conditions of NASA IRTF. Our observations of HDO and H_2O at the close wavenumbers of 2722

OBSERVATIONS OF WATER VAPOR IN THE MARTIAN MIDDLE ATMOSPHERE ON MARS-EXPRESS

A. Fedorova¹, J.-L. Bertaux², F. Montmessin², D. Betsis¹, O. Korablev^{1,4}

¹*Space Research Institute of Russian Academy of Sciences (IKI RAS),
117997, 84/32 Profsoyuznaya str., Moscow, Russia*

²*LATMOS-UVSQ, 11 Bd d'Alembert, F-78280 Guyancourt, France*

³*AIM/Cea-Saclay, France*

⁴*Center for Space Physics, Boston University, Boston, USA*

Contact: fedorova@iki.rssi.ru

We present long-term observations of water vapor in the middle atmosphere of Mars performed by SPICAM on Mars-Express. Since 2004 the SPICAM IR spectrometer carries out measurements of the vertical distribution of water vapor in the 1.38 μm band and aerosol properties by means of solar occultations. The seasonal, spatial and interannual variations will be presented. The data will be considered in connection with dissipation rate of hydrogen corona on Mars.

ACKNOWLEDGEMENTS:

A.Fedorova and D.Betsis acknowledges support of the RFBR grant 15-02-07812

MARS CLIMATE HISTORY: A GEOLOGICAL PERSPECTIVE

James W. Head

*Brown University, Department of Earth, Environmental and Planetary
Sciences, Providence RI 02912 USA
Contact: james_head@brown.edu*

INTRODUCTION AND APPROACH:

Deciphering climate history has been one of the major goals of the scientific exploration of Mars because of the significance of climate as a proxy for understanding: 1) planetary volatile accretion, 2) outgassing history, 3) the distribution and stability of water and the nature and evolution of the water cycle, 4) the surface weathering environment, 5) the presence, stability, and abundance of liquid water, 6) the implications for environments conducive to the origin and evolution of life [1], and 7) the influence of climate on the cratering process. Recent intensive exploration has contributed significantly to the understanding of current Mars weather, and lengthening observational baselines are beginning to reveal the basic elements of climate. This baseline knowledge is essential to the proper understanding of the longer-term history of climate. Assessing longer-term climate change and its history can be approached from a process-response standpoint through the identification of cause and effect [2] (Fig. 1). Among the most important causes of climate change (input parameters) are external forcing functions linked to spin-axis and orbital variations, elements whose nature and history have recently become much more well-understood in both the time and frequency domain [3]. The influence of these external forcing functions on the climate system (the internal response mechanism) are becoming more well known through increasingly more sophisticated atmospheric general circulation models [4-7], including the behavior of water. Finally, the consequences of the causes (the external forcing functions, spin-axis/orbital parameters, operating on the internal response mechanism, the climate system) produces an effect in the time and frequency domain (the geological record); increasing availability of global data is providing a more comprehensive view of over four billion years of geological history [8]. Specifically, increased knowledge of the structure of current polar deposits [9], the location of geological deposits that chronicle the distribution and history of non-polar ice [10], and the context in which to interpret ice deposits in extremely cold hyper-arid Mars-like conditions [11], have all contributed to an increased understanding of the climate history of Mars.

AMAZONIAN:

(present to ~3 Ga; [20-22]) A robust prediction of the spin-axis/orbital parameter-based insolation input to the climate system has been developed for the last 20 Ma [3] and these predictions have been used to begin to decipher the history of the polar cap [12-14], the nature of recent ice ages [15], the timing of active layers at high latitudes [16], and the conditions under which liquid water might form gullies during this time [17]. Prior to the last 20 Ma, deterministic predictions are not currently possible because solutions based on the input parameters become chaotic; nevertheless exploring this parameter space, Laskar et al. produced 15 scenarios showing candidate obliquity histories over the last 250 Ma (Fig. 2), and predicted that mean obliquity would be ~38° [3]. Analysis of these 15 examples shows the huge range of options for Late Amazonian climate history. In contrast to the last 20 Ma, where input parameters to the climate system are well-known, there is no robust prediction for a specific input parameter history to use as a test in interpreting the geological record. Therefore, we have adopted a different approach and use the geological record of non-polar ice deposits [10] (the output of the external forcing function and climate system) and a general knowledge of the behavior of the GCM and climate system under different obliquity baselines, to evaluate the 15 candidate scenarios of the obliquity component of the external forcing function.

EARLIER AMAZONIAN:

Using a general knowledge of the behavior of the GCM under different obliquity conditions, we chose four mean baselines to form a framework for evaluating the 15 candidate obliquity scenarios for the last 250 Ma (Fig. 2) [18]. We applied the geological observations, in terms of interpreted latitude and time

[10], to assess the candidate obliquity scenarios and found that the obliquity scenario that was most consistent with age and obliquity constraints (Fig. 2-8) is characterized by 45° obliquity at the times of both the early and late TMGs, and obliquity at or close to 35° during mid-latitude glaciations. Examination of the geological record of non-polar ice deposits, together with related information strongly suggests that the climate of Mars throughout the Amazonian was much like at is today, but with migration of surface ice in response to variations in spin-axis/orbital parameters, primarily obliquity. A corollary is that the hydrological cycle was horizontally stratified during the Amazonian [19].

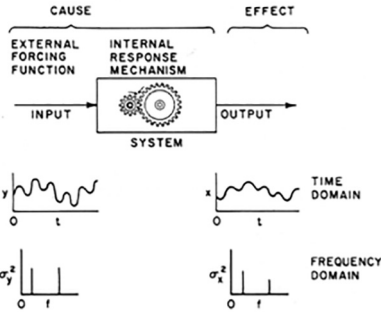


Fig. 1. Process-response framework for analysis of the climate system on Mars [2].

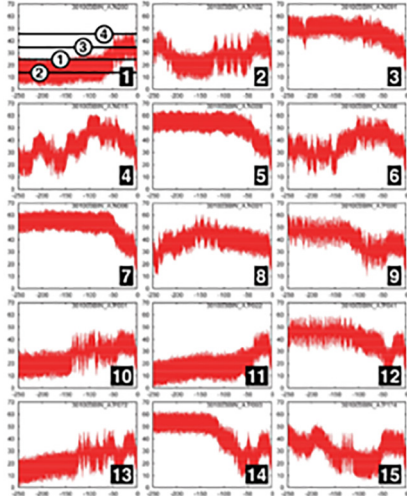


Fig. 2. Examples of possible evolution of Mars' obliquity over the past 250 Myr [3]. Numbered lines in 1 indicate four obliquity scenarios.

THE HESPERIAN PERIOD:

(~3-3.6 Ga; [20-22]): The martian outflow channels debouched into the northern lowlands primarily in the Late Hesperian Period [1] and their characteristics suggest to many workers that a large standing body of water, or ocean, was produced as a result. Characteristics of northern lowland deposits in the Early Amazonian Period suggest that by this time that if such an ocean existed it was gone. The evolution of water loaded with sediments emplaced by outflow channel formation has been modeled [23]; results suggest that it would freeze and sublime on very short time scales. The Late Hesperian Vastitas Borealis Formation may be the sublimation residue of the ocean [23]. In the Early Hesperian Period, a significant flux of volcanism occurred in the form of the Hesperian ridged plains, and this may well have represented a major pulse of volatiles into the atmosphere [24-25]. In addition, there is clear evidence of interaction of these volcanic deposits and large volatile-rich deposits in the south polar region [26], causing melting and drainage of liquid water.

Over the last 80% of the history of Mars, permafrost and the cryosphere dominate the surface. Although there is compelling evidence that liquid water formed occasionally on the surface and moved locally, there is no compelling evidence that indicates that the global cryosphere was absent at any time throughout the most recent 80% of the history of Mars. Mars surface conditions appear to have been cold and dry throughout most of its history, very similar to the way they are now. Further evidence of this is the limited amount of aqueous chemical alteration detected from orbit [27] and in martian meteorites [28]. Obliquity extremes, and intrusive volcanic activity related to the two major rises, Tharsis and Elysium, appear to have redistributed some water but liquid water was transient on the surface for the vast majority of Mars' history.

THE NOACHIAN PERIOD:

(>3.6 Ga; [20-22]): Geological evidence has been cited to support a 'warm, wet' era [29] in the late Noachian Period (e.g., valley networks, degradation rates, etc.). Critical assessment of this evidence and new data lead to several scenarios for the emplacement style, location and fate of water on early Mars

during the first 20% of its history, and the important transition to conditions similar to those of today. This traditional view has recently been challenged by several developments [19]: 1) The growing evidence that mineralogic indicators for early phyllosilicates (interpreted to support warm and wet surface conditions [30]) could also be explained by subsurface hydrothermal effects in an early period of high thermal flux [31]; 2) The difficulty of producing and maintaining an atmosphere that could lead to a warm and wet early Mars with pluvial activity [32]; 3) Evidence that south circumpolar ice deposits are consistent with cold lower latitude surface temperatures [33]; 4) The poor integration of the surface hydrologic system (valley networks, open-basin lakes [34-35], suggesting short term activity, rather than long term integrated pluvial systems; 5) Emerging evidence in the Antarctic Dry Valleys that Mars-like fluvial and lacustrine activity can occur under surface climate conditions with mean annual temperatures (MAT) well below 0°C [11]; 6) The possibility that surface drainage features could be explained by top-down transient atmospheric effects caused by punctuated volcanism during the late Noachian-early Hesperian (LN-EH) [36]. Three alternate scenarios for a “non-warm and wet” early Mars appear to be consistent with the six new developments outlined above [19]. Could Mars have been cold and dry or cold and wet, instead of the pluvial warm and wet early Mars envisioned by many [e.g., 29]? Our current data and analyses suggest that Mars was more likely to have been characterized by a “cold and icy” early history and a horizontally stratified hydrologic system throughout most of its history. In this scenario, the Hesperian represents a *perturbation* on the historically horizontally integrated hydrological system, rather than a *transition* from vertical integration to horizontal stratification. We continue to test these scenarios.

REFERENCES:

- 1) M. Carr, *Water on Mars*, 1996; 2) J. Imbrie, *Icarus* 50, 408, 1982; 3) J. Laskar et al, *Icarus* 170, 343, 2004; 4) F. Forget et al., *JGR* 104, 24155, 1999; 5) M. Richardson and J. Wilson, *JGR* 107, 5031, 2002; 6) M. Mischna et al., *JGR* 108, 5062, 2003; 7) R. Haberle et al., *JGR* 106, 23317, 2003; 8) M. Carr, *The Surface of Mars*, Cambridge, 2006; 9) R. Phillips et al., *Science* 320, 1182, 2008; 10) J. Head and D. Marchant, *LPSC* 39 1295, 2008 and this volume; 11) D. Marchant and J. Head, *Icarus* 192, 187, 2007; 12) J. Laskar et al, *Nature* 419, 375, 2004; 13) S. Milkovich and J. Head, *JGR* 110, 2349, 2004; 14) B. Levrard et al, *JGR* 112, E06012, 2007; 15) J. Head et al., *Nature* 426, 797, 2003; 16) M. Kreslavsky et al., *MAPS* 41, 1659, 2006; 17) F. Costard et al. *Science* 295, 110, 2002; 18) J. Head et al. *LPSC* 40, 1349, 2009; 19) J. Head, *LPSC* 43, 2137, 2012; 20) W. Hartmann and G. Neukum, *SSR*, 96, 165, 2001; 21) G. Neukum et al., *SSR*, 96, 55, 2001; 22) B. Ivanov, *SSR*, 96, 87, 2001; 23) M. Kreslavsky and J. Head, *JGR*, 107, 1831, 2002. 24) T. Watters, *JGR*, 96, 15599, 1991. 25) J. Head, et al., *JGR*, 107, 1445, 2002; 26) G. Ghatan and J. Head, *JGR*, 107, 1519, 2002. [27] P Christensen et al., *JGR*, 106, 23823, 2001. [28] J. Bridges et al., *SSR*, 96, 365, 2001; 29) R. Craddock and A. Howard (2002) *JGR* 107, 5111;30) J.-P. Bibring et al. (2006) *Science* 312 400; 31) B. Ehlmann et al. (2011) *Nature* 479, 53; 32) R. Wordsworth et al. (2013) *Icarus*, 222, 1-19; 33) J. Fastook et al. (2012) *Icarus*, 219, 25-40; 34) C. Fassett and J. Head (2008) *Icarus* 195, 61; 35) C. Fassett and J. Head (2008) *Icarus* 198, 37; 36) I. Halevy and J. Head, (2014) *Nature Geoscience*, 1-4.

GLOBAL AND LOCAL TRENDS IN OBSERVATION OF SUBSURFACE WATER IN GALE CRATER FROM DAN/MSL DATA

M.L. Litvak, I.G. Mitrofanov, D. Lisov¹, A.B. Sanin

Space Research Institute of Russian Academy of Sciences (IKI RAS)

Profsoyuznaya Str, Moscow, Russia, 117997

Contact: mlitvak.iki@gmail.com

Four years ago in August, 2012, NASA's Curiosity rover landed in the northern part of the Gale Crater. It is equipped with multiple instruments for imaging, sampling, and measuring including Russian active neutron spectrometer DAN developed to monitor subsurface water distribution along Curiosity traverse.

Curiosity is collecting data as it moves across the plain towards Aeolis Mons, a mountain at the center of Gale Crater. In our study we report about global observed trends in subsurface water variations measured by DAN along 14 km rover's path. This water is likely held in pores or in clay minerals formed at the previous aqueous history of Mars. We also paid special attention to the results of water estimation during of special campaigns conducted at local unique areas such as high silica spots in the lacustrine Murray formation and Martian active dunes.

DOSIMETRY INVESTIGATIONS ONBOARD EXOMARS MISSIONS. RESULTS FROM RADIATION MEASUREMENTS DURING EXOMARS 2016 TGO CRUISE TO MARS

J. Semkova¹, T. Dachev¹, St. Maltchev¹, B. Tomov¹, Yu. Matviichuk¹, P. Dimitrov¹, R. Koleva¹, K. Kanev¹, I. Mitrofanov², A. Malakhov², M. Mokrousov², A. Sanin², M. Litvak², A. Kozyrev², V. Tretyakov², D. Golovin², S. Nikiforov², A. Vostrukhin², F. Fedosov², N. Grebennikova², V. Benghin³, V. Shurshakov³

¹*Space Research and Technology Institute, Bulgarian Academy of Sciences, Sofia, Bulgaria*

²*Space Research Institute of Russian Academy of Sciences (IKI RAS) Profsoyuznaya Str, Moscow, Russia, 117997*

³*State Scientific Center of Russian Federation, Institute of Biomedical Problems, Russian Academy of Sciences, Moscow, Russia*
Contact: jsemkova@stil.bas.bg

Radiation risk on long-duration deep space manned missions appears to be one of the basic factors in planning and designing the mission.

The paper relates to the scientific objectives and instrumentation for investigation of the radiation environment to be carried out during the ExoMars 2016 and 2018 missions to Mars.

Presented are the scientific objectives and instrumentation for investigation of the radiation environment onboard the ExoMars 2016 and 2020 missions to Mars. Described are: 1) The charged particle telescope and the experiment Liulin-MO for dosimetric measurements onboard the ExoMars 2016 Trace Gas Orbiter (TGO) satellite as a part of the Fine Resolution Epithermal Neutron Detector and 2) Liulin-ML experiment and instrument for dosimetric measurements on Mars surface as a part of the active detector of neutrons and gamma rays on the Surface Platform for ExoMars 2020 mission.

The preliminary results from the dosimetric measurements during the TGO cruise to Mars are discussed.

MARTIAN COMPUTING CLOUDS: A TWO USE CASE STUDY

**J.L. Vázquez-Poletti¹, I.M. Llorente¹, M.P. Velasco², A. Vicente-Retortillo³,
C. Aguirre⁴, R. Caro-Carretero⁵, F. Valero³, L. Vázquez¹,**

¹*Universidad Complutense de Madrid, Facultad de Informática, Calle Profesor José García Santesmases 9, 28040 Madrid, Spain*

²*Universidad Politécnica de Madrid, Escuela Técnica Superior de Ingeniería y Sistemas de Telecomunicación, Ctra. de Valencia Km. 7, 28031 Madrid, Spain*

³*Universidad Complutense de Madrid, Facultad de Ciencias Físicas, Avda. Complutense s/n, 28040 Madrid, Spain*

⁴*Universidad Autónoma de Madrid, Escuela Politécnica Superior, Calle Francisco Tomás y Valiente 11, 28260 Madrid, Spain*

⁵*Universidad Pontificia Comillas de Madrid, Escuela Técnica Superior de Ingeniería - ICAI, Calle Alberto Aguilera 25, 28015 Madrid, Spain*

Contact: jlvezquez@fdi.ucm.es, llorente@dacya.ucm.es,
velascom@unizar.es, alvarodv@ucm.es, carlos.aguirre@uam.es,
rcaro@comillas.edu, valero@ucm.es, lvazquez@fdi.ucm.es.

The study of the Martian atmosphere has generated a great amount of computing efforts by means of simulations and data analysis. However, as applications and data processed grow in size and complexity, more computing power is needed.

Cloud computing is seamless paradigm that allows a dynamic, elastic and on-demand provision of computing resources such as CPU and storage. Moreover, public cloud infrastructures (following a “pay as you go” basis) represent in many situations a valid alternative to in-house solutions such as supercomputers, which increase the budget considerably and not always act as dedicated resource.

However, cloud offerings add complexity to the equation, as one has to decide the optimal setup (number and type of resources) be means of performance and cost.

In the present work we are introducing two use cases of work in progress related to the studies of the Martian atmosphere. The first one is the modeling of atmospheric dust dynamics using fractional differential equations. The second one is the study of the solar radiation propagation by using radioactive transfer codes with different levels of complexity.

MARS HUMAN SCIENCE EXPLORATION AND RESOURCE UTILIZATION: THE DICHOTOMY BOUNDARY DEUTERONILUS MENSÆ EXPLORATION ZONE

J.W. Head¹, J. Dickson¹⁰, J. Mustard¹, R. Milliken¹, D. Scott¹, B. Johnson¹,
D. Marchant², J. Levy³, K. Kinch⁴, C. Hvidberg⁴, Francois Forget⁵,
D. Boucher⁶, J. Mikucki⁷, J. Fastook⁸, K. Klaus⁹, A. Weir¹¹.

¹Brown University, Providence, RI USA

²Boston University, Boston, MA USA

³University of Texas Institute for Geophysics, Austin, TX USA

⁴Nils Bohr Institute, University of Copenhagen, Copenhagen, Denmark

⁵Laboratoire de Météorologie Dynamique, Université Pierre et Marie Curie, Paris, France

⁶Deltion Innovations, Capreol, Ontario CA

⁷Middlebury College, Middlebury, VT USA

⁸University of Maine, Orono, ME USA

⁹LPI, Houston, TX USA

¹⁰Caltech, Pasadena CA USA

¹¹San Francisco, CA USA

Contact: James_head@brown.edu

The Dichotomy Boundary Deuteronilus Mensae (DBDM) Exploration Zone (EZ) (39.11° N, 23.199° E) combines: 1) Fundamental MEPAG scientific objectives for the exploration of Mars (geology, atmosphere/climate history, hydrology, astrobiology)(1-6; 8-18); 2) Samples/questions from each of the three major geologic eras (Noachian, Hesperian, Amazonian); 3) The certainty of ISRU (1), including access to abundant stores of water ice mapped by SHARAD (16); and 4) Civil Engineering (CE) opportunities, including manipulating material/ice and reducing reliance on Earth supplies. We combine these four themes into the term *Science/ICE*. We illustrate the *Science/ICE* theme in the selection of our current top priority EZ along the DB (Figure 1), among numerous candidate DB EZ sites we have investigated (Figure 2).

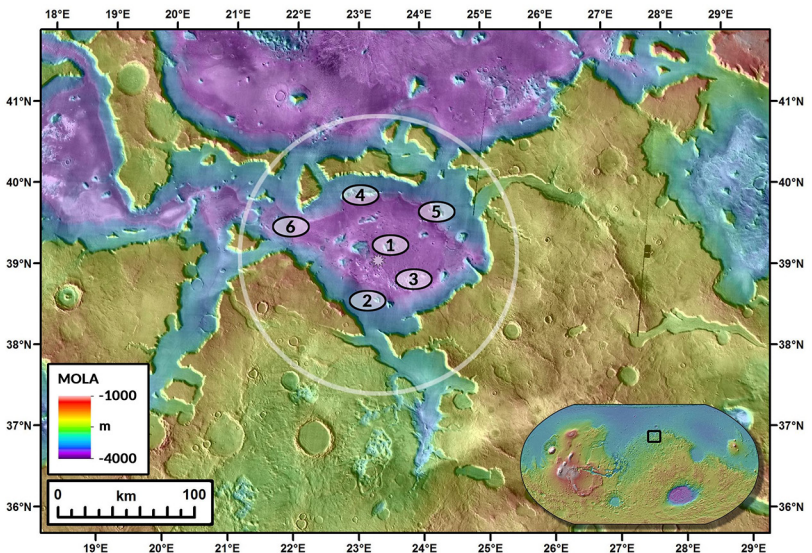


Fig. 1. The Dichotomy Boundary Deuteronilus Mensae (DBDM) Exploration Zone (EZ) outlined as a circle of 100 km radius, with the Landing Site/Surface Field Station (denoted by star) centrally located and slightly separated to assure safe descent and ascent. Science and Resource ROIs (always combined) are indicated by numbers and described in the text. For geological units within EZ, see (18); floor is HNps (smooth plains); LDA is Ada (debris aprons); Flat plateaus are Nplsu (upper smooth plateau material). Basemap is a THEMIS daytime IR mosaic overlain on MOLA gridded topography.

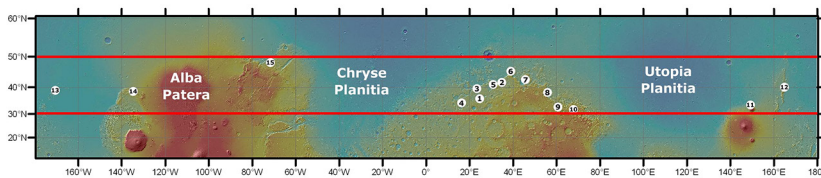


Fig. 2. Location of additional EZs with similar objectives that have been investigated. See references for guide.

EZ RATIONALE:

Science goals/ROIs are based on abundant study and analysis by our group (see selected references), span the entire geologic history of Mars, and include: 1) *Amazonian* climate record and nature of glacial processes in Latitude-Dependent Mantle (LDM) deposits on the crater floor, and ice in Lobate Debris Aprons (LDA) and Lineated Valley Fill (LVF); 2) *Hesperian/Noachian* Ridged Plains (Nhr), composition and mode of emplacement (basaltic talus in LDA), and possibility of a northern lowlands ocean. 3) *Noachian* crustal composition, diversity, history of alteration (hydrothermal, groundwater, surface, subsurface; relation to global remote sensing signatures), climate history (comparison of A/H/N suite of rocks), and origin of the dichotomy boundary (shocked rocks from Borealis basin?) in surface materials and LDA talus.

All of our Science ROIs (Figure 1) are in the same areas as our I/CE ROIs as the LDAs and surrounding terrains provide access to water and CE tasks for surface manipulation, resource access and infrastructure emplacement and protection. This DBDM/EZ *Science/ICE* concept is very robust as it has abundant backup EZs (Figure 2) for exploring trade space and optimizing science and engineering synergism.

ISRU ACTIVITIES:

These activities should focus on life support and mission support. Water ice is the most important commodity, and the most important factors are: *grade* (how clean or chemically contaminated is the product) and *concentration* (how much ice per kg of debris “waste”), followed very closely by *site logistics and extraction feasibility*. Atmospheric modeling suggests ice cement at shallow depths, and layered deposits similar to the LDM are prominent on the floor and may provide relatively pure ice or ice lenses. The key locations for water ice resources, however, are the LDA, shown by SHARAD results to be *high-grade, high concentration* (nearly pure) water ice, lying below less than 10-15 meters of sublimation till, itself a major resource for construction and shelter, as well as of fundamental scientific interest.



Fig. 3. LDA at ROI 4

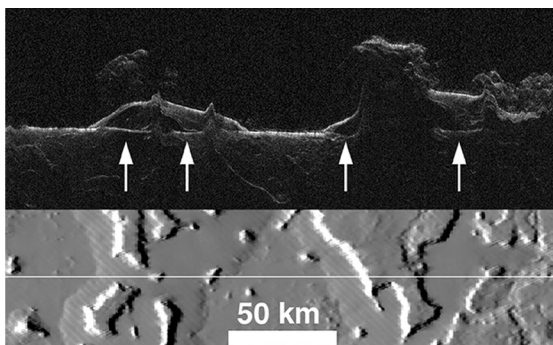


Fig. 4. SHARAD profile N-S across central DBDM EZ (16).

Science-Resource ROI 1: Located nearby the landing site, this ROI is represented by the Noachian-aged crater central peak, uplifting and exposing deeper crustal material, and by LDM fragments that expose the climate record and are a potential water resource. **Science-Resource ROI 2:** Base of the LDA with water ice resources at shallow depths and a rock material suite that will include samples brought from the broader region to the south. **Science-Resource ROI 3:** Extensive flat-lying LDM several tens of meters thick, containing an Amazonian climate record and nearly pure ice intercalated with ice-cemented debris. **Science-Resource ROI 4:** Distinctive LDA protruding through ridge represent-

ing potential peak ring of Noachian-aged crater (Figure 3). Access to water ice in near subsurface and suite of samples from terrain to the north. **Science-Resource ROI 5:** Ridge representing potential peak ring of Noachian-aged crater; LDA banked behind with LDA lobes on both sides of the outcrop of ancient crustal material. **Science-Resource ROI 6:** Outlet from Noachian-aged crater floor to west provides access to additional LDA and wrinkle-ridge-like structure that may mark the location of ancient lavas.

We utilize our Apollo experience in site selection and mission operations and engage our Immersive Virtual Reality (IVR) capability (7) in visualizing mission concepts and architectures, Landing Site selection, Surface Field Station placement, traverse planning, and resource extraction planning. We also engage IVR in EDL, surface operations and public impact and outreach assessments. Detailed exploration concepts are being developed for each ROI.

REFERENCES:

- 1) D. Baker et al. (2010) Flow patterns of lobate debris aprons and lineated valley fill north of Ismeniae Fosse, Mars: Evidence for extensive mid-latitude glaciation in the Late Amazonian, *Icarus*, 207, 186-209, doi: 10.1016/j.icarus.2009.11.017. 2) J. Dickson and J. Head (2008) Late Amazonian glaciation at the dichotomy boundary on Mars: Evidence for glacial thickness maxima and multiple glacial phases, *Geology*, 36, 411-414, doi: 10.1130/G24382A.1. 3) J. Dickson et al. (2012) Patterns of accumulation and flow of ice in the mid-latitudes of Mars during the Amazonian, *Icarus*, 219, 723-732, doi: 10.1016/j.icarus.2012.03.010. 4) J. Fastook and J. Head (2014) Amazonian mid- to high-latitude glaciation on Mars: Supply-limited ice sources, ice accumulation patterns, and concentric crater fill glacial flow and ice sequestration, *Planet. Space Sci.*, 91, 60-76, doi: 10.1016/j.pss.2013.12.002. 5) J. Fastook et al. (2011) Evidence for Amazonian northern mid-latitude regional glacial landsystems on Mars: Glacial flow models using GCM-driven climate results and comparisons to geological observations, *Icarus*, 216, 23-39, doi: 10.1016/j.icarus.2011.07.018. 6) J. Fastook et al. (2014) Formation of lobate debris aprons on Mars: Assessment of regional ice sheet collapse and debris-cover armoring, *Icarus*, 228, 54-63, doi: 10.1016/j.icarus.2013.09.025. 7) J. Head et al. (2005) ADVISER: Immersive Scientific Visualization Applied to Mars Research and Exploration, *Photogrammetric Engineering and Remote Sensing*, 71, 1219-1225. 8) J. Head et al. (2006a) Modification of the dichotomy boundary on Mars by Amazonian mid-latitude regional glaciation, *Geophys. Res. Lett.*, 33, L08S03, doi: 10.1029/2005GL024360. 9) J. Head et al. (2006b) Extensive valley glacier deposits in the northern mid-latitudes of Mars: Evidence for Late Amazonian obliquity-driven climate change, *Earth Planet. Sci. Lett.*, 241, 663-671, doi: 10.1016/j.epsl.2005.11.016. 10) J. Head et al. (1998) Oceans in the past history of Mars: Tests for their presence using Mars Orbiter Laser Altimeter (MOLA) data, *Geophys. Res. Lett.*, 25, 4401-4404. 11) J. Head et al. (2010) Northern mid-latitude glaciation in the Late Amazonian period of Mars: Criteria for the recognition of debris-covered glacier and valley glacier landsystem deposits, *Earth Planet. Sci. Lett.*, 294, 306-320, doi: 10.1016/j.epsl.2009.06.041. 12) J. Holt et al. (2008) Radar sounding evidence for buried glaciers in the southern mid-latitudes of Mars, *Science*, 322, 1235-1238, doi: 10.1126/science.1164246. 13) J. Levy et al. (2007) Lineated valley fill and lobate debris apron stratigraphy in Nilosyrtris Mensae, Mars: Evidence for phases of glacial modification of the dichotomy boundary, *J. Geophys. Res.*, 112, E08004, doi: 10.1029/2006JE002852. 14) J. Levy et al. (2014) Sequestered glacial ice contribution to the global martian water budget: Geometric constraints on the volume of remnant, midlatitude debris-covered glaciers, *J. Geophys. Res.*, 119, 1-9, doi: 10.1002/2014JE004685. 15) S. Mackay et al. (2014) Cold-based debris-covered glaciers: Evaluating their potential as climate archives through studies of ground-penetrating radar and surface morphology, *J. Geophys. Res.*, 119, 2505-2540, doi: 10.1002/2014JF003178. 16) J. Plaut et al. (2009) Radar evidence for ice in lobate debris aprons in the mid-northern latitudes of Mars, *Geophys. Res. Lett.*, 36, L02203, doi: 10.1029/2008GL036379. 17) J. Head et al. (2002) Recent ice ages on Mars, *Nature*, 426, 797-802. 18) F. Chuang and D. Crown (2009) Geologic map of MTM 35337, 40337, and 45337 quadrangles, Deuteronilus Mensae region of Mars: U.S. Geological Survey Scientific Investigations Map 3079.

ALUMINUM PHYLLOSILICATES: IMPLICATIONS FOR PAST CLIMATE HISTORY OF MARS

S.V. Kaufman¹, J.W. Head¹, J.F. Mustard¹

¹*Brown University, Providence, RI 02912, United States of America*

Contact: sierra_kaufman@brown.edu

Widespread detections of Al-phyllsilicates on Mars have raised compelling questions on their implications for the early Martian climate [1, 2]. This group of minerals may be indicative of extensive leaching of parent rock by liquid water [3]. However, the climate of early Mars has not been sufficiently constrained to determine if these same mechanisms we see on Earth are responsible for the formation of the phyllosilicates observed there. Whether Mars was “warm and wet” [4] or “cold and icy” [5, 6] would have had a profound influence on the formation mechanism of these phyllosilicate deposits.

The stratigraphically layered deposits [7] around the Nilli Fossae and Mawrth Vallis regions (**Figure 1**) have had several workable formation and emplacement hypotheses proposed, but their emplacement histories continue to be largely unresolved. A substantial portion of hypotheses include environments consistent with a warm and wet early Mars: weathering of primary basaltic rock by aqueous alteration [2], water deposition of transported sediments in an aqueous environment [8], and aqueous alteration of volcanic ash [8, 9]. Each of these hypotheses requires large amounts of either standing or precipitated water to be consistently available. No existing climate model has been able to convincingly create a sustainable surface environment in which such conditions exist, especially in the Southern Highlands, where, in the “cold and icy” model, altitude dependent cooling takes effect under atmospheric pressures above a few hundred millibars [5].

The change from Fe/Mg smectites to Al-phyllsilicates in the stratigraphic column is hypothesized to be indicative of larger environmental change. The Fe/Mg smectites are able to be produced in a low water to rock ratio and closed system that does not require exchange of fluids with its surroundings [10]. On Earth, the ferrous phase material found between the contact of the aluminum and iron/magnesium phyllosilicates could be indicative of microorganisms causing a change in pH or cation activity; this same change on Mars could be explained via hydrothermal processes [11]. The Al-phyllsilicates however, are a more advanced weathering or alteration product than the Fe/Mg-smectites which still contain some relatively soluble elements. They form in an open system and a high water to rock ratio [3]. This requires the environment would be able to undergo ion transport, changing the bulk composition of the primary rock. At a moderate pH, Mg, Ca, Cl, Na, and K are relatively to highly mobile, which allows them to be removed from the system and produce the low activity levels required to form aluminum clays [10].

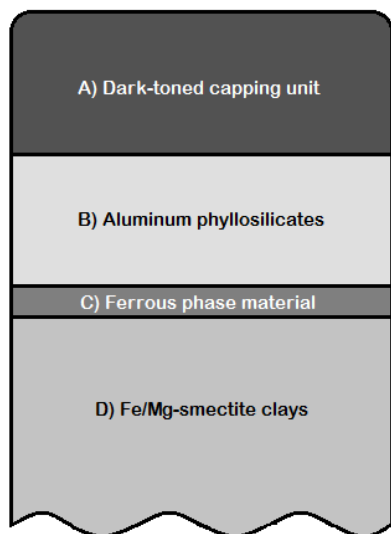


Fig. 1. Generalized upper stratigraphic column for the Mawrth Vallis and Nilli Fossae layered phyllosilicates [7, 11].

A) Spectrally neutral capping unit, bottom few tens of meters are banded and olivine-rich in the Nilli Fossae region.
 B) Light colored layer with small polygonal fractures on montmorillonite-rich units and smooth textured kaolinite-bearing units, commonly intermixed with hydrated silica.
 C) Fe²⁺ (ferrous) phase material seen sandwiched between the phyllosilicate deposits.
 D) Light colored layer containing larger scale polygonal fractures; nontronite and saponite are most common minerals, however chlorite has been detected in significant amounts as well.

Alternative methods of phyllosilicate formation have been examined as possibilities for Mars, including: 1) aeolian phyllosilicate deposition [5], 2) impact-driven alteration during the Late Heavy Bombardment [8], and 3) widespread hydrothermal alteration [2]. The aeolian deposition model has no viable source [8], impact-driven alteration appears to have difficulty producing such even and widespread deposits [8, 12], and hydrothermal processes assume sufficient volatile content present in the crust at that time to alter the minerals appropriately [2]. The mineral assemblages and morphology of Fe/Mg-phyllosilicate deposits exhumed from impact events and observed in their central peaks, crater walls, and ejecta show significant evidence for deep hydrothermal emplacement [10].

We are investigating the morphology and characterizing areas by their locally dominant Al-clay, montmorillonite or kaolinite. Establishing these relationships will prove useful in distinguishing between a "warm and wet" and a, "cold and icy" early martian climate.

REFERENCES:

- [1]-Poulet, F. et al. (2005) *Nature*, 438, 623-627. [2]-Bibring, J.-P. et al. (2006) *Science*, 312, 400-404. [3]-Chevrier, V. et al. (2007) *Nature*, 448, 60-63. [4]-Craddock, R.A. & Howard, A.D. (2002) *J. Geophys. Res.*, 10. [5]-Wordsworth, R. et al. (2013) *Icarus*, 222, 1-19. [6]-Head, J.W. & Marchant, D.R. (2014) *Antarct. Sci.*, 26, 774-800. [7]-Mustard, J.F. et al. (2008) *Nature*, 454, 305-309. [8]-Loizeau, D. et al. (2007) *J. Geophys. Res.*, 112. [9]-Bishop, J.L. & Rampe, E.B. (2016) *Earth Planet. Sci. Lett.*, 448, 42-48. [10]-Ehlmann, B.L. et al. (2011) *Nature*, 479, 53-60. [11]-Bishop, J.L. et al. (2008) *Science*, 321, 830-833. [12]-Murchie, S.L. et al. (2009) *J. Geophys. Res.*, 114.

FRETTED TERRAIN ORIGINS AND THE PROBLEMS OF ARABIA TERRA, WITH A FOCUS ON STRATIGRAPHIC AND TEMPORAL RELATIONSHIPS

C.A. Denton, J.W. Head

Brown University, Providence, RI, 02912, USA

Contact: camille_denton@brown.edu

INTRODUCTION

Many martian geologic structures and terrains, while identified almost half a century ago, remain mysterious in terms of their formation mechanisms and their ties to Martian climatic and geologic history. One such enigmatic terrain is the **fretted terrain**, which lies in the transitional region between the smooth northern lowlands and the ancient, cratered highlands to the south.

GEOLOGIC BACKGROUND

Fretted terrain is traditionally characterized by abrupt escarpments in highly irregular configurations, with isolated, island-like mesas and buttes of highland material [1]. These escarpments tend to be of uniform height (~1-2 km) and are separated by wide, flat-floored chasms, but do not construct regular patterns across the landscape [2]. Large debris aprons are associated with most escarpments, extending up to 20 km across the flat northern plains [3]. The debris aprons are likely the results of recent erosion, however, and are thus not associated with the formation of the fretted terrain [4].

The most compelling observations of fretted terrain occur in the northern section of **Arabia Terra** (between 30 and 50 N and 270 and 360 W). In the case of Arabia Terra, sections of fretted terrain appear to be dominated by **fretted channels**, which appear as sinuous, wide valleys with steep walls, flat floors, and unusually stout tributaries [1]. These features are both much wider than typical valley network channels and much less dendritic, with few if any tributaries and no obvious source. Many fretted channels have longitudinal striae on their floors, which suggests that: a) these channels are not fluvial (as no channels or obvious floodplains are present), b) mass-wasting was involved to an undetermined extent, interpreted earlier as debris flows [3, 5], and c) involvement of debris-covered glaciers [6, 7]. In addition, collapse structures seen in the channels and in the terrain in general imply mobilization and/or erosion of the subsurface.

Early theories for the formation of fretted terrain have suggested initiation via tectonic alteration of the older, cratered surface, creating escarpments that then recede through a mechanism that undermines the terrain (such as groundwater sapping), developing the more complicated configurations of escarpments seen in the present [2]. Because fretted channels have no obvious source, a collapse or sapping mechanism is typically assumed to be involved [1]. The striae are presumed to form through the mobilization of large amounts of debris shed by the retreating escarpments and lubricated via ice and/or groundwater [1, 4]. Sharp [2] also suggested that dissolution of massive quantities of ice could have shaped the fretted terrain, which the debris-covered glacial hypothesis [6, 7] connects to the lineated valley fill. In any case, most sources agree that large amounts of highland material were dissected and removed to produce the existing geometry seen in the fretted terrain. Processes of removal and subsequent redeposition of material appear to have occurred much earlier than the largely Amazonian modification represented by the lineated valley fill [6, 7].

ARABIA TERRA

To assess possible formation mechanisms for the fretted terrain and fretted channels, we must place them within the context of the geologic history of the region in which they exist: Arabia Terra. Arabia Terra, like most of the Martian surface, is covered in multiple geologic structures that make tracing the geologic history difficult; these include impact craters, volcanic plains, tectonic structures (wrinkle ridges, etc.), and the aforementioned fretted terrain. It is also intriguing for being the northernmost block of highland material, as well as anomalously low relative to the average reference elevation [8].

The first recorded geologic process in Arabia Terra, like most of Mars, is the formation of the hemispheric dichotomy and the differentiation of the lowlands vs. the highlands in the Early Noachian, most likely by a huge oblique impact [9]. Afterwards, extensive regional geologic mapping by McGill [4] determined that large-scale flood volcanism took place in the Middle Noachian, emplacing the plateau materials, and a second major resurfacing took place in the Late Noachian (though these dates are approximate). This second era of volcanism left some older plateau lava exposed and in general acted to resurface areas on a local rather than regional scale. The major erosional event that formed the fretted terrain and the fretted channels took place after both of these volcanic episodes, likely in the early Hesperian but possibly between the middle Noachian and the middle Hesperian [4]. The formation of the fretted channels removed and isolated large sections of highland material, as well as producing numerous isolated and connected depressions. It is possible that the formation of the fretted terrain coincided with a second volcanic resurfacing event, as the uncertainties overlap.

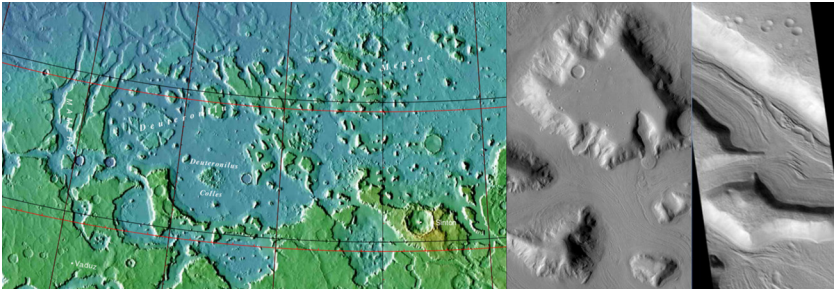


Fig. 1. A: MOLA topographic map of Arabia Terra, with labeling of smaller regions. B: CTX image of mesas and buttes within Arabia Terra. C: HiRISE image of lineated floor deposits of Hyspas Valles, presumed to be glacial in origin.

CONCEPTUAL MODEL

We propose a revised model for the formation of the fretted channels based on Cassanelli and Head [10]. Previous studies have suggested that large amounts of ice (and the melting and drainage thereof) may have been involved in channel and terrain formation, without specifying what such a mechanism might entail or where such ice might originate [e.g., 2]. More recent climate work [11, 12] has suggested that, as a result of a cold, icy early Mars, regional ice sheets may have populated large swathes of the highlands [e.g., 13], providing a source of ice which might be involved in producing the channels.

Recent modeling work suggests that volcanism that occurs in the presence of an ice sheet is mostly likely to emplace the lava flow on top of the ice sheet via either advance from a nearby non-ice covered source or through dike emplacement through the ice sheet itself [14]. The presence of a lava flow on top of the ice sheet will either induce contact melting or deferred melting depending on the amount and number of lava flows emplaced [10]. The amount of meltwater and the timing of meltwater formation are likewise tied to the properties of the lava; little to no melting could occur, or alternatively meltwater flows could be activated at the base of the ice sheet. Additionally, meltwater produced by ice sheet heating and loading will likely infiltrate the underlying sediments, destabilizing the cryosphere and increasing groundwater flow.

Considering the predictions of the above model, volcanic-induced deferred and/or contact melting of a preexisting ice sheet in the late Noachian could activate the large amounts of water needed to produce the fretted channels. Additionally, destabilization and localized collapse of the ice sheet and cryosphere beneath it could cause the collapse features and asymmetric depressions seen in sections of the fretted terrain. The late Noachian volcanic flows are a likely source, as McGill [4] notes that they are more local than regional events, suitable for locally melting an ice sheet. The waves of flooding produced by deferred melting (on the kyr timescale) are consistent with predictions that the fretted channels formed over a relatively long time period [2, 4].

The proposed mechanism for formation of the fretted channels places their inception in the late Noachian rather than the early Hesperian, which is within the uncertainty range previously predicted [4]. The mechanism also provides an impetus for large-scale groundwater and/or icy debris flows via the heating

and loading of an ice sheet, an impetus which has heretofore been ambiguous. However, this model remains purely conceptual. Future work must assess: a) how much ice realistically existed in the region to be melted and mobilized, b) the amount needed to form the fretted channels, c) which mechanisms are most likely (lubricated debris flows, groundwater/below surface motion, or something else entirely), and d) if the amount of ice available is consistent with a more detailed conceptual model.

REFERENCES

- [1] Carr, M.H. *Water on Mars*. 1996. [2] Sharp, R.P. (1973) *JGR* 78, 20. 4073-4083. [3] Squyres, S.W. (1978) *Icarus* 34. 600-613. [4] McGill, G.E. (2000).” *JGR* 105, E3. 6945-6959. [5] Carr, M.H. (1995) *JGR* 100. 7479-7507. [6] Head et al. (2006). *Earth Planet. Sci Lett.* 241. 663-671. [7] Head et al. (2006) *GRL* 33, L08S03. [8] Smith, D.E., et al. (1999) *Science* 284. 1495-1503. [9] Andrews-Hanna, J. et al. (2008) *Nature* 452. 1212-1215. [10] Cassanelli, J.P and Head, J.W. (2016) *Icarus* 271. 237-264. [11] Forget, F. et al. (2013) *Icarus* 222, 1. 81-99. [12] Wordsworth, R. et al. (2013). *Icarus* 222, 1. 1-19. [13] Head, J.W., and Marchant, D.R. (2014). *Antarctic Science* 26 (6). 774-800. [14] Wilson, L. and Head, J.W. (2002) *Geol. Soc. Lond. Spec. Publ.* 202, 5-26.

PRECISION CARTOGRAPHIC MAP OF THE EXOMARS SCHIAPARELLI LANDING SITE ON MARS DERIVED FROM MARS RECONNAISSANCE ORBITER CONTEXT CAMERA IMAGES

T.C. Duxbury

¹George Mason University, Department of Physics and Astronomy, Fairfax, Virginia, 22039, USA

Contact: tduxbury@gmu.edu

The European Space Agency (ESA) has launched its Trace Gas Orbiter (TGO) and Schiaparelli Entry, Descent and Landing Demonstrator Module (EDL) to Mars with orbit insertion and landing on 17 October 2016 (ESA, 2014). A precision cartographic map, tied to the MOLA reference surface, has been produced from NASA Mars Reconnaissance Orbiter (MRO) Context Camera (CTX – Malin, 2007) images and associated NAIF SPICE kernels. Forty-eight (48) CTX image strips that provided overlapping and stereo coverage of the Schiaparelli landing site in Meridiani Planitia were processed in a stereo photogrammetric reduction scheme to not only yield the cartographic map but also determine the geometric, alignment and pointing parameters of the CTX camera and all 48 image strips. Fifty-seven MOLA features were used for absolute control in the data reduction to yield precise camera mounting alignment angles on the MRO spacecraft and the CTX focal length. Over one thousand smaller features, only seen in the CTX images, were used as tie points to precisely determine the CTX optical distortion parameters, the individual camera pointing of each of the 48 image strips and constrain the focal length. The cartographic reduction estimated over 3000 control and tie point Mars-fixed position components, 150 camera pointing and alignment angles and the CTX focal length and distortion parameters. All tie points were observed in at least 3 CTX image strips and in as many as 15 strips to allow an over determination of the estimated parameters by a factor of 3. After the processing, all of the 48 CTX image strips could be map projected into controlled photomosaics with no visible seams in image overlap due to mis-registration or mis-camera modeling.

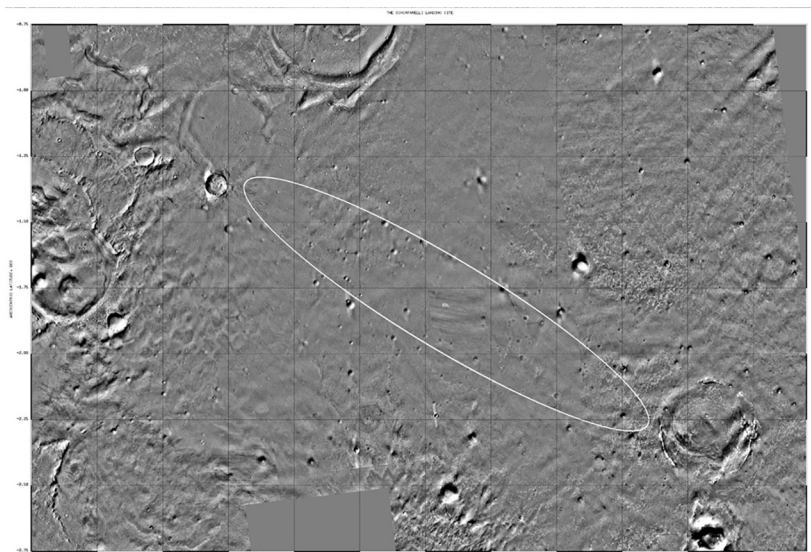


Fig. 1. Example of a precision controlled CTX photomosaic of the ESA ExoMars 2016 Schiaparelli landing site

REFERENCES:

1. Schiaparelli: the ExoMars Entry, Descent and Landing Demonstrator Module., ESA. 2013. Retrieved 1 October 2014.
2. Malin, et. al., Context Camera investigation on board the Mars Reconnaissance Orbiter, JGR, 12, ES, DOI: 10.1029/2006JE002808, May 2007.

PARAMETERS OF SATURATED INTERNAL GRAVITY WAVES IDENTIFIED IN THE MARTIAN ATMOSPHERE FROM AN ANALYSIS OF *MARS GLOBAL SURVEYOR* RADIO OCCULTATION DATA

V.N. Gubenko, I.A. Kirillovich, V.E. Andreev

Kotelnikov Institute of Radio Engineering and Electronics of the RAS, Vvedenskogo square 1, 141190 Fryazino, Moscow region, Russia
Contact: vngubenko@gmail.com

INTRODUCTION:

An original method of determining the characteristics of an internal gravity wave (IGW) has been developed using the data of an analysis of individual vertical temperature or buoyancy frequency square profile in the planetary atmosphere. A threshold criterion of IGW identification is formulated and justified, by which, analyzed fluctuations can be considered as wave manifestations [Gubenko *et al.*, 2008, 2011, 2012]. The method is based on an analysis of relative wave amplitude determined from a vertical profile, as well as on the assumption of the IGW linear theory, according to which the wave amplitude is saturated by processes of dynamic (shear) instability in the atmosphere. It is supposed that, when the amplitude of the internal wave reaches the shear instability threshold as the wave propagates upward, a dissipation of wave energy occurs such that the IGW amplitude is maintained at the atmospheric instability threshold. An application of the developed method to vertical temperature profiles obtained from radio occultation (RO) measurements of the *Mars Global Surveyor* (MGS) mission made it possible to identify IGWs in the Martian atmosphere and determine the values of key wave parameters such as intrinsic frequency, amplitudes of the vertical and horizontal disturbances of wind velocity, vertical and horizontal wavelength, intrinsic vertical and horizontal phase (and group) velocities, kinetic, potential, and total energy of IGWs per unit mass, vertical fluxes of wave energy and horizontal momentum [Gubenko *et al.*, 2015]. Identified in the Martian atmosphere IGWs, with a vertical wave-length of 4.5–8.2 km, are waves with low intrinsic frequencies close to inertial frequency. Their kinetic energy, as a rule, is greater than potential energy by an order of magnitude. The propagation of these waves causes a significant modulation of the stability of atmospheric stratification that leads to shear instability and the occurrence of thin layers of intermittent turbulence in the Martian atmosphere.

EXPERIMENTAL DATA FOR AN ANALYSIS:

The data on the vertical temperature profiles of the MGS mission were taken by us from NASA's archive of the planetary data system (<http://starbrite.jpl.nasa.gov/pds/...>, Planetary Data System) and they were the primary material for processing and analysis in order to identify IGWs and reconstruct wave characteristics in the Martian atmosphere. The vertical resolution of these temperature profiles, which depends on the geometry of the experiment and the wavelength of the sounding signal, is limited by diffraction effects and is ~1 km. Near the planet's surface, where the restored profiles are most accurate, the standard deviation of temperature fluctuations is equal to about 0.4 K, which corresponds to the value of relative data spread of ~0.2% [Hinson *et al.*, 2001]. The vertical resolution of the temperature data was significantly different for different profiles, but it was not worse than 1250 m [Creasey *et al.*, 2006]. Therefore, to ensure consistency in data processing and to simplify the spectral analysis of investigated fluctuations, the altitude interpolation of temperature values was performed each 1250 m. The high-frequency filtration of temperature fluctuations with a cutoff at 10 km allowed us to exclude structures with the vertical wavelengths more than 10 km, which may not be caused by IGWs but instead by thermal tides, occurring most often in the atmosphere above the mountains, particularly over the Tharsis region [Creasey *et al.*, 2006]. At the next step of data processing, the method of an analysis of wave manifestations and IGW parameter determination was applied to the vertical temperature profiles. As can be seen from [Gubenko *et al.*, 2008, 2011, 2012], in the case of a positive identification of IGWs, we can determine key wave parameters such as the intrinsic frequency, amplitudes of vertical and horizontal disturbances of wind velocity, vertical and horizontal wavelength, intrinsic verti-

cal and horizontal phase velocities, density of kinetic, potential, and total energy, vertical fluxes of wave energy and horizontal momentum, and others. For the further analysis of profiles in order to identify wave events, we have selected vertical profiles where noticeable quasi-periodic temperature variations were observed, and intervals of wave observation were determined for each of the selected profiles [Gubenko et al., 2015].

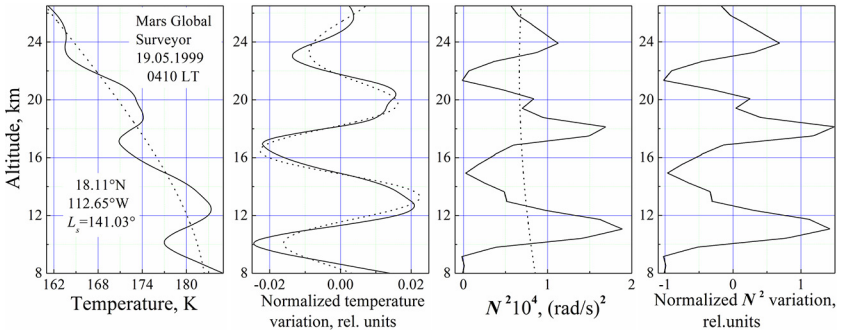


Fig. 1. Manifestation of the fully saturated IGW (sat. degree ≥ 0.95) in the Martian atmosphere (Tharsis region) from the vertical temperature profile (data file: 9139G18A.TPS) retrieved from MGS RO on 19 May 1999. The season was summer in the northern hemisphere (celestial longitude $L_s = 141.03^\circ$) and the local true solar time was 04:10 h, corresponding to early morning. Wave parameters: $\lambda_p = 6.6$ km; $\lambda_h = 580$ km; $E = 42.7$ J/kg; $p = E_p/E = 1.4$; $E = 17.6$ J/kg; $f/\omega = 0.42$; $T^n = 2\pi/\omega = 16.6$ hrs; $a_s = 0.95$; $|u| = 9.2$ m/s; $|v| = 3.9$ m/s [Gubenko et al., 2015].

Figure 1 shows an example of altitude profiles of variations of temperature and square of the buoyancy frequency in the range of 8–26.5 km restored from the measurements of the MGS mission on 19 May 1999 in the Martian atmosphere. The indicated measurements were performed during the Martian summer ($L_s = 141.03^\circ$) at 4:10 of local time in the atmospheric region with coordinates 18.11° N and 112.65° W (data file: 9139G18A.TPS) located above the Tharsis mountain volcanic massif. Powerful quasi-periodic variations of T and N^2 with a vertical wavelength of ~ 6.6 km are identified as manifestations of saturated IGW in the planet's atmosphere. Two independent estimates of the wave amplitude, $a_s = 0.95$ and $A^{rel}_N = 1$, in good agreement with each other, testify that the saturation degree of the wave amplitude is not less than 95%, since for saturated IGW with any intrinsic frequency ω , the relative threshold amplitude does not exceed one. The intrinsic frequency of the internal wave is greater than the inertial frequency approximately by a factor of 2.4 ($f/\omega = 0.42$), and its kinetic energy is greater than potential energy by a factor of 1.4. It is seen from Figure 1 that IGW propagation leads to a strong modulation of the stability of atmospheric stratification. Local values of parameter N^2 reach zero near levels of 9, 15, and 21 km, which assumes here not only dynamic, but also convective instability, and the occurrence of thin layers of intermittent turbulence in the atmosphere. These thin layers of turbulence having a thickness significantly less than λ_z and a horizontal extent of the order of magnitude of λ_h cannot destroy the structure of the wave field [Gubenko et al., 2015].

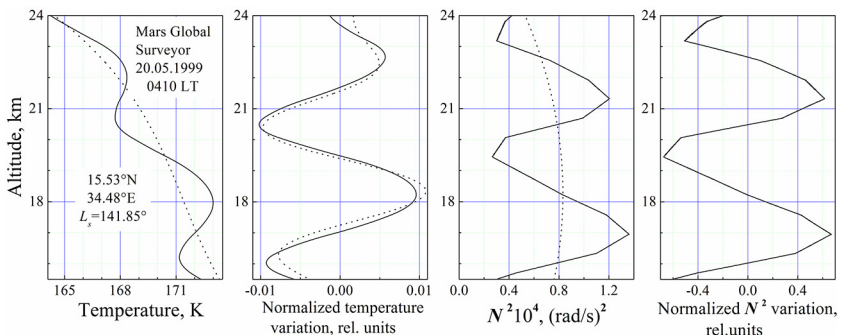


Fig. 2. The same as Figure 1 except from radio occultation (data file: 9140V32A.TPS) conducted in summer ($L_s = 141.85^\circ$) at 04:10 h LT on 20 May 1999. Example of “clean” wave observations, where noise was not discovered in the spectrum of analyzed temperature fluctuations. Wave parameters: $\lambda_p = 4.5$ km; $\lambda_h = 2080$ km; $E = 39.9$ J/kg; $p = E_p/E = 8.4$; $E_p = 4.2$ J/kg; $f/\omega = 0.89$; $T^n = 2\pi/\omega = 40.7$ hrs; $a_s = 0.63$; $|u| = 8.9$ m/s; $|v| = 7.9$ m/s [Gubenko et al., 2015].

Figure 2 shows a rare example of so-called “clean” wave observations, where noise was not discovered in the spectrum of analyzed temperature fluctuations. Coordinates of the probing atmospheric region and information about the time of the measurements are shown in Figure 2. Quasi-periodic variations of T and N^2 with a vertical wavelength of ~ 4.5 km have been identified as signatures of propagation of inertial IGW in the Martian atmosphere. The intrinsic frequency of the internal wave is close to the inertial frequency ($f/\omega = 0.89$), and its kinetic energy is greater than potential energy by a factor of 8.4. The very good correspondence of the values of the wave parameters reconstructed by two different ways should be noted. We find that the value $A^{rel}_2 = 0.63$ coincides with the estimate of the wave amplitude a_0 obtained from an analysis of the temperature data. A comparison shows that the results of reconstruction of the IGW parameters obtained by two different methods are practically identical [Gubenko *et al.*, 2015].

CONCLUSION:

An original method of identifying the internal waves and determining their characteristics has been developed based on the analysis of the vertical temperature, density or buoyancy frequency square profile in a planetary atmosphere. Application of the method to the analysis of the vertical temperature profile of the MGS mission enables the identification of IGWs in the Martian atmosphere and the determination of the values of key wave parameters such as intrinsic frequency, amplitudes of the vertical and horizontal disturbances of wind velocity, vertical and horizontal wavelength, density of kinetic and potential energy, vertical fluxes of wave energy and horizontal momentum. Internal waves with vertical wavelength of 4.5–8.2 km identified in the Martian atmosphere are the waves with low intrinsic frequencies close to the inertial frequency, and their kinetic energy, as a rule, exceeds potential energy by an order of magnitude. The propagation of these waves causes a significant modulation of the vertical stability of atmospheric stratification that leads to shear instability and the occurrence of thin layers of intermittent turbulence in the Martian atmosphere.

ACKNOWLEDGMENTS:

This work was partially supported by the Program No. 7 of the RAS Presidium.

REFERENCES:

- Creasey J.E., Forbes J.M., Hinson D.P. (2006). Global and seasonal distribution of gravity wave activity in Mars' lower atmosphere derived from MGS radio occultation data. *Geophys. Res. Lett.*, V. 33, No. L01803, DOI: 10.1029/2005GL024037.
- Gubenko V.N., Pavelyev A.G., Andreev V.E. (2008). Determination of the intrinsic frequency and other wave parameters from a single vertical temperature or density profile measurement. *J. Geophys. Res.*, V. 113, No. **D08109**, DOI:10.1029/2007JD008920.
- Gubenko V.N., Pavelyev A.G., Salimzyanov R.R., Pavelyev A.A. (2011). Reconstruction of internal gravity wave parameters from radio occultation retrievals of vertical temperature profiles in the Earth's atmosphere. *Atmos. Meas. Tech.*, V. 4, No. 10, P. 2153–2162, DOI:10.5194/amt-4-2153-2011.
- Gubenko V.N., Pavelyev A.G., Salimzyanov R.R., Andreev V.E. (2012). A method for determination of internal gravity wave parameters from a vertical temperature or density profile measurement in the Earth's atmosphere. *Cosm. Res.*, V. 50, No. 1, P. 21–31, DOI: 10.1134/S0010952512010029.
- Gubenko V.N., Kirillovich I.A., Pavelyev A.G. (2015). Characteristics of internal waves in the Martian atmosphere obtained on the basis of an analysis of vertical temperature profiles of the Mars Global Surveyor mission. *Cosm. Res.*, V. 53, No. 2, P. 133–142, DOI: 10.1134/S0010952515020021.
- Hinson D.P., Tyler G.L., Hollingsworth J.L., Wilson R.J. (2001). Radio occultation measurements of forced atmospheric waves on Mars. *J. Geophys. Res.*, V. 106, No. E1, P. 1463–1480.

LUNAR NEUTRONS, AS SIGNATURES OF WATER

A.B. Sanin¹, I.G. Mitrofanov¹, M.L. Litvak¹, B.N. Bakhtin¹, J.G. Bodnarik², W.V. Boynton², G. Chin³, L.G. Evans^{3,4}, K. Harshman², F. Fedosov¹, D.V. Golovin¹, A.S. Kozyrev¹, T.A. Livengood^{3,5}, A.V. Malakhov¹, T.P. McClanahan³, M.I. Mokrousov¹, R.D. Starr^{3,6}, R.Z. Sagdeev⁵, V.I. Tret'yakov¹, A.A. Vostrukhin¹

¹*Space Research Institute of Russian Academy of Sciences (IKI RAS), 117997, 84/32 Profsoyuznaya str., Moscow, Russia*

²*Lunar and Planetary Laboratory, University of Arizona, Tucson, AZ 85719, USA*

³*Solar System Exploration Division, NASA Goddard Space Flight Center, Greenbelt, MD 20771, USA*

⁴*Computer Science Corporation, Lanham, MD 20706, USA*

⁵*University of Maryland, College Park, MD 20742, USA*

⁶*Catholic University of America, Washington DC 20064, USA*

Contact: sanin@np.cosmos.ru

The Lunar Exploration Neutron Detector (LEND) is operating on orbit around the Moon on-board the Lunar Reconnaissance Orbiter (LRO) spacecraft more than six years. LEND has been designed and manufactured to investigate presence and determine average amount of hydrogen in upper (~1 m depth) sub-surface layer of the Lunar regolith with spatial resolution ~10 km from 50 km orbit and to check the hypothesis what the permanently shadowed regions (PSRs) at circumpolar regions are the main reservoirs of a large deposition of water ice on the Moon.

A method of water equivalent hydrogen (WEH) abundance in top ~ 1 meter regolith estimation using LEND data has been developed. Maps of WEH distribution in North and South Polar Regions will be presented and discussed. It was found from the LEND observations that not all large PSRs contain a detectable amount of hydrogen but there are neutron suppression regions (NSRs) with statistically significant suppression of neutron flux. The NSRs partially overlap or include PSRs in some craters, like Cabeus, Shoemaker, Haworth (on South) and Rozhdestvensky U (on North), but significant part of their area spread out at sunlit territory. This means that hydrogen may be preserved for a long time or even accumulated at a subsurface regolith layer of sunlit areas. WEH estimation in case of hydrogen bearing regolith layer coverage by a dry regolith will be presented for largest NSRs.

HIGH CONCENTRATIONS OF HYDROGEN-BEARING VOLATILES AT THE BASE OF POLEWARD-FACING SLOPES IN THE MOON'S LARGE SOUTHERN PERMANENTLY SHADOWED REGIONS

T.P. McClanahan¹, I.G. Mitrofanov², W.V. Boynton³, G. Chin¹, R.Z. Sagdeev⁴, T.A. Livengood^{4,1}, M. Litvak², A. Sanin², R.D. Starr^{5,1}

¹NASA Goddard Space Flight Center, Greenbelt MD, USA

²Space Research Institute, Moscow, Russia

³University of Arizona, Tucson, Arizona, USA

⁴University of Maryland, College Park, MD, USA

⁵Catholic University, Washington D.C, USA

Contact: timothy.p.mcclanahan@nasa.gov

In this paper we review evidence that indicates that high concentrations of hydrogen-bearing volatiles are biased towards the base of poleward-facing slopes (PFS) in the Moon's southern permanently shadowed regions (PSR). Results are derived from a correlated study of Lunar Reconnaissance Orbiter instrument maps of epithermal neutron leakage flux from the Lunar Exploration Neutron Detector (LEND), topography from the Lunar Observing Laser Altimeter (LOLA) and surface thermal maps from the Diviner radiometer. Maximum concentrations of hydrogen-volatiles, likely as water ice, are shown in Cabeus crater's PSR, 0.62 wght% water-equivalent-hydrogen. Detailed studies show that hydrogen-volatiles at the base of (PFS) are correlated with the locations of low PSR temperatures of Cabeus, Haworth, Shoemaker and Faustini. High volatile concentrations in these regions may reflect down-slope volatile transport on PFS or thermally constrained volatile losses. 15-km Full-width at Half-Maximum (FWHM) is shown to be an upper-bounds condition for the LEND collimated sensor's spatial resolution, observed from a cross-section profile that transects Cabeus' largest permanently shadowed region and the LCROSS impact point. LEND's high-resolution spatial response is further illustrated in a 220-km long transect of the co-aligned permanently shadowed regions and partially-illuminated ridges of Haworth, Shoemaker, Faustini and Amundsen craters.

PETROLOGICAL MAPPING OF REGIONS IN THE SOUTH POLE-AITKEN BASIN

D. Rommel¹, A. Grumpe¹, C. Wöhler¹, H. Hiesinger², A.A. Berezhnoy³, K.J. Kim⁴

¹Dortmund Technical University, Image Analysis Group, Dortmund, Germany

²Westfälische Wilhelms-Universität Münster, Institut für Planetologie, Münster, Germany

³Sternberg Astronomical Institute, Moscow State University, Moscow, Russia;

⁴Geological Research Division, Korea Institute of Geosciences & Mineral Resources, Daejeon, Republic of Korea

Contact: daniela.rommel@tu-dortmund.de

INTRODUCTION:

The formation of the South Pole-Aitken basin (SPA) took place in the pre Neotectonic time range, i.e. about 4 billion years ago. It is the oldest, deepest, and largest impact basin [1] with an extent of about 2500 km in diameter [2]. Since the SPA is a deep basin and has been subject to further impacts, the composition of the SPA and its craters is highly relevant for models of the lunar crust. In this study, we map four interesting craters, namely Alder, Antoniadi, Dryden, and Lyman that show high abundances of Mg-rich rock. The analysis is based on spectral reflectance derived elemental abundance maps.

METHODS AND DATASET:

We base our analysis on the hyperspectral dataset of the Moon Mineralogy Mapper (M³) [3]. Since the apparent reflectance of the surface highly depends on the illumination geometry, we apply a normalization procedure. Afterwards, we derive maps of spectral parameters that closely resemble the spectral absorption troughs of common lunar minerals. Finally, we construct elemental abundance maps based on these spectral parameters and Lunar Prospector Gamma Ray Spectrometer derived elemental abundance maps of low lateral resolution.

NORMALIZATION OF THE SPECTRAL DATA.

Due to the loss of the spacecraft's star sensors, the geo-referencing of the M³ data was not sufficient and has been refined after the mission [4]. To remove the residual errors of the geo-referenced positioning data, we manually computed a projective transform that maps each M³ image onto the LROC WAC mosaic [5], respectively.

Since the lateral resolution of available digital elevation models (DEM), e.g. the GLD100 [6], does not match the lateral resolution of the M³ images, we apply a shape-from-shading based method [7, 8] to increase the lateral resolution of the GLD100. The Hapke model [9, 10] was used to describe the reflectance of the surface. We compute a low-resolution local estimate of the single-scattering albedo and adopt the remaining parameters from [11]. Since the radiance measured by the M³ instrument includes a thermal emission component, we compute the refined DEM based on the M³ channel centered at 1369 nm. Based on the refined DEM, the M³ spectra are normalized to standard geometry, i.e. 30° incidence angle and 0° emission angle [12].

CONSTRUCTION OF ELEMENTAL ABUNDANCE MAPS.

We adopt the spectral parameters from [13] to describe the spectral absorption features. These spectral parameters are the depth, width, position and continuum slope of the absorption band near 1 μm and the continuum slope and depth of the absorption band near 2 μm .

Following the steps outlined in [13, 14], we map the M³ derived low-resolution mosaic of spectral parameters to Lunar Prospector Gamma Ray Spectrometer [15, 16] derived elemental abundance maps of low spatial resolution using a polynomial regression model. The regression parameters are then applied to the full resolution M³ data of the target regions, resulting in maps of the elemental abundances of Ca, Al, Fe, Mg, Ti and O. From the Fe and Mg maps we derive a petrological map based on the model suggested in [17], which is defined by the endmembers mare basalt (18 wt% Fe, 6.5 wt% Mg), Mg-rich rock (4 wt% Fe, 13 wt% Mg, e.g. troctolite or orthopyroxene-rich norite) and feldspathic rock (0.5 wt% Fe, 1 wt% Mg, especially ferroan anorthosite).

The relative fractions can be read out from the ternary Fe-Mg diagram [17] and are visualized in terms of an RGB image, where the red channel corresponds to basaltic material content, the green channel corresponds to Mg-rich rock content, and the blue channel corresponds to the fraction of feldspathic rock.

RESULTS AND DISCUSSION:

The crater Alder (82 km in diameter, centered at 48.6° S, 177.9° E) is located in the center of the SPA. It features a large ferroan anorthosite patch in the southern part (Fig. 1). This structure looks like a huge debris flow of about 20 km in extent. The core of the central peak and the eastern part of the crater rim show a high Mg-rich content. The crater floor and the surrounding regions show a basaltic signature.

In the southern region of the SPA lies the large crater Antoniadi (137.9 km in diameter, centered at 69.3° S, 173.1° W). Its central peak and the inner mountain range show an increased content of Mg-rich rock, while the crater floor is covered by basaltic lava [18]. This fact is also captured by the petrological map (Fig. 2). There is, however, a large patch of ferroan anorthosite in the western region of the Antoniadi crater wall that looks rather like an outcrop rather than a debris flow. In order to examine this structure, we will include morphologic data in future studies.

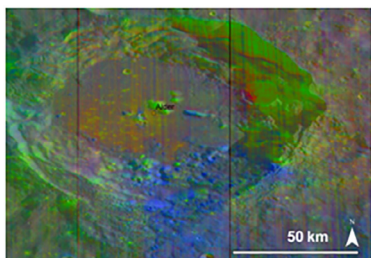


Fig.1. The crater Alder. The central peak region is composed of Mg-rich rock. A basaltic composition is found around the crater core. More important, there is an outflow patch of ferroan anorthosite content in the southern part. Furthermore, the northern and western areas of the crater rim show structures of increased Mg-rich rock.

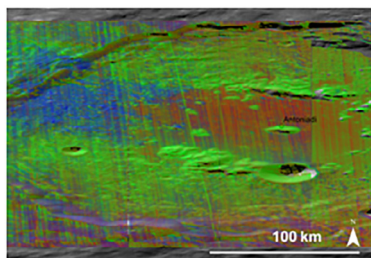


Fig.2. The crater Antoniadi. The Mg-rich rock content of the central peak and the inner mountain range that encloses the basaltic lava is well known [e.g. 18]. There is however, a large anorthositic patch on the western wall of the rim.

The crater Dryden (54.5 km in diameter, centered at 33.2° S, 156.2° S) lies in the eastern part of the SPA basin. This crater shows a significant Mg-rich rock content in the central peak and the crater rim (Fig. 3). The basaltic lava partially covers the floor but still shows a small signature of Mg-rich rock. A closer look on the northeastern part reveals an anorthosite signature of unknown origin. Again, further morphologic analysis is required to identify the origin of this highly interesting structure.

The crater Lyman (83 km in diameter, centered at 65° S, 162.5° E) resides in the western part of the SPA basin. Again, this crater shows a significant content of Mg-rich rock all over the central peak and the crater rim (Fig. 4). Due to the large gap of missing data, however, it is hard to identify further important structures.

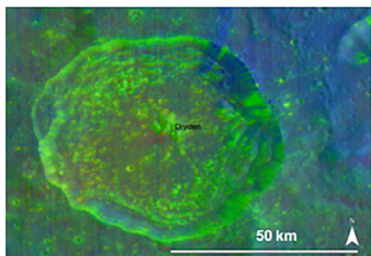


Fig.3. The crater Dryden. Mg-rich rock is found in high abundance on the terraces of the crater rim and the central peak. The basaltic lava on the crater floor partially covers underlying Mg-rich material.

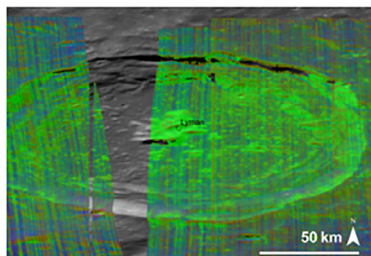


Fig. 4. The crater Lyman. The central peak and the crater rim are mainly composed of Mg-rich material.

SUMMARY AND CONCLUSION:

We presented petrological maps of four interesting craters, namely Alder, Antoniadi, Dryden, and Lyman. All craters show an increased Mg-rich rock content in the central peak region and the crater rims. More important, the craters Alder, Antoniadi, and Dryden show structures containing high abundances of anorthosite on the crater rim indicating geologically interesting events. We will include morphologic data into future studies to further analyze these interesting structures.

REFERENCES:

- [1] Petro, N.E. and Pieters, M. C. (2004) *J. Geophys. Res.*, 109, E06004. [2] Kim, K.J. et al. (2012) *Adv. Space Res.* 50, 1629-1637. [3] Pieters, C.M. et al. (2009) *Curr. Sci.*, 96(4), 500–505. [4] Boardman, J.W. (2011), *J. Geophys. Res.* 116(E6), E00G14. [5] Speyerer, E.J. et al. (2011), 42nd LPSC, Abstract #2387. [6] Scholten, F. (2012) *J. Geophys. Res.* 117(E12), E00H17. [7] Grumpe, A. et al. (2014) *Adv. Sp. Res.* 53(12), 17351767. [8] Grumpe, A. and Wöhler, C. (2014) *ISPRS J. Photogramm. Remote Sens.* 94, 3754. [9] Hapke, B. (1984) *Icarus* 59, 4159. [10] Hapke, B. (2002) *Icarus* 157, 523534. [11] Warell, J. (2004) *Icarus* 167(2), 271286. [12] Pieters, C.M. (1999) Workshop New Views of the Moon II, Abstract #8025. [13] Wöhler, C. et al. (2011) *Planet. Space Sci.* 59, 92-110. [14] Bhatt, M.U. et al. (2015) *Icarus* 248, 72-88. [15] Lawrence, D.J. et al. (1998) *Science*, 281 (5382), 1484-1489. [16] <http://www.mapaplanet.org/explorer/moon.html> [17] Berezhnoy, A.A. et al. (2005) *Planet. Space Sci.* 53, 1097–1108. [18] Sruthi, U. (2014) *Icarus*, 242, 249-268.

DEGRADATION OF SMALL CRATERS IN LUNAR HIGHLANDS

M.A. Kreslavsky¹, N.A. Kozlova², A.T. Basilevsky³, I. Zavyalov²

¹*Earth and Planetary Sciences, University of California - Santa Cruz, 1156 High Str., Santa Cruz, CA, 95064, USA*

²*MIIGAiK Extraterrestrial Laboratory, Moscow State University of Geodesy and Cartography (MIIGAiK), Moscow, Russia*

³*Vernadsky Institute, Moscow, Russia*

Contact: mkreslav@ucsc.edu

INTRODUCTION:

Small impact craters are the dominant surface features on almost all terrains on the Moon and many other bodies. On the Moon craters with diameter D smaller than a few hundred meters form an equilibrium population, that is the formation of new craters is balanced by obliteration of old ones: craters degrade getting shallower and softer with time and finally disappear. Since small fresh craters of the same D are approximately similar, crater depth can be used as a proxy for crater degradation state and therefore, its age. High-resolution digital topography models (DTM) that have become available recently enabled its quantitative analysis [1-3]. Here we report preliminary results from our new quantitative study for two typical highland sites.

MEASUREMENTS:

For morphometric measurements of small craters we used high-resolution DTM obtained by photogrammetric processing of stereo pairs of LROC NAC images. We chose two typical highland areas referred in the official LROC PDS release as "LUNA20-1" (4°N 56°E, 137 km²) and "FEOKTISTOV" (32°N 140°E, 194 km²) DTM products. These DTM have 2 m/pix sampling. We identified all small impact craters sufficiently well resolved by the DTM (~9000 for both sites combined) and measured their D with Cratertool plugin for ArcGIS [4]. Size-frequency distributions (Fig. 1) suggest that the survey is close to complete for $D > \sim 20$ m and $D > \sim 30$ m for these two sites, respectively. We applied an original ArcGIS plugin [5] for automated extraction of several other morphometric parameters: crater depth d' with respect to surroundings (Fig. 3), rim height $d-d'$, and missing volume. All these measurements are taken with respect to inclined plane approximating surrounding surface at the distance of D from the rim; this is essential due to the ubiquity of kilometer-scale slopes (6 - 10°) in the highlands [6].

AGE ESTIMATES:

We use d'/D as a measure of crater degradation state; traditionally used depth d with respect to the rim is not suitable for small craters, because degraded craters usually do not have apparent elevated rims. Since the craters degrade down to disappearance, identification of the most degraded craters cannot be objective. We have found [1] that craters with $d'/D > 0.05$ are identified reliably; we use only such craters for further quantitative analysis. Fig. 1 shows size-frequency distributions for craters with $d'/D > 0.05$ for both sites (exclusion of craters with $d'/D < 0.14$ in Fig. 1 has a very minor effect; see the next paragraph). It is seen that the equilibrium crater density on the ancient farside highlands (FEOKTISTOV) is greater than on Crisium basin ejecta (LUNA20), although both are typical highland terrains. We assumed that the crater population is in equilibrium, D does not change in the course of degradation and cratering rate is described by Neukum production function (NPF) [7]. Under these assumptions, the spatial density of craters of a given size gives the time needed to reach $d'/D = 0.05$. This time, for example, for $D \sim 80$ m craters is ~ 110 Ma (170 Ma) for LUNA20 (FEOKTISTOV) site.

FAST AND SLOW DEGRADATION REGIMES:

Cumulative frequency distributions of d'/D are shown in Fig. 2. The distributions for both sites are remarkably similar to each other; moreover, they are also similar to those for mare sites studied in [1]. If we assume that the crater population is in equilibrium and that crater diameters are not changed in the course of degradation, the steepness of the distributions in Fig. 2 is proportional to the crater degradation rate [1]. Fresh craters with high d'/D degrade quickly, and the degradation rate decreases sharply in the course of degradation. When d'/D decreases down to ~ 0.14 , the degradation rate becomes constant or only slowly decreasing. We have argued [1] that quick degradation of fresh ($d'/D > \sim 0.14$) craters occurs primarily due to regolith slides and avalanches on steep crater walls, while further slow degradation ($d'/D < \sim 0.14$) occurs due to regolith gardening processes. The

particular transition $d'/D \sim 0.14$ calculated as described in [1] is the same for high-land (this study) and mare [1] craters. This transition corresponds to the steepest slopes of the crater walls of $\sim 26^\circ$. This angle is likely close to the dynamic angle of repose of the lunar regolith under low lunar gravity [10].

TOPOGRAPHIC DIFFUSION MODEL:

Topography evolution caused by small-meteorite-induced regolith gardening has been shown [8] to be described by diffusion equation. In [9] degradation of larger ($D = 0.8 - 5$ km) mare craters has been successfully modeled with diffusion equation, and diffusivity estimate $K = 5.5 \text{ m}^2/\text{Ma}$ has been obtained. We tried to model degradation of small craters in the slow regime ($d'/D < 0.14$) with diffusion equation. We chose a realistically-looking initial radial profile of an axially symmetric model crater (black line in Fig. 3) conveniently described by simple functions (a Gaussian dome with a paraboloid cavity; this enables analytic solution of the diffusion equation). For this model the initial $d/D = 0.2$ (with respect to the rim), and there is no missing volume. Under these assumptions, the time needed to evolve from $d'/D = 0.14$ (red curve in Fig. 3) to $d'/D = 0.05$ (green curve) is $0.048D^2/K$. We again assumed that the crater population is in equilibrium, D does not change in the course of degradation, and cratering rate is described by NPF [7]. The modeled size-frequency distribution is shown in Fig. 1 with blue line. It is seen that K from [9] correctly predicts the order of magnitude for the equilibrium crater density, however, the modeled distribution is much shallower than the observed ones. Variation of K would shift the modeled distribution (Fig. 1) up or down, but would not change its slope: the slope is defined by the NPF slope and the fact that for diffusion the all times are proportional to D^2 .

DISCUSSION:

The discrepancy between the model and the observed population is caused by failure of one or several model assumptions. Although the absolute value of cratering rate for small craters is not well defined, the slope of the NPF is hardly too wrong, and our choice of NPF cannot account for the discrepancy. Our assumption of constant D is certainly wrong: craters expand in the course of degradation. For the particular model shown in Fig. 3 this expansion is insufficient to account for the observed discrepancy. However, our measurements show that, unlike for the model in Fig. 3, real craters often have non-zero missing volume. Modeling shows that expansion of craters with missing volume is more pronounced than in Fig. 3. We are working on a more realistic diffusive evolution model that takes crater expansion into account. It is possible, however, that crater evolution is not described by topographic diffusion, for example, it is not excluded that deposition of ejecta from distal impacts plays a greater role in crater degradation than local transport induced by tiny meteorites and described by the diffusion equation. Finally, it is not excluded, that the "equilibrium" population of craters is not in the detailed equilibrium state, for example, crater degradation and obliteration might be dominated by rare resurfacing episodes (earthquakes, large distal impacts, etc.) with gradual accumulation and minor degradation between them.

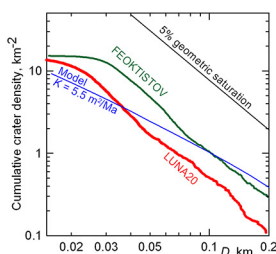


Fig. 1.

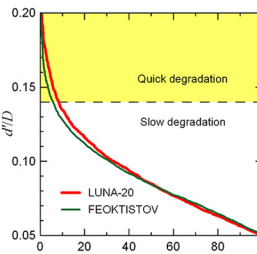


Fig. 2.

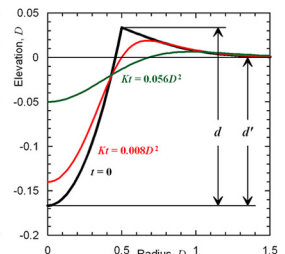


Fig. 3.

ACKNOWLEDGEMENTS:

All technical work on crater morphology was carried out by NK and IP at MIIGAiK under Russian Science Foundation support, project 14-22-00197

REFERENCES:

- [1] Basilevsky A. et al. (2014) *PSS* 92 77-87. [2] Mahanti P. et al. (2015) *LPSC* 46, 1615. [3] Mahanti P. et al. (2016) *LPSC* 47, 1202. [4] Kneissl T. et al. (2011) *PSS* 59, 1243-1254. [5] Kokhanov A. et al. (2015) *Solar System Res.* 49, 295-302. [6] Kreslavsky M. and Head J. (2016) *Icarus* 273, 329-336. [7] Neukum G. et al. (2001) *Space Sci. Rev.* 96, 55-86. [8] Soderblom L. (1970) *JGR* 75, 2655-2661. [9] Fassett C. and Thomsson B. (2014) *JGR* 119, 2255-2271. [10] Kleinhans, M. G. et al. (2011) *JGR* 116, E11004.

COLD AND HOT MODELS OF THE LUNAR MANTLE

E.V. Kronrod, V.A. Kronros, O.L. Kuskov

Vernadsky Institute of Geochemistry and Analytical Chemistry, RAS, Kosygina st., 19, Moscow, Russia

Contact: e.kronrod@gmail.com

The empirical dependences of the lunar silicate fraction bulk concentration of Al_2O_3 , FeO and #Mg on the average volume temperature (T_{mean}) in the range of $780^\circ\text{C} < T_{\text{mean}} < 1100^\circ\text{C}$ have been estimated. All of the models of the Moon can be conventionally divided into "cold" models ($T_{\text{mean}} \approx 780\text{-}880^\circ\text{C}$, $\text{Al}_2\text{O}_3 \approx 3.4\text{-}4.4$ wt.%, FeO ≈ 11.5 wt.%) and "hot" models ($T_{\text{mean}} > 970^\circ\text{C}$, $6.8 > \text{Al}_2\text{O}_3 > 5.0$ wt.%, FeO $\sim 11\text{-}12$ mac.%, with monotonic linear trend between them. Alumina content of "cold" model is similar to that of the Earth's mantle; "hot" models are considerably enriched in alumina as compared with the Earth.

INTRODUCTION:

Internal structure of the Moon is determined by its thermal regime, composition and magmatic evolution. The aim of this study was to estimate effect of the temperature on the bulk chemical composition of the silicate Moon for the model of magma ocean with joint inversion of gravitational, seismic and petrological data.

MODEL AND METHOD

In our modeling we used the hypothesis of lunar magma ocean LMO [1;2;3]. Monte-Carlo method was applied for the calculations. With inversion of gravitational (mass, moment of inertia (MOI)) [4], seismic (P- and S- waves velocities) and petrological (mass balance relations) data we investigated the effect of temperature distribution in the lunar mantle on bulk crust+mantle chemical composition. The model of chemical differentiation of LMO into crust, upper mantle, middle mantle and lower mantle with primitive undifferentiated composition was assumed.

Our model assumes that the Moon consists of five spherical layers: crust (0-40 km), upper mantle (40-230 km), middle mantle (230-750 km), lower mantle and Fe-S core. Core sizes were estimated from constraints on mass and MOI. Main oxides concentrations, mineral composition and physical properties in the each mantle zone were calculated with inversion of geophysical (mass, MOI, seismic velocities) and geochemical data [5,6]. Constraints on seismic velocities were assumed from model [7]. Modeling of the phase composition and physical properties of the mantle was performed for the dry system CaO-FeO-MgO-Al₂O₃-SiO₂ (CFMAS) [5,6,8] including the phases of nonideal solid solutions with the software and database THERMOSEISM [8]. The Monte-Carlo method was used to solve the problem.

To estimate the effect of mantle temperature on the composition of the silicate fraction of the Moon we calculated multiple models of the Moon with wide temperature range. Based on these models qualitative and quantitative dependencies between lunar composition and temperature distribution were estimated.

In order to provide all possible temperature variants from the majority of available temperature models of the Moon the group of temperature profiles models was selected. On the base of available published data and our numerical modeling ranges of possible mantle temperatures were specified as follows: in the upper mantle at the depth of 150 km ($470^\circ\text{C} < T_{150} < 750^\circ\text{C}$); in the lower mantle at the depth of 1000 km ($1000^\circ\text{C} < T_{1000} < 1400^\circ\text{C}$) [9, 10, 11]. In the middle mantle we imposed condition of positive vertical temperature gradient. For each selenotherm from selected range physical properties (density, seismic velocities) and main oxides concentrations in the mantle were calculated. As an integral characteristic of the thermal field of the Moon the volume-averaged mantle temperature T_{mean} was selected, which implies total temperature level in the mantle. In our calculations T_{mean} is within $780^\circ\text{C} - 1090^\circ\text{C}$.

RESULTS

The dependencies between Al_2O_3 , FeO bulk and silicate Moon's fraction concentrations and #Mg and bulk mantle temperature (T_{mean}) were estimated. All considered modes can be conventionally divided into "cold" models ($T_{\text{mean}} \approx 780\text{-}880^\circ\text{C}$, $\text{Al}_2\text{O}_3 \approx 3.4\text{-}4.4$ wt.%, FeO ≈ 11.5 wt.%) and "hot" models ($T_{\text{mean}} > 970^\circ\text{C}$, $6.8 > \text{Al}_2\text{O}_3 > 5.0$ wt.%, FeO ≈ 11 wt.%) with monotonous linear trend between them. Al_2O_3 content in "cold" models is similar to that of Earth's value and "hot" models are considerably enriched in alumina as compared to Earth. Magnesium number #Mg is 0.82-0.83 for all temperatures. Increasing of T_{mean} in the lunar mantle

under constant pressure and composition conditions leads to decreasing of both density and P- and S- velocities in each mantle layer. On the contrary, velocity and density can remain almost constant if increasing of temperature with depth are compensated by the corresponding pressure and composition variations. Increase of Al_2O_3 concentration ($C_{Al_2O_3}$) results in density increase as well as seismic velocities increase, particularly in the lower mantle by reason of the garnet portion increase [9]. Therefore the solution for “cold” and “hot” models is generally determined through $C_{Al_2O_3}$ variation, C_{FeO} и MG# remain almost constant.

Linear dependences between probable bulk concentrations (Al_2O_3 , FeO, wt. %), #MgO and parameter T_{mean} were revealed. These dependences provide bulk silicate Moon composition estimation from given temperature profile in the lunar mantle. It is enough to define temperature at three points of the temperature profile – at the depth of 150, 500 and 1000 km (T_{150} , T_{500} , T_{1000}) and calculate T_{mean} . In the Table 1 estimations of T_{mean} , $C_{Al_2O_3}$, C_{FeO} , #MgO for two variants (for “hot” and “cold” Moon) are represented.

Table 1. Parameters T_{mean} , $C_{Al_2O_3}$, C_{FeO} , #MgO for “cold” and “hot” models of the Moon

Model	T_{150}	T_{500}	T_{1000}	T_{mean}	$C_{Al_2O_3}$	C_{FeO}	#MgO
Cold	600	900	1200	880	4.3	11.4	0.82
Hot	700	1100	1300	1020	5.9	11.0	0.83

According to calculations the size of Fe-S core is almost independent of thermal regime in the mantle. For models from Tab.1 we obtained the following results: $R_{core\ hot} = 315 \pm 37$ km, $R_{core\ cold} = 310 \pm 32$ km.

CONCLUSIONS

Average volume temperature (T_{mean}) as well as mass, moment of inertia and seismic velocities is important parameter which controls chemical and mineralogical composition of the Moon. All temperature models of the Moon can be divided into “cold” models ($T_{mean} \sim 780-880^\circ C$) and “hot” ($T_{mean} > 970^\circ C$). Bulk alumina content for “cold” models ($Al_2O_3 \sim 3.4-4.4$ wt.%) is similar to bulk silicate Earth (BSE), whereas “hot” models are considerably enriched in Al_2O_3 ($\sim 5.0-6.8$ wt.%) against BSE. Magnesium number for both type of models is oppositely almost constant (MG# 82-83) and concentration of FeO is $\sim 11-12$ wt.%, which is considerably different from that for BSE (FeO $\sim 8\%$ and MG# 89).

For all variants of temperature distribution the silicate Moon is enriched in SiO_2 , FeO and depleted in MgO against Earth’s mantle, which indicates significant difference in Moon’s and Earth’s compositions.

The size of Fe-S core weakly depends on the thermal regime in the lunar mantle.

ACKNOWLEDGMENTS:

This research was supported by the RFBR grant 15-05-0257 2 and 15-05-01161.

REFERENCES:

- [1] Shearer, C.K. et al., 2006. Thermal and magmatic evolution of the moon. *New Views Moon Rev. Mineral. Geochem.* 60, 365–518.
- [2] Wieczorek M.A. et al., 2006. The constitution and structure of the lunar interior. *Rev. Mineral. Geochem.* 60, 221–364.
- [3] Elardo, S. M. et al., 2011. Lunar magma ocean crystallization revisited: bulk composition, early cumulate mineralogy, and the source regions of the highlands Mg-suite. *Geochim. Cosmochim. Acta* 75, 3024–3045.
- [4] Williams J.G. et al., 2014. Lunar interior properties from the GRAIL mission. *J. Geophys. Res. Planets*, 119, 1546–1578
- [5] Kronrod V.A., Kuskov O.L., 1997. Chemical composition, temperature, and radius of the lunar core from geophysical evidence. *Geochem. Int.*, 35, 4–12.
- [6] Kuskov O.L., Kronrod V.A., 1998. A model of the chemical differentiation of the Moon. *Petrology*, 6, 564–582.
- [7] Gagnepain-Beyneix, J. et al., 2006. A seismic model of the lunar mantle and constraints on temperature and mineralogy. *Phys. Earth Planet. Interiors* 159, 140–166.
- [8] Kronrod, V.A., Kuskov, O.L., 2011. Inversion of seismic and gravity data for the composition and core sizes of the Moon. *Izv. Phys. Solid Earth* 47, 711–730.
- [9] Kuskov, O.L., Kronrod, V.A., Kronrod, E.V., 2014. Thermo-chemical constraints on the interior structure and composition of the lunar mantle, *Physics of the Earth and Planetary Interiors*, doi: <http://dx.doi.org/10.1016/j.pepi.2014.07.011>
- [10] Kuskov O.L., Kronrod V.A., Kronrod E.V., 2016. Testing the reference Moon model in respect of the thermal regime and chemical composition of the mantle: Thermodynamics versus seismology. *Izvestiya, Physics of the Solid Earth* 52, 3, 344–352
- [11] Kuskov O.L., Kronrod V.A., Kronrod E.V., 2015. Thermochemical constraints on the thermal state, composition, and mineralogy of the upper mantle of the Moon: Evidence from the seismic models. *Astronomicheskii Vestnik*, 49, No. 2, 83–99

RECENT RESULTS FROM THE LUNAR RECONNAISSANCE ORBITER MISSION

J.W. Keller¹, N.E. Petro¹

¹Goddard Space Flight Center, Greenbelt, MD, USA

Contact: john.keller@nasa.gov

INTRODUCTION:

Since entering lunar orbit on June 23, 2009 the Lunar Reconnaissance Orbiter (LRO) has made comprehensive measurements of the Moon and its environment. The seven LRO instruments use a variety remote sensing techniques to obtain a unique set of observations. These measurements provide new information regarding the physical properties of the lunar surface, the lunar environment, and the location of volatiles and other resources. Scientific interpretation of these observations improves our understanding of the geologic history of the Moon, its current state, and what its history can tell us about the evolution of the solar system. Scientific results from LRO observations overturned existing paradigms and deepened our appreciation of the complex nature of our nearest neighbor. LRO has been in orbit for seven years, in that time it has been a witness and leader of a remarkable era of lunar science where a paradigm shift is taking place from the view of the Moon as a static planet to one with active processes on multiple scales. With ample fuel to remain in orbit (for up to eight more years) and a healthy suite of instruments and spacecraft systems, LRO is ready to continue uncovering and addressing key planetary science questions.

The mission is underwent Senior Review in May, in order to extend the mission two more years. The Cornerstone Mission will take LRO to 2018, meaning that LRO will have been at the Moon for ~100 lunar days, and will shed light on the processes that continue to shape and re-shape the Moon today.

As part of the Senior Review process, we proposed to return the Mini-RF instrument to a fully operational status. The Mini-RF team has investigated possibly using an antenna at Goldstone as a transmitter at X-band wavelength (4.3cm). This addition, as well as new operational modes from several other instruments enables LRO to make new measurements during the next two years of operation.

SPACECRAFT STATUS:

The LRO spacecraft and instrument suite are in good health, with no significant degradation. The orbit we are in is quasi-stable allowing us to preserve the small amount of fuel we have left so that we can possible rephrase the orbit in order to observe scientifically unique events (e.g., spacecraft impacts). The LRO spacecraft has been in an elliptical, polar orbit with a low perilune over the South Pole since December 2011 (Figure 1). This orbit minimizes annual fuel consumption, enabling LRO to use fuel to maximize opportunities for obtaining unique science.

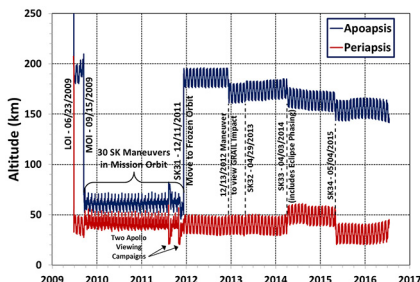


Fig. 1. Apsis History of the LRO Spacecraft

LRO DATA:

The LRO instrument teams deliver data to the Planetary Data System (PDS) every three months, data that includes raw, calibrated, and gridded/map

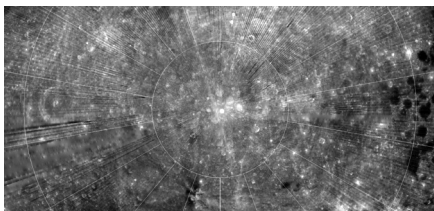


Fig. 2. LOLA-derived 1064nm albedo of the South Pole. Map uses an orthographic projection centered on the South Pole, with the lunar nearside at the top.

products [3]. New higher-level data products are regularly added to the PDS archive; here we highlight just a few of those products and data tools.

LOLA GLOBAL ALBEDO:

Using the energy of the reflected laser pulse from LOLA, a global albedo map at 1064 nm and 0° phase angle [4] has been produced (Fig. 2). That these maps are generated using the active LOLA instrument, areas that are otherwise in permanent shadow are visible (note the relatively brighter interior of Shackleton Crater [5]). The maps are available via the PDS at a range of resolutions, globally at 10 pixels per degree (ppd) or at 1km per pixel for areas poleward of 50° N/S.

LROC NAC DTM:

Repeated imaging of selected targets enables the generation of localized, high-resolution digital terrain models (DTMs). Hundreds of these DTMs are available at scales of ~2 meters per pixel for a range of targets and areas of interest (e.g., Apollo and Luna landing sites, LADEE impact site, other areas of interest).

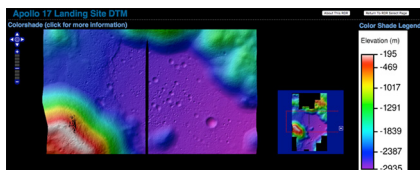


Fig. 3. Example of the web interface with the Apollo 17 DTM [6].

LROC WAC MOSAICS:

There are a number of WAC products available [6] including empirically normalized reflectance maps, low and high sun angle mosaics, and a number of low-sun mosaics from several months-long imaging campaigns (Figure 4). These products are extremely useful for characterizing surface morphology.



Fig. 4. WAC Mosaic systematically acquired in June 2012. Orthographic projection centered on the farside.

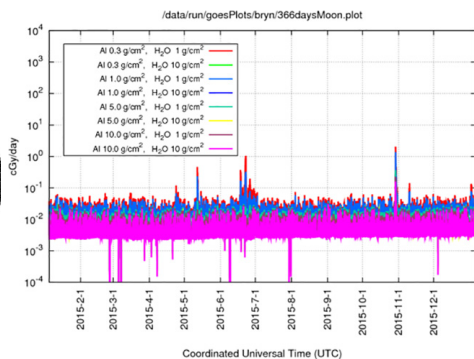


Fig. 5. Plot of the radiation received at the Moon, with various modeled doses received behind thicknesses

CRaTER Data: The CRaTER instrument provides data to the Prediccs website, an on-line system to predict and forecast the radiation environment at the Moon [7]. The on-line tool allows the user to view the radiation dose (at the Earth, Moon, or Mars) over the past 366 (Figure 5), 31, or 7 days.

SMALL LUNAR CRATERS SIZE-FREQUENCY DISTRIBUTION: DEGRADATION AND WIDENING

B.A. Ivanov

Institute for Dynamics of Geospheres, Russian Academy of Science, Leninsky Prospect 38-1, Moscow, Russia, 119334
 Contact: baivanov@idg.chph.ras.ru

INTRODUCTION:

New LROC images and DTM expand our understanding of small (diameters less than ~100m) impact crater evolution [1, 2, 3]. The new data allow us to measure crater degradation [2, 3] and to discuss small crater equilibrium in the new data context.

SMALL CRATER DEGRADATION:

It is well known that the number of small craters per unit area is limited as older craters vanish due to degradation and younger crater overlapping. Key ideas and references one can find in [4, 5, 6]. The observation of just formed new impact craters [7] creates the basis for study of the crater shape evolution from the crater birth to the degradation toward the unobservable state.

DEGRADATION MODELING.

We repeat the most simple modeling of the crater erosion due to smaller impacts. The downslope material motion is numerically simulated with the diffusion model [8, 9, 10]. To mimic the possible non-linear diffusion [11] we test the option to have 2 to 10 times faster diffusion at steep slopes – in the spirit of [2] where landslides at steep crater slopes move material faster than by small cratering mass motion in [8]. The main new observation is that the diameter at the crater rim (taken as the point of the maximum altitude) is increased about twice before the depth/diameter ratio decreased to the unobservable value of about 0.03 [2, 3]. The effect is visible but not discussed explicitly in [9], and missed in [8] where the author have used only one Bessel function having constant max and min distances. The correct expanding over Bessel functions is used in [10].

COMPARISON WITH OBSERVATIONS.

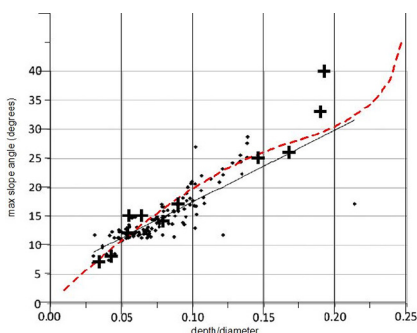


Fig. 1. The maximum slope vs. depth/diameter ratio for craters in various degradation stage: small dots are from [2], crosses are for craters with D from 200 to 900 m (this work); the red dashed curve is numerical model (this work).

The most abundant data over the depth/diameter and slope evolution are presented in [2]. We use publicly available LROC DTM with 2 m/pix resolution for larger craters than in [2] to check the universalism of the relations.

Fig. 1 demonstrates that small craters measured in [2] and larger simple craters obviously have very similar “degradation trajectory”. The simple diffusion model reproduces the “trajectory” pretty well. However the detailed comparison with crater profiles measured in this work (black crosses in Fig. 1) are not well reproduced with the model. The current impression is that the simple diffusion model overestimates the crater widening.

The attempt to mimic the “high rate evolution” of steep slopes we assumed artificially 2 to 10 times larger diffusion coefficient at the slope above some critical inclination. These model variants give much faster evolution in time, but do not change dramatically the model “evolution trajectory” shown in Fig. 1 as the red dashed curve.

The main consequence of our modeling – the demonstration of the fact that small craters during the evolution from A to B to C type may increase their visible diameter factor of 1.5 to 2. It means that at the crater counts with a standard $2^{1/2} = 1.41$ logarithmic step craters with the same initial diameter but in different degradation state may occupy neighboring bins, affecting the general size-frequency distribution (SFD).

EQUILIBRIUM AREAL DENSITY:

We have made an attempt to test the crater widening effect with a simple Monte-Carlo modeling. The model generate “craters” in a wide range of diameters with the random number generator. The SFD of fresh craters gives $N_{>D} \sim D^{-3}$. Each crater evolves in a time according to the model, shown in Fig. 1. While a “crater” reaches the critical depth/diameter ratio of ~ 0.03 it is removed from statistics. The absolute value of the diffusion coefficient in the degradation model is chosen arbitrary to have the establishing of the equilibrium state near $D=10$ m. As the model assumes the constant diffusion coefficient, the absolute size of craters may be chosen arbitrary.

The modeling run include 10 trials, 3 millions “craters from 1m to 100 m are generated in each trial. This number of craters allow us to use relatively narrow diameter bins $D_{\text{right}}/D_{\text{left}} = 1.1$. Number of craters in each bin is averaged over trials.

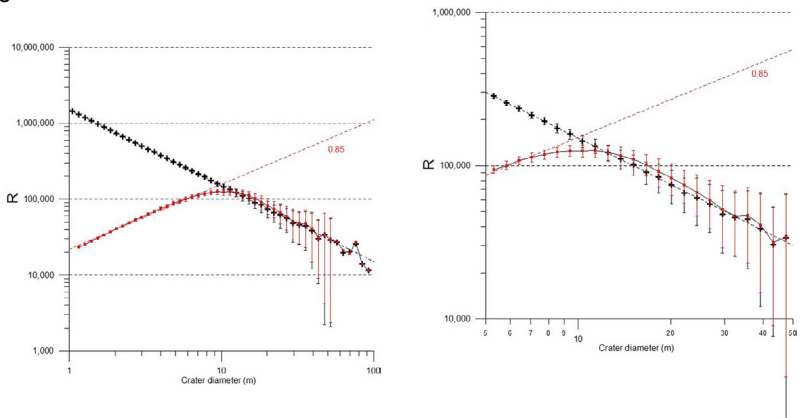


Fig. 2. Left panel – the relative plot (R-plot) of small crater SFD counted by the initial diameter (black crosses and error bars) and by the model diameter increasing with the degradation (red points and error bars). Right panel – the fragment of the left figure outlining the transition to equilibrium.

Fig. 2 illustrates changes of a simple crater SFD due to degradation with the crater widening. The main (trivial) effect is the rollover of the SFD curve for small craters due to erosion of craters. To the right of the bending point the SFD is slightly uplifted due to crater widening. However the effect is in the limits of 1 sigma error bars. At the same time the formal slope of the SFD here is slightly more steep than for the primary (fresh) crater population.

CONCLUSIONS:

The crater degradation along the line A-B-C craters [2] is complying with the crater widening. This modest widening (less than a factor of 2 in the crater diameter) results in the minor change of the SFD slope in comparison with the fresh crater SFD. This fact should be taken into account in the SFD comparison of just formed (“new”) small lunar craters [7] with standard A-B-C crater counts.

The degradation model (at least – tested variants) also result in the R-plot slope of small craters in equilibrium below 1 (-2 exponent in the cumulative shape). The value of this slope (Fig. 2) about 0.85 is close to the “empiric value” of 0.78, previously proposed by Hartmann [12].

ACKNOWLEDGEMENTS:

The project is supported by Russian Academy of science Presidium’s Program 9.

REFERENCES:

- [1] M. Robinson, et al. (2010) *Space science reviews* 150(1):81.
- [2] Basilevsky, A.T. et al. (2014) *Planetary and Space Science*, 92, 77-87.
- [3] Mahanti, P. et al. (2015) *LPSC 46th*, abs. #1615.
- [4] Richardson, J.E. (2009) *Icarus*, 204, 697-715.
- [5] Fassett, C.I., and B.J. Thomson (2014) *Journal of Geophysical Research (Planets)*, 119, 2255-2271.
- [6] Xiao, Z., and S.C. Werner (2015) *Journal of Geophysical Research (Planets)*, 120, 2277-2292.
- [7] Thompson, S.D. et al. (2014) *LPSC 45th*, abs. # 2769.
- [8] Soderblom, L.A. (1970) *Journal of Geophysical Research*, 75, 2655-2661.
- [9] Fassett, C.I., and B.J. Thomson (2014) *Journal of Geophysical Research (Planets)*, 119, 2255-2271.
- [10] Xie, M., and M.-H. Zhu (2016) *Earth and Planetary Science Letters*, 440, 71-80.
- [11] Minton, D.A., and C.I. Fassett (2016) *LPSC 47th*, abs. # 2623.
- [12] Hartmann, W. K. (1984) *Icarus*, 60, 56–74.

THREE-STAGE ERUPTION SEQUENCE IN LUNAR SHIELD VOLCANOES AND THE PRODUCTION OF MAGMATIC FOAM

L. Wilson^{1,2}, J. Head¹

¹Brown University, Providence, RI USA

²Lancaster University, Lancaster, UK

SUMMARY:

Volcanic eruptions on the Moon take place in conditions very different from those on Earth. Obvious differences are (i) the lower acceleration due to gravity on the Moon and (ii) the absence of any significant atmospheric pressure. Additional differences are (iii) the propensity for lunar eruptions to be fed by dikes that extend through the crust and into the upper mantle delivering only mafic magmas, and (iv) the likelihood that all lunar eruptions begin with an explosive phase. An important similarity between lunar and terrestrial mafic eruptions is the importance of the presence of magmatic water exsolved in the final stages of approach of magma to the surface. However, we show that water release in lunar magmas can produce an extremely highly vesicular foam that is stable on the time scale of an eruption. Subsequent destruction of this foam by micrometeorite bombardment can lead to interesting consequences.

INTRODUCTION:

The absence of any atmosphere on the Moon means that, on approaching the surface, all magmas will attempt to release all of the volatile species that they contain in solution or can generate by chemical reactions at low pressures. A common component of mafic melts in the lunar mantle is graphite, and reactions between graphite and various metal oxides produce CO gas at a pressure of ~40 MPa (1-6) which occurs at ~10 km depth. This gas production ensures that essentially all lunar eruptions begin with an explosive phase. The initial stage of the eruption is fed by a dike that is likely to extend completely through the lunar crust into the upper mantle (7) and the great width of this dike ensures a high magma discharge rate. As the initially high excess pressure in the dike is lost and the dike begins to close due to the elastic response of the crust, the discharge rate must decrease and eventually become very small. The discharge rate, i.e. the volume flux, is the product of the cross sectional area of the dike and the magma rise speed within it. As the dike closes, wall friction becomes ever more important and the magma rise speed decreases. Initially, the magma rise speed is so great that gas bubbles nucleating in the magma will have buoyancy-driven rise speeds through the magmatic liquid that are many orders of magnitude less than the rise speed of the magma itself through the dike. This means that a uniform distribution of gas bubbles exists in the magma as it reaches the surface, and the expansion of these bubbles into the lunar vacuum causes the magma to fragment into sub-mm-sized droplets that emerge in a nearly steady Hawaiian-style eruption. However, as the magma speed decreases, the difference between the magma speed and the bubble speeds becomes less, and the greater transit time allows large bubbles to overtake small ones and coalesce with them. At a sufficiently small magma rise speed the process reaches a run-away state, with occasional very large gas bodies emerging though a pond in the vent and bursting as they expand into the vacuum - this is Strombolian activity. As the magma rise speed at depth approaches zero, the last magma to pass through the 40 MPa pressure level delivers the last Strombolian explosion at the surface and the remaining closure of the dike squeezes out magma in which the only gas production is the release of water vapor. At the several hundred ppm water contents typical of many lunar magmas (9-11) the gas bubble sizes are so small that surface tension forces allow them to remain stable against the internal gas pressures and so to form a foam that can have a vesicularity up to ~95%. This is the last material to be extruded and can extend for a few to several hundred meters below the surface.

HAWAIIAN EXPLOSIVE PHASE:

With negligible separation of gas bubbles and liquid, steady Hawaiian fire fountains under lunar conditions will have had the same morphology as the umbrel-

la-shaped plumes on Io (7) but with a very different opacity. Total released gas contents in lunar eruptions were up to a few thousand ppm, whereas those on Io involve up to 30% by mass volatiles (12). As a result, the maximum ranges of pyroclasts in steady lunar eruptions are from ~1 to less than 10 km (7) to be contrasted with ranges up to 300 km on Io. The much greater crowding of pyroclasts in lunar fire fountains makes them optically dense so that heat cannot escape from the interior and clasts land at magmatic temperatures to coalesce into a lava pond feeding lava flows. An outer shell of cooled pyroclasts can form a cinder/spatter cone around the central lava pond. Some small shield volcanoes on the Moon may be constructed largely from pyroclastics in this way if the magma volume eruption rate is relatively small and the volatile content is relatively large. In other cases, where the volume eruption rate is relatively large and the volatile content is relatively small, essentially all of the pyroclasts enter the pond and feed lava flows that reach cooling-limited lengths of at most a few tens of km, the length being determined by the volume flux (13).

STROMBOLIAN EXPLOSIVE PHASE:

As the volume flux declined towards the end of an eruption, the rise speed of the magma decreased and it became ever more likely that CO bubbles would have had time to coalesce as they ascended through the rising magma. This would have led to a change in eruption style towards Strombolian activity. Large bubbles of CO would have risen through the lava pond, updoming the lava surface, and clots of the fragmented skin of the bubble would have been ejected as pyroclasts as the bubbles burst. Loss of magma from the vent to form these pyroclasts would have been compensated by the slow rise of magma through the dike and near-surface conduit, and H₂O gas bubbles would have continued to nucleate in the rising magma as it neared the surface. Generalization of the model developed by (14) for terrestrial Strombolian activity to lunar conditions suggests that bubble coalescence will be efficient as long as magma rise speeds are less than ~5 m s⁻¹, easily satisfied in the late stages of lunar eruptions.

FOAM EXTRUSION STAGE

The final stage of an eruption occurs when the magma rise speed becomes vanishingly small. No further CO is produced because no magma is passing through the 40 MPa level, and a final large bubble of CO emerges at the surface in a final Strombolian explosion. The dike is now relaxing elastically as the excess pressure in the magma vanishes and residual dike magma is squeezed towards the surface. The top of the magma column consists in part of pyroclastic material of a range of sizes that fell back into the vent after the last CO bubble burst and otherwise of uncooled magma exposed to the overlying vacuum. Bubbles of water vapor that have nucleated in this magma will expand as a result of the decompression they experience as the magma skin overlying the last CO bubble is ejected and the bubble gas pressure is lost. If these bubbles survive for long enough, they will also grow by continued diffusion of H₂O molecules through the magmatic liquid, and larger bubbles will grow at the expense of smaller ones with which they are in contact by the process of Ostwald ripening. It is possible that bubbles in contact with the magma surface will explode in a mini-strombolian fashion because they have gas at a finite pressure on one side of the liquid film forming the bubble wall but have a hard vacuum on the other side. This tendency will be resisted by capillary forces controlled by the surface tension of the magma, σ , ~0.37 J m⁻². Specifically, the bubbles will be able to avoid rupture as long as the gas pressure inside them is less than a critical value, P_c , given by (15) as $P_c = [(4 \sigma) / R]$ where R is the bubble radius.

The internal pressure and bubble size can be calculated by assuming a value for the vesicularity of the magma under these conditions. In a series of experiments in which melted samples of terrestrial basalts were exposed to progressively lower pressures in a vacuum system, (16) found that vesicularities of up to 94% were produced. This is comparable to the vesicularities of up to 96% in reticulite clasts from basaltic eruptions measured by (15). Bubble sizes in the experimental foams were mainly in the range 100-1000 microns, and some bubble bursting occurred as the pressure decreased below ~3 kPa. These findings are in good agreement with the above equation and suggest using a vesicularity of 96%. The solubility of water as a function of pressure in mafic magma given by (17) can be used to find the mass fraction exsolved, $n_{\text{H}_2\text{Oe}}$, at any given pressure given an assumed total amount present in the pre-eruption magma, and an assumed magma temperature allows

the density of this vapor to be found. The implied vesicularity is then calculated from the mass fractions and densities of the H_2O vapor and the magmatic liquid, and the pressure, P_f , is varied until the required 95% vesicularity is found. The water vapor bubble radii are found by assuming that they nucleate at the saturation pressure relevant to the assumed total amount of water, n_{H_2O} , with a radius of 10 microns (18) and expand isothermally to a radius R at the pressure P_f . The value of P_c corresponding to this radius is then found.

As long as P_f is greater than P_c the foam is stable. If the reverse is true, bubbles at the top of the foam burst and the bursting process propagates down into the foam producing a loosely-packed layer of bubble wall magma fragments with a density ρ of order half that of the magma, say 1500 kg m^{-3} . The underlying foam becomes stable when the depth of the fragmental layer reaches a value $D = (P_f - P_c) / (\rho g)$ where g is the acceleration due to gravity. The table below shows representative examples of the relevant parameters.

This latter stage of foam development should be characteristic of dikes and conduits beneath summit pit craters on small shield volcanoes (19-20) and extrusion and modification may provide an explanation for some of the unusual textures and features observed in these environments.

Table: Foam parameters. Values of water vapor pressure, P_f , in bubbles near the surface of magmatic foam with 95% vesicularity as a function of the total pre-eruption magma water mass fraction, n_{H_2O} . The mass fraction of water exsolved into the vapor bubbles is n_{H_2Oe} , the typical bubble radius is R , and the capillary pressure preventing rupture of the foam is P_c . When P_f exceeds P_c , as in the case for $n_{H_2O} = 1000$ ppm, a thickness D of accumulated pyroclastic debris is needed to stabilize the foam.

n_{H_2O}	P_f	n_{H_2Oe}	R	P_c	D
/ppm	/kPa	/ppm	/m	/kPa	/m
1000	85.4	807	21.9	67.5	7.36
500	40.8	385	20.1	73.4	not needed
250	19.2	182	18.6	79.6	not needed

REFERENCES:

- (1) Sato, M., 1976. Proc. Lunar Sci. Conf. 7, 1323–1344.
- (2) Sato, M., 1979. Proc. Lunar Sci. Conf. 10, 311–325.
- (3) Fogel, R., Rutherford, M., 1995. GCA 59, 201–215.
- (4) Nicholis, M.G., Rutherford, M.J., 2006. Lunar Planet. Sci. 37. Abstract 2061.
- (5) Nicholis, M.G., Rutherford, M. J., 2009. GCA 73, 5905–5917.
- (6) Wetzel, D.T., et al., 2015. Nature Geoscience 8, 755–758.
- (7) Wilson, L. and Head, J., 2016. Icarus, <http://dx.doi.org/10.1016/j.icarus.2016.05.031>
- (8) Saal, A. E., et al., 2008. Nature 454 (7201), 192–195.
- (9) Hauri, E.H., et al., 2011. Science 333, 213–215.
- (10) Hauri, E.H., et al., 2015. Earth Planet. Sci. Lett. 409, 252–264.
- (11) Kieffer, S.W., 1982. in Satellites of Jupiter, edited by D. Morrison, pp. 647–723, Univ. of Ariz. Press, Tucson.
- (12) Pinkerton, H. & Wilson, L., 1994. Bull. Volcanol. 56 (2), 108–120.
- (13) Parfitt, E.A. and Wilson, L., 1995. Geophys. J. Internat. 121, 226–232.
- (14) Mangan, M.T. and Cashman, K. V., 1996. J. Volcanol. Geotherm. Res., 73, 1–18.
- (15) Fielder, G., Guest, J. E., Wilson, L. and Rogers, P. S., 1967. Planet. Space Sci. 15 (11), 1653–1666.
- (16) Dixon, J.E., 1997. American Mineralogist 82, 368–378.
- (17) Sparks, R.S. J. 1978. J. Volcanol. Geotherm. Res., 3, 1–37.
- (18) Head, J. and Gifford, A. 1980. Moon and Planets, 22, 235–258.
- (19) Head, J. and Wilson, L., 2016. Icarus, doi:10.1016/j.icarus.2015.12.039.

STATUS OF LUNA-25 LANDING SITE SELECTION

I.G. Mitrofanov

Space Research Institute of Russian Academy of Sciences (IKI RAS), 117997, 84/32 Profsoyuznaya str., Moscow, Russia
Contact: imitrofa@space.ru

INTRODUCTION:

Luna-25 is the first Russian robotic mission to the Moon since the last Soviet mission Luna-24 of 1976. Luna-25 is the polar lander, which is currently under development for the launch in 2019. There are two main goals of this mission. The scientific goal is to perform the first studies of lunar polar regolith and lunar polar exosphere, which are thought to be quite different from the well-known regolith and exosphere at moderate and equatorial latitudes. The technological goal is to test and to validate the main systems of the spacecraft at all main stages of the mission: cruise flight, pre-landing orbital flight, soft landing, surface operations at the day-time period with solar illumination and survival capabilities at the night-time period of darkness. Successful accomplishment of these two goals depend on the proper choice of landing site, which should be based both on the engineering requirements, as well as on demands of scientific investigations.

ENGINEERING REQUIREMENTS FOR LANDING SITE SELECTION:

The landing site for Luna-25 should be selected in accordance with the following requirements: The first, local slopes should not exceed 7 degrees to avoid overlapping of the spacecraft at the moment of touching of the surface. The second, total fraction of illumination period of a lunation cycle should be large enough, about 40%. The third, spacecraft should have the permanently reliable radio link with the ground stations on the Earth. The fourth, solar irradiation during the lunation mid-day should not result to overheating of the spacecraft. There are available data from the NASA's LRO mission (LOLA laser altimeter, LROC cameras, etc.), which are used to look for possible landing sites in accordance with these criteria.

SCIENCE DEMANDS FOR LANDING SITE SELECTION:

The area for on-surface investigations should have enhanced content of water in the regolith in comparison with the regolith at mid-latitudes. The data of LEND neutron telescope onboard the LRO will be used for estimation of amount of water in the shallow subsurface.

LANDING SITE CANDIDATES:

The ellipse of landing uncertainty of the first polar lander Luna-25 is rather large: it is 30 km along the meridional direction and 15 km along the latitudinal direction. The process of landing site selection should take into account such large uncertainty for targeting on the surface, and it was the main difficulty to satisfy all selection criteria, as named above, for such large region on the surface. The list of selected landing site candidates will be presented. For each candidate the set of parameters are evaluated, which are determined in correspondence with the selection criteria. The prioritization of these candidates will be suggested, as based on these parameters.

DISCUSSION:

The proposed landing sites have been considered in the special workshop at October 9, 2016. Conclusions of this workshop will be presented for joint discussion at the Lunar session of this Symposium. The final decision for the primary landing site and the spare sites will be made by the Space Council of the Russian Academy of Science later at this year.

CANDIDATE LANDING SITES FOR THE LUNA-GLOB MISSION

J. Flahaut¹, C. Wöhler², A.A. Berezhnoy³, D. Rommel², A. Grumpe²,
E.A. Feoktistova³, V.V. Shevchenko³, C. Quantin¹, P. Williams⁴
¹1LGL, TPE, CNRS/Université Lyon 1, 69622 Villeurbanne Cedex, France
²Image Analysis Group, TU Dortmund University, Dortmund, Germany
³Sternberg Astronomical Institute, Moscow State University, Moscow, Russia
⁴Dept. of Earth and Space Sciences, University of California, USA
⁵Goddard Space Flight Center, USA
 Contact: jessica.flahaut@ens-lyon.org

INTRODUCTION:

The last decades have been marked by increasing evidence for cold trapped volatiles, including water, at the lunar poles (e.g., Keller et al., 2016). Lunar volatiles are targets of interest both as scientific repositories and for exploration purposes. Orbital measurements reveal an enhancement in hydrogen at both poles, which is interpreted as evidence for surface or subsurface water ice (e.g., Feldman et al., 1998). In addition, recent Moon Mineralogy Mapper (M³) data reveal hydroxylation of the lunar surface (Pieters et al., 2009a).

Determining the exact nature, extent and origin of the hydroxyl/water and other volatiles at and near the surface at the poles required *in situ* analyses via lander or rover missions. Several upcoming projects and missions are targeting these chemical compounds such as the Luna-25 (also referred to as Luna-Glob) and Luna-27 Russian missions. The present study focuses on potential volatile-rich and science-rich targets with the landing area of the Luna-Glob mission, with the aim to determine and characterize all potential landing areas.

SELECTION CRITERIA:

Potential landing sites for Luna-Glob must meet the following engineering and science criteria (Mitrofanov et al., 2016):

- The latitude and longitude of the supposed landing site must be between 65-85°S and 0-60°E;
- The landing ellipse dimensions must be 15×30 km (spread in longitudinal direction);
- Surface slopes in landing site must not be greater than 7° on a 2.5 meters scale;
- The mean illumination within the landing area must be maximal;
- The Earth visibility (for radio communication) within the landing area must be maximal;
- The hydrogen abundance as estimated from orbit must be maximal.

In order to select terrains that meet these conditions (+ present eventual additional science benefits), datasets and derived products from various instruments were collected and co-analyzed into a Geographic Information System (GIS).

Our data collection includes:

- LOLA DEM at 60 m/pixel (Neumann et al., 2016) and derived slope map,
- LOLA-based average illumination and Earth visibility maps (Mazarico et al., 2011),
- LPNS and LEND H abundance maps (Elphic et al., 2007, Mitrofanov et al., 2010),
- Diviner average, minimum, and maximum temperature maps (Paige et al., 2010),
- USGS geologic map (Fortezzo et al., 2013, renovation of the Wilhelms and McCauley 1971 maps),

Elemental and petrologic maps derived from a polynomial regression that relates LP GRS elemental abundances (Lawrence et al., 1998) to M³ (Pieters et al., 2009b) spectral parameters (see details on the method in Wöhler et al., 2014; Rommel et al., 2016). The resulting maps include elemental abundances of Ca, Al, Fe, Mg, Ti and O at 0.05 degrees per pixel and a petrologic map constructed using the method of Berezhnoy et al. (2005), which is a RGB composite of a mare basalt endmember (18 wt% Fe, 6.5 wt% Mg, red channel), a Mg-rich rock endmember (4 wt% Fe, 13 wt% Mg, green channel, e.g. troctolite or orthopyroxene-rich norite) and feldspathic rock (0.5 wt% Fe, 1 wt% Mg, blue channel, especially ferroan anorthosite) (Rommel et al., 2016).

ELLIPSES DEFINITION AND CHARACTERIZATION:

Twelve ellipses have already been proposed by the Russian Space Research Institute team (Mitrofanov et al., 2016). By eliminating all areas of slope $> 7^\circ$ and illumination $< 40\%$ (blackened on Figure 1), we propose six additional candidate ellipses located in the remaining terrains and being characterized by high H abundance with both the LPNS and LEND instrument data (Cyan outlines on fig. 1a). These ellipses are labelled as 13-18 and are all located north of -70° in latitude.

Table 1. Mean values of selected parameters, computed for each of the 18 proposed ellipses.

Ellipse #	Earth Visibility	Illumination	H abundance from LPNS (ppm)	H abundance from LEND	LOLA elevation (m)	LOLA slope at 60 m ($^\circ$)	Avg T from Diviner ($^\circ$ K)	Geologic unit	Unit description
1	1.000	0.468	62	High	688	7.6	165	Ntp	Nectarian terra mantling and plains material
2	0.999	0.433	43	High	-2499	6.2	162	Ip	Imbrian plains material
3	1.000	0.417	45	High	-2536	5.8	161	Ip	Imbrian plains material
4	0.979	0.457	57	High	828	8.3	162	Ip	Imbrian plains material
5	0.999	0.464	41	Intermediate	938	7.8	160	Ntp	Nectarian terra mantling and plains material
6	0.997	0.454	78	High	460	9.5	161	pNbr	pre-Nectarian basin material, rugged
7	0.921	0.443	69	High	2068	16.9	165	pNc	pre-Nectarian crater material
8	0.992	0.430	37	High	1772	10.3	154	Isc	Imbrian secondary crater material
9	0.999	0.408	64	Intermediate	-819	9.1	155	Esc	Erastosthenian secondary crater material
10	0.999	0.406	74	High	119	15.6	165	Ec	Erastosthenian crater material, younger than most mare materials
11	0.996	0.435	54	Low	-872	6.5	158	Ntp	Nectarian terra mantling and plains material
12	0.923	0.401	57	High	974	16.8	156	pNc	pre-Nectarian crater material
13	0.994	0.458	66	High	353	9.0	163	pNb	pre-Nectarian basin materials
14	0.987	0.428	42	High	-1959	8.0	165	pNc	pre-Nectarian crater material
15	0.999	0.464	93	Intermediate	1542	7.9	166	pNt	pre-Nectarian terra material
16	0.994	0.466	84	High	377	9.0	159	pNb	pre-Nectarian basin materials
17	0.995	0.467	74	High	623	9.2	160	pNb	pre-Nectarian basin materials
18	0.996	0.468	87	High	103	8.6	160	pNb	pre-Nectarian basin materials

Zonal statistics were then performed to compute mean values and standard deviations for the elevation, slope, illumination, Earth visibility, H abundance, minimum, maximum and average Diviner temperature, composition and age of each of the 18 proposed ellipses (Table 1). There are discrepancies between the H abundances as estimated from the LPNS and LEND dataset (e.g., ellipse 8 show high values with the LEND data but low values with the LPNS data), but some ellipses (e.g., 16, 17, 18) have high H abundance values according to both instruments data. All the ellipses fall within the same average temperature range as estimated from the Diviner polar maps, however these values will be further improved with thermal modelling calculation. It is important to notice that the composition of terrains is very homogeneous within the investigated latitude/longitude range even though the ages of terrains vary (Fig. 1b). Terrains within the region of investigation are likely composed of anorthositic material.

CANDIDATE LANDING SITES RANKING:

Based on the computed statistics, we suggest to discard ellipses 7, 10, 12 (high slopes), 3, 9 (low illumination), 4 (low Earth visibility), 5 and 8 (low H abundance). Ellipses 1, 13 and 16 appear to be more suitable landing sites and should be considered of higher priority. Ellipse 1 presents slightly better illumination conditions but lower H abundances and higher Diviner average and maximum temperature than ellipses 13 and 16 (suggesting that less volatile species might be present). Ellipses 2, 6, 15, 17, and 18 are retained with intermediate priority (Fig. 1b). Future work will include high resolution scientific characterization of the three preferred ellipses (e.g., estimate of surface temperatures from thermal modelling as described in Wöhler et al. (2016), age estimation from crater counts).

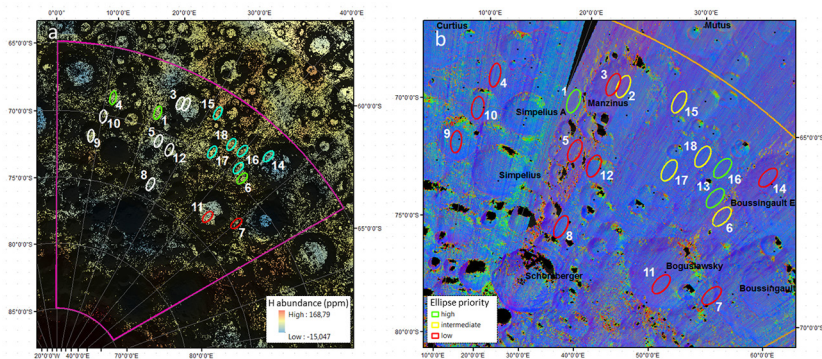


Fig. 1. a - Location of the 18 proposed ellipses on a LPNS H abundance map (low = blue, high = red). Blackened areas correspond to zones where the slope and illumination do not meet the defined criterias (see text); red, white and green outlines represent the low, intermediate and high priority ellipses from Mitrofanov et al. (2016), whereas cyan outlines represent the newly suggested, additional ellipses (this study). b - Ranking of the proposed ellipses (green = higher priority, red = lower priority). Background is the petrologic map derived from the correlation between M3 spectral parameters and LP GRS elemental abundance maps (e.g., Rommel et al., 2016).

ACKNOWLEDGEMENTS:

This work is partially supported by joint RFBR-DFG grant No. 15-52-12369 / WO 1800/7-1. J. Flahaut is supported by a CNES postdoctoral fellowship.

LITERATURE:

Keller J. W. et al. (2016), *Icarus*, 273, 2-24. Feldman W. C. et al. (1998), *Science*, 281, 1496-1500. Pieters C. M. et al. (2009a), *Science*, 326, 568-572. Mitrofanov I. et al. (2016), ELS abstract. Neumann G. A. (2016), LRO LARDR DPSIS, available on the PDS. Mazarico E. et al. (2011), *Icarus*, 211, 1066-1081. Elphic R. C. et al. (2007), *JGR* 34, 13. Mitrofanov I. et al. (2010), 330.483-486. Paige D. A. et al. (2010), 330, 479-482. Fortezzo C. M. et al. (2013), 44, 2114. Wilhelms D. E. and J. F. McCauley (1971), USGS. Lawrence D. J. et al. (1998), *Science*, 281, 1484-1489. Pieters C. M. et al. (2009b), *Science*, 96, 500-50. Wöhler C. et al. (2014), *Icarus* 235, 86-122. Rommel D. et al. (2016), ELS abstract. Berezhnoy A. A. et al. (2005), *Planet. Space Sci.* 53, 1097-1108. Wöhler C. et al. (2016), *submitted to Icarus*.

GEOLOGICAL CHARACTERIZATION OF THE THREE MOST PROMISING LANDING SITES FOR THE LUNA-GLOB MISSION

M.A. Ivanov¹, A.M. Abdrakhimov¹, A.T. Basilevsky¹, N.E. Demidov¹, E.N. Guseva¹, J.W. Head², H. Hiesinger³, S.S. Krasilnikov¹

¹Vernadsky Inst., RAS, Moscow, Russia

²Brown Univ. Providence, USA

³Münster Univ., Münster, Germany

Contact: mikhail_ivanov@brown.edu

INTRODUCTION:

A new assessment of the science/engineering requirements and constraints and the distribution of volatiles within the previously selected region for the Luna-Glob (LG) mission has brought into consideration a series of twelve new landing sites for the mission [Mitrofanov, pers. comm.]. Among these, the former primary mission site in the crater Boguslawsky has the lowest priority, whereas three new sites, Site 1 at 68.7S, 21.2E (WS of crater Manzinus), Site 4 at 68.6S, 11.6E (S of crater Pentland-A), and Site 6 at 69.5S, 43.5E (N of crater Boguslawsky) are considered as the most promising ones from an engineering and volatiles standpoint. These three sites show the highest concentration of hydrogen in the regolith and appear as reasonably smooth terrains. Although the main goal of the LG mission is water/volatiles, it is also important to understand what different types of geologic materials can be analyzed at the different landing sites. Here we briefly describe the geological settings of the most promising sites and document the possible sources of materials that can be found within the landing ellipses (30 by 15 km for all sites).

THE LANDING SITES:

The landing ellipse for Site 1 is ~20-25 km from the SW portion of the rim of the pre-Nectarian [1] crater Manzinus. Two morphologically distinctive units, rolling and flat plains, characterize the landing ellipse (Fig. 1a). Rolling plains have a morphologically smooth, gently undulating surface and occur in a narrow band along the eastern side of the ellipse. The plains form local highs that on the average are ~80-100 m higher than the mean level of the flat plains. Outcrops of the rolling plains occur around the ellipse and always appear as remnants of older materials embayed by flat plains. Flat plains have a subhorizontal surface with abundant small (less than several hundred meters) impact craters. The visual density of craters on the flat plains is higher than that on the adjacent rolling plains.

The landing ellipse of Site 4 (Fig. 1b) is 40-45 km to the SE of the rim of the crater Curtius (67.1°N, 4.5°E, ~100 km), which is Nectarian in age [1]. In this area, as in the case of Site 1, the rolling and flat plains are two major units that make up the surface of the landing ellipse and the adjacent territory. The flat plains occur in local lows that are ~100-150 m lower than the neighboring rolling plains and apparently embay them. In contrast to this stratigraphic relationship, the density of the smaller (less than 100 m) craters is larger on the flat plains. The rolling plains to the SW of the landing ellipse show numerous chains of relatively large (1-3 km) secondary craters that extend from the crater Moretus (70.7S, 5.8W, 115 km). These chains suggest that the landing ellipse is at the very edge of the Moretus ejecta deposit [1].

The landing ellipse of Site 6 (Fig. 1c) is within an area of ancient, pre-Nectarian terrain [1] between the rims of three large, pre-Nectarian craters: Boguslawsky (~100 km), Boussingault (~75 km), and an unnamed crater at 67S, 46E (110 km). Two units make up the surface of the landing ellipse: more and less rugged terrains. The more rugged terrain is located in a broad (several kilometers wide) zone along the ellipse edges and is more abundant in the landing area; less rugged terrain occupies the central portion of the ellipse and is less abundant. Significant topographic variations (100-200 m over the distance of 1-2 km) characterize both units. On average, the more rugged terrain occurs at higher elevations and there is no visual contrast in crater density between these units.

DISCUSSION/CONCLUSIONS:

The characteristic features and locations of the most promising landing sites recommended for the LG mission allow us to reach the following conclusions about the nature of the units that occur in the landing ellipses.

Site 1 is close to the rim of Manzinus and overlies a zone of continuous ejecta from this crater. Thus, the occurrences of the rolling plains along the eastern side of the ellipse are likely to be ejecta from Manzinus. Since this pre-Nectarian crater is ~80 km in diameter, its depth of excavation is ~8 km [e.g., 2]. This depth well exceeds the total thickness of ejecta from the pre-Nectarian (including SPA) lunar basins estimated by methods of either [3], 1-1.2 km, or [4], 2.5-3.1 km. Thus, materials from beneath the composite layer of the basin ejecta should contribute to the Manzinus ejecta. The zone of contiguous ejecta is the place where materials excavated from the deepest horizons are concentrated [5]. Materials deposited by the SPA impact almost completely compose the basin ejecta layer (~95-98% of its thickness) in the South Polar Region (SPR) and form the stratigraphically lowest portion of the layer. Thus, the contiguous ejecta from Manzinus should contain a significant proportion (~60-80%) of materials predating the SPA impact. These materials are likely to form the rolling plains in the Site 1 landing ellipse.

Flat, sub-horizontal plains cover the rest of the landing ellipse. These plains belong to the population of small plains-forming occurrences that fill local lows in the SPR. The topographic characteristics of such plains around Manzinus are not highly consistent with a volcanic nature and instead favor an impact origin for the plains [6] by emplacement of the finer-grained fraction of ejected materials [7]. This interpretation is supported by numerous chains of small impact craters oriented about perpendicular to the long axis of the landing ellipse and pointing to the Nectarian [1] crater Curtius (67S, 4.7E, 100 km). As in the case with Manzinus, the excavation depth of the Curtius impact exceeded the total thickness of the Nectarian/pre-Nectarian basins in the SPR. However, the flat plains within the landing ellipse are distal facies of the Curtius ejecta and, thus, they likely consist of the stratigraphically upper portions of the basins ejecta.

Two major units, rolling plains and smooth plains, make up the surface of the Site 4 landing ellipse. These units are morphologically similar to those that are presented in the Site 1 ellipse and probably have the same nature. The Site 4 ellipse is near the edge of ejecta blanket from Eratosthenian [1] crater Moretus. Thus, the major units in the ellipse are likely the rougher and finer facies of ejecta from this crater. Because Moretus is Eratosthenian in age, it should excavate materials deposited by all nearby lunar basins. However, the contribution of all post-Nectarian basins to the SPR is negligible in comparison with the volume/thickness of materials ejected from the SPA. Estimates of the thickness of the basin ejecta show that in the site of Moretus the contribution of all other basins are 2-3% of the total thickness. Depending on the model, the total thickness of ejecta in the Moretus site vary from ~1100 m [3] to 2700 m [4]. The diameter of Moretus, ~115 km, indicates that its depth of excavation was 4 to 10 times greater than the thickness of the composite layer of the basin ejecta. Thus, the presence of materials older than the SPA impact is expected in the zone of the contiguous ejecta around Moretus. The distal facies of the ejecta, however, should contain a larger fraction of the uppermost layers and, thus, materials related to the basin ejecta. Even in this case, however,

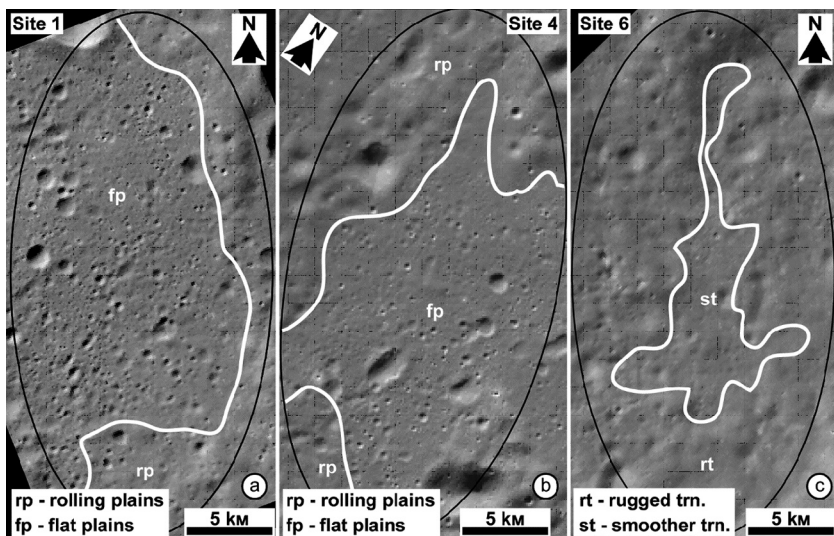


Fig. 1. Sketch geological maps of the most promising landing sites for the Luna-Glob mission.

the SPA ejecta, which represent materials that predated the SPA impact, should dominate the Site 4 landing ellipse.

The Site 6 landing ellipse is in a local low between the three large pre-Nectarian craters that are likely to have contributed to the materials in the landing ellipse. The crater Boguslawsky is anomalously shallow [6] and was partly filled. The analysis of possible scenarios of the filling reveals that the crater was partly covered by ejecta from the neighboring crater Boussingault [6]. Among the three largest craters near the Site 6 landing ellipse, Boussingault appears as the freshest and youngest. Ejecta from this crater, thus, should dominate materials within the landing ellipse and form the rugged unit in the ellipse. The smoother terrain in the ellipse, which occurs in local lows, may represent the mass-wasted portions of the rugged unit. The depth of excavation of Boussingault, ~7.5 km, is about 2-4 times larger than the thickness of ejecta from the nearby pre-Nectarian basins and, thus, the zone of the contiguous ejecta around Boussingault should contain a large fraction of materials predating the SPA impact.

REFERENCES:

1) Wilhelms, D. et al., USGS Map I-1192, 1979. 2) Melosh, J. Impact Cratering: A Geologic Process, pp. 253, 1989. 3) McGetchin, T. et al., EPSL, 20, 226-236, 1973. 4) Petro, N. and C. Pieters, MPS, 43, 1517-1529, 2008. 5) Oberbeck, V., RGSP, 13, 337-363, 1975. 6) Ivanov et al., PSS, doi:10.1016/j.pss.2015.05.007, 2015. 7) Oberbeck, V. et al. The Moon, 12, 19-54 1975.

HEAT RADIATION IMPACT MODELING ON THE SPACECRAFT LOCATED ON MOON POLAR REGIONS

S.S. Filimonov¹, S.A. Aksenov²

¹HSE Moscow Institute of electronics and mathematics, Russia

²Space Research Institute of Russian Academy of Sciences (IKI RAS),

117997, 84/32 Profsoyuznaya str., Moscow, Russia

Contact: sfilms89@gmail.com, akxenov.s.a@gmail.com

In this work a computer simulation tool for calculation of thermal fluxes acting on a spacecraft placed at the Luna surface is presented. The information obtained by this instrument can be then used to provide the boundary conditions for thermal simulation of a landing complex located at the South pole of the Moon. The mathematical model implemented in the developed software involves the simulation of indirect solar radiation, infrared radiation associated with a temperature of the Moon surface including reflection of the thermal fluxes by the spacecraft elements. The position of the Sun relative to the spacecraft located at the specific point of the Moon surface is calculated using NAIF SPICE observation geometry system. The computer software was developed using C++ programming language in a form of console application. Input and output information is provided by txt files. A study of thermal fluxes acting on selected elements of Luna-25 landing complex for Luna-Glob mission.

COMPUTER SIMULATION OF LUNAR SURFACE SPUTTERING FOR LUNA-RESOURCE MISSION

V. Ermakov^{1,2}, D. Trufanov²

*¹Space Research Institute of Russian Academy of Sciences (IKI RAS),
117997, 84/32 Profsoyuznaya str., Moscow, Russia*

*²National Research Nuclear University "MEPHI", Moscow, Russia
Contact: ermakovvova@mail.ru*

Secondary neutral particles sputtered from the lunar surface by solar wind ions impact provide a way to study the lunar surface. Remote measurements of sputtered neutral particles by the instrument onboard the Luna-Resource satellite of the Moon, allow one to make the map of lunar surface composition and of magnetic anomalies regions.

In order to determine the characteristics of particles sputtered from the lunar surface one needs to know the efficiency of neutral particle measurement instrument. Also, estimations of sputtering yields and angular distributions of sputtered particles can assist to choose the most efficient orientation of the instrument on the spacecraft.

Results of computer simulation of sputtering of the surface, imitating the lunar regolith, are presented. Energy spectra and angular distributions of neutral particles sputtered from the lunar surface by solar wind ions with different angles of incidence are presented.

ROBOTIC PRECURSORS TO HUMAN EXPLORERS: ESA LUNAR MISSION ACTIVITIES AND STUDIES

J. Carpenter, B. Houdou, R. Fisackerly, D. De Rosa, J. Schiemann, J. Huesing

*ESTEC, Keplerlaan 1, 2201 AZ, Noordwijk, The Netherlands
Contact: james.carpenter@esa.int*

INTRODUCTION:

Exploration of the Moon is the next step for human spaceflight, building on the experience of the International Space Station, which has seen human spaceflight restricted to Low Earth Orbit (LEO). This transition from LEO to Moon requires the development of new technologies, new capabilities and new knowledge across multiple domains and the progression of international partnerships exemplified through the ISS. The progression to lunar surface will be achieved through a combination of developments in robotic and human spaceflight systems and missions.

ESA's strategic approach to lunar exploration, the approach to technology development and synergies with other exploration destinations will be presented elsewhere in this meeting. Here we describe the current precursor robotic mission activities.

CONTRIBUTIONS TO THE RUSSIAN LUNAR EXPLORATION PROGRAMME:

In advance of human surface missions robotic missions to the surface provide an opportunity to drive up the technology and system maturities of key elements for the future, to generate relevant operational experience, to build partnerships and to generate knowledge.

To this end ESA is investing in a series of robotic precursor missions that will be implemented as a collaborative effort with Russia. The first mission in this campaign is the Russian Luna-25 ('Luna-Glob Lander') lander mission in 2019. ESA will provide an imaging system for this mission as a precursor of a complete precision landing and hazard avoidance system, PILOT, which will be deployed on the Luna-27 lander mission in 2021. The Precise Intelligent Landing using On-board Technology system, PILOT, is a generic exploration product, which will be available as a European contribution to future missions to enable pin-point and safe landing.

The Russian Luna-27 ('Luna-Resurs') mission also includes the "Package for Resource Observation and in-Situ Prospecting for Exploration Commercial exploitation and Transportation", PROSPECT. This system will be used to investigate the presence, provenance and viability of lunar resources at the Luna-27 landing site. This mission also provides the basis for future deployments of PROSPECT as a system for comprehensive resource evaluation across the lunar surface. PROSPECT emphasises cold trapped polar volatiles but is intended to provide a broader investigatory capability, which could be deployed more broadly across the lunar surface.

ESA will provide communications support across the sequence of Russian missions including both landers and the Luna-26 orbiter.

MISSION STUDIES:

Following these flights ESA is looking to build on the demonstrated capabilities and further support the definition of Europe's path to the lunar surface. To this end a number of mission studies are on-going including sample return and mobile surface exploration. It is important that these next steps address key knowledge and capability gaps for human exploration, build strong partnerships and build the user base for the exploration missions that will follow.

Two mission robotic mission concepts are being studied; a lunar polar sample return mission, in cooperation with Russia and a Lunar Volatile Prospecting rover missions. Both of these missions would investigate lunar polar volatiles.

Precursor missions integrating human and robotic capabilities are also being investigated as potential future international partnerships.

PARTNERSHIPS:

International partnerships have been and continue to be an essential element in ESA's approach to exploration. The ability to work and operate together in space also represents one of the key benefits delivered by exploration. In addition a new partnership model with the private sector is being explored, with initial pilot phases into commercially led activities to prepare robotic capabilities and infrastructure for the future.

CONCLUSIONS:

We will present the current robotic precursor activities in ESA to prepare for future human exploration to the surface. Emphasis will be placed on the development activities for PILOT and PROSPECT, mission studies which are on-going with European industry, as part of a partnership between ESA and Russia, on the LPSR and LVP mission studies and on activities related to developing partnerships with the private sector.

THE MULTI-SCALE MAPPING OF MONS RUMKER AREA FOR DESIGNING LUNAR ROVER'S ROUTE PURPOSE

M.A. Zakharova¹, E.N. Slyuta¹

¹Vernadsky Institute of Geochemistry and Analytical Chemistry, Moscow, Kosygina str. 19, Russia

Contact: mari.al.zakharova@gmail.com

INTRODUCTION:

The paper mainly describes the process of multi-scale mapping the Mons Rumker area for designing a Russian lunar rover's route - "Lunar geologist". The Mons Rumker area is the primary target for Lunar Geologist research because here we can see lunar mare basalts of all ages, which makes it quite a valuable source of information for the study. The study area was carried out in the context of the cartographic method of research. This method allows us to analyze the spatial configuration of the area using GIS analysis technology. There were compiled two small-scale overview maps showing topography and geological features of the territory, and large-scale maps of the relief. The maps formed the basis for the design of the route the Lunar geologist. The small-scale maps were used for the preliminary design and large-scale ones - for the safest route planning, taking into account the technical characteristics of the rover. The maps were compiled mostly using Lunar Reconnaissance Orbiter data. And the basis for geologic map was formed using several maps from Geologic History of Moon [2].

MAPPING THE MONS RUMKER AREA:

At the beginning it was necessary to conduct a preliminary study of the Mons Rumker area. Due to the information received there was planned the general trend of rover's route. For this purpose there were compiled two overview maps of the area (Fig. 1, 2). The relief map was compiled using laser altimeter data obtained by LRO [3]. It shows general relief features of the area. The geological map represents the age and origin of the rocks covering the Mons Rumker area. The map was compiled using mainly "Geologic History of Moon [2]", afterwards the borders, separating different rocks, were detailed using LRO NAC images and relief map of the area. The primary Lunar Geologist's task is to collect samples of all rocks represented at the Mons Rumker area. Due to this fact the rover's route is supposed to cross the area from west to east, covering the mare basalts of all ages and volcanic province. The next step was the detailed planning of the optimal route based upon the Lunar geologist's technical requirements. For this purpose several digital elevation models were compiled. The models are done using the high-precision images LROC NAC also obtained by LRO [4]. The DEMs are the result of automatic stereophotogrammetric processing the images using ISIS [5] and ASP [6] software. Afterwards the models have been used to produce large-scale hypsometric map covering the volcanic province western part (Fig. 3). The main factor for the rover's route planning was the slope of the surface. So DEMs have also been used for the surface slope map compiling. The calculated surface slope values of the Mons Rumker area were classified in accordance with the technical specifications of the Lunar geologist. Figure 4 shows the fragment of the final map with several prospective rover's routes.

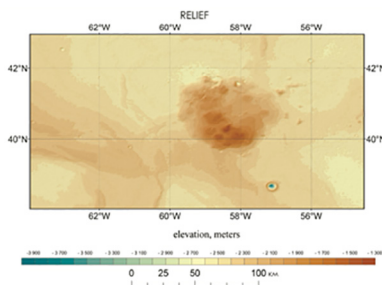


Fig. 1.

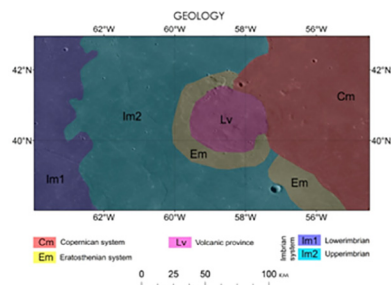


Fig. 2.

CONCLUSION:

The final cartographic results accumulate the relief and geological information at the Mons Rumker area. The DEMs obtained during the work are also the most

detailed source of information about Mons Rumker's relief. Future research plans include obtaining larger number of 3D models covering the area of study while increasing the number of LROC NAC images of the Mons Rumker.

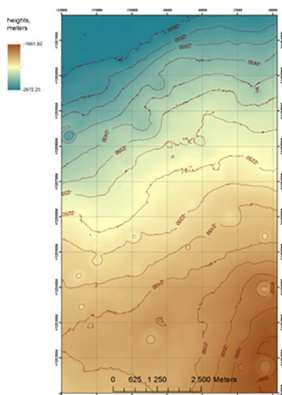


Fig. 3.

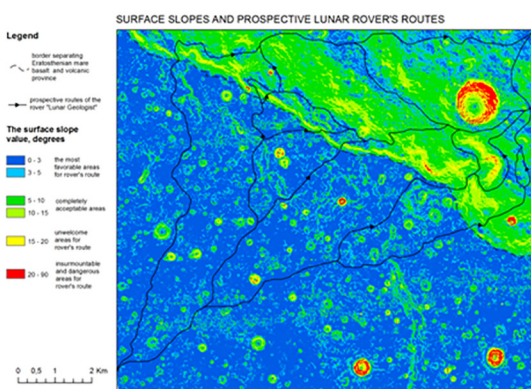


Fig.4

REFERENCES:

- [1] Lunar Reconnaissance Orbiter // USGS, NASA, 2015.
URL: <http://lunar.gsfc.nasa.gov/index.html>
- [2] Wilhelms Don E. The geologic history of Moon. U.S. Geological Survey Professional Paper 1348. United States government printing office, Washington, 1987. – 329 p.
- [3] LOLA – Lunar Orbiter Laser Altimeter // LRO LOLA TEAM, USGS, NASA, 2016.
URL: <http://lunar.gsfc.nasa.gov/lola/>
- [4] The Lunar Reconnaissance Orbiter Camera archive // LRO LROC TEAM, USGS, NASA, 2016
- [5] USGS ISIS – Integrated Software for Imagers and Spectrometers, 2009.
URL: <http://isis.astrogeology.usgs.gov>
- [6] Broxton M. J., Beyer R. A., Moratto Z., Lundy M., Husman K., 2012. The Ames Stereo Pipeline: NASA's Open Source Automated Stereogrammetry Software. A part of the NASA NeoGeography Toolkit. Version 2.0.0. Intelligent Robotics Group, NASA Ames Research Center, 88 p.

LUNAR POLAR ILLUMINATION AND IMPLICATIONS FOR FUTURE LANDING SITES

J. Oberst^{1,2,3}, P. Gläser¹

¹*Technische Universität Berlin, Institute of Planetary Geodesy, Straße des 17. Juni 135, 10623 Berlin, Germany*

²*German Aerospace Center, Institute of Planetary Research, Rutherfordstrasse 2, 12489 Berlin, Germany*

³*Moscow State University for Geodesy and Cartography (MIIGAiK), Gorokhovskiy pereulok 105064, Moscow, Russia*

Contact: philipp.glaeser@tu-berlin.de

ABSTRACT

We investigate the polar illumination conditions of the Moon based upon data from the Lunar Orbiter Laser Altimeter (LOLA). We simulate the received sunlight for a solar-panel of a lander or rover at a height of 2 m above the ground. Several landing sites, each located near the pole, were identified with average illumination intensities of ~80%. Here, a lander could reside in sunlight for a total of up to ~330 days out of the year. Permanently Shadowed Regions (PSRs), possibly containing polar volatiles, are found within kilometre-range of the proposed sites.

INTRODUCTION

The lunar synodic day lasts about 29.5 Earth days. As the lunar rotational axis is tilted wrt the ecliptic plane by only a small angle (1.54°), areas near the lunar equator have equally long illumination and shadow periods throughout the year. However, polar illumination, is more complex. The combination of grazing sunlight and local topography leads to extreme conditions.

Permanently Shadowed Regions (PSRs), for instance, exist in close proximity to regions receiving illumination for the greater part of the year [1][2][3]. Accordingly, PSRs are amongst the coldest areas on the Moon [4] and have long been suspected to harbor enhanced concentrations of hydrogen compounds and hence possibly also water ice [5].

Landing sites in quasi-continuous illumination and close proximity to PSRs will be ideal exploration sites for robotic missions. Landing units and rovers at such sites can rely on solar power and are able to explore polar volatiles in nearby PSRs.

DATA/METHOD

For this study consistent, large-scale and high-resolution Digital Terrain Models (DTMs) were produced. Similar to the generation of a south polar DTM using Lunar Orbiter Laser Altimeter (LOLA) data as shown in [3], a north polar LOLA DTM was created using co-registration techniques [6]. Both DTMs cover areas of 400 x 400 km at a resolution of 20 m/pixel, respectively (Fig. 1). Based on the polar LOLA DTMs illumination conditions can, for instance, be simulated by applying the horizon method [1][3]. Here, illumination conditions at 2 m (height of a solar panel on a lander or rover) above ground were evaluated for 50 x 50 km regions (see Fig. 1) near each pole.

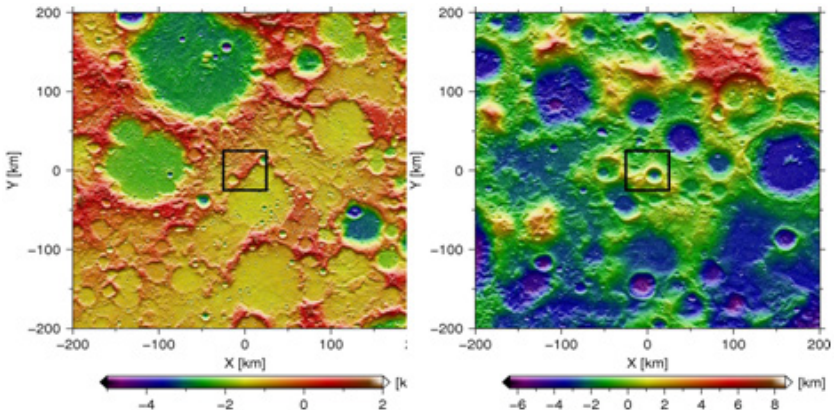


Fig. 1. Lunar polar LOLA DTMs, 400 x 400 km and 20 m/pix resolution. The investigated 50 x 50 km regions are outlined in black. Left: North pole. Right: South pole.

ACKNOWLEDGEMENT

This project was funded by a grant of the German Research Foundation (FOR 1503, OB 124/8-1). J. Oberst gratefully acknowledges being hosted by MIIGaIK and supported by the Russian Science Foundation under project 14-22-00197. We wish to thank the LOLA and LROC Science Team for releasing such great data products.

REFERENCES

- [1] Mazarico, E., Neumann, G.A., Smith, D.E., Zuber, M.T., Torrence, M.H., 2011. Illumination conditions of the lunar polar regions using LOLA topography. *Icarus* 211, 1066–1081.
- [2] Speyerer, E.J., Robinson, M.S., 2013. Persistently illuminated regions at the lunar poles: Ideal sites for future exploration. *Icarus* 222, 122–136.
- [3] Gläser, P., Scholten, F., De Rosa, D., Marco Figuera, R., Oberst, J., Mazarico, E., Neumann, G.A., Robinson, M.S., 2014. Illumination conditions at the lunar south pole using high resolution Digital Terrain Models from LOLA. *Icarus* 243, 78–90.
- [4] Paige, D.A. et al., 2010. Diviner Lunar Radiometer Observations of Cold Traps in the Moon's South Polar Region. *Science* 330, 479.
- [5] Watson, K., Murray, B., Brown, H., 1961. On the possible presence of ice on the Moon. *JGR* 66, 1598–1600.
- [6] Gläser, P., Haase, I., Oberst, J., Neumann, G.A., 2013. Co-registration of laser altimeter tracks with digital terrain models and applications in planetary science. *PSS* 89, 111–117.

SCIENTIFIC OBJECTIVES AND PARAMETERS OF ARIES-L INSTRUMENT QUALIFICATION MODEL FOR LUNA-GLOB MISSION

D. Moiseenko¹, O. Vaisberg¹, R. Zhuravlev¹, A. Shestakov¹, S. Shuvalov¹,
P. Moiseev², V. Letunovsky³, M. Mitjurin², A. Koziura², E. Rodkin²,
I. Nichushkin²

¹Space Research Institute of Russian Academy of Sciences (IKI RAS),
117997, 84/32 Profsoyuznaya str., Moscow, Russia

²«Astron Electronics»

³Orel, Russia, SKB KP, Tarusa, Russia

Contact: modaldi@iki.rssi.ru, olegv@iki.rssi.ru, zhuravlev_roman@iki.rssi.ru

Study of lunar regolith is an important part of investigation of origin, evolution, and properties of the Moon. The purpose of experiment is investigation of solar wind interaction with the surface of the Moon, desorption of surface layer, and composition of surface layer. Secondary Ion Mass Spectrometry is common methods of analysis solid bodies. Experiment on the Moon allows one to use the solar wind flux as primary ion beam.

We are presenting results of functional tests and calibrations of qualification model ARIES-L instrument for LUNA-Glob mission. Panoramic ions and neutrals analyzer ARIES-L is an energy-mass spectrometer with field-of-view $\sim 2\pi$. Scheme of the ARIES-L electronic optics is presented in Figure 1. ARIES-L qualification model before preliminary laboratory tests is presented in Figure 2. Wide viewing angle allows this instrument to measure simultaneously the solar wind flux and characteristics of secondary ion flux sputtered from lunar regolith. Instrument also includes converter of neutral atoms located within the field of view of instrument. Secondary neutrals sputtered by the solar wind are ionized on the surface of converter and are measured by the same ion energy-mass analyzer. Secondary goal of experiment is the study of solar wind interaction with Earth's magnetosphere and magnetotail.

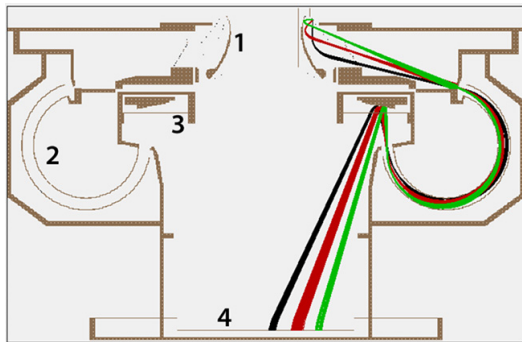


Fig. 1. Scheme of the ARIES-L electronic optics:
1 – mirror M1 with gate; 2 – electrostatic analyzer;
3 – mirror M2; 4 – position-sensitive MCP-detector.



Fig. 2. ARIES-L qualification model before preliminary tests of electronic optics.

TIDAL-LIBRATIONAL DISSIPATIVE DYNAMICS OF THE MOON AND RADIO/LASER BEACONS VLBI/LRR/LLR TECHNOLOGIES FOR CHANGE-5/6, LUNA-25/26/27, ILOM MISSIONS

A. Gusev¹, H. Hanada², A. Kosov³, Z. Meng⁴, J. Ping⁴, O. Titov⁵, M. Vasilyev⁶

¹Kazan federal University, Kazan, Russia

²NAOJ, Mizusawa, Japan

³IKI RAS, Moscow, Russia

⁴NAOC CAS, Beijing, China

⁵Geoscience Australia, Canberra, Australia

⁶IPA RAS, S-Petersburg, Russia

Contact: agusev33@gmail.com

Tidal phenomena play a key role in the spin-orbital evolution of the moons. The gravitational force exerted by planets deforms the moons (tides) and periodically changes their rotation and space orientation (librations). The largest tidal terms of the Moon have a 1month period, lesser terms are at 2weeks and 6years, and smaller terms occur at other periods. Of the two arguments, the tidal component is phase shifted. As a result of tidal dissipation, the Moon and Deimos that form beyond the synchronous radius will move gradually outwards with time, and moons within the synchronous radius will move inwards (Phobos). Early analyses of the effect of tides and tidal dissipation on physical librations by Yoder (1981) and Eckhardt (1981) found a few of the largest terms. Now we know the two sources of dissipation on the Moon: 1) tides in lunar mantle and 2) viscoelastic fluid motion at the core-mantle boundary on the Moon (Gusev et al., 2015). There is a small tide-induced libration terms at the differential periods. Tides also affect the moments of inertia of the Moon. And vice versa lunar librations also little changes the lunar tides. (Williams, Boggs, 2015).

The lunar structure includes a rigid crust, viscoelastic mantle and liquid core. The temperature increases with depth, the structure and composition change with depth, and the deep mantle strongly attenuates seismic waves. We expect the dissipation to vary with depth and that variation may include discontinuities. Weber et al., (2011), Harada et al., (2014) found a 150km thick attenuating zone with low seismic velocity, low-viscosity layer of partial melt (1016 Pas) and low quality factor Q. The dissipation of energy during distortion by tides or seismic waves depends on the behavior of materials at microscopic scales. Tidal dissipation is mainly concerned with shear. There are multiple mechanisms of dissipation that can depend on frequency, temperature, stress, rheology models. In the Moon at tidal frequencies, the application of shear stress to a material is thought to cause mineral grains to slide by one another at their boundaries. The mineral grains have defects that can impede the motion so that shear stress across the grains can oppose the sliding force. The anelastic mechanism dissipates energy, but the distortion from sliding is limited by pinning due to defects on the grains. At high temperatures and long time scales the pinning becomes weak and the sliding will be a free (Henning et al., 2009).

Tidal deformations of lunar surface are described by the sum of periodic terms. The maximum of vertical tidal displacement is characterized by amplitude about 100 mm and by anomalistic period in 27.555d (period of mean anomaly). Other significant tidal term has the period 27.212 d (period of node crossing of lunar orbit on ecliptic). Others tidal deformations of the elastic Moon with amplitudes about 10 mm are characterized by the periods in 1 and 1/2 months, and amplitudes about millimeters are characterized by the periods: 1/3, 7 months, 1 year and 6 years. Horizontal tidal displacements of lunar surface are characterized by amplitudes approximately twice smaller in comparison with mentioned above.

The Sun perturbs the lunar orbit causing major variations at periods of 2weeks, 1 month, 7months, and 1year. Solar tides on the Moon has amplitude 2 mm. For such a wide span of periods, we must consider the tidal distortion, Love numbers, and dissipation to depend on period. For lunar tidal dissipation, this anelastic behavior is thought to arise from sliding at grain boundaries. Defects in the grains can inhibit sliding allowing shear stress across grains to resist the motion. For a second type of dissipation, a constant stress causes

unlimited viscous distortion. Displacement measurements with accuracies of a few tenths of a millimeter become useful for dissipation studies. The Apollo LLR arrays should display monthly (29.531day) thermal expansion cycles of ~1mm. At 1m above the surface, the Lunokhod arrays should show thermal motion of several millimeters. Laboratory experiments have provided important information on the mechanisms of dissipation in materials over a range of temperatures, time scales, grain sizes, and presence of melt. (Williams, Boggs, 2015).

The lunar core is much smaller than the Earth's core, the rotation rate is less, and the flattening of the CMB is less; the associated core precession period is some centuries (Gusev et al, 2015). The influence of a liquid core results in decreasing of the period of librations in longitude on 0.316 day, and in change of the period of free wandering a pole of the Moon on 25.8 days. In the first approximation the liquid core does not render influence on the value of Cassini's inclination and on the period of precession of the angular momentum vector. However, it causes an additional "quasi-diurnal" librations with period about 27.165 days. In comparison with model of rigid nonspherical of the Moon the presence of a liquid core should result in increase of amplitudes of the Moon librations on 0.06 % (Barkin et al., 2006).

The new prospects for establishment of a liquid/rigid core model and for studying its contribution in physical librations of the full Moon for direct studies of tidal and non-tidal "breath" of the Moon with new multi-parametric rheological interior (Maxwell, Voigt-Kelvin, SAS, Burgers, Andrade models) will be viewed. New differential radio (VLBI/SBI, LRR) and optical (one way of LLR) technologies (Turyshv et al., 2010) have been proposed for measurements of Lunar physical librations and Lunar dissipative tides (Gusev et al., 2015). Modern designs for corner cubes include single corner cubes that would not spread the pulse in time (Otsubo et al., 2010). An alternative to retroreflectors, optical transponders would provide a strong signal (Bender et al., 1990; Yoshino et al., 1999), but they require power. For this a new big size corner cubes reflectors (bsCCR) and a stable long-lived radio beacons should be located on new Lunar landers. Sensitivities to a dissipative physical libration and tidal displacements would be enhanced by a broad geographical spread of the bsCCR, radio beacons, seismometers and optical telescopes on Lunar poles at ChangE-5/6, Luna-25/26,27, ILOM projects (Hanada H., et al., 2014).

REFERENCES:

- Barkin Yu., Gusev A., Petrova N., (2006), Study of spin-orbit and inner dynamics of the Moon: Lunar mission applications. *Advances in Space Research*, v. 37, p. 72 – 79.
- Bender P. et al. (1990), Microwave and Optical Lunar Transponders, *AIP Conf. Proc.*, 207, 647–653.
- Eckhardt D.H., (1981), Theory of the librations of the Moon. *Moon*, v. 25, p. 3 – 49.
- Gusev A., Hanada H., Petrova, N., Kosov A., Kuskov O., Kronrod V&K., (2015), Rotation, physical librations and interior structure of the active and multi-layer Moon, Monograph, Kazan, 328pp.
- Hanada H., et al., (2014), Some technological problems in development of a small telescope for gravimetry, *Proc. of conf. "Space Gravimetry and Geodesy"*, TGSMM2013, S-Petersburg, p.198-203.
- Harada Y., et al, (2014). Strong tidal heating in an ultralow-viscosity zone at the core-mantle boundary of the Moon. *Nature Geoscience*, v.7, p.569 – 572.
- Henning W.G., et al., (2009), Tidally heated terrestrial exoplanets: Viscoelastic response models, *Ap. J.*, v.707, p. 1000–1015.
- Otsubo T. et al., (2010), Simulation of optical response of retroreflectors for future lunar laser ranging, *Adv. Space Res.*, 45, 733–740.
- Turyshv S., et al., (2010), "dvancing Tests of Relativistic Gravity with Laser Ranging to Phobos, *Experimental Astronomy*, v. 28, Issue 2, pp 209–249.
- Weber R. et al, (2011), Seismic detection of the lunar core, *Science*, v.331, p.309–312
- Williams J. G., D. H. Boggs, (2015), Tides on the Moon: Theory and determination of dissipation, *J. Geophys. Res. Planets*, v.120, p. 689 –724.
- Yoder C.F., (1981), The free librations of a dissipative Moon. *Phil. T.R.Soc. Lond. Ser.A*, p. 32–338.
- Yoshino T., et al., (1999), Lunar laser ranging by optical transponder collocated with VLBI radio sources on the moon, *Proc. SPIE 3865, laser radar ranging and atmospheric lidar techniques II*, 20-26.

INSTRUMENTATION FOR POLAR REGOLITH ANALYSIS OF LUNA-25 AND LUNA-27 SPACECRAFTS

M.L. Litvak, I.G. Mitrofanov

Space Research Institute of Russian Academy of Sciences (IKI RAS), 117997, 84/32 Profsoyuznaya str., Moscow, Russia
Contact: mlitvak.iki@gmail.com

The current Russian lunar space program proposes several launches of orbital and landing robotic missions scheduled in 2019-2021. All landing missions will provide comprehensive science investigations of lunar regolith properties combining remote measurements with sampling probes analysis. The main goal is to study mineralogical, chemical, elemental and isotopic content and search for volatiles in bulk subsurface within 20-200 cm depths in of south high latitude and polar areas of Moon.

The Luna-25 is reconnaissance mission, which deliver science instruments to the Moon's south high latitudes and study elemental composition of regolith using active gamma and neutron spectroscopy methods and laser mass spectroscopy to analyze probes taken from shallow depths. The most comprehensive investigations are planned onboard Luna-27 lander, which will be equipped with cryogenic drilling system and three sampling instruments to evaluate elemental, isotopic composition and search for volatiles preserved in lunar regolith at polar southern latitudes (>80S). It will be implemented through a very intensive international cooperation between Russian Federal Space Agency (Roscosmos) and European Space Agency (ESA).

In this presentation we will focus on requirements, capabilities and expected science outcome applicable to the drilling system, sampling instruments and remote instrumentation developed to study lunar polar regolith properties.

RUSSIAN LUNAR ORBITER MISSION

**A. Petrukovich, L. Zelenyi, K. Anufrejchik, O. Korablev, I. Mitrofanov,
I. Polyansky**

*Space Research Institute of Russian Academy of Sciences (IKI RAS), 117997,
84/32 Profsoyuznaya str., Moscow, Russia*

Contact: a.petrukovich@cosmos.ru

Russian Lunar orbiter mission Luna-26 (Luna-Resource-1 Orbiter) will have onboard 160 kg of science instrumentation to probe lunar surface and subsurface, as well as exosphere. We discuss orbital scenario planning issues, relevant to implementation of instrument coverage requirements. Expected launch date is end of 2020.

RADAR COMPLEX IN THE “LUNA-RESOURCE” PROJECT

V.M. Smirnov¹, O. Yushkova¹, V. Marchuk¹, A. Pavelyev¹, S. Matyugov¹,
O. Yakovlev¹, V. Abramov², I. Dutishev², B. Chernishev², M. Laptev²

¹Kotel'nikov Institute of Radio Engineering and Electronics RAS, Fryazino
Branch, Russia

²Special Design Bureau IRE RAS, Fryazino, Russia Institute

Contact: vsmirnov@ire.rssi.ru

INTRODUCTION:

Study of the Moon is an intensively developing direction in space research. The practical importance of the Moon exploration consists in the expansion of knowledge about formation and development of the Solar System; a choice of the disposition places for the future expeditions, the estimation of potential use of lunar resources. The main resource is water ice. Water is important for the activity of the Lunar bases. For this reason, detecting of water ice in subsurface layer of the Moon is a priority problem in lunar researches. Radiolocation is the most efficient methods of subsurface exploration. Drilling in situ is a more accurate method but it is less efficient and more expensive and it can be used to refine the soil structures detected by radar.

Multi-purpose radar complex (RLC-L) is planned to be installed on the orbital module “Luna – Resource 1”. RLC-L aims at:

- detection, identification and study of lunar subsurface structures;
- assessment of the dielectric constant of lunar soil;
- localization of places with high conductivity;
- study of large-scale irregularities of the lunar surface;
- registration of electromagnetic radiation in the lunar space.

HARDWARE:

RLC-L complex is developed in cooperation of Kotel'nikov Institute of Radio Engineering and Electronics of the Russian Academy of Science and Special Design Bureau IRE RAS. Designed radar complex RLC-L consists of two subsurface sounding radars: Radar-20 and Radar-200. The main characteristics of locators are given in Table 1 and Table 2, respectively.

Table 1. Radar-20 technical characteristics

- Range of accepted frequencies on the minus 3 dB level	17.5 up to 22.5 MHz;
- Bandwidth of intermediate frequency in an active location mode on the minus 3 dB level	5 KHz up to 5 MHz;
- radiated power, not less than	30 W;
- radiated signal	pulse, chirp signal;
- Duration of a radiated impulse	250 μs;
- Duration of registration of the received signal	350 μs
- Repetition frequency, not less than	1 Hz;
- Range of radiated frequencies on the minus 1 dB level	17 up to 23 MHz;
- Average power consumption, no more	20 W.

Table 2. Radar-200 technical characteristics

- Range of accepted frequencies on the minus 3 dB level	175 up to 225 MHz;
- Bandwidth of intermediate frequency on the minus 3 dB level	5 KHz up to 5 MHz;
- Bandwidth of intermediate frequency in a bistatic location mode on the minus 3 dB level	300 KHz;
- radiated power, not less than	30 W;
- radiated signal	pulse, chirp signal;
- Duration of a radiated impulse	250 μs;
- Duration of registration of the accepted signal	350 μs
- Repetition frequency, not less	1 Hz;
- Range of radiated frequencies on the minus 1 dB level	170 up to 230 MHz;
- Average power consumption, no more than	20 W.

OPERATIONAL MODES:

The work of RLC-L radar complex is planned in three modes.

Mode 1: Radar-20 and Radar-200 will operate in monostatic *mode 1* in the range of 50 to 100 km altitude. Chirp modulation of signals will be used

for active sounding. Radar will determine the structure of the lunar ground to a depth of several kilometers with the vertical resolution not worse than 25 m. Radar-200 is supposed to investigate the surface properties and vertical distribution of physical characteristics in the lunar top layers up to ten meters depth with the vertical resolution of about 1 m. The Radar-20 and Radar-200 radars will operate in succession with a minimum switching time. Received lunar echoes are stored in the onboard memory of the Radar-20 and Radar-200, and then transmitted to the Earth for analysis.

Mode 2: In this mode the radar RLK-L will operate in bistatic regime to study the lunar subsurface structure by use of signals emitted by an Earth-based transmitter.

Mode 3 is applied to study the spatial and frequency distributions of electromagnetic emission produced by cosmic sources.

Radarograms are used for displaying results of radar measurements. They are obtained during the radar's movement along the satellite orbit and show a delay of the reflected signal with respect to time of arrival of the signal scattered from the lunar surface. Influence of reflections from the relief features on the results of subsurface sensing can be removed from radarograms by use of 3-D model of the Moon topography. Parameters of the lunar subsurface structure will be restored by use of special method of inverse problem solution.

LGNS INSTRUMENT FOR LUNA-26 MISSION

A.B. Sanin, I.G. Mitrofanov, M.L. Litvak, M.I. Mokrousov

Space Research Institute of Russian Academy of Sciences (IKI RAS)

Profsoyuznaya Str, Moscow, Russia, 117997

Contact: sanin@np.cosmos.ru

The primary goal for the Lunar Gamma and Neutron Spectrometer (LGNS) is investigation of lunar regolith composition from the Luna-26 spacecraft orbit by the nuclear planetology methods. The methods are based on measuring of the neutron and gamma-ray albedo from the lunar surface generated in subsurface regolith by high energy particles of Galactic Cosmic Rays (GCRs). The main component of the GCR flux is protons and alpha particles with energies above 100 MeV. These energetic particles penetrate into the surface of the Moon, interact with the nuclei of the regolith and produce fast neutrons as a result of nuclear interactions. In their turn, neutrons interact with major rock forming nuclei and excite them with following emission of characteristic gamma rays. Both neutrons and gamma-rays may escape from lunar surface and be detected by an instrument on orbit. By measuring energy and intensity of observed gamma-ray lines it is possible to determine the amount and spatial distribution of the main rock forming elements such as: H, O, Na, Mg, Al, Si, K, Ca, Fe, Th, U.

By the LGNS orbital measurements of neutron and gamma-rays flux various energies the composition of lunar regolith to a depth of ~1 meter will be obtained. These data will be used to create maps of abundance of main rock forming and natural radioactive elements. Also the radiation doze will be measured of lunar orbit during Luna-26 mission.

LSTK - LUNAR STEREO TOPOGRAPHIC CAMERA FOR «LUNA-RESURS-1» ORBITAL MISSION

I. Polyanskiy¹, B. Zhukov¹, A. Zubarev², I. Nadezhdina²

¹Space Research Institute of Russian Academy of Sciences (IKI RAS)

Profsoyuznaya Str, Moscow, Russia, 117997

²Moscow State University of Geodesy and Cartography

Lunar stereotopographic camera LSTK intended for stereo imaging of the lunar surface with the goal of high-resolution 3D mapping that will be used to provide an autonomous optical navigation in subsequent lunar missions.

Imaging will be performed from the spacecraft located on lunar near-circular orbit with altitude of 50 to 100 km, optimized for maximum coverage of the territory. The triaxial SC orientation and stabilization system of angular position in the orbital coordinate system will be used. The principle of LSTK is based on successive frame survey of the moon surface by means of two optical heads, oriented forward and backward relative to the direction of SC flight, providing the pairs of images by the method of oblique-convergent stereo photography.

The expected results of the experiment – building a digital three-dimensional maps of the moon in the range of 30-80° North and 30-80° South latitude with a horizontal resolution of 2,5...3 m and a height accuracy better than 10 m.

ADVANCED GLOBAL TOPOGRAPHIC MAPPING OF THE MOON: AN IMPORTANT OBJECTIVE OF UPCOMING LUNAR ORBITAL MISSIONS

M.A. Kreslavsky^{1,2}, A.E. Zubarev¹, I.P. Karachevtseva¹

¹Moscow State University of Geodesy and Cartography (MIIGAIK)
MIIGAIK Extraterrestrial Laboratory (MExLab), Moscow, Russia

²University of California - Santa Cruz
Contact: mkreslav@ucsc.edu

INTRODUCTION:

Global topographic data are indispensable for scientific understanding and robotic exploration of planetary bodies. Such data are essential for a wide range of geodynamic studies, for proper interpretation and inversion of gravity data, for global and regional geological studies, geological mapping, mission planning, and many other applications. A spectacular illustration for the role of such data is how the first global topographic data set for Mars has revolutionized our knowledge about that planet. Since the first data from laser altimeter MOLA onboard Mars orbiter Mars Global Surveyor were returned in 1997, about 180 peer-reviewed journal papers have mentioned MOLA data as their major data source. The flux of such data analysis papers have not petered out yet. MOLA-based topographic maps superseded image mosaics and became the most used geographic reference; as such, MOLA data have been used in countless other works. Successful landing of three rovers would be impossible without such a data set. Here we assess the currently available global topographic data sets for the Moon and argue for advanced stereo imaging as prospective objective of a lunar orbital mission.

PRESENTLY AVAILABLE GLOBAL LUNAR TOPOGRAPHIC DATA AND THEIR SHORTCOMINGS:

A brief and complete overview of all presently available lunar topographic data sets can be found in [Barker *et al.* 2016]. The most advanced global topographic data set is so-called SLDEM2015. It covers low and midlatitudes of the Moon (60°S to 60°N) with 512 pixels per degree sampling in the simple cylindrical projection. This sampling corresponds to ~60×60 m pixel at the equator. This data set was produced [Barker *et al.*, 2016] by combination of LOLA data with SLDEM2013 data set [Haruyama *et al.*, 2014]. The latter was generated by photogrammetric processing of stereo images obtained by Terrain Camera (TC) onboard Kaguya mission to the Moon. SLDEM2013 data set has 10 m sampling approximately equal to sampling of the source TC images, an inconveniently coarse 1 m vertical quantization, and internal vertical precision ~10 m. The actual resolution of this data is worse than the pixel size, because photogrammetric processing inherently yields the actual resolution of topography lower than the original image. According to estimates by Barker *et al.* [2016] this actual resolution is ~100 m. Both vertical and horizontal accuracy of TC-derived topography is lower than its internal precision due to imperfect knowledge of the Kaguya orbit, errors in camera pointing, imperfect knowledge of focal length, flat-field, distortion, as well as the spacecraft jitter, which is especially harmful since TC is a push-broom camera. LOLA data [Smith *et al.*, 2010] are characterized by superb internal vertical precision (~10 m) and ~57 m along-orbit spacing of individual elevation measurements, however, the gaps between orbit tracks typically are much wider than ~100 m actual resolution of the TC-derived topography, therefore, the actual resolution is lower. The orbital knowledge of LRO is thought to be much better than for Kaguya, and the absolute vertical accuracy of LOLA data is better than for the TC-derived data, although imperfect knowledge of the spacecraft attitude may introduce some spatial inaccuracy. Combination of LOLA and TC-derived data into SLDEM2015 yielded a data set with spatial resolution of the original TC-derived topography, somewhat better positional accuracy and much better absolute elevation accuracy. No doubt, SLDEM2015 will become a widely used data set.

This data set, however, has a number of shortcomings. First, its geodetic (= absolute spatial) accuracy is probably still not adequate to its resolution. Second, quality of the original SLDEM2013 data set and therefore the derived SLDEM2015 is not uniform because of (1) gaps in the original TC coverage,

and (2) shadows in the original TC images. The latter mostly occur at high latitudes. For some regions TC took images under too low Sun, and the area lost in shadows is significant. Although the data gaps are cosmetically filled with interpolated LOLA topography, they still significantly limit usability of the data set, especially for such applications as statistical analysis of topography, systematic study of impact craters (where they have shadows), regional geologic studies, including potential prospective in-situ exploration sites for the areas that happen to be imaged under not optimal illumination conditions, etc.

OBJECTIVES OF AN ORBITAL EXPERIMENT:

The shortcomings described above make it essential to improve the existing global topographic data sets. Such data set of uniform quality would enable a wide range of scientific studies based on statistical analysis of topography, which promise a breakthrough in understanding of surface modification processes on the Moon. A reference topographic data set of a uniformly high quality would be extremely useful in regional photogeological studies, including geological mapping. Such data set is also essential for planning in-situ exploration, both robotic and human. Improved geodetic accuracy of such reference data set would facilitate planning of remote sensing experiments from the orbit.

PROSPECTIVE APPROACHES TO IMPLEMENTATION:

Properly planned stereo imaging from the orbit with a resolution comparable of slightly exceeding that of TC would enable necessary improvement of the global topographic data set. To provide essential improvement, stereo imaging should: (1) provide observation and illumination geometry favorable for photogrammetric processing; (2) cover the gaps in TC coverage; (3) provide repeated and complimentary (in terms of shadow configuration) coverage for regions with abundant shadows in the TC data set; (4) have a better geodetic accuracy. Ideal illumination geometry for photogrammetric processing is when both imaging forming a stereo pair are taken with the same location of the Sun on the sky. A pair of identical imagers pointing at proper angles fore and aft of the orbiter automatically provides almost ideal illumination geometry. The same approach has been used for TC camera. Proper choice of the looking angles with respect to the nadir would provide proper observation geometry. The necessity of imaging of high-latitude regions (where the TC data suffer from shadowing) requires high orbit inclination (close to polar orbit). A frame camera has a potential for better geodetic accuracy in comparison to push-broom cameras: data from push-broom cameras suffer from the spacecraft jitter, while overlapping frames of frame cameras potentially allow compensation of the uncertainty in the knowledge of the spacecraft attitude and camera pointing. The technical requirements are considered in more detail in [Zubarev *et al.*, 2016].

CONCLUSIONS:

Despite the availability of useful global topographic data sets, their improvement in terms of coverage and geodetic accuracy is an essential objective for future orbital mission(s) to the Moon. This objective can be achieved through imaging with a dedicated frame stereo camera from a polar orbit.

REFERENCES:

- Barker M. K. et al. (2016) *Icarus* 273, 346-355, <http://dx.doi.org/10.1016/j.icarus.2015.07.039>.
 Haruyama J. et al. (2014) *LPSC* 45, 1304, <http://www.hou.usra.edu/meetings/lpsc2014/pdf/1304.pdf>
 Smith, D. E. et al. (2010) *Space Sci. Rev.* 150, 209–241. <http://dx.doi.org/10.1007/s11214-009-9512-y>.
 Zubarev A. E. et al. (2016), this conference.

CHALLENGES OF THE 3D MOON SURFACE MAPPING

M.A. Zakharova, E.N. Slyuta

Vernadsky Institute of Geochemistry and Analytical Chemistry, Moscow,

Kosygina str. 19, Russia

Contact: slyuta@mail.ru

INTRODUCTION:

There is a large enough pool of data today about the lunar surface, obtained from various space missions. The paper describes the analysis of the existing problems, which we face during the 3D modeling of the lunar surface. The sources of challenges include data types, methods of processing, data access, databases organization, existing software etc. Also based on NASA's experience we can offer a set of solutions that should optimize the workflow and organization of the potential future Russian space imaging database.

3D MOON SURFACE MAPPING:

Nowadays, the biggest lunar surface database consists of data obtained by the Lunar Reconnaissance Orbiter [1], which operates with a number of instruments, collecting different types of information. Regarding 3D modeling the lunar surface there are two most popular methods of obtaining information about the topography of celestial bodies - laser altimetry and stereo photogrammetric processing. The necessary data can be obtained after a shooting surface by appropriate instruments - a laser altimeter or optical camera. But the main difference is the output height and spatial resolution of the final 3D model. The laser altimetry data give us an excellent height resolution, and for example LROC NAC images have a high spatial precision, which allows us to obtain the most detailed digital elevation models of the lunar surface. Here we can draw the conclusion that we need to use both types of data in order to achieve the highest spatial and height resolution. We can easily get the both types of data due to Planetary Data System [2] with open access. But in the case of LROC images, we need spatial reference of images, which could be obtained only by using the special software produced by NASA to operate with SPICE database [3].

Consider the process of creating a 3D model by stereophotogrammetric processing the LROC NAC images. First of all images metadata or kernels are needed which could be extracted from SPICE database using ISIS (The Integrated System for Imagers and Spectrometers) software [4]. ISIS – is a free software package developed by NASA for processing space data purposes. Image metadata allows us to attach the spatial reference to the image, and then the stereophotogrammetric processing goes. It could be accomplished using a number of different programs depending on which processing user needs - whether or not automatic. Such programs as ERDAS Imagine, PHOTOMOD and etc. comprise the manual processing, while the ASP (Ames Stereo Pipeline)[5] contain an automatic imaging mode. Its advantage lies in the fact that ASP is the only existing free program for stereo processing the space imagery data. Figure 1 shows several models with the highest spatial (~1.5 m) and height (~5 m) resolution, obtained using ASP and covering the Mons Rumker area.

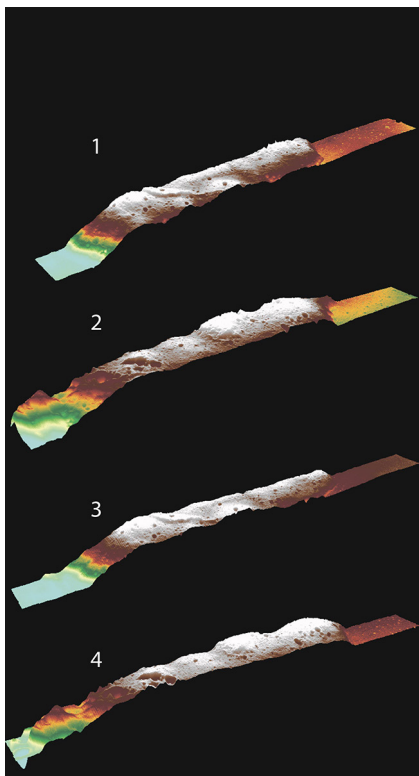


Fig. 1.

CONCLUSIONS:

In fine – the LROC NAC images are the best source of data for obtaining the most detailed 3D models of the lunar surface. Also the ISIS and ASP are the most affordable current software for 3D modeling purposes. But the workflow has several disadvantages such as two different databases for images and images metadata which causes processing difficulties. Despite this, the future prospective Russian space database should incorporate the best features of NASA development. It needs a strict data structure, user-friendly interface and special software for extracting and processing the data collected by Russian lunar missions, exactly Luna-26. All the types of data should be classified in appropriate categories. It also the web platform should be developed to work with them, which includes special tools to facilitate the search and download the necessary data.

Such a large development requires a lot of effort and design, so at this stage there is a need to create a special commission that oversees the development of Russian space database and its supporting components.

REFERENCES:

- [1] Lunar Reconnaissance Orbiter // USGS, NASA, 2015. URL: <http://lunar.gsfc.nasa.gov/index.html>
- [2] PDS: The Planetary Data System // NASA, 2016. URL: <https://pds.nasa.gov/>
- [3] SPICE – An Observation Geometry System for Planetary Science Missions // USGS, NASA, 2016. URL: <http://naif.jpl.nasa.gov/naif/index.html>
- [4] USGS ISIS – Integrated Software for Imagers and Spectrometers, 2009. URL: <http://isis.astrogeology.usgs.gov>
- [5] Broxton M. J., Beyer R. A., Moratto Z., Lundy M., Husman K., 2012. The Ames Stereo Pipeline: NASA's Open Source Automated Stereogrammetry Software. A part of the NASA NeoGeography Toolkit. Version 2.0.0. Intelligent Robotics Group, NASA Ames Research Center, 88 p.

PRIORITIES FOR IMAGING FOR LUNAR ORBITAL MISSIONS CONSIDERING FURTHER PHOTOGRAMMETRIC PROCESSING

A.E. Zubarev¹, I.E. Nadezhkina¹, I.P. Karachevtseva¹, M.A. Kreslavsky^{1,2}, Oberst J.^{1,3,4}

¹*Moscow State University of Geodesy and Cartography (MIIGAiK), MIIGAiK Extraterrestrial Laboratory (MExLab), 105064, Gorokhovskiy per., 4, Moscow, Russia*

²*University of California - Santa Cruz, USA*

³*Technical University of Berlin, Berlin, Germany*

⁴*German Aerospace Center (DLR), Berlin, Germany*

Contact: a_zubarev@miigaik.ru

The Moon is the most studied celestial body. Modern lunar missions such as LRO [1] and Kaguya [2] provided full stereo image coverage of its surface from which detailed DEMs and orthoimages (i.e., rectified images) could be derived. Nowadays, topographic data with vertical resolution of 3-6 meters are available for 80% of the lunar surface [3]. Therefore, it is important to select targets for the new orbital missions in a way to complement already available data, which would allow addressing scientific problems as well as planning future landing missions to the Moon.

We analyzed and summarized the images obtained by those latest missions that provide the most comprehensive currently available visual data. We have studied regions which are of most interest e.g. landing sites of former and future missions, or geologic studies, including known "young" craters. We also included the sites of lunar laser ranging (LLR) [4] into our inventory; they are essential for accurate navigation in the near planetary space, orbit refinement, and reliable post-processing of obtained images. We performed comprehensive analysis of the conditions for technical feasibility of photogrammetric processing and formulated special requirements for the orbit characteristics and for imaging equipment.

As a result, taking into account all factors mentioned above, we have indicated a number of important constraints on the parameters of the orbit and observation geometry, which allow us to obtain data, especially for areas with high scientific priorities, as well for areas where DEMs of limited quality area available only. Properly planned stereo imaging from the orbit with a resolution comparable or slightly exceeding that of the available data sets would enable significant improvements of the global topographic data. Such imaging should have a better geodetic accuracy, cover gaps in the existing coverage, and provide repeated and complimentary coverage for regions with low quality of presently available data.

ACKNOWLEDGEMENTS:

The authors are very grateful to GEOIKHI RAS and to Mikhail Ivanov personally for providing valuable information.

REFERENCES:

1. Robinson M.S. et al. 2010, The Lunar Reconnaissance Orbiter Camera (LROC) instrument overview. *Space Sci. Rev.* 150, pp.81-124.
2. Haruyama, J. et al. 2012, Lunar global digital terrain model dataset produced from SELENE (Kaguya) terrain camera stereo observations. In: *Lunar and Planetary Science Conference*, p. 1200.
3. Barker M.K., et al. 2016, A new lunar digital elevation model from the Lunar Orbiter Laser Altimeter and SELENE Terrain Camera. *Icarus*, 273, pp. 346-355.
4. Williams J.G., Boggs D.H., Folkner W.M. DE430 Lunar orbit, physical librations, and surface coordinates. 2013, Jet Propulsion Laboratory, Report No. IOM 335-JW, DB, WF-20130722-016.

THE EFFECT OF IMAGE COMPRESSION ON DTM QUALITY

A.E. Zubarev¹, I.E. Nadezhdina¹, I.V. Polyanskiy²

¹Moscow State University of Geodesy and Cartography, MIIGAiK
Extraterrestrial Laboratory (MExLab), 105064, Gorokhovskiy per., 4, Moscow,
Russia

²Space Research Institute of Russian Academy of Sciences (IKI RAS)
Profsoyuznaya Str, Moscow, Russia, 117997

Contact: a_zubarev@miigaik.ru

Modern satellite imagery systems provide very high resolution that requires large amounts of data storage and transmissions to Earth. Reduction of resolution leads to a loss of useful information, therefore it is important to retain data with maximum resolution without generalization. However, in resource-limited storage and limited capacity of transmission channels, as well as other restrictions, we face up to the task of data compression. Lossless compression can provide optimization in an average of 1.5 times, which is not enough for high resolution imagery. Compression with normalized losses provides a significant reduction in volume, but it is necessary to determine the acceptable level of losses in data quality for the particular case of lunar topographic stereo imaging. JPEG2000 standard [1] has a successful history of use in imaging equipment for various purposes and is supported by the hardware used in outer space as well. It is important to assess the quality of the recovered data, especially with different heights of the Sun, since a large percentage of the observation targets on the Moon are located in shaded areas or terminators. We have performed an experiment on reconstruction and post-processing of high resolution lunar images obtained with different illumination conditions and undergone different compression., LRO NAC stereo pairs [2] with different resolution (0.5 - 1.3 m) and the various sun heights (19 - 56 degrees) were selected to analyze the accuracy of DTM recovery. Then, the selected raw images were compressed using JPEG2000 compression algorithm [1] with coefficients 3x, 4x, 5x, 8x, and 10x. DTMs were formed for each compression ratio and then they were compared with the original DTM (obtained based on the images without compression). As a result, the dependence of the DTM accuracy from compression ratio was determined, threshold compression value was defined, and areas which are most influenced by compression were indicated.

REFERENCES:

1. Information technology - JPEG 2000 image coding system - Part 1: Core coding system / Note: new national adoption*Approved 2002-08-29. ISO/IEC 15444-1.
2. Robinson M.S., Brylow S.M., Tschimmel M., Humm D., Lawrence S.J., Thomas P.C., Denevi B.W., Bowman-Cisneros E., Zerr J., Ravine M.A., Caplinger M.A., Ghaemi F.T., Schaffner J.A., Malin M.C., Mahanti P., Bartels A., Anderson J., Tran T.N., Eliason E.M., McEwen A.S., Turtle E., Jolliff B.L., Hiesinger H. 2010, the Lunar Reconnaissance Orbiter Camera (LROC) instrument overview. Space Sci. Rev. 150, pp.81-124.

NITROGEN ISOTOPE RATIO IN THE SOLAR SYSTEM AND ITS EVOLUTION ON TITAN

V.A. Krasnopolsky

*Catholic University of America, Department of Physics, 620 Michigan Avenue,
N.E., Washington, DC 20064, USA
vlad.a.krasn@gmail.com*

Isotopic ratios in atmospheric species imply significant constraints on origin and evolution of the atmosphere. Measurements of $^{14}\text{N}/^{15}\text{N}$ on Venus, in Mars' meteorites, chondrites, and the solar wind gave the ratios close to that on Earth, 272. This favored a uniform distribution of nitrogen isotopes in the Solar System.

The concept was broken by the Galileo probe that measured $^{14}\text{N}/^{15}\text{N} = 435 \pm 65$ in Jupiter. Later improved analysis of the solar wind gave 440 ± 130 . This was explained by N_2 with $^{14}\text{N}/^{15}\text{N} \approx 440$ as a dominant nitrogen species in the protosolar nebula with NH_3 and HCN ices having $^{14}\text{N}/^{15}\text{N} \approx 270$. Almost all N_2 was captured by the Sun and Jupiter, while comets delivered NH_3 and HCN to the terrestrial planets and Titan. NH_3 was converted to N_2 by photolysis and/or thermolysis.

However, the Huygens probe measured $^{14}\text{N}/^{15}\text{N} = 167.6 \pm 0.7$ in N_2 on Titan. Furthermore, recent observations of comets resulted in $^{14}\text{N}/^{15}\text{N} = 130 \pm 30$ in ammonia in comets. This requires further development of the problem of nitrogen isotopes in the Solar System.

Another puzzle is the observed $^{14}\text{N}/^{15}\text{N} \approx 60$ in HCN on Titan, much smaller than that in N_2 . Liang et al. (2007) studied predissociation in the N_2 bands at 80-100 nm and found that small isotope shifts of the $^{14}\text{N}^{15}\text{N}$ lines put them in windows between the N_2 lines and increase the $^{14}\text{N}^{15}\text{N}$ predissociation on Titan by a factor of 8. Our model (Krasnopolsky 2014) accounts for all processes of dissociation, ionization, and dissociative ionization of N_2 on Titan by the solar EUV photons, photoelectrons, magnetospheric electrons and protons, and cosmic rays. Using all these data, the calculated $^{14}\text{N}/^{15}\text{N} = 57$ in nitriles, in excellent agreement with the observations.

According to Krasnopolsky (2014), the irreversible loss of nitriles on the surface removes $390 \text{ g cm}^{-2} \text{ Byr}^{-1}$ of nitrogen with fractionation factor $F = 168/60 = 2.8$. Another loss by sputtering is $60 \text{ g cm}^{-2} \text{ Byr}^{-1}$ (De la Haye et al. 2007) with $F = 0.73$ (Mandt et al. 2014). The young Sun was brighter in EUV by a factor of 6 at $t = 1 \text{ Byr}$ than now ($t_0 = 4.6 \text{ Byr}$), and the solar wind was stronger by a factor of 20 (Penz et al. 2005). Assuming hydrodynamic escape with very low isotope fractionation in the first billion years (Mandt et al. 2014), we calculated fractionation of nitrogen isotopes in two models.

The first model adopts a linear response of the atmosphere to the varying solar EUV and wind; it gives the initial $^{14}\text{N}/^{15}\text{N}$ ratio of 108. The square root response is adopted in the second model that gives the initial $^{14}\text{N}/^{15}\text{N}$ ratio of 125. In both cases the initial nitrogen isotope ratio on Titan was close to that of ammonia in comets.

ACKNOWLEDGEMENTS

This work is supported by Grant 16-12-10559 of the Russian Science Foundation to Moscow Institute of Physics and Technology (PhysTech) and V.A. Krasnopolsky.

REFERENCES

- De la Haye, V., et al., *J. Geophys. Res.* 112, A07309, 2007.
Krasnopolsky, V.A., *Icarus* 236, 83-91, 2014
Liang, M.C., et al., *Astrophys. J. Lett.* 664, L115-L118, 2007.
Mandt, K.E., et al., *Astrophys. J. Lett.* 788, L24 (5 pp), 2014.
Penz, T., et al., *Adv. Space Res.* 36, 241-250, 2005.

ON THE IRON CHLORIDE AEROSOL IN THE CLOUDS OF VENUS

V.A. Krasnopolsky

*Catholic University of America, Department of Physics, 620 Michigan Avenue,
N.E., Washington, DC 20064, USA*

Contact: vlad.a.krasn@gmail.com

Iron chloride in the Venus clouds is under discussion for three decades, and the saturated vapor pressure of this species is of crucial importance for its modeling. There is a great scatter in the published data, and the preferable results are by Rustad and Gregory (1983, *J. Chem. Eng. Data* 28, 151-155) and those based on thermodynamic parameters by Chase (1998, *J. Phys. Chem. Ref. Data Monograph* 9). Using these data, loss by coagulation with sulfuric acid, and transport by eddy diffusion and the Stokes precipitation, the model confirms conclusions of our early study (Krasnopolsky 1985, *Planet. Space Sci.* 33, 109-117) that FeCl_3 in the Venus clouds (1) agrees with the near UV and blue reflectivity of Venus (Zasova et al. 1981, *Adv. Space Res.* 1, #9, 13-16), (2) was observed by the direct X-ray fluorescent spectroscopy, (3) explains the altitude profiles of the mode 1 aerosol in the middle and lower cloud layers and (4) the decrease in the NUV absorption below 60 km. Here we add to these conclusions that (5) the delivery of FeCl_3 into the upper cloud layer and the production of sulfuric acid are just in proportion of 1 : 100 by mass that is required to fit the observed NUV albedo. Furthermore, (6) the mode 1 and 2 particle sizes fit this proportion as well. Finally, (7) the required Fe_2Cl_6 mixing ratio is 17 ppbv in the atmosphere and the FeCl_3 mole fraction is 19 ppbv in the Venus surface rocks.

ULTRAVIOLET ABSORBER IN THE CLOUDS OF VENUS

HOW CAN WE KNOW THAT WE ARE NOT SAMPLING BACTERIA IN THE CLOUDS OF VENUS IF THEIR PHYSI- CAL AND SPECTRAL PROPERTIES ARE SIMILAR?

S.S. Limaye

University of Wisconsin

Contact: SanjayL@ssec.wisc.edu

The nature of the ultraviolet absorber on Venus has been a puzzle for more than a half century. Imaging of the Venus cloud cover (Titov et al., 2008) has provide ample evidence of the short and long term changes in the appearance, spatial scales and distribution as well as magnitude of the contrasts globally, but the identity/ies of the absorber remains un-confirmed. Further, the distribution of the ultraviolet absorber is spatially and temporally variable on a variety of scales and the reasons for the ultraviolet contrasts remain unknown, except that they are not due to Rayleigh scattering (Travis, 1975). Photochemistry and convection are not very convincing mechanisms for their existence in the very stable equatorial and mid-latitude regions of Venus in the upper portions of the cloud layer. Why the ultraviolet absorber(s) is/are not well mixed is a puzzle and suggests some active mechanism for their existence. Optical observations of glory (Markiewicz provide inferences of the index of refraction somewhat higher than that of sulfuric acid which led to the original identification of the nature of the clouds (but not the ultraviolet absorber) by Hansen and Hovenier (1974).

Although the first detailed suggestion for possible life in the clouds of Venus was discussed by Morowitz and Sagan in 1967, interest in the topic dimmed as the results about the composition of the clouds , atmosphere and surface conditions trickled in from the Venera and Pioneer Venus missions. Cockell (1999) presented the first detailed discussion of life conducive conditions in the clouds of Venus. Subsequently Schulze-Makuch et al. (2003; 2004), Grinspoon and Bullock (2007), Grinspoon et al. (2011) and others suggested potential life on Venus and mission concepts to follow them. Since then information from the biology of acid resistant bacteria regarding their properties. Schulze-Makuch and Irwin (2006) suggested that the S8 proposed as a possible constituent responsible for ultraviolet contrasts seen in the clouds of Venus could be due to microbiological sources. But there are many other species of acid resistant bacteria found on Earth which can likely survive in the Venus clouds it appears, and similar species could have evolved independently on Venus during its period when there was a liquid water reservoir on the surface (Donahue et al., 1982; Donahue and Hodges, 1992) which could have lasted as long as two billion years.

A literature survey of potential bacteria candidates suggests that there is a great deal of resemblance in the physical and spectral properties of the Venus cloud particles and those of certain species of acid resistant bacteria. The particle size (sub-micron to 1.2 micron radius) as well as ultraviolet absorption below 400 nm and variable absorption between 2 and 3 microns which are key characteristics of the Venus cloud particles are comparable. From thousands of ultraviolet images of Venus in which the cloud contrasts at 283, 365 and 410 nm images have been seen (Mariner 10, Galileo and Venus Express missions), the short term evolution of the features has been a challenge to explain unambiguously from purely physical processes. A resource limited environment such as that in the clouds of Venus where water in liquid or vapor form is not abundant may be consistent for their growth and decay characteristics. How can we know that the instruments on the probes that have sampled clouds did not sample bacteria? Recent research suggests that Venus could have harbored liquid water on its surface for about 2 billion years, so it is conceivable that life migrated to the clouds when surface became warmer. How can we look for the distinctive properties of the clouds to know if the ultraviolet absorber is organic or inorganic?

Alternately, it is also possible that bacteria riding on interplanetary dust entering Venus atmosphere can reside in the Venus clouds similar to what is suspected on Earth (Wainwright et al., 2006) where bacteria have been discovered at altitudes as high as 42 km (Wainwright et al., 2002; Narlikar et al., 2003)

REFERENCES

- Cockell, C.S., Life on Venus, *Planetary and Space Science*, 47, 1487-1501, 1501, 1999. DOI:10.1016/S0032-0633(99)00036-7.
- Donahue, T.M., J.H. Hoffman, R.R. Hodges, and J. Watson, Venus was wet: a measurement of the ratio of D to H., *Science*, 216, 630-633, 1982.
- Donahue, T.M. and R.R. Hodges, Past and present water budget of Venus, *J. Geophys. Res.*, 97, 6083-6091, 1992.
- Grinspoon, D. H., & Bullock, M. A. (2007). Astrobiology and Venus exploration. *Exploring Venus as a Terrestrial Planet*, (176), 191.
- Hansen, J. E., and J. W. Hovenier, Interpretation of the polarization of Venus, *J. Atmos. Sci.* 31, 1137-1160, 1974.
- Markiewicz, W.J., E. Petrova, O. Shaligyna, S. M. Almeida, D.V. Titov, S.S. Limaye, N. Ignatiev, T. Roatsch, T. and K.D. Matz, Glory on Venus cloud tops and the unknown UV absorber, *Icarus* 234:200-203, May 2014. DOI: 10.1016/j.icarus.2014.01.030
- Narlikar, J. V., Lloyd, D., Wickramasinghe, N. C., Harris, M. J., Turner, M. P., Al-Mufti, S., et al. (2003). A balloon experiment to detect microorganisms in the outer space. *Astrophysics and Space Science*, 285(2), 555-562.
- Kawabata, K., D. L. Coffeen, J. E. Hansen, W. A. Lane, M. Sato, and L. D. Travis, Cloud and haze properties from Pioneer Venus polarimetry, *J. Geophys. Res.*, 85,, 8129-8140, 1980.
- Morowitz, H.D. and C. Sagan, Like in the clouds of Venus, *Nature*, 215, 1259-1260, 1967. doi:10.1038/2151259a0
- Schulze-Makuch, D., & Irwin, L. N. (2002). Reassessing the possibility of life on Venus: Proposal for an astrobiology mission. *Astrobiology*, 2(2), 197-202.
- Schulze-Makuch D, Grinspoon DH, Abbas O, Irwin LN, & Bullock MA (2004). A sulfur-based survival strategy for putative phototrophic life in the Venusian atmosphere. *Astrobiology*, 4 (1), 11-8 PMID: 15104900
- Schulze-Makuch, D., & Irwin, L. N. (2006). The prospect of alien life in exotic forms on other worlds. *Naturwissenschaften*, 93(4), 155-172.
- Titov, D. V., Taylor, F. W., Svedhem, H., Ignatiev, N. I., Markiewicz, W. J., Piccioni, G., & Drossart, P. (2008). Atmospheric structure and dynamics as the cause of ultraviolet markings in the clouds of Venus. *Nature*, 456(7222), 620-623.
- Travis, L. D., On the origin of ultraviolet contrasts on Venus, *J. Atmos. Sci.* , 32, , 1190-1200, 1975.
- Wainwright, M., Wickramasinghe, N. C., Narlikar, J. V., & Rajaratnam, P. (2002). Microorganisms culture from stratospheric air samples obtained at 41 km. *FEMS Microbiology Letters*, 10778, 1-5.
- Wainwright, M., Alharbi, S., & Wickramasinghe, N. C. (2006). How do microorganisms reach the stratosphere? *International Journal of Astrobiology*, 5(1), 13-15. DOI: <http://dx.doi.org/10.1017/S1473550406002825>.

SULPHUR BEARING SPECIES AT THE NIGHT SIDE OF VENUS' UPPER MESOSPHERE

D.A. Belyaev¹, D.G. Evdokimova¹, M.S. Luginin¹, A.A. Fedorova¹,
O.I. Korablev¹, F. Montmessin², E. Marcq², J.-L. Bertaux²

¹Space Research Institute of the Russian Academy of Sciences (IKI), 84/32
Profsoyuznaya Str., Moscow 117997, Russia

²LATMOS - UVSQ/CNRS/IPSL, 11 bd d'Alembert, 78280 Guyancourt, France
Contact: bdenya.iki@gmail.com

INTRODUCTION

The cycle of sulphur bearing species on Venus is directly connected to the chemistry of sulphur dioxide (SO_2), which photolysis and oxidation influences formation of the planet's clouds. They consist of sulphuric acid droplets (75-80% of concentration in water) that totally enshroud Venus at altitudes 50-70 km. It is possible that SO_2 abundance within and above the clouds is a major observable chemical indicator of recent volcanic activity on Venus [1]. Another possible evidence of actual eruptions comes from Venus Express VIRTIS and VMC surface observations at the 1- μm transparency window [2, 3]. A volcanic outburst may cause a disturbance in vertical diffusion and the lower air masses rich in sulphur dioxide may reach above the clouds. Such releases may last from a few weeks to a few months as observed in the Earth atmosphere.

Recent ground-based observations [4-7] and continuous monitoring from the Venus Express orbiter [8-10] have shown high temporal and spatial variability of SO_2 abundance mostly on the day side: from 20 to 500 ppbv above the clouds. Nevertheless, there is a gap in the detailed analysis at the night-time mesosphere, in absence of photo dissociation processes. Around midnight interactions of sulfur dioxide with the global subsolar-antisolar (SS-AS) circulation become dominant at altitudes ~ 100 km, and chemical reactions with atoms of Cl, OH, O are significant as well.

In this paper we present vertical distribution of SO_2 content at the night side of Venus upper mesosphere that resulted from stellar occultations made by the SPICAV UV spectroscopy. This mode of occultation occurred for the entire VEx mission, and it gave us possibility to observe yearly variations for period 2006-2014 at altitudes 85-100 km. In parallel, we have reprocessed the terminator dataset from the UV solar occultations at the same altitude range [8] up to 2014. Like this, we have got (for the first time) whole the night-time coverage of SO_2 distribution from the sunset to the sunrise twilights of the upper mesosphere.

RESULTS

In this paper we present new results from sulphur dioxide observations made by SPICAV UV spectrometer onboard Venus Express orbiter [11] in regimes of stellar (STELL) and solar (SOL) occultation. In the mode of stellar occultation the instrument observes night-side mesosphere while at solar occultation it sounds evening/morning twilights at altitude range 85-100 km. SPICAV UV can register SO_2 absorption bands at 190-220 and 270-300 nm and CO_2 bands at 120-200 nm with spectral resolution 1-2 nm. As a result, vertical distribution of SO_2 mixing ratio was retrieved in observation period from June 2006 to April 2014. On average, the volume mixing ratio (VMR) increases with altitude from 20 to 200 ppbv (Fig. 1.).

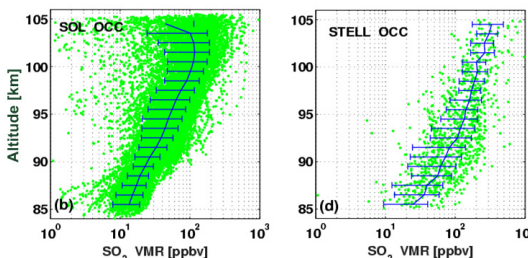


Fig. 1. Altitude distribution of SO_2 mixing ratio from SPICAV UV solar (a) and stellar (b) occultations. Solid lines are weighted mean values with standard deviations. Error bars of individual dots (not shown) are less than the dispersion of the data.

The resulting inter-annual diagram at altitude range 90-95 km is presented in Figure 2, showing time intervals with respectively high (> 100 ppbv) and low (< 50 ppbv) SO_2 contents from both regimes of occultation. We found that the long-term behavior was identical for stellar and solar occultations with 1.5-2 times higher in SO_2 content at the STELL's case.

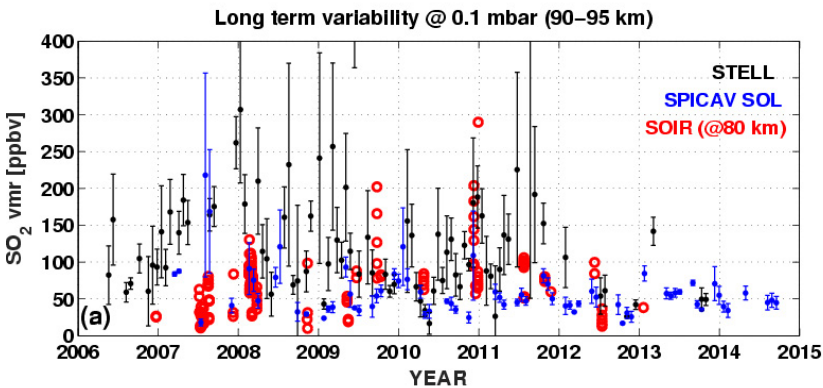


Fig.. 2. Time Long term variability of SO_2 mixing ratio at the altitude range 90-95 km. Each point (black dot for STELL and blue dot for SOL occultations) is a result of the grouping density profiles over 10 orbits. Red circles were taken from SOIR occultation profiles at altitude ~ 80 km [10].

In order to observe night time variations of SO_2 content, we grouped altitude profiles of the VMR in intervals of 0.5 hours of Solar local time on Venus, e.g. from the evening to the morning terminators. The result is presented in Figure 3 for all observed altitudes binned by 1 km between 85 and 105 km. We found that at lower altitudes (85-90 km) a difference between the midnight and the twilights was almost negligible: 30-50 ppb of SO_2 vmr. At higher altitudes (>95 km) the midnight content appears to be 3-4 times more than at twilights: 150-200 ppb versus 50 ppb.

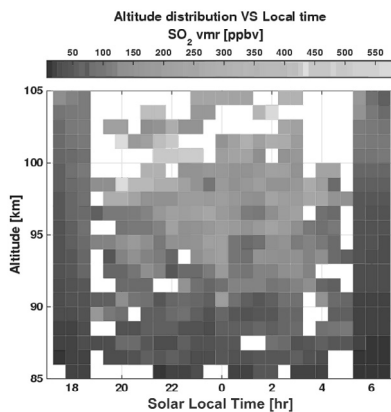


Fig.. 3. Altitude distribution of SO_2 mixing ratio as varied with Solar local time. Data around 18:00 and 06:00 correspond to SOL occultations while all the rest are from STELL.

Additional analysis is going on together with properties of aerosol particles, retrieved from the same sessions of the SOL occultations by the IR channel of SPICAV ($0.7-1.7 \mu\text{m}$) [12]. This study would help us to check if the aerosol droplets can be a significant reservoir of SO_2 in the upper mesosphere.

ACKNOWLEDGEMENTS

Venus Express is an ESA scientific mission. SPICAV development and operations were funded by CNES and Roscosmos. D. Belyaev, D. Evdokimova and M. Luginin acknowledge support from the program №9 from the RAS. A. Fedorova and O. Korabiev acknowledge support from the RFFI # 16-52-16011. F. Montmessin, E. Marcq and J.-L. Bertaux acknowledge support from the Centre National d'Études Spatiales (CNES) and from the Centre National de la Recherche Scientifique (CNRS).

REFERENCES:

- [1] Esposito L.W., 1984. Sulfur dioxide: Episodic injection shows evidence for active Venus volcanism. *Science* 223, 1072–1074.
- [2] Smrekar S.E. et al., 2010. Recent hotspot volcanism on Venus from VIRTIS emissivity data. *Science* 328, Issue 5978, pp. 605-608. DOI: 10.1126/science.1186785.
- [3] Shalygin E. et al., 2015. Active volcanism on Venus in the Ganiki Chasma rift zone. *Geophys. Res. Lett.*, 2015: p. 10.1002/2015GL064088.
- [4] Encrenaz T. et al., 2012. HDO and SO₂ thermal mapping on Venus: evidence for strong SO₂ variability. *A&A* 543, A153.
- [5] Krasnopolsky V.A., 2010. Spatially-resolved high-resolution spectroscopy of Venus. 2. Variations of HDO, OCS, and SO₂ at the cloud tops. *Icarus* 209, 314-322.
- [6] Sandor B.J. et al., 2010. Sulfur chemistry in the Venus mesosphere from SO₂ and SO microwave spectra. *Icarus* 208, 49–60.
- [7] Jessup et al., 2015. Coordinated Hubble Space Telescope and Venus Express observations of Venus' upper cloud deck. *Icarus*. <http://dx.doi.org/10.1016/j.icarus.2015.05.027>.
- [8] Belyaev D. et al., 2012. Vertical profiling of SO₂ and SO above Venus' clouds by SPICAV/SOIR solar occultations. *Icarus* 217, 740–751.
- [9] Marcq E. et al., 2013. Variations of sulphur dioxide at the cloud top of Venus's dynamic atmosphere. *Nature Geoscience*, vol. 6, 25-28. DOI: 10.1038/NGEO1650.
- [10] Mahieux A. et al., 2015. Venus mesospheric sulfur dioxide measurement retrieved from SOIR on board Venus Express. *Planet. Space Sci.* v.113-114, p.193–204.
- [11] Bertaux J.-L. et al., 2007. SPICAV on Venus Express: three spectrometers to study the global structure and composition of Venus atmosphere. *Planet. Space Sci.* 55, 1673–1700.
- [12] Luginin M. et al., 2016. Aerosol properties in the upper haze of Venus from SPICAV IR data. *Icarus* 277, p. 154–170.

VENERA 9, 10 AND VENERA 15, 16 BISTATIC RADAR RESULTS: THE VENUS SURFACE AND LOWER ATMOSPHERE

A.G. Pavelyev, S.S. Matyugov, A.A. Pavelyev, V.N. Gubenko

Kotelnikov Institute of Radio Engineering and Electronics RAS, Space Radio Physics Department, Vvedenskogo sq. 1, Fryazino, Moscow region, 141190, Russian Federation

Contact: alxndr38@mail.ru

INTRODUCTION:

Aim of this contribution is to present results of reanalysis of the first bistatic radar investigations of the Venus equatorial and polar regions provided using Venera-9, 10 and 15, 16 satellites. Bistatic radar results are compared with the first monostatic radio images obtained by the Venera 15,16 and Magellan orbiters [1-5]. Bistatic and monostatic radar studying the physical properties of Venus surface, subsurface structures, and atmosphere in the different wavelength band (from 3 cm up to several tens of meters) is important direction in the future radio science of Venus research [6,7].

RADIO IMAGES AND CHARACTERISTICS OF THE VENUS SURFACE:

Below are shown radio images and results of bistatic measurements of reflectivity and roughness in two equatorial and four polar regions. The first bistatic radar measurements with spatial resolution 10-20 km have been carried out during autumn of 1975 year in the Venus equatorial regions using the Venera-9 and 10 satellites.

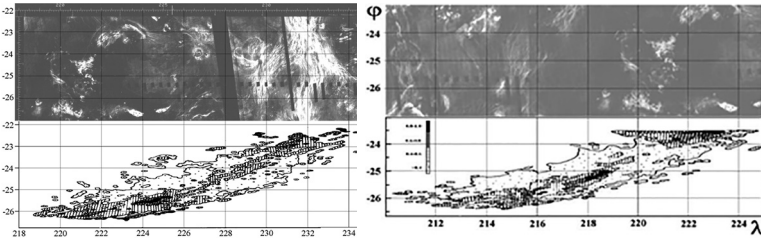


Fig. 1. Monostatic SAR (1994) Magellan (top) and bistatic monochromatic (1975) Venera-10 (bottom) radio images of two parts of equatorial plain obtained at wavelengths 12.4 cm and 32 cm.

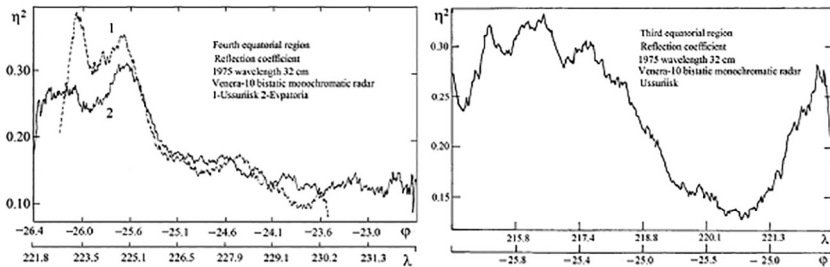


Fig. 2. Bistatic monochromatic reflection coefficient in the two parts of equatorial area (Venera-10).

Bistatic and monostatic radars used specular and diffuse part of reflections. The first bistatic radar measurements with spatial resolution 10-20 km have been carried out during autumn of 1975 year in the five Venus equatorial regions using the Venera-9 and 10 satellites. Small roughness and, in general, plain character of relief in the investigated regions have been revealed (Figures 1,2).

In 1983, the satellites Venera 15 and 16 have carried out new bistatic radar experiments with spatial resolution in the interval 5 - 10 km (Figure 3). New information on the large-scale topography and roughness of small-scale relief has been obtained in Northern polar areas of the planet. Some features have been detected. 1. The significant variations of the reflectivity 2-4 times (Figure 4, left) were found in the first region (Figure 3, left). The second area (Figure 3,

left) of reflectivity magnitude was far below (by three – four times) the previously measured values in the equatorial regions of Venus. The reflectivity magnitude in the second area was far below (by three – four times) the previously measured values in the equatorial regions of Venus. These significant reflectivity variations may be related to changes in the conductivity of the ground. 2. Extremely small values roughness parameter with rms of slopes equal to 0.15 degrees were recorded in the Northern area centered at coordinates 73.4 N and 228 E.

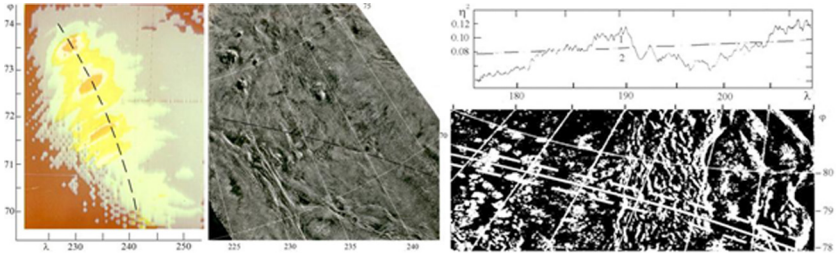


Fig. 3. Bistatic (left) and monostatic SAR (middle and bottom, right) Venera-15 radio images of the North polar plain obtained at wavelengths 32 cm and 8 cm, respectively. Dashed lines indicate the trajectory of specular point during bistatic radar investigation. Experimental and theoretical dependence of the reflection coefficient along the trajectory of specular point (continuous and dashed curves, respectively). Dashed curve is reduced to 4 times for convenience of comparison (top, right).

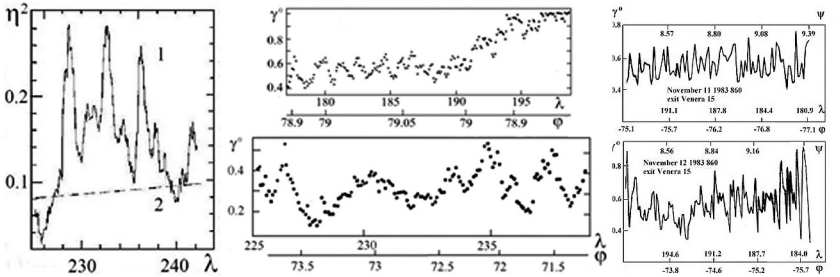


Fig. 4. Bistatic reflection coefficient in the first region (left). Curves 1 and 2 correspond to the experimental data and reflectivity calculated under assumption of homogeneous ground with dielectric constant 5.1. Curve 2 is reduced to 4 times for convenience of comparison. Surface roughness in the first (bottom) and second (top) Northern polar regions (middle). Surface roughness in the first (bottom) and second (top) Southern polar regions (right).

CONCLUSIONS:

To obtain the information on the Venus subsurface structure up to depth 1 km it is necessary to use radio waves in the Medium Frequency (MF), or High Frequency (HF) bands with wavelength from 1 m up 30 m at different polarizations states. For investigations of the layered structures of the Venus atmosphere a new eikonal acceleration/intensity technique is proposed [7]. This technique allows: (1) one frequency high-precision measuring the total absorption of radio waves in the atmosphere; (2) estimating vertical gradients of the refractivity, and determining the height, slope, and horizontal displacement of the atmospheric and ionospheric layers.

REFERENCES:

- [1] Pavelyev A.G. et al. (1990) *Cosmic Research*, 28, 125-133.
- [2] Pettengill G. H. et al. (1996) *Science*, (272), 1628–1631.
- [3] Simpson R.A. et al. (2009), *JGR*, 114, E00B41.
- [4] Pavelyev A.G. et al. (1976) *Radio Engineering and Electronic Physic*, 21(9), 6–11.
- [5] Kolosov M.A. et al. (1981) *Icarus*, 48, 188–201.
- [6] Head J.W. and Basilevsky A.T. (1998) *Geology*, (26), 35–38.
- [7] Pavelyev A. G. et al. (2011) *Radio Sci.*, (46), RS1009.

TOPOGRAPHIC CHARACTERISTICS OF RIFT ZONES ON VENUS

E.N. Guseva

Vernadsky Institute, Moscow, 11999, Russia

Contact: guseva-evgeniya@ya.ru

INTRODUCTION:

Rift structures of Venus are concentrated mainly in the equatorial part of the planet. The most expressive in relief are the rift valleys (canyons). They are propagated from the tops of large domes of Atla and Beta Regions and form a giant triangular structure – BAT (Beta-Atla-Thetis) [1-3]. Also important are the rift valleys that cut Eistla Regio and valleys in the southern hemisphere along the margin between Lavinia Planitia (to the north) and Lada Terra (to the south). Less expressive are belts of graben that often continue the trends of the canyons. The belts represent wide (hundreds of kilometers) zones of grabens and troughs that cross all of the structural and material complex, except for the younger lobate plains [4].

GOAL OF THE STUDY:

was establishing the possible correlations between topographic and morphometric characteristics of the rift valleys and the belts of graben.

RESULTS:

The rift valleys are spatially associated with dome-shaped rises [5]. The largest rises with rifts are presented by Atla and Beta Regions [6; 7]. The structures of rift valleys are propagated from the crest of the domes and represent individual deep canyons, which extend for thousands of kilometers. The obvious spatial associations of the rift valleys with the rift domes are indicate their genetic relationships. The morphological and topographic characteristics of the rift zones in this case are inspected to be controlled by uplift of the domes. In the places where rifts valley cross the domes, the depth of the rift correlates with the height of domes. Complete absence of correlation is observed between the widths of domes and the depth of rift valleys and the heights of domes and widths of the rift valleys. Perhaps, the absent of the correlations is explained by prolonged and possibly multistage process of domes formation. Probably, the formation of domes in the Atla and Beta regions take place after the regional plains formation because the pattern of wrinkle ridges does not indicate the presence of the rises by the time of the formation of the ridges [8]. The topographic and morphometric characteristics of rifts (depths and widths) demonstrate a positive correlation for N branch of rift in Beta Regio and a negative correlation for SE branch of rift in Atla Regio (Fig. 1).

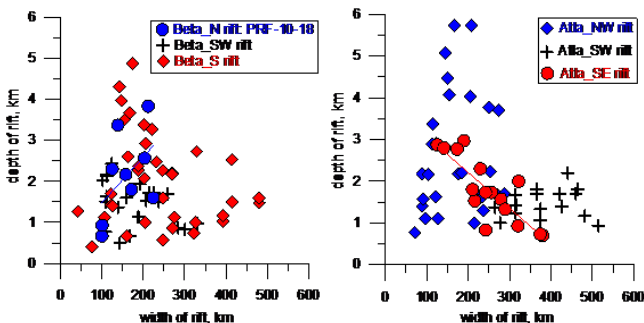


Fig. 1. Correlation between width and depth of rifts in Atla and Beta Regions: for N rift of Beta a weakly expressed trend is observed (the correlation coefficient is ~ 0.5); for SE rift in Atla Regio there is a trend of increasing of the rift width with decreasing of its depth (the correlation coefficient is ~ 0.8).

Perhaps the rifts of the studied regions are at different stages of geological evolution: N rifts of Beta Region can be characterized as “growing”, and SW rift of Atla Regio - as “ancient”.

The graben belts have no spatial association with dome-shaped rises and often continue the trend of rift valleys on the slope of domes and far beyond.

In some places, the graben belts connect the dome-shaped rises. Structures of the graben belts are expressed in relief as series of closely spaced individual grabens and horsts. Topographic and morphometric characteristics (depths and widths) of these structures have no correlation with each other (Fig. 2). Thus, the large width of the belts is not characterized by the greater depth. The absence of such a correlation probably suggests their morphological maturity, when increase of the width is not accompanied by the increase of the depth.

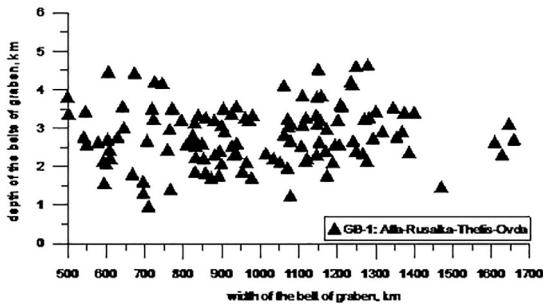


Fig. 2. Maximum depth vs. maximum width for the graben belts in the Atla-Rusalka-Thetis-Ovda regions.

CONCLUSIONS:

The structures of rift valleys and graben belts form two distinct facies of rift zones of Venus (Fig. 3). The absence of relationship between width and depth of the rift valleys and their correlation with widths of the domes perhaps reflects the long and multistage evolution of topography.

Domes formation and lithosphere cracking [7; 9] occurred in the Atla and Beta regions over the central parts of the uplift [10-12]. Diapirs interacted with presumably "dry" and "stiff" [13] and perhaps thick (to 300 km [14; 15]) lithosphere of Venus. Within the domes, the deep and relatively narrow rift valleys formed, extending outward from the central parts of the domes. The average depth of the rift valleys was increased at the initial stages of the rifts evolution (circles and rhomb in Fig. 3). The rift valleys are replaced by the graben belts when rift zones propagated beyond the domes (Fig. 3). For graben belts, there is no correlation between their maximum width and depth (Fig. 2). The lack of such correlation suggests a more mature stage of evolution of the graben belts compared with the rift valleys. If this interpretation is correct, the rift valleys are the result of more recent deformation during the ongoing uplift of the domes.

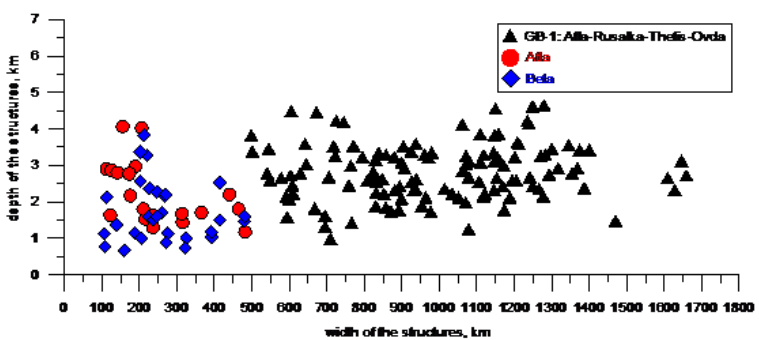


Fig. 3. Maximum depth vs. maximum width for the structures in the middle part of the Atla and Beta regions and for graben belts in Atla-Rusalka-Thetis-Ovda regions.

REFERENCES:

- [1] Masursky et al. JGR. 1980. V.85. P.8232-8260; [2] Shaber. GRL. 1982. V.9. P.499-502; [3] Head et al. JGR. 1992. V.97. P. 13,153-13,197; [4] Ivanov and Head. PSS. 2013. V. 84. P. 66-92; [5] Ivanov et al., SSR. V. 49. P.1-11. 2015; [6] Stofan et al. JGR. V.100. P.23,217-23,327. 1995; [7] Kiefer and Hager. GJR. V.96. P.20,497-20,966. 1991; [8] Basilevsky and Head. ICR. V.192. P.167-186. 2007; [9] Smrekar et al.//in Venus II, eds. Bougher et al. Univ. of Arizona Press. 1997. P. 845-878; [10] Esposito et al. ICR. V.51. P.448-459. 1982; [11] Stofan et al. GSA Bull. V.101. P.143156. 1989; [12] Senske et al. GRL. 1991. V.18. P.1159-1162; [13] Mackwell et al. JGR. V.103. P.975. 1998; [14] Kucinskas and Turcotte. ICR. V. 112. P.104-116. 1994; [15] Veizolainen et al. JGR. 2004. V. 109. P.1-8.

THE JAPANESE VENUS ORBITER AKATSUKI AND ITS INITIAL SCIENTIFIC RESULTS

Chikako Hirose, Masato Nakamura, Nobuaki Ishii, Takeshi Imamura, Atsushi Yamazaki, Manabu Yamada, Takao M. Sato, Takehiko Satoh, Junichi Nakatsuka, Tomoaki Toda, Hiroyuki Toyoda, Sumitaka Tachikawa, Masatoshi Ebara, Takeshi Oshima, Hiroshi Terada, Chiaki Ukai, Kota Matsushima, Tomoya Fujita, Kozo Otani, Yukio Kamata, Makoto Suzuki, Naomoto Iwagami, Makoto Taguchi, Tetsuya Fukuhara, Shigeto Watanabe, Yukihiko Takahashi, Munetaka Ueno, George L. Hashimoto, Toru Kouyama, Kazunori Ogohara, Ko-ichiro Sugiyama, Hiroki Kashimura, Shoko Ohtsuki and Hiroki Ando,
Japan Aerospace Exploration Agency
Contact: <hirose.chikako@jaxa.jp>

The Japanese Venus orbiter, AKATSUKI (PLANET-C), was launched on May 21, 2010 and it arrived at Venus on December 7, 2010. However, due to a malfunction of the propulsion system, it failed in Venus orbit insertion. Using the reaction control system, instead of the broken orbital maneuvering engine, the recovery maneuver was conducted on December 7, 2015. AKATSUKI became a Venus orbiter at the second attempt of Venus orbit insertion. It rotates around Venus with a period of 10.5 days. Its periapsis is about 400 – 10,000 km and its apoapsis is about 360,000 km. AKATSUKI currently transmits important scientific data on a daily basis.

JSDT :SCIENTIFIC GOALS AND ARCHITECTURE OF THE MISSION VENERA-D

L. Zasova¹, D. Senske², A. Ocampo³, T. Economou⁴, N. Eismont¹, L. Esposito⁵, M.Gerasimov¹, D. Gorinov¹, N. Ignatiev¹, M. Ivanov⁶, K. Jessup⁷, O. Korablev¹, T. Kremic⁸, S. Limaye⁹, M. Martynov¹⁰

¹Space Research Institute of the Russian Academy of Sciences (IKI), 84/32 Profsoyuznaya Str., Moscow 117997, Russia

²Jet Propulsion Laboratory, Pasadena, USA

³NASA Headquarters, Washington DC, USA

⁴Enrico Fermi Institute, Chicago, USA

⁵University of Colorado, Boulder, USA

⁶Vernadsky Inst. RAS, Moscow, Russia

⁷Southwest Research Institute, Boulder, USA

⁸Glenn Research Center, Cleveland, USA

⁹Univ. of Wisconsin, St Madison, USA

¹⁰Lavochkin Assoc., Moscow, Russia

Contact: zasova@iki.rssi.ru

Introduction:

The Venera-D project was previously included in the Russian Federal Space Program for 2006-2015. The mission concept is based on the highly successful Soviet Veneras and VEGA, the American Mariners and Pioneer Venus missions of the 1970s and 80s, the NASA Magellan mission (early 1990s), and the impressive ESA mission Venus Express. Several mission elements have been evaluated for inclusion in the Venera-D project. These include two baseline elements: an orbiter and a lander. There is also the potential for the inclusion of an additional elements, i.e. a sub satellite, a long-lived station on the surface and balloons [1]. Venera-D mission architecture, the notional scientific payloads for each baseline element, and the scientific goals of the mission are studied by Roscosmos/IKI- NASA Joint Science Definition Team on Venera-D (JSDT). In the definition of the science priorities, the JSDT is evaluating the overlap with the NASA VEXAG goals and the Decadal Survey (2013-2022) roadmap. The Venera-D concept will be able to address the outstanding science problems concerning the formation and evolution of Venus. The synergy with NASA goals could potentially lead to the contribution of an element to enhance the scientific return of the to Venera-D mission.

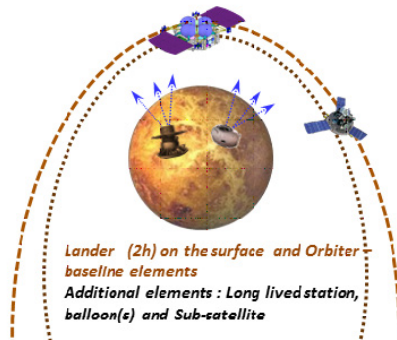


Fig. 1. Concept of Venera-D mission

WHY EXPLORE VENUS?

Located in the same part of the solar system and formed out of the same protoplanetary material, Venus is the Earth's twin sister. Although these two 'sisters' have nearly the same size, mass, and density, the climate of Venus, fueled by a massive CO₂ atmosphere with a surface pressure of 90 atm. has an enormous greenhouse effect and a surface temperature of 470°C. The atmosphere undergoes a superrotation, with the upper clouds rotating at a rate 60 times faster than the surface. Shrouded in clouds of sulfuric acid, the surface lacks water and has been sculpted by volcanism and deformed by faulting and folding forming belts of rifts and mountains. The lack of an intrinsic magnetic field suggests the planet's interior structure is different from that of Earth.

Why did Venus take an evolutionary path so different from Earth and what are the implications for making a planet habitable? Earth is shielded from the solar wind by its magnetic field and is abundant by water supporting the active biosphere. Why and at what stage did the evolutionary paths of these planet-twins diverge? Did the conditions exist on Venus at one time that could have fostered the origin of life? Are the remains of this life (some bacteria) survive somewhere on Venus after catastrophic eruptions during last billions of years? A place of survival maybe the clouds layer where both a water and solar light exist. The study of Venus will help us to better understand our own world and the possible future evolution of our climate. In particular, the instability of our climate and the increase of the amount of greenhouse gases: can we be slowly moving in the Venus' direction? These questions are addressed by the Venera-D mission scientific goals. They are: evaluation of the structure and chemical composition of the atmosphere, abundances and isotopic ratios of the light and noble gases; study of the thermal structure, dynamics and superrotation; thermal balance as related to the greenhouse effect; cloud composition, structure, microphysics and chemistry; study of the surface mineralogy and elemental composition including the key radioactive isotopes; measurement of the iron distribution by its oxidation states; assessment of potential current volcanic, electrical, and seismic activity; study of the structure of exosphere and ionosphere; interaction of the solar wind and magnetosphere and atmospheric gases dissipation

ARCHITECTURE OF THE MISSION AND POTENTIAL CONTRIBUTION:

The baseline elements of the mission concept include an Orbiter and a Lander (Lavochkin Assoc.). The priority of science goals for the Orbiter are study of the dynamics and superrotation of the atmosphere, characterization of the thermal structure of the atmosphere, assessment of UV-absorbers and thermal balance, quantification of the composition of the atmosphere and clouds. The scientific payload would include several spectrometers, a plasma package and a radio science experiment. The payload would build upon the instruments flown on Venus Express and would provide additional capability for the study of Venus. (for example VIRTIS VEX to VENIS Venera-D).

Understanding the surface composition and surface-atmospheric interaction is a high priority for Venera-D and a Lander is a key mission element. As the last landing with surface measurements was more than 30 years ago, high-fidelity modern instruments would provide for revolutionary advancement in the understanding of atmosphere during descent and mineralogy and element composition of surface rocks. High accuracy in situ measurements in the atmosphere, will provide greater insight into questions about the origin and evolution of the atmosphere and climate of Venus.

POTENTIAL AUGMENTATION TO THE BASELINE ELEMENTS:

The JSDT has emphasized the importance of atmospheric in situ measurements. As such, an atmospheric platform, floating or free-flying, is identified as important element for the mission to investigate atmospheric circulation. Experiments on an aerial would address questions regarding the nature of the UV absorber (are organics of any kind involved?), evaluation of the spatial distribution of different chemical species, and measurement of cloud composition. The maximum lifetime of the earlier Venera landers was on the order of 2 hours. Although important measurements were made by the previous missions, they were not able to address the following questions: what are the conditions in the near surface boundary layer; what is the meteorology of the near-surface atmosphere; how topography influences the atmosphere in such a way that the extreme topographic features are revealed in the temperature fields, cloud structure and zonal wind at least up to altitude of about 100 km with shift in longitude? The inclusion of properly instrumented long-lived sondes (landed in different regions of the planet) may give answers to these questions. The JSDT recognized that a possible sub-satellite would be important in measuring plasma, gases escape, the solar wind and magnetic fields at two points (with orbiter) as well as to conduct radio science occultation experiments.

VENERA-D BUILDING ON THE RESULTS OF VENUS EXPRESS (ESA) AND AKATSUKI (JAXA):

It is worth comparing the scientific goals of three orbiters: Venera-D, Venus Express and Akatsuki. The most important measurement types performed by

Venus Express are also included in the payload of Venera-D orbiter but with the advanced capability. In addition, Venera-D would perform investigations focused on science goals such as dynamics, superrotation, thermal structure and thermal balance. Example instruments for carry out such investigations are: Planetary Fourier Spectrometer, UV – spectrometer, and MM- radiometer. The Akatsuki payload includes several cameras for different spectral ranges. In Fig.2 one may see the spectral bandwidth of the Akatsuki cameras (blue) superimposed on the spectrum of night side of Venus. For comparison, spectral resolution of VIRTIS VEX (green) and VENIS Venera-D (red) are also given. Even taking into account the advantages of the cameras in the obtaining of the image for all points of FOV simultaneously, one may see [2] that camera bandwidth include the parts of spectra corresponding to different levels of the atmosphere. Spectrometers of Venera-D cover the spectral ranges of the Akatsuki cameras. However, Akatsuki does not have a spectral measurement capabilities. The data from Venera-D will be complementary to both Venus Express and Akatsuki.

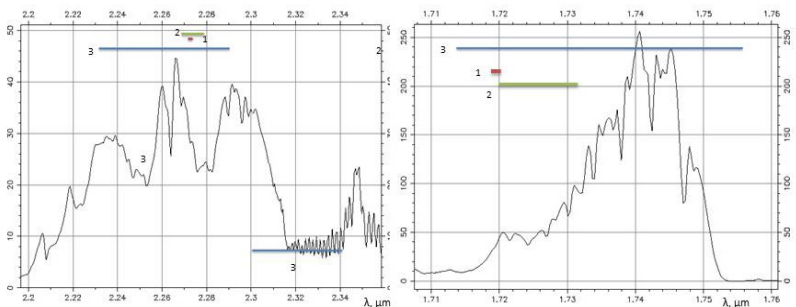


Fig. 2. Examples of the spectral bandwidth of Akatsuki cameras [3] (blue) superimposed on the spectrum of night side of Venus. For comparison, spectral resolution of VIRTIS VEX (green) and VENIS Venera-D (red) are also given in the left plot.

CONCLUSION:

The JSDT concluded that the Venera-D concept would address fundamental key scientific objectives for Venus exploration, both the atmosphere and the surface. The JSDT also identified science that could be enhanced via augmentation (NASA) via a free-flying atmosphere element or long-lived drop sonde. The conclusion of the JSDT is that the Venera-D concept would aid in providing context for the ever growing number of extra-solar planets, provide insight into how planetary systems form, and what makes a planet potentially habitable. In comparison to Venus Express (VEX) and Akatsuki, the Venera-D orbiter notional payload would include several spectrometers, including imaging, for the spectral ranges from UV to mm. Several of the Venera-D spectrometers have never been used around Venus (like mapping UV-spectrometer), others have been effectively used on previous missions (like FS on Venera-15 and VIRTIS-VEX). Even in the case of similarity in spectral coverage of instruments, the scientific capability of the instruments on the Venera-D orbiter significantly exceeds the capacity of the instruments on VEX and Akatsuki.

REFERENCES:

- [1] L. Zasova, et al., Future Venus Exploration: mission Venera-D. LPI Contribution No. 1781, id.6037, 2014
- [2] L. Zasova et al., Venus atmosphere and extreme surface topography. EPSC Abstracts, Vol. 10, EPSC2015-876, 2015
- [3] I. Khatuntsev et al. Cloud level winds from the Venus Express Monitoring Camera imaging. *Icarus*, 226 (2013), 140-158
- [4] M. Nakamura et al., Planet-C: Venus Climate Orbiter mission of Japan. *Planetary and Space Science* 55 (2007), 1831-1842

THE LANDING POTENTIAL OF TERRAINS ON THE SURFACE OF VENUS: PROGNOSIS FOR THE VENERA-D MISSION

M. Ivanov¹, T. Economou², N. Eismont³, L. Esposito⁴, M. Gerasimov³,
D. Gorinov³, N. Ignatiev³, K. Jessup⁵, O. Korablev³, T. Kremic⁶, S. Limaye⁷,
M. Martynov⁸, A. Ocampo⁹, D. Senske¹⁰, L. Zasova³

¹Vernadsky Inst. RAS, Moscow, Russia

²Enrico Fermi Institute, Chicago, USA

³Space Research Institute of the Russian Academy of Sciences (IKI),
84/32 Profsoyuznaya Str., Moscow 117997, Russia

⁴University of Colorado, Boulder, USA

⁵Southwest Research Institute, Boulder, USA

⁶Glenn Research Center, Cleveland, USA

⁷Univ. of Wisconsin, St Madison, USA

⁸Lavochkin Assoc., Moscow, Russia

⁹NASA Headquarters, Washington DC, USA

¹⁰Jet Propulsion Laboratory, Pasadena, USA

Contact: mikhail_ivanov@brown.edu

INTRODUCTION:

Severe greenhouse effect on Venus limits the range of possible geological processes operating on this planet. The surface temperature, ~500°C, and apparently low temperature/pressure gradients cause the hyper-dry, almost stagnant near-surface environments. They preclude the water- and wind-driven geological processes and, thus, the common Earth-like geological record of sedimentary materials cannot form on current Venus. Only three processes play the major roles in the formation of material units on the surface of Venus: volcanism, tectonics, and impact cratering. There are only about a thousand impact craters on Venus. This means that 1) the surface of the planet is relatively young (the mean age estimates vary from ~750 to ~300 Ma [1-3] and 2) the contribution of impact craters to resurfacing is minor. Only volcanism and tectonics were the principal geological processes during the observable geologic history of Venus (Fig. 1).

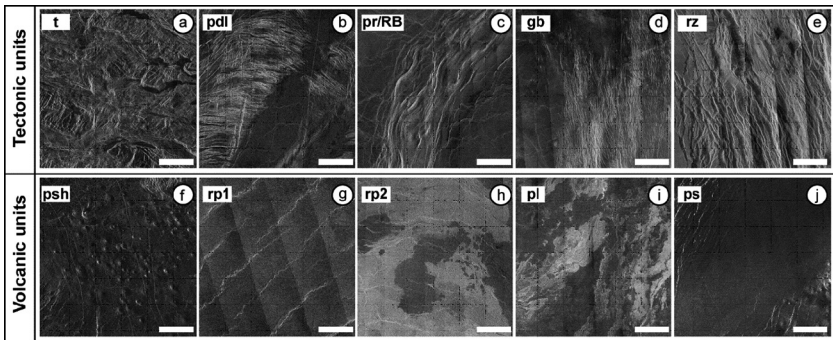


Fig. 1. Tectonic and volcanic units that make up the surface of Venus (each scale bar is 25 km).

REGIMES OF RESURFACING:

The morphologically homogenous units establish the base for the unfolding of the geologic histories of planets [4]. Inspection and comparison of units mapped by many geologists on Venus have shown that a restricted number of units adequately describes geology in different and remote regions of the planet [5]. The repeatability of these units over the surface of Venus allows compiling of a global geological map that shows the distribution of units in space and time. Since the morphologically distinct units are related to specific geological processes, the geological map allows tracing the changes of the geological activity on Venus as a function of time [6].

Analysis of the global geological map reveals that the observable geologic history of Venus consist of three different regimes of resurfacing: 1) the global

tectonic regime, 2) the global volcanic regime, and 3) global volcano-tectonic regime (Fig. 2) [7].

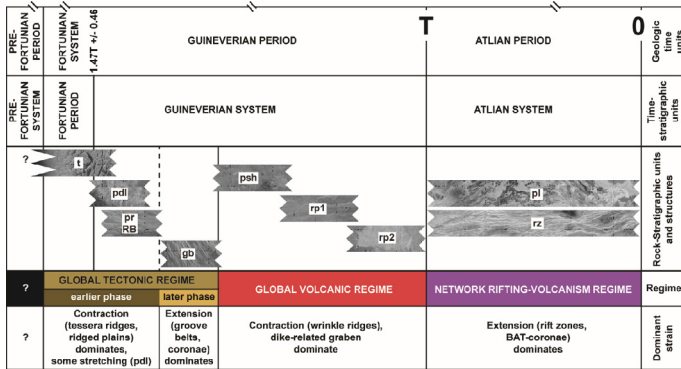


Fig. 2. Regimes of resurfacing that operated on Venus during its visible geologic history (modified from [7]).

The global tectonic regime: The tectonic resurfacing dominated during the earlier stages of the observable geologic history of Venus and caused formation of strongly tectonized terrains (Fig. 1) such as tessera (t), densely lineated plains (pdl), ridged plains/ridge belts (pr/RB), and groove belts (gb). Exposures (minimum area) of these units comprise ~20% of the surface of Venus. The global tectonic regime started with the formation of tessera, which is among the oldest material units on the planet and may represent the only “window” into the geological past of Venus. The age relationships among the tessera tectonic structures indicate that this terrain is the result of crustal shortening and may represent a mosaic of crustal blocks. The shortening of the crust suggests that the global tectonic style during the tessera formation included elements of plate tectonics such as large-scale underthrusting. No morphologic evidence of plate tectonics was found on Venus among the landforms that postdate tessera.

The global volcanic regime: During this time, volcanism overwhelmed tectonic activity and caused formation of vast volcanic plains mildly deformed by tectonic structures (Fig. 1). Three types of plains manifest the global volcanic regime (Fig. 2): 1) shield plains (psh), 2) regional plains, lower unit (rp1), and 3) regional plains, upper unit (rp2). Together, these plains compose ~60% of the surface of Venus and show a clear stratigraphic sequence from the oldest shield plains to the youngest upper unit of regional plains [8]. The density of craters on units of the tectonic and volcanic regimes suggests that they characterized about first 1/3 of the visible geologic history of Venus. During this time, however, ~80-85% of the Venus surface was renovated.

The global volcano-tectonic regime: This regime characterized the last 2/3 of the visible geologic history of Venus (Fig. 2). Three units represent the major components of the regime (Fig. 1): lobate plains (pl), rift zones (rz), and smooth plains (ps). These units have about the same area and they formed broadly synchronously. Thus, the tectonic and volcanic activities were equally important during the later episodes of the geologic history of Venus. Although the volcano-tectonic regime characterized ~2/3 of the visible geologic history of Venus, only 15-20% of the surface were renovated during this time. This means that the level of endogenous activity during the volcano-tectonic regime has dropped by about an order of magnitude comparing with the earlier regimes.

CRITERIA FOR THE SELECTION OF THE LANDING SITES:

The units of each regime have high scientific interest. Thus, their prioritization is of extreme importance during the planning of the entire configuration of the Venera-D (VD) mission. Three major criteria must be satisfied during selection of potential landing sites for the VD mission. 1) Safe landing has the top priority because it defines the success or failure of the landing part of the mission. 2) Materials that potentially can be analyzed at the landing point must have a high scientific value. 3) Materials that make up the landing point must have as simple nature as possible to decrease ambiguity of interpretation of the measurements.

TERRAINS TO SELECT:

The criterion of the safe landing strongly reduces the number of terrains to land on. For example, none of the tectonized terrains of either the global tectonic regime (t, pdl, pr, gb) or volcano-tectonic regime (rz) can be selected as safe targets. Tessera is among the most desirable scientific targets. The surface of this terrain, however, appears at Magellan resolution to be very rough with abundant steep (up to 30°) slopes and rocky scree.

The units of the global volcanic regime appear to present more safe surfaces for landing. Among the vast volcanic plains, the upper unit of regional plains (rp2) seems to be as the less desirable because it typically has a bright surface. The higher radar brightness implies an enhanced roughness at the scale of tens of radar wavelengths (i.e., at the base of ~1-2 m) and the unit may resemble the terrestrial aa lava flows landing on which is extremely dangerous.

The criterion of the geological simplicity and representability excludes shield plains. On their surface, small volcanic constructs are very abundant. They are the local (and perhaps isolated) sources of the plains materials. Another complexity of shield plains is their spatial and stratigraphic association with steep-sided domes [9], the shape of which indicate emplacement of viscous lavas [10, 11]. The higher viscosity likely reflects a higher concentration of SiO₂ in lavas, which, in turn, can be either due to remelting of the wall rocks or fractional differentiation, or both. In any case, shield plains likely have a broad variety of compositions of their materials and the only analyzed sample of these plains will not be representative.

The most attractive terrain of the global volcanic regime is the lower unit of regional plains. This unit satisfies to all three criteria. 1) It is smooth at Magellan resolution (75-100 m/px) and relatively dark on radar images. This implies that the surface of the unit is smooth at the radar-scale wavelengths. 2) It is the most widespread unit on Venus (~40% of the surface of the planet) and, thus, one of the most important volcanic terrain on the planet. The morphological homogeneity of this unit suggests that in each locality, its materials can be representative for the rest of the plains. Thus, analyzing of this unit even in one spot will give robust characteristics of the chemistry of the volcanic processes responsible for the unit formation. 3) Finally, the morphological homogeneity of the lower unit of regional plains suggests that very few processes (likely, just one) contributed to the formation of the unit and its geochemical signal would be desirable simple.

Majority of the flows of lobate plains, which is the second most important components of the global volcano-tectonic regime, are radar-bright (Fig. 1). The surface of these plains, thus, is similar to some degree to the surface of the upper unit of regional plains and likely represent the aa lava flows. Landing on the surface of lobate plains can be very dangerous. The other component of the volcano-tectonic regime, smooth plains, represents a high-priority target for the VD mission. Some portions of smooth plains surround large impact craters and consist of the fine-grained fractions of the crater ejecta. The plains have low radar albedo (Fig. 1), which means that their surface is smooth at the scale of the radar wavelength (12.6 cm) and can provide safe landing conditions. The nature of the unit implies that its material represent a very well mixed and averaged sample of the upper crust of Venus. As such, the crater-related smooth plains represent the target of very high scientific value. Their geochemical study will bring the necessary constraints on the long-standing problem of the presence or absence of the non-basaltic crustal component (analogue to the terrestrial continental crust) on Venus.

REFERENCES:

- 1) Schaber G.G., et al., JGR, 97, 13257, 1992.
- 2) Phillips, R.J., et al., JGR, 97, 15923, 1992.
- 3) McKinnon, W.B., et al., in Venus II, 969, 1997.
- 4) Wilhelms, D.E., in: Planetary Mapping, 208, 1990.
- 5) Basilevsky, A.T., Head, J.W., PSS, 48, 75, 2000.
- 6) Ivanov, M.A., Head, J.W., PSS, 59, 1559, 2011.
- 7) Ivanov, M.A., Head, J.W., PSS, 113-114, 10, 2015.
- 8) Ivanov, M.A., Head, J.W., JGR, 109, 2004.
- 9) Ivanov, M.A., Head, J.W., JGR, 104, 18907, 1999.
- 10) Pavri, B. et al., JGR, 97, 13445, 1992.
- 11) McKenzie, D. et al., JGR, 97, 15967, 1992.

VENERA-D: TECHNOLOGY IMPLICATIONS

T. Kremic¹, L. Zasova², D. Senske³, A. Ocampo⁴, T. Economou⁵,
 N. Eismont², L. Esposito⁶, M. Gerasimov², D. Gorinov², N. Ignatiev²,
 M. Ivanov⁶, K. Jessup⁷, T. Kremic⁸, O. Korablev², S. Limaye⁹,
 M. Martynov¹⁰, A. Burdanov¹¹

¹Glenn Research Center, Cleveland, USA

²Space Research Institute RAS, Moscow, Russia

³Jet Propulsion Laboratory, Pasadena, USA

⁴NASA Headquarters, Washington DC, USA

⁵Enrico Fermi Institute, Chicago, USA

⁶University of Colorado, Boulder, USA

⁷Vernadsky Inst. RAS, Moscow, Russia

⁸Southwest Research Institute, Boulder, USA

⁹Univ. of Wisconsin, St Madison, USA

¹⁰Lavochkin Assoc. and ¹¹TSNIIMASH, Moscow, Russia

Contact: tiber.kremic@nasa.gov

INTRODUCTION:

The Venera-D concept mission being developed by the Joint Russian – US Science Definition Team (JSDT) is an exciting concept for exploring Venus and is largely based on the successful approaches of heritage Soviet Veneras and VEGA missions [1]. The desired science of Venera-D seeks to build on the results on these missions and also missions implemented by other nations such as the American Mariners, Pioneer Venus, and Magellan missions, ESA's Venus Express [2], and the current Japanese Akatsuki mission [3]. A number of elements comprise the Venera-D mission concept. Core elements of the mission include a long lived orbiter (>3 years) and a short duration (~ 2 hour) but powerful lander. Several other mission elements are possible depending on mission constraints, cost being one constraint. The other possible elements include some form of mobile aerial platform (such as a balloon), long lived drosonde(s), and sub-satellite. One can imagine the diverse maturity of technologies that will be needed to support the various elements of the Venera-D mission concept. Given the long heritage and the recent orbiting missions, little technology challenges are expected for the orbiter. However it has been several decades since humanity has placed a functioning lander on the Venus surface or spent time floating in the Venus atmosphere so, for those elements, the technology challenges will be of greater concern. This briefing presents some of the results of the Venera-D technology sub-group.



Fig. 1. Venera-D Mission Concept - Potential Elements

SUMMARY OF TECHNOLOGY MATURITY AND CHALLENGES:

As discussed above, the baseline mission consists of a long-live orbiter and a short-lived lander. Because of recent mission experience such as Venus Express and Akatsuki, the only identified orbiter related technology work needed for the Venera-D concept relates to development of L and W band communication systems for atmosphere probing.

Implementation of the main lander is technically more challenging, but there have been numerous examples of successfully landing and operating missions very similar to what is planned for Venera-D. An obvious, yet not trivial, need is to build test facilities to replicated Venus surface pressures and temperatures in a CO₂ environment. At least one facility will need to be large enough to accommodate the main lander. There are existing facilities, such as the NASA Glenn Extreme Environment Rig [4] that could be used, and the example provided also can implement precise chemistry experiments, but there is no vessel large enough today to accommodate the full lander. The bulk of the technology related efforts for the lander, however, will be in development of the sample acquisition and processing system, updating components or elements of instruments and then testing and qualifying them for use inside the Venera-D land-

ing vessel in Venus conditions, and developing and testing the sensors and systems exposed to the Venus environment.

The sample handling system will need to collect a sample through a pressure lock and process / distribute portions of the sample to several potential instruments (Gas Chromatograph Mass Spectrometer "GCMS", possible Mossbauer Spectrometer/ Alpha Particle X-ray Spectrometer "APXS", possible Raman spectrometer, and possible X-ray Fluorescence Spectrometer "XRF"). These instruments would be inside the landing vessel. The acquisition and distribution system must minimize heat transfer during the sample acquisition process in order to maximize lander life. A system that ingests the required volume of sample and minimizes heat transfer has been proven on previous Venera missions. However, the sample processing and distribution system inside the vessel would be new and need complete development and testing. Sample handling and processing is a critical element of the lander and needs significant development / testing and this work should begin as soon as possible.

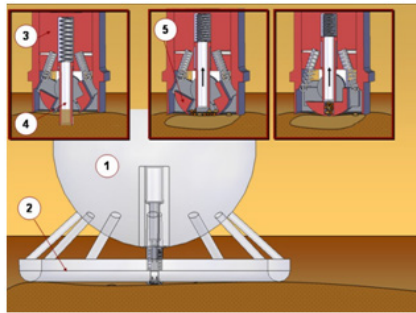


Fig. 3. Sample Acquisition Concept

Most instruments planned for the lander have some heritage to an instrument developed for another mission. However, none of the instruments have been used at Venus or from a pressure vessel, as is planned for Venera-D. The instruments would need to be tested for the environmental conditions and to calibrate and understand effects of the vessel and Venus surface conditions on the measurements. For example, tests are needed on optical effects of looking through windows and the effects of the high pressure / temperatures gases and supercritical fluids on remote sensing measurements. Lander science would benefit from instruments to precisely determine mineralogy / composition. Raman based spectroscopy may serve such needs. Finally, given the short mission life and limited power, careful planning and management of power utilization, instrument operations, and data transmission will be required.

Long term study of the Venus surface is currently not possible due to the harsh conditions. Recent advances in high temperature electronics and other subsystems may enable a paradigm shift in Venus exploration concepts and Venera-D may have opportunity to demonstrate that capability while producing new – long term (months) measurements of surface temperature, pressure, winds and basic chemistry. A concept for such an element is included in dropsonde form and could be attached as an "instrument" to the main lander.



Fig. 4. Long-lived dropsonde - Weather Station probe

TECHNOLOGY FOR POTENTIAL MISSION ENHANCING ELEMENTS:

The baseline mission can be significantly enhanced by adding other elements to the mission such as mobile aerial platform(s), a smaller orbiting sub-satellite, or the dropsonde mentioned above.



Fig. 5. JPL [5] and VEGA [6] Venus Balloon Concepts

Previous missions (E.g. VEGA) have demonstrated successful deployment and operation of free floating balloons in the Venus atmosphere. Such a platform with new instruments is of high science value and deemed relatively low risk. Some material testing work is required, particularly since longer float periods are desired than what was achieved on previous missions. Mass on such platforms is highly constrained

so ultra-low mass (and low power) versions of instruments would be sought. An increase in science, above what can be achieved by a standard balloon, could be realized with an aerial platform that has propulsive capability to control altitude and position. VAMP is such a concept and has been looked at by this JSDT. Analysis and work to date offers promise of feasibility but there is significant development required to mature the VAMP or another mobile aerial platform concept (E.g. materials qualification, deployment demonstration, flight demonstration, controlled entry, and more).



Fig. 6. Northrop Grumman VAMP Concept

Conclusion: A capable Venus mission can be developed using today's technologies with appropriate testing and qualification per the Venus conditions and supported by relevant laboratory experiments. However a much more capable and exciting mission can be realized with timely investments in key technologies such advanced instruments for quickly measuring mineral and atmospheric composition, advanced sample process and distribution system, light weight and low power aerial mobility, and high temperature sensors and systems that can survive Venus surface conditions for long periods of time. Such investments should be encouraged.

REFERENCES:

- [1] L. Zasova et al. Future Venus Exploration: mission Venera-D. *LPI Contribution No. 1781*, id.6037, 2014
- [2] H. Svedhem et al. Venus Express mission. *J. Geophys. Res.*, V. 114, CiteID E00B33, 2009.
- [3] M. Nakamura et al. Planet-C: Venus Climate Orbiter mission of Japan. *Planet. Space Science*, v. 55, 1831–1842, 2007
- [4] T. Kronic, et al. GLENN Extreme Environments Rig (GEER) for Planetary Science. *LPI Contribution No. 1903*, p.2146, 2016.
- [5] R.S. Kremnev et al. Vega Balloon System and Instrumentation, *Science*, v.231, 1408-1411, 1986
- [6] J. L. Hall, et al. Prototype design and testing of a Venus long duration, high altitude balloon, *Adv. Space Res.*, v. 42, 1648-1655, 2008

VENUS ATMOSPHERIC MANEUVERABLE PLATFORM (VAMP)- AIR VEHICLE CONCEPT AND ENTRY CONOPS

G Lee¹, S. Limay², R. Polidan³, J. Arenberg⁴

¹Northrop Grumman Aerospace System, One Space Park, Redondo Beach, California, USA

²Space Science and Engineering Center, University of Wisconsin, Madison, Wisconsin, USA

³Polidan Science Systems & Technologies, Bend, Oregon, USA Contact:

⁴Northrop Grumman Aerospace System, One Space Park, Redondo Beach, California, USA

Contact: ¹Gregory.j.lee@ngc.com, ²Sanjay.Limaye@ssec.wisc.edu,

³Ron.Polidan@psstconsulting.com, ⁴Jon.Arenberg@ngc.com

The Northrop Grumman Aerospace Systems and L'Garde team has continued to investigate a capability to provide a long-lived, maneuverable platform to explore the Venus upper atmosphere. This capability is an implementation of our Lifting Entry/Atmospheric Flight (LE/AF) system concept, and the Venus implementation is called the Venus Atmospheric Maneuverable Platform (VAMP). The VAMP concept utilizes ultra-low ballistic coefficient ($< 50 \text{ Pa}$), semi-buoyant aircraft that deploys prior to entering the Venus atmosphere, enters without an aeroshell, and provides a long-lived (months to years) maneuverable vehicle capable of carrying science payloads to explore the Venus upper atmosphere.

In this presentation we provide an update on the air vehicle design and plans for future trade studies, analyses, and prototyping to advance and refine the concept. We will discuss the air vehicle's entry CONOPs and atmospheric science operations. We will present a strawman concept of VAMP, including ballistic coefficient, planform area, percent buoyancy, inflation gas, wing span, vehicle mass, power supply, propulsion, materials considerations, structural elements, subsystems, and packaging. In this context, we will discuss four key factors impacting the design and performance of VAMP:

- 1) Air Vehicle Platform impacts on entry and science operations
- 2) Entry into the Venus atmosphere, including descent profile, heat rate, total heat load, stagnation, and average temperatures
- 3) Impact of maximum altitude on air vehicle design and entry heating
- 4) Candidate TPS requirements

We will discuss the interdependencies of the above factors and the manner in which the VAMP strawman's characteristics affect the CONOPs and the science objectives.

We will show how these factors provide constraints as well as enable opportunities for novel long duration scientific studies of the Venus upper atmosphere that support VEXAG goals 1 and 3. We will also discuss how the VAMP platform itself can facilitate some of these science measurements.

DUSTY PLASMAS IN THE SOLAR SYSTEM: RECENT DEVELOPMENTS, ADVANCES, AND UNSOLVED PROBLEMS

S.I. Popel, L.M. Zelenyi

Space Research Institute of the Russian Academy of Sciences (IKI), 84/32

Profsoyuznaya Str., Moscow 117997, Russia

Contact: popel@iki.rssi.ru

INTRODUCTION:

The area of space dusty plasma research is a vibrant subfield of plasma physics that belongs to frontier research in physical sciences. This area is intrinsically interdisciplinary and encompasses astrophysics, planetary science, and atmospheric science. Dusty plasmas are ubiquitous in our solar system; examples are interplanetary medium, circumsolar rings, asteroids, planetary rings (e.g., Saturn and Jupiter), Martian atmosphere, cometary tails and comae, dust at the Moon, etc. Dust and dusty plasmas are also found in the vicinity of artificial satellites and space stations. Here, we discuss the main aspects of the area of dusty plasma research in our solar system. Emphasis is given to the description of dusty plasmas at the Moon, which is important from the viewpoint of the future lunar missions and lunar observatory. We present new results on dusty plasmas at other atmosphereless cosmic bodies (e.g., at Phobos, the larger, of the two satellites of Mars, etc.), discuss the interaction of the solar wind with dusty cometary comae resulting in the formation of bow shock, formulate unsolved problems concerning dusty plasmas in the solar system, etc.

THE MOON:

Recently, self-consistent studies (see, e.g., [1, 2]) have been carried out which consider dusty plasma system at the Moon and take into account the charging of dust particles above the lunar surface due to the action of photoelectrons (both from the lunar surface and from the surfaces of dust particles that levitate above the Moon), electrons, and ions of the solar wind, as well as the solar radiation. Most of these studies have been performed in connection with the future lunar missions Luna-Glob and Luna-Resurs where measurements are planned to be carried out in the daytime so as to use solar power to supply the lunar station equipment. Fig. 1 presents schematically the main elements characterizing the dusty environment over the Moon. The lunar surface is charged under the influence of the solar electromagnetic radiation, the solar wind plasma, and the plasma of the terrestrial magnetosphere tail. Upon interacting with the solar radiation, the lunar surface emits photoelectrons due to the photoelectric effect. This leads to the emergence of a layer of photoelectrons above the surface. Additional photoelectrons are emitted by the dust particles levitating above the lunar surface when these particles interact with the solar electromagnetic radiation. The dust particles located on the lunar surface or in the near-sur-

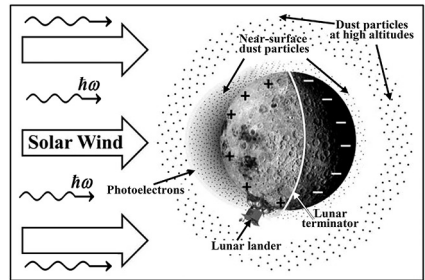


Fig. 1. The main elements characterizing the dusty plasma system over the Moon (the terminator, the photoelectrons, the near-surface dust particles, dust particles at high altitudes, photons of solar radiation ($h\omega$), and the solar wind) as well as the lunar lander at a high lunar latitude in the South Hemisphere.

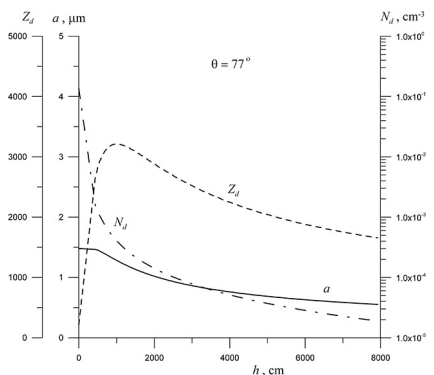


Fig. 2. Results of calculations of the characteristics of dust over Phobos' surface showing the dependences of dust number density N_d , dust particle size a , and dust charge number Z_d on the altitude h .

face layer absorb photoelectrons, photons of the solar radiation, electrons and ions of the solar wind, and (if the Moon is located in the terrestrial magnetosphere tail) electrons and ions of the magnetosphere plasma. All these processes promote charging of the dust particles, their interaction with the charged lunar surface, and the dust levitation and motion.

The consideration of the photoelectrons allows us to show a possibility of rising charged dust particles with the sizes of the order of 100 nm over the surface of the Moon in the entire range of the subsolar angles [1]. This explains the lack of the so-called “dead zone” [where dust particles, as it was previously believed [3], do not rise off the surface] at lunar latitudes of about 80°. Thus, no substantial restrictions are imposed on the choice of the landing site for future lunar spacecraft missions aimed at studying the near-surface dust on the Moon.

In the terminator region, a plasma layer exists which is similar to a sheath [2]. Dusts rise at the illuminated part of the Moon in their relative motion with respect to the terminator must enter the sheath (terminator) region with a velocity greater than the dust acoustic velocity. In the terminator region, an excitation of electric fields on the order of 300 V/m is possible. These electric fields can result in rise of dust particles of the size of 2-3 μm up to an altitude of about 30 cm that explains the effect of “horizon glow” observed at the lunar terminator by Surveyor lunar lander.

Impacts of meteoroids constitute an important source of dust microparticles in the dusty plasma system over the surface of the Moon [4]. Within the future Luna-Glob and Luna-Resurs missions, piezoelectric impact sensors can be used to detect and identify dust microparticles appearing in the dusty plasma system over the surface of the Moon owing to impacts of meteoroids. The characteristic features of such particles are high velocities (about 10–100 m/s) and micron sizes.

The relative motion of the solar wind with respect to the photoelectrons results in the excitation in a dusty plasma near the lunar surface of high-frequency oscillations with frequencies in the range of Langmuir and electromagnetic waves, while the relative motion of Earth’s magnetosphere tail with respect to the lunar dusty plasma leads to the excitation of ion-acoustic and dust-acoustic turbulence [5].

THE PHOBOS:

Phobos’ gravitational pull is only a few thousandths of that at the Moon. There could be a layer of dust four or five meters thick on the surface of the Phobos, while the dust would be easily mobilized. This indicates the presence of significant features of dusty plasma at the Phobos in comparison with that at the Moon. We develop a model of the dusty plasma system over the Phobos and show that the dusty plasma system includes charged dust, photoelectrons, and electrons and ions of the solar wind. We determine the distributions of the photoelectrons and find the characteristics of the dust which rises over Phobos’ surface. Fig. 2 [6] presents an example of results of the calculations. We compare the properties of the dusty plasmas at the Moon and Phobos. The most significant difference is that a significant share of micrometer dust is present in the dusty plasma at the Phobos.

DUST ION ACOUSTIC BOW SHOCK:

Cometary nuclei are found to be, most likely, dominated by refractories, very porous and fragile (though monolithic rather than of rubble-pile structure), and generally quite homogeneous except for dust mantling and the effects of radial migration of volatiles in the interior. Under the action of the solar light volatile components of the cometary nucleus evaporate and vapor stream entrains dust particles. The crucial point of the investigation of the interaction of the solar wind with cometary comae is the description of bow shock formed as a result of this interaction [7]. The presence of dust constituting tens per cent of the total mass of the coma can modify the bow shock. For typical cometary nucleus size of about 1 km and rather dense dusty coma ($N_d > 10^6 \text{ cm}^{-3}$) the bow shock formed as a result of the interaction of the solar wind with the coma is expected to be related to the anomalous dissipation due to the dust particle charging. The bow shock is similar, by its origin, to the dust-ion-acoustic shocks inherent in dusty plasmas.

ACKNOWLEDGEMENTS:

This work was supported in part by the Presidium of the Russian Academy of Sciences (under Fundamental Research Program No. 7, “Experimental and Theoretical Study of the Solar System Objects and Stellar Planet Systems. Transient Explosion Processes in Astrophysics” and the Russian Foundation for Basic Research (Project No. 15-02-05627-a).

REFERENCES:

1. Popel, S.I., Kopnin, S.I., Golub', A.P., Dol'nikov, G.G., Zakharov, A.V., Zelenyi, L.M., Izvekova, Yu.N., *Solar Syst. Res.*, 2013, **47**, 419
2. Popel, S.I., Zelenyi, L.M., Atamaniuk, B., *Phys. Plasmas*, 2015, **22**, 123701
3. Stubbs, T.J., Vondrak, R.R., Farrell, W.M., *Adv. Space Res.*, 2006, **37**, 59
4. Popel, S.I., Golub', A.P., Lisin, E.A., Izvekova, Yu.N., Atamaniuk, B., Dol'nikov, G.G., Zakharov, A.V., Zelenyi, L.M., *JETP Lett.*, 2016, **103**, 563
5. Morozova, T.I., Popel, S.I., 2016, this conference
6. Popel, S.I., Golub', A.P., Zelenyi, L.M., *Dusty plasmas at the Phobos*, in preparation
7. Popel, S.I., Gisko, A.A., *Nonlin. Proc. Geophys.* 2006, **13**, 223

COULOMB “EXPLOSION” OF DUST CLUSTER UNDER MICROGRAVITY

O.F. Petrov¹, M.I. Myasnikov¹, L.G. Dyachkov¹, M.M. Vasiliev¹,
V.E. Fortov¹, S.F. Savin², E.O. Serova²

¹*Joint Institute for High Temperatures, Russian Academy of Sciences, 125412
Moscow, Russia*

²*Rocket-Space Corporation “Energia”, 141070 Korolev, Moscow region
Contact: ofpetrov@ihed.ras.ru*

Physical properties of strongly coupled Coulomb systems (SCCS) are of considerable interest in various fields of science and technology. Using SCCS of dust particles, one can investigate the processes of phase transitions, waves, and instabilities on kinetic level. For confinement and investigation of SCCS of dust particles, we have proposed to use a trap based on the known possibility of the levitation of diamagnetic bodies in a nonuniform steady-state magnetic field [1, 2]. For the investigation of Coulomb systems of diamagnetic (graphite) particles in cusp magnetic field under microgravity conditions the experimental setup with the region of stable levitation about 400 cm³ and magnetic field gradient up to 0.04 T/cm was produced. A cusp magnetic field is generated by two coils placed on the same axis, in which currents circulate in the opposite directions. Experiment “Coulomb crystal” were carried out onboard of the International Space Station with graphite particles of micron size placed in the middle of the replaceable container within a cylindrical glassy cell filled with argon at atmospheric pressure. Charging of the particles was carried out using a central wire electrode that passed along the axis of the cell. For the modified experimental setup “Coulomb crystal”, a new set of replaceable containers with advanced diagnostics has been developed. The electric potential of the central electrode can be increased up to 150 V. When we applied such maximum potential, the cusp magnetic trap can not confine the graphite particles and the cluster starts to break down (Coulomb “explosion”). We have performed molecular dynamic (MD) simulations of the cluster formation in the cusp magnetic trap and then its destruction in electric field. For simplicity we take the number of particles in the simulations to be less than that in the experiment (~ 10⁴). However results of our simulations are in a good qualitative agreement with observations.

Replace these instructions with the text of your abstract. If you are including tables or figures, they MUST be imported into this file. The total abstract's text with figures and tables is no more than 1-2 pages.

This work was supported In JIHT RAS by the Russian Science Foundation through Grant No 14-50-00124. For Grant funds it was performed modification of equipment for the space experiment “Coulomb crystal”, analysis of the experimental data and MD simulation.

REFERENCES:

1. Savin S.,F., D'yachkov L.,G., Vasiliev M.,M., Petrov O.,F., Fortov V.,E. // EPL. 2009. V. 88, P. 64002.
2. Petrov O.,F., Myasnikov M.,I., D'yachkov L.,G., Vasiliev M.,M., Fortov V.,E. Savin S.,F., Kaleri A.,Yu., Borisenko A.,I., Morfill G.,E. // Phys. Rev. E. 2012. V. 86. P. 036404.

THE LUNAR DUST ENVIRONMENT: THE EFFECTS OF IMPACTS AND NEAR-SURFACE PLASMAS

M. Horanyi¹, J. Deca¹, H.-W. Hsu¹, J. Schwan¹, J. Szalay², X. Wang¹,
¹IMPACT, University of Colorado, 1234 Innovation Drive, Boulder, CO, USA,
²Southwest Research Institute, 6220 Culebra Rd, San Antonio, TX 78238, USA
 Contact: horanyi@colorado.edu

The lunar surface is continually bombarded by interplanetary dust particles generating copious amounts of secondary ejecta grains, a fraction with sufficient initial speeds to reach orbiting spacecraft. In addition, the surface is exposed to the solar wind plasma flow and UV radiation. Recent observations by the Lunar Dust Experiment (LDEX) onboard the Lunar Atmosphere and Dust Environment (LADEE) mission, that was in orbit around the Moon in the period of October 2013 - April 2014, identified an ejecta cloud forming a dust exosphere around the Moon. In addition to characterizing the spatial and temporal variability of the lunar ejecta cloud, the instrument was also capable of observing the presence of high-number-density lofted dust particles with sizes below the single detection limit of the instrument. The existence of levitated small nano-particles has been anticipated based on visual observations, and several surface experiments indicating an intermittent lunar horizon glow. The mechanism to mobilize and loft these tiny particles has been attributed to their electrostatic charging and interaction with intense electric fields. LDEX did not verify the existence of this population of high-altitude lofted particles, however these observations do not exclude electrostatic dust mobilization near the lunar surface at altitudes < 1 km.

Electrostatic dust mobilization remains a controversial issue. Simple estimates indicate that a small fraction of a characteristically micron sized particle resting on the lunar surface is likely to lose a single electron when exposed to UV, while the vast majority of the grains remain uncharged. This charge combined with an average UV sheath electric field of ~ 5 V/m is insufficient to overcome lunar gravity. However, in our recent laboratory experiments we found surprisingly large charges on particles lofted from a regolith surface exposed to UV or an electron beam. These large charges can be understood by recognizing the role of the cavity structure beneath the very surface of a dust layer. From the top layer UV or secondary

emission generated electrons are emitted and quickly returned, hence the total amount of surface charge has to match the total number of electrons 'in flight'. Contrary, if UV photons or an electron beam reach a cavity, the generated photo or secondary electrons remain trapped and the charging effects (both + and -) accumulate. The pairwise repulsive force between grains with the same sign of charge can become large enough to overcome Earth gravity. We suspect this process to remain very efficient in gardening the regolith of all airless bodies in the solar system, possibly offering an explanation for the observed dust ponds on asteroids and comets, and predicting similar features on the Martian moons Phobos and Deimos. This talk will summarize the LDEX observations, the ongoing laboratory experiments, and supporting computer simulation results.

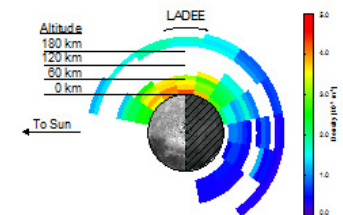


Fig. 1. Top-down view of the dust density (radii $> 0.3 \mu\text{m}$) projected onto the lunar equatorial plane. To avoid Sun pointing, LADEE did not make measurements between 12 and 18 LT. White coloring indicates regions where LADEE did not make measurements (from: Horanyi et al., Nature, 2015).

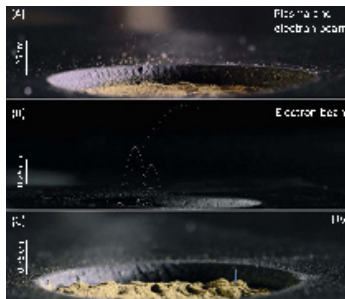


Fig. 2. Images of dust transport and hopping trajectories in (a) plasma and electron beam, (b) electron beam, and (c) UV experiments. Deposits of dust particles on the surface outside the crater also indicate their hopping motions in all three images. Large aggregates up to 140 μm in diameter are lofted in addition to individual particles in the range of 38–45 μm in diameter (from: Wang et al, GRL, 2016)

THE ROLE OF THE INNER RADIATION BELT IN DUST GRAINS LOFTING FROM THE JUPITER'S MOONS THEBE AND AMALTHEA

N. Borisov¹, H. Krüger², A. Zakharov³,

¹I.ZMIRAN, 142190, Troitsk, Moscow, Russia

²MPI for Solar System Research, 37077, Göttingen, Germany

³Space Research Institute of Russian Academy of Sciences, Moscow, Russian Federation

Contact: borisov@ipi.ru

The lofting of dust grains from the surfaces of airless cosmic bodies is caused by two reasons: 1. micrometeoroid impacts, 2. charging and motion in electric fields. In case when a moon is imbedded in the magnetospheric plasma of a planet (e.g. moons of Jupiter) up to now only micrometeoroid impacts were considered as a source of dust grains lofting from the surface.

We argue that energetic electrons in the inner radiation belt of Jupiter influence significantly dust grains lofting from Thebe and (to less extent) from Amalthea. Indeed, according to the experimental data the fluxes of energetic electrons in the inner radiation belt with the energies $W \geq 160$ keV in the vicinity of the orbit of Thebe ($L=3.1$) approximately an order of magnitude higher than the flux of thermal electrons. Near the orbit of Amalthea ($L=2.5$) the electron fluxes in the radiation belt are somewhat less (of the order of the fluxes of thermal electrons). Assuming that the electric conductivity of the moon's surfaces very small we analyze the distribution of the electric potential in space in the vicinity of the polar region of Thebe and Amalthea. It comes out that variation of the potential with the height in the double layer is not monotonic. Our estimates show that the surface of Thebe in the polar region should have very strong negative potential (up to -10^6 V and even more) and strong enough electric fields in the double layer. In such case micron and submicron sized charged grains from the surface overcome the gravity of the moon. (Note that much stronger gravity of Jupiter acts only in the radial direction and does not prevent the lofting from the moon's surface in the polar region). Our results are in accordance with some discovered peculiarities of dust grains distribution in the gossamer rings which are not properly explained in the existing models (e.g. rather smooth vertical distribution of dust having Thebe as a dust source).

ON THE PROBABILISTIC MODEL OF THE KORDYLEWSKI COSMIC DUST CLOUDS

T.V. Salnikova¹, S.Ya. Stepanov², A.I. Shuvalova³

^{1,3}Lomonosov Moscow State University, GSP-1, Leninskie Gory, 119991, Russia

²Dorodnicyn Computing Center, FRC CSC RAS, Vavilov st. 40, 119333, Russia

Contact: tatiana.salnikova@gmail.com

INTRODUCTION:

Within the mathematical model of Kordylewski clouds, the probability of formation of dust clouds in the vicinity of triangular libration points of the Earth–Moon system taking into account perturbation from the Sun is investigated. In the perturbed problem, Lyapunov stable triangular libration points become unstable. However, the Polish astronomer K. Kordylewski observed and photographed cosmic dust clouds near the libration point L5. It might be supposed that Kordylewski observed clouds in the vicinity of periodic motion that were in the line of sight of the triangular libration points at the time of observation.

PROBLEM SETTING:

The problem of determining the phase space distribution function for the system of the non interacting dust particles for the mathematical model of cosmic dust Kordylewski clouds—clusters of the non-interacting dust particles in the vicinity of the triangular libration points of the Earth–Moon–Particle system taking into account perturbation from the Sun was considered.

Let us consider an ensemble of particles with the same mass and the same probability density distribution functions in the vicinity of the Lagrangian libration points. If there is no interaction between the particles, the ensemble is statistically equivalent to the test particle $P(x, y, u, v)$ with the mass m_P and the distribution function $\rho(x, y, u, v, t)$ is described by the Liouville equation. It is a homogeneous linear partial differential equation of the first order. Its solution is constant along the characteristics, the equations of which coincide with the equations of motion of the particle.

The probabilistic model of formation of the concentrations of cosmic particles based on integration of the Liouville equation for the probability density distribution function was in qualitative agreement with the known observed clusters of Trojan asteroids in the unperturbed Sun–Jupiter– Asteroid system.

In the circular restricted three–body Earth–Moon– Particle problem, when we consider the periodical perturbation of the Sun, each of the Lagrangian libration points is captured by the two periodical stable orbits. Stability of the periodic solution implies that, in the case of small deviations of coordinates and velocities from periodic motion, we should see an ensemble of particles, moving in the vicinity of this periodic motion. In order to estimate the probability of formation of cosmic dust clouds, the Liouville equation is considered, which gives us the time evolution of the phase space distribution function for the system of the non interacting dust particles. The numerical integration of the Liouville equation in the vicinity of a periodic solution shows an increase in the density at the current position of the point on a periodic trajectory. Hence, in this model the numerical analysis shows the probability of formation of dust clouds.

CONCLUSION:

The results based on integration of the Liouville equation are in a good agreement with the parameters of the Kordylewski cloud that were shown by the Poincaré map for the equation of motion of the particle.

The probabilistic model confirmed the findings of the existence and observation condition of Kordylewski clouds.

SIMULATION OF THE DUSTY PLASMA ENVIRONMENT OF 65803 DIDYMOS FOR THE ASTEROID IMPACT MISSION (AIM)

F. Cipriani¹, D. Rodgers¹, A. Hilgers¹, S. Hess², I. Carnelli³,

¹ESTEC, Noordwijk, Netherlands

²ONERA, Toulouse, France

³ESA, Paris, France

Contact : fabrice.cipriani@esa.int

In the context of the Asteroid Impact and Deflection Assessment mission (AIDA), a joint European-US technology demonstrator mission including the DART asteroid impactor (NASA/JHU/APL) and the AIM asteroid rendezvous platform (ESA/DLR/OCA), we have developed a model describing the plasma and charged dust components of the near surface environment of the moonlet component of Near Earth binary Object 65803 Didymos, targeted by the MASCOT-2 lander and of the DART impactor. We performed numerical simulations in order to estimate the electrostatic surface potentials at various locations of the surface, resulting from its interaction with the solar wind plasma and solar photons. In addition, we describe charging levels, density profiles, and velocity distribution of regolith grains lifted out from the surface up to about 70m above the surface.

THREE DIMENSIONAL KINETIC PARTICLE-IN-CELL SIMULATION OF THE 67P ENVIRONMENT

A. Divin¹, J. Deca², H. Pierre³, M. Horanyi², S. Markidis⁴, G. Lapenta⁵

¹St. Petersburg State University, Ulianovskaya, 1, St. Petersburg, Russia

²LASP, University of Colorado, 1234 Innovation Drive, Boulder, CO, USA

³LPC2E/CNRS, Avenue de la Recherche Scientifique 3A, 45071 Orléans, France

⁴HPCViz, KTH Royal Institute of Technology, SE-100 44, Stockholm, Sweden

⁵CmPA, Department of Mathematics, KU Leuven, Celestijnenlaan 200B, bus

2400 B-3001 Leuven, Belgium

Contact: andrey.div@gmail.com

We present preliminary results of the first 3-D fully kinetic and electromagnetic simulations of the solar wind interaction with 67P/Churyumov–Gerasimenko at ~ 3 AU, before the comet transitions into its high-activity phase. We focus on the global cometary environment and the electron-kinetic activity of the interaction. In addition to the background solar wind plasma flow, our model includes also plasma-driven ionisation of cometary neutrals and collisional effects. We approximate mass loading of cold cometary oxygen and hydrogen using a hyperbolic relation with distance to the comet. We consider two primary cases: a weak outgassing comet (with the peak ion density $\sim 10x$ the solar wind density) and a moderately outgassing comet (with the peak ion density $\sim 50x$ the solar wind density).

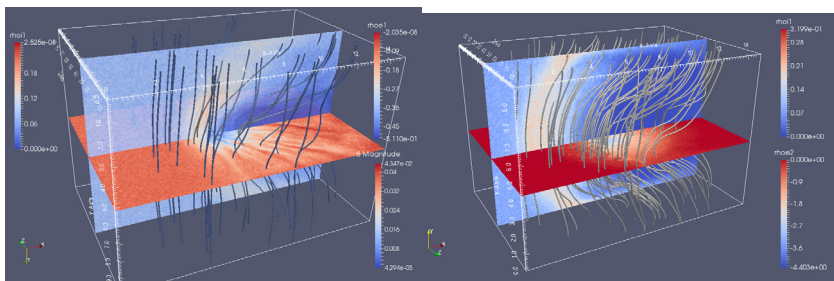


Fig. 1. Weak comet simulation; magnetic field lines. Vertical plane: solar wind ions. Horizontal plane: solar wind electrons. **Fig. 2.** Moderate comet simulations; magnetic field lines. Vertical plane: solar wind electrons. Horizontal plane: cometary electrons.

The weak comet is characterised by the formation of a narrow region containing a compressed solar wind (the density of the solar wind ion population is $\sim 3x$ the value far upstream of the comet, see Figure 1) and a magnetic barrier ($\sim 2.4x$ the interplanetary magnetic field). Blobs of plasma are detached continuously from this sheath region. Standing electromagnetic waves are excited in the cometary wake presumably due to a strong anisotropy in the plasma pressure, as the density and the magnetic field magnitude are anti-correlated.

The moderate mass-loading case shows more dynamics at the dayside region (Figure 2). The stagnation of the solar wind flow is accompanied by the formation of elongated density stripes, indicating the presence of a Rayleigh-Taylor instability. These density cavities are elongated in the direction of the magnetic field and encompass the dayside ionopause.

To conclude, we believe that our results provide vital information to disentangle the observations made by the Rosetta spacecraft and compose a global solar wind - comet interaction model.

LUNAR DUSTY PLASMA AND SPACECRAFT INSTRUMENTS INTERACTION: SPIS-DUST SIMULATION

I.A. Kuznetsov¹, A.V. Zakharov¹, S.L.G. Hess², F. Cipriani³, E. Seran⁴, S.I. Popel¹, E.A. Lisin⁵, G.G. Dolnikov¹, A.N. Lyash¹

¹Space Research Institute of Russian Academy of Sciences, Moscow, Russian Federation

²French Aerosp. Lab., ONERA, Toulouse, France

³ESTEC/TEC-EES, Noordwijk, The Netherlands

⁴Laboratoire Atmospheres, Milieux, Observations Spatiales, Paris, France

⁵Joint Institute for High Temperatures of the RAS, Moscow, Russia

Contact: kia@iki.rssi.ru

INTRODUCTION:

One of the complicating factors of the future robotic and human lunar landing missions is the influence of the dust. The absence of an atmosphere on the Moon's surface is leading to greater compaction and sintering. Properties of regolith and dust particles (density, temperature, composition, etc.) as well as near-surface lunar exosphere depend on solar activity, lunar local time and position of the Moon relative to the Earth's magnetotail. Upper layers of regolith are an insulator, which is charging as a result of solar UV radiation and the constant bombardment of charged particles, creates a charge distribution on the surface of the moon: positive on the illuminated side and negative on the night side. Charge distribution depends on the local lunar time, latitude and the electrical properties of the regolith (the presence of water in the regolith can influence the local distribution of charge).

Investigation of the effects of dusty plasma exosphere is important in terms of clarifying the interaction of the exosphere and charged dust particles as on the separate scientific instruments (for example, Langmuir probes and dust Impact sensors) and on the spacecraft systems in general.

The Spacecraft Plasma interaction Software (SPIS) has been improved to allow for the simulation of lunar and asteroid dust emission, transport, deposition and interaction with a spacecraft on or close to the surface. [1]

We present first results of modeling the influence of the exosphere on the spacecraft Luna-Glob in the soft-ware SPIS-DUST. In the simulation we took into account used spacecraft materials, its size, its landing place. The initial conditions were chosen based on the current theoretical models of formation of dusty plasma exosphere and levitating charged dust particles.

ACKNOWLEDGEMENTS:

This work was partially supported by the Ministry of Education and Science (MK-7932.2015.8), the Russian Foundation for Basic Research (the grant №15-32-211 59 and the grant №15-02-05627) and by the Presidium of the Russian Academy of Sciences.

REFERENCES:

[1] S.L.G. Hess et al., New SPIS capabilities to simulate dust electrostatic charging, transport and contamination of lunar probes, Plasma Science, IEEE Transactions on (Volume:43 , Issue: 9) Page(s): 2799 - 2807

WHERE TO LOOK FOR LIFE ON MARS – THE VIEW FROM CRYOBIOSPHERE OF EARTH

N.E. Demidov

*Institute of Physicochemical and Biological Problems of Soil Science, RAN,
Pushchino, Moscow region, 142290, Russia
Vernadsky Institute of Geochemistry and Analytical Chemistry, RAN,
Kosygin Str., 19, Moscow, 119991, Russia
Contact: nikdemidov@mail.ru*

Negative results from Viking astrobiological experiments could not be extrapolated on all planet because different parts of Mars are characterized by different composition, age, temperature etc. Speaking about the search for terrestrial-like life based on H₂O, Mars may be divided on five ecological niches according to presence and state of water (if we are speaking about the search of unknown life forms then there is no sense in using terrestrial analogs of Martian habitats).

NORTH AND SOUTH PERMANENT POLAR CAPS.

Polar caps are composed mostly of H₂O. Their diameter varies from 300 to 800 km, while thickness is 3-4 km. The age of northern and southern polar caps is estimated to be near to 100 ka and 7-17 ma, respectively (Hvidberg, 2005). Mean annual surface temperature is near to -115°C. Their closest terrestrial analog is Antarctic glacier under Vostok station, where mean annual surface temperature is -56°C, minimum temperature is -89.2°C and the age of ice at the base is estimated to be 1 ma (Siebert et al., 2001). This ice contains microorganisms (10¹⁻² cells per ml), which were brought here mostly by wind dispersal (Abyzov, 1993). In spite of presence of life in Antarctic glacier, the chances to detect life in Martian polar caps are low because they were formed from sterile condensate during lifeless Amazonian epoch. Temperature at the base of Martian polar caps does not exceed -50°C accounting for absence of subglacier lakes like Vostok lake in Antarctica.

DRY REGOLITH.

Dry regolith covers Mars from the surface everywhere except polar caps. It's thickness varies from several centimeters in the vicinity of polar caps up to hundred meters at the equator. Terrestrial analog of Martian dry regolith is dry permafrost overlaying ice-containing permafrost in Antarctic oases, where life is localized to special habitats like cryptoendoliths. Absence of water in Antarctic dry regolith puts limit to presence of life in it.

SUBPERMAFROST AQUIFERS.

Were not sampled yet, but probably exist under permafrost and are characterized by high salinity and anoxic conditions. Deep biosphere of Earth colonized by chemolithotrophs may be considered as analog of this econich. This is the only econich where life could survive all history of Mars regardless to changing conditions on the surface (Демидов и др., 2012). Great depth of burial makes them inaccessible for investigation.

CRYOPEGS.

Subzero brines (cryopegs) may be found on Mars as inside permafrost, as under it. Cryopegs found inside Arctic permafrost may be considered as their terrestrial analog. Cryopegs on Mars are hidden on inaccessible for investigation depth because even extremely salty brine with freezing temperature equal to -60°C may be stable only at depth more than 500 m.

ICE CONTAINING REGOLITH.

At high latitudes upper boundary of ice containing permafrost is located at depth less than 1 m, while lower boundary may rich depth of 4-6.5 km. In equatorial zone its presence is possible at depth from several hundred meters to 2.5-3 km. Temperature of ice containing permafrost does not exceed -75°C on its upper boundary and it rises with depth according to geothermal gradient. Antarctic ice cemented permafrost contains 10⁵⁻⁶ viable cells per gram (Gilichinsky et al., 2007). In Antarctica permafrost, from which viable microorganisms were extracted, was characterized by temperature as low as -27°C (Goordial et al., 2016) and age up to 5 ma.

To extrapolate terrestrial model of cryoconservation of microorganisms in permafrost on Mars it is necessary to look for relatively young permafrost genetically connected with Martian subpermafrost aquifers (Gilichinsky et al., 2015). From this point of view, high priority target for the search of life on Mars is represented by permanently frozen deposits of young polar volcanoes. During volcanic eruptions microorganisms from subpermafrost aquifers could propagate to the surface and survive in permafrost for million years, as it is known to happen on Earth. To develop such strategy for the search of life on Mars we perform following investigations: (1) the search for the most ancient permafrost on Earth in Antarctic Dry Valleys and revealing time limits of life survival in it, (2) study of thermophilic microorganisms isolated from frozen volcanic deposits in Kamchatka and Antarctic, (3) model experiments on studying influence of Martian – like temperatures, water vapor pressure and UV-radiation on permafrost communities in the conditions of Vostok station, (4) the search for young volcanoes at polar latitudes of Mars.

REFERENCES:

- Демидов Н.Э., Гиличинский Д.А., Миронов В.А., Шмакова Л.А. Криобиосфера Земли и поиск жизни на Марсе // Криосфера Земли. 2012. Т. 16. № 4. С. 67–82 (in Russian).
- Abyzov S.S. (1993). 'Microorganisms in the Antarctic Ice' from Antarctic Microbiology. Friedmann E. I. (ed). Wiley-Liss inc, New York, 1993.
- Gilichinsky M., Demidov N. and Rivkina E. Morphometry of volcanic cones on Mars in perspective of astrobiological research // International Journal of Astrobiology. 2015. 14 (4): P. 537–545
- Goordial J., Davila A., Lacelle D., Pollard W., Marinova M., Creer C., DiRuggiero J., McKay C. and Whyte L. Nearing the cold-arid limits of microbial life in permafrost // The ISME journal. 2016, P. 1-12.
- Hvidberg C.S. Polar caps // chapter in Water on Mars and Life. Berlin: Springer. 2005.
- Siebert M.J., Ellis – Evans J.C., Tranter M., Mayer C., Petit J. – R., Salamatin A., Priscu J.C. Physical, chemical and biological processes in lake Vostok and other Antarctic subglacial lakes // Nature. 2001. V. 144, 2001. P. 603 – 609.

MARTIAN EVOLUTION AND HABITABILITY: FROM THE PLANET FORMATION TO THE POSSIBILITY OF DNA AND RNA SYNTHESIS ON THE PLANET MARS

M. Dalir Sharami¹, S. Ebadirad²

¹ *International Occultation Timing Association in Middle East (IOTA/ME)*

² *Department of Molecular and Cellular Sciences, Faculty of Advanced Sciences and Technology, Pharmaceutical Sciences Branch, Islamic Azad University (IAUPS), Tehran, Iran.*

Contact: s_ebadirad@yahoo.com

In this presentation, first we will talk about formation and evolution of extrasolar planetary systems and their habitable zones due to the hertzsprung-russell diagram, and then we will focus on our solar system's formation and Life zone. We will also discuss the most important characteristics of Mars such as its surface environments, chemical compositions, liquid water, pressure, atmosphere, radiation, magnetic field, gravity and other conducive and unfavorable physical and biochemical conditions which may lead to life or prevent synthesis and maintenance of biomolecules. With an outlook to the unusual simulated situations and natural extreme environments on our planet as Terrestrial Mars analogs we may take steps to find Martian life; to have a better look on the possibility of life there, a better evaluation of plausible models of life and any kind of expectable biomarkers on the red planet. This also may lead to find better ways for future investigations in order to identify organic minerals and biomolecules on Mars. By the way we will have a quick look on microgravity simulation as a biomechanical and biophysical factor to estimate Mars' gravity probable effect on RNA and DNA synthesis as the most important molecular levels of life which we have found in our planet Earth.

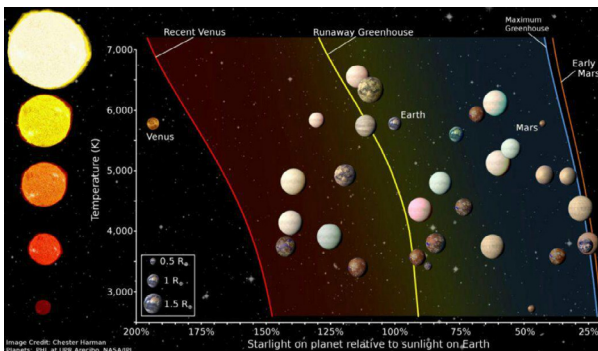


Fig. 1.

Diagram showing different HZ boundaries for stars ranging in spectral type from F0 to M7. Various planets within our solar system are shown, along with selected exoplanets.

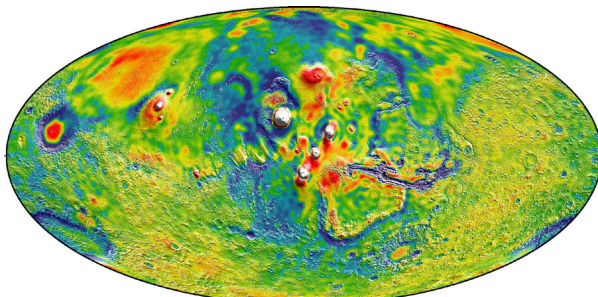


Fig. 2.

A Martian gravity map showing the Tharsis volcanoes and surrounding flexure. The white areas in the center are higher-gravity regions produced by the massive Tharsis volcanoes, and the surrounding blue areas are lower-gravity regions that may be cracks in the crust (lithosphere). Credits: MIT/UMBC-CRESST/GSFC

THE ACTUAL PROBLEMS OF ASTROBIOLOGY: FROM EMERGENCE AND SEARCH TILL DETECTION AND IDENTIFICATION OF LIFE

G.G. Managadze

Space Research Institute, Russian Academy of Sciences, 84/32

Profsoyuznaya Str, Moscow, Russia;

Contact: managa@bk.ru, managa@iki.rssi.ru

Astrobiology is the field of the science which based on new scientific achievements and studies processes of the emergence, distribution and evolution of the life in the Universe. Astrobiology is aimed at the identification and research of the life outside the Earth, and conducts the search for medium suitable for life in Solar system and beyond it and also studies a possibility of adaptation of the life under extreme conditions on Earth and in Space.

In this work results of original research of modern problems of astrobiology are presented and a number of promising assumptions are considered.

1. THE NEW PLASMA CONCEPT OF EMERGENCE OF CONDITIONS FOR ORIGIN OF LIVE MATTER IN A PLASMA TORCH OF METEORITE IMPACT [1, 2, 3].

The results of a laboratory reproduction of hypervelocity impacts of a carbon-containing meteorite on a mineral substance representing a model of planetary surfaces are considered below [3]. The properties of the impact plasma torch provide conditions for a biogenic synthesis of protein amino acids. Glycine, alanine, serine, but in smaller quantities, and organic compounds with masses about 1300 a.m.u. containing fragments of short protein peptides with masses about 300 a.m.u., composed of glycine, alanine and serine were identified in the produced material. The violation of alanine mirror symmetry with excess of L isomer over D from 1.68, with "sign" identical to the bioorganic world was found. Therefore the selection of L amino acids for the formation of proteins for living matter was not random, but it could be defined by the plasma processes occurring in the impact torch.

This indicates that the plasma torch from meteorite impacts could play an important role in the formation of biomolecular homochirality. Meteorite impacts possibly were the initial stage of this process and promoted conditions for the emergence of a living matter. Moreover, these results showed the principal possibility of appearance of the homochiralic medium identical to the biochemical one in the plasma type «dissipative structures» in impact plasma. This process belongs to the inanimate Nature and it does not face any serious contradictions.

2. RESULTS OF SYNTHESIS OF WATER IN PROCESS OF INTERACTION OF PROTONS OF STAR (SOLAR) WINDS WITH SURFACE OXIDES OF SPACE BODIES [4].

Water is the key component required for the origin and evolution of terrestrial-like life. This explains the great interest to the presence of water on celestial bodies and the mechanisms of its formation in space and on the Moon in particular.

In this experiment deuterium ions with energy 3 KeV were used as markers for reproduction of natural process of water synthesis during impact of protons of Solar wind on the surface oxides on the Moon. Products arising in the impact of deuterium ions on the powdered olivine and SiO₂ were registered by a high sensitivity mass spectrometer. Experiment was conducted in high vacuum chamber with a pressure of 10⁻⁸ mm. Hg. Ion masses measurement with high reliability has shown a possibility of OH/H₂O formation on the lunar surface under the influence of hydrogen ions of solar wind with yield about 10⁻³.

Thus, laboratory simulations of the oxide/silicate targets bombardment by solar wind protons allow us to conclude that water formation in such cases is feasible. Although the yield of the process is fairly low, we may assume that much higher amount of OH/H₂O compounds remain in the superficial layer of particles. But it is well known that very small amount of water is necessary for survival of microorganisms (MO) and the total effect can provide such conditions.

3. THE POSSIBILITY OF PRESENCE IN THE MARTIAN ATMOSPHERE OF MARTIAN MICROORGANISMS AND THEIR SPORES ARE SHOWN WITH HIGH RELIABILITY BY RESULTS OF THE MULTI-FACTOR ANALYSIS AND THE AVAILABLE MATERIAL EVIDENCES [6].

Microbial life on Mars if it exists must possess a high similarity with the life on the Earth. In this regard, today the discovery of Martian MO in atmosphere or in wind deposits on the planetary surface can be one of the most interesting breakthroughs. One of the approaches to this research combines well with the important task of determining the chemical and mineralogical composition of atmospheric dust particles with near 1 μm size and less.

It is well known that during the first billion years the Earth and Mars had similar geological history. So we can expect that MO can live in crust of Mars at depths of minimum up to a few km like on Earth.

For realization of Earth-like aerobiological processes on Mars the following conditions are necessary:

- Martian MO have to be adapted to the extreme conditions on the Martian surface and survive not only in the deep layers of the crust of the planet, but also on his surface;
- MO should be transported during dust storms and tornadoes by the wind together with the sand and dust over long distances reaching in some cases a planetary scale.

Aerobiology processes on Mars can take place if non-adapted MO are protected from direct influence of the most dangerous factor to their survival - UV radiation - in the following processes: during excavation of MO from great depths of crust and migration of MO as a part of the atmosphere over large distances under the influence of the wind.

We consider the natural processes which can promote the excavation, survival and adaptation of MO. These processes are meteorite impact and coverage from UV by the dust layer.

4. RESULTS OF LABORATORY RESEARCHES OF A NEW METHOD TO IDENTIFY A BIOMASS AND THE DESIGN OF THE ORIGINAL ONBOARD LASER MASS-SPECTROMETER FOR DETECTION OF MO IN REGOLITH AND IN ICE OF PLANETS AND ALSO IN THE ATMOSPHERE OF MARS AND VENUS [5].

We propose a new technique to detect microorganisms via **elemental composition analyses** of a sample extracted from the regolith, permafrost and ice of extraterrestrial bodies. We also describe the design of the ABIMAS instrument, consisting of the on-board time of flight laser mass-reflectron (TOF LMR) and the sample preparation unit (SPU) for biomass extraction. This instrument was initially approved to fly on-board the ExoMars lander 2018 mission. The instrument can be used to analyze the elemental composition of possible extraterrestrial microbial communities and compare it to the elemental composition of terrestrial ones. MO can be detected by the abundance ratios of biogenic markers K/Ca, P/S, C/N. This type of analysis is more reliable in comparison with macromolecular one because in this case biomarkers are not being destructed over time or under influence of radiation. This technique has been tested experimentally in numerous laboratory trials on cultures of MO and polar permafrost samples as a terrestrial analog for Martian polar soils.

We discuss various methods of extracting MO and sample preparation. The developed technique can be used to search for and identify MO in different Martian samples, and also in the subsurface permafrost and ices of other planets, satellites, comets and asteroids, in particular, Europe, Ganymede and Escalades.

5. IT IS SHOWN THAT THE PROPOSED METHOD AND INSTRUMENT ALLOWS THE IDENTIFICATIONS OF REMAINS OF LIVING BEINGS WHICH DIED HUNDRED MILLION YEARS AGO ON EARTH OR ON THE OTHER PLANETS.

Instrument can successfully be used for search of MO on Phobos or the remains of biomass in the interstellar fields from other galaxies after special modification. The first results of these studies are very promising and they are not too far from necessary perfection and precision.

6. BRIEF DISCUSSION OF IMPORTANT ISSUES.

What is the role of Prebiological Evolution in Plasma Conception of Origin of Life [1, 2]?

What is the possibility of synthesis of water in the plasma torch of meteorite impact?

What is the possibility of ammonia synthesis inside of tornado on the Mars?

May the discovery of MO in Mars atmosphere considered as a proof of their presence in crust of planet?

What are the main problems of **PLASMABIOLOGY**?

REFERENCES:

1. Managadze G.G. (2009) *Plasma of meteorite impact and prebiotic evolution*. Moscow: FIZMATLIT (in Russian).
2. Managadze G.G. (2011) *Plasma of Meteorite Impact and Prehistory of Life*. Nova Science Publishers, Inc. New York (in English).
3. Managadze, G. G., M. H. Engel, St. Getty, P. Wurz, W. B. Brinckerhoff, A. G. Shokolov, G. V. Sholin, S. A. Terent'ev, A. E. Chumikov, A. S. Skalkin, V. D. Blank, V. M. Prokhorov, N. G. Managadze and K. A. Luchnikov, *Excess of l-alanine in amino acids synthesized in a plasma torch generated by a hypervelocity meteorite impact reproduced in the laboratory*. Plan. Sp. Sc. 2016 submitted
4. Managadze G., Cherepin V., Shkuratov Y., Kolesnik V., Chumikov A. (2011) *Simulating OH/H₂O formation by solar wind at the lunar surface*. Icarus 215 449–451.
5. Managadze G., Safronova A., Luchnikov K., Vorobyova E., Duxbury N., Wurz P., Managadze N., Chumikov A., Khamizov R. (2016) *A Novel Technique and Mass-Spectrometric Instrument for Extraterrestrial Microbial Life Detection via the Elemental Composition Analyses of Martian Regolith and Permafrost/Ice*. J. Astrobiology.
6. Managadze G. (2015) *Aerobiology research on Mars and possibility of its implementation*. The sixth Moscow Solar System Symposium. 6MS3-NP-6. p. ab-154-155.

AN ESTIMATE OF A QUALITATIVE COMPOSITION OF «EXOGENOUS» PLANETARY SURFACE ORGANICS BY THE STUDY OF MODEL IMPACT-INDUCED TRANSFORMATION OF CARBONACEOUS METEORITES

M.A. Zaitsev, M.V. Gerasimov, E.N. Safonova, A.S. Vasiljeva
Space Research Institute of Russian Academy of Sciences (IKI RAS), 84/32 Profsoyuznaya str., 117997 Moscow, Russia
 Contact: mzaitsev@iki.rssi.ru

INTRODUCTION:

It's well known, planets and their satellites are exposed to hypervelocity impacts during asteroidal and cometary bombardments. Thus, «exogenous» organic matter on the planetary surfaces can be represented by both unaltered organic matter of asteroids and comets, and by impact-generated organic matter, synthesized from organic and/or mineral components of falling bodies.

The main objective of the planned missions to Jupiter's satellites Ganymede or Europa is the search for hypothetical life which can be detected by *in situ* characterization of surface organics. Adequate interpretation of results in this case is impossible without taking of «exogenous» organic compounds (OC) into consideration. This problem is also important in connection with the Mars exploration.

It's very difficult to predict a quantitative composition of «exogenous» OC. It depends on numerous factors, such as: intensity of the bombardment, speed of the icy crust renovation, etc. Nevertheless, a qualitative composition of «exogenous» organics can be characterized by the study of meteoritic organics (in general – OC of carbonaceous chondrites), and products of model impact-induced transformation of meteorites.

EXPERIMENT:

We performed a comparative study of carbonaceous CM2 (Murchison) and CO3 (Kainsaz) chondrites and condensed products of their high-temperature impact-induced evaporation, using Pyr-GC/MS.

High-temperature vapor conditions, taking place during hypervelocity impacts, were simulated by Nd-glass pulse laser ($\lambda=1,06 \mu\text{m}$), according to the standard technique [1]. Laser vaporization of meteorites was provided in helium and hydrogen gas atmospheres.

Two-stage pyrolysis of meteorites and condensates were conducted at 460°C and 900°C under the helium flow. Volatile products of pyrolysis were accumulated in a capillary cryogenic trap and their study was provided by GC/MS [2-4].

RESULTS AND THEIR DISCUSSION:

During pyrolysis at 460°C all the condensates gave lower amounts of volatiles, than the initial meteorites. «Hydrogen» condensates gave larger amounts of volatiles, than «helium» condensates.

The «helium» condensates gave volatiles, which have the higher relative amounts of N-, S-containing compounds and aliphatic hydrocarbons, than the initial meteorites, and higher amounts of CO₂ and SO₂. The «hydrogen» condensates gave volatiles, containing the higher relative amounts of aromatic and alkyl-aromatic hydrocarbons, compared to the initial meteorites. At the same time, S-containing OC were almost absent, but there were huge amounts of H₂S.

Residual pyrolysis of all the condensates at 900°C gave only carbon dioxide, sulfur dioxide, benzene and traces of other aromatics – typical products of the thermal destruction of high-molecular OC.

Carbonaceous chondrite Murchison contains higher abundances of volatiles, OC, and carbon at all [5-7], than Kainsaz [8, 9]. It was also proved by higher yield of volatile organics during pyrolysis of Murchison, compared to Kainsaz. Nevertheless, the Kainsaz condensates (both «hydrogen» and «helium») were much higher in diversity and quantity of volatile organics during pyrolysis, than

the Murchison condensates and gave lesser amounts products of oxidation – CO₂ and SO₂. This fact can be explained by differences in elemental and mineral composition of both meteorites. Kainsaz is «more reduced» chondrite, than Murchison. It contains ~5% vol. of nickel iron, compared to <0.5% vol. of the same in Murchison [10, 11]. This difference cases different redox conditions in the vapour clouds during model evaporation of chondrites. Furthermore, both nickel and iron (their nanosize particles forms in result of thermal reduction [12]) are well known as catalysts of a number of chemical reactions (e.g. Fisher–Tropsch-type of reactions). In our case, the Fisher–Tropsch-type of reactions is supposed to be a source of hydrocarbons (especially long chain aliphatic and alkyl aromatic hydrocarbons). Thus, higher yield of OC during model impact-induced transformation of Kainsaz can be a result of more intensive heterogeneous catalysis.

Despite of extreme conditions in the silicate impact-generated cloud (high temperature and pressure, presence of the free oxygen, etc.), the impact-induced transformation of carbonaceous asteroids can form various OC (not only eliminate them by oxidation), mainly, due to heterogenous catalytic reactions. Of course, composition and yield of OC are determined by elemental composition of falling bodies, and nature of a surrounding gas atmosphere. If the total abundance of carbon in two asteroids is nearly comparable, more «reduced» asteroid will give larger amounts of impact-induced OC in the same conditions. Reducing conditions (e.g. presence of hydrogen) of the surrounding atmosphere also increase the efficiency of the impact-induced synthesis of OC and contribute to the preservation of synthesized organics.

Since impactors in Ganymede or Europa conditions are most likely icy bodies, not stony ones, the question about the influence of water, the main component of such ices, on the composition of organic synthesis products remains open. Certainly, water reduces the vaporization temperature in the impact process and changes oxidation-reduction conditions in the cloud. For example, as was showed earlier [13], an increase in the water content in a homogeneous gas-vapor cloud restricts the yield and complexity of synthesized OC. However, about a half of the atoms in silicates is oxygen; in water molecules, oxygen atoms constitute one third and two thirds are formed by hydrogen, which is a reducer. In addition, even in ice bodies, there are silicate components which are a necessary catalyst for a productive synthesis of organic molecules under conditions of an impact-generated cloud.

CONCLUSION:

«Exogenous» organic matter (both delivered by falling bodies and impact-synthesized) on the icy satellites surfaces can consist of various hydrocarbons (aliphatic, and aromatic, including polycyclic, and alkyl aromatic hydrocarbons), oxygen-, sulfur- (thiophene, alkyl- and benzothiophenes), nitrogen-containing OC (nitriles, heterocyclic compounds, etc.), and high-molecular (kerogen-like) organics.

For the effective detection of «endogenous» OC, which could have a biological origin, it's necessary to obtain a database, containing information about OC, which can have a presumably «exogenous» origin. The database has also to include information about isotopic composition of OC.

Obviously, we have to choose the freshest ices as landing sites, because these ices contain lesser amounts of «exogenous» organics.

ACKNOWLEDGEMENTS:

This work was supported in part by P-22 Program of the RAS.

REFERENCES:

- [1] Gerasimov M.V., et al. (1998) *Earth, Moon, and Planets*, **80**, 205-259.
- [2] Zaitsev M.A., et al. (2013) *44th LPSC*, abs. 1905.
- [3] Ivanova M.A., et al. (2014) *45th LPSC*, abs. 1014.
- [4] Zaitsev M.A., et al. (2016) *Solar System Res.*, **50**, №2, 113-129.
- [5] Sephton M.A., Botta O. (2008) *Space Sci. Rev.*, **135**, 25-35.
- [6] Jarosewich E. (1971) *Meteoritics*, **6**, 49-52.
- [7] Jarosewich E. (1990) *Meteoritics*, **25**, 323-337.
- [8] Vdovikin G.P. (1967) *Carbon matter of meteorites*. Moscow, «Nauka». P. 64.
- [9] Ahrens L.H., et al. (1973) *Meteoritics*, **8**, 133-139.
- [10] McSween H.Y. (1977) *Geochim. Cosmochim. Acta*, **41**, 477-491.
- [11] McSween H.Y. (1979) *Geochim. Cosmochim. Acta*, **43**, 1761-1770.
- [12] Yakovlev O.I., et al. (2006) *Geochemistry International*, **44**, № 9, 847-854.
- [13] Jones T.D., Lewis J.S. (1987) *Icarus*, **72**, 381–393.

DELIVERY OF WATER AND PLANETESIMALS FROM THE FEEDING ZONE OF JUPITER AND SATURN TO FORMING TERRESTRIAL PLANETS

S.I. Ipatov^{1,2}, M.Ya. Marov¹

¹Vernadsky Institute of Geochemistry and Analytical Chemistry of Russian Academy of Sciences, Kosygina 19, 119991, Moscow, Russia

²Space Research Institute of Russian Academy of Sciences, Profsoyuznaya st. 84/32, Moscow, Russia

Contact: siipatov@hotmail.com.

INTRODUCTION:

Several sources of the delivery of water to the terrestrial planets were considered. Some scientists (see, e.g., [1]) consider the zone of the outer asteroid belt to be the main source of water on the Earth. Drake and Campins [2] noted that the key argument against an asteroidal source of Earth's water is that the O's isotopic composition of Earth's primitive upper mantle matches that of anhydrous ordinary chondrites, not hydrous carbonaceous chondrites.

There is the deuterium/hydrogen paradox of Earth's oceans (D/H ratio is different for oceans and comets), but Pavlov et al. [3] suggested that solar wind-implanted hydrogen on interplanetary dust particles provided the necessary low-D/H component of Earth's water inventory, and Delsemme [4] considered that most of the seawater was brought by the comets that originated in Jupiter's zone, where steam from the inner solar system condensed onto icy interstellar grains before they accreted into larger bodies. It is likely [2] that the D/H and Ar/O ratios measured in cometary comas and tails are not truly representative of cometary interiors.

There are a few papers devoted to computer simulations of migration of planetesimals and delivery of water to the Earth from the feeding zones of the giant planets and the outer asteroid belt. In such simulations, the present masses of the terrestrial planets usually were considered.

Our previous studies [e.g., 5-8] of the delivery of water and volatiles to the terrestrial planets were based on our computer simulations of the orbital evolution of several tens of thousands of small bodies and dust particles which orbits were close to orbits of discovered comets. Masses and orbits of planets in these simulations were the same as those of present planets. In our recent runs, we studied migration of planetesimals not only to the present terrestrial planets, but also to their embryos.

INITIAL DATA:

In our new runs, as in our previous calculations, the gravitational influence of considered planets was taken into account. Integration of the motion equations was made with the use of the symplectic method until all planetesimals were ejected into hyperbolic orbits or collided with planets. In series JS, we considered the present orbits and masses of the terrestrial planets, Jupiter and Saturn. It is considered in several cosmogonic models that Jupiter and Saturn have been almost formed when masses of forming terrestrial planets were far from the present masses. Therefore, in series JS₀₁, masses of planets in the terrestrial zone were smaller by a factor of ten than masses of the present terrestrial planets. In series JN and JN₀₁, in addition to the initial data for series JS and JS₀₁, we also considered present Uranus and Neptune. In the new series of runs, semi-major axes a of initial orbits of planetesimals varied from $a_{\min}=4.5$ to $a_{\max}=12$ AU, and the number of planetesimals with semi-major axis a was proportional to $a^{1/2}$. Initial eccentricities and inclinations of planetesimals were equal to 0.3 and 0.15 rad, respectively. Such eccentricities could be reached due to gravitational influence of planetesimals and planets [9].

COMPUTER SIMULATION RESULTS:

Our calculations of the probabilities of collisions of migrating planetesimals with planets were based on obtained arrays of orbital elements of several thousands of planetesimals during their dynamical lifetimes (until their ejections into

hyperbolic orbits or collisions with planets or the Sun). Based on the arrays of orbital elements of migrating planetesimals, we calculated the probabilities not only for the mass of the Earth's embryo that was used in a considered simulation of the evolution of a disk of planetesimals, but also for another value of the mass of the embryo. The values p_E and p_{E01} of the probabilities of collisions of a migrating planetesimal with a planet were calculated for a planet in Earth's orbit for the mass of the planet equal to m_E or $0.1m_E$, respectively, where m_E is the mass of the Earth.

In series JS and JN, the probability p_E of a collision of a planetesimal with the Earth is about 2×10^{-6} . It is smaller than the value of $\geq 4 \times 10^{-6}$ obtained in our previous calculations at initial Jupiter-crossing cometary orbits. In the recent series of runs, not all planetesimals got highly eccentric Jupiter-crossing orbits, and the probabilities of their collisions with the Earth during evolution were greater for planetesimals from the inner part of the considered disk than for the outer part of the disk. In series JS₀₁, the probability p_{E01} of a collision of a planetesimal with the Earth's embryo of mass $0.1m_E$ was obtained to be equal to 4×10^{-7} . In the series JS, JS₀₁, JN and JN₀₁, about 12–14% of planetesimals reached the orbit of the Earth during evolution. If we consider only those planetesimals that became Earth-crossers, then the probabilities of collisions of such planetesimals with the Earth are greater than 2×10^{-6} by almost an order of magnitude.

In some recent series of runs, the giant planets of present masses initially were located more close to each other than the present giant planets (the maximum values of their initial semi-major axes varied between 15 and 20 AU), and a_{\max} did not exceed 23 AU. For such runs, at least one giant planet (not Jupiter) was ejected into a hyperbolic orbit during evolution. The values of p_E and p_{E01} for such runs usually were not smaller than the values for series JS, JS₀₁, JN and JN₀₁. For the Grand Tack model, the region from 3 to 6 AU is considered free from planetesimals due to the accretion of Jupiter and Saturn which migrated inwards towards the Sun and then outwards from the Sun [10]. The probabilities of collisions of planetesimals with the terrestrial planets will be a little lower if we consider the inner border of the disk equal to 6 AU, but not to 4.5 AU.

DELIVERY OF WATER TO THE TERRESTRIAL PLANETS:

For the total mass of planetesimals in the feeding zone of Jupiter and Saturn to be about a hundred of Earth masses [9], at $p_E = 2 \times 10^{-6}$ and at the fraction of water in planetesimals equal to 0.5, one can obtain that the total mass of water delivered from these zones to the Earth can be about a half of the mass of water in Earth's oceans. About the same amount of water could be delivered to the Earth from distances greater than 12 AU. The main delivery from such greater distances could be later than from the feeding zone of Jupiter and Saturn, and could take place when the Earth was almost formed.

The ratios of the probabilities of collisions of migrating planetesimals with the Earth to the probabilities of their collisions with Venus, Mars, and Mercury were about 1, 4.6, and 13, respectively, in series JS, and were about 1.7, 2.7, and 21 in series JN. The same ratios are for the amount of water delivered to the planets. In series JS, the ratio of the probability of a collision of a planetesimal with a planet to the mass of the planet was greater by about a factor of 2 and 1.4 for Mars and Mercury, respectively, than for the Earth. The above estimates testify in favor of ancient oceans on Mars and Venus.

PROBABILITIES OF COLLISIONS OF PLANETESIMALS WITH GROWING EARTH:

Based on the arrays of orbital elements of migrating planetesimals obtained in our runs, we calculated the probabilities p_E and p_{E01} of a collision of a planetesimal with a planet in the Earth's orbit for the mass of the planet equal to m_E и $0.1m_E$, respectively. The obtained ratio p_E/p_{E01} of the probabilities mainly was between $5 \approx 10^{0.7}$ and $5.5 \approx 10^{0.74}$. Therefore, the ratio of the total mass of the planetesimals collided with a planet to the mass of the planet at the mass of the planet equal to $0.1m_E$ is greater by about a factor of 2 than at m_E . The above estimates are for planetesimals from the zone of the giant planets. Below we denote them as g-planetesimals. For the planetesimals from the terrestrial zone, their typical eccentricities are smaller than those for g-planetesimals, and the index of power could be greater than 0.74. For the increase of the mass a planet embryo of mass m due to accumulation of g-planetesimals proportional to $m^{0.74}$, the ratio of the increase of the mass of the embryo due to accumulation of g-planetesimals during the growth of the mass of the embryo from 0 to $k \cdot m_E$ to the increase of the mass of the embryo by accumulation of g-planetesimals

during the growth of the mass of the embryo from 0 to m_E is equal to $k^{1.74}$. The same estimates are for the case if the ratio of the amount of g-planetesimals collided with the embryo to the amount of 'local' planetesimals did not vary with time. In particular, $0.5^{1.74} \approx 0.3$ and $0.8^{1.74} \approx 0.68$. The fraction of g-planetesimals collided with the embryo at the growth of its mass from 0 to $k \cdot m_E$ can be smaller than $k^{1.74}$, if, at the late stages of formation of the planet, the ratio of the income of g-planetesimals to the income of "local" planetesimals was greater than at the previous stages of the growth of the planet embryo. Based on the above estimates, we concluded that at the growth of the mass of the Earth's embryo up to $0.5m_E$, the mass of water delivered to this embryo could be about 30% of all water delivered to the embryo from the feeding zone of Jupiter and Saturn. These estimates show that a considerable fraction of water could be delivered to the embryo of the Earth when its mass was smaller than the present mass of the Earth.

CONCLUSIONS:

The mass of water delivered from behind the orbit of Jupiter during the formation of the Solar System could be comparable with the mass of water in the Earth's oceans. The mass of water delivered to the Earth's embryo during the growth of its mass to a half of the Earth mass could be about 30% of all water delivered to the embryo from the feeding zone of Jupiter and Saturn during the growth of the mass of the embryo to the Earth mass.

ACKNOWLEDGMENTS:

The work was supported by the program of fundamental studies of the presidium of RAS № 30.

REFERENCES:

- [1] Petit J.-M., Morbidelli A., Chambers J. (2001) *Icarus*, 153, 338-347. [2] Drake M., Campins H. (2006) In: *IAU Symp. 229 "Asteroids, Comets, & Meteors"*. P. 381-394. [3] Pavlov A.A., Pavlov A.K., Kasting, J.F. (1999) *Journal of Geophysical research* 104, No. E1230,725. [4] Delsemme A.H. (1999) *Planetary & Space Science* 47, 125. [5] Marov M.Ya., Ipatov S.I. (2001) In: *Collisional processes in the solar system*. M.Ya. Marov, H. Rickman. Eds. Astrophys. & Space Science Library. Vol. 261. Dordrecht: Kluwer Academic Publishers. P. 223-247. [6] Marov M.Ya., Ipatov S.I., (2005) *Solar System Research*, 39, 374-380. [7] Ipatov S.I., Mather J.C. (2007) In: *Proc. IAU Symp. No. 236 "Near-Earth Objects, Our Celestial Neighbors: Opportunity and Risk"*. A. Milani, G.B. Valsecchi, D. Vokrouhlický. Eds. Cambridge: Cambridge Univ. Press. P. 55-64. [8] Ipatov S.I. (2010) In: *Proc. IAU Symposium S263. Vol. 5. "Icy bodies in the Solar System"*. J.A. Fernandez, D. Lazzaro, D. Prialnik, R. Schulz. Eds. Cambridge: Cambridge Univ. Press. P. 41-44. [9] Ipatov S.I. (1993) *Solar System Research*, 27, 65-79. [10] Rubie D.C., et al. (2015) *Icarus*, 248, 89-108.

WHERE SHOULD WE LOOK FOR RELICS OF AN EXTINCT PRIMITIVE LIFE?

V.V. Busarev

Moscow Lomonosov State University, Sternberg Astronomical Institute,
University Avenue 13, Russia
Contact: busarev@sai.msu.ru

INTRODUCTION:

Internal water oceans on planets and planetary satellites are considered as likely 'shelters' of a microbial life that could spontaneously origin in the Solar System. Widespread in the Universe three-atomic molecules of HCN and H_2O and derivative from them formamide (NH_2COH) could be initial blocks for the primitive terrestrial and extraterrestrial life forms (e. g., [1]). As shown recently in laboratory experiments (JINR, Dubna, Russia) [2], irradiation of formamide by protons in the presence of mineral or meteoritic catalyzers leads to synchronous synthesis of a wide range of prebiotic compounds (amino acids, heterocycles, alcohols, amides, sugars, etc.) potentially relevant to develop genetics (based on RNA and DNA) and metabolism underlying the terrestrial life [2, 3]. As suspected, proton irradiation of formamide creates active radicals stimulating effectively a further synthesis. Noteworthy, such types of synthesis are abiotic and run in the same chemical environments [2].

Finds of possible fossilized microbial structures in carbonaceous chondrites (e. g., [4-7]) with an extremely high age ~ 4.5 - 4.6 Gyr [8-10] points likely to origin of microbial life before the formation of Earth. Here we outline processes that could create appropriate conditions for biological synthesis at the very beginning of our planetary system formation.

A KEY ROLE OF STONE-ICE BODIES IN THE EARLY SOLAR SYSTEM:

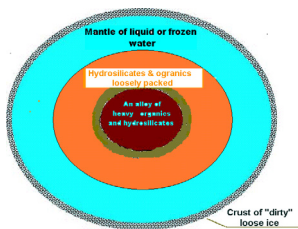


Fig. 1.

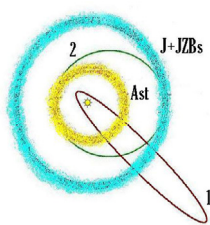


Fig. 2.

The mentioned formamide based chemical evolution in the open interstellar/interplanetary medium could not reach its logical end – origin of any biological substance. The next stages of the hypothetical synthesis needed a protection from the harsh space factors and presence of liquid water, catalysts, etc. (e. g., [3]). Protected and relatively quiet conditions might have been in the early Solar System only in interiors of proto-planetary bodies. According to our analytical calculations [11], internal water oceans could exist for some time into big enough stone-ice bodies beyond the 'snow-line'. As follows from investigations of chondritic meteorites (e. g., [12]), it was possible due to decay of short-lived isotopes (primarily ^{26}Al with $T_{1/2} = 0.72$ My) in silicate fraction of matter. The energy source would be sufficient to melt nearly all ice into the bodies ($R > 100$ km) and to create an abundant aqueous media or a global internal water ocean (with an average temperature of ~ 4 °C) existed for the first few million years after formation of calcium-aluminum inclusions (CAIs) [11]. The main

results of these processes could be aqueous differentiation of the bodies and accumulation of a considerable silicate-organic core (up to $\sim 0.7 R$) saturated with liquid water and heavy organics (of kerogen or bitumen type with density > 1 g/cm 3) [13] (Fig. 1). Important related processes in the system 'water-rock' are exothermic reaction of serpentinization (hydration) of silicates and intense release of H_2 and CH_4 gases [14, 15]. It is important to note, the processes make the material layered and microporous, hence, mechanically fragile.

EVOLUTION AND FATE OF THE STONE-ICE BODIES FROM JUPITER'S FORMATION ZONE:

Due to plenty of icy material, growth of proto-Jupiter and smaller bodies in its formation zone (JZBs) (Fig. 2, 'J+JZBs') had to run on 'runaway' scenario [16]. Then, the stone-ice bodies turned out to be bigger (~ 1000 km or more) there and had elevated temperatures in their interiors because of better insulating properties. For the reasons, there were possibly more favorable conditions for the development of more complex pre-biotic compounds (amino acids, carboxylic acids, nucleobases,

etc.) or even simplest anaerobic bacteria (prokaryotes). Nearly at the same time, when growing Jovian embryo reached in mass ~ 3 Earth's masses, its accretion of smaller bodies changed by their predominant ejection outward and inward of the early Solar System [16, 17]. The range of velocities of JZBs ('impactors') penetrating the asteroid formation zone (Fig. 2, 'Ast') is estimated from 2-3 km/s to ~ 30 km/s [17, 18]. Direct collisions of the high-velocity JZBs moving in elongated orbits (Fig. 2, orbit '1') with asteroid parent bodies ('targets') would lead to complete sweeping out the latter from the asteroid belt. However, calculations and experiments show that some fractions of 'targets' and 'impactors' could remain in vicinity of the collisional epicenter. Apparently, the quantity of remained matter is inversely proportional to the relative velocity of the colliding bodies. Those JZBs, that have been moving in less eccentric orbits (Fig. 2, orbit '2'), penetrated the asteroid belt with the lowest velocities (favorable for survival of volatile materials such as water ice, hydrated silicates and organics) and remained there for a longer time and, hence, had the highest probability to collide with asteroid parent bodies. Moreover, due to frailness of JZBs, they could crush into fragments of different sizes, up to the smallest, during collisions with mainly rocky (and probably enough strong) asteroid parent bodies. Thus, mass of JZBs' fragments (including water and carbonaceous material), or the so-called 'delivered material', remained in the asteroid belt. According to our hypothesis about origin of C-type asteroids and carbonaceous chondrites [19], the largest fragments of JZBs could replenish or even form the most numerous family of primitive asteroids with low-temperature mineralogy (of C-B-F-G close types). JZBs' smallest fragments (ice and carbonaceous material similar to CI chondrite) settled onto remained asteroids were reprocessed at subsequent collisional events and formed different carbonaceous chondrites of (CM, CO, CV, etc.) depending on collisional history and relative abundance of high-temperature millimeter-centimeter-sized inclusions or 'chondrules' as collisional products [20, 21].

PRIMITIVE LIFE RELICS MAY BE ON/IN PRIMITIVE ASTEROIDS AND IN CARBONACEOUS CHONDRITES:

Thus, according to above described chain of processes in the early Solar System, thermally altered and differentiated JZBs could be turned inside out by impact processes. Their largest fragments became likely primitive-type asteroids in the main asteroid belt. Since then, ice and carbonaceous material from JZBs' interiors could be on the surface (or under the surface) of those and other asteroids as carbonaceous chondrites of different groups including a predominant proportion of hydrated silicates (e. g., [22, 23]) and probable fossilized pseudomorphic microbial structures (e. g., [4-7]). The conclusion is confirmed by our observational data: we have found, on the one hand, spectral signs of atypical hydrated silicates on numerous asteroids of high-temperature types [24, 25] and, on the other hand, evidence of considerable proportion of water ice on primitive asteroids [26]. It is also in accordance with results of *Dawn's* investigations of the largest asteroids (4) Vesta and (1) Ceres (e. g., [27, 28]).

REFERENCES:

- [1] Pino S., Costanzo G., Giorgi A. et al. (2013) *Entropy*, v. 15, p. 5362-5383. [2] Saladino R., Carota E., Botta G. et al. (2015) *PNAS*, v. 112, E2746-E2755. [3] Mukhin L. M. (2009) In: *The problems of life origin* (Eds. A. I. Grigor'ev et al.), M.: PIN RAS, p.120-130 (in Russian). [4] Tan W. C., VanLandingham S. L. (1967) *Geophys. J. Roy. Astron. Soc.*, v. 12, p. 237. [5] Zhmur S. I. et al. (1997) *Geochem. Intern.*, v. 35, p. 58. [6] Hoover R. B. (1997) *Proc. SPIE*, v. 3111, p. 115. [7] Rozanov A. Yu. (2009) In: *The problems of life origin* (Eds. A. I. Grigor'ev et al.), M.: PIN RAS, p.158-165 (in Russian). [8] Epstein S. et al. (1987) *Nature*, v. 326, p.477. [9] Engel M. H., Masco S. A. (1997) *Nature*, v. 389, p. 265. [10] Shukolyukov A., Lugmair G. W. (2006) *Earth Planet. Sci. Lett.*, v. 250, p. 200. [11] Busarev V. V., Dorofeeva V. A., Makalkin A. B. (2003) *Earth, Moon and Planets*, v. 92, p. 345-357. [12] Srinivasan G., Goswami J. N., Bhandari N. (1999) *Science*, v. 284, P. 1348-1350. [13] Busarev V. V., Dorofeeva V. A., Makalkin A. B. (2005) *LPSC 36th*, abs. #1074. [14] Wilson L., Keil K., Browning L. B. et al. (1999) *Met. Planet. Sci.*, v. 34, p. 541-557. [15] Rosenberg N. D., Browning L., Bourcier W. L. (2001), *Met. Planet. Sci.*, v. 36, p. 239-244. [16] Safronov V. S. (1972) *Evolution of the protoplanetary cloud and the formation of the Earth and the planets / TTF-667*, Washington, 206 p. [17] Safronov V. S., Ziglina I. N. (1991) *Sol. Sys. Res.* V. 25, P. 139. [18] Vityazev A.V., Pechemikova G. V., Safronov V. S. (1990) *Planets of Earth's group. The origin and early evolution / M.: Science*, 296 p. (in Russian). [19] Busarev V. V. (2012) *Asteroids, Comets, Meteors (ACM) 2012*, abstract #6017. [20] Urey H. C. (1952) *Geochim. Cosmochim. Acta*, V. 2, P. 269-282. [21] Johnson B. C. et al. (2015), *Nature*, v. 517, p. 339-341. [22] Zolensky M., Barrett R., Browning L. 1993. *Geochim. & Cosmochim. Acta*, V. 57, P. 3123-3148. [23] Hutchison R. et al. (2005) In: *Chondrites and the protoplanetary disk / Eds Krot A. N. et al.*, *ASP Conf. Series*, v. 341, p. 933-950. [24] Busarev V. V. (2002) *Sol. Syst. Res.*, v. 36, p. 39-47. [25] Busarev V.V. (2016) *Sol. Syst. Res.*, v. 50, p. 13-23. [26] Busarev V. V., Barabanov S. I., Rusakov V. S. et al. (2015) *Icarus*, v. 262, p. 44-57. [27] McCord T. B., Li J.-Y., Combe J.-P. and 26 coauthors (2012) *Nature*, v. 491, p. 83-86. [28] Nathues A., Hoffmann M., Schaefer M. and 25 coauthors (2015) *Nature*, v. 528, p. 237-240.

MICROBIAL COMMUNITY OF THE UPPER SOIL LAYER OF NEGEV DESERT AS THE MODEL MICROBIAL SYSTEM FOR ASTROBIOLOGICAL EXPERIMENTS IN THE PLANNED MISSION PHOBOS-GRUNT 2

O.R. Kotsyurbenko

Moscow State University, Leninskie Gory, 1, 119991, Russia

Yugra State University, Chekhova str., 16, 628012, Russia

Contact: kotsor@mail.ru

Soil samples from the Negev desert have been selected for the astrobiological experiment testing the hypothesis of panspermia in the mission Phobos-Grunt in 2011. This is the unique natural ecosystem exposed to extreme environmental factors such as intensive solar radiation and highly arid climate and is the excellent model system for astrobiological experiments in the framework of the planned mission Phobos-Grunt 2 or other return space missions. Specificity of the microbial system of this soil is the present of a particular microbial group – methane producing archaea in the upper aerated layer. This microorganisms are able to develop only in the absent of oxygen. Methanogens are now considered to be the main target microbial group to be sought in different extraterrestrial ecosystems.

Methanosarcina has been found to be the main methanogenic group in the Negev desert soil. This is the most universal methanogen capable of use of full substrate spectrum characteristic for methanogenic archaea by all three known pathways. *Methanosarcina* has been also detected in different extreme environments including low-temperature ecosystems. Methanogens withstood extreme arid and aerated conditions and could be readily activated by incubating the soils under anoxic conditions with methane production within a few weeks. They appeared to contain the active oxygen detoxifying enzymes enabling them to survive. In addition to methanogenic archaea, other microbial groups have been found in the Negev desert soil composing the balance microbial community.

Experiments on influence of extreme space factors on such a microbial system will examine survival capacities of both separated microorganisms and microbial community as a whole. Soil is a matrix that is suggested to protect microorganisms and increase their survival. Additionally, enclosing microorganisms in the community with consistent trophic interactions can be also favorable for survivability.

Control laboratory and orbital experiments are planned to conduct to study survival potential of the microbial community from the above mentioned desert soil. Native soil samples and those exposed to extreme factors will be analyzed for biomarkers, microbial composition and metabolic potential.

THE PLANETARY PROTECTION REQUIREMENTS FULFILMENT DURING THE LAUNCH CAMPAIGN OF THE EXOMARS-2016 MISSION

N.M. Khamidullina², E.A. Deshevaya², A.A. Guridov², D.V. Zakharenko¹, O.N. Zaytseva¹, Novikova², O.I. Orlov²

¹*Lavochkin Association, Khimki, Moscow Region, Russia*

²*Institute of Biomedical Problems of RAS, Moscow, Russia*

Contact: nmx@laspace.ru

The major purpose of the planetary protection program in the ExoMars-2016 mission is to forestall Mars contamination by terrestrial microorganisms. Since Martian descent module is not intended for biological experiments, ExoMars-2016 mission falls under COSPAR category IVa.

Within the joint project co-sponsored by ESA and Roscosmos the European side was full responsible for ensuring a prescribed level of SC microbiological cleanliness, while the Russian side was charged with compliance of the launch services provided on Baikonur technical complex with the planetary protection requirements that is, specifically, prevention of SC recontamination. To this end, a complex of measures was executed to control microbial contamination of cosmodrome facilities on the prescribed level which included:

- regular decontamination of clean rooms using an effective disinfectant and impulse ultraviolet radiation that created favorable conditions for reliable functioning of the ESA clean tent,
- replacement of airline filters in the Thermal Conditioning Unit (TCU) air duct for SC conditioning with pure air.

Presented in the report results of microbiological tests (performed in the period of 2015 – 2016) lead to the conclusion that the Baikonur clean rooms (ISO class 8), TCU air ducts and Air Thermal Control System (ATCS) at launch site are ready for the launch campaign and that the Russian side fulfilled the planetary protection requirements of the ExoMars-2016 mission.

INTERMITTENCY IN DYNAMICS OF RESONANT KUIPER BELT OBJECTS

S.S. Efimov¹, V.V. Sidorenko^{1,2}

¹Moscow Institute of Physics and Technology, 9 Institutskiy per., 141701 Dolgoprudny Moscow Region, Russian Federation

²Keldysh Institute of Applied Mathematics, 4 Miusskaya sq., 125047 Moscow, Russian Federation

Contact: Efimov.SS@phystech.edu

The Kuiper belt is a region of the Solar System, extending from 30 AU (the orbit of Neptune) to approximately 50 AU from the Sun [D1995]. About 20% of all Kuiper belt objects exhibit mean motion resonance (MMR) with Neptune [K2008]. MMR is a dynamical situation characterized by commensurability between the orbital periods of two celestial bodies. Most of the resonant objects belong to two main groups: plutino (2:3 MMR) and twotino (1:2 MMR).

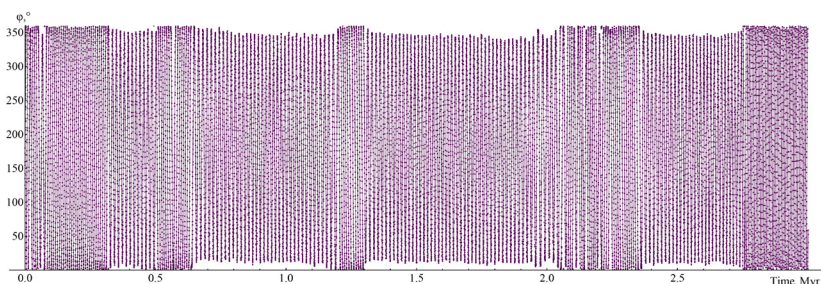


Fig. 1. Evolution of the resonant angle φ for asteroid 2011UU412

Dynamics of a small body in MMR is characterized by resonant angle – some linear combination of angular orbital elements, which varies periodically with time. During numerical simulations of known plutino's motion, we found, that for some of them (2011UU412, 1999CY131, 2001FV185) resonant angle continuously switches from oscillation to rotation and vice versa (Fig. 1). It corresponds to transitions between resonant and non-resonant regimes of motion.

Wisdom's approach [W1985] allows to develop a model Hamiltonian system, mimicking the described intermittency in the dynamics of the resonant Kuiper belt objects. Using this system, we study the long-term evolution of their eccentricity and argument of perihelion at 2:3 MMR. As an example, the possible behavior of and in the case of switches between resonant and non-resonant regimes is shown in Fig. 2. The classification of the different evolution scenarios is carried out also in [ES2016].

The interchange of resonant and non-resonant regimes gives rise to so-called adiabatic chaos [W1985], which, in particular, is responsible for non-regularity of regimes' alternation on Fig. 1. Some characteristics of chaotic motions are calculated.

REFERENCES:

- [D1995] Duncan, M.J., Levison, H.F., Budd, S.M., "The Dynamical Structure of the Kuiper Belt," *Astronomical Journal*, vol. 110, pp. 3073–3081, 1995.
- [K2008] Kavelaars, J., Jones, L., Gladman, B., Parker, J.W., Petit, J.-M., "The orbital and spatial distribution of the Kuiper belt," *The Solar System Beyond Neptune*, pp. 59–69, 2008.
- [W1985] Wisdom, J., "A perturbative treatment of motion near the 3/1 commensurability," *Icarus*, vol. 63, pp. 272–286, 1985.
- [ES2016] Efimov, S.S., Sidorenko, V.V., "Model system describing some aspects of celestial bodies' dynamics in first order mean motion resonance," Preprint 65 of Keldysh Institute of Applied Mathematics RAS, 2016.

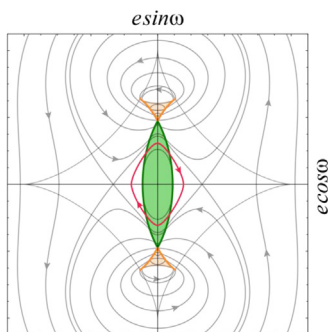


Fig. 2. Long-term evolution of orbital parameters. Green region represents the region of resonant angle rotation. Outer white region is the region of resonant angle oscillation. Orange – region with two different possible oscillation regimes. Red line represents the path of long-term evolution with oscillation-rotation intermittency

WHY COMETS REVEAL VARIOUS POSITIVE POLARIZATION?

E. Zubko^{1,2}, G. Videen^{3,4}, D.C. Hines⁵, Yu. Shkuratov²

¹*School of Natural Sciences, Far Eastern Federal University, 8 Sukhanova St., Vladivostok 690950, Russia*

²*Institute of Astronomy, V.N. Karazin Kharkov National University, 35 Sumskaya St., Kharkov 61022, Ukraine*

³*Space Science Institute, 4750 Walnut St., Boulder Suite 205, CO 80301, USA*

⁴*U.S. Army Research Laboratory, 2800 Powder Mill Road, Adelphi, MD 20783, USA*

⁵*Space Telescope Science Institute, 3700 San Martin Drive, Baltimore, MD 21218, USA*

Contact: evgenij.s.zubko@gmail.com

INTRODUCTION:

The degree of linear polarization is defined as $P = (I_{\perp} - I_{\parallel}) / (I_{\perp} + I_{\parallel})$, where, I_{\perp} and I_{\parallel} stand for intensity of the scattered sunlight that is polarized perpendicular to the scattering plane and within that plane, respectively. This polarization P differs significantly in different comets [1]. Such difference appears most noticeable at phase angles $\alpha \sim 70 - 110^{\circ}$, where P reaches its maximum value. In comets, the maximum of the degree of linear polarization P_{\max} spans the range from $\sim 7\%$ up to more than 30% [1]. Chernova et al. [1] speculated that this difference is caused by the depolarizing effect of a gaseous emission. In other words, comets with low P_{\max} have been considered to be enriched in gases; whereas, comets with high P_{\max} are dust-rich comets. On the contrary, Levasseur-Regourd et al. [2] suggested a difference in light-scattering properties of cometary dust. We thoroughly analyzed these two hypotheses and found that the gaseous-emission explanation is not consistent with numerous observations [3]. Three major issues that the gaseous-emission explanation fails to meet are as follows. (1) Gaseous emission in comets is known to be significantly weaker in red light (wavelength $\lambda \sim 0.7 \mu\text{m}$) compared to what it is in blue-green light ($\lambda \sim 0.5 \mu\text{m}$). However, the difference in P_{\max} appears nearly the same in both parts of the spectrum. (2) At least some comets with low P_{\max} were classified with confidence to be dust-rich comets. (3) Dramatic temporal variations of gaseous emission in the spectrum of a given comet do not correlate with polarization measured with continuum filters over the same time period. We refer the Reader to our work [3] where these observations are described in more details. However, taking into account these inconsistencies, we investigate the alternative explanation that suggests the difference in P_{\max} in comets results from differences in their dust.

MODELING LIGHT SCATTERING BY COMETARY DUST:

In general, there are three major factors affecting the light-scattering response from cometary dust: (1) Shape of dust particles, (2) their size distribution, and (3) their chemical composition that is described in terms of their complex refractive index m of constituent material. Modeling of light scattering by cometary dust requires adequate representation of their irregular shape. Evidently, it cannot be satisfactorily modeled with a single sphere or spheroid because light scattering by such targets reveals numerous odd features and hardly resembles what is measured in comets. Therefore, we use the model of the so-called *agglomerated debris particles* whose porosity and shape resemble what was found *in situ* in comets and in interplanetary dust particles (see discussion in [3]). On top in Fig. 1, we demonstrate ten samples of such particles; whereas, a detailed description of the algorithm for their generation can be found in [3].

Clearly, light scattering by irregularly shaped particles dramatically differs from that of spheres and spheroids. The same, however, does not hold when one type of highly irregular particle is compared to another type of highly irregular particle. In the later case, the light-scattering response tends to converge. In such circumstances, chemical composition and size distribution of model particles start playing significantly more important role compared to the true particle shape [4, 5]. This feature makes it possible to model polarization in comets using solely agglomerated debris particles. Nevertheless, this does not necessarily imply the same type of morphology in all cometary dust particles. Instead, it means that the true irregular morphology of dust particles is difficult to retrieve from their light-scattering response; whereas, chemical composition and size distribution produce a significant impact on polarization and, therefore, can be inferred from the observations [4, 5].

We compute light scattering by agglomerated debris particles using the discrete dipole approximation (DDA). DDA is a flexible numerical approach that places minimal restrictions on the morphology of the target particle [6]. We investigate 42 different refractive indices m that are representative for known and plausible species of comets in visible, such as water ice, Mg-rich silicates, Mg-Fe silicates, various types of organics, and amorphous carbon. At each refractive index m , we consider the particle radius r spanning the range from $0.08 \mu\text{m}$ up to $2.47 \mu\text{m}$ ($3.87 \mu\text{m}$ in case of water ice). The computations are repeated at two wavelengths, $\lambda = 0.4845 \mu\text{m}$ and $0.6939 \mu\text{m}$, that closely match central wavelengths of the blue continuum filter *BC* and the red continuum filter *RC* from the *International Halley Watch* (IHW) system of filters. Note, these filters are actively exploited in cometary study. It is worth noting that we perform an exhaustive averaging over particle shapes considering a minimum 500 examples of the agglomerated debris particles. Finally, we average the light-scattering response over the available particle radii r using the power law size distribution r^n . Such a size distribution has been detected *in situ* in comets with the power index n varying between 1.5 and 3 (e.g., [7]). Thus, our model is consistent with major *in situ* findings on micron-sized dust particles in comets.

RESULTS AND CONCLUSION:

We investigate the entire set of 42 refractive indices and found that none of them can reproduce the phase-angle dependence of polarization in comets with $P_{\text{max}} \geq 15\%$ by itself. A mixture of particles with at least two different refractive indices is required in order to fit observations of comets. One type of particles should consist of weakly absorbing material with imaginary part of refractive index $\text{Im}(m) \leq 0.01$. Such a constraint is consistent with Mg-rich silicates [8] that are detected *in situ* in comets [9]. $\text{Im}(m)$ in another type of material has to exceed 0.3, that corresponds to conductive materials. This is consistent with some types of organics [10] and amorphous carbon [11]; whereas, both materials have been also found in comets *in situ* [9].

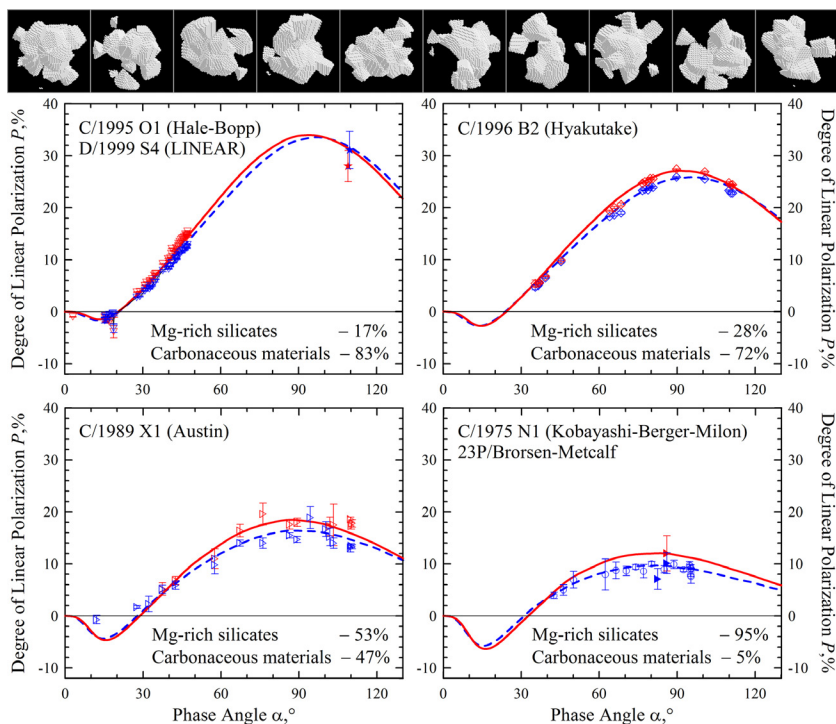


Fig. 1. Ten examples of agglomerated debris particles (top). Polarization P as a function phase angle α measured in comets with four different P_{max} (symbols) and modeling results (lines). Blue color corresponds to the measurements and modeling in blue-green light; whereas, red color – in red light.

It is significant that such a two-component mixture can satisfactorily reproduce the vast majority of polarimetric observations of comets. For instance, in Fig. 1, we demonstrate modeling results obtained with a mixture of agglomerated debris

particles with $m_1 = 1.6 + 0.01i$ and $m_2 = 1.855 + 0.45i$. Both types of particles are chosen to obey the same power-law size distribution with the index $n = 2.1$. As one can see in Fig. 1, this two-component mixture satisfactorily reproduces polarimetric responses measured with the red and the blue-green filters in four selected groups of comets. At that, the fit to each specific group of comets is obtained by varying solely the relative volume of weakly and highly absorbing particles (relative volume of each component is shown in the corresponding panels). On the contrary, when the volume ratio of weakly and highly absorbing particles is fixed to some value, solely varying the power index n cannot reproduce the entire set of observations. Thus, our modeling clearly suggests that the observed dispersion of P_{\max} in comets is caused predominantly by differences in chemical composition of their dust. At that, comets with low P_{\max} have greater abundance of Mg-rich silicates over organics and/or amorphous carbon. For more details on this research we refer the Reader to [3].

REFERENCES:

- [1] Chernova, G.P., et al. 1993, *Icarus*, 103, 144; [2] Levasseur-Regourd, A.C., et al. 1996, *A&A*, 313, 327; [3] Zubko, E., et al. 2016, *Planet. Space Sci.*, 123, 67; [4] Zubko, E., et al. 2013, *MNRAS*, 430, 1118; [5] Zubko, E., et al. 2015, *J. Quant. Spectrosc. Radiat. Transfer*, 150, 42; [6] Zubko, E., et al. 2010, *Appl. Opt.*, 49, 1267; [7] Mazets, E.P., et al. 1986, *Nature*, 321, 276; [8] Dorschner, J., et al. 1995, *A&A*, 300, 503; [9] Fomenkova, M.N., et al. 1992, *Science*, 258, 266; [10] Jenniskens, P. 1993, *A&A*, 274, 653; [11] Duley, W.W. 1984, *ApJ*, 287, 694.

CHEMICAL COMPOSITION OF THE SEMI-VOLATILE GRAINS OF COMET 67P/CHURYUMOV- GERASIMENKO

Peter Wurz¹, Kathrin Altwegg¹, Hans R. Balsiger¹, Jean-Jacques Berthelier⁵, André Bieler⁷, Ursina Calmonte¹, Johan De Keyser⁴, Bjoern Fiethe³, Stephen Fuselier⁸, Sébastien Gasc¹, Tamas I. Gombosi⁷, Annette Jäckel¹, Axel Korth², Lena Le Roy¹, Urs A. Mall², Henri Rème⁶, Martin Rubin¹, Chia-Yu Tzou¹, and ROSINA team

¹University of Bern, Bern, Switzerland

²Max Planck Institute for Solar System Research, Katlenburg-Lindau, Germany

³Technical University of Braunschweig, Braunschweig, Germany

⁴Belgian Institute for Space Aeronomy, Brussels, Belgium

⁵LATMOS Laboratoire Atmosphères, Milieux, Observations Spatiales, Paris Cedex 05, France

⁶IRAP, Toulouse, France, ⁷Univ of Michigan, Ann Arbor, MI, USA

⁸Southwest Research Inst., San Antonio, TX, USA

Contact: peter.wurz@space.unibe.ch

INTRODUCTION:

The European Space Agency's Rosetta spacecraft (Glassmeier et al., 2007) has been in orbit of the comet 67P/Churyumov-Gerasimenko (67P/C-G) since August 2014. On board is the Rosetta Orbiter Spectrometer for Ion and Neutral Analysis (ROSINA) instrument suite (Balsiger et al., 2007). ROSINA consists of two mass spectrometers, the Double Focusing Mass Spectrometer (DFMS) and the Reflectron-type Time-Of-Flight (RTOF) (Scherer et al., 2006), as well as the COmet Pressure Sensor (COPS). ROSINA is designed to detect and monitor the neutral gas and thermal plasma environment in the comet's coma by in situ investigation. The two mass spectrometers have high dynamic ranges and complement each other with high mass resolution (DFMS) and high time resolution and large mass range (RTOF). Especially the unprecedented sensitivity and mass resolution of DFMS together with the large mass range of RTOF allow determining precisely light species (e.g. isotopologues) as well as detecting heavy organic species. The pressure sensor COPS measures total gas densities, bulk velocities, and gas temperatures.

ROSINA has been collecting data on the composition of the coma and activity of comet from 3.5 AU to pericentre and out again to 3.5 AU. The Rosetta mission presents a unique opportunity to directly sample the parent species in the thin cometary atmosphere of a Kuiper-belt object at distances in excess of 2.5 AU from the Sun all the way to the pericentre of the cometary orbit at 1.24 AU. The ROSINA experiment continuously measures the chemical composition of the gases in the cometary coma. Occasionally, a dust grain from the comet enters the ion source of a ROSINA instrument where the volatile part evaporates since these ion sources are hot. We will report on the first measurements of the volatile inventory of such dust grains.

OBSERVATIONS:

Volatile release from cometary dust grains was observed with all three ROSINA instruments on several occasions. Because the volatile content of such a dust grain is completely evaporated in such an ion source after a few 100 seconds, the RTOF instrument is best suited for the investigation of its chemical composition since several complete mass spectra are recorded during this time. The rate of dust grains recorded in RTOF is small, and we report on the dust grains recorded on 11 November 2014 (1 grain), 28 March 2015 (2 grains), and 08 May 2015 (1 grain). It is estimated that these grains are of the order of 100 nm in size. We fitted the recorded mass spectra of RTOF with a set of 25 molecules, and their molecular fragments resulting from the ionisation. The major groups of chemical species are hydrocarbons, oxygenated hydrocarbons, nitrogen-bearing molecules, sulphur-bearing molecules, halogenated molecules and others (including water and CO₂). These grains are depleted in water compared to the comet, but the water content of these grains is of the order of 10%. Thus, these grains are not water-ice grains, but can be considered as semi-volatile dust grains.

The mineral phase of these grains, if there is any, cannot be investigated in these measurements. However, in an earlier investigation the bulk composition of mineral grains on the surface of the comet was inferred from solar wind sputtering of these grains (Wurz et al., 2015).

REFERENCES:

- H. Balsiger, K. Altwegg, P. Bochsler, P. Eberhardt, J. Fischer, S. Graf, A. Jäckel, E. Kopp, U. Langer, M. Mildner, J. Müller, T. Riesen, M. Rubin, S. Scherer, P. Wurz, S. Wüthrich, E. Arijs, S. Delanoie, J. De Keyser, E. Neefs, D. Nevejans, H. Rème, C. Aoustin, C. Mazelle, J.-L. Médale, J.A. Sauvaud, J.-J. Berthelier, J.-L. Bertaux, L. Duvet, J.-M. Illiano, S.A. Fuselier, A.G. Ghielmetti, T. Magoncelli, E.G. Shelley, A. Korth, K. Heerlein, H. Lauche, S. Livi, A. Loose, U. Mall, B. Wilken, F. Gliem, B. Fiethe, T.I. Gombosi, B. Block, G.R. Carignan, L.A. Fisk, J.H. Waite, D.T. Young, and H. Wollnik, *ROSINA - Rosetta Orbiter Spectrometer for Ion and Neutral Analysis*, Space Science Review 128 (2007), 745–801.
- K.-H. Glassmeier, H. Boehnhardt, D. Koschny, E. Kürt, and I. Richter, *The Rosetta Mission: Flying Towards the Origin of the Solar System*, Space Science Reviews 128 (2007), 1–21.
- S. Scherer, K. Altwegg, H. Balsiger, J. Fischer, A. Jäckel, A. Korth, M. Mildner, D. Piazza, H. Rème, and P. Wurz, *A novel principle for an ion mirror design in time-of-flight mass spectrometry*, Int. Jou. Mass Spectr. 251 (2006) 73–81.
- P. Wurz, M. Rubin, K. Altwegg, H. Balsiger, S. Gasc, A. Galli, A. Jäckel, L. Le Roy, U. Calmonte, C. Tzou, U.A. Mall, B. Fiethe, J. De Keyser, J.J. Berthelier, H. Rème, A. Bieler, V. Tenishev, T.I. Gombosi, and S.A. Fuselier, *Solar Wind Sputtering of Dust on the Surface of 67P/Churyumov-Gerasimenko*, Astron. Astrophys. 583, A22 (2015) 1–9, DOI: 10.1051/0004-6361/201525980.

THE MICROPHYSICAL PROPERTIES OF THE DUST PARTICLES ON 67P/CG NUCLEUS FROM THE MIRO DATA

Yu. Skorov, L. Rezac, P. Hartogh

Max Planck Institute for Solar System Research, Germany

Contact: skorov@mps.mpg.de

Both, the composition and also the microphysical structure of the dust grains emitted from the nucleus is one of the important open questions in understanding the comets. Since the Rosetta spacecraft arrived at the comet (Aug, 2014), a large number of dust particles emitted from the 67P nucleus have been gathered by the COSIMA instrument (Schulz et al. 2015). The image analysis of these grains indicates a rather complex structure: large agglomerates made up from smaller pieces, or agglomerates containing both, large and small tightly packed particles. Whether this complex structure is inherent in the nucleus dust (e.g. hierarchic structure of dust (Skorov & Blum 2012), or are the detected particles actually pieces (fragments) of the destroyed homogeneous porous dust layer remains is unknown. From the physical consideration of thermal and strength properties of nucleus dust layer made from the different grain characteristics are rather different.

Using the information on thermal inertia, and brightness temperature differences from the MIRO instrument (Schloerb et al 2015) we perform numerical experiments for different models of nucleus porous dust layer. The goals of the systematic numerical simulations are: 1) is it possible to select a preferred model of the surface dust layer structure based on MIRO data, 2) which observational conditions are best to address this question.

We consider a 1D heterogeneous two-layer model of nucleus, i.e. the “ice-free dust crust” is distinguished explicitly. The thickness of the crust is fixed and it is a free model parameter. The ice sublimation is included in the model. When an ice-free porous dust layer is present, the effective sublimation rate and the forward momentum of gas flow are dependent on the layer diffusive resistance. Because the characteristic times of a gas diffusion and a heat diffusion are much smaller than the variations of surface irradiation by the sun, the nucleus erosion is not included in the model. The boundary conditions on the nucleus surface and at the lower boundary of the dust layer the energy conservation. The sublimation rate is given following the Hertz-Knudsen formula. The porous surface layer reduces the effective gas flux from under it. The permeability of the ice-free porous dust layer is a function of the agglomerate radius and thickness of the dust layer. For the collisionless gas the mass flow through pore volume can be calculated via a modified Clausing formula (Skorov et al. 2011) or the experimental dependence presented in (Gundlach et al. 2015). An effective conductivity is calculated following (Gundlach & Blum 2012). In addition to the solid conductivity, the radiative conductivity as a part of the effective conductivity is considered in the model. This introduces temperature dependence to the effective conductivity and a relative increase of this value for the large dust particles. We assume that the solid conductivities of the dust crust and the ice-dust mixture are the same and that the material porosity is constant everywhere (similarly as in Skorov & Blum 2012).

REFERENCES:

- Gundlach et al. 2015, A&A, 583, A12.
- Gundlach & Blum. 2012, Icarus, 219, 618.
- Schloerb et al 2015, A&A, 583, A29.
- Schulz et al. 2015, Nature 518.
- Skorov & Blum 2012, Icarus, 221, 1.
- Skorov et al. 2011, , Icarus, 212, 867.

PINNACLES ON THE 67P/CHURYUMOV-GERASIMENKO COMET NUCLEUS

S.S. Krasilnikov^{1,2,3}, A.T. Basilevsky^{1,2,3}, U. Mall², Yu.V. Skorov^{2,4},
H.U. Keller⁴, S.F. Hviid⁵

¹Vernadsky Institute, RAS, Moscow, Russia

²Max Planck Institute for Solar System Research, Göttingen, Germany

³Moscow State University of Geodesy and Cartography, Moscow, Russia

⁴Institute of Geophysics and Extraterrestrial Physics, Braunschweig University of Technology, Braunschweig, Germany; ⁵Institute of Planetary Research, German Aerospace Center (DLR), Berlin, Germany

Contact: zergovski@geokhi.ru

INTRODUCTION:

In cometary studies, pinnacles, local promontories of varied shapes including spires with pointed tops and ranging in height from 10's m to >100 m were first described by [1] on the nucleus of the Wild 2 comet. Later they were reconsidered by [2] and [3]. The work [1] suggested that pinnacles could be erosional remnants created by loss of surrounding material, but other potential mechanisms of their formation were also mentioned, including erosion of mesas and erosion of impact ejecta blocks. They could also be cometary equivalents of hoodoos, upward-pointing spires sometimes seen in eroded volcanic ash. Hoodoo spires are erosion-resistant because they were fumarole conduits hardened by the hydrothermal process. Finally, some pinnacles might be ridges viewed edge-on. Works [2] and [3] agreed with suggestion on erosional origin of pinnacles, in particular by retreating cliffs and steep slopes of mesas. It was mentioned by [1] that if Wild 2 pinnacles are related to surface recession, then the magnitude of surface lost would be comparable to the pinnacle heights, i.e., 100 m or more. The Wild 2 pinnacles were marginally seen on the available images whose resolution was rather poor.

Pinnacles were not observed in the later rendezvous with nuclei of comets Borrelly, Tempel 1 and Hartley 2 probably because of not enough image resolutions. Interesting, that pinnacles were not reported in publications on analyses of the high-resolution images of 67P/Churyumov-Gerasimenko nucleus (e.g., [4] and [5]), probably because of great abundance of other interesting morphologies. Here we describe pinnacles seen on the surface of 67P comet nucleus (Figure 1) and consider potential implications of their presence and their characteristics.

MEASUREMENTS:

On the surface of 67P nucleus, pinnacles are well seen both in the OSIRIS [6] and NavCam [7] images (Figure 1). These images were used for primary identification of pinnacles. Then, we studied the identified pinnacles and searched for not identified in the OSIRIS and NavCam images, using the shape model SHAP4s [8], built by stereo-analysis of OSIRIS images. The model spatial resolution in most places of the nucleus is ~2 m and typical vertical accuracy is a few 10's cm. An example of the model image showing the pinnacle is presented in Figure 2. For the nucleus side, which before the perihelion was mostly in shadow, the model has the lower resolution. In this study we did not have a chance to thoroughly explore that area for the pinnacles presence and characteristics. However, in the new post-perihelion OSIRIS images of that side, a few pinnacles are clearly distinguished. After we identified pinnacles on the nucleus shape model, we compared the model images of pinnacles with what is seen in the OSIRIS NAC images (Figure 3). In the latter we could

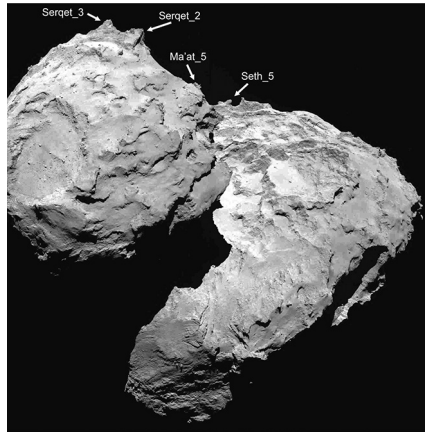


Fig. 1. Pinnacles seen on the limb of the 67P nucleus. Their names correspond to the names of regions where the given pinnacles are seen: e.g. Serget 3 is the third pinnacle identified in the Serget region. OSIRIS NAC image N20140816T195914556ID30F22.

understand if the identified in the shape model pinnacles are indeed pinnacles, and tried to suggest the nature of the pinnacle-forming material. For morphometric analysis of the considered pinnacles we used the SHAP4s shape model the shape model. For each of pinnacles were measured height from its foot and diameter near their foot. We used model `cg_spg_spc_shap4s_shap5_merged_528kgm3_ws.grav.vertex.slope_g_200k` to determine the tilt angle of the pinnacle apparent axis to local gravitational vertical (Figure 2).

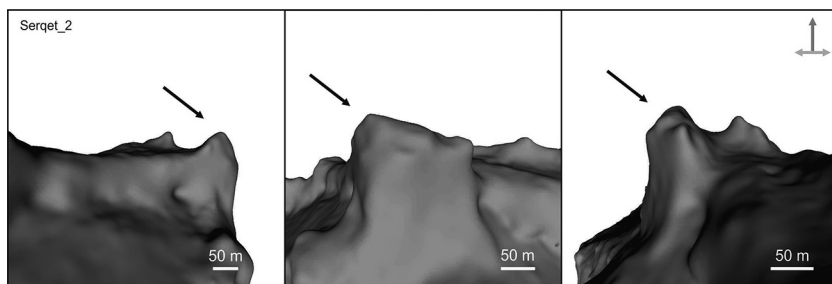


Fig. 2. The SHAP4s model 'in-profile' images of one of the considered pinnacles in three directions turning by 45°. Two arrows on the right image show the local gravitational vertical (blue arrow) and horizontal (green one). Inclined black arrows show the top of pinnacle Serqet_2.

RESULTS.

Total number of identified pinnacles on the surface of comet 67P is about 50. Most part of them have in the OSIRIS images show surfaces looking as if they were composed of the consolidated nucleus material of comet (Figure 3). They are observed both in regions with outcropped consolidated nucleus material and in areas having relatively flat surfaces probably covered by the so-called air-fall deposits [4].

Within the considered subpopulation of the pinnacles the mean value of heights (h) is 37 m, the maximum is 84 m, the minimum – 8 m. Transition of their feet to the surrounding terrain is usually gradual so it makes a problems to measure the diameter at the foot. When we made such not very accurate measurements we got the mean foot diameter (d) of 60 m. So preliminary estimate of h/d is 0,63. The slope angles in the most steep parts of the pinnacles vary from 62° to 90°. Mean tilt of pinnacle axes in relation to local horizontal plane is 79° with standard deviation 8°.

CONCLUSIONS.

If pinnacles on the comet 67P nucleus are erosional remnants created by loss of surrounding material this provides an estimate of minimal thickness of the lost material is 84 m. According to [9] the mean erosion rate for 67P nucleus is ~2 m per orbit. So for the current orbit to form pinnacles as high as 84 m it is necessary to suffer from the erosion during 42 orbits.

The reason for the significantly higher resistance of the pinnacle tops to erosion seems to be presence there of material more durable to sublimation. So the observed pinnacles suggest essential inhomogeneity of the nucleus material: inhomogeneity in density and/or in composition. The size scale of these hypothetical inhomogeneity seems to be tens of meters. In future work we plan to make more detailed morphometric analyses of pinnacles and more thorough consideration of the potential implications.

ACKNOWLEDGMENTS:

We acknowledge support of this study by MPI for Solar System Research, by Russian Science Foundation, project #14-22-00197 (KSS and BAT) as well as by Presidium of Russian Academy of Sciences, program no. 7 (KSS and BAT). We acknowledge ESA for providing the NavCam and OSIRIS images.

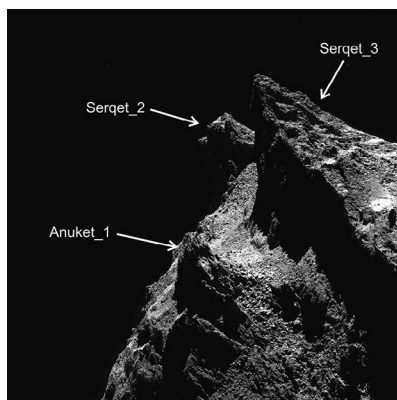


Fig. 3. Three pinnacles whose slopes are obviously composed of the consolidated material. OSIRIS NAC image N20141006T004850558ID30F22.

REFERENCES:

- [1] Brownlee D.E. et al., 2004. *Science* 304 (5678), 1764–1769. [2] Basilevsky A.T., Keller H.U. 2006. *Planet. Space Sci.* 54, No 8, 808-829. [3] Cheng A.F. et al., 2013. *Icarus* 222, 808–817. [4] Thomas N. and 58 coauthors, 2015. *Science* 347 (6220), aaa0440-1-6. [5] El-Maarry M.R. et al., 2015. *Astronomy & Astrophysics*. 583, A26. [6] Keller H.U. et al. 2007. *Space Sci. Rev.* 128: 433. [7] Geiger G. & Barthelemy M., 2015. ROSETTA ORBITER NAVCAM PRL-COM, RO-X-NAVCAM-2-PRL-COM-V1.0, ESA PSA, NASA PDS. [8] Preusker F. and 44 coauthors, 2015. *Astronomy & Astrophysics*. 583, A33. [9] Keller H.U. and 46 coauthors, 2015. *Astronomy & Astrophysics*. 583. A34.

GRAININESS OF THE MATERIAL OF THE COMET 67P NUCLEUS AS DEDUCED FROM ANALYSIS OF THE ROSETTA NAVCAM, OSIRIS AND ROLIS IMAGES

A.T. Basilevsky^{1,2}, U. Mall², H.U. Keller³, Yu.V. Skorov^{1,3}, S.F. Hviid⁴, S. Mottola⁴, S.S. Krasilnikov^{1,2}

¹Vernadsky Institute of Geochemistry & Analytical Chemistry, RAS, 119991 Moscow, Russia, atbas@geokhi.ru

²Max-Planck-Institute for Solar System Research, 37077 Göttingen, Germany

³Institute for Geophysics and Extraterrestrial Physics, TU Braunschweig, 38106, Braunschweig, Germany

⁴German Aerospace Center (DLR), Institute of Planetary Research, D 12489 Berlin, Germany

Contact: atbas@geokhi.ru

INTRODUCTION:

Two major types of the material are distinguished on the nucleus of the 67P/comet Churyumov-Gerasimenko: 1) the consolidated nucleus material and 2) the loose material covering the consolidated material in many places of the nucleus. In the NavCam [1], OSIRIS [2] and ROLLIS [3] images the consolidated material is seen in many areas of the nucleus. Its surface looks knobby, with individual knobs having dimensions ranging from a few centimeters to a few tens of meters. The knobby appearance of the surface seems to be due to inhomogeneity of the nucleus material, its graininess, with some parts more durable and less durable to surface erosion ("grains") of the scale of visible knobs. This graininess may have implications important for understanding of the comets' origin.

EXAMPLES OF THE KNOBBY TEXTURES:

Here we give several examples of the knobby surfaces of the consolidated nucleus material seen in its outcrops and in the made of it boulders (Figures 1 and 2). Below, in descriptions, several regions of the nucleus surface are mentioned. Their positions on the nucleus can be found in Figures 1 and 2 of [4].

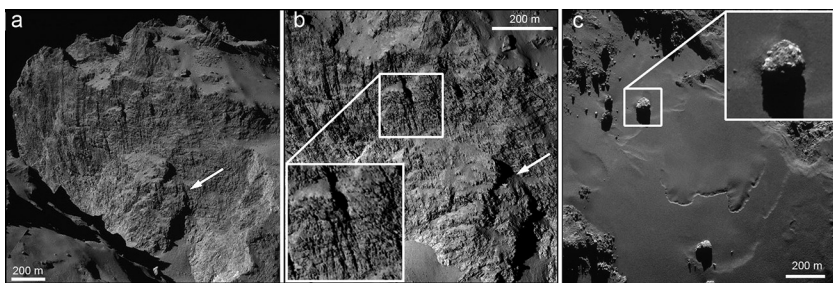


Fig. 1. a) and b) knobby texture seen on the surface of the Hathor cliff; c) knobby texture seen on the surface of ~50 m boulder Cheops in Imhotep region. NavCam image 20140920T182253, OSIRIS image N20140829T004254549ID30F22 and NavCam image 20141023T182255, correspondingly. White arrow indicates on potential landslide.

In Figure 1a is shown a surface of the Hathor cliff, close to vertical outcrop of the consolidated nucleus material [5], with dark-looking downslope lineaments and 400x400x150 m body of potential landslide [6]. It is seen that the cliff surface is covered with knobs having dimensions from several meters to a few tens of meters. As the image pixel scale in the displayed photo is about 2.5 m, the mentioned lower limit of the knob sizes is certainly not the actual limit, but a resolution dependent one. This suggestion is supported by what is seen in Figure 2b. This is a part of the OSIRIS image of the Hathor cliff, with 1 m/px resolution and numerous knobs of a few meters in diameter are observed here. Figure 1c shows an area in Imhotep region with several boulders on the smooth terrain. One of the boulders, provisionally named Cheops, is ~50 m across and shows, like other boulders of this area, the knobby surface with individual knobs of a few meters in diameter.

Figure 2 shows an outcrop of consolidated nucleus material in Apis region of the nucleus (Figure 2a) and Agilkia region where the Philae lander first time contacted with the nucleus surface [7] (Figures 2b and c). It is seen in Figure 2a that the surface of the consolidated nucleus material in the Apis region also has a knobby texture. In the OSIRIS image with the 0.18 m/px resolution knobs of a few meters in diameter, most between 1 and 3 m are seen. One can also notice that the knobby surface is fractured and outlines at least some knobs are controlled by the fractures. Figures 2b and c show the grained surface material whose compression strength was found to be very low [8]. The dominant feature seen here is a boulder of ~5 m in diameter with 0.3-1 m knobs and pits on its surface. Numerous boulders of 0.3-1 m in diameter are also seen, along with pre-dominating surface material whose texture is below the resolution limit (~5 cm). The knobs of the large boulder and the smaller individual boulders probably represent more durable components of the nucleus on the 0.3-1 m scale. Figure 2c shows the last before touchdown image with resolution of ~1 cm/px. The surface is dominantly granular with the smallest resolvable grains (particles) as small as a few centimeters. On the surface of the largest "particle" of ~1.5 m across near the image center of the image, knobs and pits of a few centimeters in size are seen. Their presence probably indicates a grainy character of the material and suggests that the dominating particles at a centimeter scale were the result of the "soft" destruction (via sublimation?) of the larger volumes of the nucleus material.

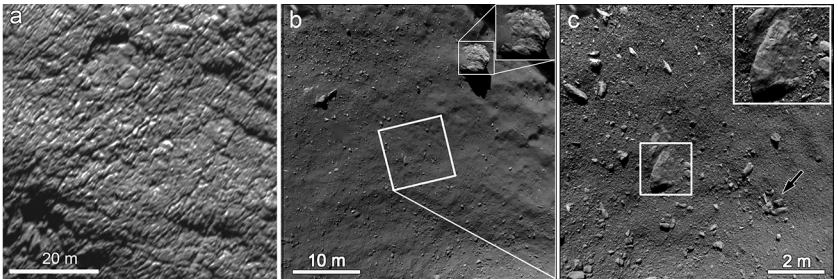


Fig. 2. a) knobby texture of the consolidated material in the Apis region; b) and c) knobby boulders seen in one before the last and the last images of the nucleus surface taken the ROLOS camera from the altitudes 39 m and 9 m above the surface. Part of OSIRIS NAC image N20150214T103553680ID30F84 and the ROLIS images, correspondingly.

There is also evidence on even finer granularity of the nucleus material: Bibring et al. [9] described images taken with the CIVA camera at the final point of the Philae landing cruise in the Abydos region. They stated that these images with a resolution of ~1 mm revealed a fractured surface with a complex structure and a variety of grain scales (down to several millimeters), possibly constituting pristine cometary material. Works [10] and [11] analyzing the OSIRIS images of this area concluded that Philae landed here on a primordial "rocky" terrain.

And finally, works [12] and [13] described fluffy aggregates of hundreds of microns in diameter captured by the Rosetta instrument COSIMA in the coma of 67P. These aggregates consist of individual particles with diameters of tens of microns, and probably represent the extension of the grainy character of the comet material into the micrometer size range.

DISCUSSION AND CONCLUSIONS:

The above consideration showed that the consolidated nucleus material of 67P comet is composed of a fractal-type agglomeration of "grains" of a broad size range, from tens of microns to millimeters, centimeters, meters and tens of meters. This phenomenon was also recently considered by [14]. These authors interpreted it as evidence for a cometary nucleus formation mechanism by *hierarchical agglomeration* and/or gravitational collapse of pebble-swarms formed by *streaming instabilities*. The mentioned pebbles are thought to be cm-sized porous aggregates initially formed in the 15-30 AU region of the Solar system ([14] and references therein). The mentioned above fluffy particles in the comet coma probably represent the building microblocks of these pebbles.

ACKNOWLEDGEMENTS:

We acknowledge ESA for providing the NavCam and OSIRIS images and supporting information (<http://imagearchives.esac.esa.int/>). This work was supported in part by Presidium of the Russian Academy of Sciences, program no. 7 (A.T. Basilevsky and S.S. Krasilnikov)

REFERENCES:

- [1] Geiger, G., Barthelemy, M., 2015. ROSETTA ORBITER NAVCAM PRL-COM, RO-X-NAVCAM-2-PRL-COM-V1.0, ESA PSA, NASA PDS; [2] Keller, H.U. and 66 coauthors, 2007. *Space Sci. Rev.* 128(1), 433-506; [3] Mottola, S., et al., 2007. *Space Sci. Rev.* 128, 241–255; [4] El-Maarry, M.R. and 53 coauthors, 2015. *Astronomy & Astrophysics*. 583, A26; [5] Thomas, N. and 58 coauthors, 2015. *Science*. 347 (6220), aaa0440-1-6; [6] Basilevsky A.T. et al., 2015. *Lunar & Planetary Science* 46. Abs. 1152. [7] Mottola, S. and 17 coauthors, 2015. *Science*. 349 (6247), aab0232-1 – 4; [8] Biele, J. and 32 coauthors, 2015. *Science* 349 (6247), aaa9816-1-6; [9] Bibring, J.-P. et al. 2015. *Science*. 349 (6247), aa0671-1-3. [10] Lamy, P. et al., 2015 EPSC Abstracts, Vol. 10, EPSC2015-783; [11] Lucchetti, A. and 47 coauthors, 2016. *Astronomy & Astrophysics*. 585, L1; [12] Schulz, R. and 24 coauthors, 2015. *Nature*. 518, 216-218; [13] Langevin, Y. et al. 2016. *Icarus*. 271, 76-97; [14] Davidson, B. and 47 coauthors, 2016. *Astronomy & Astrophysics*. (in press).

DOES REGIONAL SURFACE MORPHOLOGY OF COMETS 67P/CG AND 1P/HALLEY CARRY ANY TRACES OF THEIR ORIGIN IN LOW VELOCITY COLLISIONS?

L. Ksanfomality, L. Zelenyi

Space Research Institute of Russian Academy of Sciences (IKI RAS), 117997, 84/32 Profsoyuznaya str., Moscow, Russia

Contact: ksanf@iki.rssi.ru

Research of the 67P/CG nuclei properties and shape showed that part of the cometary nucleus may be a result of low-speed collisions of planetesimals. The hypothesis of the occurrence of the cometary nucleus as a result of collisions of planetesimals has long been known, but it is 67P/CG comet that gave it relevance. The report summarizes failure criteria and shows that in some cases the geometry of the cometary nucleus retains some information about the process of collision and allows you to find the momentum of the impactor.

ACKNOWLEDGEMENTS:

This work was supported by the Russian Foundation for Basic Research (the grant № 15-02-01989).

ROBERT FARQUHAR'S IDEAS FOR HUMAN EXPLORATION OF SPACE

D.W. Dunham, K. Stakkestad, N. Eismont, A. Ledkov, S. Aksenov, J. Kidd
KinetX Aerospace, USA
Contact: david.dunham@kinetx.com

In his doctoral dissertation, Robert Farquhar sketched out some plans for using libration points as transportation nodes for exploring the Moon and Mars. During the last years of the Apollo program, he developed his lunar exploration ideas. In 2011, we won a megagrant from the Russian Ministry of Education and Science to study "An International Program of Tasks for Human Exploration of the Solar System and for Planetary Defense". This invigorated Bob and me to further develop Bob's exploration ideas, with much help from workers and students at the Space Research Institute (IKI) and the Moscow Institute of Electronics and Mathematics (MIEM). We gave presentations and published papers about how an exploration infrastructure might be assembled in an Earth-Moon L2 (EM-L2) halo orbit, used to service space telescopes in Sun-Earth Lagrangian point orbits, and then explore, in turn, the Moon, near-Earth asteroids, Phobos, and Mars. In addition, ideas for planetary defense were studied, including placing a space telescope in a Sun-Earth L1 halo orbit to discover small asteroids approaching the Earth from the direction of the Sun (like Chelyabinsk), and using small asteroids (or asteroid boulders) with Earth Swingbys to deflect larger threatening asteroids. Some additional work to extend the exploration ideas was accomplished in 2014 and 2015, with presentations given at NASA Headquarters in April 2015 and June 2016. The latest work folds in some trajectory ideas from other studies performed at JPL and at Langley Research Center; these other studies used lunar distant retrograde orbits, as planned for the asteroid boulder to be returned by the Asteroid Redirect Mission (ARM), rather than an EM-L2 halo orbit. NASA wants to lead an international effort to send humans to Mars, preceded by a lunar exploration "proving ground", but the way this will really be undertaken is unknown, with some uncertainty in NASA's ARM mission funding that will be influenced by the winners of the November elections. But in any case, there will also be influence from Bob Farquhar's ideas that can help make this dream a reality.

ROBERT FARQUHAR'S IMPRESSIVE SPACE EXPLORATION LEGACY

D.W. Dunham

KinetX Aerospace, USA

Contact: david.dunham@kinetx.com

Robert Farquhar has left an impressive trail of accomplishments since he was born in 1932. After graduating from the University of Illinois with a BS in Aeronautical Engineering, he received a Masters in Engineering at UCLA in 1961, then his doctorate in Aeronautics and Astronautics at Stanford in 1969. At Stanford, he worked with John Breakwell to develop the first theoretical basis of "halo orbits" about the collinear libration points of the three-body problem. His doctoral thesis, "The Control and Use of Libration-Point Satellites", was published as a NASA Technical Report in 1970 for wider distribution. He showed how a satellite in a halo orbit about the Earth-Moon L2 libration point could be used as a communications link between the Earth and a farside landing. Although interest faded with the end of the Apollo program, his work laid the groundwork for other applications of libration-point orbits, especially for "post-Apollo" lunar exploration, work that is still in progress. In 1972, his interest shifted to comet flyby missions and a halo orbit about the Sun-Earth L1 point for the proposed ISEE-3 mission to study the solar wind before it reached the Earth's magnetosphere. Largely through his efforts, ISEE-3 became the first libration-point mission with its launch in 1978. But taking advantage of ISEE-3's high-energy orbit relative to the Earth, he realized a more ambitious goal, to use a complex series of lunar swingbys to send ISEE-3 to fly by Comet Giacobini-Zinner in 1985, the first comet mission. A byproduct was his discovery of the double-lunar swingby technique that was not only crucial to ISEE-3's success, but also used by other international missions that studied the Earth's geomagnetic environment. In 1989 - 1990, Bob was largely responsible for the establishment of NASA's "Discovery" program of lower-cost planetary exploration missions. The first-launched (in Feb. 1996) of these was the Near Earth Asteroid Rendezvous (NEAR) mission to (433) Eros; Bob envisioned its clever orbit and was the NEAR Mission Manager, directing its operations after launch. In 2000, it became the first spacecraft to orbit an asteroid, and the first asteroid lander a year later. Bob was the Mission Manager during the pre-launch and early operations of the MESSENGER mission, the 6th Discovery mission that launched in 2004 and in 2011, became the first spacecraft to orbit Mercury. Bob also was instrumental in establishing the first NASA "New Frontiers" medium-class planetary mission, called New Horizons that explored the Pluto system last year. As before, Bob played important roles for both the trajectory and the politics to help make the mission a success. So literally, Bob's legacy extends across the Solar System, from the nearest planet to the most distant planet explored so far. Bob lived to relish the successful New Horizons flyby of the Pluto system, but sadly, he passed away 3 months later, before all of the stunning Pluto/Charon images had been sent back to Earth. Bob's innovative trajectory designs have been used for many missions, and his ideas are bound to be applied to many missions in the future, some of which will be described later today in this session.

GRAZING ASTEROID OCCULTATION

A. Poro

International Occultation Timing Association in Middle East (IOTA/ME)

Contact: iotamiddleeast@yahoo.com

An asteroid occultation would occur when an asteroid is passing in front of a star and the apparent magnitude of the star would become lower for some seconds for the earth based observer.

“A grazing occultation of a star by an asteroid has been observed during just a few occasions. Almost every asteroid occultation features a single disappearance and reappearance at an individual observing station. But during a graze either one or more disappearances might be observed. The process of a grazing asteroid occultation is essentially identical to the lunar graze except that the surface of the asteroid is involved. If, for example, the asteroid occultation is predicted to last centrally 8 seconds, a grazing asteroid occultation at either edge could last 1 second or less. The most accurate proof is when video is taken although short blinks have occurred as seen by a visual observer. A grazing asteroid occultation is of greatest value in that it helps to determine quite accurately the actual limit of the occultation path and sheds light on asteroid topography. An example of a profile created after a successful asteroid occultation is in figure 1.

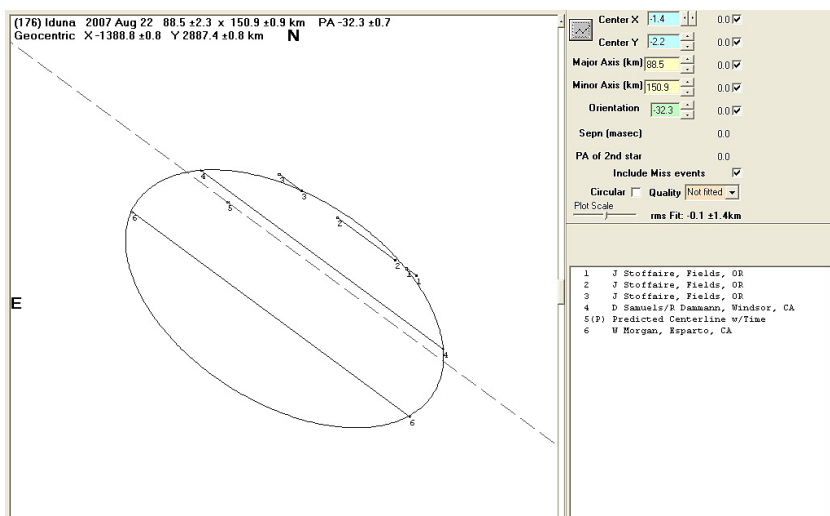


Fig. 1. The upper chord actually shows 3 disappearances and reappearances which reveal the irregular edge of the asteroid Iduna as recorded in August 22, 2007 by J. Stoffaire in Oregon, USA.”

Occultations are just one of the tools used to better understand asteroid physiology. They provide timings that equate to an instantaneous measurement of parts of an asteroid between the occulted star and the observer making the observation. If enough observations are compiled a two dimensional silhouette can be constructed at a specific location in the asteroid’s rotational light curve. Rotational mechanisms are discussed and their relation to modern day modeling of minor planets. Photometric light curves provide different information as do radar, direct observation by large telescopes or spacecraft. All of these methods are needed to provide additive solutions to develop the maximum amount of information on these distant bodies. Those asteroids passing closest to Earth offer a separate challenge. Observing asteroid occultations is now a well known part of astronomy. One of the challenges involved in this process lies in the fact that asteroids rotate about an axis which has two poles. The larger the asteroids, the slower they rotate. However, for smaller objects the rotation rate can be much faster.

Grazing asteroid occultation can have different causes than surface of asteroids. In this presentation will be talking about a new model about the cause of this event. This model is based on a survey asteroid rotated. And to examine the question posed by the rotation of the asteroids can be effective or not?

THE BREAKTHROUGH INITIATIVES – THE SEARCH FOR LIFE IN THE UNIVERSE AND MANKIND’S FIRST INTERSTELLAR VOYAGE

S.P. Worden

*Breakthrough Prize Foundation, NASA Research Park, Bldg 18, Moffett Field,
CA 94035, USA*

Contact: pete@breakthroughprize.org

On April 12, 2016 – the 55th anniversary of Yuri Gagarin’s historic flight Yuri Milner and Stephen Hawking announced at the One World Observatory in New York Breakthrough StarShot.

The objective of the Breakthrough Starshot Project is to send many lightweight spacecraft to a neighboring star system. Our initial candidate system is Alpha Centauri, 4.3 light years from Earth, and to return pictures of planets found there. The goal of Starshot is for the flight of the spacecraft to take ~20 years. With the recent discovery of an earth-size planet in the habitable zone of the Sun’s nearest stellar neighbor Proxima Centauri, it too is a target. The average speed of the spacecraft is then approximately 20% the speed of light. The concept is to use radiation pressure from an ultra high power laser installed on the Earth to quickly accelerate the spacecraft consisting of a highly reflective and low absorbing meter class sail attached to the Starchip. After achieving a speed of 0.2 c, the spacecraft is then in a coast mode (except for possibly minor course corrections from a very small on board thruster) for the remainder of its journey.

The star chip is less than one cm square and prototypes have been built on silicon nitride and have a 16-bit processor, 1 GB RAM, a one-watt burst mode laser communications downlink to earth, four 10 mW laser thrusters for mid-course corrections, four 2 mega pixel cameras, and other housekeeping items. The starchip is powered by a radioactive-decay battery embedded in the 500-micron thick silicon nitride substrate. The vision is to launch hundreds or even thousands of these from a very high orbiting mothership.

Recent technological developments are the genesis of the Starshot Project. The two principal developments are (1) the possibility of building ultra-light-weight sails and spacecraft on a chip and (2) the possibility of building ultra-high power lasers. Even so, the requirements are extremely challenging. To reach 0.2 c with a total spacecraft mass of only 1 gram and a sail optimized for speed, the average irradiance on the sail (just over 4 meters in size) is 6 GW/m² and must be maintained for 76 seconds out to a range of 2x10⁹ meters (5 times the distance to the Moon) assuming the laser has a 1 km aperture has a total power output of 100 GW and is nearly 100% efficient in compensating for atmospheric turbulence. The sail must survive the laser’s incident power density, ride the beam in a stable configuration and live through the journey to serve as an antenna for directing the downlink laser communications signals back to Earth.

The timeline for this project includes 5-10 years of R&D, beginning with \$100M of funding. Following a successful research program a prototype system costing between \$500M - \$1B is planned in the 10-15 year timeframe. Demonstration of the fastest human propelled objects within 6 years and launching interstellar starships in the 2035-40 timeframe, arrival at Alpha-Centauri and Proxima Centauri around 2060 and getting first data by 2065. This project is targeted for a total cost comparable to the largest international science experiments such as the CERN Large Hadron Collider from both public and private funding sources.

A MISSION TO THE SOLAR GRAVITY LENS FOCUS

L.D. Friedman , V. Turyshev , D. Garber
The planetary society, USA
Contact: louisdfriedman@gmail.com

The Solar Gravity Lens Focus (SGLF) is a line beginning 547 AU from the Sun extending outward toward infinity. It is the locus of points where a light from a distant object is focused after being bent by the Sun's gravity. The geometry and properties of the SGLF is given in a companion paper. In our case the distant object is an exo-planet identified a priori as being potentially Earth-like and possibly habitable. A mission to the SGLF is of high value and interest because (i) it would permit high-resolution imaging of an exo-planet to less than one kilometer resolution and (ii) it is in an unexplored region of the interstellar medium on a pathway out of our solar system. The high-resolution imaging there might be the only way to permit remote observation of habitability on another world and to provide an aspirational target for interstellar flight. The technology required to reach 547+AU from the Sun is also the precursor of the technologies that might someday permit interstellar flight.

Reaching the SGLF with a reasonable flight time (e.g. 20-30 years) is an enormously high challenge. This mission would go five times the distance of Voyager (the only spacecraft sent from Earth to reach the interstellar medium) in perhaps two-thirds the time, i.e. with a speed of 6-9 times that of Voyager. The only way we can conceive accomplishing this mission (at affordable cost) is with nano-spacecraft propelled by lightsails which have the capability of flying within 0.2 AU of the Sun to pick up the necessary speed to escape the solar system at approximately 20-25 AU/year (100-130 km/sec).

A parametric study of fast solar system exit trajectories for various nano-spacecraft masses, solar sail size and properties and solar perihelion distance will be presented. System requirements for spacecraft control, maneuverability, power, and communications will be discussed. Mission requirements for flying along the focal line to permit imaging in the SGLF will also be cited. This mission is challenging, but feasible with technology we have in hand today. Although it would extend humankind's outreach in space five-fold and into the pure interstellar medium, it still would reach only 0.4% of the distance to the nearest star. Nonetheless, we will show that the technologies required for the SGLF mission are the critical ones that may make interstellar flight feasible in the future. In fact, it will be shown that a SGLF mission is a critical milestone in a roadmap leading the interstellar Starshot fight now the subject of a privately funded study by the Breakthrough Prize Foundation.

References

1. Pasadena, CA, USA
2. Jet Propulsion Laboratory, Calif. Institute of Technology, Pasadena CA, USA
3. NXTRAC, Redondo Beach CA, USA
4. Submitted to the Seventh Moscow Solar System Symposium (7M-S3), 10-14 October 2016
5. Turyshev, et. al., Direct Multipixel Imaging of an exo-Earth with a Solar Gravitational Lens Mission, this Symposium.

DIRECT MULTIPIXEL IMAGING OF AN EXO-EARTH WITH A SOLAR GRAVITATIONAL LENS TELESCOPE

V.G. Turyshev¹, L. Friedman², M. Shao¹

*¹Jet Propulsion Laboratory, California Institute of Technology
4800 Oak Grove Drive, Pasadena, CA 91009 USA*

²www.louisdfriedman.com

Contact: turyshev@jpl.nasa.gov

Nature has presented us with a very powerful “instrument” that we have yet to explore and learn to use. This instrument is the Solar Gravitational Lens (SGL), which results from the ability of the gravity field of the Sun to focus light from faint, distant targets. In the near future, a modest telescope could operate on the focal line of the SGL and, using the enormous magnification power of the Lens, could provide high-resolution images and spectroscopy of a habitable exoplanet. We discuss the imaging properties of the SGL, when the image occupies many pixels in the region near the optical axis. We discuss a mission to the SGL focal region that could provide us with direct, multi-pixel, high-resolution images and spectroscopy of a potentially habitable Earth-like exoplanet. Based on our initial studies, we find that such a mission could produce (1,000×1,000) pixels images of “Earth 2.0” at distances up to 30pc with spatial resolution of ~10 km on its surface, enough to see its surface features. We address some aspects of mission design and spacecraft requirements, as well as capabilities needed to fly this mission in the next two decades.

ON THE STABILITY OF NANOCRAFT ORIENTATION WHILE ILLUMINATED BY INTENSE LASER BEAM

H. Popova^{1,2}, M. Efendiyev³, I. Gabitov⁴

¹*Skobeltsyn Institute of Nuclear Physics, Lomonosov Moscow State University, GSP-1, Leninskie Gory, Moscow, 119991, Russian Federation*

²*The Schmidt Institute of Physics of the Earth of the Russian Academy of Sciences (IPE RAS), Bolshaya Gruzinskaya str., 10-1, Moscow 123242, Russia*

³*Helmholtz Zentrum München Deutsches Forschungszentrum für Gesundheit und Umwelt (GmbH) Institute of Computational Biology Ingolstädter Landstr. 1 85764 Neuherberg, Germany*

⁴*Skoltech Center for Photonics and Quantum Materials, Center for Photonics and Quantum Materials, Building 3, Moscow, 143026, Russian Federation*
Contact: popovaelp@mail.ru

Breakthrough Starshot is engineering program aiming to demonstrate proof of concept for light-propelled nanocrafts. These could fly at 20 percent of light speed and capture images of possible planets and other scientific data in our nearest star system, Alpha Centauri, just over 20 years after their launch.

In this project nanocrafts are gram-scale robotic spacecrafts comprising two main parts: StarChip and Lightsail. The StarChip is gram-scale wafer, carrying cameras, photon thrusters, power supply, navigation and communication equipment, and constituting a fully functional space probe. The Lightsail is made of increasingly thin (no more than a few hundred atoms thick) and light-weight (gram-scale mass) metamaterial.

To achieve goal of the project it is necessary to solve a lot of complex scientific and engineering problems. One of these tasks is investigation stability nanocraft orientation in intense laser beam which should accelerate it up 60,000 km/s during 2 minutes.

We considered a problem of stability nanocraft orientation while illuminated by intense laser beam. In our model the nanocraft driven by intense laser beam pressure acting on its lightsail is sensitive to the torques and lateral forces reacting on surface of sail. This forces influence the orientation and lateral displacement of spacecraft. We consider stability of its position inside laser illuminated column.

The assumptions in choosing the model: 1. flat or concave (part of the sphere, conical) circular sail; 2. configuration of nanocraft is treated as solid body (applicability of Euler equations); 3. mirror reflection of laser beam from surface of the lightsail.

We discussed how sail shape and profile of the laser beam (Gaussian or flat) can affect stability of nanocraft position. We also discussed the effect of nanocraft rotation around the axis along which it is moving on the stability.

PAT-M RADIOMETER ONBOARD THE EXOMARS-2020 LANDER. CALIBRATION PROCEDURE AND POSSIBILITY OF MARTIAN ATMOSPHERE TEMPERATURE MEASUREMENTS DURING A DUST STORM

D.P. Skulachev

Space Research Institute of Russian Academy of Sciences (IKI RAS), 117997, 84/32 Profsoyuznaya str., Moscow, Russia

Contact: dskulach@mx.iki.rssi.ru

A temperature measurement of Martian regolith is one of tasks for scientific instrument set onboard the ExoMars-2020 lander. The measurement is planned to perform by microwave radiometer PAT-M. The PAT-M is a classic Dicke type radiometer with two inputs. The radiometer output is proportional to a difference between inputs power.

Two horn antennas are connected to PAT-M radiometer inputs, make it possible to perform a non-contact measurements. One antenna is pointed down to the Martian surface and other antenna is pointed upward. In this way the radiometer output is proportional to the difference between the radio-brightness temperature of the Martian regolith below and the radio-brightness temperature of the sky overhead. The Martian atmosphere is very transparent at microwaves when there is no dust storm. In this case, the radio-brightness temperature of the sky is close to the CMB temperature of 2.75 K. Point radio sources on the sky have low contributions because of rather wide antenna beam (about 50 degrees of arc). The PAT-M radiometer may works at three different frequencies that makes it possible to measure the regolith temperature at three different depths.

The upward pointed antenna has well-defined signal and is used as a calibration source for the PAT-M radiometer. To put the radiometer in calibration mode it is necessary to disconnect the radiometer first input from down pointed antenna and connect it to a source with well-known radio-brightness temperature. In RAT-M radiometer a well-matched microwave load is used for this purpose. Physical temperature of the load is measuring with high accuracy by the help of platinum resistive sensor. It is important to calibrate the radiometer when the Martian atmosphere is clear from a dust.

The PAT-M radiometer may be used not only as a regolith thermometer. If the radiometer is pre-calibrated in Martian dustless atmosphere and is standing in calibration mode, it may measure a radio-brightness temperature of the atmosphere in the case of a dust storm. The radiometer may works at three different frequencies and it is possible to measure the dust temperature at three different heights above the surface. Preliminary calculations show that the maximum height available for the measurement is about fifty kilometers.

GAS-ANALYTICAL CHROMATOGRAPHY SYSTEM FOR MISSION “EXOMARS 2020”

S.A. Aseev, M.V. Gerasimov, M.A. Zaitsev

Space Research Institute of Russian Academy of Sciences (IKI RAS),

117997, 84/32 Profsoyuznaya str., Moscow, Russia

Contact: Ser.aseev@iki.rssi.ru

In 2020 the Roscosmos together with the ESA will launch a lander and descent module to the Mars. This mission include the rover “PASTEUR” and a stationary platform on which various scientific equipment is located. A stationary platform includes a complex, consisting of a gas chromatograph (GCM) with a mass spectrometer (MS). The GCM instrument is manufactured at IKI and the MS - in China. The GC-M instrument is developed in collaboration of IKI with LATMOS (France). The main scientific objective of the GAM is a quantitative analysis of the content of Xe and Kr in the atmosphere of Mars.

In preparation for the mission, different scientific experiments were made to optimize an adsorption properties of the gas chromatograph system, to be able to store gases like Xe and Kr, because a percentages of them are too small. It is supposed to pump through the gas chromatograph system large amounts of Martian atmosphere (about 20 litres). In this system different adsorption storages will be located at various temperatures, successive passage through which should ensure the success of the experiment. Thus, one adsorption trap is used to separate carbon dioxide, water and sulfur-containing substances, a second for separating of Xe and Kr from the remaining gas mixture, and the last one - directly to the accumulation of Xe and Kr. Estimated adsorbents - Carbosieve SII, Carbosieve SII and Molsieve 5A.

According to the results of experiments we plan to clarify the content in the atmosphere of N₂, Ar, Xe, Cr, CO₂, CO and Ne. Also we would like to observe a daily and seasonal variations in water content and other trace constituents of the atmosphere in the surface layer, as well as the measurement of isotopic ratios of the main volatile elements: D/H, ¹⁷O/¹⁶O, ¹⁸O/¹⁶O, ¹³C/¹²C, ³⁴S/³²S, ³⁷Cl/³⁵Cl, isotopes of noble gases.

MARS EXPRESS OMEGA AND HRSC: DATASETS CRUCIAL FOR MMX PLANNING, SITE SELECTION AND OPERATIONS

T. Duxbury¹, J.-P. Bibring², R. Jaumann³,
J. Oberst³, B. Gondet², N. Seregina¹

¹George Mason University, Fairfax, Virginia, USA

²Institut d'Astrophysique Spatiale IAS, Orsay, France,

German Aerospace Center DLR, Berlin, Germany

³German Aerospace Center DLR, Berlin, Germany

Contact: tduxbury@gmu.edu

The JAXA Martian Moon Exploration (MMX) mission (ISAS, 2016) to launch in 2022 will rendezvous, land, obtain samples and then return these samples from Phobos to Earth. Crucial to the planning, landing site selection and mission operations are the knowledge of the surface characteristics, including topography and mineralogy/composition, and the position of the landing site in inertial space over time. The ESA Mars Express mission (MEX) has been performing a global exploration of Phobos for over 12 years and is carrying two instruments that provide crucial data needed for the successful completion of the MMX mission: the visible and infrared mineralogical mapping spectrometer (OMEGA) and the High Resolution Stereo Camera (HRSC) / Super Resolution Channel (SRC). MEX is unique in that it has had tens of Phobos flybys within 2,000 km and many as close as 50 km, providing the highest existing spatial resolution of global multispectral surface coverage under a wide range of viewing and lighting geometries. The HRSC / SRC cameras have yielded a high spatial resolution global digital terrain model (DTM) giving the size, shape and inertial orientation of the Phobos surface with detailed local topography. HRSC / SRC have also provided a full color global digital image model (DIM) and astrometric data to continually improve the orbit of Phobos. OMEGA has produced a high spatial resolution global visual and infrared multispectral dataset that can provide the mineralogy / composition of the surface needed for landing site selection. Together the OMEGA and HRSC/SRC data provide crucial data needed by the JAXA MMX mission for its successful mission planning, landing site selection and mission operation. MEX is still operational and continues to build upon the existing global datasets where many more close Phobos flybys will occur before the MMX landing. The Special Phobos Issue of Planetary and Space Science (2014) gives excellent details of the MEX mission and the scientific results from this mission that continue to increase.

REFERENCES:

«ISASニュース 2016.1 No.418» (PDF) (in Japanese). Institute of Space and Astronautical Science. 22 January 2016. Retrieved 2016-02-04.

Oberst, J., Zakharov, A. and Schulz, R., Phobos, Planetary and Space Science, Special Issue, 102, 2014.

TECTONIC HISTORY OF ENCELADUS'S SOUTH POLAR TERRAIN AND ITS TIES TO THE FORMATION OF THE TIGER STRIPE FRACTURES

C.A. Denton^{1,2}, H.M. Gonnermann¹, A. Lenardic¹.

¹Rice University, Houston TX, 77005, USA

²Brown University, Providence, RI, 02912, USA

Contact: Camille_denton@brown.edu

INTRODUCTION

Enceladus, a small, icy moon of Saturn, is an object of scientific scrutiny due to the enormous cryovolcanic eruptions originating from its South Pole. These eruptions occur at massive fractures known as the tiger stripes, which are localized in the heavily deformed South Polar Terrain (SPT) [1]. While Cassini has confirmed that the material being ejected is a combination of water vapor, micrometer-size water ice particles, and traces of sodium salts, the fundamental question of what drives deformation of the ice shell and produces these eruptions remains largely unanswered [2].

As a possible history for the formation of the tiger stripes, we present a conceptual model considering brittle deformation of the SPT through isostasy and gravity-driven flow in an ice shell that is not at equilibrium. We show that the current topographic gradient in the SPT cannot drive deformation, and suggest that a previous thermal anomaly could have caused thinning of the paleo-SPT and failure of the highlands, creating the tiger stripes, which remain active today via an unknown mechanism

GEOLOGIC BACKGROUND

The South Polar Terrain (SPT) remains mysterious in many ways – the conspicuous absence of impact craters implies that it is relatively youthful compared to the rest of the satellite, and may be only several million years old [3]. The SPT itself is a topographic low, approximately 500 to 1500 m below the surrounding highlands. Topographic profiles across the SPT show that the large-scale ridges and troughs that dominate the surface in regions outside the tiger stripe fractures are asymmetrical with respect to the tiger stripes and vary in spacing as well as height from the Leading Edge to the Trailing Edge Margin relative to Saturn [4].

Most previous work on the tiger stripes attributes their formation to tensile cracking as a result of extension of the SPT via mechanisms ranging from some sort of thermal anomaly [5], stress-induced tidal flexing [3], true polar wander [6], nonsynchronous rotation of the ice shell (provided the putative ocean is global) [7], or rifting through unspecified methods [8]. Further investigation has shown that tidal heating itself, a popular hypothesis, does not produce enough energy to match the amount of heat as measured by Cassini being released at the SPT, suggesting that several mechanisms may be operating in conjunction to produce the tiger stripes [9]. The Cassini ISS instrument determined that the SPT is a relatively warm area, with heat (170 K) centered along the axes of the tiger stripes while the surrounding highlands are much colder (80 K), indicating that the heat of the SPT is localized and not diffuse [10]. We investigate the consequences of a conceptual model that takes the asymmetrical topography of the SPT and the surrounding terrain into effect [11].

HYPOTHESIS

The formation of the tiger stripes in their current location – that is, in a large basin such as the SPT and surrounded by highlands – is not a coincidence; the tiger stripes are not disconnected from the environment in which they formed. Assuming that the highlands are isostatically compensated, the topographic gradient between the highlands and the SPT provides stresses that could have produced deformation and faulting in the ice shell, which manifests at the surface as the tiger stripes.

NUMERICAL MODEL

To test whether the measured topographic gradient could provide large enough stresses, we calculated the differential stress in the ice shell as a function of depth for the possible elevations of the highlands (based on the range given in the topographic profiles). The differential stress is determined by solving for the differences in cryostatic pressure between the highlands and the SPT and

comparing it to the brittle strength of ice, which increases linearly with depth based on terrestrial data [12].

RESULTS.

For the maximum possible value of the topography the resulting stress approaches but does not cross the lower threshold for ice strength in the ice shell. Therefore, it is likely that contemporary conditions do not drive deformation in the present ice sheet. However, Cassini data does not show current motion in the SPT outside of the eruptions from the TSF [11], and thus we do not expect that the ice shell would be experiencing deformation or collapse from the highlands in the present epoch.

We propose that the SPT as it currently exists could be in a state of post-collapse due to a prior, more extreme topographic difference that initiated failure. There is no way to constrain paleo-elevation in the South Polar Terrain or on Enceladus as a whole due to lack of data [3]. It is entirely possible that the topography in the South Pole could have had different morphology at some time in the past. Considering this new direction, we then calculated the minimum value for the highlands topography necessary to pass the threshold of tensile ice strength (2.50 km), and found it to be reasonable.

REVISED CONCEPTUAL MODEL

Taking into account these new possibilities, we can construct a new model for the development of the SPT. To increase the elevation difference between the highlands and the basin, we propose that a prior occurrence, such as a thermal anomaly, warmed the ice in the SPT at some earlier time, lowering the viscosity and increasing the pressure gradient by allowing the ice to deform and thin, increasing the height difference.

Assuming isostasy, thinning the SPT generates a response in the highlands – as the SPT thins, a corresponding elevation increase occurs in the highlands, increasing the topographic difference between them. If that elevation increase of the highlands pushes them above the calculated threshold of 2.50 km, the stress difference passes the threshold, inducing extension, failure, and normal faulting in the ice sheet. The suggested temporal sequence is shown in Figure 1.

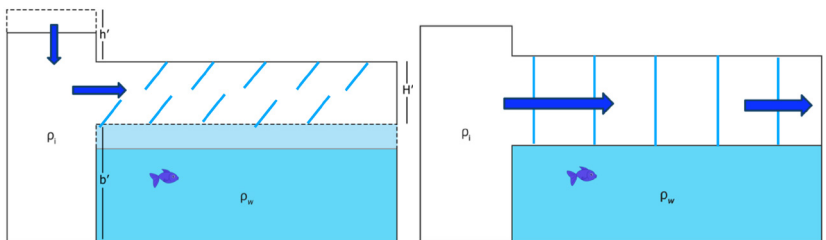


Fig. 1. A: Thinning of the SPT to a thickness H' leads to an increase in elevation of the highlands to an elevation h' . B: If h' is high enough, the differential stress crosses the strength threshold, causing collapse of the highlands to their current elevation and extension in the SPT that creates the tiger stripes.

CONSEQUENCES

Overall, the temporal sequence proposed here is a theory for inducing deformation through topographical means, while accounting for the present SPT in the context of its more tectonically active past. If this proposed temporal sequence occurred, then the subsequent extension would have caused normal faulting that could be seen by Cassini. In fact, features examined via photo-geologic surveys catalogue structures that have been interpreted as normal faults and directional indicators for extension, though more thorough investigation and better data is needed to confirm these features [8]. This theory also requires the presence of a thermal anomaly, whose origin remains to be explained in full.

REFERENCES:

- [1] Porco C.C. (2006) *Science* 311, 1393-1401. [2] Postberg F. (2009) *Nature* 459, 1098-1101. [3] O'Neill and Nimmo (2010) *Nature Geo.* 3. [4] Schenk and McKinnon (2009) *GRL* 36, 16. [5] Gioia et al (2007) *Proc. Natl. Acad. Sci USA*, 104. [6] Matsuyama and Nimmo (2008) *Icarus* 195, 459-473. [7] Patthoff and Kattenhorn (2011) *GRL* 38. [8] Walker et al. (2012) *JGR Planets* 117. [9] Spencer and Nimmo (2013) *Ann. Rev. EPS* 41, 693-717. [10] Crow-Willard and Pappalardo (2015) *JGR* 120, 928-950. [11] Yin and Pappalardo (2015) *Icarus* 260, 409-439. [12] Sammons and Thompson (2007) *Roy. Soc.*

INVESTIGATION OF POSSIBILITY OF USING MELTING PROBES FOR EXPLORATION OF ICY SATELLITES

A.E. Butenko^{1,2}, S.A. Aksenov^{2,1},

¹Space Research Institute of Russian Academy of Sciences (IKI RAS),
117997, 84/32 Profsoyuznaya str., Moscow, Russia

²Moscow state institute of electronics and mathematics NRU HSE,

Tallinskaya 34, Moscow, Russia

Contact: ostelite@gmail.com

INTRODUCTION:

Nowadays investigation of icy satellites is of great interest. They are covered with layer of ice planetary bodies: Enceladus, moon of Saturn and Europa and Ganymede, moons of Jupiter. It's believed that the internal liquid ocean exists beneath the ice, so these icy moons are the most likely places in the Solar system for detection of extraterrestrial life. The thickness of ice crust is estimated from a few hundreds of meters to tens of kilometers. One of the possibilities to investigate the ocean is to penetrate the ice by melting probe. This is device that penetrates the ice by melting and gravity force. This study consider mathematical model of melting probe's movement that allows estimating velocity of penetration and energy consumption.

MATHEMATICAL MODEL

The problem of penetration through the thick layer of ice in outer space has a lot of requirements. Melting probe is supposed to be the most suitable device for space missions due to the small weight, reliability, simplicity and absence of ice contamination comparable to other known techniques e.g. drilling. The approach presented in this study is based on mathematical and computer simulation of the probe's movement. The model can be used in order to optimize the parameters of the probe in meaning of velocity maximization, minimizing energy consumption etc.

Due to the simple energy balance, penetration velocity of cryobot with power can be expressed as:

$$v = \frac{P}{S\rho(c\Delta u + l)}$$

where S is cross section area.

his relationship of energy balance neglects all losses first of all lateral energy dissipation and can be considered as upper estimation of velocity. If we consider cylindrical coordinate system attached to cryobot that moves with constant speed, the temperature field around it will be stationary and depended on the speed. With boundary conditions the model will be:

$$D(T, v) = 0$$

$$u(M) = u^*, \quad M \in \Omega$$

$$\lim_{\rho(M, O) \rightarrow \infty} u(M) = u^0$$

$$R \left(\iint_{\Omega} |\vec{q}| ds, v \right) = 0$$

Where S is cryobot's surface, D - modified heat conduction equation, u^0 is known function, u^* is initial ice temperature and l is temperature of phase change.

The problem can be solved numerically as an iterative sequence of boundary problems for modified heat conduction equation that converges to lookup velocity value (Fig. 1). For all the simulations done absence of liquid phase is supposed due to ice sublimation under space conditions.

RESULTS OF SIMULATION

Four types of cryobot's tips are considered: conical, flat, parabolic and round (Fig. 2). Simulation performed showed increasing influence of shape and lateral energy dissipation with colder ice. With power 500W that seems to be reasonable value for space mission penetration velocity varies in range 28-36 cm/h (Fig. 3).

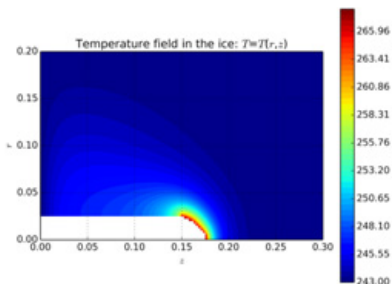


Fig. 1. Temperature field in the ice

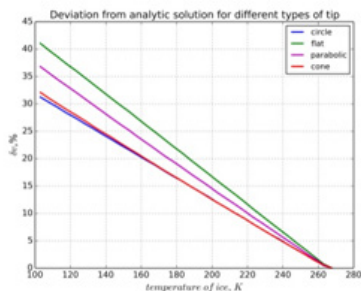


Fig. 2. Deviation from analytical solution for different types of tip

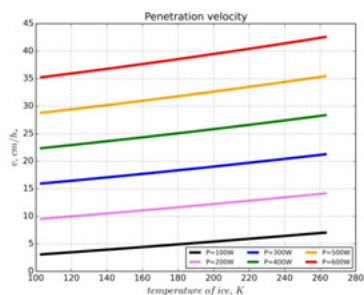


Fig. 3. Penetration velocity

CONCLUSIONS

Simulation performed showed increasing influence of shape and lateral energy dissipation with colder ice that is natural for extraterrestrial conditions. The dependence of penetration velocity on ice temperature tends to be linear for considered power supply.

THE DEVELOPMENT OF REFLECTIVE OPTICAL SYSTEMS BASED ON NANOCOMPOSITE STRUCTURES FOR SPACE RESEARCH

N.G. Chechenin, S.A. Sharakin, P.A. Klimov, M.I. Panasyuk

Lomonosov Moscow State University, Skobeltsyn Institute of Nuclear Physics, Leninskie gory 1(2), Moscow, Russia

Contact: pavel.klimov@gmail.com

In the last years new direction of space exploration – nanosatellites is actively developing. One of the main requirements for the payload of these satellites is the minimum weight at acceptable functional parameters. SINP MSU together with organizations of ROSCOSMOS is developing the technology of telescope production on the basis of new materials and structures - nanocomposites (NC). So, for a series of space experiments it has been developed a technology for production of large-size, light-weight reflective optical systems using a three-layer construction with an aluminum honeycomb core and skins of carbon layers [1-3]. One of the most difficult issues for manufacturing of such optical elements is to improve the quality of the optical reflecting surface which is significantly dependent on the design features of a mirror and carbon tissue structure at different scales [4]. With the purpose of improvement of the optical properties currently SINP MSU attempts to develop reflective surfaces on the basis of polymer composites (PMC), reinforced with carbon nanotubes (CNTs). The use of such NC allows to obtain mirror structure with a lower mass in comparison with many other materials.

The development is based on the existing experience in the SINP MSU for CNTs synthesis by different methods [5-7], the synthesis of CNT-PMC [8, 9], and study the properties of CNTs themselves [10] and the functional properties of CNT- PMC [8, 9]. Besides the quality of the reflecting surface of the mirror, the characteristics of the construction and its resistance to influence of negative factors of space environment are very important. The use of CNT-PMC gives the necessary electrical conductivity [8], thermal conductivity [9], which provides the necessary stability of the focusing properties of the reflecting surface.

REFERENCES:

1. Sergey A. Sharakin, Boris A. Khrenov, Pavel A. Klimov, Mikhail I. Panasyuk, Sergey A. Potanin, and Ivan V. Yashin. Mirror-concentrator for space telescope with wide field of view and "high" angular resolution for observation of ultrahigh energy cosmic rays and other atmospheric flashes. In **Proceedings of the SPIE**, volume 8443 of **Space Telescopes and Instrumentation 2012: Ultraviolet to Gamma Ray**, 2012.
2. A. Grinyuk, M. Slunecka, A. Tkachenko, L. Tkachev, P. Klimov, S. Sharakin, The method and results of measurement of the optical parameters of the UHECR detector for the TUS space experiment, *Nuclear Instruments and Methods in Physics Research A* 763 (2014) 604–609, DOI: 10.1016/j.nima.2014.06.019.
3. L. Tkachev, S. Biktemerova, G. Garipov, A. Grinyuk, V. Grebenyuk, B. Khrenov, P. Klimov, D. Naumov, S. Porokhovoy, B. Sabirov, O. Saprykin, M. Slunecka, A. Tkachenko, I. Yashin The optical system of the TUS space experiment *Nuclear Physics B - Proceedings Supplements*, Volume 196, December 2009, Pages 243-246.
4. Sharakin S.A., Optical system of a wide field of view orbital telescope for transient atmospheric processes measurements, International conference Manned Exploration of Space: abstract book, – Moscow: 2016. p. 59, (in Russian)
5. A. V. Makunin, N. G. Chechenin, A. A. Serdyukov, K. E. Bachurin, and E. A. Vorob'eva, Technological Characteristics of the Processes of Carbon Nanostructure Production by the Methods of Plasma Arc and Gas Pyrolytic Deposition, *Inorganic Materials: Applied Research*, 2011, Vol. 2, No. 3, pp. 252–255.
6. N.G. Chechenin, K.E. Bachurin, A.V. Makunin, E.A. Vorobyeva, P.N. Chernykh. Influence of microstructure of catalytic surface on growth of carbon nanotube by method of pyrolytic gaseous phase deposition. //Physics and chemistry of material treatment. 2012, №6, p.69-73 (in Russian).
7. N.G. Chechenin, A.A. Serdyukov, N.B. Akimov. Mesoscopic carbon structures, obtained by the method of plasma-arc-discharge deposition with pure carbon and with a catalyst usage. *Physics and chemistry of material treatment*. 2013, №3, p.18-25
8. N.G. Chechenin, P.N. Chernykh, E.A. Vorobyeva, O.S. Timofeev, *Synthesis and electroconductivity of epoxy/aligned CNTs composites*, *Appl. Surf. Sci.* (2013) том 275, с. 217-221
9. E. A. Vorobyeva, I. V. Makarenko, A. V. Makunin, V. A. Trifonov, and N. G. Chechenin. On the Synthesis and Thermal Conductivity of Nanocomposites with Multiwalled Carbon Nanotubes. *Journal of Surface Investigation. X-ray, Synchrotron and Neutron Techniques*. 2015, Vol. 9, No. 4, pp. 784–788
10. N. G. Chechenin, P. N. Chernykh, E. A. Vorobyeva, M. V. Dutka, D. I. Vainshtein, and J. Th. M. De Hosson. Structure Phases of Fe Nanoparticles in Vertically Aligned Multi-Walled Carbon Nanotubes. *Journal of Surface Investigation. X-ray, Synchrotron and Neutron Techniques*, 2015, Vol. 9, No. 5, pp. 1044–1055.

ACTIVE REMOTE SENSING OF PLANETARY ATMOSPHERES AND SURFACES

M.I. Mishchenko

NASA Goddard Institute for Space Studies, 2880 Broadway, New York, NY 10025, USA

Contact: michael.i.mishchenko@nasa.gov

Accurate aerosol and cloud retrievals from space remain quite challenging and typically involve solving a severely ill-posed inverse scattering problem. In this talk, we formulate in general terms an aerosol and aerosol–cloud interaction space mission concept intended to provide detailed horizontal and vertical profiles of aerosol physical characteristics as well as identify mutually induced changes in the properties of aerosols and clouds. We argue that a natural and feasible way of addressing the ill-posedness of the inverse scattering problem while having an exquisite vertical-profiling capability is to fly a multi-static (including bistatic) lidar system. We analyze theoretically the capabilities of a formation-flying constellation of a primary satellite equipped with a conventional monostatic (backscattering) lidar and one or more additional platforms each hosting a receiver of the scattered laser light. If successfully implemented, this concept would combine the measurement capabilities of a passive multi-angle multi-spectral polarimeter with the vertical profiling capability of a lidar; address the ill-posedness of the inverse problem caused by the highly limited information content of monostatic lidar measurements; address the ill-posedness of the inverse problem caused by vertical integration and surface reflection in passive photopolarimetric measurements; help relax polarization accuracy requirements; eliminate the need for exquisite radiative-transfer modeling of the atmosphere–surface system in data analyses; yield the day-and-night observation capability; provide direct characterization of ground-level aerosols as atmospheric pollutants; and yield direct measurements of polarized bidirectional surface reflectance. We demonstrate, in particular, that supplementing the conventional backscattering lidar with just one additional receiver flown in formation at a scattering angle close to 170° can dramatically increase the information content of the measurements. Although the specific subject of this talk is the multistatic lidar concept, all our conclusions equally apply to a multistatic radar system intended to study from space the global distribution of cloud and precipitation characteristics.

RADIATION MONITOR BASED ON DIAMOND DETECTORS FOR LONG-TERM SPACE MISSIONS

K.V. Zakharchenko¹, E.V. Gladchenkov¹, A.Yu. Istratov¹, A.F. Kaperko¹, V.A. Kolyubin¹, V.P. Kulagin¹, R.I. Kurochkin¹, S.A. Lvov², A.V. Mitenkin³, P.G. Nedosekin¹

¹Moscow Institute of Electronics and Mathematics, National Research University "Higher School of Economics", 123458, Moscow, Tallinskaya street, 34, Russia

²ITC "UralAlmazInvest", 121108, Moscow, Ivana Franko street, 4, Russia

³RPC "Mikropribor", 121108, Moscow, Ivana Franko street, 4, Russia.

Contact: nanophys@mail.ru

INTRODUCTION:

On-board equipment for new long-term space missions encounters stringent requirements to the radiation hardness. Conventional radiation defense is unable to meet these requirements especially in the space beyond the Earth radiation belts. Therefore different methods including the switching from active state to low-power-consumption state under influence of radiation streams are proposed to provide necessary lifetime of the on-board equipment. Use of such methods requires continuous radiation monitoring to identify and to predict the rise of radiation fluxes to dangerous levels. Obviously, the monitor must be much more radiation hard than the on-board equipment. Also it should resist high and low temperature, should have low power consumption and be compact etc. It is a monitor based on diamond detectors that meets all these requirements [1, 2].

The monitor is to identify electrons, protons and heavy ions in the vicinity of the spaceship. Also it should determine whether the level of the radiation rises to dangerous one. To fulfill the requirements of small size and low power consumption the monitor provides just a primary information about radiation fluxes that is processed by the external specialized computing apparatus.

In this work the structure of new radiation monitor based on the diamond detectors is described. The results of theoretical and experimental investigations of the monitor are presented.

THE STRUCTURE AND THE MODE OF OPERATION OF THE RADIATION MONITOR:

The structure of the radiation monitor is shown at the Figure 1. The monitor contains four main units: the unit of the radiation sensors (URS), the unit of the amplifying the analogous signal (UAA), the unit of primary digital processing (UPP) and the unit of the deconvolution of cosmic radiation spectra (UDR).

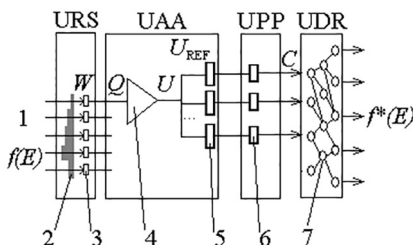


Fig. 1. The structure of the radiation monitor. The designations: $f(E)$ – the energy spectrum of cosmic radiation (1); (2) – selective filters; W – the energy transferred to the diamond detector (3); Q – the output charge of the diamond detector (3); U – the output voltage of the charge selective amplifier (4); U_{REF} – the reference voltage of the comparison device (5); C – the count rate of the particle counter (6); $f^*(E)$ – the energy spectrum restored by the artificial neural network (7).

Ionizing particles pass the selective filters and enter the diamond detectors of URS where electron-hole pairs are produced. The total number of the pairs is proportional to the energy transferred from the ionizing particle to the diamond. It is a not-monotonic function of the particle energy so using of the selective filters of different thickness shifts the maximum of the transferred energy dependence on the particle energy.

The output charge of the URS is converted to the voltage by the charge-sensitive amplifier of the UAA. The output voltage is then fed to the comparison device where the amplitude discrimination is carried out. The output of UAA unit is either logical zero or logical unit that is fed to the UPP. The particle counters are realized in the UPP unit. Their counts are the numbers of the particles having enough energy to pass the selective filters and transferring to the diamond plate enough energy to exceed the threshold of the corresponding comparison device. The UPP output signal is the set of the counts of particle counters. This set is processed in UDR using the artificial neural network. The output of the neural network is the set of the fluxes in the specified energy ranges.

THE MODEL OF THE RADIATION MONITOR:

The model describes the transformation of the input signal (the energy spectra of the cosmic radiation) to the output signal of the monitor (the set of the counts of particle counters).

The input signal of the URS unit is the set of electrons, protons and ions energy spectra. The output of the URS is the distribution of the charges passed the output contacts of five diamond detectors. The transformation of the information in the URS unit includes the transportation of the ionizing particles to the diamond detectors, the transfer of the energy from ionizing particles to the diamond sensitive element and the drift of the excited carriers produced by the radiation through the diamond plate to the output contacts. The distribution of the output charge Q passed the output contacts of the diamond detector $I(Q)$ is described by the expression (1):

$$I(Q) = \int f(E) \int g(E, W) \cdot h\left(Q, \frac{W}{W_0}\right) dW dE, \quad (1)$$

where $f(E)$ is the energy distribution of the ionizing particles; $g(E, W)$ is the distribution of the energy W transferred to the diamond depending on initial energy E of the ionizing particle obtained using Geant4 toolkit [3]; $h(Q, N_{e-h})$ is the distribution of the output charge Q depending on the initial number of electron-hole pairs N_{e-h} ; W_0 is the average excitation energy of one electron-hole pair by the ionizing particle, $W_0 = 13.2$ eV [1].

The UAA unit converts the charge to the voltage and further performs the amplitude discrimination of the signals. In the framework of the model the output of the unit is the Heaviside function depending on the signal amplitude and the reference voltage of the comparison device. So the probability P of the logical unit in the output of the comparison device is given by the formula (2):

$$P = \int I(Q) \cdot \eta(K \cdot Q - U_{REF}) dQ, \quad (2)$$

where η is the Heaviside function, K [V/C] is the conversion coefficient of the charge to the voltage and U_{REF} is the reference voltage of the comparison device. To obtain the count rate of the particle counters of UPP unit the probability P should be multiplied by the external output of the radiation source.

In the frameworks of the model the different spectra of cosmic radiation have been treated. The count rates of the particle counters have been obtained. The results show that the analysis of the count rates allows to restore of the cosmic radiation spectra. The UDR unit uses the artificial neural network for the solution of the spectra deconvolution problem. The accuracy of the spectra deconvolution better than 10% has been achieved.

EXPERIMENTAL INVESTIGATIONS OF THE RADIATION MONITOR:

The aim of experimental investigations of the radiation monitor was the validation of its mathematical model. The radiation monitor has been investigated under action of the alpha and beta radiation of standard sources using ^{239}Pu and ^{90}Sr : ^{90}Y isotopes. The sources have been placed at different distances from the diamond detectors. As for alpha radiation the selective filters have been removed during the experiment to allow alpha-particles to reach the diamond detectors.

The count rates of the particle counters have been obtained experimentally and have been computed using the model of the radiation monitor. The accuracy of the modelling was better than 8%. The restoration of the beta radiation spectrum has been carried out using the neural network. The training of the neural network has been conducted using the results of the modelling and a part of the experimental data. The accuracy of the beta spectrum restoration was better than 6%.

CONCLUSIONS:

The radiation monitor based on the diamond detectors for long-term space missions has been constructed and investigated. The monitor has been demonstrated experimentally to be suitable for ionizing particles registration. The mathematical model of the monitor has been developed. The artificial neural network trained using the results of modelling provides the deconvolution of the cosmic radiation spectra with the accuracy better than 10%. Experimental investigations of the monitor have been revealed that the accuracy of the monitor output modelling is better than 8 % and the accuracy of the restoration of the beta radiation spectra using the artificial neural network is better than 6%. So the radiation monitor is perspective for using in long-term space missions.

ACKNOWLEDGMENTS:

This work has been conducted with financial support of the Russian Federation represented by the Ministry of Education and Science of the Russian Federation (unique identifier RFMEFI 60514X0001).

REFERENCES:

- [1] Berdermann E., Pomorski M., Boer W. et al. Diamond detectors for hadron physics research // *Diam. Relat. Mater.* 2010. № 19. P. 358–367.
- [2] Kadilin V., Kolyubin V., Lvov S. et al. Diamond Techniques Prospects in Detecting Charged Cosmic Ray Particles // *Nuclear Physics and Engineering.* – 2014. – V. 5, №2. – pp. 138–144.
- [3] Geant4: A toolkit for the simulation of the passage of particles through matter. <http://geant4.web.cern.ch/geant4/>.

DUST ANALYZER DEVELOPING FOR RUSSIAN LUNAR LANDER MISSION

A.V. Zakharov¹, G.G. Dolnikov¹, I.A. Kuznetsov¹, V.V. Afonin¹, A.N. Lyash¹, E. Seran², M. Godefroy², S.L.G. Hess³, F. Cipriani⁴, V.N. Barke¹, I.A. Shashkova¹, A.V. Yakovlev¹, A.A. Venkstern¹, O.F. Petrov⁵, E.A. Lisin⁵, S.I. Popel¹, N.D. Borisov⁶, S.A. Bednyakov¹, N.S. Duxbury⁷

¹*Space Research Institute of Russian Academy of Sciences (IKI RAS), 117997, 84/32 Profsoyuznaya str., Moscow, Russia*

²*Laboratoire Atmospheres, Milieux, Observations Spatiales, Paris, France*

³*French Aerosp. Lab., ONERA, Toulouse, France*

⁴*ESTEC/TEC-EES, Noordwijk, The Netherlands*

⁵*Joint Institute for High Temperatures of the RAS, Moscow, Russia*

⁶*Institute of Earth magnetism, ionosphere and radiowaves propagation named after Nikolay Pushkov of the Russian Academy of Sciences (IZMIRAN), Troitsk, Russia*

⁷*George Mason University, Fairfax, VA, USA*

Contact: zakharov@iki.rssi.ru

One of the complicating factors of the future robotic and human lunar landing missions is the influence of the dust. Meteorites bombardment has accompanied by shock-explosive phenomena, disintegration and mix of the lunar soil in depth and on area simultaneously. As a consequence, the lunar soil has undergone melting, physical and chemical transformations.

Recently we have the some reemergence for interest of Moon investigation. The prospects in current century declare USA, China, India, and European Union. In Russia also prepare two missions: Luna-Glob and Luna-Resource. Not last part of investigation of Moon surface is reviewing the dust condition near the ground of landers. Studying the properties of lunar dust is important both for scientific purposes to investigation the lunar exosphere component and for the technical safety of lunar robotic and manned missions.

The absence of an atmosphere on the Moon's surface is leading to greater compaction and sintering. Properties of regolith and dust particles (density, temperature, composition, etc.) as well as near-surface lunar exosphere depend on solar activity, lunar local time and position of the Moon relative to the Earth's magnetotail. Upper layers of regolith are an insulator, which is charging as a result of solar UV radiation and the constant bombardment of charged particles, creates a charge distribution on the surface of the moon: positive on the illuminated side and negative on the night side. Charge distribution depends on the local lunar time, latitude and the electrical properties of the regolith (the presence of water in the regolith can influence the local distribution of charge).

On the day side of Moon near surface layer there exists possibility formation dusty plasma system. Altitude of levitation is depending from size of dust particle and Moon latitude. The distribution dust particle by size and altitude has estimated with taking into account photoelectrons, electrons and ions of solar wind, solar emission. Dust analyzer instrument PmL for future Russian lander missions intends for investigation the dynamics of dusty plasma near lunar surface. PmL consists of three parts: Impact Sensor and two Electric Field Sensors.

Dust Experiment goals are:

- 1) Impact sensor to investigate the dynamics of dust particles near the lunar surface (speed, charge, mass, vectors of a fluxes)
 - a) high speed micrometeorites
 - b) secondary particles after micrometeorites soil bombardment
 - c) levitating dust particles due to electrostatic fields. PmL instrument will measure dust particle impulses. In laboratory tests we used: min impulse so as 7·10⁻¹¹ N·s, by SiO₂ dust particles, 20-40 m with velocity about 0,5-2,5 m/s, dispersion 0.3; max impulse was 10⁻⁶ N·s with possibility increased it by particles Pb-Sn 0,7 mm with velocity 1 m/c, dispersion 0.3. Also Impact Sensor will measure the charge of dust particle as far as 10⁻¹⁵ C (1000 electrons). In case the charge and impulse of a dust particle are measured we can obtain velocity and mass of them.
- 2) Electric field Sensor will measure the value and dynamics of the electric fields near the lunar surface. Two Electric Field Sensors both are measured the concentration and temperature of charged particles (electrons, ions, dust particles). Uncertainty of measurements is 10%. Electric Field Sensors contain of Langmuir probes. Using Langmuir probes near the surface through the lunar day and night we can obtain the energy spectra photoelectrons in various periods of time.

PmL instrument is developing, working out and manufacturing in IKI. Simultaneously with the PmL dust instrument to study lunar dust it would be very important to use an onboard TV system adjusted for imaging physical properties of dust on the lunar surface (adhesion, albedo, porosity, etc), and to collect dust particles samples from the lunar surface to return these samples to the Earth for measure a number of physic-chemical properties of the lunar dust, e.g. a quantum yield of photoemission, which is very important for modeling physical processes in the lunar exosphere.

ON UNUSUAL PROPERTIES OF THE KIC 8462852 SATELLITES (KEPLER MISSION HERITAGE)

L.Ksanfomality, A.Tavrov

*Space Research Institute of Russian Academy of Sciences (IKI RAS),
117997, 84/32 Profsoyuznaya str., Moscow, Russia
Contact: leksanf@gmail.com*

Properties of the KIC 8462852 object or its exoplanets found in the KEPLER mission remain unexplained. It is shown that the assumptions about the nature of the object, as a swarm of cometary bodies, debris of a catastrophic asteroids collision, or exoplanet KIC 8462852b, encountered serious difficulties, and even contradict to the of Kepler's laws, if the eclipsing object considered as a physical body orbiting the central star. Hypothetical orbit of the KIC 8462852b does not meet the Dyson sphere hypothesis by captured energy and other requirements, too. We consider requirements to the obscuring object mass. Materials of the article (Boyajian et al., 2016) and subsequent publications have been used.

ORBITAL STELLAR STEREOSCOPIC OBSERVATORY PROJECT: MOTIVATIONS AND AUTONOMOUS NAVIGATION IN THE HELIOCENTRIC TRANSFER AND OPERATIONAL ORBITS

M.S. Chubey¹, V.V. Koupryanov¹, V.N. L'vov¹, S.D. Tsekmeister¹,
A.G. Tlatov¹, A.V. Bakholdin², S.V. Markelov³, G.V. Levko⁴

¹Central (Pulkovo) Astronomical Observatory, St. Petersburg, Russia

²Informational Technology, Mechanics and Optics University,
St. Petersburg, Russia

³Special Astrophysical Observatory of Russian Academy of Sciences,
Nizhnij Arkhyz, Russia

⁴Television Research Institute, St. Petersburg, Russia

Contact: mschubey@gmail.com

INTRODUCTION:

Orbital Stellar Stereoscopic Observatory (OStSO) project was born in 2007 as a "stellar" variant of Interplanetary Solar Stereoscopic Observatory [1]; as of now, Phase A of the OSSO project development is complete. A short description of the proposed scientific program has been outlined in [2, 3]. Spatial configuration of OStSO is formed by two identically equipped spacecrafts (SCs) in the vicinities of Lagrangian libration centers in the "Sun — Earth+Moon" system, Fig.1.

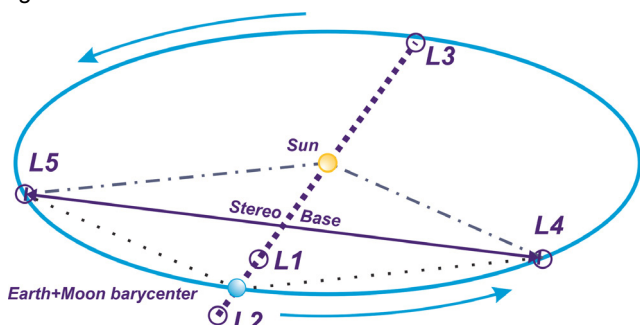


Fig.1. Space Crafts of OStSO are designing to be installed into Lagrangian points L4 and L5.

The time of insertion into these points is about 1.2 years. Requirements on the accuracy of initial conditions for the operational orbits and for the subsequent continuous operations control are rather hard. They can be satisfied by autonomous navigation using high-accuracy stellar sensors during the whole OStSO lifetime, involving the nearest Solar system objects with well-established orbits as a reference. The small solar heliograph as a solar sensor and an instrument for a number of solar research programs is also designed. According to our modeling, the accuracy of insertion of both SCs into their operational orbits by means of controlling the Hohmann transfer orbit parameters is 100 km. However, a continuous radio link between each SC and the ground-based mission control center allows us to calibrate the operational orbits with the accuracy that is by approximately 2 orders of magnitudes higher.

Stellar sensors and solar heliographs are also utilized in the pointing system of the astrophotographs during the main scientific mission.

Scientific program of the mission has been linked to study of the very Solar system (celestial mechanics, precise astrometry and photometry, Asteroid-Comet Hazard problem). Board equipment is designed for wide visual diapason observations to solve the stellar astronomy and selected astrophysical problems.

REFERENCES

- [1] Grigoriev V. M., et al. Interplanetary Solar Stereoscopic Observatory. // J. Opt. Technol. 2006, **73**, pp. 251–255.
- [2] Chubey, M. S. The Project "OStSO" // Space and Rocket Technology, 1(80) 2015, 138–147 (in Russian)
- [3] M. S. Chubey et al., Baltic Astronomy 24, 84 (2015)

LONG-TERM O₂ NIGHTGLOW OBSERVATIONS ON MARS BY SPICAM/MEX

A.A. Fedorova¹, F. Lefèvre², S.A. Guslyakova¹, F. Montmessin²,
D. Churbanov³, O.I. Korablev¹, J.-L. Bertaux²

¹Space Research Institute of Russian Academy of Sciences (IKI RAS)
Profsoyuznaya Str, Moscow, Russia, 117997

²LATMOS du CNRS/IPSL, Guyancourt, France

³MIPT, Dolgoprudnyi, Russia

Contact: fedorova@iki.rssi.ru

The oxygen nightglow is a sensitive tracer of the thermospheric circulation. In contrast to the O₂($\lambda^1\Delta_g$) dayglow that results from the ozone photodissociation on Mars, the O₂($\lambda^1\Delta_g$) nightglow is a product of the recombination of O atoms formed by CO₂ photolysis on the dayside at altitudes higher than 80 km and transported on the night side poles through the meridional circulation of Hadley cell. The first direct observation of the night-side emission were provided at limb geometry by the OMEGA spectrometer on the *Mars-Express* orbiter in 2010 (3 vertical profiles have been detected) [1] and confirmed and studied later by CRISM on *Mars-Reconnaissance-Orbiter* [2] and SPICAM on *Mars-Express* [3]. The first detections indicate that the emission is about two orders of magnitude less intense than the dayglow. All observations related to Southern and Northern poles at polar night.

Since 2010 the SPICAM IR AOTF spectrometer [4] began continuous monitoring of the O₂ nightglow in Mars' polar regions. In 2010-2016 the spectrometer provided ~300 limb observations on the night side and ~1500 stellar occultations in IR. More than 550 resulting vertical profiles of the oxygen nightglow have been obtained in both hemispheres for several Martian years.

As the emission is a result of atomic oxygen recombination in descending branch of the Hadley cell, it should be strongly sensitive to a transport of these atoms to the polar region of Mars. In this connection a comparison of the received profiles with the three-dimensional general circulation model of Mars (with photochemistry) is important [5]. The GCM calculations have been made for the same latitude, longitude, local time and Ls as in SPICAM observations. Figure presents seasonal variations of the vertically integrated emission rate in comparison with the LMD GCM. The total emission varies in SPICAM observations from 0.1 to 0.7 MR with averaged value of 0.3 MR. The emission does not show prominent interannual variations. The model also predicts that the meridional circulation is more vigorous during northern autumn and winter than during corresponding southern seasons as was also reported in [2]. But the GCM values exceed the observed emission in 2 times in the Southern hemisphere and in 1.5-4 times in the Northern hemisphere. The main disagreement relates to Ls=240-320° where the GCM emission is in 4-5 times higher the observed one near the North Pole.

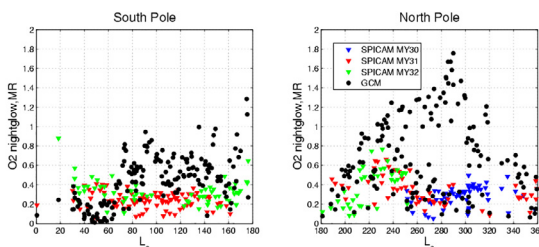


Fig. 1. Seasonal variations of the O₂ nightglow for the North (right) and the South (left) poles for 3 Martian years (30-32) in latitude bin: 65°-90°. The black circles are the corresponding GCM results.

ACKNOWLEDGMENTS:

We acknowledge the RFBR grant №15-02-07812 a for financial support.

REFERENCES:

- [1] Bertaux, J. L., et al. (2012), *J. Geophys. Res.*, 117, E00J04;
- [2] Clancy, R. T., et al. (2012), *J. Geophys. Res.*, 117, E00J10;
- [3] Fedorova, A.A. et al. (2012), *Icarus*, Volume 219, Issue 2, p. 596-608;
- [4] Korablev, O. et al. (2006), *J. Geophys. Res.*, 111, E09S03;
- [5] Lefèvre F. et al. (2004), *J. Geophys. Res.* 109. E07004;

CRYOLOGICAL MAPPING OF MARS

E.A. Grishakina

Lomonosov Moscow State University, Moscow, Russia
Institute of geochemistry and analytical chemistry V.I. Vernadsky (GEOKHI)
RAS, Moscow, Russia
 Contact: orskatya@mail.ru

On Mars, as on Earth, cryolithogenesis is widespread, what makes comparing of cryological conditions and their mapping reasonable. Temperature conditions on surface of Mars mainly specified by seasonal regime of incoming solar radiation. Amount of solar energy per area unit of Mars is about 40% of energy per area unit of Earth. As on Earth, temperature of surface depends on latitude, orographic features and exposed to more intense daily and seasonal variations of temperature compared to Earth. Amplitude of daily variations is 100°C and more. Average seasonal and latitude temperature of Mars surface is -63°C. Maximum daytime temperatures are – from +15°C during summer up to -60°C during winter; minimal night temperatures are from -65°C during summer up to -140°C during winter (in polar areas) (Mars Climate Database, 2016). Minimal temperature ever registered on Earth is -82.5°C («Vostok» station, Antarctica).

At the moment there are a lot of cryological maps of Earth and even more data accumulated for further mapping. There are enough data already to make cryological conditions maps, similar to Earth ones. There are global estimations of cryolithosphere thickness (Komarov, Isaev, 2010).

For mapping was used legend based on next layers: topographical, geological and geocryological (Komarov et al, 2013). Topography was processed using MOLA (Mars Orbital Data Explorer, 2016) data. Classification of geological sediments provided from Tanaka map (Tanaka et al, 2014).

Geocryological map is main among other layers of digital map. It will consist of several layers, which will reflect aspects of geocryology of Mars. First of all, «crater method» of defining border of frozen and cryogenic rocks was visualized, which was developed during second half of XX century (Kuzmin, 1983), using most detailed images and digital terrain models available at the moment for humanity several decades after. Secondly, also using remote probing data, by decipherment high-resolution HIRISE images, classification of geomorphological processes on surface was made, and spreading of exogenous cryogenic phenomena – polygonal forms of relief, pingo, thermokarst et al (HIRISE, 2016). Provided materials can be used for regional level of mapping. Thirdly, models of cryolithosphere of Mars are show in global scale (Komarov, Isaev, 2010).

All processing of images is made using ArcGIS software. Scale of map is 1:2500000, with scale of more detailed incuts – 1:200000. Coverage of mapped territory is 10°10' which is approx. equal to 590*590 km.

Thus, based on newest remote data of Mars surface and using crater method and calculated models of cryolithosphere new opportunities appeared for mapping cryological aspect on regional level.

REFERENCES

- Komarov I.A., Isaev V.S. Cryology of Mars and other Solar system planets. – Moscow: Scientific World, 2010. – 232 p.
- Komarov I.A., Isaev V.S., Abramenko O.N., Balmasheva V.V. Creating base of legend for digital cryological map of Mars // Conference by geocryological mapping, Geological, MSU, 2013.
- Kuzmin R.O. Cryolithosphere of Mars. – Moscow: Science, 1983. – 144 p.
- Kuzmin R.O., Komarov I.A., Kozlov A.N., Abramenko O.N., Isaev V.S. The map of polygonal forms of microrelief on Mars // Proceedings of Earth Cryosphere as a medium of life support, Pushino, Russia, 2003, p.195.
- Tanaka K.L., Skinner J.A., Dohm J.M., Irwin R.P., Kolb E.J., Fortezzo C.M., Platz T., Michael G.G., and Hare T.M., 2014. Geologic map of Mars: U.S. Geological Survey Scientific Investigations Map 3292, scale 1:20000 000, pamphlet 43 p., <http://dx.doi.org/10.3133/sim3292>.
- High resolution imaging science experiment. NASA/JPL/University of Arizona, 2016. URL: <http://hirise.lpl.arizona.edu/>
- Mars Climate Database. Laboratoire de Météorologie Dynamique, CNRS-UPMC, Paris, France, 2016. URL: <http://www-mars.lmd.jussieu.fr/>
- Mars Orbital Data Explorer. Planetary Data System Geosciences Node, Washington University in St. Louis, 2016. URL: <http://ode.rsl.wustl.edu/mars/>

LATE NOACHIAN ICY HIGHLANDS CLIMATE MODEL: EXPLORING THE POSSIBILITY OF TRANSIENT MELTING AND FLUVIAL/LACUSTRINE ACTIVITY THROUGH PEAK TEMPERATURES

A. Horan¹, J. Head¹

¹Department of Earth, Environmental, and Planetary Sciences, Brown University, Providence, RI, 02912

Contact: Ashley_Horan@Brown.edu.

INTRODUCTION:

Ancient fluvial features on the surface of Mars, including valley networks (VN) [1], open-basin lakes and closed-basin lakes (OBL/CBL) [e.g. 2,3], are indicative of liquid water on the surface of the southern highlands and related fluvial and lacustrine processes [4] during the Late Noachian and Early Hesperian. Here we address the question: Does formation of the fluvial and lacustrine features require long-term “warm and wet” conditions with mean annual temperatures (MAT) consistently above the melting point of water, or can they form through transient warming and melting of surface snow/ice in a “cold and icy” background climate?

BACKGROUND:

Recent climate models [5,6] have found that under the influence of a younger Sun, emitting approximately 75% the current luminosity [7], early Mars would be forced into a cold steady state with temperatures consistently below the triple point of water (MAT ~225 K). In these models, greenhouse gases and CO₂ clouds are incapable of producing the additional warming necessary to cause consistent “warm and wet” conditions (MAT >273 K) with persistent rainfall and runoff [e.g. 5,6,8,9]. Spin-axis/orbital parameters also differed in the Noachian from current values [10]. However, adjusting these parameters also does not induce a large enough temperature increase to permit the continuous existence of stable liquid water at the surface [5].

Due to the aforementioned difficulties in producing the continuous natural clement conditions [5,6] typical of a “warm and wet” early Mars climate [e.g. 11], we consider the possibility of a “cold and icy” background climate characterized by periods of episodic or punctuated heating to permit transitory rainfall or snow-melt, runoff, and fluvial/lacustrine processes. General circulation model (GCM) studies [5,6] show that when atmospheric pressure exceeds tens to hundreds of millibars, an altitude-dependent temperature effect is induced and H₂O preferentially accumulates in the highlands, producing a “Late Noachian Icy Highlands” scenario [6,12]. In this context, [13] studied where precipitation would occur under a natural “cold and icy” scenario compared to a gray gas/increased solar flux forced “warm and wet” scenario, finding that snow accumulation in a “cold and icy” climate is better correlated with the VN distribution than precipitation in a “warm and wet” climate. Correspondingly, the VN and OBL/CBL are commonly observed at distal portions of the ice sheet [12]. However, melting of the accumulated surface snow/ice must occur to permit fluvial/lacustrine activity [12,14,15].

Several candidates have been proposed for transient warming processes to melt surface snow/ice, including periods of intense volcanism releasing high concentrations of SO₂ into the atmosphere [9,16], impact cratering-induced warming [17-19], and transient annual melting from peak daytime or seasonal

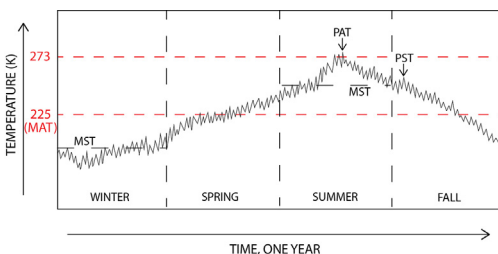


Fig. 1. Illustration of PAT, PST, MST, and MAT.

temperatures (PDT/PST) that exceed 273 K in a climate that is otherwise characterized by MAT ~ 225 K [e.g. 12]. Here, we focus on the latter of the aforementioned hypotheses, using the Laboratoire de Meteorologie Dynamique (LMD) GCM to test whether peak annual, daytime or seasonal temperatures (PAT, PDT, PST) in a “cold and icy” Late

Noachian climate [5,6] can produce transient snowmelt and subsequent runoff in sufficient quantities and at the appropriate locations to explain the nature and distribution of VN. Additionally, we investigate the importance of PDT and PST variation, in contrast with MAT, when discussing snow/ice melt in a “cold and icy” climate (Fig. 1).

METHODS:

We employ the LMD GCM [e.g. 5,6,13,21] for early Mars to test for transient melting under the conditions of peak temperatures, focusing on a range of pressures (600-1000 mbar pure CO₂ atmosphere, specifically 600, 800, 1000) and exploring the effects of different spin-axis orbital conditions [10] including obliquity (25-55°, specifically 25, 35, 45, 55°) and eccentricity (0, 0.097). We search for regions with substantial snow accumulation and PAT above the melting point of water, permitting transient snowmelt and runoff. We assess whether or not transient melting of snow/ice may be responsible for VN formation by testing whether repetitive yearly seasonal melting events in similar locations over long periods of time could be responsible for significant fluvial/lacustrine activity, a situation that is observed in the Antarctic Dry Valleys on Earth [12,20]. Additionally, we place further constraints on the spin-axis orbital parameter space by determining which conditions maximize any transient melting in comparison with the VN distribution.

Regions of peak temperatures above 273 K. We begin our study with the comparison of MAT and PAT maps, validating the importance of seasonal temperature variation: much of the equatorial region has PAT >273 K. To ensure that our PAT values represent max daytime temperatures, we collect GCM data four times per martian day, every ~6 model hours, throughout the entire model year. However, it is possible that temperatures defined in PAT maps may not last for more than a few hours yearly, conditions that would likely be insufficient to cause the necessary scale of melting and erosion [14]. To address this, we also analyze temperature time-series at three specific VN systems from various locations across the globe (Table 1) to determine the yearly time duration of heating and whether or not the peak temperatures last long enough to provide sufficient melting [21,14].

WHERE IS THE MELT; HOW MUCH IS THERE?

For parameter combinations where the aforementioned tests predict melting in VN-rich regions, we complete two follow-up global tests to deduce information about the melting: (1) produce parallel time-series movies for changes in ice thickness (sublimation/melting), snowfall, and temperature to determine if temperatures >273 K correlate with possible melting of snow/ice; and (2) determine annual meltwater volume by using a positive degree day (PDD) method (following [14]; 1.08 mm/PDD).

Table 1. VN included in this study and corresponding latitudes and longitudes.

Parana Valles	24.1 S 10.8W
Evros Valles	12 S 12 E
Networks near Kasei Outflow Channels	23 N 55 W

CONSIDERING ADDITIONAL WARMING.

Finally, we consider the addition of a small amount of greenhouse gas surrogate in the atmosphere to strengthen the greenhouse effect slightly and assess how much seasonal warming could occur under slightly increased MAT conditions while still keeping a “cold and icy” climate scenario. Because of the uncertainty in sources and sinks for specific greenhouse gases, we account for additional greenhouse warming by adding in gray gas, an artificial gas that absorbs evenly across the spectrum at a defined absorption coefficient (here, we choose $\kappa = 2.5e-5 \text{ m}^2 \text{ kg}^{-1}$, increase of ~10 K). We repeat all previously discussed steps of this study for all obliquities, pressures, and eccentricities with the additional greenhouse warming.

RESULTS AND DISCUSSION:

In this work, we answer multiple important questions that assist in our understanding of early Mars climate history. These results underline the critical importance of peak temperatures, in addition to MAT. As is the case of the Antarctic Dry Valleys [12], PDT can exceed 273 K despite the much lower MAT (~225 K), permitting transient top-down melting of snow and ice and resulting in fluvial and lacustrine activity. As such, MAT >273 K are not required to explain the Noachian fluvial and lacustrine surface features.

1) IN THE NOMINAL LATE NOACHIAN ‘COLD AND ICY HIGHLANDS’ CLIMATE MODEL (MAT ~225 K), DO PAT EVER EXCEED 273 K ANYWHERE?

The PAT maps produced in this study are evidence that temperatures exceed 273 K despite the much lower MAT. Conditions most suitable to equatorial melting are low obliquity, high pressure.

2) HOW DO VARIATIONS IN OBLIQUITY INFLUENCE THE LOCATIONS WHERE PAT >273 K AND THEIR DURATION?

We explored the obliquity range 25-55° [10] and found that obliquity variations do not influence the abundance of areas with PAT >273 K, but causes the temperature distribution to shift northward at higher obliquities.

3) HOW DO VARIATIONS IN ECCENTRICITY INFLUENCE THE LOCATIONS WHERE PAT >273 K AND THEIR DURATION?

We explored the eccentricity range 0-0.097 [10] and found that eccentricity variations influence the abundance of areas with PAT >273 K, with a more eccentric orbit creating a warmer summer season; however, this does not cause the distribution of high temperatures to shift with varying eccentricity.

4) HOW DO VARIATIONS IN PRESSURE INFLUENCE THE LOCATIONS WHERE PAT >273 K AND THEIR DURATION?

We explored the pressure range 600-1000 mbar [6] and found that variations influence the abundance of areas with PAT >273 K, increasing overall temperatures as pressure increases. Additionally, the inclusion of other greenhouse gases in the atmosphere, done here through a gray gas, increases overall temperatures further. In either case, increasing pressure or the greenhouse effect does not change the global distribution of warm temperatures.

5) FOR LOCATIONS WHERE PAT >273 K, HOW OFTEN DOES MEAN SEASONAL TEMPERATURE (MST) EXCEED 273 K?

Despite PAT exceeding 273 K, the duration is not long enough to increase MST above 273 K.

6) ARE LOCATIONS WHERE PAT EXCEEDS 273 K ALSO LOCATIONS WHERE SNOW AND ICE IS PREDICTED TO OCCUR IN THE ‘‘COLD AND ICY’’ MODEL?

We compared the locations where peak temperatures exceed 273 K with the ice distribution predicted by the models and found a close correspondence in the equatorial and near equatorial regions.

7) ARE THE DURATIONS OF TEMPERATURES >273 K SUFFICIENTLY LONG TO CAUSE TOP-DOWN MELTING OF SNOW AND ICE AND RUNOFF?

We utilize temperature time-series to determine the duration of melting, finding that under certain conditions, specifically when accounting for additional greenhouse warming, the duration is sufficient to cause top-down melting of snow and ice at the studied VNs and in equatorial regions. Additionally, we are completing melt PDD-based volume calculations to determine total melt volume per year and number of years required to produce sufficient meltwater to form the VN and OBL/CBL for all cases in the studied parameter space.

8) ARE GREENHOUSE GASES REQUIRED TO EXPLAIN THE OBSERVED VN AND OBL/CBL?

We have shown that the locations and duration of PDT >273 K are sufficient to induce limited top-down heating and melting and are aided when including modest greenhouse warming.

REFERENCES:

- [1] Hynek et al. (2010), *J. Geophys. Res. Planets* **115**, E09008. [2] Fassett and Head (2008a), *Icarus* **195**, 61–89. [3] Goudge et al. (2015), *Icarus* **260**, 346-367. [4] Fassett and Head (2008b), *Icarus* **198**, 37–56. [5] Forget et al. (2013), *Icarus* **222**, 81-99. [6] Wordsworth et al. (2013), *Icarus* **222**(1), 1-19. [7] Gough (1981), *Sol Phys.*, **74**, 21-24. [8] Wolf and Toon (2010), *Science* **328**, 1266. [9] Halevy and Head (2014), *Nature Geosci. Lett.* [10] Laskar et al. (2004), *Icarus* **170**, 343-364. [11] Craddock and Howard (2002), *J. Geophys. Res. Planets* **107**, E11, 511. [12] Head and Marchant (2014), *Antarctic Science* **26**, 774-800. [13] Wordsworth et al. (2015), *J. Geophys. Res. Planets* **120**, 1201-1219. [14] Fastook and Head (2015), *Planet. Space Sci.* **106**, 82-98. [15] Rosenberg and Head (2015), *Planet. Space Sci.* **117**, 429-435. [16] Kerber et al. (2013), *Icarus* **223**, 149-156. [17] Segura et al. (2002), *Science* **298**, 1997-1980. [18] Segura et al. (2008), *J. Geophys. Res.* **113**. [19] Toon et al. (2010), *Earth Planet. Sci.* **38**, 303-322. [20] Marchant and Head (2007), *Icarus* **192**, 187-222. [21] Scanlon et al. (2013), *Geophysical Res. Lett.* **40**, 4182-4187.

GLOBAL PATTERNS OF PARAGLACIAL ACTIVITY IN THE MARTIAN MID-LATITUDES

E.R. Jawin, J.W. Head

Department of Earth, Environmental, and Planetary Sciences,
Brown University, Providence, RI 02912 USA
Erica_Jawin@brown.edu

INTRODUCTION:

Extensive evidence of non-polar ice exists on Mars, predominantly in the form of debris-covered glaciers in the mid-latitudes including lobate debris aprons (LDA), lineated valley fill (LVF), and concentric crater fill (CCF) [1–3]. These deposits are believed to have accumulated in periods of higher obliquity ($\sim 35^\circ$) in the last few hundred million years [4–7]. Stratigraphically younger latitude-dependent mantle (LDM) suggests that ice ages have continued to occur in the geologically recent past [8, 9]. Integral to the discussion of glaciation and ice ages on Mars is the role of deglaciation. In terrestrial glacial regions, the period directly following deglaciation is referred to as the paraglacial period, in which the environment returns to “equilibrium” or interglacial conditions [10, 11]. Recently, a paraglacial period has been identified in martian mid-latitude crater glacial deposits [12]. This paraglacial period is expected to have initiated within the past 5 Ma based on modeled obliquity variations [13], and the current climate setting in these craters is an interglacial period, while the paraglacial period may still be ongoing [14].

This work builds upon previous paraglacial analyses of martian glaciated craters [12, 14], and seeks to determine the degree of variability in paraglacial reworking within the martian mid-latitudes. On Earth, paraglacial modification often exhibits a specific suite of geomorphic features [11], a subset of which are also seen on Mars [12]. It is therefore expected that this suite of geomorphic units will be present in the glaciated craters in the martian mid-latitudes. The variations seen in this analysis will aid in assessing patterns of accumulation and ablation during recent glacial periods on Mars.

METHODS:

The analysis of paraglacial features was carried out by assessing the population of CCF-bearing craters in the mid-latitudes as described by [15], and documenting the paraglacial features present in each crater. Specific paraglacial features include spatulate depressions, gullies, washboard terrain, crater wall polygons, and broad pits [12]. Observations were made using a combination of visual images: 6 m/pixel Context Camera (CTX) and 30 cm/pixel High Resolution Imaging Science Experiment (HiRISE) [16, 17]. The fine-scale nature of these features are most accurately resolved in HiRISE data; however, exten.

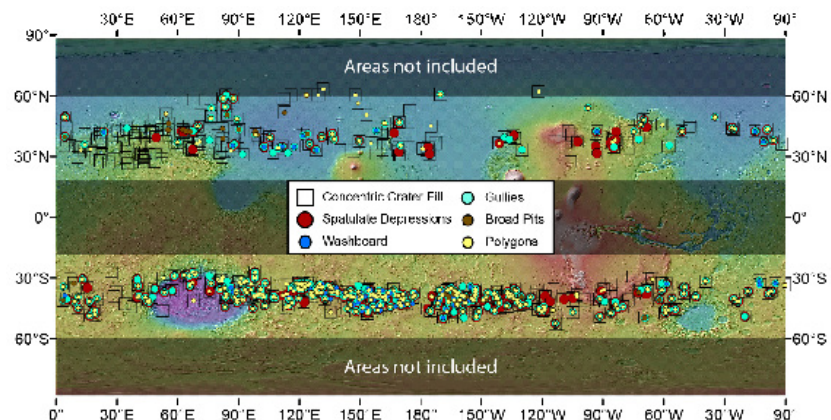


Fig. 1. Distribution of paraglacial features in glaciated craters across the mid-latitudes. CCF crater database from [15]. sive CTX coverage allowed at least initial observations to be made in all craters.

OBSERVATIONS:

The analysis of mid-latitude glaciated craters showed that the degree of paraglacial reworking is variable across the planet (Fig. 1, Table 1). This analysis yielded several observations: **(1)** ~70% of mid-latitude glaciated craters contain some evidence of paraglacial reworking. **(2)** Many more paraglacial craters are present in the southern hemisphere than in the northern; this is predominantly due to the older average age of the southern highlands relative to the northern lowlands, and therefore a larger crater population which can be glaciated; however, proportionally there are more paraglacial craters in the south than in the north: 89% and 44% respectively contain at least 1 feature (Table 1). **(3)** The distribution of features is not ubiquitous across all craters. Many craters contain multiple paraglacial features (Fig. 2A, Table 1), while some craters contain CCF, but no paraglacial features (Figure 2B). Features are generally present on pole-facing slopes, as has been reported in previous studies assessing gully orientation and CCF flow orientation [15,18]. **(4)** Northern hemisphere craters are often more completely filled with CCF than southern hemisphere craters, inhibiting the formation of paraglacial features in the crater wall (such as crater wall polygons and washboard terrain). **(5)** The highest concentrations of paraglacial features in the southern hemisphere are located in regions that have been predicted to experience melting conditions at higher obliquities in the last few hundred million years [19], including Newton crater, the eastern rim of Hellas, and Terra Cimmeria. The region west of Hellas (~30°E) is distinct in the southern hemisphere for its lack of paraglacial features. In the northern hemisphere, the highest concentration of glaciated craters exists in the Deuteronilus-Protonilus Mensae region, although almost all of these craters do not exhibit paraglacial reworking. The highest concentration of craters with multiple paraglacial features in the northern hemisphere is in Utopia Planitia, although on average the concentration of paraglacial features in this area (and the hemisphere on the whole) is lower than in the southern hemisphere (Table 1).

	Total (n=631)	North (n=246)	South (n=385)
1 Feature	71	44	89
2 Features	55	23	76
3 Features	44	15	62
4 Features	31	9	44
5 Features	17	5	24

Table 1. Percent of glaciated craters with evidence of paraglacialiation. Paraglacial features include spatulate depressions, gullies, washboard terrain, crater wall polygons, and broad pits. For example, 24% of glaciated craters in the southern hemisphere contain all 5 paraglacial features.

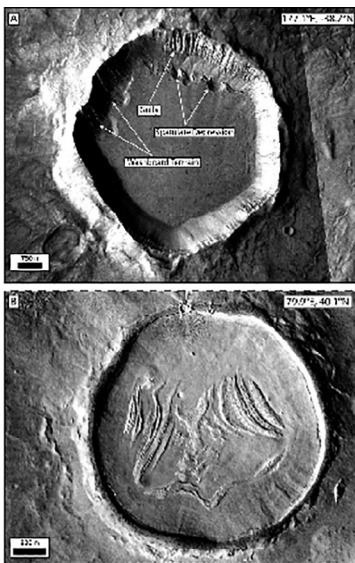


Fig. 2. Variation in morphology and distribution of paraglacial features in glaciated craters. (A) Crater with evidence of paraglacial modification. CTX image G09_021635_1405. (B) Crater containing no paraglacial features. CTX image P16_007437_2220.

DISCUSSION:

The variations in paraglacial reworking suggest that accumulation and ablation are not completely dependent on latitude; primarily, regional circulation patterns will affect the distribution of precipitation throughout the mid-latitudes. The highest concentrations of glaciated craters in the northern hemisphere are broadly located in regions predicted to be areas of enhanced winter precipitation in periods of higher obliquity by general circulation models [5]. This prediction is confirmed by the higher degree of fill in northern hemisphere craters. The relative paucity of paraglacial features in much of the northern hemisphere, specifically in the Deuteronilus-Protonilus Mensae region which is noted for its concentration of glacial features, may be attributed to differences in many factors including circulation patterns, elevation, atmospheric pressure and temperature which led to lower ablation rates and less paraglacial reworking.

Another potential source of variability in the paraglacial features is the presence of latitude-dependent mantle (LDM) [9]. In many craters, particularly in the northern hemisphere, deposits of CCF are mantled by

LDM, obscuring the presence of paraglacial features on the crater wall and floor (see the "mantled" class in [25]). In some craters, the LDM has been modified by subsequent gully formation [26], but this deposit complicates the identification of paraglacial features. Subsequent analyses of the detailed nature and distribution of LDM and its relation to larger glacial cycles will aid in interpreting the paraglacial response in glaciated craters.

REFERENCES:

1. Levy et al. (2007), *JGR*, 112.
2. Levy et al. (2010), *Icarus*, 209.
3. Head et al. (2010), *EPSL*, 294.
4. Mangold et al. (2003), *JGR*, 108.
5. Madeleine et al. (2009), *Icarus*, 203.
6. Morgan et al. (2009), *Icarus*, 202.
7. Fassett et al. (2014), *Geology*, 42.
8. Mustard et al. (2001), *Nature*, 412.
9. Head et al. (2003), *Nature*, 426.
10. Church & Ryder (1972), *GSA*, 83.
11. Ballantyne (2002), *Quat. Sci. Rev.*, 21.
12. Jawin et al. (2014), LPSC 45th, #2241.
13. Laskar et al. (2004), *Icarus*, 170.
14. Jawin et al. (2015), LPSC 46th, #2016.
15. Dickson et al. (2012), *Icarus*, 219.
16. Malin et al. (2007), *JGR*, 112.
17. McEwen et al. (2007), *JGR*, 112.
18. Dickson et al. (2007), *Icarus*, 188.
19. Dickson et al. (2015), LPSC 46th, #1035.
20. Costard et al. (2002), *Science*, 295.
21. Williams et al. (2009), *Icarus*, 200.
22. Lachenbruch (1962), *GSA*, 70.
23. Marchant et al., *GSA*, 114 (2002).
24. Marchant & Head (2007), *Icarus*, 192.
25. Harrison et al. (2015), LPSC 46th, #1625.
26. Dickson et al. (2015), *Icarus*, 252.

HELLAS BASIN FLOOR, MARS: IS THE HONEYCOMB TERRAIN FORMED BY SALT OR ICE DIAPIRISM?

D.K. Weiss¹, J.W. Head¹,

¹*Brown University, Department of Earth,
Environmental and Planetary Science,
324 Brook Street, Box 1846, Providence, RI, USA
Contact: david_weiss@brown.edu*

INTRODUCTION:

The “honeycomb” terrain is a Noachian-aged cluster of ~7 km wide cell-like depressions located on the northwestern floor of Hellas basin, Mars [1] (Fig. 1). A variety of origins have been proposed for the honeycomb terrain, including deformation rings of subglacial sediment [2], frozen convection cells from a Hellas impact melt sheet [3], a swarm of igneous batholiths [4], salt diapirism [1, 3-5], and ice diapirism [1, 2]. Recent work has shown that the salt and ice diapirism scenarios appear to be most consistent with the morphology and morphometry of the honeycomb terrain [1] (Fig. 2). Hellas basin is a distinctive environment for diapirism on Mars due to its thin crust (which reduces surface heat flux), low elevation (which allows Hellas to act as a water/ice/sediment sink), and location within the southern highlands (which may provide proximity to inflowing saline water or glacial deposits). In this analysis, we assess the salt and ice diapirism scenarios.

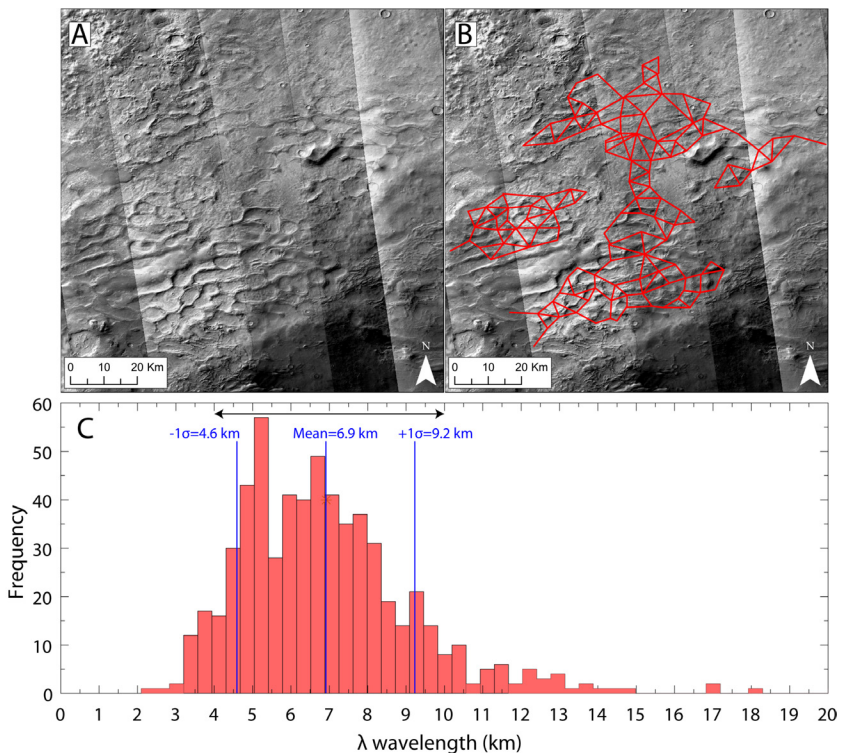


Fig. 1. A) A section of the honeycomb terrain in Hellas basin (50.65° E, 34.78° S). B) The wavelength of the cells are measured as the distance between the centroid of adjacent cells (red lines). C) Histogram of the N=604 diapir wavelength (λ) measurements. The mean is 6.9 km and the standard deviation (σ) is 2.3 km. The black arrow shows λ range explored in our study (4 to 10 km).

The salt diapirism hypothesis requires large volumes of saline water to flow into Hellas, whereas the ice diapirism scenario requires a cold climate with a source of glacial ice or frozen water to form massive subsurface ice. The distinction between salt and ice diapirism in Hellas basin is important because both origins have different (but major) implications for the ancient martian climate and

hydrological cycle. Here, we evaluate the thermal stability limits of ice and salt in the martian subsurface (as it relates to diapir cell wavelengths; Fig. 1) in order to determine whether ice or salt diapirism remains a candidate formation mechanism for the Hellas basin honeycomb terrain.

In this study, we specifically test whether the honeycomb terrain is consistent with an ice or salt diapir origin. We use thermal modeling to assess the limits on the thermally stable thickness of an ice or salt (gypsum and halite) diapir-forming layer at depth within Hellas (dashed red line in Fig. 2), and then apply analytical models [6] for diapir formation in order to evaluate the diapir wavelengths (λ) predicted for these ice and salt thicknesses for comparison with observation (Fig. 2).

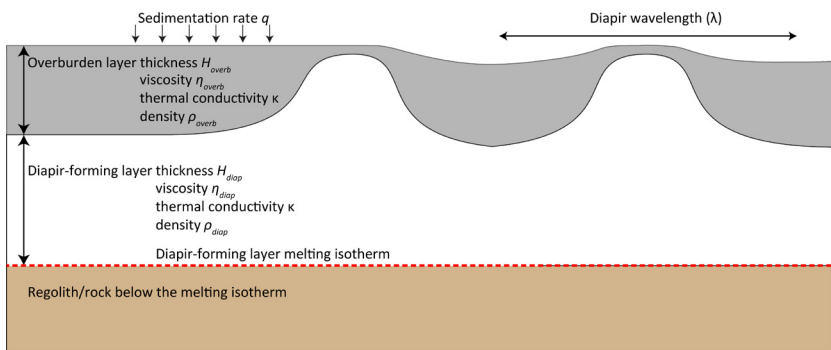


Fig. 2. Thermal and diapir wavelength model configuration and variables.

The thermal stability models apply important constraints on stable diapir-forming layer configurations: they show that large thicknesses (~ 1 - 2 km) of both ice and gypsum are stable over a confined range of surface temperatures and heat fluxes. Halite remains thermally stable across the entire parameter range. In order to establish the layer thickness relationships that reproduce the observed diapir dimensions, we adopt recent scaling laws derived from a 2-D semi-analytical thick plate model [6], which relate diapir wavelength (λ) to the diapir-forming layer thickness (H_{diap}) and the overburden thickness (H_{overb}).

In our analysis, we find that the consistency of ice diapirism is heavily dependent upon surface temperature and overburden thickness. The viability of salt diapirism is dependent more-so upon the ability for sufficiently thick evaporite deposits to accumulate in Hellas, rather than specific climatic conditions or overburden thickness. Both scenarios have significant implications for the ancient martian climate and hydrological cycle.

REFERENCES:

- [1] Bernhardt et al., *JGR Planets* 121(4), 714-738 (2016);
- [2] Moore and Wilhelms, *Icarus* 154(2), 258-276 (2001);
- [3] Mangold and Allemand, *6th Int'l. Conf. on Mars*, abstract #3047 (2003);
- [4] Kite et al., *40th LPSC*, abstract #1248 (2009);
- [5] Diot et al., *PSS* 121, 36-52 (2016);
- [6] Fernandez and Kaus, *Geophys. Journal Int'l.*, 202(2), 1253-1270 (2015).

MODELIZATION AND SIMULATIONS OF THE ATMOSPHERIC DUST DYNAMIC THROUGH FRACTIONAL CALCULUS

M.P. Velasco¹, D. Usero², S. Jimenez³, J.L. Vazquez-Poletti⁴, L. Vazquez⁴

¹*Universidad Politecnica de Madrid, Escuela Tecnica Superior de Ingenieria y Sistemas de Telecomunicacion, Ctra. de Valencia Km. 7, 28031 Madrid, Spain;*

²*Universidad Complutense de Madrid, Facultad de Quimicas, Avda. Complutense s/n, 28040 Madrid, Spain*

³*Universidad Politecnica de Madrid, Escuela Tecnica Superior de Ingenieros de Telecomunicacion, Avda. Complutense 30, 28040 Madrid, Spain*

⁴*Universidad Complutense de Madrid, Facultad de Informatica, Calle Profesor Jose Garcia Santesmases 9, 28040 Madrid, Spain*

Contact: mp.velasco@upm.es, um david@mat.ucm.es, s.jimenez@upm.es, jl vazquez@fdi.ucm.es, lvazquez@fdi.ucm.es.

The dust aerosols play a fundamental role in the behavior of the Martian atmosphere. They have a direct effect on both surface and atmospheric heating rates, which are also basic drivers of atmospheric dynamics. Aerosols cause an attenuation of the solar radiation traversing the atmosphere. This attenuation is modeled by the Lambert-Beer-Bouguer law, where the aerosol optical thickness plays an important role. Through Angstrom law, the aerosol optical thickness can be approximated and this law allows to model attenuation of the solar radiation traversing the atmosphere by a fractional diffusion equation. We present a possible fractional model together with numerical simulations.

PHOBOS EVOLUTION UNDER THE TIDAL ACTION OF MARS

S.A. Voropaev¹

¹Vernadsky Institute geochemistry and analytical chemistry (GEOKHI) RAS,
119991 Moscow, Kosygina Str., 19, Russia
Contact: voropaev@geokhi.ru

INTRODUCTION:

The unusual dynamical behavior of Phobos, its global network of grooves, internal structure and orbit evolution make it an intriguing object. Unfortunately, Russian sample return mission "Phobos-Grunt" to Phobos launched on 9 November 2011, failed due to the problem with the main engine of the interplanetary module. So, the task of the soil delivery from Phobos and determination of the rock composition is still relevant. We are looking forward to the project "Phobos-Grunt-2" and have time to make some preliminary calculations. In this study, the Martian satellite is modeled as homogeneous, elastic triaxial ellipsoid which was subjected to tidal, rotational and self-gravitational stress. As Phobos is near or crossed the Roche limit for Mars satellite, we can estimate the strength of its rocks and compare it with the known data of asteroids of various types.

ANALYTICAL PROCEDURE:

Phobos is well approximated by a triaxial ellipsoid model with the following principal semiaxes: $a = 13,4$ km, $b = 11,2$ km, $c = 9,2$ km. The mean density, ρ_b , was equal to $1,876$ g/cm³ [1]. The gravitational potential inside of the satellite can be described by the quadratic equation [2]

$$V_G = G\rho_b\pi abc [-U_0 + x^2U_a + y^2U_b + z^2U_c], \quad (1)$$

where G is a gravitational constant; (x,y,z) are Cartesian coordinates directed along the a -, b -, c - axes, respectively; U_0 , U_a , U_b , U_c are constants calculated as

$$U_0 = \int_0^\Delta \frac{1}{\Delta} ds, \quad U_c = \int_0^\Delta \frac{1}{(c^2 + s) \cdot \Delta} ds, \quad U_b = \int_0^\Delta \frac{1}{(b^2 + s) \cdot \Delta} ds, \quad U_a = \int_0^\Delta \frac{1}{(a^2 + s) \cdot \Delta} ds$$

where $\Delta = \Delta = \sqrt{(a^2 + s) \cdot (b^2 + s) \cdot (c^2 + s)}$. As any synchronized satellite, Phobos

rotates around its z -axis (axis of greatest inertia) at a constant angular rate $\omega = 2\pi/T$, where the rotation period $T = 7,39$ h. The longest x -axis is directed toward Mars. In this case, the centrifugal forces may be expressed by means of the rotational potential

$$V_\Omega = -\frac{1}{2} \omega^2 (x^2 + y^2) \quad (2)$$

In addition, Phobos is subject to significant tidal forces when orbiting Mars of mass M at a distance $d = 9377$ km, that corresponds to 2.76 Mars radii. The tidal potential can be expressed to lowest order in a/d as

$$V_T = -GM (x^2 - y^2/2 - z^2/2) / d^3 \quad (3)$$

If we assume that the Phobos composition is homogeneous and isotropic, its elastic properties are completely described by two Lamé parameters, λ and μ

$$\lambda = E\nu / (1 - 2\nu)(1 + \nu), \quad \mu = E / 2(1 + \nu), \quad (4)$$

where E is Young's modulus and ν is Poisson's ratio. Hooke's law is characterized by the well-known relation between strain and stress tensors, ε_{ij} and σ_{ij} (indexes $i, j = 1, 2, 3$), $\varepsilon = \varepsilon_{11} + \varepsilon_{22} + \varepsilon_{33}$, as

$$\sigma_{ij} = \lambda\varepsilon + 2\mu\varepsilon_{ij}, \quad \partial\sigma_{ij} / \partial x_j = -\rho_b \text{grad}(V), \quad (5)$$

where $V = V_G + V_\Omega + V_T$. According to Dobrovolskis [2], we can decompose the deformation vector (u_j) by twelve dimensionless constants (referred to as A, B, C , etc.) like in the following equation

$$u_x = x(A + Bx^2/a^2 + Cy^2/b^2 + Dz^2/c^2), \quad u_y = y(\dots), \quad u_z = z(\dots) \quad (6)$$

However, the boundary conditions we define differently from those applied in [2], where a balanced (equilibrated) model of Phobos was assumed. For a rigid body, the boundary condition as surface free from load can be expressed as zero value of one of the main component of the stress tensor (analogue of lithosphere pressure). In this case, we have 12 equations for 12 coefficients and receive analytical expressions for the all deformation and stress tensor components [3].

RESULTS AND DISCUSSION:

As it turned out from the general solution for a 3-axial rigid small body, the following 6 dimensionless coefficient are of a great importance: $\lambda/2\mu = \nu/(1 - 2\nu)$, $t_1 = c^2/a^2$, $t_2 = c^2/b^2$, $V_g = G(\rho_b)^2 \pi bc/2\mu$, $V_\omega = 1/2 \omega^2 a^2 \rho_b/2\mu$, $V_t = GM/d^3 \rho_b a^2/2\mu$. If we take into account the characteristic parameters of Phobos and the known elastic parameters of chondrites [4] ($\nu = 0.46$, $\mu = 3 \cdot 10^4$ bar), the above mentioned coefficients would have the following values; $t_1 = 0,471$; $t_2 = 0,675$; $\lambda/2\mu = 5,75$; $V_g = 12,667$ (ppm); $V_\omega = 1,46$ (ppm); $V_t = 2,912$ (ppm), in relation to double rigidity (shear) modulus ($2\mu = 6$ GPa). With such intensive potentials the inner part of Phobos is compressed by the self-gravity, mainly. However, along the xz-plane (cross-section directed to Mars and perpendicular to the equator, "north pole" is $x = 0$), the tidal force is sufficient to stretch Phobos and provide the tensile stress of about 0,05 (ppm) (see Fig.1)

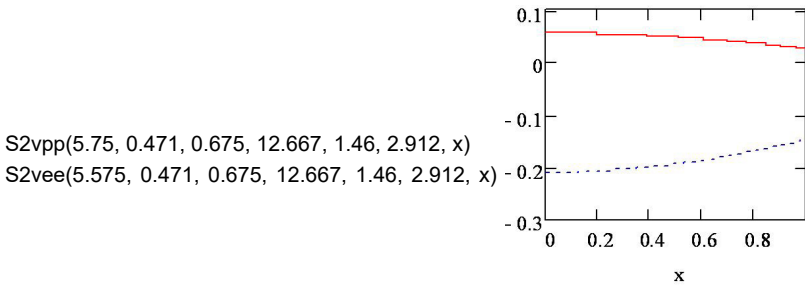


Fig. 1. $d = 9377$ km

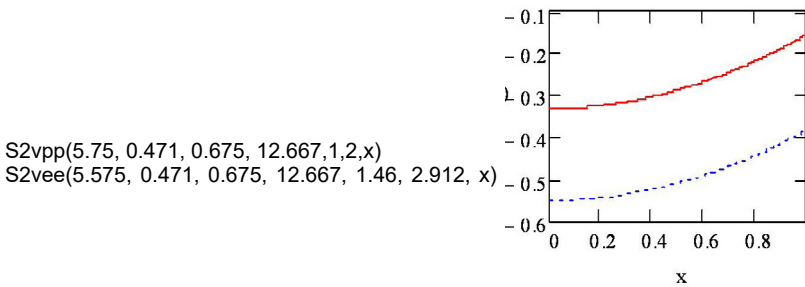


Fig. 2. $d = 10\ 640$ km

$S2v$ is the second main value of the stress tensor on the surface (in ppm): pp is the longitudinal plane or xz-cross-section; ee is the equatorial plane or xy-cross-section. $S1v = 0$, $S3v$ is negative (compressive stress).

This tensile stress is very sensitive to the distance between Phobos and Mars. At a little greater distance (see Fig.2), the compression on the surface would prevail everywhere. The estimated tensile stress on the surface is equal to ca 0,3 kPa which is obviously not enough to break the body. So, in case of slow, quasi-stationary, movement of Phobos to Mars, preserving the synchronous rotation, the tensile stresses do not occur until the current time. This allows us to understand better the possible genesis of the Phobos grooves, while the detailed analysis of its orbit dynamics is needed.

REFERENCES:

- [1] Andert, T. P., P. Rosenblatt, M. Pätzold, B. Häusler, V. Dehant, G. L. Tyler, and J.C. Marty (2010), Precise mass determination and the nature of Phobos, *Geophys. Res. Lett.*, 37, L09202, doi:10.1029/2009GL041829.
- [2] Dobrovolskis, A. R. (1982), Internal stresses in Phobos and other triaxial bodies, *Icarus*, 52, 136-148.
- [3] Voropaev S.A. (2016) Phobos orbit dynamics and evolution under the tidal action of Mars (to be published).
- [4] Dobrovolskis, A. R. (1990), Tidal disruption of solid bodies, *Icarus*, 88, 24-38.

STATIC STRESSES ESTIMATES IN MARS WITH AN ELASTIC MANTLE

A.V. Batov¹, T.V. Gudkova², V.N. Zharkov²

¹Institute of Control Sciences of RAS, 65 Profsoyuznaya street, Moscow, Russia

²Schmidt Institute of Physics of the Earth of RAS, 10-1Bolshaya Gruzinskaya street, Moscow, Russia

Contact: batov@ipu.ru

INTRODUCTION:

The recent progress in developing the gravity and topographic models of Mars [1-3] allows to study the stress field in detail and to recalculate previous estimates of static stresses [4]. It is of importance to identify areas of high values of shear and tension-compression stresses as possible marsquakes focuses, as in 2018 NASA's Discovery Program mission InSight (Interior Exploration using Seismic Investigations, Geodesy and Heat Transport) will place a single geophysical lander with a seismometer on Mars to study its deep interior. In this paper we will consider the case of an elastic mantle of Mars.

METHOD:

Numerical simulation is based on a static approach, according to which the planet is modeled as an elastic, self-gravitational spherical body. It is assumed, that deformations and stresses which obey Hooke's law are caused by the pressure of relief on the surface of the planet and anomalous density $\delta\rho(r, \theta, \lambda)$, distributed by a certain way in the crust and the mantle. A self-consistent technique of the solutions of this problem (by way of the Green's functions or loading factors technique) has been developed in [4-6]. The anomalous density field is represented in the form of weighted thin layers positioned at different characteristic depths. Imposing the anomalous density waves (ADW) on the surface or in the interior leads to the deformation of the planet interior and the distortion of the surface and the boundary interfaces. With the addition of ADW to the planet it goes to a new state of elastic equilibrium, that is, it "adjusts" to the ADW. So, the problem is reduced to the determination of Green's response function for the case of a single ADW located at some depth level.

STRESSES ESTIMATES:

To avoid uncontrollable stresses and deformations in the mantle of the planet due to the significant deviation of Mars from hydrostatic equilibrium state, an outer surface of a hydrostatical model is taken as a reference surface [7, 8]. Only unequilibrium components of gravity and topography fields have been considered: they were obtained by subtracting the equilibrium component from the observed external field.

As a benchmark real model for the planetary interior we have used a model of Mars M7 from [9], which satisfies all the currently available geophysical and geochemical data. The density of the crust is 3000 kg m^{-3} , the thickness of the crust is 50-100 km. In present paper we have started with a simple model – an elastic model. The model allows one to calculate all stresses (tension-compression stresses and shear stresses).

It is impossible to unambiguously determine ADW from the data on the gravitational field of a planet, therefore to solve the problem we assume that there are two levels of concentration of anomalies in Mars – on its surface and at the crust-mantle boundary. Loading coefficients for deeply buried density anomalies k_n and h_n of n -th harmonic of ADW located at depth r_n defines the total change in the gravitational potential on the surface of Mars and deformation of the planets surface under the action of load, respectively (Fig. 1).

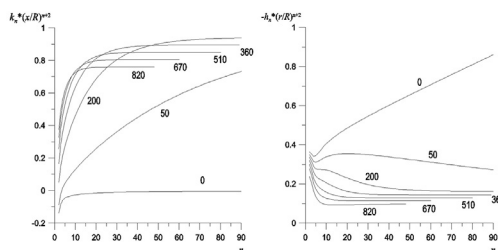


Fig. 1 . Load numbers k_n and h_n for various depths of the density anomaly as a function of the order n . Values correspond the depths (in km) of loading.

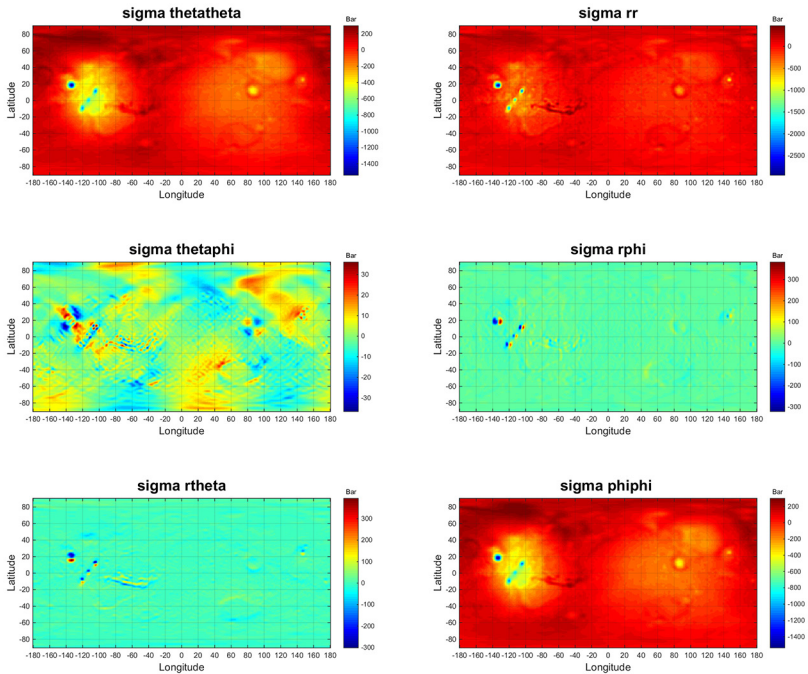


Fig. 2. Stress tensor components.

Figure 2 shows the components of complete stress tensor σ_{ij} for a test model, calculated for the level beneath the 50km-crust. Then this tensor is reduced to diagonal form with the principal stresses $\sigma_3 \leq \sigma_2 \leq \sigma_1$, and the compression-tension stresses and maximum shear stresses are calculated as $(\sigma_1 + \sigma_2 + \sigma_3)/3$ and $(\sigma_1 - \sigma_3)/2$, respectively (Fig. 3). As seen in the fig. 2 and 3 most of stress intensity is accumulated in the Tharsis region, with maximum compression stresses at a location of Olympus Mons. Such topographic structures as Valles Marineris and Elisium region have much smaller values of stresses, but clearly visible in the figures. The presented sub-crustal stresses are somewhat lower than the values obtained in [10].

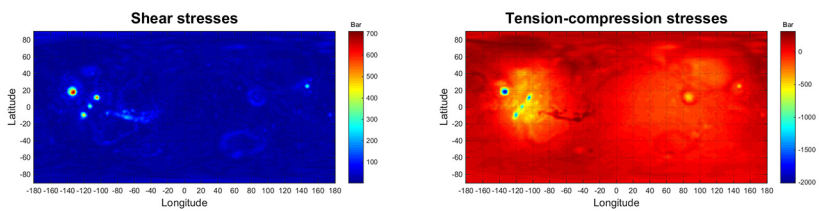


Fig. 3. Shear stresses (left) and tension-compression stresses (right) beneath the 50km-crust

ACKNOWLEDGMENTS:

This work was undertaken during the preparation phase of the SEIS experiment on InSight mission. The work was supported by the Russian Foundation for Basic Research, project no. 15-02-00840.

REFERENCES:

- [1] Smith D.E., Zuber M.T., Frey H.V. et al. 2001. J.Geophys.Res. 106 (E10), 23689-23722;
- [2] Konopliv A.S., Park R.S., Folkner W.M. 2016. Icarus 274, 253-260;
- [3] Genova A., Goossens S., Lemoine F.G. et al. 2016. Icarus 272, 228-245;
- [4] Zharkov V.N., Koshlyakov E.M., Marchenkov K.I. 1991. Solar Syst. Res. 25, 515-547;
- [5] Marchenkov K.I., Lubimov V.M., Zharkov V.N. 1984. Doklady Acad.Nauk, SSSR, Earth Sci.Sect. 279, 14-16;
- [6] Zharkov V.N., Marchenkov K.I., Lubimov V.M. 1986. Sol.Syst.Res. 20, 202-21;
- [7] Zharkov, V.N., Gudkova, T.V., 2000. PEPI, 117: 407-420;
- [8] Zharkov, V.N., Gudkova, T.V., 2016. Sol.Syst.Res. 50, 252-267;
- [9] Zharkov V.N., Gudkova T.V., Molodensky S.M. 2009. PEPI, 172, 324-334;
- [10] Tenzer R., Eshagh M., Jin S. 2015. EPSL 425, 84-92.

ON THE MODEL STRUCTURE OF THE GRAVITY FIELD OF MARS

V.N. Zharkov, T.V. Gudkova

Schmidt Institute Physics of the Earth RAS, B. Gruzinskaya, 10, Russia

Contact: zharkov@ifz.ru

Introduction:

The areoid heights and gravity anomalies for the model of Mars are calculated. Mars deviates much more strongly from the hydrostatic equilibrium than the Earth. It is suggested that the average thickness of the Martian elastic lithosphere should exceed that of the Earth's continental lithosphere. Our approach is as follows: we use the Martian interior structure model, which retains the values of M , R and ω – the mass, the average radius, and angular velocity of the planet's rotation. The model [1, 2] satisfies the values of the mean moment of inertia, Love number k_2 , and the weight ratio Fe/Si must be closed to the chondritic value 1.7.

DATA ANALYSIS:

We have used the detailed gravity and topography models: the high resolution MOLA (Mars Orbiter Laser Altimetry) global topography [3] and gravity field MRO110B2 and MRO110C models from Jet Propulsion Laboratory [4]. The definition of the "topography" needs the choice of a reference surface. An outer surface of a hydrostatical model is taken as a reference surface [5, 6]. Only nonequilibrium components of gravity and topography fields have been considered: surface relief (or topography) was referenced to the standard equilibrium spheroid in the first approximation, and the hydrostatically equilibrium field of the Martian spheroid was subtracted from the full potential [7].

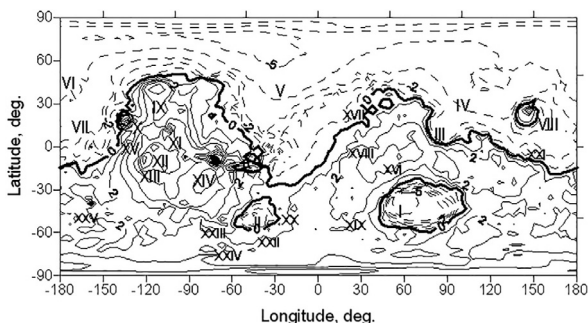


Fig. 1. Contour map of heights of the surface relief of Mars to degree and order 90. The zero level (thick solid line) corresponds to the equilibrium figure.

The solid lines correspond to positive heights; the dashed ones, to negative heights. The interval between contours is 1 km. The map legend: I – the Hellas basin, II – the Argyre basin, III – the Isidis basin, IV – Utopia Planitia, V – Acidalia Planitia, VI – Arcadia Planitia, VII – Amazonis Planitia, VIII – the Elysium uplift, IX – Alba Patera, X – the volcano Olympus Mons, XI – the volcano Asraeus Mons, XII – the volcano Pavonis Mons, XIII – the volcano Arsia Mons, XIV – Valles Marineris, XV – Biblis Patera; the craters: XVI – Huygens, XVII – Cassini, XVIII – Schiaparelli, XIX – Darwin, XX – Gale, XXI – Gale, XXII – Phillips, XXIII – Lowell, XXIV – Schmidt, XXV – Newton.

Figure 1 shows a map based on the data for the heights of the surface relief of Mars after expansion to degree and order 90. The map demonstrates one of the main features of the Martian topography: the elevation of the southern, heavily cratered regions relative to the northern planetary depression. One can see also the main geological structures such as the Tharsis and Elysium uplift, the Hellas, Argyre, and Isidis circular basins, the volcano Olympus Mons, Alba Patera, etc..

AREOID HEIGHTS:

It is clear, that the Martian potential field is strongly dominated by long-wavelength components. The reason that the amplitudes of the harmonics of degrees $n=2-6$ in the potential spectrum far exceed the amplitudes in the rest

of the spectrum and carry information mainly on the global Tharsis anomalies. For the identification of the small-scale structure Fig. 2 shows the areoid heights starting from the seventh harmonic, i.e., after the elimination of the long-wavelength background. In Fig. 2 along with the strong anomaly from Olympus Mons, one can clearly see a number of other local anomalies associated with such regions as Utopia Planitia, the Elysium uplift, Valles Marineris, the volcanoes Arsia Mons and Ascraeus Mons, Alba Patera, etc. Noteworthy is the regions of negative areoid heights around Olympus Mons.

GRAVITY ANOMALIES:

Figure 3 shows a map of the δg contours on the surface of Mars. In addition to the pronounced global Tharsis anomaly, which is characterized by $\delta g \sim 200$ - 300 mGal, one can clearly see others, more local anomalies, corresponding to specific topographic structures. The Hellas basin has no substantial perturbations in gravity acceleration: within the basin δg varies from 130 to 50 mGal and the Hellas basin can be considered as an isostatically compensated structure, or in the case of a thick crust, even as a mascon.

Utopia Planitia (IV) is characterized by a vast anomaly of 150-330 mGal, which together with the 1 – 2 km lowering in the terrain, allows one to consider Utopia as a gigantic impact basin, perhaps, the most ancient one on Mars. It is a gigantic Martian mascon. To the northwest of the Hellas basin, there is the Isidis impact basin (III), which is an analogue of the lunar mascons and has a positive anomaly reaching a maximum of 600 mGal. To the east, the circular contours δg outline the Elysium uplift (VIII); at the center of the uplift, $\delta g = 850$ mGal.

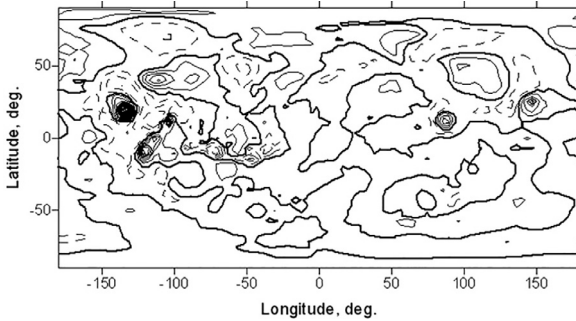


Fig. 2. Map of areoid heights for harmonics of degree 7 through 90 relative to the equilibrium figure. The solid lines correspond to positive heights, the dashed ones, to negative heights; the zero level is shown by a thick solid line. The interval between the contour lines is 50 m.

A number of characteristic features of the gravity field are clearly seen in the neighborhood of the Tharsis uplift against the background of the associated global anomaly. The lowering of the relief along Valles Marineris (XIV) is indicated by negative values of δg down to -380 mGal. The somewhat attenuated anomaly with the amplitude of 500 mGal corresponds to the Alba Patera (IX). There are distinct anomalies associated with two of the three central shield volcanoes on the Tharsis uplift – Ascraeus Mons (XI) and Arsia Mons (XIII), the tops of which have δg , of 2500 and 2000 mGal, respectively. Pavois Mons (XII), located right between the two, has a δg value of 1700 mGal. Noteworthy is the area of Biblis Patera (XV), where, amidst values of ~ 300 mGal, there is a sharp drop in δg to zero and further, to negative values, which are seen around Olympus Mons (X) in the inset to Fig. 3 for harmonics n from 7 to 90.

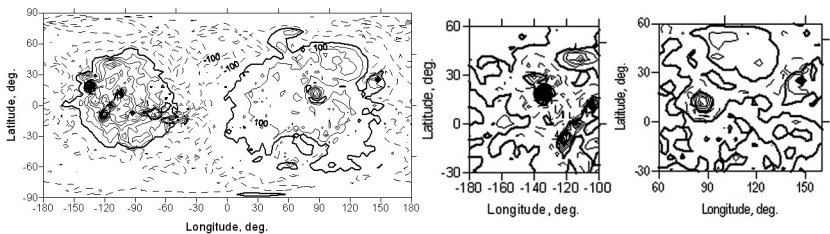


Fig. 3. Map of the deviations of the gravity from the hydrostatic-equilibrium values δg on the Surface of Mars for harmonics of degree 2 through 90. The solid lines corre-

spond to positive values; the dashed lines, to negative ones. The interval between the contour lines is 100 mGal. The insets show the deviations of gravity from the hydrostatic-equilibrium values δg for the area of Olympus Mons and the Isidis and Elysium basin for harmonics of degree 7 through 90.

This feature was already noted above when discussing the areoid heights and, together with the absence of lowering in the relief, may mean the presence at the Moho of a crust thickening, which is a part of an extended compensation «root» supporting Olympus Mons (X), above which the gravity anomaly reaches an amplitude of 3300 mGal. It is possible that the Elysium uplift and the Isidis mascon have a similar structure.

Also noteworthy are the negative anomalies corresponding to Amazonis Planitia (VII, - 215 mGal), the Argyre impact basin (II, - 280 mGal) and Acidaliu mare (V, - 215 mGal). The south pole is characterized by an almost zero value of δg , at the north pole, $\delta g = -145$ mGal.

Here we give values for several impact craters of the more ancient southern hemisphere with diameters of several hundreds of kilometers (see Fig.1). A part of the craters have negative anomalies: Galle (-267 mGal), Gale (-216 mgal), Lowell (-206 mgal), Schmidt (-67 mGal), Newton (-134 mGal); another part have positive values, close to zero: Huygens (57 mGal), Cassini (15 mGal), Schiaparelli (30 mGal), Darwin (19 mGal), Phillips (38 mGal), which is evidence of a state close to isostasy.

ACKNOWLEDGMENTS:

The work was supported by the Russian Foundation for Basic Research, project no. 15-02-00840.

REFERENCES:

- [1] Zharkov, V.N., Gudkova, T.V., 2005. Solar System Res., 39: 343-373.
- [2] Zharkov, V.N., Gudkova, T.V., 2016. Solar System Res., 50, 235-250.
- [3] Smith, D.E. et al., 2001. J.Geophys. Res., 106 (E10): 23689-23722;
- [4] Konopliv et al, 2011. Icarus, 211: 401-428;
- [5] Zharkov, V.N., Gudkova, T.V., 2000. PEPI, 117: 407-420.
- [6] Zharkov V.N. et al., 2009. PEPI 172, 324-334;
- [7] Zharkov V.N. et al., 1991, Sol.Syst.Res. 25,515-547.

GARS INSTRUMENT - AN IMITATOR OF EXOMARS-2016 TGO TRANSMITTER

A.S. Kosov, V.M. Aniskovich, V.M. Gotlib, L.S. Roshkov, V.S. Roshkov
Space Research Institute of Russian Academy of Sciences (IKI RAS)
Profsoyuznaya Str, Moscow, Russia, 117997

INTRODUCTION:

Autonomic Generator of Radio Signals (instrument GARS) has been developed and produced under IKI - Russian Space Agency contract for creation the Russian Ground Facilities for Receiving Scientific Data (RKPNI). RKPNI is intended for receiving scientific data from ESA Trace Gas Orbiter (TGO) spacecraft launched on March 2016 according to Exomars-2016 project. Actually GARS is low power transmitter which can produce same radio signals as main TGO transmitter intended for data transmitting from Mars to Earth. GARS is independent from ground-based station and intended for autonomous evaluation of ground-based station down-link radio channel, including ground antenna, analog and digital parts of ground station, modulation and coding algorithms. The instrument satisfy the CCSDS 401.0-B and 506 1-B-1 standards, can imitate Doppler shift and effects of radio waves propagation.

GARS DESCRIPTION:

According to TGO transmitter working algorithm the data to be transmitted are treated by computer program "Waveform Generator". The program performs errors correction encoding (Reed-Solomon or Turbo), creates frames and generates baseband digital signals using three types of modulation modes:

1. PCM(NRZ-L)/PSK/PM on square-wave subcarrier for transmitted coded-symbol rates up to 60 ksp/s:
 - 8.190 kHz subcarrier to be used from 21.3333 sp/s to 1023.75 sp/s.
 - 263.1579 kHz subcarrier to be used from 2.05592 ksp/s to 52.632 ksp/s.
2. GMSK (BT=0.5) for transmitted coded-symbol rates from 62.5 ksp/s to 2 Msp/s.

As a result the waveform.prd file is created. Figure 1 shows "waveform generator" algorithm and GARS structure chart.

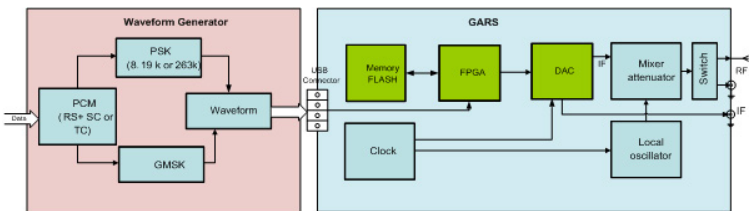


Fig. 1. Waveform generator algorithm and GARS chart.

The waveform.prd files are downloaded into GARS flash memory via USB connector. The memory value 64 GB is enough to store all types of TGO transmitter signals. During working the needed waveform is selected and downloaded into DAC, where radio signal at intermediate frequency (IF=70 MHz) is created. Then IF signal is up-converted into RF=8.410654321 GHz signal which comes to RF connector or RF patch antenna. GARS is clocking by precise quartz oscillator OCXO-8607, space version of which is used in TGO transmitter. The short term frequency stability of OCXO-8607 is about 10^{-13} , which allows simulating



Fig. 2. Spectra of GARS signals: A - GMSK modulation; B - PCM(NRZ-L)/PSK/PM with 263.1579 kHz subcarrier frequency; C - PCM(NRZ-L)/PSK/PM with 8.190 kHz subcarrier frequency

Doppler shift and fine effects of signal propagation.

Testing of GARS instrument in RKPNI station near Kalyazin town on this June has shown compatibility of GARS signals with TGO transmitter signals. Spectra of GARS signals measured on RF connector are shown on figure 2. Figure 2 shows three types of modulations implemented in TGO transmitter: GMSK modulation, PCM(NRZ-L)/PSK/PM with 263.1579 kHz subcarrier frequency and 8.190 kHz subcarrier frequency.

MECHANICAL AND CLIMATIC FEATURES OF GARS:

- GARS is the portable instrument with mass no more than 5 kg and volume no more than 5 liters;
- the instrument has outdoor implementation and wet protection;
- the instrument is powered from DC 9-15 V source;
- the consumption power is no more than 20 W;
- the working temperature range is from minus 40° C to plus 50° C;
- GARS control and uploading of test information files is making by Ethernet using telnet and ftp protocols respectively.

SUMMARY

GARS instrument, autonomic imitator of TGO transmitter signals has been developed and successfully tested in RKPNI station near Kalyazin town. GARS is very useful for evaluation of new stations or in unpredictable events of communication losses in working station. GARS satisfy the CCSDS 401.0-B and 506 1-B-1 standards. GARS is prototype for new modern onboard transmitters.

SCIENTIFIC PROGRAM OF LUNA-25 AND LUNA-27 LANDERS

V.I. Tretyakov¹, I.G. Mitrofanov¹, V.P. Dolgoplov²

¹*Space Research Institute of Russian Academy of Sciences (IKI RAS),
117997, 84/32 Profsoyuznaya str., Moscow, Russia*

²*Lavochkin Space Association, Moscow*

Contact: vladtr@mx.iki.rssi.ru, imitrofa@space.ru, komarov@laspaces.ru

Obviously that future Lunar exploration should be developing on step-by-step extending of technical and scientific heritage: 1st stage with robotic Landers and Orbiters only, 2nd one with cooperation between manned orbiters and robotic spacecrafts on surface and on orbit, 3rd - manned mission with operation on orbit, and support the robotic spacecrafts on surface.

Scientific goals for first Russian Landers Luna-Glob (Luna-25) and Luna-Resource-1 (Luna-27) missions will be presented. Both Lander designed and aimed on landing, long time surviving and operation in Moon Polar Regions and its will be base for the next steps to future exploration of Moon resources.

Science payload for search the volatiles and water ice in upper layer of regolith, for investigation of structure and content of regolith and for studies of moon's exosphere will be described. Preliminary plans of surface operations during moon days will be considered.

KEYWORDS:

Moon, Polar Regions, spacecraft, robotic missions, regolith, exosphere, volatiles

INA PIT CRATER: ORIGIN AS A DRAINED SUMMIT LAVA LAKE AND MAGMATIC FOAM EXTRUSIONS MODIFIED BY SEISMIC SIEVING

L. Qiao^{1,2}, J.W. Head², L. Xiao¹, L. Wilson³, J. Dufek⁴

¹Planet. Sci. Inst., China Univ. Geosci, Wuhan 430074, China

²Dep. Earth, Env. & Planet. Sci., Brown Univ., Providence, RI, 02906, USA,

³Lancaster Env. Centre, Lancaster Univ., Lancaster LA1 4YQ, UK

⁴Sch. Earth & Atmos. Sci., GA Tech, Atlanta, GA, 30332, USA

Contact: le_qiao@brown.edu, james_head@brown.edu

INTRODUCTION:

Ina is an enigmatic feature in Lacus Felicitatis, ~170 km southwest of the Imbrium basin, first discovered in Apollo data [1]. It is an ~2×3 km D-shaped depression consisting of dozens of bleb-like mounds surrounded by unusually bright floor hummocky and blocky terrains. Notable for its irregular shape, well-preserved state of relief, significantly low optical maturity and few superposed impact craters, Ina is generally interpreted to be formed/modified by geologically recent processes. However, the specific formation mechanism has been long debated. Previous hypotheses proposed for its origin include a collapsed summit caldera with the mounds formed by later individual lava extrusions [2], very recent extrusive volcanic activity [3], very recent venting of magmatic volatiles [4], and lava flow inflation process [5]. But no single hypothesis yet successfully explains the regional setting, and all the observed properties of the interior units at Ina. Here, we use new LRO data and terrestrial analogs to assess the regional setting of Ina and the nature and origin of the suite of units within it.

REGIONAL GEOLOGIC SETTING:

New LRO altimetry and image data show that Ina is not only located within the lunar maria, but also at the summit of a small round shield volcano, ~22 km in diameter and ~300 m high (Fig. 1), at the upper end of the size range of >200 small shield volcanos on the Moon [6]. The diameter of Ina also lies on the summit diameter/shield base diameter base line [6]. These small lunar shield volcanoes are generally interpreted to be formed by multiple eruptions from a common pit crater source, and to be dominated by accumulating low-ef-fusion rate, cooling-limited flows [7]. Summit pit craters are common at small terrestrial shield volcanoes in Hawai'i, Iceland and elsewhere. How will summit crater context and terrestrial analogs assist in understanding the properties and origin of Ina interior?

NATURE OF THE INA INTERIOR TERRAINS:

The Ina interior is defined by an inward-facing wall (5–10°) and a relatively flat basal terrace/ledge with a steep (10–30°) inward-facing scarp up to ~12 m high (Fig 2–4). The floor is generally flat, slopes gently (<2°) toward the interior, and mainly lies about 40–60 m below the rim crest. About 50% of the interior terrain is made up of the unusual bleb-like mounds with the remainder composed of two floor units: 1) a hummocky unit (44%), composed of relatively optically immature terrain with ridged and pitted textures, and 2) an optically immature blocky unit (6%) with a rougher texture, and 1–5 m exposed blocks. The meniscus-like mounds are convex upward, rise up to ~20 m above the floor, and have marginal slopes typically in the range of ~10–30°. About 88 of these mounds (including 6 in depressions) are arrayed across the floor of Ina, some continuous with the regolith sur-

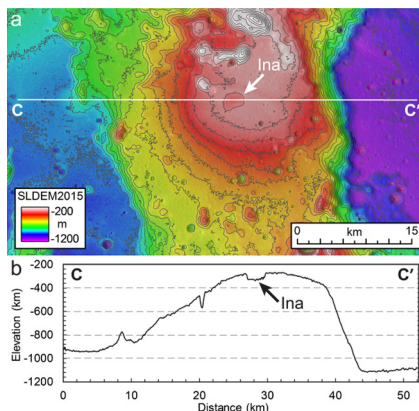


Fig. 1. Topography of the middle portion of Lacus Felicitatis.

face of the walls and rim of Ina, and others forming coalescing bleb-like features on the floor. The summits of the mounds are always below the rim of Ina (Fig. 3); the average elevation of mound summits is ~ 37 m below the rim, with a range of about ~ 33 m; mound summit elevations decrease toward the center of Ina. The optical maturity of the mounds lies between the mature mare surrounding Ina and the very optically fresh hummocky and blocky floor units [8]. Moat-like features, 1–3 m wide and several meters deep and sometimes containing blocks (Fig. 2), are often observed around the edges of mounds, and at the foot of the scarp bounding the Ina interior.

TERRESTRIAL ANALOGS:

The 1959 eruption at Pu'u Pua'i on Kilauea that flooded the Kilauea Iki pit crater ($\sim 0.9 \times 1.6$ km) [9] provides a very well documented example of cyclic pit crater flooding, lava lake formation and drainage. During the eruption, the extruded lava flooded the Kilauea Iki crater floor several times, inflating the lava lake and surface crust by 100s of meters, accompanying by the formation of a rigid and platy thermal boundary layer (TBL). During lava lake inflation and deflation, the magma continuously degassed and bubbles and foams accumulated below the lava crust. In summary, the results of the final stage of dome-building activities are 1) a steep-sided solidified lava ledge or terrace around the lake margins, 2) highly porous surface deposits, and 3) shallow surface layers with abundant vesicles, with porosity up to 40–60 % [10–11].

A NEW MODEL FOR INA FORMATION.

On the basis of geologic context and terrestrial analogs studies, we interpret that the size, location, morphology, topography, optical maturity and spectroscopic characteristics of Ina are consistent with an origin as a drained summit pit crater lava lake atop a 22 km diameter, ~ 3.5 billion years old shield volcano. Latest stage summit activity during the formation of the shield was characterized by very low magma rise rates, final volatile production, and the creation of a highly macro-vesicular floor, the TBL of the summit pit crater lava lake. Concurrently, magmatic foam buildup occurred just below the TBL. The final stages of dike stress relaxation and closure [7] caused the magmatic foam to extrude to the surface through cracks in the TBL to produce the mounds, resulting in final floor subsidence, and drainage of residual lava from the partially solidified floor TBL. The final pit-crater floor deposit consisted of a macro-vesicular chilled floor unit superposed by numerous micro-vesicular magmatic foam mounds. Two factors governed the subsequent evolution of the caldera floor. The micro-vesicular nature of the extruded foams altered the nature of subsequent impact craters (the aerogel effect), causing them to be significantly deeper and smaller in diameter, characterized by less abundant and finer-grained ejecta, and leading to the buildup of a regolith formed predominantly from crushed micro-vesicular foam material [12–13]. Compared to the adjacent ancient surfaces of the shield volcano flanks, these factors led to poor crater retention, more rapid crater

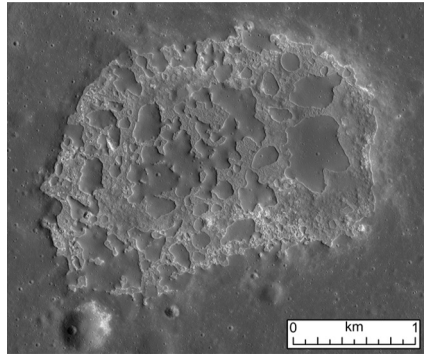


Fig. 2. Image of Ina pit craters.

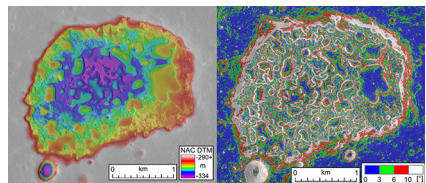


Fig. 3. LROC NAC DTM (left) Topography and (right) of the Ina pit crater.

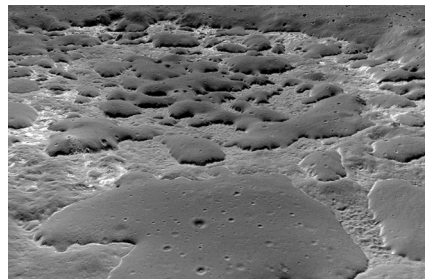


Fig. 4. Perspective view of the interior of Ina. View is looking from east to west across Ina. Vertical exag-geration is ~ 3 .

degradation and anomalously young apparent crater-retention ages for the mounds. The topographically rougher, hummocky and blocky portions of the caldera floor, the macro-vesicular lava lake TBL, is underlain by significant void space caused by late-stage lava lake drainage and TBL buckling and deformation. Subsequent impacts are also influenced by this unusual substrate, forming blockier ejecta than the mounds, and causing finer-grained ejecta to drain into the macro-vesicular substrate, assisted by subsequent impact-induced seismic shaking and sieving. The blocky and relatively optically immature nature of the hummocky pit-crater floor is caused by the loss of fines by persistent seismic sieving, a process that also inhibits regolith buildup and crater retention and recognition. Together, the physical properties of the pit-crater floor mound and hummocky materials both exert an influence on the nature of the regolith substrate and crater formation and retention processes, resulting in an anomalously young age for the Ina summit pit crater floor that more plausibly [7] formed contemporaneously with the underlying shield volcano about 3.5 billion years ago.

REFERENCES:

- [1] Whitaker (1972) NASA SP-289.
- [2] Strain and El-Baz (1980), *LPSC XI*, 2437–2446. [3] Braden et al. (2014) *NGEO* 7, 787-791.
- [4] Schultz et al. (2006) *Nature* 444, 184-186.
- [5] Garry et al. (2012) *JGR* 117, E00H31.
- [6] Head & Gifford (1980) *Moon & Planets* 22, 235-258.
- [7] Head & Wilson (2016) *Icarus*, doi:10.1016/j.icarus.2016.05.031.
- [8] Garry et al. (2013) *LPSC XLIV*, #3058.
- [9] Eaton et al. (1987) *USGS SP-1350*, 1307–1335.
- [10] Richter & Moore (1966) USGS PP-537 -B.
- [11] Mangan & Helz (1986) USGS OPR 86–424.
- [12] Housen & Holsapple (2003) *Icarus* 163, 102-119.
- [13] Flynn et al. (2010) *LPSC LXXI*, #1078.

DID THE ORIENTALE IMPACT MELT SHEET UNDERGO LARGE-SCALE IGNEOUS DIFFERENTIATION BY CRYSTAL SETTLING?

J.P. Cassanelli, J.W. Head

Brown University Department of Earth, Environmental, and Planetary Sciences,
324 Brook St., Box 1846, Providence, RI 02912, USA

Contact: James_Cassanelli@Brown.edu

INTRODUCTION:

The formation of the Moon's primary crust has been followed by over 4 Gyr of surface modification processes, predominantly in the form of impacts [1,2]. Impacts are a powerful erosive agent [3], modifying the primary crust through fracturing, brecciation, physical mixing, and through shock-induced melting. The shock-induced melting caused by large impact events (e.g. those producing a crater ~300 km in diameter or greater; [4]) is predicted to generate significant volumes of melt [5,6]. Given the concentration of large impacts distributed across the surface of the Moon, up to ~5% of the Moon's crust [7] may now be comprised of impact melt products. Despite the potentially significant contribution of impact melt to the compositional variability of the lunar crust, the processes involved in impact melt sheet cooling and crystallization are not well understood.

Following an impact event, impact melt is collected in the excavated crater [5] and begins cooling and solidification. Crystallization of the impact melt may then proceed by one of two end-member scenarios: (1) The melt may undergo igneous differentiation during solidification [7] resulting in a newly developed crustal stratigraphy, or (2) The melt may undergo homogeneous solidification and crystallize in equilibrium [7], thus homogenizing the crustal stratigraphy. A critical requirement for igneous differentiation is the ability of nucleated crystals to separate from the impact melt by sinking or flotation driven by density differences.

Here, we perform a case study on the lunar Orientale basin to explore the possibility for igneous differentiation of the Orientale impact melt sheet by assessing the thermal and physical processes driving cooling and crystallization, focusing on crystal settling.

COOLING AND SOLIDIFICATION:

Following the impact event, melt created through shock heating collects in the excavated crater [5]. Morphologic measurements of the Orientale impact structure suggest the thickness of the initial molten impact melt sheet, z , was ~15 km [7] (Fig. 1). Given the observed radius of the melt sheet, this yields an initial melt volume of $\sim 1.5 \times 10^6 \text{ km}^3$ [7], in agreement with scaling law predictions [5,6].

The melt sheet is predicted to initially exist in a completely molten state [3] at a temperature, T_p , with heat radiating away from the upper surface of the impact melt sheet. Radiative top-down cooling leads to the formation of an unstable upper thermal boundary layer (Fig. 1) [8] resulting in a large temperature gradient across the melt sheet, with a configuration characterized by very high Rayleigh

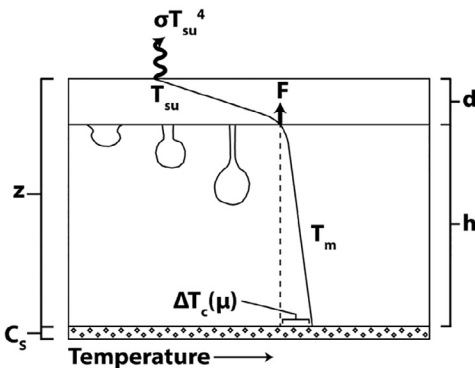


Fig. 1. Configuration of the convectively cooling Orientale impact melt sheet showing the upper thermal boundary layer (d) and the well-mixed interior (h) (where convection maintains a relatively constant interior temperature T_m). The system is divided into the crystal-melt mixture region which contains a fluid phase (z), and the accumulating layer of settled crystals (C_s) which contains no fluid phase.

numbers ($\sim 10^{19}$). Under these conditions vigorous convection would take place in the impact melt sheet interior [8] with down-going plumes of cool dense material formed at the base of the upper thermal boundary layer (Fig. 1).

The convective cooling of the Orientale impact melt sheet can be estimated with empirically derived relationships which describe the thermal convection processes of terrestrial lava lakes [8] due to the generally analogous geometry and thermal processes, and because a flotation crust is not predicted to form (none of the crystallizing products are buoyant in melt of the upper crust; [7]). Cooling of the impact melt sheet is governed by the amount of heat that can be transported through the upper thermal boundary layer (F) and radiated to space (Fig. 1). The heat flux across the upper thermal boundary layer depends critically on the temperature contrast within the mixed interior (ΔT_c) (Fig. 1) which has been shown to be controlled only by the viscosity (μ) contrast across the layer [8]. We model cooling of the Orientale impact melt sheet by estimating total heat loss from the system and by tracking the solid fraction of the melt sheet (Fig. 2a) as well as the evolution of the system viscosity which is dependent upon temperature and suspended crystal content.

CRYSTALLIZATION PROCESSES:

On the basis of analogous scale and convective vigor, we adopt a crystallization framework developed for vigorously convecting terrestrial magma chambers [9] to assess the crystallization processes involved in impact melt sheet solidification. In this framework [9], vigorous convection within the well-mixed interior of the melt sheet holds crystals in suspension and prevents settling. Instead suspended crystals settle at the boundaries of the system, where convective velocities decay to zero. The crystals in suspension settle out at the boundaries over a characteristic residence time [10] which is dependent on crystal size. Terrestrial and lunar impact melt rocks generally exhibit fine-grained holocrystalline to glassy matrices containing up to $\sim 25\%$ mineral clasts ranging in size from ~ 0.1 -1 mm along with a much smaller volume fraction of lithic fragments up to tens of meters in size [11]. Here we adopt a conservative nominal crystal size of 1 mm and later explore the effects of variable crystal size.

We compare the time required to nucleate crystals within the impact melt sheet to the residence time of suspended crystals, to derive the fraction of suspended

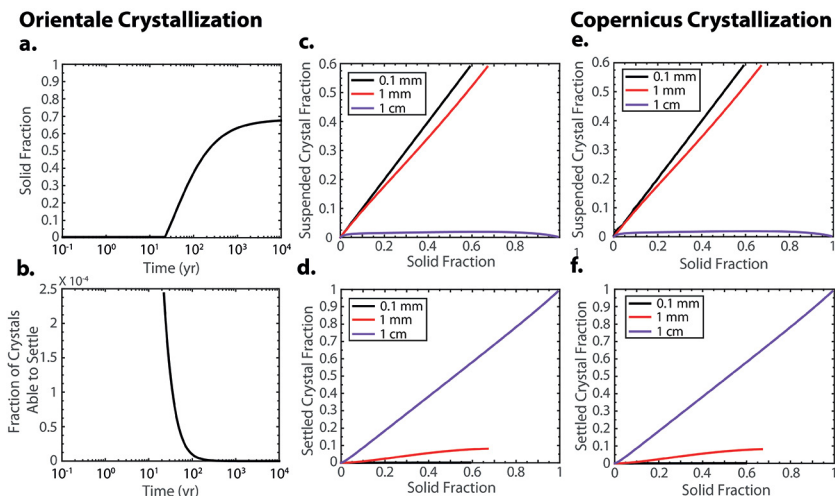


Fig. 2. (a.) Solid fraction of the Orientale impact melt sheet as a function of time during the cooling and crystallization process with a crystal size of 1 mm. (b.) Fraction of 1 mm crystals suspended within the melt which are able to settle throughout cooling and solidification of the impact melt sheet. (c.) Fraction of crystals within the Orientale impact melt sheet that remain in suspension throughout the cooling and solidification process for a range of crystal diameters from 0.1 mm to 1 cm. (d.) Fraction of crystals that have settled out of suspension throughout the cooling and solidification process for crystal diameters from 0.1 mm to 1 cm. As the crystal size decreases, the fraction of crystals kept in suspension throughout cooling and solidification increases while an increase in crystal size causes an increase in the fraction of crystals settled. (e. & f.) Same as (c.) and (d.) for the Copernicus impact melt sheet, showing similar trends in predicted crystallization history

crystals able to settle throughout the cooling process (Fig. 2b). This fraction is used, with the total solid fraction of the melt sheet (Fig. 2a), to estimate the relative fraction of crystals suspended (Fig. 2c) versus settled (Fig 2d) throughout the cooling and solidification process.

CONCLUSIONS:

Analysis of the cooling and crystallization processes of the Orientale impact melt sheet indicates that crystals typical of impact melts 1 mm in size or smaller are not able to efficiently settle out at the boundaries of the convecting melt system (Fig. 2c & 2d). As a result, crystals nucleated within the melt remain in suspension, causing a near-linear increase in the suspended crystal fraction (Fig. 2c) throughout solidification until a maximum value of 0.6 [12] is reached after ~10 kyr (Fig. 2a). Once the maximum suspended crystal fraction is reached the crystal-melt mixture takes on a solid-like behavior [13], subduing convective and settling motions, and causing any further cooling and crystallization to occur in situ. Therefore, the Orientale impact melt sheet is predicted to solidify by equilibrium crystallization with no large-scale igneous differentiation. Analysis of the effects of variable crystal size indicate that equilibrium crystallization is predicted to occur for a dominant crystal size of 0.1 mm, but fractional crystallization is predicted for a crystal size of 1 cm (Fig. 2c & 2d). Assessment of the crystallization history of the thinner Copernicus crater impact melt deposits (Fig. 2e & 2f) indicates that impact melt sheet thickness does not significantly influence crystallization history. The predictions of this analysis are supported by results from petrologic studies [7] which also predict that the Orientale impact melt sheet underwent equilibrium crystallization. These results suggest that crystallization of lunar basin impact melt deposits may have compositionally homogenized up to ~5% [7] of the upper lunar crust.

REFERENCES:

- [1] Hartmann (1980) *Dropping Stones in Magma Oceans*. [2] Head et al. (2010) *Science*, 329, 1504. [3] Melosh (1989) *Impact Cratering*. [4] Baker et al. (2012) *JGR Plan.*, 117. [5] Cintala and Grieve (1998) *Meteorit. Plan. Sci.*, 33, 889. [6] Abramov et al. (2012) *Icarus*, 218, 906. [7] Vaughan et al. (2013) *Icarus*, 223, 749. [8] Davaille and Jaupart (1993) *GRL*, 20, 1827. [9] Martin and Nokes (1988) *Nature*, 332, 534. [10] Suckale et al. (2012) *JGR Plan.*, 117. [11] Onorato et al. (1978) *JGR Sol. Earth*, 83, 2789. [12] Marsh (1981) *Contrib. Mineral. Petrol.*, 78, 85. [13] Pinkerton and Stevenson (1992) *J. Volcanol. Geotherm. Res.*, 53, 47.

MINERAL ASSOCIATIONS IN ENSTATITE CHONDRITES: POSSIBLE INSIGHTS INTO MINERALS ON MERCURY

S.V. Kaufman^{1,2}, C.M. Corrigan¹, T.J. McCoy¹, E.S. Bullock³

¹Smithsonian National Museum of Natural History, Washington, D.C. 20560, USA

²Brown University, Providence, RI 02912, USA

³Carnegie Institution of Washington, Washington, D.C. 20005, USA

Contact: sierra_kaufman@brown.edu

INTRODUCTION:

The parent body for enstatite chondrites and the planet Mercury share many elemental characteristics, as discovered by MESSENGER. Both bodies have high abundances of magnesium and volatile elements such as sulfur, potassium, sodium, and chlorine [1-4]. Due to their similarities, the two bodies are thought to have formed under similar conditions in the same area of the protoplanetary disk. Thus, enstatite chondrites may provide a useful proxy for determining the mineral phases that host elements on Mercury [5].

Djerfisherite, a potassium sulfide [6] $[K_6(Fe, Cu, Ni)_{26}S_{26}Cl]$, has been suggested as a host for chlorine on Mercury [4]. Djerfisherite is hypothesized to form through the sulfidization of roedderite [6], the potassium silicate $[(Na, K)_2(Mg, Fe)_2(Mg, Fe)_3Si_{12}O_{30}]$. Roedderite crystallizes under peralkaline conditions $[(Na+K)/Al > 1]$ on an atomic basis. Both minerals form in highly reducing environments such as those thought to have been present during the formation of enstatite chondrites and Mercury [5]. While the composition of Mercury is not peralkaline, the possible association of djerfisherite and roedderite could provide insights into the mineralogy and petrogenesis of the planet.

Although the association of roedderite and djerfisherite in enstatite meteorites has been suggested, few studies have critically examined this relationship. In this study, we examine occurrences of these phases in enstatite chondrites to assess their mechanism of formation.

METHODS:

Thirty-eight enstatite chondrites were analyzed using reflected light microscopy in order to optically search for djerfisherite.

Of those 38, only seven contained djerfisherite. These seven were analyzed using the semi-quantitative electron dispersive spectrometry (EDS) mapping feature of the FEI Nova Nano SEM 600 scanning electron microscope (SEM) based in the Department of Mineral Sciences at the Smithsonian's National Museum of Natural History. Five of these meteorites were determined to contain roedderite. Of these five, three EH3 meteorites - ALHA 77156, ALH 84250, and MIL 07139 - had obvious associations between the roedderite and djerfisherite. Obvious associations were defined as instances where the minerals were touching or in very close proximity with the hypothesized reaction minerals, such as sodium feldspar, in between.

RESULTS AND DISCUSSION:

Mineral associations suggest three possible modes for the formation of djerfisherite and roedderite.

As found in the Pena Blanca Spring aubrite and suggested for the formation of djerfisherite in enstatite chondrites by [6], the co-existence of roedderite and sodic feldspar could suggest evolution of the silicate melt composition. While roedderite requires peralkaline conditions, feldspar requires metaluminous melts. The co-existence of these phases suggests melt evolution from peralkaline to metaluminous causing resorption of roedderite. Elements (notably K) become incorporated into the subsequently crystallizing djerfisherite, as well as sodic feldspar, ensta-

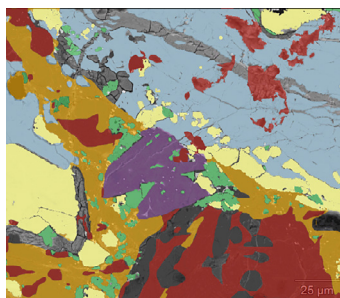


Fig. 1. False color image of djerfisherite (blue) and roedderite (purple) with Fe, Ni metal (yellow), feldspars (red), daubreelite and troilite (green), and enstatite (orange) in ALH 84250. The irregular border of djerfisherite may suggest resorption and formation of roedderite.

tite, and, in some cases, diopside. This texture is observed in two of the three enstatite chondrites (Fig. 1).

While a changing silicate melt composition is required to explain the co-existence of roedderite and plagioclase, sulfidization/de-sulfidization (Fig. 2) reactions may also help explain the transition from roedderite to djerfisherite. If roedderite crystallizes early, an increase in sulfur fugacity – perhaps resulting from sulfur enrichment in the melt during crystallization – might allow crystallization of djerfisherite instead of other K-bearing phases (e.g., potassium feldspar).

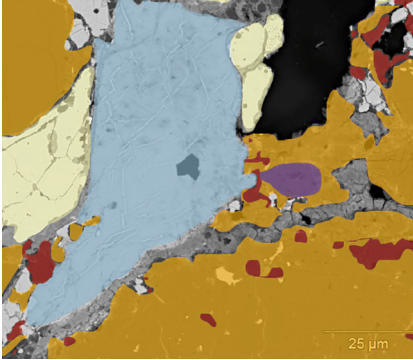


Fig. 2. False color image of djerfisherite (blue), roedderite (purple) and sodic feldspar (red) with metal (yellow) and enstatite (orange) in ALHA 77156. The transition from roedderite to djerfisherite might require both evolving melt compositions and sulfidization.



Fig.3. False color image of co-crystallization of djerfisherite (blue) and roedderite (purple) in Fe,Ni metal (yellow) in ALH 84250.

In some cases, djerfisherite and roedderite co-exist in the absence of any other silicate or sulfide phases, at least in the two dimensions of the thin section (Fig. 3), trapped in Fe,Ni metal. This strongly suggests that the trapped melt was both peralkaline and sulfur-rich and the two phases co-crystallized from this melt.

FUTURE WORK:

Although we have documented the occurrences of roedderite and djerfisherite, quantitative mineral analyses would allow us to better assess possible reactions, particularly given the occurrence of Na and K in subequal abundances in roedderite [6].

If early crystallization of roedderite is an essential first step for the formation of djerfisherite through either chemical evolution of the melt or sulfidization/desulfidization reactions, the identification of djerfisherite as the carrier of chlorine on Mercury could alter our view of melt evolution on that planet. Neither the surface of Mercury as a whole nor any of the distinct geochemical terranes [7] are peralkaline. However, bulk enstatite achondrites (aubrites) are also not peralkaline, yet roedderite occurs in aubrites [8], suggesting an early peralkaline phase to melt evolution. The best opportunity to determine the carrier of chlorine may be provided by the Mercury Radiometer and Thermal Infrared Spectrometer (MERTIS) to be flown on the BepiColombo mission to Mercury [9]. Mid-infrared spectroscopy has already proven useful for constraining feldspar composition and may prove equally useful in detecting the presence of other minerals indicative of the petrogenesis of Mercury.

REFERENCES:

- [1] Nittler et al (2011) *Science* 333, 1847-1850. [2] Peplowski et al. (2011) 333, 1850-1852. [3] Peplowski et al (2014) *Icarus* 228, 86-95. [4] Evans et al (2015) *Icarus* 257, 417-427. [5] McCoy and Nittler (2013) *Treatise on geochemistry* [6] Fuchs (1966) *Science* 153: 166–167. [7] Weider et al. (2015) *EPSL* 416, 109-120. [8] McCoy and Bullock (2016) *Planetesimals Chap. 12* (in press), [9] Hiesinger et al. (2010) *Planetary Space Sci.* 58, 144-165.

CONSTRAINING THE AGES OF ICE DEPOSITS AT MERCURY'S NORTH POLAR REGION: IMPLICATIONS FOR WATER-ICE DELIVERY MECHANISMS

A.N. Deutsch¹, J.W. Head¹, C.I. Fassett², N.L. Chabot³,

¹*Department of Earth, Environmental and Planetary Sciences, Brown University, Providence, RI 02912, USA*

²*Department of Astronomy, Mount Holyoke College, South Hadley, MA 01075, USA*

³*The Johns Hopkins University Applied Physics Laboratory, Laurel, MD 20723*
Contact: Ariel_Deutsch@brown.edu

INTRODUCTION:

Earth-based radar observations and results from the MErcury Surface, Space ENvironment, GEOchemistry, and Ranging (MESSENGER) mission have provided strong evidence that permanently shadowed regions near Mercury's poles host water-ice deposits. Radar-bright deposits near the planet's poles [1] collocate with regions of permanent shadow [2], and enhanced hydrogen concentrations measured by MESSENGER in the north polar region are consistent with models for the radar-bright deposits to be composed primarily of water ice [3].

Although the polar ice deposits have a well-characterized spatial distribution [1–4], their age and source are poorly constrained. One approach to constraining the age of the ice is to determine the age of the host craters in which the ice deposits occur. Here we present crater counts done using images acquired by MESSENGER and available on the Planetary Data System, and use crater size-frequency distributions (CSFDs) to estimate the maximum age of polar deposits in Mercury's north polar region. Determining the age of the youngest ice-bearing craters is an important constraint for Mercury, because it provides an upper limit for the age of their polar ice deposits. Such a constraint has implications for the source, history, and evolution of water and other volatiles in the inner Solar System.

AGE CALCULATIONS OF POLAR ICE DEPOSITS:

Using a geologic map of Mercury from 70°N to 90°N [5], we identified all Kuiperian and Mansurian craters ≥ 40 km in diameter. From maps of permanent shadow and radar-bright deposits [4], we identified which of these craters host water-ice deposits. We investigated the morphology of each permanently shadowed crater hosting a radar-bright deposit using MESSENGER images. Each crater was evaluated for the degree of freshness: the freshest craters display bright, radial rays, crisp rim crests, crisp wall terraces, distinct floor-wall boundaries, radially textured continuous ejecta deposits, well-defined continuous fields of secondary craters, and a general lack of superposed craters [6]. Based on crater morphology, we classified Prokofiev, Kandinsky, and Stieglitz as three of the youngest, primary impact craters ≥ 40 km in diameter between 70°N and 90°N that host water-ice deposits and are large enough to obtain useful CSFDs. Other permanently shadowed primary craters may be younger than Prokofiev, Kandinsky, and Stieglitz, but they do not host a radar-bright deposit [1].

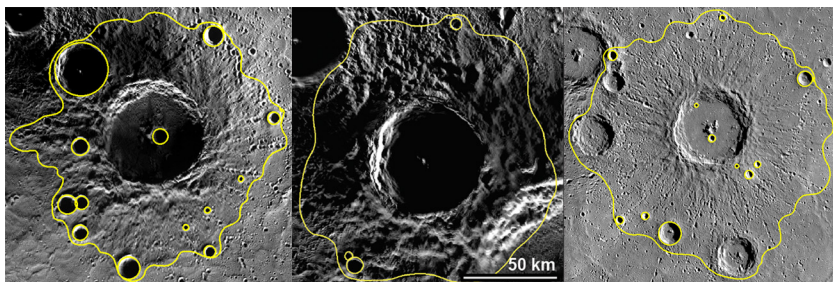


Fig. 1. Mosaics of regions surrounding (a) Prokofiev, (b) Kandinsky, and (c) Stieglitz craters. The ejecta deposits of these three craters are traced in yellow and primary

impact craters (≥ 4 km in diameter) that post-date the craters (within the crater and ejecta) are circled.

Crater counts for these three specific craters were completed using the crater interior and ejecta deposit as the count area (Fig. 1). To avoid including secondary craters, only fresh, circular impact craters ≥ 4 km in diameter were included; a more strict limit of craters ≥ 10 km in diameter does not significantly change the calculated ages. We estimate the absolute ages of Prokofiev, Kandinsky, and Stieglitz craters using CraterstatsII [7] and a range of chronology and production systems (Table 1).

Stieglitz and Kandinsky date younger than Prokofiev. These results and the craters' morphologies [11] imply that the craters are Calorian-to-Mansurian in age. These ages provide upper limits for the age of the ice present within Prokofiev, Kandinsky, and Stieglitz. If the polar ice deposits were emplaced all at once, then the age of Stieglitz and Kandinsky craters provides a maximum age for all water-ice deposits in the north polar region of Mercury.

Crater	Chronology System			
	[8]	[9]	[10] non-porous	[10] porous
Prokofiev ($N = 13$)	3.9Ga+0.1-0.1Ga	3.9Ga+0.1-0.1Ga	3.6Ga+0.1-0.1Ga	3.8Ga+0.1-0.1Ga
Kandinsky ($N = 3$)	3.7Ga+0.1-0.4Ga	3.7Ga+0.1-0.3Ga	1.0Ga+0.7-0.7Ga	3.7Ga+0.1-2.0Ga
Stieglitz ($N = 11$)	3.7Ga+0.1-0.2Ga	3.7Ga+0.1-0.2Ga	1.2Ga+1.0-1.0Ga	3.7Ga+0.1-0.3Ga

Table 1. Ages of Prokofiev, Kandinsky, and Stieglitz derived from a range of chronology and production systems [8–10]. Errors are from counting statistics alone and neglect systematic errors in the age model or fit.

IMPLICATIONS FOR THE SOURCE OF ICE DEPOSITS:

It has been suggested that water ice was delivered to Mercury via episodic impacts of large comets or asteroids [12]. A recent impact could explain the fresh appearance of the sharp boundaries of the low-reflectance layers that insulate the majority of the polar deposits, for there is little positive evidence of regolith gardening having occurred [13]. If a water-bearing impact did deliver the ice deposits to Mercury, then the maximum age of ~ 3.7 Ga determined here for the water ice also constrains the timing of the delivery to an impact that happened more recently than ~ 3.7 Ga.

Radar observations [14] indicate a dominantly pure water-ice composition for the polar deposits, suggesting that the ice was emplaced all at one time. If the ice was delivered in a single event, the estimated ~ 3.7 Ga endmember age provides an upper boundary for the age of the ice-delivering impactor. Identifying the crater caused by an ice-delivering impactor can further constrain this estimation. Recently, mass estimations [15] suggest that the Hokusai impact could have contributed an amount of water ice comparable to the estimated total water mass on Mercury [3]. Hokusai is one of the largest and youngest craters on Mercury [11], with an extensive ray system and lack of superposed craters. The presence of rays indicates that Hokusai was formed in the Kuiperian period, and thus is younger than ~ 1 Ga [6], or possibly younger than ~ 140 – 320 Ma, as suggested by recently revised age constraints [16]. If Mercury's polar ice deposits were delivered in the Hokusai-producing impact, then the age of the polar deposits is much younger than the estimated host crater maximum of ~ 3.7 Ga, and could have been emplaced as recently as the Kuiperian (1 Ga [6] or 320 Ma [16]).

Alternatively, ice from multiple impacts may have accumulated over time, or ice may have been deposited, sublimated, and resupplied (these possibilities being not mutually exclusive). If the water-ice deposits are as old as the ~ 3.7 Ga host craters, then it is plausible that multiple impacts have delivered ice over this substantial geologic time. It is unlikely that Hokusai is unique as a candidate for delivering substantial amounts of ice, and many large impacts could have delivered ice over the last ~ 3.7 Ga.

Finally, it is possible that some of Mercury's polar ice deposits originate from planetary outgassing, and this possibility needs to be explored further, given the substantial evidence for effusive and explosive volcanic activity on Mercury [16]. Most of the volcanic activity on Mercury is ancient (~ 3.7 – 3.9 Ga [18]), although some small-scale and pyroclastic eruptions appear to be more recent.

COMPARISON TO LUNAR POLAR DEPOSITS:

The Moon lacks the concentrated surface ice deposits observed on Mercury. The source of lunar ice deposits has also been suggested to be an episodic delivery mechanism, rather than a steady state source, because of the heterogeneity of the deposits [19]. A recent impact event on Mercury could resolve the lack of Mercury-type polar deposits on the Moon; if Mercury experienced a large cometary impact in the relatively recent past that delivered the majority or all of its observable water-ice deposits, then perhaps the Moon has not experienced a similar event as recently as Mercury.

REFERENCES:

- [1] Harmon J.K. et al. (2011) *Icarus*, 211, 37–50. [2] Chabot N. L. et al. (2013) *JGR Planets*, 118, 26–36. [3] Lawrence D.J. et al. (2013) *Science*, 339, 292–296. [4] Deutsch A.N. et al. (2016) *LPS*, 47, abstract 1134. [5] Prockter L.M. et al. (2016) *LPS*, 47, abstract 1245. [6] Spudis P.D. and Guest J.E. (1988) in *Mercury*, Univ. of Ariz. Press, 118–164. [7] Michael G.G. and Neukum G. (2010) *Earth Planet. Sci. Lett.*, 294, 223–229. [8] Strom R.G. and Neukum G. (1988) in *Mercury*, Univ. of Ariz. Press, 336–373. [9] Neukum G. et al. (2001), *Planet. Space Sci.*, 49, 1507–1521. [10] Le Feuvre M. and Wieczorek M. A. (2011) *Icarus*, 214, 1–20. [11] Kinczyk M. J. et al. (2016) *LPS*, 47, abstract 1573. [12] Paige D.A. et al. (2013) *Science*, 339, 300–303. [13] Chabot N.L. et al. (2014) *Geology*, 42, 1051–1054. [14] Butler B.J. (1993) *JGR*, 98, 15003–15023. [15] Ernst C.M. et al. (2016) *LPS*, 47, abstract 1374. [16] Banks M.E. et al. (2015) *DPS*, 47, abstract 215.06. [17] Head J.W. et al. (2009) *EPSL*, 285, 227–242. [18] Denevi B.W. et al. (2013) *JGR Planets*, 118, 891–907. [19] Spudis P.D. et al. (2010) *GRL*, 37, L06204.

LUNAR CRUSTAL POROSITY, THERMAL CONDUCTIVITY AND URANIUM CONCENTRATION IN THE CRUST AND MANTLE.

V.A. Kronrod, O.L. Kuskov, E.V. Kronrod

Vernadsky Institute of Geochemistry and Analytical Chemistry, RAS

Contact: va_kronrod@mail.ru

The problem of agreement between thermal conductivity coefficient and porosity of the lunar crust and heat source intensities in crust and mantle is discussed. Heat flows and temperature at the depth of lower boundary of the crust satisfy constraints from seismic data. Input parameters of the model are uranium concentrations in crust and mantle, relation between heat conductivity coefficient and porosity, crustal thickness. Constraints on distribution of porosity and heat conductivity coefficients in the crust were obtained. If lunar crust thickness is 34-44 km bulk uranium concentration of the Moon is 17-23.5 ppb and uranium concentration of the crust is 60-210 ppb.

INTRODUCTION:

The thickness and structure of the lunar crust are key constraints on bulk composition, evolution, and formation of the Moon. The Gravity Recovery and Interior Laboratory (GRAIL) mission is providing unprecedentedly high-resolution gravity data, which provide new information on the thickness, density and porosity in the crust [1]. On the other hand, we obtained surface and mantle heat flow and upper mantle temperature estimations in the Moon with inversion of seismic data into temperature [2, 3]. In this work the results of lunar crust modeling are presented. These results are based on matching of thermal constraints and new information about crustal structure.

THERMAL MODEL.

Heat transfer in the crust is described by one-dimensional steady-state thermal conductivity equation. At the upper boundary the temperature $T_0 = 0^\circ\text{C}$ and heat flow J_0 are defined. Heat flow J_0 is calculated from the average uranium concentration (U_{bulk}) in the Moon with the assumption that ratios Th/U and K/U are standard. Heat source intensity in the crust q_{cr} and thermal conductivity coefficient k as a depth (H) function are model parameters. Total average heat source intensity in the crust or average uranium concentration in the crust is defined in the range $U_{\text{cr}} = 40\text{-}240$ ppb. Besides boundary conditions, the temperature at the lower boundary of the crust and its derivative should satisfy constraints obtained from the calculations of probable temperature profiles in the upper mantle of the Moon: $dT/dH_{\text{crust-mantle}} \cong 1.17$ град/км, $T_{\text{crust-mantle}} \approx 300^\circ - 600^\circ\text{C}$ [2, 3].

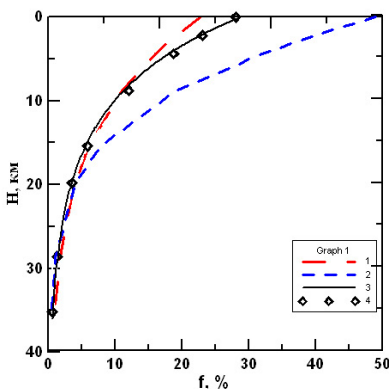


Fig. 1. The porosity (f) dependence on depth (H) in the lunar crust.

- (1) - $P_c = 300$ MPa; $f(0) = 23\%$;
- (2) - $P_c = 200$ MPa; $f(0) = 49\%$;
- (3) - $P_c = 250$ MPa, $f(0) = 28\%$;
- (4) - the model of best approximation from gravitational data [1].

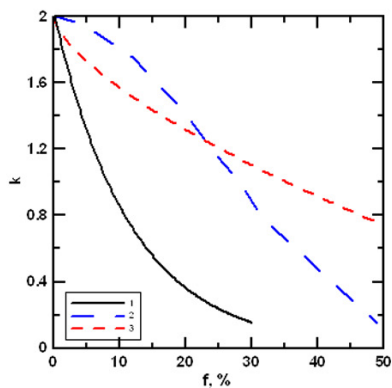


Fig. 2. The heat conductivity coefficient (k) dependence on porosity (f).

- (1) - approximation of experimental data shown in [4];
- (2) - model [5];
- (3) - geometric model [6]

POROSITY.

Effective heat conductivity coefficient considerably depends on material porosity. The lunar crust at the depth of 2 to 10 km (probably to several tens km) was formed as a result of multiple fallings of bodies on lunar surface, its impact destruction and fragmentation. The porous layer of mixed in a random way rock fragments (megaregolith) was formed. Porous crustal medium can be represented as a homogeneous two-phase material (rock) with heat conductivity coefficient k and local average density of the material. Porosity distribution (f) in the generally accepted models of the earth's sedimentary rocks is described by the simple exponential function, which depend on mechanical properties of the rock (P_c). P_c is the characteristic closure pressure of the material. We applied similar approach to the lunar crust to choose coefficients in the exponential model with estimating of porosity distribution from gravitational data. [1], fig. 1.

Heat conductivity. To calculate temperature profiles one must have effective heat conductivity coefficient dependence on depth. Laboratory lunar rocks samples experiments show that porosity is very important cause which controls thermal conductivity of the lunar crust. We considered three methods of k calculation (fig. 2). The most successful results were obtained for the model with approximation of experimental data shown in [4].

HEAT GENERATION IN THE CRUST.

Heat generation in the unit of volume in the crust depends on porosity and concentration of radioactive elements in the matter. In our model exponential mass heat source intensity ($q_m(z)$) distribution with depth was accepted (fig. 3), H_e – the depth where intensity decreases in e times.

CONSTRAINTS ON THE PHYSICAL PROPERTIES IN THE CRUST.

The calculation of the temperature field in the crust revealed that the most strict restriction on the model was the condition $T_{\text{crust-mantle}} \geq 300^\circ\text{C}$, which can be satisfied only in case of very low values of k in the upper layers of the crust. The requirement of low values of k leads to strict restrictions on porosity, fig.2. The porosity distribution should in turn satisfy the data from gravitational estimations, fig. 1. The temperature profile is also affected by the distribution of heat sources in the mantle which depends on the porosity and H_e . To satisfy all these constraints many numerical experiments have been made. It was revealed that the models of the crust with porosity on the surface $f \approx 28\%$ function $f(H)$, which is in agreement with gravitational data (fig. 1), dependence $k(f)$ obtained by the approximation of experimental data (fig. 2), value of $H_e \approx 30$ km, closure pressure $P_c \approx 250$ MPa satisfy all given constraints.

URANIUM CONCENTRATION IN THE MANTLE.

Model parameters calculated enable us to obtain tolerance range of bulk concentration U_{bulk} and mean concentration in the crust U_{cr} , fig. 4. In case of crust depth 34 km U_{bulk} is in the short range of 20 – 23.5 ppb and $U_{\text{cr}} = 125 - 210$ ppb; if $H_{\text{cr}} = 34$ km - $U_{\text{bulk}} = 17-22.5$ ppb, $U_{\text{cr}} = 60 - 160$ ppb correspondingly.

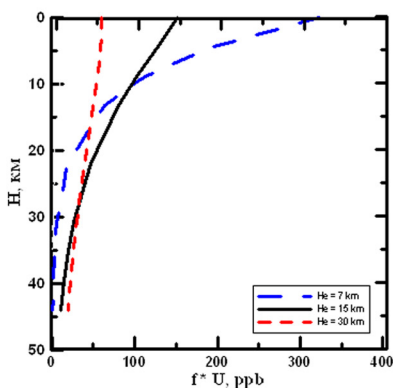


Fig.3. Dependence of uranium concentration $U \cdot f$ with depth H in the lunar crust at different values H_e . $U_{\text{cr}} = 60$ ppb.

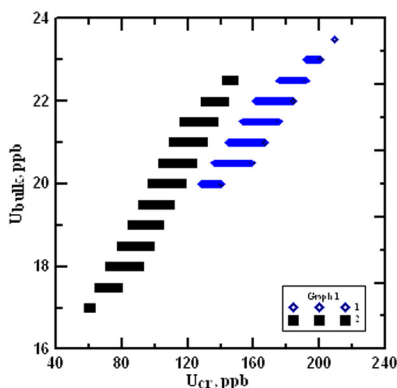


Fig.4. Dependence between bulk uranium concentration U_{bulk} and mean uranium concentration in the crust U_{cr} . $T_{\text{cr-mantle}} \geq 300^\circ\text{C}$. (1) – $H_{\text{cr}} = 34$ km; (2) – $H_{\text{cr}} = 44$ km

CONCLUSION.

Constraints on the temperature $T_{\text{crust-mantle}} \geq 300^\circ\text{C}$ in case of heat flow $dT/dH|_{\text{crust-mantle}} \cong 1.17^\circ\text{C/km}$ ($H_{\text{cr}} = 34\text{--}44\text{ km}$) can be satisfied if crust parameters are as follows: porosity on the surface $f \cong 28\%$, $H_{\text{cr}} \cong 30\text{ km}$, closure pressure $P_c \cong 250\text{ Mpa}$. If $H_{\text{cr}} = 34\text{ km}$ bulk uranium concentration is $20 - 23.5\text{ ppb}$, uranium concentration in the crust - $125 \div 210\text{ ppb}$; if $H_{\text{cr}} = 44\text{ km}$, bulk concentration is $17\text{--}22.5\text{ ppb}$ and crustal concentration is $60\text{--}140\text{ ppb}$ consequently.

ACKNOWLEDGMENTS:

This research was supported by the RFBR grant 15-05-0257 2 and 15-05-01161.

REFERENCES:

- [1] Besserer J. F. et al. 2014. GRAIL gravity constraints on the vertical and lateral density structure of the lunar crust. *Geophys. Res. Lett.*, 41, doi:10.1002/2014GL060240.
 [2] Kronrod V. A., Kronrod E. V., Kuskov O. L. 2014. Constraints on the Thermal Regime and Uranium Content in the Moon: Evidence from Seismic Data. *Doklady Earth Sciences*. V. 455, Part 2, pp. 485–489. http://exp-geochem.ru/JPdf/01_Planetology/01_Rus/29_01_Rus.pdf. [3] Kuskov O.L., V.A. Kronrod, Kronrod E.V. 2014. Thermo-chemical constraints on the interior structure and composition of the lunar mantle. *Phys. Earth Planet. Interiors*. <http://dx.doi.org/10.1016/j.pepi.2014.07.011>. [4] Keihm S.J., Langseth M.G. 1977. Lunar thermal regime to 300 km. *Proc. Lunar Sci. Conf.* 8th p. 499–514. [5] Shoshany Y.D. et al. 2002. Monte Carlo modeling of the thermal conductivity of porous cometary ice. *Icarus*, 157(1), p. 219–227. [6] Smoluchowski, R. 1981. Amorphous ice and the behavior of cometary nuclei, *Astrophys. J.*, 244, L31–L34.

PRELIMINARY DATA ON AGE OF MONS RUMKER REGION

G.V. Makhatadze¹, A.A. Dmitrovsky¹, M.A. Zakharova¹, E.N. Slyuta¹

¹Vernadsky Institute of Geochemistry and Analytical Chemistry, Moscow, Kosygina str. 19, Russia

Contact: makhatadzeg36@gmail.com

INTRODUCTION:

Mons Rumker are known as volcanic dome midst the Oceanus Procellarum (Fig. 1). It is exceptionally attractive place because of spatial superposition of unexplored volcanic features and marine materials of wide spectrum of ages (from Lower Imbrian Series to Copernican System) in the nearest neighborhood around it [1]. That is why this region is supposed for being primary target for russian heavy rover "Lunar Robot-Geologist" [2, 3]. In order to prepare for the mission, the study of morphology, history and matter of the volcanic province has been begun.

The dome's relative elevation is about 1 km and about 70 km in diameter [4]. It has asymmetric slopes, the eastern is gentler. The rise consists of at least ten individual volcanoes, as they are understood. Some of them have calderas at the top.

METHODOLOGY:

The whole research is based upon the LRO WAC images mosaic with mean resolution 100 m/pixel. The crater counting was performed using CraterTools for ArcGIS. The crater statistics was performed using Craterstats.

According to morphologic, topographic [4] and albedo characteristics of the region, the analyzed area was divided in a first approximation into two opposite parts: volcanic province and surrounding marine plain (Fig. 1). Mean ages for both of them were obtained from craters size-frequency distribution [5, 6]. There were used only craters with diameter more than 500 m (Fig. 2, 3).

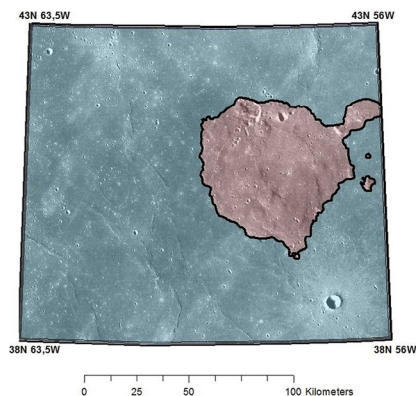


Fig. 1. Study area: red – Mons Rumker volcanic province, blue – surrounding part of Oceanus Procellarum.

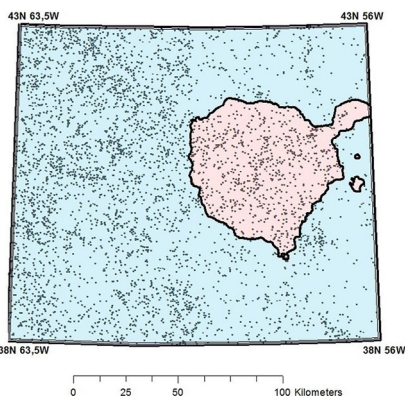


Fig. 2. Craters (black dots) distribution on the study area. Only the craters with radius more than 500 m are taken into account.

RESULTS:

The mean age for the whole volcanic province is seemed to be 3.79 Ga (Fig. 4) corresponding to Lower Imbrian Series [1]. The mean age for the surrounding plain it is 3.77. Though these values are too close, they were derived with statistically significant distinction. It should be noted that there are basalts of different ages in the surrounding plain - from the most common of the Lower and Upper Imbrian Series (3.85 – 3.2 Ga) to less common Eratosthenian (3.2 – 1.1 Ga) and Copernicus (~1.1 Ga) Systems [1].

DISCUSSION:

The resulting mean age of the volcanic province about 120 Ma older than the oldest age obtained by [7] (3.67 Ga). Volcanic province is seemed to overlaying

the Eratosthenian marine lavas and to be covered by Copernician materials [1]. We can suggest that volcanic province was formed as Lower Imbrian focus of marine volcanism on its earliest stages. But only the following could give the exact answer. In order to receive it, we have to provide geomorphologic and geologic mapping in details with obtaining ages for different parts of surrounding plain and volcanic province including mapping on the basis of a high resolution mosaic images and DEMs [4, 8].

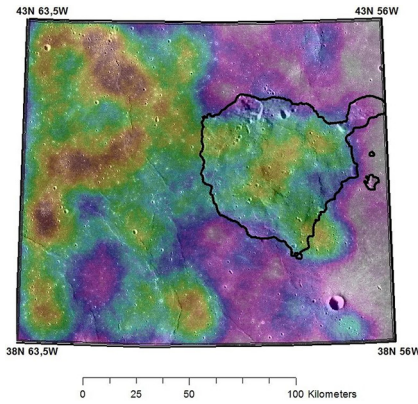


Fig. 3. Crater density on the study area. Calculated by sliding window method. Rainbow color scheme: red – the most dense area, purple – the least dense area.

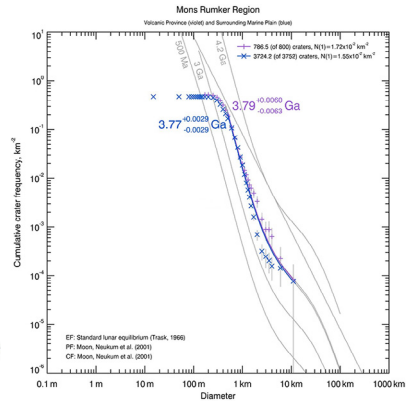


Fig. 4. Cumulative crater density on the surrounding plain (blue) and the volcanic province (purple).

REFERENCES:

- [1] Wilhelms D. E. (1987) The Geologic History of the Moon. Washington. US Government Printing Office.
- [2] Slyuta E. N., Galimov E. M., Marov M. Ya. (2014) Thematic geological survey on the Moon. In: Fundamental space research. V. 2. Solar System. Ed. G.G. Raikunov. Moscow, Fizmatlit. P. 103-128.
- [3] Slyuta E. N. (2016) Project «Lunar Robot-Geologist»: concept, scientific problems, scientific equipment, technical configuration (In this issue).
- [4] Zakharova M. A. and Slyuta E.N. (2016) The multi-scale mapping of Mons Rumker area for designing lunar rover's route purpose (In this issue).
- [5] Trask N. J. (1966) Size and spatial distribution of craters estimated from the Ranger photographs. NASA Technical Report.
- [6] Neukum G. et al. (2001) Cratering Records in the Inner Solar System in Relation to the Lunar Reference System. Chronology and Evolution of Mars. 96, 55–86.
- [7] Zhao J. et al. (2016) The Mons Rumker volcanic complex of the Moon: a candidate landing site for Chang'E-5 mission. 47th Lunar Planet. Sci. Conf. Abst. #1758.
- [8] Zakharova M. A. and Slyuta E.N. (2016) Challenges of the 3D Moon surface mapping (In this issue).

PROJECT «LUNAR ROBOT-GEOLOGIST»: CONCEPT, SCIENTIFIC PROBLEMS, SCIENTIFIC EQUIPMENT, TECHNICAL CONFIGURATION

E.N. Slyuta

*Vernadsky Institute of Geochemistry and Analytical Chemistry, Moscow,
Kosygina str. 19, Russia
Contact: slyuta@mail.ru*

INTRODUCTION:

Research and development of the Moon as a geological object, i.e. the same object as the Earth and other planetary of the Solar system, is the main task of the Lunar Program of research at the present stage, with the involvement of all geological research methods. It is practically impossible to carry out a geological survey around 500 km long route on the Moon at the next few decades with the help of a manned expedition for various reasons. But such routes can be implemented by means of the lunokhod "Lunar Robot-Geologist" at the next 10-15 years. The machine can easily cope with the tasks of thematic geological, geochemical and geophysical survey. The most interesting and important from a scientific and practical point of view area of the Moon should be the main objective of such routes. Such studies should be carried out not only at the stage of automatic research, but also on the stage of manned missions in accordance with their rational combination and interaction.

LUNOKHOD "LUNAR ROBOT-GEOLOGIST":

Lunokhod is developed by Central Research and Development Institute of Robotics and Technical Cybernetics (St.-Petersburg) on the instructions of the Russian Space Agency (Roskosmos) in accordance with the initiative and recommendations of Vernadsky Institute (Moscow). Lunokhod is projected on the basis of universal six-wheel platform, which will also be used for double manned lunar rover, and for freight and other vehicles for movement on the lunar surface (Fig. 1). The concept of the lunar rover "Lunar Robot-Geologist" with a boring rig on board has been designed to perform well-defined scientific and practical tasks at the present stage lunar exploration [1]. The main task of the automatic "Lunar Robot-Geologist" is a thematic geological, geochemical and geophysical survey with sampling of lunar soil and shallow (3-6 m) drilling a few (5 and more) wells for sampling stratified core of regolith (Fig. 2). Planned length of the route rover is about 400 km. The magnetometry, gravimetry, active and passive seismic experiment and logging measurements are also planned. One of the tasks of the "Lunar Robot-Geologist" is also deploying of the automatic research station of long-term monitoring (ARS) in accordance with the project Lunar Basic Network [2]. On the board of "Lunar Robot-Geologist" is planned

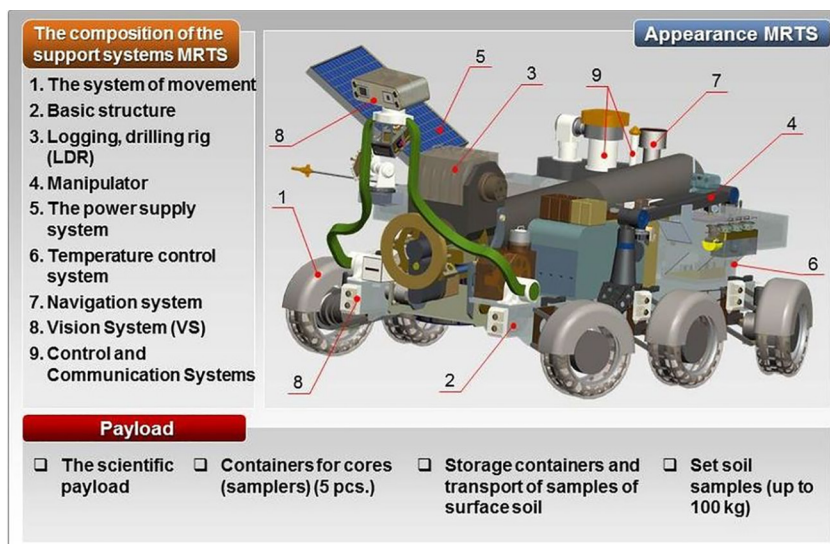


Fig. 1. Appearance of the lunokhod "Lunar Robot-Geologist"

Fig. 2. Lunar regolith

- Delivery of samples of lunar rock back to the Earth is a necessary and key element at lunar research. The important element of information content delivered samples is the method and place of their selection.
- Lunar regolith has a complex layered structure in the form of a stratified sequence of layers of material from nearby impact craters since the formation of the bedrock.
- The larger crater, the farther fly jets. Stratified core of regolith contains information about the composition and age of the regolith and bedrock not only in drilling site, but also quite a large surrounding area.
- If in the vicinity of the borehole are even minor displays of rare composition of lunar rock, which can not be detected on the surface, with a high probability these rock will also be presented in the form of one of the layers in the core regolith.
- Drilling depth up to 15 meters is sufficient almost the entire surface of the Moon and with the necessary reserve will provide the complete stratified column of regolith since the formation of the bedrock.

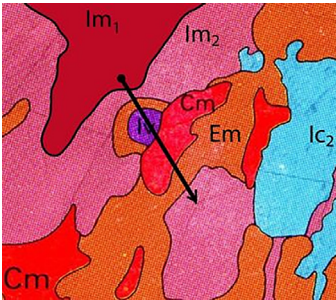
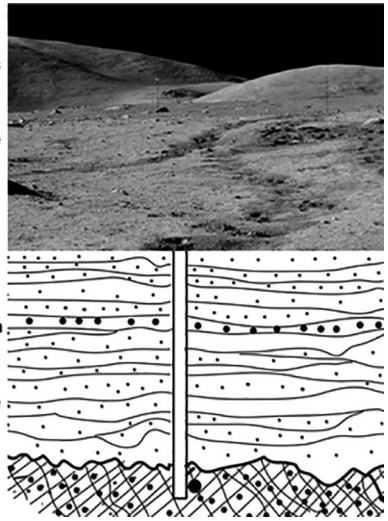


Fig. 3. Geologic map of Mons Rümker region [3]. Im1 – Lower Imbrian Series basalts; Im2 – Upper Imbrian Series basalts; Em – Eratosthenian System basalts; Cm – Copernican System basalts; lv – volcanic province; Ic2 – crater material from Mare Imbrium basin. The arrow length is ~400 km.

to install the following scientific equipment: 1) Scientific navigation devices – radio beacon, TV-spectrometer, IR-spectrometer, TV-camera working field; 2) Instruments for geophysical research – set for active and passive seismic survey, geological radar, logging device, magnetometer and gravimeter; 3) Instruments for studying the composition of the lunar soil and gases – gas analyzer for the study of weakly bound volatiles in lunar regolith and for the study of gas concentration and composition of the lunar atmosphere, gamma-spectrometer and neutron detector; 4) The sampler devices – drilling rig and manipulator with cassettes for the collection and storage of core samples and soil samples.

The rover to be used in areas where there are a variety of complexes of rocks of different ages, genesis, composition and spectral classes. According to the geological structure the Mons Rümker region in the northwestern

part of the Oceanus Procellarum is one of the primary landing sites and research areas for the lunokhod “Lunar Robot-Geologist” [2] (Fig. 3).

The second major problem that can be solved with the help of the lunokhod “Lunar Robot-Geologist”, is a search and reconnaissance to assess the content

Table 1. Features “Lunar-Geologist”	
Time active functioning, year	1-1,5
Cruising range - not less, km	400
The maximum speed, km/h	5
Average speed, km/h	2-3
Long gradeability, degrees	25°
The angle of the longitudinal dynamic stability, degrees	32°
The angle of the longitudinal dynamic stability, degrees	38°
The height threshold surmounted obstacles, mm	250
The radius of the working area of manipulator, m	3
The total weight of scientific equipment, kg	300-400
The total weight of the “Lunar-Geologist”, kg	1200-1400

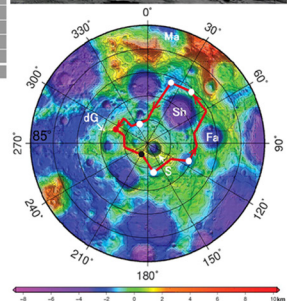
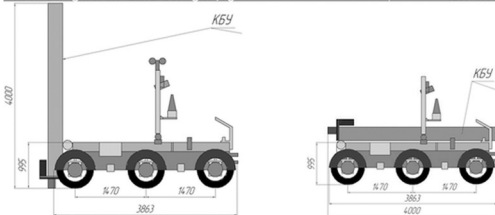


Fig. 4. The outline route (~400 km) at the South Pole (bottom). Topographic map by SC «Kaguya» [4]. S – Crater Shackleton, dG – Crater de Gerlache, Sh – Crater Shoemaker, Fa – Crater Faustini, Ma – Mount Malapert. A - South Pole (Shackleton crater); B (up) – black circle (89.225° S, 240° E); C - red circle; D - Sverdrup crater rim; M - Mount Malapert [5].

and distribution, and delineation of lunar resources, such as loosely coupled gas and frozen volatiles in the Polar regions of the Moon, as well as pre-exploration of the potential deployment location of the Lunar Polar Observatory (Fig. 4).

On board the rover is planned to install a manipulator and drilling device of the next generation LB10, with a potential drilling depth up to 15 meters, which is being developed taking into account the experience of successfully operated LB9 on board the "Luna-24". Delivery to Earth of samples collected is planned by the automatic transport spacecraft, which meets the rover at the end point of the route, and later with the help of the crews of manned missions.

REFERENCES:

- [1] Slyuta E.N., Galimov E.M., Marov M.Ya. (2014) Problems of Selenology. In: Fundamental space research. V. 2. Solar System. Ed. G.G. Raikunov. Moscow, Fizmatlit. P. 52-97.
- [2] Slyuta E.N., Galimov E. M., Marov M.Ya. (2014) Thematic geological survey on the Moon. In: Fundamental space research. V. 2. Solar System. Ed. G.G. Raikunov. Moscow, Fizmatlit. P. 103-128.
- [3] Wilhelms D.E. (1987) The Geologic History of the Moon. Washington. US Government Printing Office.
- [4] Araki H., et al. Science. 2009. V.323. P. 897-900.
- [5] Bussey D. B. J., et al. Nature. 2005. V. 434. P. 842.

EXPERIMENTAL RESEARCH OF THERMAL SENSORS USING CONTROL SAMPLES OF LUNAR SOIL IMITATORS

V.Yu. Makovchuk, D.A. Belov, E.G. Savelev, E.N.Slyuta

Institute of geochemistry and analytical chemistry V.I. Vernadsky (GEOKHI) RAS, Laboratory of the Lunar and Planetary geochemistry, Moscow, Russia
Contact: makovchuk.vladislav@yandex.ru

INTRODUCTION

THERMO-L scientific equipment designed for measuring thermal properties (thermal conductivity, thermal capacity) of surface layer of Moon regolith on board of landing modules on their land sites using active and passive modes. In passive mode temperature of regolith surface is measured. Active mode allows to estimate thermal properties by measuring heat flux. Further this data can be used to calibrate remote measures. Measuring temperature dependence of thermal conductivity coefficient of regolith also gives an estimation of its dispersion. Physical properties of measured characteristics, measurement instruments and expected accuracy of measurements are provided in table 1.

TESTING OF THERMO-L SCIENTIFIC EQUIPMENT

Tests were conducted in laboratory of GEOKHI RAS using analogue of THERMO-L scientific equipment.

Effect of environment temperature and pressure on thermal sensors readings was measured. Control equipment provided measurement of pressure with accuracy $\pm 20\%$. Temperature registration with error below 0,5 K was done for 3 points of vacuum chamber and 12 points of climate chamber. Equipment signals were registered with frequency of 1 Hz using 16-bit analog-to-digital converter and after were saved on computer.

Main goal of vacuum tests was determining degree of rarefaction required for correct equipment work. Test were conducted using active mode. Results have proven the dependence of sensors readings from pressure, specific for switching from convective to molecular and further to vacuum heat transfer. (Fig.1). As seen on graph, when pressure is below 10^{-4} bar the readings of sensors become stable. Measures were done for next pressure levels: $5 \cdot 10^{-6}$, 10^{-5} , 10^{-4} , $2 \cdot 10^{-3}$, $8 \cdot 10^{-2}$, 10^{-1} . According to this, the optimal pressure for reliable measures is at most 10^{-4} bar.

Active measures in vacuum were conducted in short circuit mode (SC) and idle mode (IM).

Short circuit mode matches the maximum rate of heat transfer from inner heater, it's done by making contact of thermal sensitive surface of sensor with thermal conducting mass (copper plate). Thermal contact was ensured by KPT-8 thermal paste. Idle mode matches minimal rate of heat transfer from heater (thermal sensitive surface of sensor was contacting fluoroplastic plate)

As a result, were obtained records of work cycles of scientific equipment with synchronous measurements of temperature in fixed points. This data allowed to conduct a thermal graduation of thermal sensors.

Below provided data, obtained during one of work cycles of thermal sensors in idle mode (Fig.2) and short circuit mode (Fig.3). Color shows data from similar groups of sensors in different blocks of sensors (red – TM1, TM4, TM7; blue – TM2, TM5, TM8; brown – TM3, TM6, TM9). Signals of sensor block SB1 – continuous line, SB2 – dashed line, SB3 – dot line.

SUMMARY

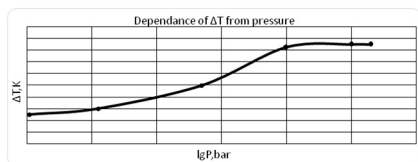
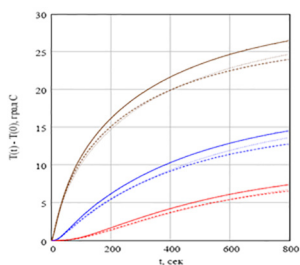
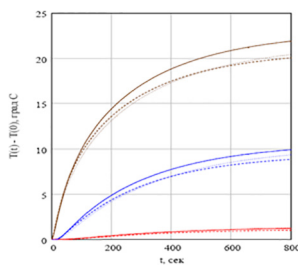
1. Measurements provided univocal results. During measurements, readings for each of samples were different, that shows interpretability of obtained results.
2. To make a model of thermal properties definition more measurements must be conducted for more reliable statistic data.

REFERENCES:

1. Alifanov O.M. Inverse problems of heat exchange. M.: Mashinostroyeniye, 1988. 200p. (in russian)
2. Tichonov A.N., Arsenin V.Ya. Methods of solution of ill-posed problems. M.: Nauka, 1979. 285 p. (in russian)

Table 1. Objectives and goals of THERMO-L scientific equipment

Goals of experiment	Scientific objectives	Measured characteristics	Physical properties of measurements	Measurement instruments	Expected accuracy of measurements
Measurement of thermal properties of lunar soil	Measurement of lunar soil temperature	Measurement of temperature of surface layer in passive mode	Interval of measured temperatures $\pm 150\text{ }^{\circ}\text{C}$	Surface sensors based on cermet and platinum thermometers	$\pm 0,1\text{ }^{\circ}\text{C}$
	Measurement of thermal conductivity and thermal capacity	Measurement of temperature of surface layer in active mode	Interval of measured temperatures $\pm 150\text{ }^{\circ}\text{C}$	Surface sensors based on cermet and platinum thermometers	$\pm 0,1\text{ }^{\circ}\text{C}$

**Fig. 1.** Dependence of temperature difference between sensors near heater and near thermal sensitive surface from pressure. Reading were made after 300 seconds of heating.**Fig. 2.** Dependence of temperature change from time (conversion of signals TM1-TM9) in idle mode**Fig. 3.** Dependence of temperature change from time (conversion of signals TM1-TM9) in short circuit mode

IMITATORS OF THE LUNAR SOIL FOR LARGE-SCALE FIELD EXPERIMENTAL RESEARCH

E.A. Grishakina, V.Yu. Makovchuk, E.A. Ivleva, E.G. Savelev, D.A. Belov, E.N. Slyuta

*Institute of geochemistry and analytical chemistry V.I. Vernadsky (GEOKHI) RAS, Laboratory of the Lunar and Planetary geochemistry, Moscow, Russia
Contact: orskatya@mail.ru*

INTRODUCTION:

All lunar soil models and imitators are usually made for imitating one or two main properties required for research, modelling and carrying out experiments. It's almost impossible to make full analog of moon regolith which matches all main properties – physical, thermal, electromagnetic and also chemical and mineral composition [1]. Depending on objectives of research and required amounts of lunar soil imitator, used components and production technologies can vary significantly. For example, for testing instruments and soil intake devices using cryovacuum stands in low temperatures and with varying humidity, high quality lunar soil imitator is needed, similar not only by granulometric composition and main physical properties, but also by main rock forming mineral contents different for maria and highland areas of the Moon. For this types of research small amounts of lunar soil imitators of tens and hundreds of kilograms are required. For large-scale natural experiments, for example for drop tests and landing tests of «Luna» mission spacecrafts, building a moon dromes (lunadromes) for testing self-moving and other vehicles made for movement on moon surface, for projecting and testing of moon infrastructure elements, for development and building processing facilities for extraction and enrichment of required resources etc. significantly larger amounts of soil imitators (tens and hundreds of tons) are required. This means that technologies for making small amounts of soil imitators for more precise research are not applicable here, because fine milling of components in large quantities, spreading using sieves and partial mixing require expensive technologies and cost a lot.

LUNAR SOIL IMITATORS:

Several main requirements were considered in process of choosing components of soil imitators:

1. Lunar soil model must imitate only main mechanical properties.
2. Components of soil imitators must be relatively cheap and easily obtainable in large quantities.
3. Making (mixing) of soil imitators and its laying must be doable using accessible industrial methods and instruments.

According to initial requirements next components were chosen: «Slag sand 0.1-5 mm», «Crashed stone and sand mixture 0.1-10 mm», «Granulated slag», « Fly-ash from Cherepetskaya State District Power Plant(SDPP)(№1)», «Fly-ash from Cherepetskaya SDPP (№2)», «Fly-ash from Ryazanskaya SDPP», « Quartz sand 0.5-1.0 mm». Product names were unchanged.

Next properties of chosen components were defined: granulometric composition, volumetric weight, specific gravity, porosity, humidity, modulus of deformation, static and dynamic modulus of elasticity, poisson's ratio, shear modulus, bearing capacity, angle of internal friction, cohesion, uniaxial compression strength (for cohesive soil components). After defining listed properties of each of chosen components, they were mixed in next mass proportions: lunar soil imitator №1 (LS1) – «Slag sand 0.1-5 mm», «Fly-ash from Ryazanskaya SDPP», « Quartz sand 0.5-1.0mm»; lunar soil imitator №2 (LS2) – «Crashed stone and sand mixture 0.1-10 mm», « Fly-ash from Cherepetskaya SDPP (№1)», «Quartz sand 0.5-1.0 mm» (Tables 1,2,3).

SUMMARY:

Both lunar soil imitators are almost similar to original lunar soil, measurement errors are acceptable for choosing lunar soil imitator for large-scale field experimental research.

REFERENCES:

[1] Slyuta E.N. (2014) Physical and mechanical properties of the lunar soil (A review). Solar System Research. V. 48, № 5. P. 330–353

Table 1. Physical properties of soil imitators LSI1 and LSI2

Sample	Constitution	Humidity, %	Density of soil in loose constitution, g/cm ³	Density of air-dry soil, g/cm ³	Particle density, g/cm ³	Porosity, %	Porosity coeff., u.f.	Compactibility, u.f.
LSI1	loose	0	1.50	1.50	2.56	41.30	0.70	1.14
	compact		1.93	1.93		24.72	0.33	
LSI2	loose	0	1.35	1.35	2.35	42.34	0.73	0.98
	compact		1.71	1.71		27.02	0.37	

Table 2. Deformation properties of soil imitators LSI1 and LSI2

Sample	Constitution	Vertical pressure P, MPa	Relative deformation ϵ , u.f.	Porosity coeff. e, u.f.	Compressibility coeff. m, 1/MPa	Odometric modulus of deformation E _{oed} , MPa	Constrained Modulus E _k , MPa	Static elastic modulus E, MPa	
LSI1	loose	0	0.000	0.668					
		0.025	0.085	0.491	7.109	0.1	0.1	5.3	
		0.05	0.099	0.463	1.094	0.9	0.8	12.5	
		0.1	0.109	0.443	0.416	2.4	2.1	18.7	
		0.3	0.127	0.405	0.190	5.3	4.7	42.7	
	0.5	0.136	0.385	0.095	10.5	9.3	99.6		
	compact	0	0.000	0.383					
		0.025	0.002	0.379	0.126		7.9	5.9	15.7
		0.05	0.003	0.378	0.047		21.1	15.7	23.5
		0.1	0.006	0.375	0.071		14.1	10.4	47.0
0.3		0.012	0.366	0.041		24.1	17.9	75.2	
0.5	0.016	0.361	0.028		36.2	26.9	224.9		
LSI2	loose	0	0.000	0.878					
		0.025	0.112	0.668	8.392	0.1	0.1	8.3	
		0.05	0.121	0.651	0.708	1.4	1.3	13.8	
		0.1	0.132	0.630	0.419	2.4	2.1	20.7	
		0.3	0.153	0.590	0.199	5.0	4.5	47.3	
	0.5	0.163	0.571	0.094	10.6	9.5	165.6		
	compact	0	0.000	0.528					
		0.025	0.013	0.508	0.786		1.3	0.9	10.6
		0.05	0.015	0.505	0.157		6.4	4.7	14.2
		0.1	0.019	0.498	0.122		8.2	6.1	21.3
0.3		0.029	0.483	0.076		13.1	9.7	42.5	
0.5	0.036	0.474	0.048		20.8	15.5	135.6		

Table 3. Strength properties of soil imitators LSI1 and LSI2

Sample	Constitution	Density, g/cm ³	Friction coeff., tg φ	Inner friction angle, φ	Cohesion C, MPa

THE NATURAL RESOURCES OF THE LUNAR PROCELLARUM KREEP TERRANE

S.G. Pugacheva, E.A. Feoktistova, V.V. Shevchenko

Sternberg Astronomical Institute, Moscow State University, Universitetsky 13, Moscow 119992, Russia, sve-pugacheva@yandex.ru

INTRODUCTION:

The report provides a data on the chemical composition of the lunar soil in the area of PKT (Procellarum KREEP Terrane). This area encompasses the main part of the "Marea" basaltic volcanism of the visible side of the Moon. KREEP in the name of Procellarum KREEP Terrane title (PKT) means potassium (K), rare earth elements (REE) and phosphorus (P). In the area of PKT according to the data of Lunar Prospector it is observed elevated contents of Thorium, that is a sign of the presence of KREEP-rocks. The area of PKT is located on the visible hemisphere of the Moon. The chemical composition of the surface layer of the Moon in the area of PKT was determined by a gamma spectrometer of the spacecraft Lunar Prospector in 1998 [1,4].

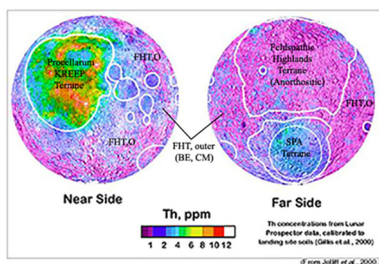


Fig.1. Pore spaces filled with thorium can be seen in PKT areas at the Moon surface space images [photo NASA].

VOLCANIC ACTIVITY IN THE REGION OF PROCELLARUM KREEP TERRANE.

According to lunar soil samples collected by AMIE/SMART, Apollo-17 and Luna-16 expeditions all the Maria on the Moon area of volcanic origin. Age of mare basalt is evaluated starting from 4,3 Ga up to 0,9 Ga billion years ago [2, 3]. Photographs taken by in-orbit satellites of the Moon show the lunar Maria covered with volcanic lava, meandering lava flows, cones, domes and destroyed depressions. Pore spaces filled with thorium can be seen in PKT areas at the Moon surface space images. The researches of a spacecraft Lunar Prospector give a basis to suggest that deep deposits of KREEP-rocks (in the crust, and possibly in the mantle of the Moon) are located in the More Crisium, the More Orientale, and in the South Pole–Aitken basin.

The presence of radioactive elements in the crust of (and/or the mantle of the Moon) in the area of Procellarum KREEP Terrane with a high degree of probability is connected with a volcanic activity on the visible side of the Moon [5].

During the period of volcanic activity (4.3 billion years ago): basalt lavas were spreaded over the lunar surface, filling old dents and other lowlands. Almost a third of the visible side of the Moon is covered with ancient traps, but on the other side, where the crust is thicker, there are still less of them. It was found that almost the entire lunar volcanism was basaltic rather than silicic, i.e. lunar lavas are rich in minerals containing iron and magnesium rather than silicon and aluminum [6].

CHEMICAL COMPOSITION OF THE SURFACE AT THE PKT.

The contents of elemental chemical composition of the soil in the surface layer of the Moon is cited in the catalogs of Lawrence D.J., Feldman W.C. etc. and on the geological maps of the Moon [1, 4]. The catalogs of contain 12 chemical elements of the soil of the surface layer of the Moon. These

include the following chemical elements: oxygen, silicon, titanium, aluminum, iron, magnesium, calcium, uranium, potassium, thorium, hydrogen, iron oxide. The highest spatial resolution of 0.5 degrees is available with the measurements of elemental contents of thorium, hydrogen and iron oxide. The remaining elements of the chemical composition are measured with a spatial resolution of 5 degrees. In the surface layer of the area of PKT it is observed a maximum value of thorium, iron, and oxide iron.

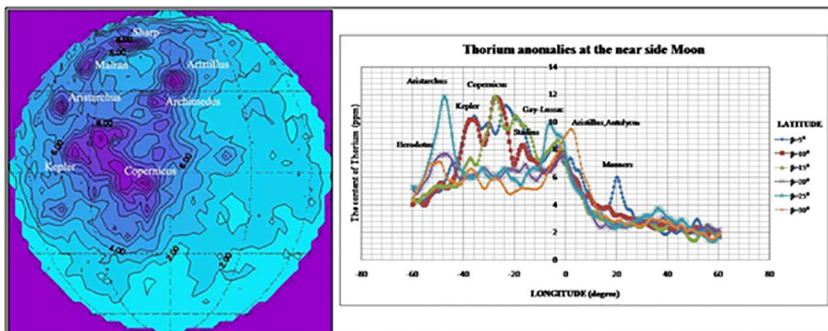


Fig. 2. The names of craters located in thorium anomalies at the PKT. These data are in units of ppm. Thorium data as described by Lawrence [4]. Figures are profiles of Thorium content in the soil regions, which are located along the Latitude.

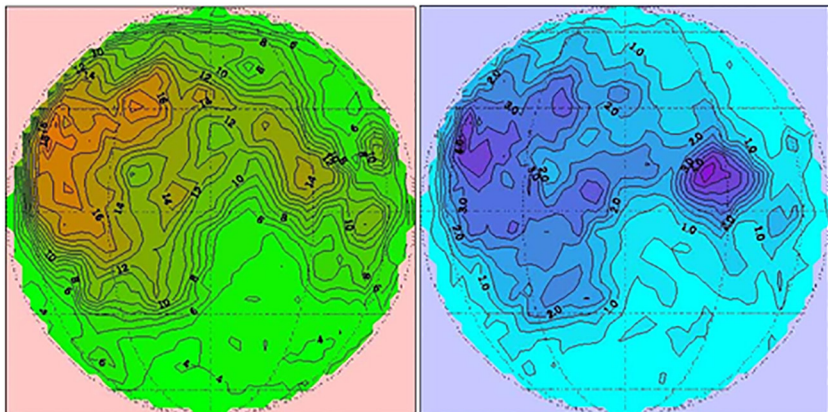


Fig.3. Iron Distribution at the PKT (on the left). Titanium Distribution at the PKT (on the right). All data are in units of weight percent. Iron and Titanium data as described by Lawrence [4].

In the upper layer of soil of PKT in the article to be cited the distribution schedules of elemental contents of titanium, hydrogen, iron oxide and other chemical elements. The maps are localized with the regions of the maximum values of the elemental composition of substances in the soil in the area of PKT. It is cited a comparative table of a composition of lunar samples in the areas of Apollo-17 and the Luna-16 and measurements of Lunar Prospector.

CONCLUSION.

Abounding reserves of thorium on the Moon are the important natural resource. Besides, the metals required for the industry and innovative technologies development have been found out in the lunar regolith. These are vanadium, tantalum, niobium, cadmium, zirconium, yttrium and strontium rare earth metals. The lunar ground investigation via the space vehicles allow us to suppose that the rare earth rocks, thorium and ferric hydroxide underlie in the lunar Maria covered with volcanic lava, on the surface or shallow depth of the lunar surface.

REFERENCES:

- [1] Gillis, J.J., Jolliff, B.L., and Korotev, R.L. (2004) Lunar surface geochemistry: Global concentrations of Th, K, and FeO as derived from Lunar Prospector and Clementine data. *Geochimica et Cosmochimica Acta*, v. 68, p. 3791-3805. [2] Ambrosel W.A., (2009) Timing, Emplacement, and Distribution of Mare-Fill Units in Oceanus Procellarum, a Large Nearside Lunar Basin, Search and Discovery Article #70063. [3] Grimm, R.E.

ON THE POSSIBILITY OF THE EXISTENCE OF DEPOSITS OF VOLATILES COMPOUNDS IN THE AREA NORTHWEST OF THE BOGUSLAWSKY CRATER

S.G. Pugacheva¹, E.A. Feoktistova¹, V.V. Shevchenko¹

¹*Sternberg Astronomical Institute, Moscow University, Moscow, Russia*

Contact: Hrulis@yandex.ru

INTRODUCTION:

The area with high hydrogen concentration was revealed by neutron spectrometer LEND onboard the probe LRO [1]. This area is located to the northwest of the Boguslawsky crater, near the satellite craters Boguslawsky G (71,5°S, 34,3° E), Boguslawsky M (70,5° S, 34,8° E) and Boguslawsky L (70,7° S, 36,5° E) [1]. As we know the high abundance of hydrogen on the surface may be due to the presence of volatiles deposits on the surface and in the subsurface. The goal of this study was to investigate possibility of the existence deposits volatiles in this region.

TEMPERATURE REGIME AND ILLUMINATION CONDITIONS IN THE AREA NEAR THE CRATERS BOGUSLAWSKY G, BOGUSLAWSKY M AND BOGUSLAWSKY L :

Stability of lunar polar volatiles deposits is controlled by the rate of evaporation. Since the evaporation rate is a function of temperature, we have investigated the temperature regime and illumination conditions of this region. To do this, we used the data from altimeter LOLA on board the probe LRO [2]. We used an algorithm Zevenbergen and Thorne (1987) [3] for calculation the morphometric terrain parameters elevation, slope and aspect of each element. Studied region was divided into a grid with a number of elements with step in latitude 0,03 degrees and step in longitude 0,08 degrees. The results of the calculations are shown in Fig. 1. The elevation varies from 0,01 km on the floor of crater Boguslawsky G to 4,5 km on the western part of the walls of crater Boguslawsky. The maximal slopes of this region reach 35° on walls of crater Boguslawsky G and 25° on walls of craters Boguslawsky L. All three craters have flat bottoms (the slope does not exceed 10°) and located on a flat surface (slope values are varied from 0° to 11°). According to our estimates the size of the flat sections inside craters reach 14, 7× 12, 13,5 × 12,5 and 7× 7 km in craters Boguslawsky M, Boguslawsky L and Boguslawsky G, respectively.

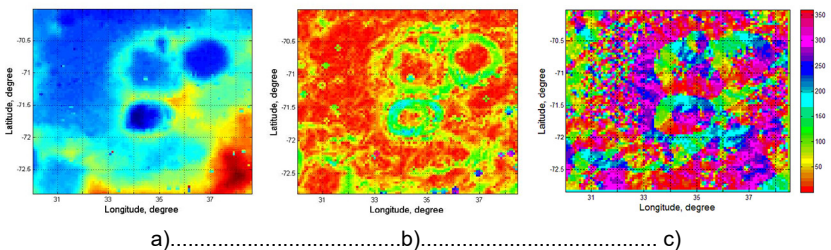


Fig. 1. The height (a), slope (b), and orientation (c) of the studied area.

Figure 2 shows the illumination conditions, average and maximum surface temperatures in the studied area over one diurnal period. For calculation the illumination conditions, we take into account the elevation model constructed as described above. To determine the position of the sun at each time step its angular height and the orientation were calculated. Our results show that the permanently shaded regions are exists in the crater Boguslawsky G and in the crater Boguslawsky L (Fig. 2a). These regions are located in the northern parts of crater's interior. We estimate their areas as the 6 and 0,3 km², respectively. The bottoms of investigated craters remain shaded for 60 - 70% of the diurnal period.

The maximum temperatures within studied craters reach 350K on the southern parts of the inner walls, 270 – 320 K on the their bottoms and 250 – 300 K on the northern parts of the inner walls (Fig.2c). Areas where the maximum

temperatures does not exceed 110 K exist on the northern slopes of the craters Boguslawsky G and Boguslawsky L. The average temperatures of studied region are shown on Fig. 2b.

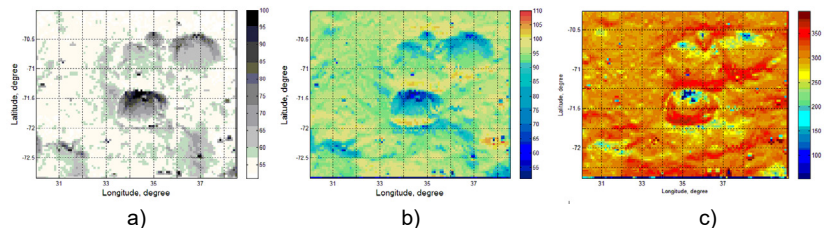


Fig. 2. Illumination conditions (a), average (b) and maximum (c) temperatures in the studied region. 100 % corresponds to permanently shaded area on (a).

We considered the possibility of the existence of deposits of volatile species on the surface and subsurface in the study area. In order to study we chose compounds similar to those found during the LCROSS impact experiment in the crater Cabeo, such as CH_4 , CO_2 , H_2S , NH_3 , SO_2 , C_2H_4 , CH_3OH and water [4,5]. Previous studies [6,7] have been studied temperatures at which the deposition of the volatile compounds are relatively stable against to evaporation. For CO_2 , NH_3 , SO_2 and water are the values 60, 70, 78 and 112 K [6], and for CH_3OH , H_2S , C_2H_4 , CH_4 and CO - 100, 57, 40, 22 and 17 K (Berezhnoy et al, 2012), respectively. According to our calculations, in the northern part of the crater Boguslawsky G, there are areas where possible the existence of stable deposits compounds such as H_2O , CH_3OH , SO_2 , NH_3 , CO_2 and H_2S at the surface. The area of these regions is 10, 9, 7.7, 7.5, 7.4 and 7 km^2 , respectively.

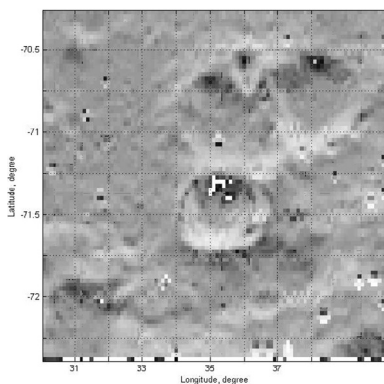


Fig. 3. Locations of areas where the existence of volatiles deposits is possible.

We also studied the possibility of the existence of deposits of volatile species buried by a layer of regolith in the study area. The temperature distribution with depth was obtained by the solution of nonlinear heat-diffusion equation by method of finite differences. As in the model described in [6] the surface of the Moon was modeled as consisting of two layers (top layer with a low density and low thermal conductivity and lower layer with more density and higher thermal conductivity) with parameters described in [6]. To investigate the loss rate of buried volatile species we apply the model from [8]. We find that the existence of volatiles compounds deposits on the surface and subsurface is possible only small area in the northern part of Boguslawsky G crater. The location this area is shown in Fig. 3.

REFERENCES:

1. Mitrofanov I. et al., 2012, JGR, 117, no. 27, p. E00H27.
2. (<http://www.pds.wustl.edu/>)
3. Zevenbergen L.W. and Thorne C.R. 1987, Earth Surface Processes and Landforms, 12(1), p. 47–56.
4. Colaprete A. et al., 2010, Science, 330, p. 463-468.
5. Gladstone G.R. et al., 2010, Science, 333, p. 1703.
6. Vasavada A.R., Paige, D.A. and Wood, S.E. 1999, Icarus, 141, p. 179-193.
7. Berezhnoy A.A. et al. 2012, Advances in Space Research, 50, Is. 12, p. 1638-1646, 2012
8. Schorghofer N. and Taylor G.J. 2007, JGR, 112, E02010.

RELATION BETWEEN MAGNETIC FIELD AND DUST DISTRIBUTION ON THE LUNAR SURFACE

Yangxiaoyi¹ Lu, V.V. Shevchenko²

¹Beijing Planetarium, Beijing, China

²Sternberg Astronomical Institute, Moscow, Russia

Contact: luyangxiaoyi@gmail.com

INTRODUCTION:

From Chang'E-3 orbiter and descent imaging data analysis, we discover distributed highness of lunar surface over the surface landing area - 34 meters. Surveyors 5, 6, and 7 captured the first evidence of dust transport on airless bodies with their television cameras. The conductivity of lunar soil is very low, due to the space environmental effects, the lunar dust is easy to get static electricity. It is also static floating and has strong adsorption capacity due to the interaction among electrostatic lunar dust electrostatic. When the moon probe or astronauts land on the lunar surface, lunar soil and the moon probe, as well as the most parts of the space suits material will produce static electricity in the process of friction with grit and dust. From the Apollo return samples analysis, we know that in lunar soil and dust there are many iron nanoparticles, so these particles' movement are under the influence of a transverse magnetic field.

MOVEMENT OF LUNAR DUST ON MAGNETIC FIELD :

Moon has no global magnetic dipole field. However, data from LP show that the lunar magnetic field is very weak, local intensity usually just a few nT, but had been found the largest concentrations of strong lunar crustal magnetic fields are in regions antipodal to four young large lunar basins: Orientale, Imbrium, Crisium, and Serenitatis. The Chang'E mission spacecraft and rover landed within the mappable area of the higher FeO. There are many magnetic field anomalies in the Imbrium basin, and if there are correlation between depth and formation times, the older anomaly is. Iron uneven distribution is also the important reason. With this work, we know that there are many magnetic anomalies area on the surface of the young basin. The soil particles which have more iron, are moving along electromagnetic belt over "magnetic bubble" or from one bubble to another.

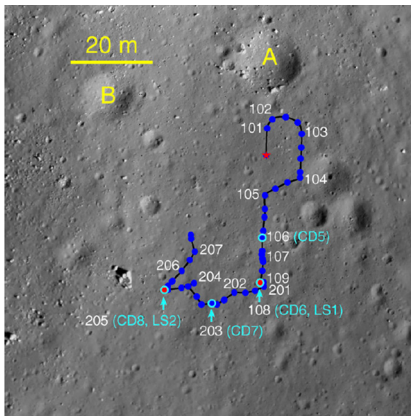


Fig.1. Chang'e-3 landing site and the rover Yutu's track.

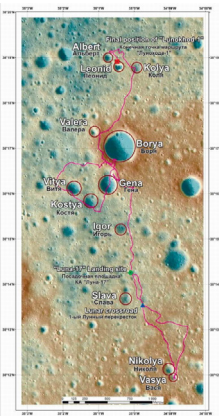


Fig.2. Luna-17 landing site and the rover Lunokhod-1's track.

REFERENCES:

- [1] B.C. Eimer and L.A. Taylor. Lunar regolith, soil, and dust mass over on the moon. 38th LPSC. [2] K. Hemant et.al. NLSI LSC. 2008. Interpreting magnetic anomaly signatures observed over the nearside lunar mare basins. [3] V.Shevchenko et.al. Comparison of Physical and Chemical Properties of the Surface in the Regions of Operation of the Lunokhod-1 and Yutu Rovers on the Moon. Solar System Research, 2016, Vol. 50, No. 2, pp. 81–89. [4] Rene A. Wiesli et.al. Space weathering processes on airless bodies: Fe isotope fractionation in the lunar regolith. Earth and Planetary Science Letters 216 (2003) 457–465 [5] Syou MAKI et. al. Magnetism of Simulated Lunar Regolith of FJS-1. Biomedical Soft Computing and Human Sciences, Vol.19, No.2, pp.35-38.

CUTOFF FREQUENCY – MOMENTUM SCALING LAW FOR IMPACTS INVERTED FROM APOLLO SEISMIC DATA

T. Gudkova¹, Ph. Lognonné², K. Miljković^{2,3}, J. Gagnepain-Beyneix²

¹*Schmidt Institute of Physics of the Earth RAS, B. Gruzinskaya, 10, 123995 Moscow, Russia*

²*Institut de Physique du Globe de Paris, Sorbonne Paris Cité, Univ Paris Diderot, CNRS, F-75013 Paris, France,*

³*Department of Earth, Atmospheric and Planetary Sciences, Massachusetts Institute of Technology, Cambridge, MA 02139-4307, USA*

Contact: gudkova@ifz.ru

INTRODUCTION:

By using a proxy to the local porosity, based on the density of surface craters [1, 2] and well correlated to the most recent GRAIL observations [3], we demonstrate that the seismic cutoff frequencies for 40 selected impacts from the Apollo lunar seismic network correlate with this proxy and therefore likely with the porosity at the impacted areas. Our finding shows that lunar seismic records of meteoroid impacts represent unique geophysical data documenting medium to high-energy (0.1-1 kt TNT yield) impact processes, including the interaction of shock waves with porous media. This work can be applied to the analysis of the seismic data and the investigation of the lateral variations in the Martian regolith.

ANALYSIS OF METEOROID IMPACTS RECORDED BY THE APOLLO SEISMOMETERS:

Source spectra are typically characterized by a plateau at low frequencies and a roll-off slope for high frequency. The frequency corresponding to the intersection of the horizontal low-frequency asymptote and the sloping high-frequency asymptote is called the corner frequency (or cutoff frequency). The cutoff frequency is determined by the source size and material properties of the impacted medium (e.g., porosity).

Meteoroid impacts are well explained by the seismic impulse approach method, which integrates both the impactor and the ejecta momentum [4, 5]. This model fits both impacts: an impact at a short distance and an impact at a long distance, and allows the analysis of meteoroid impacts events occurring in two geologically diverse regions: in the lunar maria and highlands regions.

IMPACT CUTOFF FREQUENCY - MOMENTUM RELATION:

Let us compare the impact momentum and the cutoff frequency (or the time-duration of the seismic excitation process τ) on a log-log scale and determine the power law relationship between these two parameters, such that $\tau = \tau_0 (mv/10^7)^\beta$, where m , v are the mass (kg) and velocity of the impactor (m/s), τ (in s) is the cutoff time and β is the scaling power. The latter is obtained by least square fit of the data set for the momentum transfer of the impactor and seismic impact duration. We find that the values for the time-duration of the seismic excitation process for all data sets (black line, Fig. 1) are described reasonably well by a power law dependence on the seismic moment with $\tau_0 = 0.65$ s and a power of about 0.14.

ESTIMATING THE REGOLITH POROSITY IN THE VICINITY OF THE IMPACTS:

The impacts are sampling very different areas on the Moon, from mare basalts to highlands regions. Therefore, significant variations in the regolith properties can be expected to exist, depending on the surface impact cratering history.

Lunar porosity is a poorly known parameter. The latest porosity map derived from the GRAIL gravity measurements [3] provided estimates of porosity in the farside highlands but not in the nearside maria regions. In this study, we use an indirect proxy to the porosity, based on the impact history of this region. Regolith is generated and sustained by the constant meteoroid bombardment, a process that fractures and ejects surface material. Mega-regolith

has been continuously bombarded by smaller impact events, which contributed to the formation of the upper-most finely grained regolith layer.

We introduce a new function, impact-regolith function approximated to be proportional to the sum of the ejecta created by a number of successive impacts on the lunar surface. Areas with higher crater density are expected to have deeper regolith than the areas with lower crater density. The impact-regolith function used here is considered as a relative measure of the regolith maturity: it is correlated with the porosity and the thickness of regolith as well as the shear velocity of the subsurface layers. In our approach, this function is directly related to the final (present day) thickness of the regolith.

The impact-regolith function is calculated as the sum of the ejecta from the lunar craters between 20 and 500 km in diameter (see crater catalog [1, 2]). Our model assumes a uniform distribution of ejecta around each crater and no mixing of ejecta layers. We do not consider a small number of craters larger than 500 km under assumption that the ejecta from those impacts would have global effects to the Moon that formed the oldest and deepest mega-regolith, which have been buried and compacted by subsequent impacts.

We use the impact model of Housen et al and Holsapple and the HTML software [6-8], to calculate the crater diameter and depth for a range of impact parameters. The estimates of the radial deposition of the ejecta blanket produced by a single impact, and the ejection velocity are related by the ballistic equation. Our model for the ballistic deposition of impact ejecta for a single crater is represented by two components. The central component is defined as a cylindrical core around the impact point that contains 50% of ejecta volume (V_{ejecta}). Its radius is equal to twice the radius of the crater (or one crater diameter D). By applying this calculation to all lunar craters considered in this study and by rigidly stacking the ejecta layers without mixing, we approximated the distribution of the global lunar regolith thickness. Considering the simplifications used in this approach, we defined the obtained distribution as a proxy estimates for the impact-regolith function that is proportional to the real regolith thickness over the entire Moon. Figure 2 shows the locations of the considered meteoroid impact events on the map of the proxy estimates for crustal porosity as described above, and the contour of the GRAIL coverage from [3]. Our porosity estimates [9] are consistent with the GRAIL-derived crustal porosity [3].

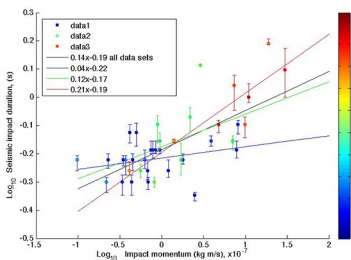


Fig. 1. Trade-off between the impact duration, momentum transfer of the impactor and the impact-regolith thickness at the observed impact locations. The estimated impact-regolith thickness is shown by color. Color lines display the least squares solution for the cutoff frequency for three groups of impacts depending on the regolith thickness in the vicinity of the impact: (1) blue line, impact-regolith function is between 0 and 8; (2) green line, 8 - 13; (3) red line, 13 - 20. Black line is a fit for all Apollo-recorded impacts considered in this study.

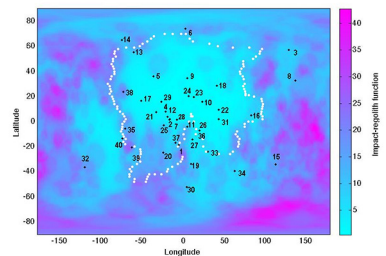


Fig. 2. Locations of the meteoroid impacts are shown on the map of the modeled impact-regolith function. White points represent the contour of the GRAIL coverage from [3]

TRADE-OFF BETWEEN SEISMIC SOURCE PARAMETERS AND THE REGOLITH MATURITY:

By comparing impact momentum, its cutoff frequency (or the time-duration of the seismic excitation process) and the location of the events, we find that the larger the impact, the lower the cutoff frequency, for the impacts occurring in the same surface area. We assume that the difference between

the source cutoff frequencies for the impacts with the same momentum are caused by excitation processes in different geologic regions (the lunar maria and highlands). Let us go back to Fig. 1 and analyze the relationship between the impact duration, the momentum transfer of the impactor and the thickness of the lunar regolith in the vicinity of the impact (or the impact-regolith function). As noted above, the seismic impact duration for all impacts under consideration can be approximated by a power law $\tau = \tau_0 (mv/10^7)^\beta$ with $\tau_0 = 0.65$ s and $\beta = 0.14$ (black line). For our analyses, we divided the available data sets into three groups, depending on the regolith thickness in the vicinity of the impact: the minimum, the mean, and the maximum regolith thickness. The first group involves impact events located where the impact-regolith function is between 0 and 8, the second group between 8 and 13, and the third group between 13 and 20. Color lines display the least squares solution for the power law dependence of the cutoff frequency (or the time-duration of the seismic excitation process τ) for each group. The power law fit in the first group yields values of $\tau_0 = 0.6$ s and $\beta = 0.04$ (blue line, impact-regolith function is between 0 and 8), the second group: $\tau_0 = 0.67$ s and $\beta = 0.12$ (green line, impact-regolith function is between 8 and 13), and the third group: $\tau_0 = 0.64$ s and $\beta = 0.21$ (red line, impact-regolith function is between 13 and 20). Our goal was mainly limited to modeling the variation in the cutoff frequency with the regolith porosity in the vicinity of the impact. Figure 1 shows that the larger the impact, the higher the impact duration, as well as the slopes of the lines increase with the increase of the regolith thickness (the scaling power β is increasing with the regolith thickness). An overlay of the observed seismic cutoff with the map of the lunar regolith distribution shows that there is indeed a correlation between the regolith depth and the seismic cutoff frequency of an impact event.

ACKNOWLEDGMENTS:

This work was undertaken during the preparation phase of the SEIS experiment on InSight mission. The work was supported by the Russian Foundation for Basic Research, project no. 15-02-00840.

REFERENCES:

- [1] Head, J.W. et al. 2010. *Science* 329, 1504–1507;]
- [2] Kadish, S.J. et al. 2011., 42nd Lunar Planet. Sci. Conf. abstr. 1006;
- [3] Wieczorek M.A. et al. 2013. *Science*. 339, 671–675;
- [4] Lognonné, Ph. et al. 2009. *J. Geophys. Res.* 114, E12003;
- [5] Gudkova, T. V. et al.. 2011. *Icarus* 211, 1049–1065;
- [6] Holsapple, K. A. 1993. *Annu. Rev. Earth Planet. Sci.* 21, 333–373;
- [7] Housen, K. R. et al. 1983. *J. Geophys. Res.* 88, 2485–2499;
- [8] Housen, K. R., Holsapple, K. A. 2011. *Icarus* 211, 856–875;
- [9] Gudkova T. et al. 2015. *EPSL*, 427, 57–65.

NEW VELOCITY-DEPTH PROFILES FROM RE-EVALUATION OF APOLLO 17 LUNAR SEISMIC PROFILING EXPERIMENT

A. Heffels¹, M. Knapmeyer¹, J. Oberst^{1,2,3}, I. Haase²

¹German Aerospace Center (DLR), Inst. of Planetary Research, Rutherfordstr. 2, 12489 Berlin, Germany

²Technical University Berlin, Inst. for Geodesy and Geoinformation Sciences, Straße des 17. Juni 135, 10623 Berlin, Germany

³Moscow State University for Geodesy and Cartography (MIIGAiK), Extraterrestrial Laboratory (MEXLab)

Contact: alexandra.heffels@dlr.de

INTRODUCTION:

We re-evaluated seismic data streams of the Apollo 17 Lunar Seismic Profiling Experiment (LSPE). The data streams were filtered using a Wiener filter, enabling new arrival time readings for seismic P-waves. Combining these new travel time readings with geometrically accurate positions of the seismic equipment derived from high-resolution pictures taken by the Lunar Reconnaissance Orbiter Camera (LROC) [1] leads to new estimates for the velocity-depth profiles beneath Taurus-Littrow valley.

In this study positions of only six of the eight Explosive Packages (EP) were used, since the locations of the other two could not be determined in LROC-data. Therefore, we used a set of 24 individual lunar seismograms for our evaluations.

Analysis of this data set leads to either two- or three-layer models. In both cases, data points of the four closest detonations represent the uppermost layer. Arrival times from the other two explosions give some indication, but not compelling evidence, for additional layers. We solve for thickness and seismic P-wave velocities of the layers. We compared results derived with old source-receiver distances published by Cooper et al. [2] and new LRO-derived coordinates.

TWO-LAYER MODELS:

Old distances from Cooper et al. [2] lead to P-wave velocities of 275 m/s for the uppermost layer and 790 m/s for the layer below. The interface between the two layers can be observed at a depth of 169 m. With new LROC-derived coordinates, the results change slightly. The P-wave velocity of the uppermost layer rises to 285 m/s. In contrast, the velocity of the layer below decreases to a value of 775 m/s. The boundary between the two layers is at 170 m.

THREE-LAYER MODELS:

When solving for the three-layer case and using old Cooper distances, we get P-wave velocities of 275, 876, and 2074 m/s for the uppermost, second, and third layer, respectively. The layer boundaries are calculated to depths of 188 and 986 m. Using new LROC-derived coordinates, the velocity

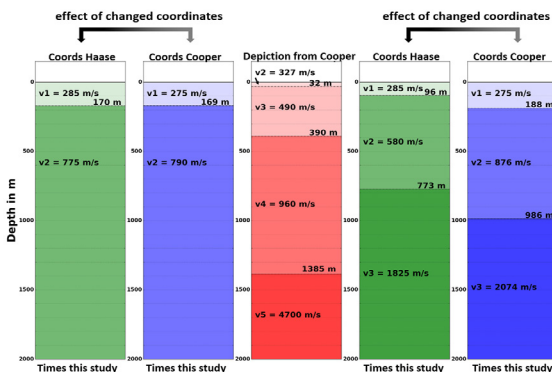


Fig. 1. Comparison of our 2- and 3-layer models to the Cooper model. Red chart represents the velocity-depth profile of Cooper et al. (1974) [3], for better readability of the uppermost 100 m/s-layer with a thickness of 4 m is not depicted here. Blue charts were generated with old coordinates from Cooper et al. (1974) [2], green charts were generated with new LROC-derived coordinates from Haase et al. (2013) [1].

of the first layer slightly rises to 285 m/s, whereas the velocities of the layers below decrease to values of 580 and 1825 m/s. The interfaces between the layers can be found at the reduced depths of 96 and 773 m.

DISCUSSION:

Our results show that the uncertainties in the experiment geometry led to a significant underestimation of the overall velocity increase. Both, the two- and three-layer models, show a strong increase of seismic velocity with depth. Our new models show that the uppermost layers tend to be thinner and have higher velocities when using new LROC-derived coordinates, whereas layers below tend to have lower P-wave velocities. Both effects lead to a more drastic increase of seismic velocity with depth compared to previous analyses (Cooper et al., 1974, [3]). The same trends can be observed when using old p-wave arrival times from Kovach [4] instead of the new p-wave arrival time readings from this study.

ACKNOWLEDGEMENTS:

This study is supported by the Helmholtz Alliance "Robotic Exploration of Extreme Environments – ROBEX", which aims at development of a new seismic experiment concept that can be conducted autonomously by robotic rovers on the Moon.

J. Oberst gratefully acknowledges being hosted by MIIGaIK and supported by the Russian Science Foundation under project 14-22-00197.

REFERENCES:

[1] I. Haase et al. (2013), LPSC XLIV, p. 1966 (abstract). [2] Cooper and Kovach (1975), Proc. Lunar Sci. Conf. 6th, 2863-2879. [3] Cooper and Kovach (1974) *Reviews of Geophysics and Space Physics*, Vol. 12, No. 3, 291-308. [4] R. Kovach (2015), from personal communication.

ILLUMINATION DEPENDENT BEHAVIOR OF THE LUNAR 3 μm ABSORPTION BAND DEPTH IN THE LUNAR CRATER DRYDEN

A. Grumpe¹, C. Wöhler¹, A.A. Berezhnoy², E.A. Feoktistova²,
N.A. Evdokimova³, K. Kapoor¹, V.V. Shevchenko²

¹Dortmund Technical University, Image Analysis Group, Dortmund, Germany

²Sternberg Astronomical Institute, Moscow State University, Moscow, Russia

³Space Research Institute of the Russian Academy of Sciences (IKI), 84/32 Profsoyuznaya Str., Moscow 117997, Russia

Contact: arne.grumpe@tu-dortmund.de

INTRODUCTION:

The behavior of the OH/H₂O on the Moon has been addressed by numerous studies. The present scientific consensus is the existence of OH/H₂O on the Moon in several forms, i.e. water ice, separate H₂O molecules, and OH/H₂O-bearing minerals. The presence of OH/H₂O in the uppermost layer of the lunar regolith was shown by a prominent 2.83.0 μm absorption band measured by the Moon Mineralogy Mapper (M³) which is attributed to the OH/H₂O-bearing minerals [1]. This observation was confirmed by other infrared studies [e.g. 2, 3, 4]. In addition, the 3 μm absorption band was shown to be dependent on the local lunar time [4]. In this study, we show the behavior of the 3 μm absorption band based on M³ data of the lunar crater Dryden (51 km in diameter, centered at 33.0° S, 155.2° W). The M³ data comprise four different local times including the lunar morning, the lunar mid-day and the lunar evening. The analyzed images were not necessarily acquired during the same lunation, but the illumination conditions are nearly identical within each set of local times, i.e. the Euclidean distance of the sub solar coordinates is about 2°.

NORMALIZATION OF THE MOON MINERALOGY MAPPER (M³) DATA:

Due to the loss of the spacecraft's star sensors, the geo-referencing of the M³ data was not sufficient and has been refined after the mission [5]. To remove the residual errors of the geo-referenced positioning data, we manually computed a projective transform that maps each M³ image onto the LROC WAC mosaic [6], respectively.

Since the lateral resolution of available digital elevation models (DEM), e.g. the GLD100 [7], does not match the lateral resolution of the M³ images, we apply a shape-from-shading based method [8, 9] to increase the lateral resolution of the GLD100. The Hapke model [10, 11] was used to describe the reflectance of the surface. We compute a low-resolution local estimate of the single-scattering albedo and adopt the remaining parameters from [12]. Since the radiance measured by the M³ instrument includes a thermal emission component, we compute the refined DEM based on the M³ channel centered at 1369 nm.

In the wavelength range, which was used for the DEM refinement, the thermal emission component is negligible. However, the thermal emission component starts to become significant at a wavelength of about 2 μm and severely distorts properties of the 3 μm absorption band. It is well known that the officially supplied surface temperature maps (<http://pds-imaging.jpl.nasa.gov/volumes/m3.html>) tend to result in an incomplete removal of the thermal emission component [13, 14]. To derive an accurate estimate of the local surface temperature, we compute the pixel-wise local single-scattering albedo of the Hapke model based on the refined DEM and follow the thermal equilibrium based approach in [15]. Since the estimate of the single-scattering albedo depends on the measured radiance and thus on the thermal emission component, we iterate this approach until the temperature changes by less than 0.01 K.

Finally, the M³ spectra are normalized to standard geometry, i.e. 30° incidence angle and 0° emission angle [16]. To measure the time dependence of the 3 μm absorption band, we apply this method to each image, respectively. The strength of the 3 μm absorption band is measured by the R_{2657}/R_{2817} value, the ratio of reflectance at 2657 nm (M³ channel 77) and 2817 nm (M³ channel 81). An increased OH/H₂O content of the surface leads to an increased R_{2657}/R_{2817} value.

RESULTS AND DISCUSSION:

The four M^3 radiance images are shown in Fig. 1. The available images span a range from lunar morning (69 hours after sunrise) to the lunar evening (276 hours after sunrise). The estimated surface temperatures nicely reflect the local daytime and shows increased temperatures at illuminated surface slopes (see Fig. 2). The estimated temperature of the crater floor rises from 330 K in the morning to 370 K at midday. The maximal temperature at the steeply illuminated southern crater wall exceeds 380 K.

Fig. 3 shows the time dependent behavior of the R_{2657}/R_{2817} value. The average R_{2657}/R_{2817} value starts high (1.05 at 08:20 local time), rises slightly (1.06 at 10:12 local time) during the first quarter of the lunar day and is minimal (1.02 at 11:48 local time) at mid-day. Sunrise and sunset occur at 06:00 and 18:00 local time, respectively. Interestingly, the average R_{2657}/R_{2817} value starts to increase in the afternoon (1.04 at 15:20 local time), showing an increasing absorption strength as the surface cools down. The increased R_{2657}/R_{2817} value at 10:12 local time shows a weak positive correlation with the surface temperature with a correlation coefficient of about 0.5, while at the other analyzed local times no correlation is apparent. Neither of the remaining density plots shows a correlation between the R_{2657}/R_{2817} value and the surface temperature (Fig. 4).

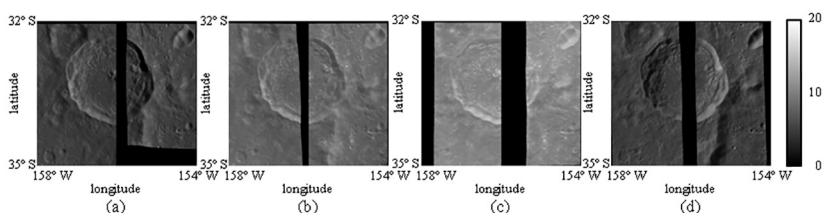


Fig. 1. M^3 radiance at 1579 nm (channel 50) at different local times after sunrise: a) 69 hours (08:20 local time). b) 124 hours (10:12). c) 172 hours (11:48). d) 276 hours (15:20).

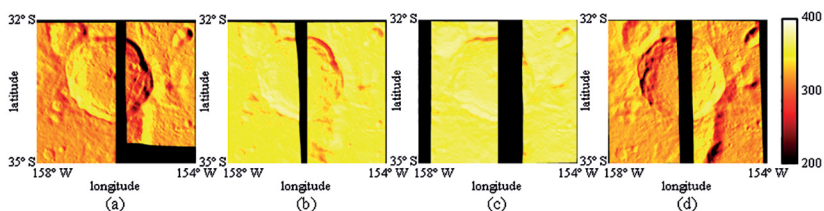


Fig. 2. Estimated surface temperature at different local times after sunrise: a) 69 hours. b) 124 hours. c) 172 hours. d) 276 hours.

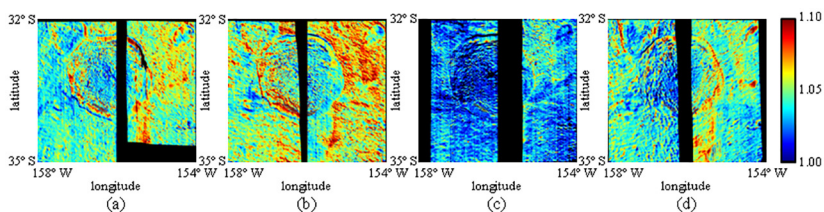


Fig. 3. R_{2657}/R_{2817} values at different local times after sunrise: a) 69 hours. b) 124 hours. c) 172 hours. d) 276 hours.

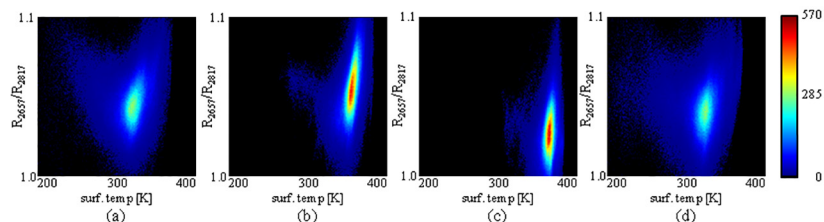


Fig. 4. Density plots showing the dependence of the R_{2657}/R_{2817} values on the surface temperature at different local times after sunrise: a) 69 hours. b) 124 hours. c) 172 hours. d) 276 hours.

SUMMARY AND CONCLUSION:

In this study we analyzed the 3 μm band as seen by the M³ instrument on the near-equatorial crater Dryden. The R_{2657}/R_{2817} value, as a measure of the absorption strength, starts at a high value in the lunar morning, increases slightly and falls to the lowest value in the lunar mid-day. In the lunar late afternoon, the R_{2657}/R_{2817} value increases again but does not reach the high values of the lunar morning. Obtained results can be preliminary explained by solar wind delivery of H₂O/OH to the surface of the Moon during the lunar day. Consequently, we will analyze further regions and compare the results to the lunar crater Dryden.

ACKNOWLEDGEMENTS:

This work is supported by the joint RFBR-DFG grant No. 15-52-12369/WO 1800/7-1.

REFERENCES:

- [1] Pieters C.M. (2009) *Science* 326, 568-672. [2] Clark R.N. (2009) *Science* 326, 562-564. [3] Sunshine J.M. et al. (2009) *Science* 326, 565-568. [4] McCord T.B. et al. (2011), *Geophys. J. Res.* 116(E6), E00G05. [5] Boardman J.W. (2011), *Geophys. J. Res.* 116(E6), E00G14. [6] Speyerer E.J. et al. (2011), 42nd LPSC, Abstract #2387. [7] Scholten F. (2012) *Geophys. J. Res.* 117(E12), E00H17. [8] Grumpe A. et al. (2014) *Adv. Sp. Res.* 53(12), 1735-1767. [9] Grumpe A. and Wöhler C. (2014) *ISPRS Photogrammetry J. Remote Sens.* 94, 3754. [10] Hapke B. (1984) *Icarus* 59, 4159. [11] Hapke B. (2002) *Icarus* 157, 523-534. [12] Warell J. (2004) *Icarus* 167(2), 271-286. [13] Clark R.N. et al. (2011) *Geophys. J. Res.* 116, E00G16. [14] Bandfield J.L. et al. (2016) 47th LPSC, Abstract #1594. [15] Shkuratov Y. et al. (2011) *Planet. Sp. Sci.* 59, 1326-1371. [16] Pieters C.M. (1999) Workshop New Views of the Moon II, Abstract #8025.

SOLAR WIND INTERACTION WITH LUNAR MAGNETIC ANOMALIES: REINER GAMMA

**J. Deca, A. Divin, T. Ahmadi, X. Wang, B. Lembege, S. Markidis,
G. Lapenta, M. Horanyi**

Laboratory for Atmospheric and Space Physics,

University of Colorado Boulder

Contact: jandeca@gmail.com

Discovered by early astronomers during the Renaissance, the Reiner Gamma formation is one of the most peculiar lunar swirls. Observations show that the famous tadpole-shaped albedo marking found on the Oceanus Procellarum is co-located with one of the strongest magnetic anomalies (LMAs) on the Moon. Even more, all available data indicate that every lunar swirl can be associated with a magnetised region. The opposite, however, does not hold and their evolutionary scenario has been under debate since the early Luna missions.

In previous work, using a horizontal dipole, we described the formation of a mini-magnetosphere structure, capable of locally shielding the underlying lunar surface from the impinging solar wind, and hinted at a correlation between the surface albedo brightness and the observed visual surface density pattern. Having implemented now the observed magnetic field vector mapping model by Tsunakawa et al. (2015) in our 3-D fully kinetic and electromagnetic framework iPic3D, we are able to reproduce a surface weathering pattern closely resembling the Reiner Gamma swirl. This clear correlation provides strong evidence that the solar wind standoff theory for lunar swirl formation is the dominant process responsible for the large-scale albedo signatures of the Reiner Gamma region.

This work was supported by NASA's SSSERVI/IMPACT and by the Swedish National Space Board, Grant No. 136/11. Resources supporting this work were provided by the NASA High-End Computing (HEC) Program through the NASA Advanced Supercomputing (NAS) Division at Ames Research Center. Test simulations utilised the Janus supercomputer, supported by NSF (CNS-0821794) and CU Boulder.

ANALYSIS OF EPITHERMAL NEUTRON FLUX FROM BOUGUER ANOMALIES

M.P. Sinitsyn

Sternberg Astronomical Institute Moscow State University,
13 Universitetsky pr., Moscow

Contact: Russia. msinitsyn.sai@gmail.com

INTRODUCTION:

Recently, GRAIL spacecraft recognized a large number of gravity anomalies located concentrically inside of the ring and multi-ring basins of the Moon. In addition, with well-known basins the gravity anomalies located in so called probable impact formations, which arranged under any layers of lava or ejections from neighboring impact processes. As a result, some reliable information has appeared for identification of this unconfirmed impact structures that not have enough any clear external signs. Investigations of the same shock formations using LEND neutron spectrometer data have shown that these structures are characterized by a relative increased epithermal neutron (EN) flux in comparison with areas located just outside the outer ring. Furthermore, directly in the field of gravity Bouguer anomalies, even more increasing EN fluxes have been observed. The neutron flux also tends to increase from the barely distinguishable or completely unknown ring basins that absolutely can't be identified visually. Finally, according to changing of EN flux it is possible to confirm the existence of some invisible circular basins that have no gravitational anomalies.

THE RESULTS OF LUNAR IMPACT BASINS IDENTIFICATION BY GRAIL

According to GRAIL data, there are positive Bouguer gravity anomalies into the center of impact basins with diameters greater than 200 km. and negative ones at the outer ring boundary [1, 2]. The positive anomaly formed due to process of reducing the crust thickness within the inner ring and the raising of upper mantle. A negative Bouguer anomaly is recognized at the vicinity of outer ring as a consequence of increasing the crust thickness. Such phenomena occur due to development of impact process [3, 4].

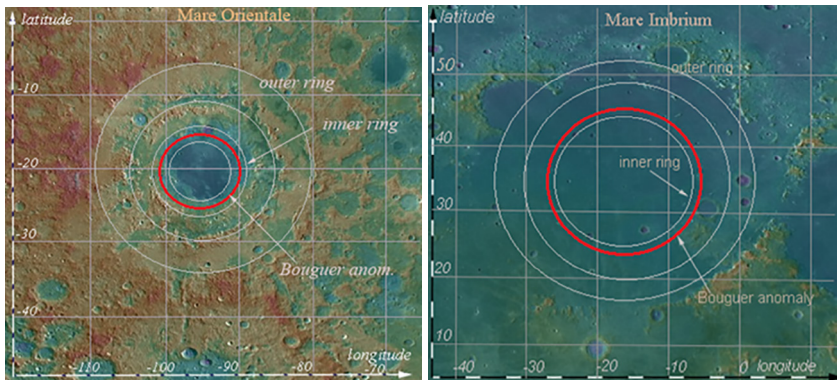


Fig.1. Mare Orientale is a multi-ring basin on the far side and contains of few rings. A wide red line denotes the so-called gravitational Bouguer anomaly. Its size is approximately equal the size of inner ring. Inside the gravity anomaly located one more, smaller ring (left). Mare Imbrium is near side multi-ring basin with ring structures which had been hidden under the later lava flows (right).

Together with well-known basins like mare Orientale and mare Imbrium (fig.1), both requiring confirmation ring structures and unknown ones are included in a list objects under study [1] (tab.1). Such basins are Balmer-Kapteyn, Fitzger-Jackson, Szilard-North and others [5,6,7]. Visually the ring structures may be indistinguishable, as they are under the later impacts and volcanic formations. These structures are particularly numerous on the far side due to its greater age. The age of ones is mainly attributable to Pre-Nectarian. It should be said that the gravitational method of identifying of invisible impact basins allows us to release their structures from the later accretions and recover their actual number.

ANALYSIS OF EPITHERMAL NEUTRON FLUX FROM LUNAR IMPACT BASINS

For analysis of neutron flux the epithermal neutron count rates, obtained by spectrometer LEND have been used [8]. To quantify the EN flow from the surface of the selected area it is necessary to choose a so-called reference zone. The estimation of neutron flux has been produced in comparison with one. In this case, the reference area located immediately behind the outer ring and encompasses the entire ring structure. We estimate the relative changing of neutron flux δ (suppression factor) [9] inside the ring or multi-ring basin compared to these outer reference zone. If the neutron flux is reduced then $\delta > 0$, otherwise the suppression factor is negative.

Table.1. The suppression factors for some lunar impact basins both with Bouguer gravity anomalies and without ones. Most standard errors of δ are not less than 3σ .

Impact basin	lat.	long.	outer ring suppr. (δ)	inner ring suppr. (δ)	Bouguer anomaly suppr. (δ)	Bouguer anomaly (mGal)
well known lunar basins with b. a. recognized by GRAIL						
1.Hamboldt.	57.3	82.0	-0.016	-0.017	-0.022	404
2.Imbrium	37.0	-18.5	+0.003	-0.011	-0.011	375
3.Leibnitz	-38.2	179.2	-0.020	-	-0.038	66
4.Moscoviense	26.1	147.	-0.017	-0.028	-	632
5.Oriental	-20.1	-94.8	-0.014	-0.021	-0.023	720
probable and previously unknown basins with Bouguer anomaly by GRAIL						
6.Fitzger- ackson	25.1	-169.4	-0.008	-0.012	-0.013	224
7.Szilard North	34.3	105.6	-0.020	-	-0.026	182
probable lunar basins without any gravity anomalies						
8.Al-Khwarizmi King	1.0	112	-0.012	-0.015	-	-
9.Bailly-Newton	-73	-57	+0.008	-	-	-
10.Silves- ter-Nansen	83	45	+0.012	+0.012	-	-

We give preliminary results concerning suppression factors for some impact basins commonly for near and far sides (tab.1). In case of absence the gravity anomaly the epithermal neutron suppression factor can confirm the existence of hidden impact basin. These ones are, for example, Al-Khwarizmi King, Bailly-Newton and others.

DISCUSSION

It should be noted that EN neutron flux coming from upper layer of surface (up to 2 meters) and it is mainly determined by the hydrogen content and, perhaps, additional absorbers [10]. However, the crust thickness in gravity Bouguer anomaly is about 10 km. and more [11]. Therefore, the question remains about the reason of the neutron flux changes within the anomaly. Note that the suppression factor is mostly negative for ring structures on the far side, while it is positive on the near side. This may be due to really different hydrogen content in lavas on the different sides of the Moon.

REFERENCES:

- [1] Neumann, G.A. et al., Science Advances, Vol.1, 9 (2015) [2] Zuber, M.T. et al., Science, Vol.266, 5192,1839-1843 (1994) [3] Melosh, H.J., MvKinnon, W.B. Geophys. Res. Lett. Vol. 5, 11, 985-988 (1978) [4] Melosh, H.J., Impact Cratering: A Geologic Process, Oxford Univ. Press, New York, (1989) [5] Wilhelms, D.E., The Geologic History of the Moon, U.S. Geol. Surv. Prof. Paper 1348, Govern. Print. Office, Washington, DC (1987) [6] Cook, A.C. et al. JGR, Vol.105, 12023-12033 (2000) [7] Frey, H.V. et al., Special Paper 477, Geological Society of America, Boulder, CO, pp. 53-75. (2011) [8] Mitrofanov, I.G. et al. Space Sci. Rev. 150(1-4), 183-207(2010b) [9] Boynton, W.V. et al. JGR, 117, E00H33(2012) [10] Lawrence, D.J. et al. Icarus, Vol.255, 127-134 (2015) [11] Wieczorek, M.A. et al. Science, Vol.339, 6120, 671-675 (2013)

STUDYING MOON'S EDGE WITH OCCULTATION METHODS

P. Abouhamzeh

International Occultation Timing Association in Middle East (IOTA/ME)

Contact: parya_abouhamzeh@yahoo.com

INTRODUCTION:

Important type of the occultations with the moon is called grazing occultation. It happens when the moon and target star have occultation for a short time in one of the lunar poles and the target star crosses one of the lunar poles in a so called grazing way. This type of star occultation is one of the shortest kinds of star occultations with the moon. In a grazing occultation, it would be possible to observe the appearance and disappearance of the target star for many times. The causes of this phenomenon are the lunar mountains and edge features. The grazing occultation is one of the most exciting astronomical occultations. You will observe a star that passes slowly in a grazing manner through one of the lunar poles mountains in absence of atmosphere and in this interval the star appears and disappears repeatedly.

Normally the observers who are interested to observe a grazing occultation should wait for a long time in order to observe such an event in their regional location. Therefore in many cases people who want to observe such an event need to travel.

As it was mentioned before, in past few years, the scientific values of grazing occultations have changed. Even a visual observation with the precision of 0.5 second, would lead to very precise information about the moon edge features. More precise information about the exact lunar edge would lead to better determination of the stars' positions. Right now, after the passing of Japanese spacecraft, Kaguya, from the lunar poles, accurate laser topography of that region, where the grazing occultations happen, were performed. These features are almost known with a high accuracy; however the visual or instrumented observations are still valuable and might lead to the improvement of Kaguya mapping. Therefore as it was mentioned before, the grazing occultations are still very useful.

In many cases, the observers of grazing occultations are placed on a line in order to obtain more precise data. In many of occultations' observations team work is an important factor while without a good team work obtaining the accurate and appropriate information is almost impossible.

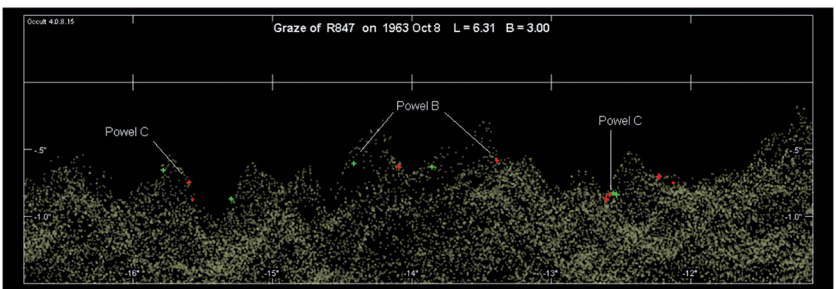


Fig. 1. Reduction of grazing occultation observations

In order to obtain an accurate demonstration of moon poles, many grazing occultations have been observed. In spite of different types of photographs provided by various satellites, the characteristics of moon polar features are still improved by grazing occultations. In past few years, the scientific value of grazing occultations has changed. Understanding the precise structure of the moon edge, which is detectable during a sun eclipse, has still a great significance for instance, for measuring the variation in sun diameter by using the observation of Bailey's beads. Therefore as it was mentioned before, the grazing occultations are still very useful. Sometimes there are two simultaneously grazing occultations at two poles of the moon. This event is a very good opportunity for improvement of the moon diameter via timing.

MOON AS A GIANT DETECTOR FOR NEUTRINO STREAMS FROM PULSARS

O.B. Khavroshkin, V.V. Tsyplov

Institute of Physics of the Earth, Russian Academy of Sciences,

Contact: khavole@mail.ru

Unaddressed existence of extraterrestrial sources of high energy neutrinos was discovered in 2013y. But the most promising addition to supernovae includes objects such as pulsars and closes multiple systems. Relying mainly on its own experience in the search and registration of the seismic response at frequencies of pulsars and close binary stars on Earth and the Moon and using the results to detect solar neutrinos work on the study of modulated neutrino fluxes were continued. The study of the spectra of lunar seismic noise revealed a number of significant spectral peaks that match the frequency to 3-4 significant figures with the frequencies of sending energy pulses from pulsars. At the same time availability of seismic peaks and their characteristics are strongly associated with the shape and depth of the radioactive geological structures of the lithosphere of the Moon. That is the energy of interaction modulated beam of neutrinos from the pulsar radioactive elements Moon differently converted into energy of seismic noise. There have also been recorded seismic peaks well coincides with the period of close binary stars. Some of the peaks previously registered not only as a purely seismic frequency, but as the frequency inherent to radioactive laboratory sources, which further confirms their astrophysical neutrino origin and similarity search became part of high-energy neutrino astronomy.

THE MOON AND PHOBOS: SPECIFIC RESPONSES OF TWO SATELLITES MOVING OFF AND NEARER THEIR RESPECTIVE PLANETS

G.G. Kochemasov

*IGEM of the Russian Academy of Sciences, 119017 Moscow, Staromonethy 35
kochem.36@mail.ru*

Several enigmatic structural and petrologic features of two satellites are widely discussed: origin and global spreading of the high-Ti lunar basalts, mascons, swirls and intercrossing ripples of Phobos (Fig. 1-5). The rippling covers the whole surface of this small satellite constantly moving towards Mars, thus narrowing its orbit and increasing its orbital frequency and speed of rotation. The increasing speed of rotation means increasing angular momentum of Phobos and this must be compensated by diminishing radius. Very "fresh" overall rippling cutting majority of structural forms of Phobos is a trace of this global contracting process (Fig. 1).

Another trend is in the moving off Moon. Loosing its angular momentum due to slowing rotation a necessary compensation is fulfilled by sending dense materials into the crust (Fig. 4, 5). Varying density basalt flows (high, low, very low-Ti) reflect various stages of the slowing rotation process. Various contents of dense mineral component – ilmenite in basalts means various densities of the rock. Iron in basalts can be in less dense dark minerals and denser ilmenite thus influencing overall basalt densities corresponding to requirements of "healing" diminishing angular momentum.

Spectral mapping of basalt types [9] indicate that for large parts of Oceanus Procellarum younger basalts are more titanium rich than the older basalts, thus somewhat reversing the trend found in the returned samples [5]. In some smaller basins spectral mapping also shows titanium richer basalts being older than titanium pure ones [4]. Thus, one may conclude that decreasing rotation rate of the Moon was not smooth but rather uneven.

The deepest SPA Basin must be filled with denser rocks than the shallower Procellarum Ocean filled with basalts and Ti basalts. The Clementine spectral data show presence of orthopyroxene and absence of plagioclase [10] favoring some dense ultrabasic rock. An obvious tendency to approach this type of rock would be to observe it in the Luna 24 samples from also very deep (up to 4.5 km) Mare Crisium. In fragments there prevail pyroxene and VLT-ferrobasalts (Mg-poor). Unusual melt matrix breccia with globules and crystals of Fe metal were also found [1]. Among glass droplets there 40-54 % are irons. Nearly half of the black and brown droplets have either vesicles or iron droplet trains or both [1]. The melt-matrix breccias observed in thin section may be represented in the > 1 mm fragments by the high FeO, high metallic iron particles observed by Morris [2, 8]. A significant portion of Mg enriched fragments in the Luna 24 soil is also observed.

The lunar global magnetic map (Fig. 3) favors a conclusion about some important Fe metal admixture increasing not only magnetism but also overall density infilling of the deepest Basins and Mares. An association of Mg-pyroxene enstatite with Fe-Ni metal is well known in cosmic materials (for an example, E-chondrites). On the Moon enigmatic but characteristic swirls with high albedo, elevated magnetism and diffused boundaries could be presented by this type of high-Mg (light in color) with Fe metal rock. The SPA Basin is one of the enriched with swirls relatively magnetic areas (Fig. 3). In the Reiner Gamma swirl area some small rifts are detectable.

With this rock in mind, we could construct a ladder of ascending UB-basic rocks densities against descending topography (relief): KREEP basalts, low-Ti basalts, high-Ti basalts, VLT-Mg-poor ferrobasalts, and pyroxene (with metal) rich rocks of UB or enstatite metal rich meteorites affinity [6].

Another not less important repairing instrument for the diminishing momentum is an introduction into the crust additional dense masses – mascons. Their bodies are rather typical and characteristic in the lunar crust.

An important role of dense minerals (ilmenite, native Fe) in basaltic-UB covers in the lunar crust witnesses a compensating role of these effusions for loosing angular momentum of moving off satellite. Mascons appear in the crust for the same reason.



Fig. 1. Phobos

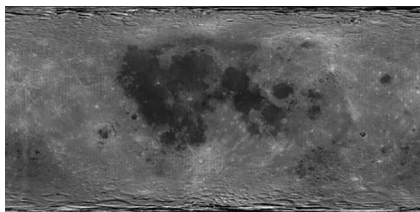


Fig.2. Moon. Albedo: Black- lowland, basalts.

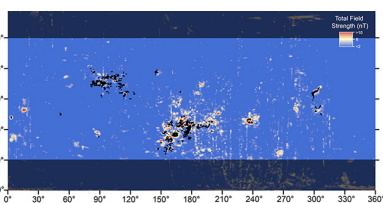


Fig. 3. Moon, magnetism, swirls [3]

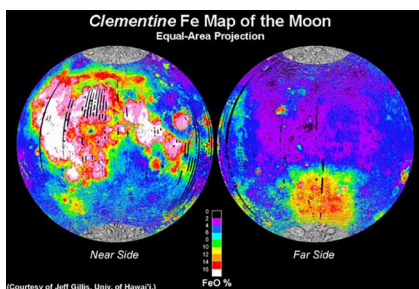


Fig. 4

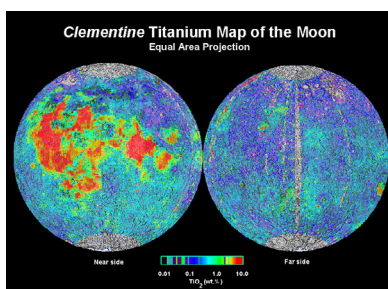


Fig. 5

REFERENCES:

- [1] Basu A., D.S. McKay, U. Clanton, G. Waits, and R.M. Fruland.(1977) Glass particles in Luna 24 drill core soils // Conference on Luna 24, Houston, LPI Contribution 304, p. 14-17.
- [2] Basu A., D.S. McKay, and Ruth M. Fruland. (1977) Petrography, mineralogy and source rocks of Luna 24 drill core soils // the same, p. 18-21.
- [3] Denevi B.W., M.S. Robinson, A.K. Boyd, D.T. Blewett, and R.L. Klima (2016) The distribution and extent of lunar swirls // *Icarus*, v, 273, 15 July 2016, 53-67. doi.10.1016/j.icarus.2016.01.017
- [4] Hiesinger H., R. Jaumann, G. Neukum, J.W. Head, III. Ages of mare basalts on the lunar nearside // *J. Geoph. Res.*, 2000, v.185, #E12, 29239-275.
- [5] Hiesinger H. and J.W. Head III. Ages of Oceanus Procellarum basalts and other nearside mare basalts // Workshop on New Views of the Moon II, 2016, abs.8030.
- [6] Kochemasov G.G. (1999) The deepest lunar SPA Basin and its unusual infilling: constraints imposed by angular momentum considerations // In Workshop on New Views of the Moon II: Understanding the Moon throughout the integration of diverse datasets. Sept.22-24, 1999, Flagstaff, Arizona. LPI Contribution # 980, Lunar and Planetary Institute, Houston, p. 34.
- [7] Milbury C., Schubert G., Raymond C., and Smrekar S. Joint analysis of gravity and magnetic anomalies on the Moon // NLSI Lunar Science Conference (2008), 2164.pdf.
- [8] Morris R.V. (1977) FMR and magnetic properties of Luna 24 soils and >1 mm soil particles// the same, 121-124.
- [9] Pieters C.M.// Proc. Lunar Planet. Sci. Conf., 9th, 1978, 2825-2849.
- [10] Pieters C.M. (1997) *Annales Geophysicae*, Suppl. III to v. 15, p. 792.

REFERENCES:

- [1] Kochemasov G.G. Universe of oscillations: sound-radiowaves-gamma-rays-ether // Geophysical Research Abstracts, Vol. 5, 02159, 2003;
- [2] Kochemasov G.G. Wave modulations in the Solar system bodies and their radio emissions // Geophysical Research Abstracts, Vol. 10, EGU2008-A-01272, 2008. SRef-ID: 1607-7962/gra/EGU2008-A-01272, EGU General Assembly 2008.
- [3] Kochemasov G.G. Radiowaves and tectonic dichotomy: two sides of one coin // Geophysical Research Abstracts, Vol. 4, 2002, European Geophysical Society XXVII General Assembly, Nice, France, 21-26 April 2002.
- [4] Chan K.L., K. T.Tsang, B. Kong, Y-C. Zheng . Lunar regolith thermal behaviour revealed by Chang'E-1 microwave brightness temperature data // EPSL, v. 295, (1-2), 2010, 287-291.
- [5] Zheng Y.C., Tsang K.T., Chan K.L., Zou Y.L., Zhang F., Ougang Z.Y. First microwave map of the Moon with Chang'E-1 data: The role of local time in global imaging // Icarus, May 2012, v. 219, issue 1, p. 194-210

THEORY ROTATIONAL OF THE MOON IN THE FRAMEWORK OF THE “MAIN PROBLEM”

A. Zagidullin, N. Petrova, Yu. Nefed'ev¹

Kazan Federal University

Contact: arhtur.zagidullin@ya.ru

INTRODUCTION:

In the planned lunar experiments the solution of the many problems require a good level of knowledge of the parameters of lunar physical libration (PhLM). The exact theory of lunar rotation will allow the accurate solving the navigation tasks in the near-Moon space and on the lunar surface. Research of the PhLM provides a cheap (without the using the expensive equipment of the space experiments) method to study the internal structure of the Moon. At the present time, there are only a few scientific centers in the world, where the physical libration of the Moon is being developed. The dynamics of the Moon has a lot of differences from other celestial bodies. In the Kazan University the investigation of the PhLM is traditional; a good experience has been accumulated. Everything this allows building and developing the theory of physical libration taking into account the growing requirements for the accuracy of libration observations. Presented work is dedicated to development of a numerical approach in the theory of PhLM. The first step in the implementation of the task is associated with the development of theory in the framework of the main problem of the PhLM.

The paper of the N.K. Petrova [1] has been taken as a basis, the results of whose were used for comparison when the residuals were analyzed.

THE MAIN PROBLEM:

In the construction of the theory libration in the frame of the main problem we have taken the three permissible simplification.

1. The orbital and rotational movements do not affect each other, so we can get solution for libration separately from orbital motion. We used the theory of Schmidt & Brown [3] for the lunar orbital motion, this theory lies as basis in the theory of Petrova.
2. The body of the Moon is considered as a rigid triaxial ellipsoid of revolution. Thus, the Earth-Moon system in this theory is conservative.
3. The Earth and the Sun are considered as the main sources of perturbation. When interacting with the Earth we take into account the 2nd and the 3rd harmonics of selenopotential, and when the Sun the 2nd harmonics is only considered.

HAMILTON'S EQUATIONS IN GENERAL FORM:

To describe the Moon's rotation was used the Hamiltonian approach. The Hamiltonian is the sum of kinetic and potential energy. Since the potential energy is not depended on the rates of change of the canonical coordinates, the construction of Hamiltonian system can be divided into two tasks: obtaining expression of the kinetic energy and obtaining of the potential. The potential can be expanded in a power series on spherical harmonics, and only the first two terms ($n = 2, 3$) were left in the expansion.

$$V(\rho\theta\lambda) = \frac{GM}{\rho} \sum_{n=1}^N \sum_{m=0}^n \left(\frac{a}{\rho}\right)^n [C_{nm} \cos(m\lambda) + S_{nm} \sin(m\lambda)] P_{nm}(\cos(\theta)) \quad (1)$$

The aircraft angles μ - ν - π have been taken as angles describing the lunar physical libration [4]. The origin of the coordinate systems (CS) have been moved to the center of mass of the Moon. The transformation from the inertia CS (ecliptic system) to the dynamic CS (axes are oriented along the axes of inertia of the Moon) was performed using the rotation matrixes (Eq. 2, Fig. 1):

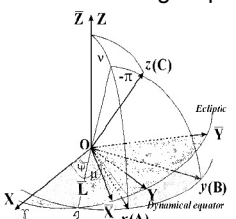


Fig. 1. The main plane of the aircraft angles are shown

$$\begin{pmatrix} \tilde{O} \\ y \\ z \end{pmatrix}_{DSC} = R_x(-\pi) R_y(\nu) R_z(\mu + L) \begin{pmatrix} x \\ y \\ z \end{pmatrix}_{Ecliptic} \quad (2)$$

Thus, the Hamilton system have taken the form (Eq.3), where the linear part has been allocated to obtain the eigenfrequencies of the system.

$$\begin{aligned}
 \dot{q}_1 &= p_1 + F_1(\bar{\mathbf{q}}, \bar{\mathbf{p}}) \\
 \dot{q}_2 &= (1+k_1) \cdot p_2 - k_1 \cdot n \cdot q_3 + F_2(\bar{\mathbf{q}}, \bar{\mathbf{p}}) \\
 \dot{q}_3 &= (1+k_2) \cdot p_3 - q_2 \cdot n + F_3(\bar{\mathbf{q}}, \bar{\mathbf{p}}) \\
 \dot{p}_1 &= F_4(\bar{\mathbf{q}}, \bar{\mathbf{p}}) + Q_1(\bar{\mathbf{q}}) \\
 \dot{p}_2 &= -n^2 \cdot q_2 + n \cdot p_3 + F_5(\bar{\mathbf{q}}, \bar{\mathbf{p}}) + Q_2(\bar{\mathbf{q}}) \\
 \dot{p}_3 &= -k_1 \cdot n^2 \cdot q_3 + k_1 \cdot n \cdot p_2 + F_6(\bar{\mathbf{q}}, \bar{\mathbf{p}}) + Q_3(\bar{\mathbf{q}})
 \end{aligned} \tag{3}$$

The eigenperiod in the longitude has the value of 1057.48 days, and the eigenperiods in the latitude and the node have the values of 27.29 the day and of 62.62 year respectively.

THE RESIDUAL DIFFERENCE:

On the fig.2 the residuals in latitude ($q_2 = v$) and longitude ($q_1 = \mu$) are shown at the interval of 150 years.

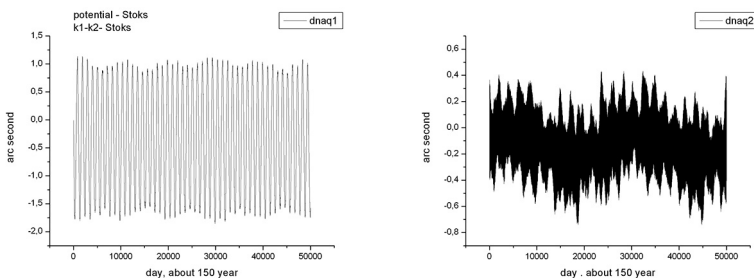


Fig. 2. The residual differences in longitude and latitude

The amplitudes of the residual differences have the values greater than the accuracy of the physical libration. After constructing the Schuster periodograms it was found that the main component in longitude has the period of 1059.57 days and in the latitude/node the periods are of 27.3 days and of 68 years respectively. These periods are close to the resonant periods, so such amplitudes depends on correct calculation in the analytical theory. The similar conclusion was done by G.I Eroshkin [2]. The accuracy of Petrova's theory matches with other analytical theories within ± 0.01 seconds of arc, it can be argued that the accuracy of the solution obtained in the present study is not worse than respective analytical solution.

Let's consider the residuals in comparison with the numerical theory Rambaux, Williams [5] fig. 3.

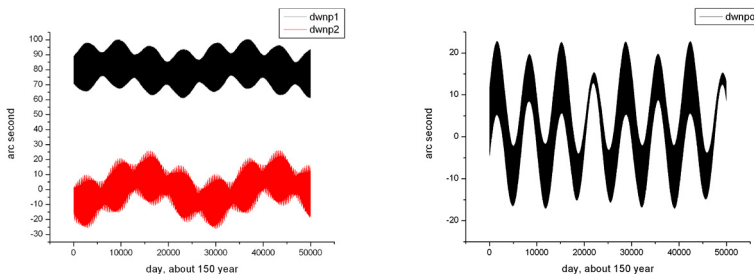


Fig. 3. The residual difference in the direction cosines and inclination

As it can be seen at Fig. 3, in addition to large, tens of seconds, amplitudes of periodic nature the appreciable systematic shifts are observed. That manifests that between the main problem model of PhLM and the exact theory DE, there are significant differences. Part of the differences may be explained by several reasons: 1) Different constants in both theories; 2) Influences of the harmonics 4-th - 6th orders in the expansion selenopotential taken into account in DE; 3) Direct and indirect planetary perturbations are not included in the main problem; 4) In DE the more complicated internal structure of the Moon is considered.

CONCLUSIONS:

In this paper the numerical theory of the physical libration of the Moon was constructed in the framework of the main problems. Analysis of the residuals showed that the quality of the comparison between analytical and numerical solutions depends on the correct consideration of resonant and small denominators terms in the analytical approach. Eroshkin G.I. came to the same results in 1987 year after similar comparisons [2]. This fact is independent proof of the correctness of our development of the numerical theory.

REFERENCES:

- [1] Petrova N, 1996, Earth, Moon and planets v 73, pp. 71-99.
- [2] Eroshkin G.I., 1986, Symp. Figure and Dynamics of the Earth, Moon, and Planets.
- [3] Schmidt, D. S., 1980, Moon and the Planets, vol. 23, pp. 135-164.
- [4] Khabibullin Sh.T, 1998, Kinematics and physics of celestial bodies v.4, N1, pp. 35-42.
- [5] Rambaux N , Williams J. G.,2011, Celest Mech Dyn Astr , v109, pp. 85–100.

ORBITAL IMAGES OF HIGH RESOLUTION AND THEIR ROLE IN THE STUDY OF THE MATTER STATE IN LUNAR CRATERS

M.I. Shpekin¹, R.T. Ferreyra², Ch.R. Mukhametshin¹, A.A. Semenov¹, T.F. Rysayev¹

¹Kazan Federal University, Kazan, Russia

²National University of Cordoba, Cordoba, Argentina.

Contact: MichaelS1@yandex.ru

HIGH RESOLUTION IMAGES:

The concept of high and super-high resolution came into use since the LRO mission. The images with a resolution of 10-20 meters on the lunar surface began to refer to the high resolution and images with a resolution of 1-2 meters - to the super-high. So images of the spacecrafts "Apollo-15, -16, -17" metric cameras are included in the group of high-resolution, and images of the same spacecrafts, obtained by panoramic cameras, this is super-high resolution images. As for the unique images «LRO», it is necessary to emphasize the experimental survey from low orbit, when the resolution reaches two feet on the lunar surface. This is not just a low-orbit, but it was the risky orbit, taking into account the elevation changes on the Moon, which is comparable with an orbital altitude of 25 km.

It is interesting to note that the images of panoramic cameras "Apollo-15,-16, -17", have been digitized recently. At open access these images were posted online almost simultaneously with images «LRO», although the "Apollo" film were taken and delivered to Earth nearly 40 years earlier.

In our study we used "Apollo-15, -17" digitized images (metric camera) as well as "LRO" digital images (narrow-angle camera).

ANALYSIS AND DISCUSSION:

The lunar territory sites in the area of young impact craters Tsiolkovsky and Aitken were selected for the analysis.

We have already paid attention to some features selected craters. So we found quite unusual objects at the bottom of the crater Tsiolkovsky that are not found in other lunar craters [1]. In addition, we paid attention to the glacial-like tongue, slipping from the south-western slope of the crater Tsiolkovsky central peak [2].

The albedo and magnetic anomalies of the crater Aitken has long attracted the attention of [3]. The nature of these anomalies is still a mystery. Just as in the crater Tsiolkovsky crater Aitken has the glacier-like tongue. This tongue also is located in the south-western slope of the central peak of the crater Aitken. However, in contrast to the tongue in the crater Tsiolkovsky, sliding down the slope of the central hill, the tongue of the crater Aitken like "creeps" from the central peak.

These features of two impact craters have been discovered and studied mainly on single images. Due to the unusual elements of the relief it is important to carry out more detailed survey of these areas in a variety of ways. To do this, we have tried to build a 3D-model of the craters on the basis of high-resolution images taken metric cameras "Apollo 15" and "Apollo -17" to look at the study sites from different sides together panoramic images «LRO».

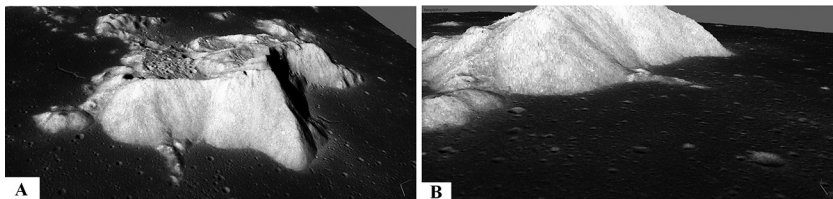


Fig. 1. Fragments of 3D-model for Tsiolkovsky crater. South-western slope of the central peak is shown from two perspectives: the view from the south-west (A) and from the west (B). There are sure visible structural details of glacial-like tongue, and the track of his movements on the slopes of the central peak.

Three-dimensional models were built on the technology embodied in computer program Agisoft Photoscan [4].

3D-model for the central peak of the crater Tsiolkovsky allows better view of the above mentioned glacier-like tongue. Figure 1 presents fragments of the model in the foreshortenings where the tongue is seen from the west and from the south-west. In contrast to the single images details of the tongue structure itself are visible, as well as the place of the slope, where tongue slips out.

Another interesting features of the bottom of the crater Tsiolkovsky is located to north of the central peak. This inclined plateau between the northern part of the central peak and the inner slope of the crater wall. On Figure 2 the plateau is located in the center. From the west the plateau area is adjacent to the tectonic fault, which is located at crater bottom and oriented along crater radius. This part of the plateau far above the eastern edge of which lies directly on the bottom of the crater. On the single panoramic images «LRO» we can see the cluster of boulders at about the center of the plateau, as well as on the western slope of said radial tectonic fault at the crater bottom. There are no other craters on the Moon where similar "structures" take place.

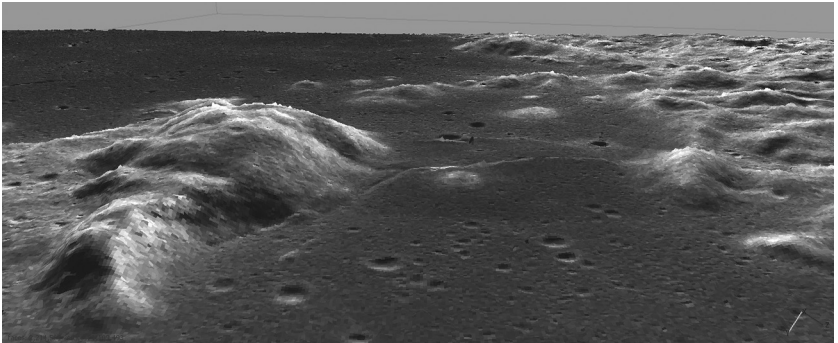


Fig. 2. 3D-model fragment with a sloping plateau at the bottom at the northern part of the crater Tsiolkovsky (itself a plateau in the center of the figure). Barely visible outlines of the far crater wall crest could be seen in the left part of the horizon.

The boulders traces left by them on the slopes of the central peak of the crater Tsiolkovsky are made strong impression. Figure 3 shows the traces of the boulders left on the southern slopes of the central hills. So the size of the disc-shaped boulder at the center of the figure is about 24-30 meters. The topography of boulder trace indicates that the depth of the dent in the lunar soil is comparable to the boulder size. Even if a dent is a quarter the size of a boulder, it must be recognized that the depth of the dent in the lunar soil is about 6-8 meters! Such a significant value can indicate unusual mechanical properties of the soil at a specified slope and the bottom of the crater during the rolling boulders down the slope of the central hills, which in turn raises the question about the state of matter in the crater.



Fig. 3. Site of the crater Tsiolkovsky bottom on «LRO» satellite image, where the disc-shaped «boulder» has stopped after rolling from the slope of the central peak.

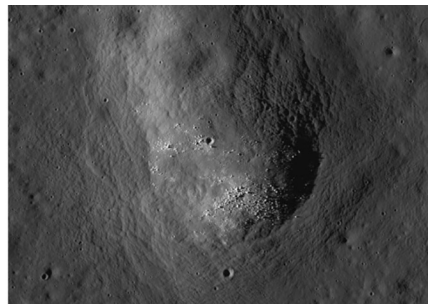


Fig. 4. The front part of the glacier-like tongue of the crater Aitken central peak on high resolution images «LRO» satellite.

Unfortunately, the resolution of the models constructed for the crater Tsiolkovsky, is not enough to carry out a detailed analysis of the bottom territory near the volcano and the plume found by us in 2009 [1].

The analysis of the crater Aitken structure is also linked to its central peak. Figure 5 shows the fragment of the crater model. The figure clearly shows the central crater slide (view from the south-west), as well as the isolated peaks of the crater bottom. The number 5 denotes glacial-like tongue, which

“creeps out” from the south-western slopes of the central peak. The structure of tongue confidently viewed in photographs «LRO». Figure 4 shows a close-up of the front part of the tongue. There are clearly visible boulders scattered radially around the epicenter.

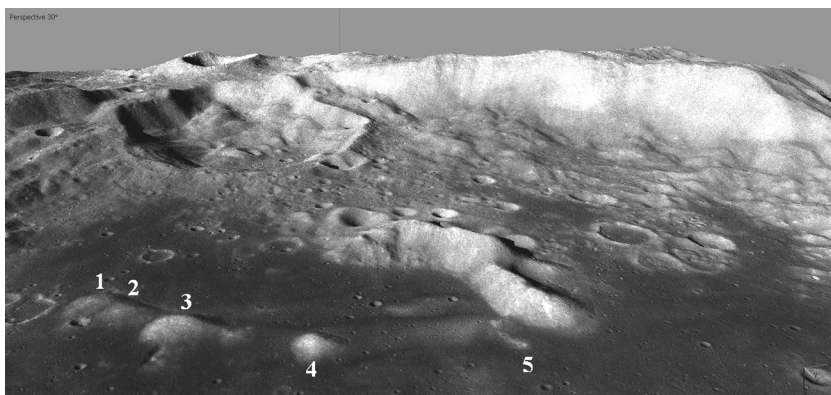


Fig. 5. Fragment of 3D-model for the crater Aitken central part. The digits from 1 to 4 are numbered isolated mountain peaks to the west of the central peak. Digit 5 is marked with glacier-like tongue “getting out” of the south-western slopes of the central peak. 5 impact craters, which may be related to isolated peaks, are visible on the other side of the central peak (to the east).

Nature of glacial-like tongue and isolated mountain peaks is of undoubted interest. There are several versions of its origin. Earlier, we pointed out the similarity of the tongue with the Martian “hourglass”, where the soil contains a significant quantity of frozen water ice and begins to move under the influence of solar heat. Another version of the tongue behavior can be linked to the central peak substance, which have not cooled down yet and continues to give out the energy, accumulated in the cratering process.

“Driving force” of the central peak tongue can be also linked to the shock-wave effect from the later falls in its vicinity. It may be small craters formed on the bottom to the east of the central peak. The shock wave from the impact sites in this case is moving to the west directly on the slopes of the central peak. Furthermore, in this place the most central peak edge outlines are concave, which should lead to increased shock wave effect on the material of peak. That may be enough to release the material of the central peak in the shock wave direction. It should simulate the dynamics of the shock-wave process and conduct quantitative assessments. It is possible that 5 impact craters that lie to the east of the central peak, may be the cause of four isolated mountain peaks to the west of the central peak, and the fifth isolated peak is formed at the moment, and is under the glacial-like tongue state.

CONCLUSION:

Orbital high-resolution images are the basis for the construction of 3D-models. Such models have been built to the most interesting areas of the lunar territory. On the example of two young impact craters is shown that a detailed examination of the relief elements can contribute to the study of the lunar craters matter state.

The experience of the building three-dimensional models convincingly demonstrated the high requirements that apply to the computer's power. Powerful computer with a large operational memory may be suitable

if 3D-model is based on several images of one orbit revolution. Embedding of the two or more images of the orbit turns leads to a significant increase in resources consumed. Complete spatial model with a large number of high-resolution images require processing power class personal supercomputers.

REFERENCES:

1. Shpekin M.I., Barenbaum A.A. Proceedings of 17 Russian sci.conf. student-physicists and young scientists. Ekaterinbourg 2011, p. 476-477
2. Shpekin M.I., Barenbaum A.A. The fourth Moscow Solar System Symposium 14-18 October 2013, Space Research Institute.
3. Hideo Tsunakawa and all. Journal geophysical research, Volume 120, Issue 6, June 2015, p.1160–1185, DOI: 10.1002/2014JE004785.
4. Agisoft PhotoScan Professional Edition, ver. 1.0.0, 2013 AgiSoft LLC.

INTEGRAL AUTOMATED GIS-ALGORITHM FOR COMPLEX ANALYSIS OF PLANETARY SURFACE AND LANDING SITE CHARACTERIZATION

A.A. Kokhanov, A.E. Zubarev, I.P. Karachevtseva

Moscow State University of Geodesy and Cartography (MIIGAiK), MIIGAiK Extraterrestrial Laboratory (MExLab), Gorokhovskiy per., 4, 105064, Moscow, Russia

Contact: a_kokhanov@miigaik.ru

For studying of various factors, which influence on safety of spacecrafts landing, we are developed the integral GIS-algorithm for complex surface analysis based on remote sensing data. Evaluation of surface suitability is carried out involving ephemerides of celestial bodies [1] and origin data: DTM, distribution of scientific interest factors, e. g. LEND [2] and geological mapping [3] for polar Moon missions. The algorithm includes several modules: 1) automated calculation of surface parameters – slopes and roughness [4] – on base-lines defined by DTM; 2) detecting of visibility zones of Earth and Sun during the period of observation [5]; 3) for relative depth of crater calculation as indicator of fresh small craters [4]; 4) module overlay analysis [6].

On base of user-defined range of suitable values for each of studied factors the algorithm implements overlay analysis and outlines zones satisfying the conditions of landing. Results of automated analysis allows to characterize distribution of suitable for landing areas by the small scale spatial data - GLD100 [7] and LDEM1024 [8], and to detect hazardous relief forms by the large scale data - LROC NAC [9] and Kaguya [10].

ACKNOWLEDGEMENTS:

This work was carried out at MIIGAiK and supported by Russian Science Foundation, project #14-22-00197.

REFERENCES:

- [1] Acton, 1996, PSS, V. 44 (1), pp. 65-70.
- [2] Mitrofanov et al., 2016, Doklady Physics, V. 61 (2), pp. 98-101
- [3] Ivanov et al., 2015, PSS, V. 117, pp. 45-63.
- [4] Kokhanov et al., 2016, Int. Arch. Photogramm. Remote Sens. Spatial Inf. Sci., XLI-B4, 431-433.
- [5] Zubarev et al., 2016, Int. Arch. Photogramm. Remote Sens. Spatial Inf. Sci., XLI-B4, 529-536.
- [6] Kokhanov, 2016, Izv. Vuzov. Geodesy and aerophotosurv. V. 60 (3), pp 61- 67.
- [7] Scholten et al., JGR, 2012, № 117, E00H17.
- [8] Neumann et al., 2011, <http://imbrium.mit.edu/DOCUMENT/ARCHSIS.PDF>.
- [9] Robinson et al., 2010, SSR, V. 150, pp. 81–124.
- [10] Haruyama et al., 2014, LPSC 45, p. 1304.

LUNAR ROVER LOCALIZATION METHOD USING JOINT PROCESSING OF ORIGINAL SURFACE IMAGES WITH ARTIFICIALLY MODELLED ONES

N.A. Kozlova, A.E. Zubarev, V.D. Patratiy, A.A. Konopikhin

Moscow State University of Geodesy and Cartography, MIIGAIK

Extraterrestrial Laboratory (MExLab), 105064, Gorokhovskiy per., 4, Moscow,

Contact: Russia – n_kozlova@miigaik.ru

A new method for determination of rover observation point coordinates will be presented. Innovation of the method is in using of artificial image modelling techniques to assist processing and localization of surface images obtained by the rover.

Rover positioning and navigation is very important nowadays because of a comprehensive Lunar program (Khartov et al., 2015) that is planned by Russian Space Agency for the next few years. It includes both lander and orbiter missions, as well as a unique automatic rover "Robot-Geologist" (Vasilyev, 2015), which aim will be to study samples from the depth up to 2 m and from different regions. So it will have to cover very long distances (about several hundred kilometers) on the lunar surface to travel between the regions of study.

The proposed method includes usage of detailed DEMs in order to create synthetic (artificial) images to help with rover orientation and navigation. Special software has been created for this purpose – module OrthoDEM2Cam (Zubarev et al., 2016). The module allows us to transform a DEM into a synthetic surface image which could have been obtained by the rover from the indicated position and orientation. For correct geometry of the modelled image the program supports different types and parameters of cameras providing the opportunity to implement it for different rovers or different sensors on one rover (incl. past Lunokhod missions as well as planned Lunar landers and rovers). High-resolution orbital images are used to form the texture for synthetic surface images to help in search for navigation orienteers and control points.

Such artificial images (modelled in a proper way) can be used in precise rover localization as a supplement to real images obtained by the rover during the mission. Using photogrammetry software PHOTOMOD (<http://www.racurs.ru/>) we adjust together original surface image with the modelled ones. Known exterior orientation for artificial models becomes the base for coordinate determination for original surface image. Their relative orientation is carried out by measurements of tie-points in overlapping areas and ground control points. Then we adjust all the images and measurements to get the position of observation point for the original image. Tests on models with parameters of Lunokhod missions showed good results (Kozlova et al., 2016).

ACKNOWLEDGEMENTS:

This work was carried out at MIIGAIK and supported by Russian Science Foundation, project #14-22-00197.

Lunokhod panoramic image processing received funding from the European Community's Seventh Framework Program (FP7/2007-2013) under grant agreement № 312377 Planetary Robotics Vision Data Exploitation (PRoViDE), 2013-2015.

REFERENCES:

Khartov V.V. Ot issledovaniya k osvoeniyu resursov Luny'. Vchera i zavtra (k 50-letiyu kosmicheskoy deyatel'nosti NPO imeni S.A. Lavochkina) // Vestnik NPO imeni S.A. Lavochkina. 2015. № 3 (29). S. 8-14.

Kozlova N.A., Zubarev A.E., Patratiy V.D., Konopikhin A.A., Oberst J. Method of a planetary rover localization based on synthetic lunokhod images, *Int. Arch. Photogramm. Remote Sens. Spatial Inf. Sci.*, XLI-B4, 435-439, doi:10.5194/isprs-archives-XLI-B4-435-2016, 2016.

Vasilyev A.V. The mobile robotic system (lunokhod) "Robot-Geologist" for thematic geological mapping and geological exploration on the Moon. Seminar of the Department of Planetary Research and Cosmochemistry under the leadership of M. Marov, 2015.

Zubarev A.E., Nadezhdina I.E., Kozlova N.A., Brusnikin E.S., Karachevtseva I.P. Special software for planetary image processing and research, *Int. Arch. Photogramm. Remote Sens. Spatial Inf. Sci.*, XLI-B4, 529-536, doi:10.5194/isprs-archives-XLI-B4-529-2016, 2016.

UNIFIED APPROACH TO BUILDING SOFTWARE FOR OPERATIONAL PLANNING OF LUNAR SURFACE IMAGING AND PROVIDING BROAD ACCESS TO RESULTED IMAGES USING 3D WEB-GIS

A.A. Garov, A.E. Zubarev, I.P. Karachevtseva

*Moscow State University of Geodesy and Cartography (MIIGAiK),
MIIGAiK Extraterrestrial Laboratory (MExLab), Gorokhovskiy per., 4, 105064,
Moscow, Russia
Contact: icar2003@mail.ru*

One of the tasks, occurring throughout orbital mission course is operational planning of the shooting. While shooting planning can be done at mission preparation stage it is preliminary and not based on actual orbit. Many factors (and possible failures) can come into play and make initial plan non-fit for achieving mission goal. Therefore mission crew needs a tool which would allow monitoring of shooting progress and making operative changes to initial shooting plan, based on corrected data. Ideally this tool should be visual and based on GIS technologies.

As new data becoming available, the task of its publication to the broader audience arises. At most basic level this could be done via ftp. However the most intuitive way for end-user to get to the data is web publication of footprints via some form of geo-portal.

Both tasks are important and should to be accomplished before mission start. It can be noticed that while target audience and operational environment are different for these two (restricted desktop environment and protocols for planning software, web-stack for publishing solution) they have much in common; the key components are shared (access to image DB, visualization layer). Therefore we think that the most rational approach for implementation is developing using a single codebase. We present our current proposal which is based on using single cross-platform solution for both tools. This approach has been formed in process of major refactoring of the initial implementation of MIIGAiK planetary data geoportal (<http://cartsrv.mexlab.ru/geoportal/>) which currently is at testing stage and represent a subset of a more broad concept [1].

We believe using this approach facilitates tighter linkage between image planning and publishing and thus shortens path for an image from orbiter to end-user. It also enables new form of involvement of scientific users in shoot planning – for example they could place requests on geoportal.

REFERENCES:

[1] Garov A.S., Karachevtseva I.P., Matveev E.V., Zubarev A.E., and Florinsky I.V. Development of heterogenic distributed environment for spatial data processing using cloud technologies. 2016, In: *Int. Arch. Photogramm. Remote Sens. Spatial Inf. Sci.*, XLI-B4, 385-390. doi:10.5194/isprs-archives-XLI-B4-385-2016.

ANALYSIS OF UPPER HAZE OF VENUS FROM VENUS EXPRESS SPICAV-IR DATA

M. Luginin^{1,2}, A. Fedorova¹, D. Belyaev¹, F. Montmessin³, V. Wilquet⁴, O. Korabiev¹, J.-L. Bertaux³, A.-C. Vandaele⁴

¹Space Research Institute of the Russian Academy of Sciences (IKI), 84/32 Profsoyuznaya Str., Moscow 117997, Russia; ²Moscow Institute of Physics and Technology, Russia; ³LATMOS, France; ⁴Belgian Institute for Space Aeronomy, Belgium. Contact: mikhail.luginin@phystech.edu

INTRODUCTION:

The upper haze of Venus located at 70-90 km is composed of submicron aerosol particles of H_2SO_4 (Esposito et al., 1983). Three channels of SPICAV/SOIR instrument onboard the VEX orbiter provided the occultation profiles in three spectral ranges that resulted in discovery of a bimodality in size distribution in the upper haze with a small mode of radius 0.1-0.3 μm , and a large mode of radius 0.4-1.0 μm as well as presence of a detached haze layers (Montmessin et al., 2008; Wilquet et al., 2009).

Recently, results from 222 SPICAV-IR solar occultations observed from May 2006 to November 2014 were reported (Luginin et al., 2016). Microphysical

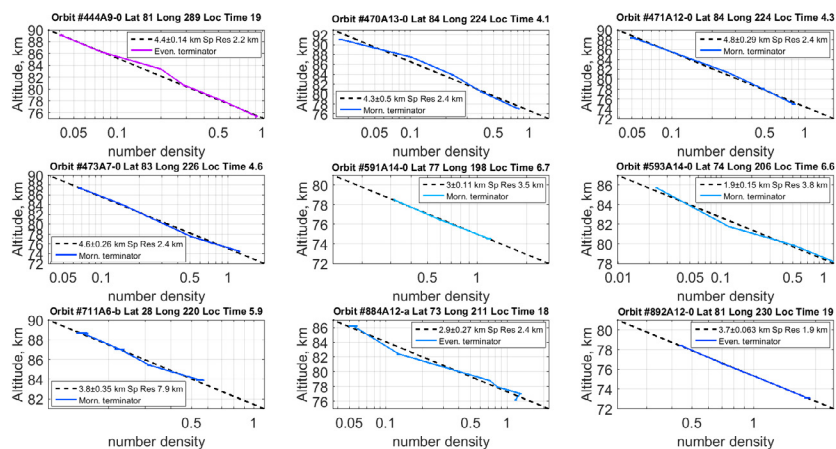


Fig. 1. Number density profiles for a series of orbits assuming unimodal particle size distribution, retrieved scale heights corresponding profiles.

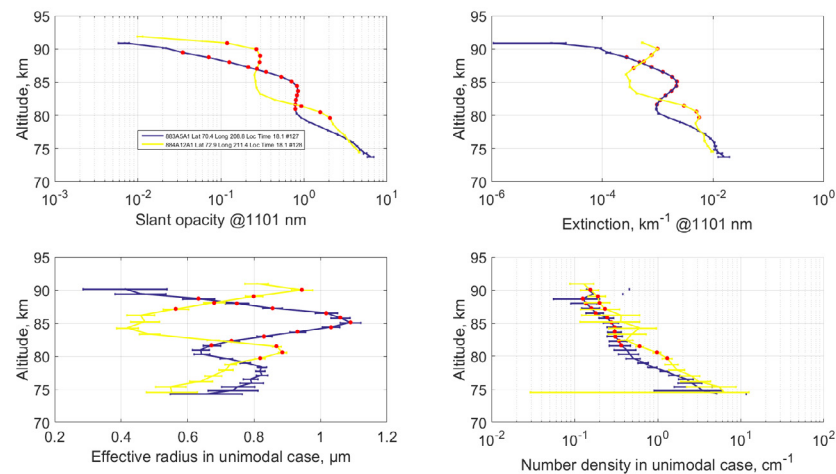


Fig. 2. Vertical profiles of the slant optical depth (top left), vertical profiles of the extinction coefficient at 1101 nm (top right), vertical profiles of effective radius (bottom left) and of the number density (bottom right) for orbits #883 and #884. Detached haze layers are shifted in altitude, but the form of the layers remains the same.

properties of the mesospheric haze were derived from the vertical profiles of atmospheric extinction obtained at 10 near-IR wavelengths. Bimodal distribution of particles was found to be consistent with data for some orbits with mean radius for mode 1 $r_{eff1}=0.12\pm 0.03\ \mu\text{m}$ and $r_{eff2}=0.84\pm 0.16\ \mu\text{m}$ for mode 2. The radius for the single mode case equaled $R_{eff}=0.54\pm 0.25\ \mu\text{m}$, it was also 1.5-2 times smaller at polar region ($60^\circ\text{N}-90^\circ\text{N}$) than at nonpolar ($60^\circ\text{S}-60^\circ\text{N}$). In the bimodal case the number density profiles decreased smoothly for both modes, from $\sim 500\ \text{cm}^{-3}$ at 75 km to $\sim 50\ \text{cm}^{-3}$ at 90 km for mode 1, and from $\sim 1\ \text{cm}^{-3}$ at 75 km to $\sim 0.1\ \text{cm}^{-3}$ at 90 km for mode 2.

In this paper, we continue our study of the aerosols in the Venus' upper haze. Scale heights were retrieved from 36 number density profiles in unimodal case: see examples for a couple of orbits in Fig. 1. The mean scale height is found to be $3.6 \pm 0.7\ \text{km}$. Retrieved scale heights allow us to estimate the vertical wind speed to be $\sim 1\ \text{mm/s}$ at 80 km and $\sim 1\ \text{cm/s}$ at 90 km.

In some occultations, detached haze layers at the altitudes between 70 and 90 km were observed. The structures sometimes can be observed over consecutive orbits. In some instances, detached haze layers are shifted in altitude, but the form of the layers remains the same (Fig. 2). In other cases, the altitude of the layers keeps constant (Fig. 3).

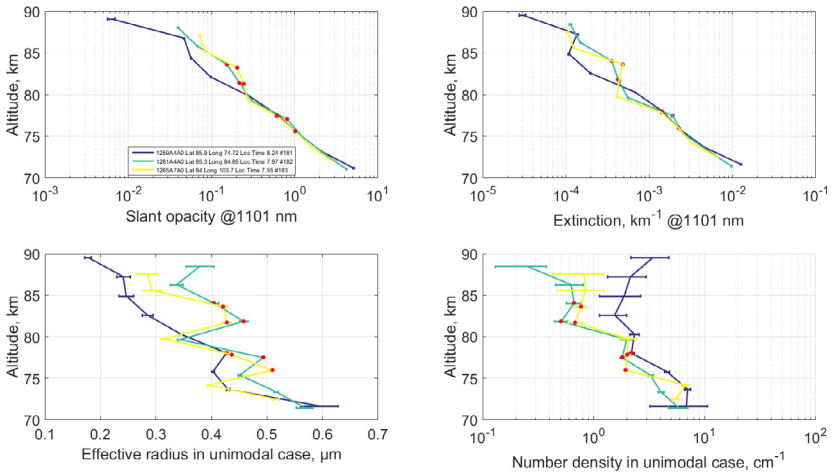


Fig. 3. Vertical profiles of the slant optical depth (top left), vertical profiles of the extinction coefficient at 1101 nm (top right), vertical profiles of effective radius (bottom left) and of the number density (bottom right) for orbits #1259, #1261, and #1265. Detached haze layers of orbits #1261 and #1265 remain the same in the form and in the altitude.

ACKNOWLEDGMENTS:

Russian team acknowledges support from the RFFI grants № 16-02-00633a and № 16-52-16011.

REFERENCES:

- Esposito et al., 1983. Venus. Univ. of Arizona, Ch. 16. The clouds and hazes on Venus, 484–564
- Luginin et al., 2016. Aerosol properties in the upper haze of Venus from SPICAV IR data. *Icarus*, 277, 154–170. <http://doi.org/10.1016/j.icarus.2016.05.008>
- Montmessin et al., 2008. Venusian Upper Haze Properties: Detection of a Multimodal Distribution at High Altitude by SPICAV/SOIR. American Geophysical Union, Fall Meeting 2008
- Wilquet et al., 2009. Preliminary characterization of the upper haze by SPICAV/SOIR solar occultation in UV to mid-IR onboard Venus Express. *JGR*, 114, E00B42. doi:10.1029/2008JE003186

OXYGEN NIGHTSIDE AIRGLOW ON VENUS IN RELATION TO ATMOSPHERIC DYNAMICS BASED ON VIRTIS-M OBSERVATIONS

D. Gorinov, L. Zasova

Space Research Institute of the Russian Academy of Sciences (IKI), 84/32 Profsoyuznaya Str., Moscow 117997, Russia
Contact: gorinov-dmitry@yandex.ru

INTRODUCTION:

Atmospheric oxygen $O_2(a^1\Delta_g)$ on Venus forms on the dayside in high altitudes and emits on the $1.27 \mu\text{m}$ wavelength on the nightside, thus being an important indicator of the day-night circulation of the atmosphere.

This work studies the distribution of the O_2 nightside airglow using both nadir (southern hemisphere) and limb (northern hemisphere) measurements made by the M-channel of VIRTIS instrument on-board of Venus Express spacecraft.

DATA ANALYSIS:

After processing 718 data cubes the following analyses were made:

- Comparison between northern and southern hemispheres
- Variability of the airglow with time
- Comparison with the underlying topography of the planet
- Comparison with the wind velocities
- Appearances of the double peaks in the vertical intensity profiles

IMPLICATION:

The global map of the O_2 nightglow distribution, based on data from 718 data cubes, indicates a complex character of the circulation in this transition region. Appearance of maximum intensity before midnight (from equator up to high latitudes) cannot be explained in terms of known modes of circulation: superposition of zonal retrograde and sub-solar – anti-solar modes of circulation of the Venus atmosphere. No influence on the O_2 night airglow horizontal distribution of the zonal retrograde superrotation in the global map for Southern hemisphere was found: the averaged intensity of the O_2 nightglow emission before midnight (0.43 MR) exceeds the averaged intensity after midnight (0.26 MR), the opposite of how it would be in the case of the presence of the zonal superrotation. Wave activity may affect the observed O_2 nightglow distribution.

REFERENCES

1. Gérard, J.-C., Saglam, A., Piccioni, G., Drossart, P., Cox, C., Erard, S., Hueso, R., and Sánchez-Lavega, A., 2008 Distribution of the O_2 infrared nightglow observed with VIRTIS on board Venus Express. *Geophys. Res. Lett.* V35. L02207. doi:10.1029/2007GL032021
2. Hueso, R., Sánchez-Lavega, A., G. Piccioni, Drossart, P., Gérard, J. C., Khatuntsev, I., Zasova, L., Migliorini, A., 2008. Morphology and dynamics of Venus oxygen airglow from Venus Express/Visible and Infrared Thermal Imaging Spectrometer observations, *J. Geophys. Res.*, 113, E00B02, doi:10.1029/2008JE003081.
3. Piccioni, G., Zasova, L., Migliorini, A., Drossart, P., Shakun, A., García Muñoz, A., Mills F. P., Cardesin-Moinelo, A., 2009. Near-IR oxygen nightglow observed by VIRTIS in the Venus upper atmosphere. *J. Geophys. Res.*, 114, E00B38, doi:10.1029/2008JE003133.
4. Shakun, A. V., Zasova, L. V., Piccioni, G., Drossart, P., Migliorini, A., 2010. Investigation of oxygen $O_2(a^1\Delta_g)$ emission on the nightside of Venus: Nadir data of the VIRTIS-M experiment of the Venus Express mission. *Cos. Res.*, Volume 48, Issue 3, pp.232-239, doi: 10.1134/S0010952510030044

ON POSSIBLE GW ORIGIN OF “METEORIC” LAYERS IN VENUSIAN IONOSPHERE

M. Bondarenko¹, A. Gavrik¹

¹*Institute of Radio Engineering (RAN), 1, Academician Vvedensky square, Fryazino, Moscow region, Russian Federation*

Contact: linuxoid2013@mail.ru

As more data were being collected from radio science occultation experiments on Venus and Mars (PVO, VEX, MGS, MEX), a number of ionospheric electron density (N_e) profiles were produced with additional layers, around 100-120km on Venus, below the smaller Chapman ionization layer V1, and correspondingly below M1 on Mars. Drawing an analogy with studies of Earth ionosphere, these layers were hypothesized to be “meteoric ionization layers” supposedly caused by ablation of meteoric dust, cometary ejecta, meteoric showers and other similar mechanisms in the lower ionosphere of the two planets. Numeric models developed in the early 2000s provided estimates roughly similar to or bracketing the parameters of the observed “layers”.

While the existence of these signal features is indisputable, their interpretation as “meteoric layers”, cautious first, then more and more accepted as a default explanation, needs to be reexamined.

Such reexamination can be started from a little known data set of 8 daytime occultations spanning the range of $[-56 \div -82]$ deg latitude, obtained 14÷30 October 1983 in VENERA-15, VENERA-16 joint mission to Venus, as part of its occultation season 1, the strongest of the three in this earlier Soviet study of the planet.

In contrast to the recent publications, we examined signals processed to level 02 rather than completed N_e profiles. All signals in the series up to the V1 altitudes, and possibly higher, feature wavelike variations with growing amplitudes, which exceed uncertainty levels, in one case looking spectacularly like a very well expressed sine with a near-exponential envelope. Using a Morlet wavelet transform combined with subsequent wavelet filtering, the signals were decomposed into the lower frequency component, reflecting the Chapman layers of the ionosphere (and responsible for the N_e profile shape after further processing), and what appeared to be a set of nearly-harmonic components at higher frequencies with bell-shaped envelopes growing to a certain “dissipation altitude”, then subsiding, superimposed on the lower frequency component.

These higher-frequency oscillations with wavelengths approximately between 5km and 15km were further inspected as possible recordings of gravity wave activity at ionospheric altitudes. Knowing background profiles of pressure/density and temperature, it is possible to estimate GW parameters from its dissipation altitude, if it dissipates due to kinetic viscosity and thermal dumping, which affect GWs at ionospheric heights. Profiles determined in other VEX experiments were used for this estimation for both VENERA-15,16 and VEX data. This calculation for the analyzed signal components produced hypothetical GW parameters matching those of real GWs observed on UV daytime photographs of the upper cloud layer of Venus at 66km (Peralta et al, 2008), as well as GWs at 115-135km on images from CO2 non-LTE emissions (Garcia et al, 2009). Additionally, numeric estimates demonstrated that the real GWs identified by Peralta at the upper cloud levels would dissipate at the same altitudes as the components of our signals, if propagating upwards, and moreover that the dissipation altitudes lie at the turbopause heights. The matches conflate these separate observations from two missions into a coherent description of a physical phenomenon, which also seems to be a permanent feature of the Venusian ionosphere (VENERA-15,16 measurements and VEX mission are spaced 23-30 years apart).

A new interpretation of lower ionospheric “layers” below V1 (if the above considerations are correct) immediately follows: what appears on N_e profiles as “additional layers” below V1 may in fact be the last, largest periods of GWs rising from the top of the cloud layer level (65-70km) and being on the verge of dissipating at turbopause altitudes, which were registered in high-quality occultation data. Not only of non-meteoroid origin, they do not seem to appear as “layers” (which would imply more stability), but according to this interpretation are dynamic and local phenomena.

The overall distribution of N_e profiles with “layers” in the VEX mission, as seen in a recent recalculation of the profiles, falls geographically into higher latitudes

(appr. 60-65 degrees poleward for both hemispheres, also noted in various previous works). This also appears to strengthen the GW interpretation, as these are the latitudes of the “cold collar” encircling the polar vortex formations where atmospheric parameters permit propagation of GWs in our range upwards, possibly originating from the top of the cloud layer below.

IS THE GW INTERPRETATION OF “LOWER IONOSPHERIC LAYERS” SUPPORTED BY THE VEX VERA DATA?

In the more recent Western missions, radio science experiment designers standardized on much shorter wavelengths, in an attempt to emphasize atmospheric studies. The Soviet VENERA-15.16 emitted an S-band signal at 32cm and X-band at 8cm, with most power allocated to the S-band thus producing a signal with a much stronger ionospheric signature. In case of VEX VeRa (S-band = 13cm, X-band = 3.8cm, most power to the X-band) the X-band power (i.e. closed-loop AGC) signal at *ionospheric altitudes* is digital noise.

The Soviet mission experiment design involved comparison between the derivative of the differential Doppler frequency residual (channel one) and accordingly normalized signal power (channel two), which permits separation of signal variations synchronous between the channels and noise. On signals in this form smaller variations are much more obvious. For the VEX VeRa X-band data the lack of meaningful power signal at ionospheric altitudes precludes using the same processing methods.

For the VEX VeRa S-band signal the problem was further compounded by a malfunction: S-band channel power sharply dropped after the first occultation season in 2006, rendering it scientifically useless and for the rest of the mission leaving researchers with data from X-band channels only.

But, even during VEX VeRa Season 1 with a valid S-band channel signal, it has been presented in the archives downsampled to 1Hz, i.e. as points 1 second apart on the time scale, which is too crude to resolve smaller signal variations.

It is also possible that the rest of the occultation measurements, even when sampled at 10Hz in Level 02 processed data, were downsampled to 1Hz for the calculation of N_e profiles, also reducing resolution and possible recognition of GW patterns.

THUS a set of design decisions and an unfortunate technical failure in the VEX mission (combined with a certain tradition in interpreting occultation results) probably prevented researchers from even considering the idea that GWs propagating to ionospheric altitudes may have become registered in the results of occultation experiments and subsequently seeped into N_e profiles as additional “layers” of unknown origin.

HOWEVER, as a result of the above analysis of VENERA-15,16 data it becomes possible to recognize possible GW patterns in VEX VeRa data and use this data in further study of the “low-altitude ionospheric layer” phenomenon in support of the new GW interpretation.

RELEVANCE OF GW INTERPRETATION TO MARS STUDIES.

A preliminary and cautious optimism may be expressed that this interpretation may also account for the appearance of “meteoric layers” on Mars, where, in the absence of atmospheric superrotation, GWs (and therefore additional “layers” on N_e profiles) may be expected to show up less frequently and follow a different pattern. On the other hand, the interpretation leads us to a hypothesis that (rather than Mars orbit comet crossings and similar events, proposed by the “meteoric ion layer” theory) the appearance of “layers” may correlate with GW producing events such as dust storms. And indeed dust opacity is a parameter with which the “meteoric layers” demonstrated the highest positive correlation out of many tested in a review by P.Withers et al, 2008. This hypothesis requires further investigation.

In conclusion, while leaving the possibility of ionization from meteoric ablation at heights below V1, and leaving the question of existence of layers of truly meteoric origin on Venus outside the bounds of this discussion, we propose that the signal features widely reported and branded as “meteoric layers” in recent studies may in fact be traces of GW activity at near-turbopause altitudes.

MERCURY-SUN DISTANCE FROM THE TRANSIT OF MERCURY

S. Shamyati

International Occultation Timing Association in Middle East (IOTA/ME)

Contact: Samaneh_shamyati@yahoo.com

What will be examined in this study is measuring mercury distance from the sun, by passing through it's surface. we Calculated it by using spherical trigonometry and it's formulas.

It should be noted that through the passing of Mercury across sun, we consider parallax too and we also obtained distance. To reach this aim, This data points were collected over view from points that apperceive the transit.

STUDYING OF CLOUD VARIATIONS USING NIGHT OBSERVATIONS DATA OF SPICAV IR IN 2016-2011

D. Evdokimova¹, A. Fedorova¹, D. Belyaev¹, O. Korablev¹, J.L. Bertaux²

¹Space Research Institute of the Russian Academy of Sciences (IKI), 84/32 Profsoyuznaya Str., Moscow 117997, Russia

²LATMOS, CNRS/UVSQ/IPSL, Guyancourt, France

Contact: evd.dar@yandex.ru

Venus is totally covered by cloud layer consisted of concentrated sulfur acid aerosol. Clouds locate within altitude range of 50-70 km and can be divided into three layers according to sizes of prevailed aerosol particles [1]. The upper haze at altitudes above 70 km contains sub-micron particles of mode 1 which radius is less than 0.4 μm . The upper cloud layer within 50-70 km consists of mode 1 and mode 2 particles. Radius of mode 2 particles is $\sim 1 \mu\text{m}$. The particles of mode 3 with radius 3-4 μm and mode 2 are prevailed in the middle (50-57 km) and lower (47-50 km) layers and in the lower haze. Mode 3 particles determine the mass and opacity of the Venus clouds [1].

Clouds form the current Venus climate and cause a great greenhouse effect. Cloud characteristic variations may influence the thermal balance of the atmosphere and lead to changes in atmospheric dynamic and composition. There is a probability of both short and long term variations of the cloud layer [2, 3, 4].

Venus clouds are optically thick that made remote observations of their lower layer parameters almost impossible. However, the weak thermal emission escaping Venus atmosphere below clouds in narrow IR spectral windows was detected in the mid-1980s on the planet night side [5]. These intervals named "transparency windows" locate between strong absorption bands of CO_2 .

This work is studying cloud characteristics using 1.28- μm window emission formed at altitudes of 15-30 km. There are no absorption bands of minor gases in this range except far wings of strong CO_2 lines. However, oxygen airglow at 1.27 μm formed in night atmosphere at altitudes about 100 km also is observed within 1.28- μm window [10]. The spectral interval near maximum of window intensity is chosen in the way to eliminate the airglow emission line from consideration. Thus, thermal emission is sensitive to scattering within clouds. The most great impact is done by the biggest particles of mode 3 concentrated in the lower cloud layer.

The nadir observations of 1.28- μm window were made in time period of 2006-2011 by IR channel of the SPICAV instrument onboard Venus Express. According to these measurements the emission intensity changes from 0.05 to 0.1 $\text{W}/\text{m}^2/\mu\text{m}/\text{ster}$. Modeling of the night-side window and comparison of theory and experimental spectra are used to analyze cloud properties. The direct model is build according to multiply scattering radiative transfer model calculated by SHDOMPP program realizing the spherical discrete ordinate [6] method for plane parallel atmospheres [7, 8, 9]. VIRA temperature profile is used. The surface emissivity is accepted equal to 95% of the black body one. The 75% solution of sulfur acid is taken as the composition of aerosol particles to calculate the scattering. The other cloud parameters (optical depth, single scattering albedo, asymmetry parameter, lower boundary of the cloud layer) are analyzed to find out the level of their influence to the intensity of the 1.28- μm transparency window.

REFERENCES

1. Esposito L.W. et al., 1997. Chemistry of lower atmosphere and clouds. *Venus II, The University of Arizona Press*. 415–458.
2. McGouldrick K. et al., 2011. Quantification of middle and lower cloud variability and mesoscale dynamics from Venus Express/VIRTIS observations at 1.74 μm . *Icarus*, 217. 615-628.
3. McGouldrick K., Toon O.B., 2007. Investigation of possible causes of the holes in the condensational Venus cloud using a microphysical cloud model with a radiative-dynamical feedback. *Icarus*, 191. 1–24.
4. McGouldrick K., Toon O.B., 2008. Modeling the effects of shear on the evolution of the holes in the condensational clouds of Venus. *Icarus*, 196. 35–48.
5. Pollack J.B., et al., 1993. Near-infrared light from Venus' nightside: a spectroscopic analysis. *Icarus*, 103. 1–42.
6. Evans, K. F., 1998. The spherical harmonic discrete ordinate method for three-

- dimensional atmospheric radiative transfer. *J. Atmos. Sci.*, 55, 429-446.
7. Bezdard B. et al., 2009. Water vapor abundance near the surface of Venus from Venus Express/VIRTIS observations. *J. Geophys. Res.*, 114, E00B39.
 8. Bezdard B. et al., 2011. The 1.10- and 1.18- μm nightside windows of Venus observed by SPICAV-IR aboard Venus Express. *Icarus*, 216, 173-183.
 9. Fedorova et al., 2014. The CO_2 continuum absorption in the 1.10- and 1.18- μm windows on Venus from Maxwell Montes transits by SPICAV IR onboard Venus Express. *Planetary and Space Science*, 113–114, 66–77. (DOI: 10.1016/j.pss.2014.08.010)
 10. Crisp, D. et al., 1996. Ground-based near-infrared observations of the Venus nightside: 1.27- μm $\text{O}_2(\text{a}\Delta_g)$ airglow from the upper atmosphere. *Journal of Geophysical Research*. 101, E2, 4577-4594.

SUPERROTATION STUDY IN THE ATMOSPHERE OF VENUS BY MEANS OF BALLOON PROBES

V.M. Linkin, A.N. Lipatov, A.P. Ekonomov

*Space Research Institute of the Russian Academy of Sciences (IKI),
84/32 Profsoyuznaya Str., Moscow 117997, Russia
Contact: alekonomo@yandex.ru*

The atmosphere of Venus was remotely studied for about 100 years, and with the spacecraft nearly half a century. As a result, there was a dramatic modernization of views. The main finding is the detection of a unique phenomenon - atmosphere superrotation. For the first time it is detected from orbit in 1974 with the spacecraft Mariner, and it is the main element of the atmospheric dynamics. The superrotation study was conducted in the UV range at altitudes of 65-69 km and in the IR range of 51-59 km, and in the course of the experiment VEGA balloon at 53-55 km. At intermediate altitudes systematic measurements was not carried out. It is proposed to introduce into the atmosphere at different altitudes balloon lightweight probes, but of increased durability. Envelopes are made of metalized PET foil. Mass of payload on each probe is 1 kg. The diameter of the envelope depends on the altitude and in altitude range 50-70 km is in the range of 1-3 meters. The expedition should be about 30 Earth days long.

WINDS IN THE MIDDLE CLOUD DECK FROM THE NEAR-IR IMAGING BY THE VENUS MONITORING CAMERA ONBOARD VENUS EXPRESS

I.V. Khatuntsev¹, M.V. Patsaeva¹, D.V. Titov², N.I. Ignatiev¹, A.V. Turin¹, W.J. Markiewicz³

¹Space Research Institute of the Russian Academy of Sciences (IKI), 84/32 Profsoyuznaya Str., Moscow 117997, Russia

²ESA/ESTEC, PB 299, 2200AG Noordwijk, The Netherlands

³Max-Planck-Institute for Solar System Research, Max-Planck-Str. 2, 37191 Göttingen, Germany

Contact: khatuntsev@iki.rssi.ru

INTRODUCTION:

More eight years Venus Monitoring Camera (VMC) onboard the Venus Express orbiter has observed the upper cloud layer of Venus. Unprecedentedly largest set of images of Venus was obtained in the UV (365nm), visible (513nm) and two infrared channels – 965nm and 1010nm. UV dayside images were used to study the atmospheric circulation at the Venus cloud tops (Khatuntsev et al., 2013; Patsaeva et al. 2015). Mean zonal and meridional profiles are presented in Fig.1. In low latitudes the mean retrograde zonal wind at the cloud top (67 ± 2 km following Rossow et al., 1990) is about 95 m/s with a maximum of about 102 m/s at 40-50°S. Poleward from 50°S the zonal wind quickly fades out with latitude. The atmospheric rotation period at the cloud top has a maximum of about 5 days at the equator, decreases to approximately 3 days in the middle latitudes and stays almost constant poleward from 50°S. The mean poleward meridional wind slowly increases from zero value at the equator to about 10 m/s at 50°S. Poleward from this latitude, the absolute value of the meridional component monotonically decreases to zero at the pole. Influence of Venus topography on the speed of zonal flow was found by Bertaux et al. (2016).

Here we present results of wind tracking from IR images obtained by VMC from 2006/12/17 till 2010/03/14.

WINDS IN THE MIDDLE CLOUD DECK:

The brightness contrast in the near-IR is much weaker than in UV images and does not exceed 4% (Titov et al., 2012). 2D-wavelet filters were applied to enhance the contrast of cloud details and decrease the high-frequency noise. Digital wind tracking technique was modified with respect to UV and applied to meso-scale details in IR images.

IR dayside images (965nm) for 150 orbits were processed by automated (digital) method. More 32000 vectors were obtained with satisfactory longitude-latitude coverage in South hemisphere of Venus.

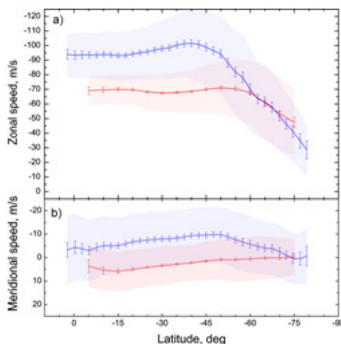


Fig. 1. Mean zonal (a) and meridional (b) profiles of the wind speed derived from UV (blue, Khatuntsev et al., 2013) and IR (red) images for all period of observations. Error bars correspond to 99.9999% (5) confidence interval based on the standard deviation of the weighted mean. Standard deviations are presented by shadowed areas.

Mean zonal and meridional components of horizontal flow obtained from IR dayside images are shown on Fig.1. In the low latitudes the mean retrograde zonal wind in the middle cloud deck (55 ± 4 km) is about 68-70 m/s (Fig.1a). Mean meridional speed has a positive sign in latitude range 5-65°S (Fig.1b). It implies an equatorward transfer of air masses along meridians. The maximum of the meridional speed $+5.8\pm 1.0$ m/s is observed at latitude 15°S, and then the meridional speed slowly decreases to 0 near 65-70°S.

It is thus reasonable to suggest that in the IR (965nm) the lower branch of cloud-level Hadley cell is observed.

LONGITUDE-LATITUDE VARIATIONS OF WIND SPEED:

Contour maps for mean zonal and meridional components of horizontal flow in the middle cloud deck were calculated (Fig.2). As in UV, we can see a similar evidence for the influence of Venus topography on the zonal and meridional speed. Obviously, Aphrodite Terra and Atla Regio (60-200°E and 0-30°S in Fig.2) significantly influence on the circulation in middle cloud deck. Moreover, Aphrodite Terra generates a “braking” effect for the meridional speed. Maximal meridional speeds (~5-6m/s) were observed above depression regions (-50-50°E and 5-25°S in Fig. 2).

According to Crisp et al. (1990) VEGA-2 balloon was pushed on 500 km toward the equator during its 47 hours flight on 53 km altitude. For comparison the trajectory of VEGA-2 balloon has been drawn in Fig.2 (red line). VEGA-2 balloon has an entry point at 6.5°S latitude and 181.5°E longitude. Meridional speed of VEGA-2 has been estimated about +2.5 m/s. This value is in agreement with our estimates near Aphrodite Terra 1-3.5m/s.

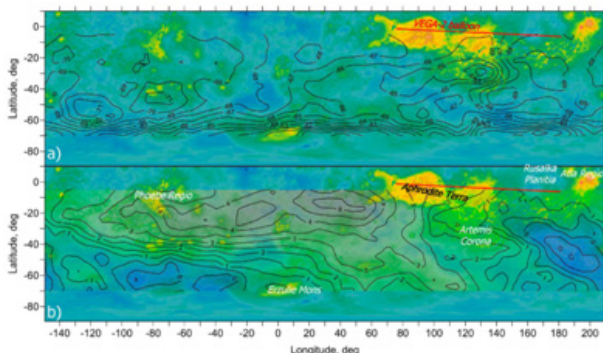


Fig. 2. Venus geographic map with zonal (a) and meridional (b) speed contour maps. Red line in the upper right corners of each panel denotes the VEGA-2 balloon trajectory.

RESULTS:

- 1) IR (965nm) dayside images of Venus clouds obtained by VMC onboard Venus Express can be used for wind tracking;
- 2) The mean retrograde zonal wind in the middle cloud deck (55 ± 4 km) is about 68-70 m/s in low and middle latitudes;
- 3) Sign of the meridional component indicates the air-mass flow towards the equator. The maximum of the meridional speed $+5.8 \pm 1.0$ m/s is observed at latitude 15°S;
- 4) Venus topography has an influence on the velocity of the horizontal flow. Aphrodite Terra and Atla Regio have a significant influence on the circulation in the middle cloud deck (55 ± 4 km).

REFERENCES:

1. Bertaux, J.-L., I. V. Khatuntsev, A. Hauchecorne, W. J. Markiewicz, E. Marcq, S. Lebonnois, M. Patsaeva, A. Turin, and A. Fedorova (2016), Influence of Venus topography on the zonal wind and UV albedo at cloud top level: The role of stationary gravity waves, *J. Geophys. Res. Planets*, 121, 1087–1101, doi:10.1002/2015JE004958.
2. Crisp, D., Ingersoll, A.P., Hildebrand, C.E., Preston, R.A. (1990), VEGA balloon meteorological measurements, *Adv. in Sp. Res.*, vol. 10, no. 5, p. 109-124
3. Khatuntsev, I.V., M.V. Patsaeva, D.V. Titov, N.I. Ignatiev, A.V. Turin, S.S. Limaye, W.J. Markiewicz, M. Almeida, T. Roatsch and R. Moissl (2013), Cloud level winds from the Venus Express Monitoring Camera imaging., *Icarus*, 226, 140-158.
4. Patsaeva, M.V., I.V. Khatuntsev, D.V. Patsaev, D.V. Titov, N.I. Ignatiev, W.J. Markiewicz, A.V. Rodin (2015), The relationship between mesoscale circulation and cloud morphology at the upper cloud level of Venus from VMC/Venus Express, *Planet. Space Sci.* 113(08), 100-108, doi:10.1016/j.pss.2015.01.013.
5. Rossow, W.B., Del Genio A.T., Eichler, T., 1990. Cloud-tracked winds from Pioneer Venus OCPP images. *J. Atmos. Sci.* 47, 2053-2084.
6. Titov, D.V., Markiewicz, W.J., Ignatiev, N.I., Li Song, Limaye, S.S., Sanchez-Lavega, A., Hesemann, J., Almeida, M., Roatsch, Th., Matz, K.-D., Scholten, F., Crisp, D., Esposito, L.W., Hviid, S.F., Jaumann, R., Keller, H.U. Moissl, R., 2012. Morphology of the cloud tops as observed by the Venus Express Monitoring Camera. *Icarus* 217, 682-701.

INFLUENCE OF VENUS TOPOGRAPHY ON VARIATIONS OF ZONAL AND MERIDIONAL WINDS ACCORDING TO MEASUREMENTS IN UV AND NEAR-IR CHANNELS OF VMC/VENUS EXPRESS

M.V. Patsaeva, I.V. Khatuntsev

Space Research Institute of the Russian Academy of Sciences (IKI),
84/32 Profsoyuznaya Str., Moscow 117997, Russia

Contact: marina@irn.iki.rssi.ru

INTRODUCTION:

A set of UV and IR images obtained by the Venus Monitoring Camera (VMC) was used to study the circulation of the mesosphere at two levels. The results were obtained by visual and digital methods for observation period from 2006 to 2014 for UV images (Khatuntsev et al. 2013, Patsaeva et al. 2015) and from 2006 to 2012 for IR images. The long observation period and good longitude-latitude coverage by single measurements allowed us to focus on the study of the slow-periodic component. The influence of the underlying surface topography on the change of speed of the average zonal wind at UV level is published in Bertaux et al. (2016). Analysis of the longitude-latitude distribution of the zonal and meridional components for 172,241 (257 orbits) digital individual UV wind measurements and for 32,000 (150 orbits) digital individual IR wind measurements allows us to compare the influence of Venus topography on the change of the zonal and meridional components at both cloud levels.

RESULTS:

Average zonal and meridional wind components and average longitudinal profiles of surface altimetry were constructed for latitudinal ranges of 10° at low latitudes. Then correlations between altimetry profiles and profiles of speed were considered. Shifts between correlated profiles were defined for the maximum correlation coefficient for zonal and meridional components.

Analysis of the *zonal component* at the UV level demonstrates increase of the correlation shift when the maximum height decreases and thus confirms the influence of the underlying surface topography on the change of speed of the average zonal wind. At the IR level (55 ± 4 km), there are amorphous formations and a number of elongated structures (streaks) along the entire planetary disk. This fact decreases the accuracy of zonal component in comparison with the UV level at low latitudes. Moreover, the average speed of the zonal flow in latitudes of Aphrodite Terra is slower than that at the UV level by about 20 m/s, and the speed of the meridional flow is on the contrary faster. This circumstance does not allow us to establish reliable correlation between the zonal wind at the IR level and the surface.

At the IR level, the dependence between surface topography and *meridional component* was found for latitude bins in the region 10 - 30° S. Fig.1 shows average profile of surface altimetry and profiles of meridional component before and after shift for latitude bin 15 - 25° S.

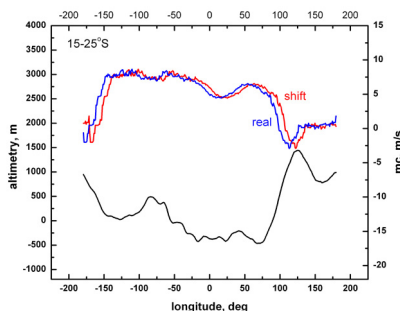


Fig. 1. Average profile of the surface altimetry (black line), average profiles of the meridional component before (blue line) and after the shift (red line). Each point is an average of all values within the latitudinal region 15 - 25° S and longitudinal region $\pm 15^\circ$. The interval between points is 1° .

At the IR level, the meridional flow is equatorward ("+"). The meridional velocity decreases to zero in the region of maximum of the average surface altimetry (longitudes from 100° to 150°). The meridional flow is poleward (about -3 m/s) at the maximum. The equatorward meridional component reaches its maximum (up to +10 m/s) in the region of minimum of the average surface altimetry (longitudes from -100° to +60°). The correlation shift varies from -10 to +10 for various latitudinal bins. The shift has no visible dependence on altitude. At the UV level, the meridional flow is directed to the pole, where the surface altimetry decreases, i.e. the flow does not encounter obstructions. There is no visible correlation at the UV level between the meridional flow and the surface altimetry.

CONCLUSION:

The influence of the underlying surface topography on the change of speed of the average zonal wind takes place at the UV level, and the influence on the change of speed of the average meridional wind is observed at the IR level.

REFERENCES:

- Khatuntsev, I.V., M.V. Patsaeva, D.V. Titov, N.I. Ignatiev, A.V. Turin, S.S. Limaye, W.J. Markiewicz, M. Almeida, T. Roatsch and R. Moissi (2013), Cloud level winds from the Venus Express Monitoring Camera imaging., *Icarus*, 226, 140-158.
- Patsaeva, M.V., I.V. Khatuntsev, D.V. Patsaev, D.V. Titov, N.I. Ignatiev, W.J. Markiewicz, A.V. Rodin (2015), The relationship between mesoscale circulation and cloud morphology at the upper cloud level of Venus from VMC/Venus Express, *Planet. Space Sci.* 113(08), 100-108, doi:10.1016/j.pss.2015.01.013.
- Bertaux, J.-L., I. V. Khatuntsev, A. Hauchecorne, W. J. Markiewicz, E. Marcq, S. Lebonnois, M. Patsaeva, A. Turin, and A. Fedorova (2016), Influence of Venus topography on the zonal wind and UV albedo at cloud top level: The role of stationary gravity waves, *J. Geophys. Res. Planets*, 121, 1087–1101, doi:10.1002/2015JE004958.

ADIABATIC TRAPPING OF ELECTRONS AND LOCALIZED WAVE STRUCTURES IN LUNAR DUSTY PLASMAS AND EARTH'S MESOSPHERE

T.I. Morozova¹, S.I. Kopnin², S.I. Popel¹

¹Space Research Institute of the Russian Academy of Sciences (IKI), 84/32 Profsoyuznaya Str., Moscow 117997, Russia

²Moscow Institute of Physics and Technology, Institutskii per. 9, Dolgoprudny, Moscow oblast 141700, Russia

Contact: timoroz@yandex.ru

INTRODUCTION:

Dusty plasma system in the near-surface layer on the illuminated side of the Moon involves photoelectrons, solar-wind electrons and ions, neutrals, and charged dust grains. Solutions in the form of dust acoustic (DA) solitons corresponding to the parameters of the lunar dusty plasma system have been found [1]. DA wave structures are also important in Earth's dusty mesosphere [2]. In [1, 2] adiabatic trapping of electrons when considering the solitons has not been taken into account. However, DIA localized wave structures (in particular, solitons) can be accompanied by either positive or negative electrostatic potential ϕ , the positive ϕ being the potential well for electrons. The purpose of the present work is to determine the localized wave structure properties with taking into account the influence of the effect of adiabatic trapping.

ADIABATIC TRAPPING OF ELECTRONS:

Adiabatic trapping of electrons should be taken into account when

$$t_{\text{sol}} \geq L_{\text{sol}} / v_{Te}$$

where t_{sol} is the characteristic time of the soliton formation, L_{sol} is the soliton width, and v_{Te} is the electron thermal velocity. In this case, distribution of electrons is modified due to their adiabatic trapping [3] and is described by the Gurevich formula:

$$\frac{n_e}{n_{e0}} = \exp\left(\frac{e\phi}{T_e}\right) \operatorname{erfc}\left(\sqrt{\frac{e\phi}{T_e}}\right) + \frac{2}{\sqrt{\pi}} \sqrt{\frac{e\phi}{T_e}}$$

where $\operatorname{erfc}(\zeta) \equiv 1 - \operatorname{erf}(\zeta)$ is the complimentary error function, n_e is the electron number density, T_e is the electron temperature, the subscript 0 denotes unperturbed values, $-e$ is the electron charge. The first term in the above equation corresponds to free electrons, while the trapped electrons are represented by the second term. Note that the Gurevich distribution presumes trapped electrons to be collisionless. For practical purposes, this means that the average time between electron-neutral collisions should be longer than the time during which the soliton exists.

GOVERNING EQUATIONS:

To describe localized dust structures (solitons) on the DA time scale we use (in addition to the above equation for the electron number density) the basic equations for investigating DA structure:

$$\partial_t n_d + \partial_x (n_d v_d) = 0,$$

$$\partial_t v_d + v_d \partial_x v_d = \frac{Z_d e}{m_d} \partial_x \phi,$$

$$n_i = n_{i0} \exp\left(-\frac{e\phi}{T_i}\right),$$

$$\partial_x^2 \phi = 4\pi e (n_e + Z_d n_d - n_i),$$

$$I_e(q_d) + I_i(q_d) + I_{ph}(q_d) = 0,$$

where $n_{d(0)}$ is the dust (ion) number density, v_d is the dust speed, $q_d = -Z_d e$ is the average dust grain charge, m_d is the dust particle mass, T_i is the ion temperature, I_e and I_i are microscopic electron and ion currents on the grain surface, respectively, and I_{ph} is the photoelectric current.

Localized structures (solitons) are usually formed from nonlinearly propagating waves that are ubiquitous in space plasmas and in Earth's mesosphere. We do not consider the processes of the soliton structure formation. Such a consideration requires special development of numerical methods for DA nonlinear perturbations somewhat analogous to those developed already for the case of the dust ion-acoustic perturbations. This is a problem for future investigations. Here, we use the standard approach to the investigation of solitons and restrict ourselves to the consideration of the steady-state structures under the assumption that they already exist.

We look for solutions in the form of solitons moving with a constant velocity U in the x direction with respect to the background. We assume that $Z_d = \text{const}$, use the standard Sagdeev potential approach, and reduce the problem to the analysis of the effective energy integral

$$\frac{1}{2}(\varphi_\xi)^2 + V(\varphi) = 0$$

where the Sagdeev potential is

$$V(\varphi) = 4\pi n_{e0} T_e \left((1 - Z_d d)(e^{-\varphi} - 1) - \tilde{\varphi} \left(1 + \frac{\tilde{\varphi}}{2} - \frac{8}{15\sqrt{\pi}} \tilde{\varphi}^{3/2} \right) + 2dM(\sqrt{M^2 - \tilde{\varphi}} - M) \right).$$

Here, the normalizations $e\varphi/T_e \rightarrow \tilde{\varphi}$, $U/c_d \rightarrow M$ are used, $d = n_{d0}/n_{e0}$, and $c_d = \sqrt{T_i/m_d}$.

SOLUTIONS:

For the existence of localized DA structures, the Sagdeev potential $V(\varphi)$ must have a local maximum at $\varphi = 0$, and the equation $V(\varphi) = 0$ must have at least one more real solution $\varphi_0 \neq 0$. A local maximum of the Sagdeev potential $V(\varphi) = 0$ at the point $\varphi_0 \neq 0$ exists if $M^2 > dZ_d^2$, which is a consequence of the inequality $d^2 V(\varphi = 0) < 0$.

We find solutions characterizing the localized DA structures for the situations inherent in the lunar dusty plasmas and Earth's mesosphere plasmas under the conditions described in [1, 2]. An example of the dependence of the soliton amplitude on the Mach number and the height over the lunar surface is given for lunar dusty plasmas containing positively charged dust.

The common conclusions for the lunar dusty plasmas and Earth's mesosphere are that DA solitons in the presence of trapped electrons can exist in both these situations. Their main properties are determined mainly by the signs of the local dust charges. DA structures containing positive grains appear as electron-density humps and ion-density dips, and those with negative grains appear as electron-density dips and ion-density humps. Thus, our results can help in the determination of the sign of the dust grain charge.

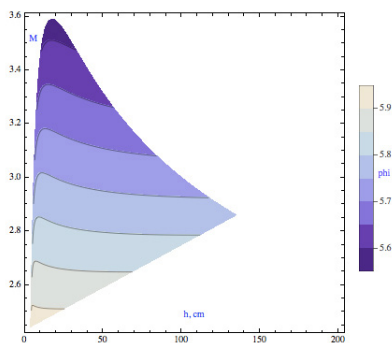


Fig. 1. An example of calculation of soliton amplitude "phi" dependence on M and the height h over the lunar surface for lunar dusty plasmas containing positively charged dust (photoelectric effect significant).

ACKNOWLEDGEMENTS:

This work was supported in part by the Presidium of the Russian Academy of Sciences (under Fundamental Research Program No. 7, "Experimental and Theoretical Study of the Solar System Objects and Stellar Planet Systems. Transient Explosion Processes in Astrophysics") and the Russian Foundation for Basic Research (Projects Nos. 15-02-05627-a and 16-32-00814-mol_a).

REFERENCES:

1. Morozova, T.I., Kopnin, S.I., Popel, S.I., Plasma Phys. Rep., 2015, **41**, 799
2. Popel, S.I., Kopnin, S.I., Kosarev, I.N., Yu, M.Y., Adv. Space Res., 2006, **37**, 414
3. Lifshitz, E.M., Pitaevskii, L.P., Physical Kinetics, Pergamon, Oxford, 1981

WAVES IN THE REGION OF INTERACTION BETWEEN EARTH'S MAGNETOSPHERE AND LUNAR DUSTY PLASMA

T.I. Morozova, S.I. Popel

Space Research Institute of the Russian Academy of Sciences (IKI), 84/32 Profsoyuznaya Str., Moscow 117997, Russia
Contact: popel@iki.rssi.ru

INTRODUCTION:

Wave processes in a lunar dusty plasma caused by its interaction with Earth's magnetotail are studied. This is a continuation of the investigation of waves in lunar dusty plasmas [1], where the relative motion of the solar wind with respect to the photoelectrons was shown to be a reason for the excitation of high-frequency oscillations with frequencies in the range of Langmuir waves. Here, we show that the relative motion of Earth's magnetotail with respect to the Moon leads to the excitation of ion acoustic and dust acoustic waves.

DUSTY PLASMA PARAMETERS:

Dusty plasma constituents in the situation considered are electrons and ions of Earth's magnetosphere, electrons and ions of the solar wind, charged dust particles, as well as photoelectrons which are formed due to the photoelectric effect on the surface of the Moon and on the surfaces of the levitating dust particles. To determine number densities and temperatures of plasmas in the solar wind and in the magnetotail in the vicinity of the Moon we use the data [2] presented in Fig. 1. Both ion n_i and electron n_e number densities decrease by about two/three orders of magnitude from the solar wind to the magnetosphere, the ion temperature T_i increases from several dozens eV to about 1000 eV, while the electron temperature T_e changes less dramatically (from about 10 eV to ~100 eV). The velocity u of the lunar dusty plasma with respect to the magnetotail plasma (determined by the relative motion of the Moon and the magnetotail) is about 1 km/s. However one has to take into account that in the plasma sheet the flow speed u can be much higher (say, of the order of 10 km/s). The solar wind speed is supposed to be $u_s \approx 400$ km/s.

Table 1 presents the parameters of photoelectrons calculated [3] for $\cos\theta = 1$ (where θ is the subsolar angle) in the near-surface layer of the illuminated part of the Moon for the solar activity level corresponding to (column A) an X28 Class solar flare, (column B) the solar maximum, and (column C) the solar minimum for various quantum yields (subscripts Y1 and Y2 correspond to the quantum yield from [4] and that from [5], respectively). It can be seen that, because of the significant difference between the quantum yields, the calculated characteristics of photoelectrons near the surface of the Moon are strongly different. The dependence of the parameters $n_{e(ph)}$ and $T_{e(ph)}$ on the solar activity level is not so strong. The difference between the quantum yields presented in [4] and [5] much more strongly affects the calculation than the variation of the work function in the range of 5–6 eV. The $n_{e(ph)}$ values for $\cos\theta \neq 1$ are obtained by multiplying the values from the table by $\cos\theta$. The electron temperature $T_{e(ph)}$ is independent of $\cos\theta$.

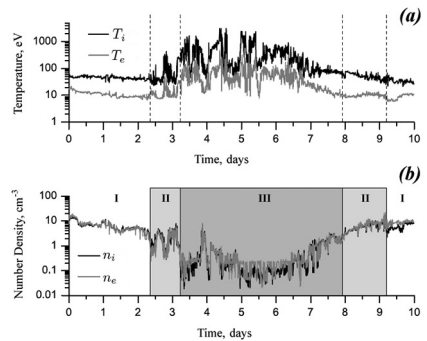


Fig. 1. Ion and electron temperatures (a) and number densities (b) of the solar wind and Earth's magnetosphere on the orbit of the Moon measured by the ARTEMIS P2 spacecraft during a crossing of the magnetotail from 2013 January 22 to 31 [2]. Roman numerals characterize the regions of the solar wind (I), the magnetosheath and/or boundary layer (II), and the inner magnetosphere (III) including the plasma sheet. The boundaries between the regions I-III are shown by the vertical lines in both upper (a) and lower (b) panels.

Table 1. Parameters of photoelectrons in the near-surface layer of the illuminated part of the Moon for various solar activity levels and various quantum yields

	A	B	C
$n_{e(ph)Y1}, \text{ cm}^{-3}$	$2.2 \cdot 10^5$	$2.1 \cdot 10^5$	$1.9 \cdot 10^5$
$T_{e(ph)Y2}, \text{ eV}$	0.2	0.1	0.1
	A	B	C
$n_{e(ph)Y1}, \text{ cm}^{-3}$	$8.6 \cdot 10^2$	$2.9 \cdot 10^2$	$1.3 \cdot 10^2$
$T_{e(ph)Y2}, \text{ eV}$	2.1	1.9	1.3

Dust number density n_d can easily be determined by the relationship $n_d \sim n_e / |Z_d|$, where Z_d is the dust particle charge number. Using this estimate and taking into account that for 100 nm-sized dusts $|Z_d| \sim 10-50$, we find (for the illuminated part of the Moon) $n_d \sim 10^3 - 10^4 \text{ cm}^{-3}$ for the quantum yield presented in [4] and $n_d \sim 10 \text{ cm}^{-3}$ for the quantum yield presented in [5], and (for the dark side of the Moon) $n_d \sim 10^{-2} - 10^{-1} \text{ cm}^{-3}$.

INSTABILITIES AND WAVE EXCITATION:

The simplest instability is the hydrodynamical instability (like Buneman instability). It is realized under the conditions $kv_{Td} \ll (kv_{TiM}, kv_{TiS}) \ll \omega \ll (kv_{Te(ph)}, kv_{TeS}, kv_{TeM})$, where $v_{Te(j)}$ is the electron (ion) thermal velocity, v_{Td} is the dust thermal velocity, the subscripts M, S, (ph) describe parameters of the magnetosphere, solar wind, and photoelectrons, respectively. The linear dispersion equation in this case takes the form

$$1 + \frac{1}{k^2 \lambda_{DeM}^2} + \frac{1}{k^2 \lambda_{DeS}^2} + \frac{1}{k^2 \lambda_{De(ph)}^2} - \frac{\omega_{piM}^2}{\omega^2} - \frac{\omega_{piS}^2}{(\omega - ku_S)^2} - \frac{\omega_{pd}^2}{(\omega - ku)^2} = 0$$

where λ_{De} is the electron Debye length, $\omega_{pi(d)}$ is the ion (dust) plasma frequency. Taking into account the plasma parameters from the previous section we find that there is a possibility of excitation of the ion acoustic waves with the dispersion law

$$\omega = \frac{\omega_{piM}}{\sqrt{1 + 1/k^2 \lambda_D^2}}$$

$$\frac{1}{\lambda_D^2} = \frac{1}{\lambda_{DeM}^2} + \frac{1}{\lambda_{DeS}^2} + \frac{1}{\lambda_{De(ph)}^2}$$

The maximum growth rate of the instability is

$$\gamma_{\max}^{\text{Hydro}} = \frac{\sqrt{3}}{2^{4/3}} \omega_{piM} \sqrt{1 - \frac{u^2}{\omega_{piM}^2 \lambda_D^2} \left(\frac{n_d Z_d}{n_{iM}} \frac{n_d Z_d}{m_d} \right)^{1/3}} = \frac{\sqrt{3}}{2^{4/3}} \omega_{pd} \sqrt{1 - \frac{u^2}{\omega_{piM}^2 \lambda_D^2} \left(\frac{n_{iM}}{n_d Z_d} \frac{m_d}{Z_d m_i} \right)^{1/6}}$$

Here, $m_{i(j)}$ is the mass of ion (dust particle). The hydrodynamical instability is effective in the magnetosheath and/or boundary layer in the situation when the quantum yield is given by the results [5], i.e., for the parameters of photoelectrons given in the lower part of Table 1. In this situation the characteristic time of the instability development is $\tau \sim 1 \text{ s}$ which is much less than the time during which the interaction of the lunar dusty plasmas with the magnetosheath and/or boundary layer occurs. Thus in the situation considered one can expect developed ion acoustic turbulence in the magnetosheath and/or boundary layer.

Another instability which can develop due to the interaction of the magnetotail with the lunar dusty plasma is the kinetic one which is realized for $kv_{Td} \ll \omega \ll (kv_{TiM}, kv_{TiS})$. In this case the dust acoustic waves with the dispersion law

$$\omega_k = \frac{\omega_{pd} \lambda_D k}{\sqrt{1 + k^2 \lambda_D^2}}$$

$$\frac{1}{\lambda_D^2} = \frac{1}{\lambda_{DeM}^2} + \frac{1}{\lambda_{DeS}^2} + \frac{1}{\lambda_{De(ph)}^2} + \frac{1}{\lambda_{DiM}^2} + \frac{1}{\lambda_{DiS}^2}$$

are excited. The growth rate is

$$\gamma \sim \omega_{pd} \frac{T_{e(ph)}}{T_{iM}} \frac{n_{iM}}{n_{e(ph)}} \frac{u}{v_{TiM}}$$

The kinetic instability is much slower than the hydrodynamical one ($\tau \sim 1 \text{ hour}$). It can be realized also in the situation when the quantum yield is given by the results [5], i.e., for the parameters of photoelectrons given in the lower part of Table 1. It can result in the development of dust acoustic turbulence in the region of interaction between Earth's magnetosphere and lunar dusty plasma.

ACKNOWLEDGEMENTS:

This work was supported in part by the Presidium of the Russian Academy of Sciences (under Fundamental Research Program No. 7, "Experimental and Theoretical Study of the Solar System Objects and Stellar Planet Systems. Transient Explosion Processes in Astrophysics") and the Russian Foundation for Basic Research (Project No. 15-02-05627-a).

REFERENCES:

1. Morozova, T.I., Kopnin, S.I., Popel, S.I., Plasma Phys. Rep., 2015, 41, 799
2. Vaverka, J., Richterová I., Pavlů J., Šafránková J., and Němeček Z., Astrophys. J., 2016, 825, 133
3. Popel, S.I., Golub', A.P., Izvekova, Yu.N., Afonin, V.V., Dol'nikov, G.G., Zakharov, A.V., Zelenyi, L.M., Lisin, E.A., Petrov, O.F., JETP Lett., 2014, 99, 115
4. Walbridge, E., J. Geophys. Res., 1973, 78, 3668
5. Willis, R.F., Anderegg, M., Feuerbacher, B., Fitton, B., in: Photon and Particle Interactions With Surfaces in Space, ed. by R.J.L. Grard, D.Reidel, Dordrecht (1973), p. 389

DUST VORTEX MOTIONS IN THE ATMOSPHERES OF EARTH AND MARS

Yu.N. Izvekova, S.I. Popel.

*Space Research Institute of the Russian Academy of Sciences (IKI), 84/32
Profsoyuznaya Str., Moscow 117997, Russia
Contact: izvekova@iki.rssi.ru*

INTRODUCTION:

We develop a continuously stratified model of nonadiabatic terrestrial atmosphere [1] in order to study a possibility of instability development of acoustic-gravity waves. We consider the interaction of acoustic-gravity (AG) vortices with nanoscale dust particles at altitudes of the ionosphere. Here, we study the following possibilities: capture and evolution of dust particles in AG-vortices, formation of dust vortices as a result of involving a great number of dust particles into vortical motions, and formation of vertical and horizontal dust flows (streamers and zonal flows) in dusty ionospheric plasma. We also model dust particle dynamics in the so-called Dust Devils (DDs) [2], which are a widespread event on Earth and Mars. We develop methods for the description of dust particle charging in DDs, discuss the ionization processes in DDs, and model charged dust particle motion. Our conclusions are consistent with the fact that DDs can lift a big amount of dust from the surface of a planet into its atmosphere.

DUST IN INTERACTION WITH AG-WAVES:

We study the instability of acoustic-gravity waves in the atmosphere with taking into account thermal flows of solar radiation, infrared emission of the atmosphere, water vapor condensation, as well as thermal conductivity. The interest in such investigations is caused by the fact that AG-vortices at the altitudes of about 110 km (i.e., at those altitudes where dust particles are in the ionosphere) are formed and self-sustained owing to dissipation processes, similarly to autosolitons. Moreover, vortical structures can catch and transit particles of the medium. We construct the dispersion equation for AG-waves in non-adiabatic atmosphere and obtain dispersion surfaces in wave-number space for altitudes up to 130 km. Instability regions for different wave numbers are studied. Fig.1 shows instability growth rates for all 4 dispersion surfaces characterizing AG-waves at 110 km altitude. Our results show that in Earth's atmosphere (at the tropospheric and ionospheric altitudes) there are regions where the instability develops. We have considered the behavior of nanoscale dust particles in the acoustic-gravity vortex which is formed as a result of the development of the convective instability at the altitudes of 110 – 120 km. It has been shown that dust particles of the size of 10 nm can exist in the vortex of the size of 3 km during the time of about 10 minutes, while smaller particles are inside the vortex longer than 10 minutes. The speeds acquired by the grains as a result of their interaction with the vortex can be of the order of the sound speed. Hence, the layers of meteoritic dust at the altitudes of 110 – 120 km (which have usually the width of about 1 km) can change their form, the dust can be redistributed over the whole existence region of the vortex. Moreover, transition of dust particles up to the altitudes of 130 km, where AG-vortices can form and exist, becomes possible. The presence of the regions with positive gradients of density against the background of the dipole vortices can result in the generation of streamers and zonal flows as a result of the nonlinear interaction with the dust vortex. We have illustrated also a possibility of the formation of acoustic-gravity vortices with the parameters close to those of large-amplitude vortices observed in Earth's troposphere.

DUST TRAJECTORIES IN DUST DEVILS:

We study trajectories of dust particles in DDs under the conditions of the atmospheres of Earth and Mars with taking into account forces of different nature. We investigate the influence of the electric field configuration on the dynamics of dust particles. We use the self-consistent model which gives us the electric field distributions. We compare also the obtained numerical results with those valid for the field of electric dipole when considering the trajectory of a dust particle far from the center of the vortex. Fig. 2 shows the trajectories of posi-

tively charged 40 μm -sized dust particles in DD with the size $r_0=20 \text{ m}$ in Earth's atmosphere with self-consistent electric field (curve 2) and with dipole electric field (curve 3). For this case the dipole moment ($0.0667 \text{ C}\cdot\text{m}$) is calculated using the value of the electric field near the surface of the planet. The charge of the particle is $8\cdot 10^{-15} \text{ C}$. Fig. 2b displays the imitation situation when electric field is turned off above some low altitude. The results given in Fig. 2b correspond to the fact that the electric field influences strongly the dust particle trajectory only at the stage of the dust particle capture. Moving upward in the vortex, the dust particle acquires the speed which is large enough to make the influence of the electric field negligible.

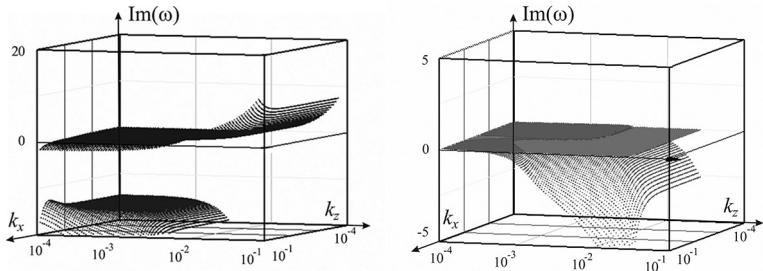


Fig. 1. Instability growth rates for all 4 dispersion surfaces characterizing AG-waves at 110 km altitude in k -space.

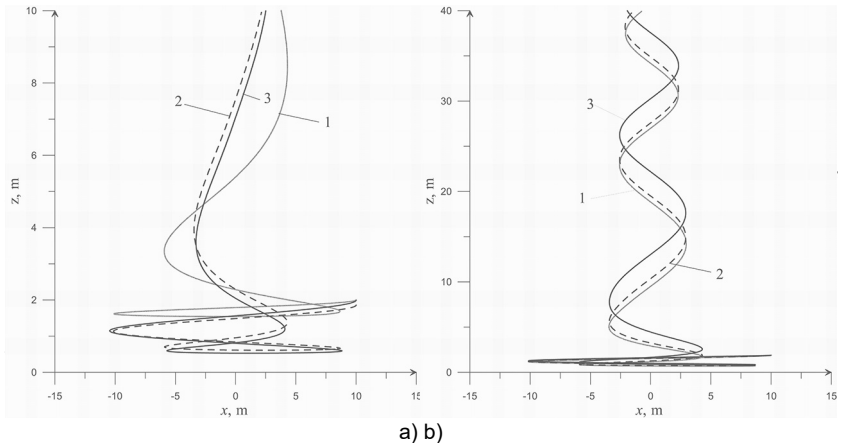


Fig. 2. DD in Earth's atmosphere. 40 μm -sized dust particle having the charge $Q=8\cdot 10^{-15} \text{ C}$. In the panel a) the grey solid curve 1, the dashed curve 2, and the black solid curve 3 correspond to the situations of the absence of the electric field, of the self-consistent electric field, and of the electric field of dipole, respectively. The panel b) shows the vertical projection of the trajectory of dust particle for the situation of the self-consistent electric field (the black solid curve 1), the imitation situation when electric field is turned off above the altitude of 1.88 m (the dashed curve 2) and above the altitude of 1.78 m

ACKNOWLEDGMENTS:

This work was supported by the Russian Federation Presidential Program for State Support of Young Scientists (project no. MK-6935.2015.2).

REFERENCES:

1. Izvekova, Yu. N., Popel, S. I., & Chen, B. B. (2015). Nonlinear acoustic-gravity waves and dust particle redistribution in earth's atmosphere. *Journal of Atmospheric and Solar-Terrestrial Physics*, 134, 41-46.
2. Izvekova, Yu. N., & Popel, S. I. (2016). Charged Dust Motion in Dust Devils on Earth and Mars. *Contributions to Plasma Physics*, 56(3-4), 263-269.

LIFE IN THE ALIEN ENVIRONMENTS: SIMULATION OF THE PHYSICAL PARAMETERS OF EXTRATERRESTRIAL HABITATS ON THE EARTH ANALOG ENVIRONMENTS

E.A. Vorobyova^{1,2}, V.S. Cheptsov¹, A.K. Pavlov³, M.A. Vdovina³,
V.N. Lomasov⁴, G.A. Osipov⁵, S.A. Bulat⁶, G.G. Dol'nikov²,
I.A. Shashkova², I.A. Kuznetsov², A.V. Zakharov²

¹M.V. Lomonosov Moscow State University, Leninskie gory, 1/12, Moscow, Russia; ²Space Research Institute of the Russian Academy of Sciences, Profsoyuznaya street, 84/32, Moscow, Russia

³Ioffe Physical-Technical Institute of the Russian Academy of Sciences, Politekhnikeskaya str., 29, Saint-Petersburg, Russia

⁴Saint-Petersburg State Polytechnical University, Politekhnikeskaya str., 29, Saint-Petersburg, Russia

⁵A.N. Bakulev Center for Cardiovascular Surgery, Moscow, Russia

⁶Saint-Petersburg B.P. Konstantinov Institute of Nuclear Physics, NRC "Kurchatov Institute", Gatchina, Saint-Petersburg, Russia.

Contact: elsaut@gmail.ru

At the heart of astrobiology research paradigm is the concept of the universal principles of the origin of life, and possible spreading of life through the space environment. Is life as we know it only a product of our planet's evolution? Could it be spread beyond the Earth and adopt to an alien environments? Studies of extreme habitats of the Earth significantly changed the ideas concerning of sustainability of the cell as of the biological unit. They demonstrated microbial interactions and the role of the environment in the long-term maintenance of the viability and metabolic activity of microbial communities. Alien habitats suggest great diversity in combinations of physical and chemical factors, which should be quite different from terrestrial conditions. Opportunities for long-term existence of complex living systems in these conditions have not been studied.

In a series of experiments we simulated the effects of different combinations of physical and chemical factors known as characteristics of the Martian regolith, and close to the space environment, on the natural microbial communities inhabiting xerophytic harsh habitats with extreme temperature conditions: polar permafrost and desert soil. The aim of the study was to examine the cumulative effect of factors (gamma radiation or electron irradiation of high-energy, low temperature, low pressure, UV exposure, the presence of perchlorates), to identify the limiting factor, to assess the possibility of metabolic reactions, and to find limits of the viability of natural microbial communities after exposure to the given conditions. Microbial viability was evaluated on a wide range of indicators: total cells' count, metabolic activity of microbial communities *in situ*, evaluation of *in situ* microbial community composition and structure by analyzing lipid markers and by phylogenetic sequence analysis of 16S rRNA genes of bacterial phylotypes, as well as by cytomorphological analysis (TEM) and isolation of sustainable cultures.

It was found that microbial biomarkers could be reliably detected in soil samples after radiation dose accumulation up to 1 MGy (not further investigated) in combination with exposure to low temperature and low pressure and in the presence of oxidants. High concentration (5%) of oxidants (perchlorate) and UV have shown the most obvious inhibitory effect on viable bacteria *in situ*. Nevertheless, it has been found that a long exposure of soil samples in the UV under high vacuum does not lead to an irreversible loss of viability and biodiversity of bacterial communities *in situ*. Also it has been confirmed that when the temperature is changed, subsurface ice sublimated, and moistened the overlying soil layer with the following activation of the metabolic activity of microbial communities.

Resistance to extremely high doses of radiation in simulated conditions proves that if there was an Earth-like Biosphere on the early Mars microorganisms could survive in the surface or subsurface layers of the Martian regolith for more than hundreds of millions of years after climate change. The study gives also some new grounds for the approval of transfer of viable microorganisms in space.

PHYSICAL AND THERMAL CONDITIONS FOR EXISTENCE OF LIQUID WATER OCEANS WITHIN ICY SATELLITES CALLISTO AND TITAN

A.N. Dunaeva, V. Kronrod, O. Kuskov

Vernadsky Institute of Geochemistry and Analytical Chemistry, Russian Academy of Sciences, Kosygin Str., 19, 119991 Moscow, Russia
 Contact: dunaeva.an@gmail.com

INTRODUCTION:

The study and interpretation of the Galileo and Cassini-Huygens spacecraft's data have led to the hypothesis that a water or water-salt oceanic layer could exist beneath the icy crusts of Jupiter's and Saturn's satellites Callisto and Titan. Since the water-rock interactions may lead to production of heat and organic materials the presence of such internal oceans imparts great exobiological significance to these satellites.

Although the existence of a liquid subsurface oceans in Callisto and Titan supported by a number of experimental measurements, there is no reliable evidence on the volume of the hypothetical ocean, its thickness, depth of occurrence, temperature, and chemical composition. At the same time, these parameters reflect the main problems in the understanding of processes controlling the origin and distribution of liquids in Callisto and Titan in general. In this paper we investigated the main physical and thermal conditions which make possible existing of internal oceans within Callisto and Titan using the model of partially differentiated satellites.

MODEL DESCRIPTION:

Within the proposed model, Callisto and Titan were assumed to consist of three major structural domains: the outermost water-ice shell, intermediate undifferentiated rock-ice mantle and the central rock-iron core. Significant restrictions on the application of such model are the values of the satellites' moment of inertia (I/MR^2), and their heat fluxes (F), which determine the stability of the rock-ice mantle (solid state of H_2O -phases), as well as the existence and depths of the inner ocean, and the thickness of the outer icy crust.

The values of the Titan's and Callisto's moments of inertia were estimated as $I/MR^2 = 0.342$ [1] and $I/MR^2 = 0.3549$ [2] respectively. However, the uncertainty in the moment of inertia calculation caused by the non-hydrostatic effects, is about 10% [3], resulting in the scatter in the true values of I/MR^2 in the range of $0.32 < I/MR^2 < 0.355$ [4]. There is no clarity concerning the actual values of Callisto's and Titan's heat fluxes, and the available literature data are obtained from approximate assessments. Therefore, in this paper, in the range of the satellites moments of inertia of $0.31 < I/MR^2 < 0.36$ we have investigated all possible satellites' heat fluxes values which provide the suitable thermal condition inside satellites' interiors to keep stability of the ice-rock mantle and existence of the internal ocean. This approach allows to take into account uncertainty in I/MR^2 experimental measurements, to assess the influence of the moment of inertia value on the extent of the satellites' differentiation, as well as to obtain independent constraints on the satellites' heat fluxes values which ensure the stability of undifferentiated satellites structure.

MAIN RESULTS:

The results of model calculations have shown that the models of partially differentiated satellites Callisto and Titan, containing an internal ocean, can be implemented with the following agreed parameters I/MR^2 and F :

- For Titan the condition for internal ocean and rock-ice mantle existence is the moment of inertia values equal to $0.312 < I/MR^2 < 0.366$ with the heat flux value of $3.3 < F < 7.1$ mW/m². With Titan's moment of inertia of $I/MR^2 > 0.366$ and the heat flux $F < 3.3$ mW/m² the existence of the internal ocean in the satellite is not possible. With the moment of inertia equal to $I/MR^2 < 0.312$ the satellite becomes fully differentiated into an inner silica core and an outer water-ice shell (Ganymede-like structure), and an undifferentiated rock-ice mantle is absent. At the heat flux values $F > 7.1$ mW/m² the external ice

Ih-crust of Titan becomes hydrostatically unstable due to the density inversion with depth in the outermost icy layer. So if the higher heat fluxes in the satellite are possible, it requires the further study of the H_2O -shell stability. The obtained values of Titan's moment of inertia and heat flux values allowed us to specify its admissible thickness and possible structure of the outer water-ice shell, to determine the thickness of the Ih-icy crust, depth of the internal ocean and size of central Fe-Si core. Depending on the moment of inertia value Titan's outer water-ice shell could reach the sizes from 230 km ($I/MR^2 = 0.36$) to 800-900 km ($I/MR^2 = 0.312$) with the corresponding radius of the inner core from 1000 km to 1700 km. Depending on the heat flux values of $3.3 < F < 7.1$ mW/m² the sizes of the satellite's outer icy Ih-crust could change respectively in the range of $160 > H_{in} > 80$ km and the depth of the inner ocean does not exceed 320 km.

- For the model of partially differentiated Callisto the following results were obtained: at the moment of inertia $I/MR^2 = 0.3549$ the allowable heat flux values vary in the range of 3.3-3.7 mW/m². The maximum thickness of the water-ice shell corresponds to the interval of 330 km, the radius of the inner core is 1280 km. The admissible thickness of Callisto's external Ih-crust is $170 > H_{in} > 110$ km, the depth of the internal ocean is less than 195 km.

ACKNOWLEDGMENTS:

This research was supported by the RFBR grant 15-05-02572.

REFERENCES:

- [1] Iess L. et al. // *Science*, V. 337(6093), pp. 457-459, 2012.
- [2] Anderson J.D., et al. // *Icarus*, 2001, 153, 157-161.
- [3] Gao P., Stevenson D.J. // *Icarus*. V. 226. No. 2. pp. 1185-1191, 2013.
- [4] Lefevre A. et al. // *Icarus*. V. 237. pp. 16-28, 2014.

REMOTE SENSING AND IN SITU MINERALOGIC SURVEY OF THE CHILEAN SALARS: AN ANALOG TO MARS EVAPORATE DEPOSITS?

J. Flahaut¹, M. Martinot^{1,2}, J.L. Bishop³, G.R. Davies², N.J. Potts⁴

¹Univ Lyon, Université Lyon 1, ENS-Lyon, CNRS, UMR 5276 LGL-TPE, F-69622, Villeurbanne, France

²Faculty of Earth and Life Science, VU University Amsterdam, De Boelelaan 1085, 1081HV Amsterdam, The Netherlands

³Carl Sagan Center, The SETI Institute, Mountain View, CA 94043, USA

⁴School of GeoSciences, University of Edinburgh, King's Buildings, Edinburgh, EH9 3FE, UK

Contact: jessica.flahaut@ens-lyon.org

The identification and characterization of hydrated minerals within ancient aqueous environments on Mars are high priorities for determining the past habitability of the planet. Few studies, however, have focused on characterizing the entire mineral assemblage, even though it could aid our understanding of past environments. In this study we use both spaceborne and field (VNIR spectroscopy) analyses to study the mineralogy of various salt flats (salars) of the northern region of Chile as an analog for Martian evaporites. This data is then compared to laboratory based Raman and XRD analyses for a complete overview on mineral assemblages. Core and marginal zones within the salars are easily distinguished on the Landsat 8 band color composites. These areas host different mineral assemblages that often result in different landscape types. The lower elevation Salar de Atacama, located in the Andean pre-depression, is characterized by a unique thick halite crust at its center, whereas various assemblages of calcium sulfates (gypsum, basanite, anhydrite) and sodium sulfates (mirabilite, thenardite, blodite, glauberite), borates (ulexite, pinnoite), Al/Fe- clays and carbonates (calcite, aragonite) were found at its margin. Sulfates form the main crust of the Andean salars to the east, although various compositions are observed. These compositions seem to be controlled by the type of feeder brine (Ca, SO₄ or mixed), a result of the local geology among other factors. Sulfate crusts were found to be generally thin (<5 cm) with a sharp transition to the underlying clay, silt, or sand-rich alluvial deposits. Coupled with morphologic analyses, VNIR spectroscopy, provide a powerful tool to distinguish among different types of salt crusts. XRD analysis allowed us to quantify the mineral assemblages and discuss the limitations of VNIR techniques in the presence of hydrated sulfates, which tend to mask the signatures of other minerals such as clays, chlorides, and carbonates. We found that the Atacama's unique arid and volcanic environment, coupled with the transition recorded in some of the salars has a strong Mars analogue potential. Characterizing the outcrop mineralogy at a variety of environments from alkaline, lake waters to more acidic salar brines may facilitate constraining geochemical environments on Mars (Flahaut et al., 2016).

REFERENCES:

Flahaut J. et al. (2016), Remote sensing and in situ mineralogic survey of the Chilean salars: An analog to Mars evaporate deposits?, *Accepted to Icarus*.

JUPITER: NEW CONFIRMATIONS OF THE AMMONIA ABSORPTION DEPRESSION AT LOW NORTHERN LATITUDES

V.G. Tejfel, V.D. Vdovichenko, A.M. Karimov, P.G. Lysenko, G.A. Kiriienko, N.N. Bondarenko, G.A. Kharitonova, V.A. Filippov
Fessenkov Astrophysical Institute, Almaty, Kazakhstan
 Contact: tejf@mail.ru

INTRODUCTION

In 2014 we first detected on Jupiter a strange depression of the 787 nm ammonia absorption band in the Northern hemisphere at low latitudes [1]. In subsequent years, an existence of this depression was annually confirmed by spectral observations, although we were noticing its variable character [2]. A special important confirmation of this feature on Jupiter is a significant depletion of gaseous NH_3 discovered recently. It also has been found at the same low latitudes of the Northern hemisphere in the region of the NEB with using of the big radio telescope's system - Very Large Array (VLA) with high angular resolution [3].

NEW OBSERVATIONS AND PROCESSING

From February to April of 2016, we carried out a special series of spectrophotometric observations of Jupiter to continue the study of the current behavior of the ammonia absorption bands centered at 645 and 787 nm. During these observations we have obtained more than 2,500 CCD-spectrograms, including the spectra of the central meridian, the GRS, and 12 scans of Jovian disk on different dates (70 zonal spectra in each scan). The measurements of the ammonia absorption bands are certainly rather difficult, since they are overlapped with more intense methane bands. The 787 nm NH_3 absorption band was extracted with using of ratios of the Jovian spectra to the Saturn's disk spectrum that was taken as a reference. «Clear» profiles of the NH_3 bands are shown in Figure 1.

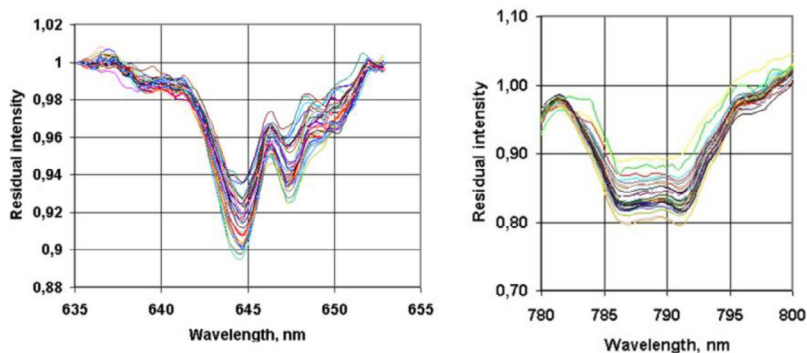


Fig. 1. The NH_3 absorption bands after extracting

Figure 2 presents the latitudinal variations of the NH_3 absorption bands' depths derived from about 800 zonal spectra. The equivalent widths of the bands give the same picture of latitudinal changes. The depression of the ammonia

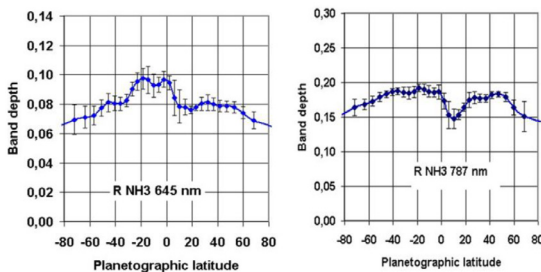


Fig. 2. Latitudinal variations of the 645 and 787 nm NH_3 absorption bands' depths on Jupiter in 2016.

absorption is more expressed for the 787 nm NH₃ band. It begins almost from the equator, and its maximum occurs at the planetographic latitude of 10°N; then the absorption again increases approaching to the latitude of 20°N. The equivalent bandwidths corresponding to these latitudes are equal to 18.7 ± 1.4 Å, 14.4 ± 1.0 Å and 17.8 ± 0.8 Å. The 645 nm NH₃ absorption band also shows depletion at the low latitudes of the Northern hemisphere, but it is less pronounced. At the temperate latitudes of the Northern hemisphere this band's absorption is systematically lower than the Southern Hemisphere's ones.

DISCUSSION

The differences of latitudinal variations for both ammonia absorption bands shown in Figure 2 were qualitatively kept in the past 12 years. So it can be considered as one of the characteristics of the distribution of the ammonia absorption on Jupiter mainly associated with the conditions of these two bands' formation. Figure 3 (in the left) shows equivalent widths of the 645 and 787 nm NH₃ absorption bands normalized to the zero latitude.

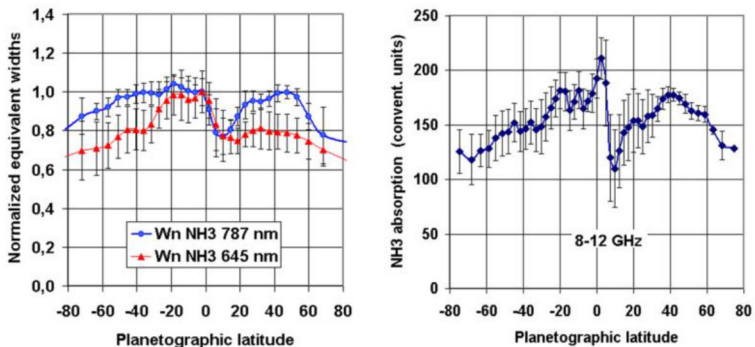


Fig. 3. Left - Normalized to the EZ equivalent widths of the NH₃ bands; Right – Longitudinally averaged latitudinal variations of the ammonia absorption according VLA map of Jupiter at 8-12 GHz.

This graph illustrates the observed differences in the absorption of ammonia, although there is a small depression in the north of the equator and it is visible from the 645 nm weaker band. We analyzed the radio map of Jupiter's gigahertz radiation [3] in order to compare the observed absorption in the course of such a different range. For this there were longitudinally averaged the profiles of brightness temperature at 8 -12 GHz. The resulting picture is upside-down, and conditionally displays the variations of the ammonia absorption or the ammonia gas content. A research of ammonia gas in the Jovian NEB in the thermal infrared range leads to a similar conclusion about the lower abundance [4], also showing the longitude and time variations of the ammonia absorption.

By comparing the observed effects, we, of course, conclude that it's necessary to take into account the fact that the cloud layer does not affect on the passage of millimeter radiation through the atmosphere, whereas the role of multiple scattering in the clouds may be significant for the transfer of the visible and infrared radiation.

REFERENCES:

- [1] V.Tejfel et al., Strange Latitudinal Variations of the Ammonia Absorption on Jupiter. Bull.AAS, 2005, Vol. 37, p.682
- [2] N. N.Bondarenko. The study of the ammonia absorption band NH₃ 787 nm variations in the atmosphere of Jupiter. Astronomical and Astrophysical Transactions. - Vol. 28. - Issue 2. - 2013. - P.81-86.
- [3] I. de Pater et al. Peering through Jupiter's clouds with radio spectral imaging. . Science, 2016, Vol. 352, Issue 6290, p.1290-1294
- [4] L.N. Fletcher et al. Mid-Infrared Mapping Jupiter's Temperatures, Aerosol Opacity and Chemical Distributions with IRTF/TEXES. Icarus, 2016 (In press).

LIGHT SCATTERING BY CHEMICALLY HETEROGENEOUS PLANETARY REGOLITH

N. Zubko¹, M. Gritsevich^{1,2,3}, E. Zubko^{4,5}, T. Hakala¹, J.I. Peltoniemi¹

¹Finnish Geospatial Research Institute, Geodeetinrinne 2, Masala, FIN-02430, Finland

²Institute of Physics and Technology, Ural Federal University, 19 Mira St., Ekaterinburg 620002, Russia

³Department of Physics, University of Helsinki, Gustaf Hällströmin katu 2a, Helsinki, FI-00560, Finland;

⁴School of Natural Sciences, Far Eastern Federal University, 8 Sukhanova St., Vladivostok 690950, Russia;

⁵Institute of Astronomy, V.N. Karazin Kharkov National University, 35 Sumskaya St., Kharkov 61022, Ukraine

Contact: nataliya.zubko@nls.fi

INTRODUCTION:

Analysis of the light-scattering response from an unknown target requires a comparison with well-characterized reference samples. In this sense, laboratory measurements are very useful for validation of the retrievals. In the present work we investigate two-component mixtures, consisting of bright and dark powders. We study how the volume ratio of bright and dark components affects the reflectance and the degree of linear polarization in particulate surfaces. This study is useful in interpretation of the data obtained from space missions. For instance, recent observations of the dwarf planet Pluto by *New Horizons space probe* [1] have revealed broad surface markings with bright and dark areas. Evidently, some parts of the Pluto surface consist of mixed bright and dark components. Our laboratory measurements can help to estimate the mixing ratio of dark and bright materials.

LABORATORY MEASUREMENTS:

The measurements were carried out with the Finnish Geodetic Institute Field Gonio-spectropolarimeter (FIGIFIGO) [2]. FIGIFIGO allows measurements of the reflectance and linear polarizations of the target, both in laboratory and in field conditions. In our laboratory measurements the target was illuminated with a halogen lamp. The fore-optics is connected to an ASD FieldSpec Pro FR 350-2500 nm spectroradiometer with an optical fiber. For the spectrometer calibration, a Labsphere Spectralon 99% is used as a white reference. The presented measurements have been obtained in the principal plane at phase angle range from -20° to 120° (except for the range from -6° to 6°). To estimate the accuracy of the measurements, each target was repeatedly measured up to 10 times.

Five different powder samples were measured (Fig. 1). Volcanic sand and NaCl were used as constituents in a two-component mixture. Pure volcanic sand, pure salt and 3 different mixtures of sand and salt were prepared.

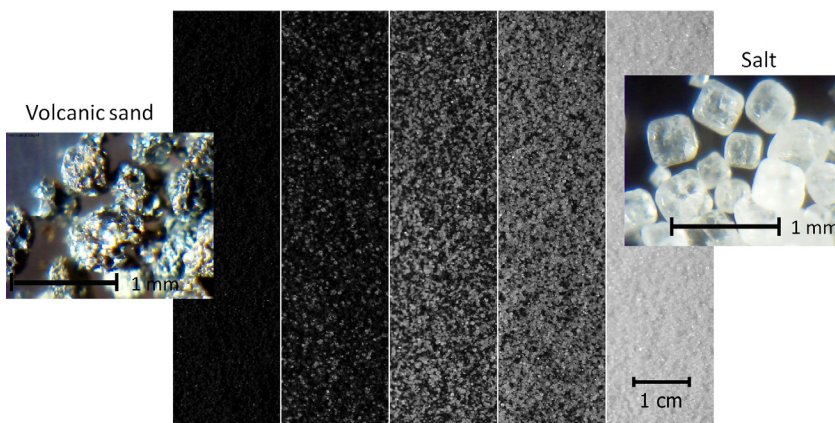


Fig.1. Samples of volcanic sand, salt and their mixtures

RESULTS AND CONCLUSION:

We conduct photometric and polarimetric measurements, using the FGI field goniospectropolariphotometer [3]. Reflectance at phase angle of $\alpha = 6^\circ$

varies from 4% (in pure volcanic sand) up to 86% (in pure salt) as compared to an equivalent Lambertian surface. As one can see in Fig. 2, changing the volume ratio of salt and volcanic sand monotonically affects light-scattering by particulate surface. While the sample is getting brighter, its phase function gets more flattened. Relative amount of dark and bright components unambiguously affects angular profile of the degree of linear polarization. This effect is the most apparent at side scattering, where degree of linear polarization acquires its maximum value P_{\max} . In the pure volcanic sand we found $P_{\max} \approx 55\%$; whereas, in the pure salt it is only $\sim 1\%$. In the mixtures of volcanic sand and salt, P_{\max} takes on intermediate values (Fig. 2, middle). Our measurements unambiguously reveal an inverse correlation between the geometric albedo (reflectance near backscattering) and P_{\max} that, in the literature, is referred to as the *Umov effect* (e.g., [4]). However, comparison of the Umov effect in the two-component mixtures with what was previously found in the lunar soils suggests that the effect takes somewhat different form in these two different types of surface.

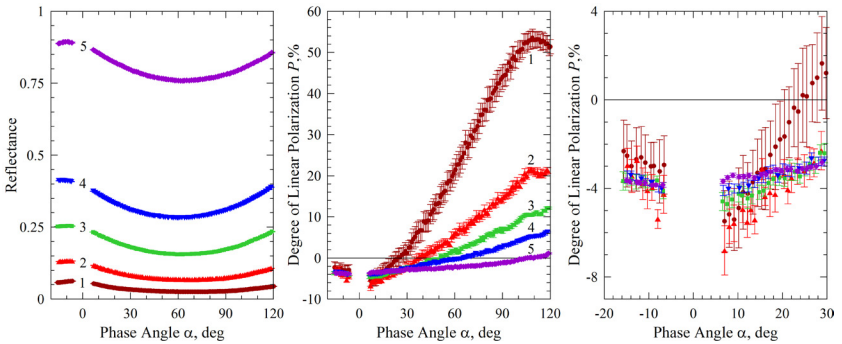


Fig.2. Phase curves of the reflectance (left) and the degree of linear polarization (middle and right) measured in the samples at wavelength $\lambda = 630$ nm (curves 1 – pure volcanic sand, 2 – 75% volcanic sand & 25% salt, 3 – 50% volcanic sand & 50% salt, 4 – 25% volcanic sand & 75% salt, 5 – pure salt).

Finally, it is worth noting that the previous study of two-component mixture of bright MgO and dark Fe_2O_3 powders has revealed a significant increase of the *negative polarization*, phenomenon that is commonly observed in regoliths at small phase angles, $\alpha < 30^\circ$ [5]. However, our present research suggests that the negative polarization changes monotonically in the mixture of volcanic sand and salt (see on right in Fig. 2). Thus, the enhancement of the negative polarization does not necessarily appear in all high-contrast mixtures. For more details on this research we refer the Reader to [3].

REFERENCES:

- [1] <http://www.nasa.gov/feature/nasa-s-new-horizons-sees-more-detail-as-it-draws-closer-to-pluto>
- [2] Peltoniemi, J., et al. 2014, *J. Quant. Spectrosc. Radiat. Transfer*, 146, 376.
- [3] Zubko, N., et al. 2016, *J. Quant. Spectrosc. Radiat. Transfer*, 178, 422;
- [4] Shkuratov, Yu.G. & Opanasenko, N.V. 1992, *Icarus*, 99, 468;
- [5] Shkuratov, Yu., & Ovcharenko, A. 2002, In: Videen, G. & Kocifaj, M., (eds.). *Optics of cosmic dust* (NATOScience Series). London: Kluwer Academic Publishers, pp. 225–238.

INFLUENCE OF GAMMA IRRADIATION IN SIMULATED MARTIAN CONDITIONS ON CATALASE ACTIVITY AND REACTIVITY OF EXOMETABOLITES OF *KOCURIA ROSEA* AND *ARTHROBACTER POLYCHROMOGENES*

V.S. Cheptsov¹, E.A. Vorobyova^{1,2}, A.H. Tambiev¹, A.K. Pavlov³,
M.A. Vdovina³, V.N. Lomasov⁴,

¹Lomonosov Moscow State University, GSP-1, Leninskie Gory 1-12, Moscow, 119991, Russia

²Space Research Institute of Russian Academy of Sciences, 84/32 Profsoyuznaya Str, Moscow, 117997, Russia

³Ioffe Physical-Technical Institute of the Russian Academy of Sciences, Polytechnicheskaya street, 26, Saint-Petersburg, 194021, Russia

⁴Saint-Petersburg State Polytechnical University, Polytechnicheskaya street, 29, Saint-Petersburg, 195251, Russia

Contact: cheptcov.vladimir@gmail.com

INTRODUCTION:

Ionizing radiation is one of the key factors at the analysis of the impact of cosmic or extraterrestrial environment as a potential habitat. Specifics of influence of this factor, from the point of view of astrobiology, consist not only in the wide range of a variation of parameters in for different objects of the Solar system, but also in the accumulation of doses for biological objects. Limits of resistance of a terrestrial life form to influence of ionizing radiation are authentically not defined, and many experiments on the influence of radiation on bioobjects don't take into account the cumulative effect of environmental factors that modify the effects of ionizing radiation. In this regard further researches and modeling in the conditions closest to parameters of target astrobiological objects are necessary.

In the present study, we investigated the reactivity of exometabolites and activity of enzymes of oxidative stress on the example of catalase after gamma ray irradiation of bacteria *Kocuria rosea* SN_T60 and *Arthrobacter polychromogenes* SN_T61 under conditions simulating the basic physical parameters of the surface layer of regolith of Mars (-50°C, 1 Torr).

MATERIALS AND METHODS:

Strains *Kocuria rosea* SN_T60 and *Arthrobacter polychromogenes* SN_T61 isolated from the sample of described earlier gray soil (Negev desert, Israel) [3] were objects of research. For the irradiation the biomass was immobilized in a sterile montmorillonite. Samples were irradiated by K-120000 gamma-ray facility with ⁶⁰Co sources in the climatic chamber allowing to maintaining pressure of 1 Torr and temperature of -50°C during the whole time of irradiation. In addition to the original control culture we investigated variant after the influence of low pressure and temperature without carrying out gamma irradiation.

The number of culturable bacteria was determined using solid Peptone Yeast Glucose (PYG) culture medium. Reactivity of exometabolites (RE, oxidizing – OA and anti-oxidizing – AOA activity) was measured by method of chemical models with 0,04% solution of 3,4-dioxyphenylalanine (DOPA) in distilled water [7]. OA and AOA determined respectively by increase or reduction in the rate of oxidation of DOPA in control (net PYG liquid medium) and at addition of the cultural liquid of bacteria containing native exometabolites. Acceleration or deceleration of oxidation of DOPA was defined by a tangent of angle of an inclination of a curve of increase of optical density in time at a constant temperature of 45°C on the «Akvakon-4» device [7]. Catalase activity in cultural liquid was measured using gasometrical method [8].

RESULTS AND DISCUSSION:

After irradiation in simulated Martian conditions number of colony forming units (CFU) of *K. rosea* and *A. polychromogenes* has increased by 1.7-2.6 times. In the control experiment after exposure to low temperature and pressure (without irradiation) the number of CFU of *K. rosea* has increased by 6.5 times. Thus,

increase in number of the culturable cells was the response to influence of low temperature, and, perhaps, the low pressure, but not gamma radiation. Desiccation of the culture immobilized in a mineral in vacuum promoted an additional immobilization of cells that could lead to changes in their physiological state and metabolism. It is known that freezing-thawing could promote cell proliferation activation [6]. According to the literature, 2 kGy gamma radiation dose resulted in the death of 90% of the cells of *K. rosea* population [4]. However, in our experiment 1 kGy dose in a vacuum at a low temperature didn't suppress the number of the reproducing cells. It can be explained variously: a) reduction of radiation damage of the cells due to irradiation at a low temperature [1]; b) heterogeneity of the bacterial populations [4] and compensation of the inhibiting ionizing radiation impact on the population components due to activation of other components owing to the impact of temperature fluctuations and vacuum which was shown in unirradiated control; c) high resistance to a multiple stress of the strains that are adapted to extremely xerophytic habitats [5]. Influence of a number of extreme physical factors manifested through oxidative stress, which allows the microorganisms to intensify quite universal response mechanisms with subsequent adaptation in stable adverse conditions [2].

Extreme influence of the studied combination of physical factors significantly has affected reactivity of exometabolites of bacterial strains (fig. 1, 2). RE of *K. rosea* SN_T60 strain after exposure in simulated Martian conditions sharply changes in the same points (6 h, 30 h, 72 h, 10 days) as that of the control variant. However, during the period 6-48 hours of growth exometabolites of exposed strains have up to 27% higher oxidative activity. Further, both exposed variants (irradiated and unirradiated) have significantly higher antioxidant activity than the control: in the period from 3 to 25 hours AOA exceeds the control level by 40-90%.

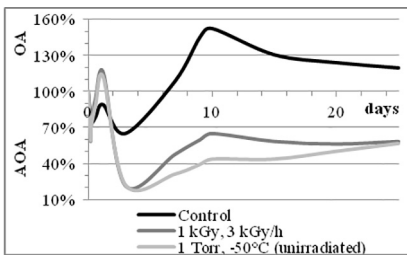


Fig. 1. RE of *K. rosea* SN_T60. OA – area of oxidizing activity; AOA – area of anti-oxidizing activity.

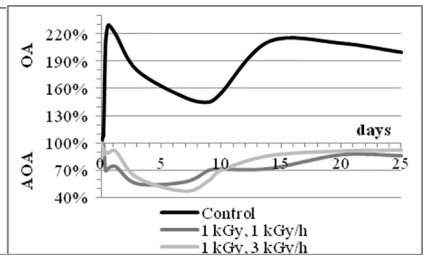


Fig. 2. RE of *A. polychromogenes* SN_T61. OA – area of oxidizing activity; AOA – area of anti-oxidizing activity.

RE of control strain of *A. polychromogenes* SN_T61 for the entire period of measurements was in oxidizing area, RS of the irradiated strains – in anti-oxidizing area. From 10 h to 25 days of growth, AOA in the irradiated variants exceeded control level by 75-150%. Principal divergences were not observed between the strains, which were irradiated at equal doses but with various intensity of radiation.

Increasing of AOA of exometabolites is consistent with increasing of catalase activity of *K. rosea* culture liquid after irradiation. During the period till 3 days of growth catalase activity of the initial strain and irradiated variant was the same. However, further activity of irradiated culture increased twice concerning control. Increasing of AOA of exometabolites and enhancing of catalase activity indicates the complex response of antioxidant system of the studied bacterial strains to the impact of multifactorial stress.

CONCLUSION:

The studied strains of bacteria have shown high resistance to influence of gamma radiation, low pressure and low temperature. Exposure to model conditions of the surface layer of the Martian regolith did not led to the death of microorganisms, but, on the contrary, caused active cell reproduction and adaptive response to stress. Results of research testify to a possibility of a survival and adaptation of bacteria in a surface layer of Martian regolith in case of transport to Mars of microorganisms from Earth or in event of formation on early Mars of the biosphere of terrestrial type.

Low pressure and low temperature significantly have reduced radiation damage. In this regard, it is possible to suppose that duration of potential preservation of microorganisms and their resistance in extraterrestrial conditions (on objects where radiation is the main limiting factor) is underestimated.

Results of research presented new evidence of interconnected reactions of the response to a multiple stress in bacteria. The practical prospect of application of this knowledge lies as in the field of improvement of methods of astrobiological search (the choice of key biomarkers in relation to object of research), and development of new technologies, in particular, in extraterrestrial conditions.

ACKNOWLEDGMENTS:

This work was supported by RFBR grant No. 13-04-01982 and by RSF grant No. 14-50-00029 (in part of culturing and identification of bacteria).

REFERENCES:

- [1] Baumstark-Khan C., Facius R. (2002). Life under conditions of ionizing radiation. In *Astrobiology* (pp. 261-284). Springer Berlin Heidelberg. [2] Chattopadhyay M.K. et al. (2011). Increase in oxidative stress at low temperature in an Antarctic bacterium. *Current microbiology*, 62(2), 544-546. [3] Cheptsov et al. (2015). Influence of gamma radiation, low pressure and low temperature on viability of microbial community of the gray soil as analytical model of Martian regolith. *Modern Problems of Science and Education*, 3. (In Russian). [4] Cox M.M., Battista J.R. (2005). *Deinococcus radiodurans*—the consummate survivor. *Nature Reviews Microbiology*, 3(11), 882-892. [5] Erkus O. et al. (2013). Multifactorial diversity sustains microbial community stability. *The ISME journal*, 7(11), 2126-2136. [6] Soina V.S., Vorobyova E.A. (2004). Adaptation of Bacteria to the Terrestrial Permafrost Environment. In *Origins* (pp. 427-444). Springer Netherlands. [7] Tambiev A.H. (1984). Reactivity of plant exometabolites. (In Russian). [8] Zvyagintsev D.G. (1991). Methods of soil microbiology and biochemistry. (In Russian).

LIMITS OF RESISTANCE OF SOIL MICROBIAL COMMUNITIES TO IMPACT OF GAMMA RADIATION

V.S. Cheptsov¹, E.A. Vorobyova^{1,2}, S.A. Bulat³

¹Lomonosov Moscow State University, GSP-1, Leninskie Gory 1-12, Moscow, 119991, Russia

²Space Research Institute of Russian Academy of Sciences, 84/32 Profsoyuznaya Str., Moscow, 117997, Russia

³B.P. Konstantinov Petersburg Nuclear Physics Institute, National Research Centre "Kurchatov Institute", Orlova Roscha, Gatchina, 188300, Russia
Contact: cheptcov.vladimir@gmail.com

INTRODUCTION:

Ionizing radiation is one of the major factors that can hinder the preservation and distribution of life in the Solar system. In this regard, data on resistance of a terrestrial life form to influence of ionizing radiation have great importance for an assessment of possibility of origin and preservation of life on various space bodies and for the choice of objects and regions, which are perspective for astrobiological search.

Currently, it is shown that the most radioresistant species of microorganisms in pure culture capable withstand gamma irradiation by doses about 20-25 kGy, and with the temperature decreasing during the irradiation up to 80 kGy [3, 5]. The resistance of microbial communities inhabiting natural habitats to the effects of ionizing radiation is less well studied. Gamma radiation is used in some cases for the sterilization of the soil, but scant data about sterilizing doses are contradictory, and conditions conducive to the high resistance of microorganisms, remain unclear [8]. According to various authors, soil was sterilized by gamma radiation dose from 15 kGy to 50 kGy [8, 11]. It is also shown that in the case of irradiation under conditions of low pressure and low temperature the microbial communities of extreme habitats are able to withstand gamma irradiation by doses up to 1 MGy [1, 2]. In general, the radioresistance of the microbial communities is poorly studied, and the sterilizing doses are not determined.

We irradiated soddy-podzolic soil (Moscow region) and gray soil (Negev desert, Israel) by gamma rays with dose gradient from 159 kGy to 1.35 MGy in conditions close to normal (+ 16°C, 1 atm.) in order to find limit of resistance of soil microbial communities to gamma radiation.

MATERIALS AND METHODS:

The samples of soddy-podzolic soil (Moscow region) and gray soils (Negev desert, Israel), taken from a depth of 5-10 cm (horizon A) were objects of research. This choice of objects of study was caused by the fact that the radioresistance of microorganisms associate with resistance to a number of other extreme factors [7, 12, 13] and a comparison of the reaction to irradiation communities of extreme and non-extreme habitats have high importance in terms of adaptive capacity of microbial communities in situ.

Samples were irradiated by «Isslodovatel'» gamma-ray facility with ⁶⁰Co sources at radiation intensity from 3.7 to 10.8 kGy/h and at a temperature of + 16°C. The temperature during irradiation was logged by a thermocouple thermometer-recorder ATE-9380 («Aktakom», Russia). The samples were irradiated by doses of 159 kGy, 343 kGy, 463 kGy, 741 kGy, 1 MGy and 1.3 MGy. Non-irradiated samples served as controls. After irradiation and before analysis samples were kept at the temperature of -18°C.

Determination of the number of cultured bacteria in soils was determined using solid Peptone Yeast Glucose (PYG) medium [14]. The total number of prokaryotic cells was measured using epifluorescence microscopy (EFM) with acridine orange [1]. Assessment of the potential metabolic activity of soil microbial communities was conducted using the multisubstrate testing method (MST) [1, 6]. During the MST, it was used a set of 47 test-substrates belonging to different classes of organic compounds: sugars, alcohols, amino acids, salts of organic acids, polymers and others.

RESULTS AND DISCUSSION:

In a sample of soddy-podzolic soil the number of aerobic heterotrophic bacteria capable to growth on a PYG nutrient medium decreased from 4.7×10^7 to 60

colony forming units (CFU) per gram of soil after irradiation by 159 kGy dose. Bacteria culturable on PYG medium were not detected after irradiation by higher radiation doses. The total number of prokaryotes (determined using EFM) decreased by almost an order of magnitude - with the 4×10^8 to 5.5×10^7 cells/g after impact of 159 kGy dose. Microbial community of control sample had high metabolic activity and was able to consume 28 substrates (out of 47 tested), belonging to different classes of organic compounds. The irradiation by 159 kGy dose led to sharp reducing of the potential metabolic activity of the microbial community - only one substrate (peptone) was consumed. At higher doses of irradiation the metabolic activity by the MST method was not detected.

In the control sample of gray soil and after irradiation by doses of 159 kGy, 343 kGy and 463 kGy number of culturable bacteria was 8×10^7 , 2×10^5 , 1.5×10^5 and 2.8×10^3 CFU/g, respectively. Cultured bacteria were not found in the samples irradiated with doses above 463 kGy. The total number of cells after irradiation with 463 kGy dose decreased by more than 40 times - from 1.3×10^9 to 3×10^7 cells/g. A variety of substrates which were consumed by the microbial community was sharply reduced after irradiation - with 27 substrates in the control of up to 3 (peptone, cysteine, glucose) after a dose of 159 kGy and 2 (peptone, cysteine) after a dose of 343 kGy. At higher doses of irradiation metabolic activity was not detected by the MST method.

In general, investigated microbial communities showed high resistance to high doses of gamma radiation. Culturable bacteria were found in samples of soddy-podzolic soil and gray soil even after irradiation with doses of 159 kGy and 463 kGy, respectively, which substantially exceeds the existing estimates of radioresistance of microorganisms. At the same time, the lack of culturable cells after irradiation with higher doses cannot be unambiguously interpreted as samples sterilization. It is known that bacteria can pass into not culturable state under influence of stress conditions (including gamma irradiation) [9, 10]. In this regard, attempts of reactivation of microbial communities are assumed in continuation of present work.

Exposure to gamma radiation has caused a sharp decline in the potential metabolic activity and functional diversity of microbial communities, which may also indirectly indicate a reduction in species diversity. It is not clear whether it is possible full or partial recovery of the microbial community and its functioning as an integrated system with realization of its biospheric functions.

Microbial community of gray soil showed significantly higher radioresistance. It is probably connected with high resistance to multiple stresses of microorganisms adapted to extreme xerophytic habitats [4].

CONCLUSION:

Soil microbial communities are able to withstand gamma irradiation by doses of at least 463 kGy. The received data suggest that the resistance of the soil microbial communities to the effects of ionizing radiation significantly underestimated. It gives grounds for a more optimistic analysis of the possibility of life existence on the some objects and bodies in the Solar system.

ACKNOWLEDGMENTS:

This work was supported by RFBR grant № 16-34-01275.

REFERENCES:

- [1] Cheptsov et al. (2015a). Influence of gamma radiation, low pressure and low temperature on viability of microbial community of the gray soil as analytical model of Martian regolith. *Modern Problems of Science and Education*, 3. (In Russian).
- [2] Cheptsov et al. (2015b). The microbial community inhabiting ancient arctic permafrost withstands gamma irradiation dose of 1 MGy in simulated Martian conditions. In International Conference Permafrost in XXI century: basic and applied researches. Program and Conference materials, Pushchino, pp. 105–106.
- [3] Dartnell et al (2010). Low-Temperature Ionizing Radiation Resistance of *Deinococcus radiodurans* and Antarctic Dry Valley Bacteria. *Astrobiology*, V. 10, N. 7, pp. 717-732.
- [4] Erkus et al. (2013). Multifactorial diversity sustains microbial community stability. *The ISME journal*, 7(11), 2126-2136.
- [5] Ferreira et al. (1999). Characterization and radiation resistance of new isolates of *Rubrobacter radiotolerans* and *Rubrobacter xylanophilus*. *Extremophiles*, 1999, 3, pp. 235-238.
- [6] Gorlenko M.V., Kozhevnikov P.A. (2005). Multisubstrate testing of natural microbial communities, MAKS Press, Moscow. (In Russian).
- [7] Mattimore V., Battista J.R. (1996) Radioresistance of *Deinococcus radiodurans*: functions necessary to survive ionizing radiation are also necessary to survive prolonged desiccation. *Journal of Bacteriology*, 178(3), pp. 633–637.

- [8] McNamara et al. (2003). Effects of acute gamma irradiation on chemical, physical and biological properties of soils. *Applied Soil Ecology*, V. 24, N. 2, pp. 117-132.
- [9] Mulyukin et al. (2001). Synthesis of anabiosis autoinducers by non-spore-forming bacteria as a mechanism regulating their activity in soil and subsoil sedimentary rocks. *Microbiology* 70(5), pp. 535-541.
- [10] Pitonzo et al. (1999). Effect of Gamma Radiation on Native Endolithic Microorganisms from a Radioactive Waste Deposit Site. *Radiation Research*, V. 152, N. 1, pp. 64-70.
- [11] Rainey et al. (2005). Extensive diversity of ionizing-radiation-resistant bacteria recovered from Sonoran Desert soil and description of nine new species of the genus *Deinococcus* obtained from a single soil sample. *Applied and environmental microbiology*, 71(9), pp. 5225-5235.
- [12] Romanovskaya et al. (1999). Sensitivity of soil bacteria isolated from the alienated zone around the Chernobyl Nuclear Power Plant to various stress factors. *Microbiology*, 68(4), pp. 465-469.
- [13] Wassmann et al. (2010). Adaptation of *Bacillus subtilis* cells to archean-like UV climate: relevant hints of microbial evolution to remarkably increased radiation resistance. *Astrobiology*, 10(6), pp. 605-615.
- [14] Zvyagintsev D.G. (1991). Methods of soil microbiology and biochemistry. (In Russian).

GROUND-BASED DUSTY EXOSPHERE SIMULATION CHAMBER FOR THE DEVELOPING AND CALIBRATION OF LUNAR LANDER INSTRUMENTS

I.A. Kuznetsov¹, E.A. Lisin², A.V. Zakharov¹, G.G. Dolnikov¹,
I.A. Shashkova¹, A.N. Lyash¹, S. Bednyakov¹

¹Space Research Institute of Russian Academy of Sciences, 84/32
Profsoyuznaya Str, Moscow, 117997, Russia

²Joint Institute for High Temperatures of the RAS, Moscow, Russia
Contact: kia@iki.rssi.ru

The surface of the Moon, as well as the surface of any space body without an atmosphere, is subjected to the solar wind and ultraviolet radiation. As a result, a charge appears on the surface and electric fields near it are induced. Dust particles from the lunar regolith occurring in the near-surface plasma can levitate over the surface, forming dusty plasma clouds. One of the main problems of future missions to the Moon is associated with lunar dust.

In order to gain a better understanding of mass transfer processes occurring on surfaces of the moon and other atmosphereless celestial bodies it is necessary to conduct physical simulations in a laboratory. Usually, when the UV impact on dust particles is experimentally studied, dust levitation is provided by electric fields of a non-photoemission nature [1], or is not observed at all [2].

Our poster presents the Vacuum Dust Particles Simulating Chamber and first results with the lunar dusty exosphere simulation. We are also to present first results of SPIS-Dust numerical modelling of Dust-Instrument interaction investigation in comparison with lunar exosphere numerical modelling.

REFERENCES:

- [1] Sickafoose A.A., Colwell J.E., Horányi M., and Robertson S., J. Geoph. Res., 107, 1408 (2002)
- [2] Filippov A.V., Babichev V.N., Fortov V.E., Gavrikov A.V., Petrov O.F., Starostin A.N., and Sarkarov N.E., J. Exp. Theor. Phys., 11 2, 884 (2011)

NEURAL NETWORK BASED SIMULATIONS FOR AUTONOMOUS EXPLORATION OF THE OCEAN FLOOR BY ROBOTIC SYSTEMS

I.E. Digel, N. Berger, H. Bonsmann

Institute for Bioengineering, Aachen University of Applied Sciences, Heinrich-Mußmann-Str. 1, D-52428 Jülich, Germany

Contact: digel@fh-aachen.de

INTRODUCTION:

Autonomous robotic systems displaying features of intelligent adaptation to a highly dynamical environmental situation are now under intensive investigation and development in the frames of various international projects. Such studies are of great importance for military and surveillance applications as well as atmospheric, oceanic, and, especially, space research. Taxis, the ability of living organisms to sense and actively response to three-dimensional chemical or physical gradients, is a well-studied phenomenon. In natural biological systems, various forms of taxis (chemotaxis, gravitaxis, phototaxis, etc.) create an important basis for ecological flexibility, better competitiveness, and ultimately, higher survival rate. Yet another compelling fact is that this relatively complex behavior is accomplished in many animals by surprisingly simple neural networks, containing just a few neurons.

In our study we have derived several simple neural models and tested their chemotactic responses in 2D environment. One of our goals was to demonstrate feasibility and usability of the approach applying the ideas of NeuroEvolution of Augmenting Topologies for the purposes of autonomous navigation, for instance, on an ocean floor.

MATERIALS AND METHODS:

The neural network design and all simulations were performed using MatLab® code running on a PC. Gaussian-shaped distributions were used to model two-dimensional chemical attractant gradients. The initial positions of the probe within a circular gradient field were chosen arbitrarily.

RESULTS AND CONCLUSIONS:

Though some further (self-) adjustments seem to be necessary for better system performance in our experiments, combining of neural networks with genetic machine-learning algorithms for autonomous navigation has shown very promising probe behavior (Fig).

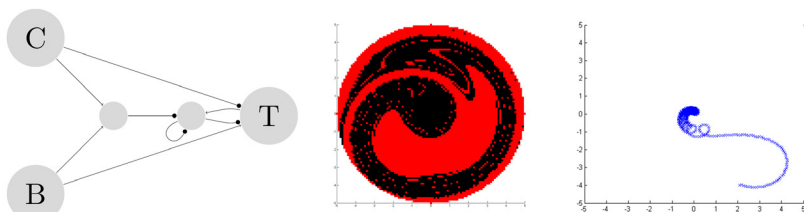


Fig. 1. **Left:** one of the tested network variants (C: attractor concentration as an input signal; B: bias; T: Angle of rotation (dynamically ranged from -50° to 50°). Excitatory and inhibitory connections are indicated by arrows and black circles, correspondingly. **Center:** an example of the color-coded efficacy map: from the black-labelled starting points it was possible to reach the "spot of interest" within 500 steps. **Right:** an example of a successful searching trajectory simulation.

OUTLOOK:

A vitally important property of a successful robotic system for future space exploration will be the capability to adjust its performance autonomously, depending on a real-time flow of multiple signals, relevant for decision-making. Future work will involve both improvement of the model and analysis of the resulting solutions. Improvements might include introducing realistic performance constraints, optimization of the synaptic connections, eliminating redundancy etc. Analyses will be aimed also at determining the role and contribution of individual network features in chemotactic behavior.

DIFFERENTIAL OPTICAL DETECTION OF “BLACK SMOKERS” SULFUR COMPOUNDS USING SELF-ORGANIZING MAPS

I.E. Digel, Th. Sichtermann, D. Porst

Institute for Bioengineering, Aachen University of Applied Sciences, Heinrich-Mußmann-Str. 1, D-52428 Jülich, Germany

Contact: digel@fh-aachen.de

INTRODUCTION:

Primary goal of many space exploration programs is finding organic material and extraterrestrial life (extant or extinct). Appropriate tools for life detection must be highly sensitive and ideally would require little to no sample handling. Spectroscopic techniques are perfectly suited for this task, since no sample acquisition and no reagents of any kind are needed and a measurement requires little time and energy. Life-specific organic molecules known so far typically possess conjugated aromatic structures and therefore exhibit high intrinsic fluorescence. Although extraterrestrial life might be composed of any kind of molecules, fluorescent conjugated structures are so functional that they likely will be a part of extraterrestrial biochemistry. Meanwhile, fluorescence spectroscopy, in particular Excitation-Emission Matrices (EEM) methodology, has become an indispensable tool for studying aquatic ecosystems. EEMs provide valuable multidimensional information about the composition of fluorescent chemical mixtures. However, regarding huge amounts and heterogeneity of obtained data, interpretation and the statistical treatment of EEM currently represent a significant challenge for (astro-)biogeochemists.

In this study we propose usage of Self-Organizing Maps (SOMs) for detection and classification of fluorescence signatures (sulfur compounds and bacteria) typical for the black smoker ecosystem. The SOMs approach belongs to the group of unsupervised (self-learning) neural network algorithms and has proved to be an excellent tool to explore patterns in large data sets. The SOM projects high-dimensional data sets onto a space of lower dimension, while preserving the topological relationships of the input data sets. Furthermore, we argue that the SOM-approach can significantly facilitate the extraterrestrial life search.

MATERIALS AND METHODS:

In this work the spectroscopic fingerprints of black smoker-specific molecules have been investigated using the SOM-methodology. We analyzed large and heterogeneous EEM data sets, including various inorganic compounds (such as sulfates, sulfides, thiosulfates etc.) For the detection of bacterial cells and bacteria-specific organic molecules, a cell culture of the proteobacterium *Thiobacillus thioeparus* was prepared. This chemoautotroph microorganism depends on sulfur and therefore can be taken as an example for chemoautotroph organisms living in deep water marine environments. Neurons in the SOM were used to represent the spectral characteristics of different compounds.

RESULTS AND CONCLUSIONS:

Some experimental data and processing examples are shown in Figure 1.

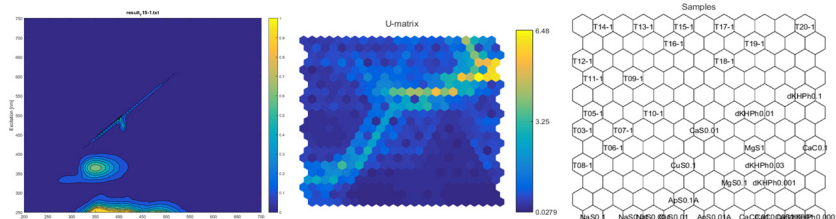


Fig.1. left: An excitation-emission matrix of a black smoker resident bacterium *Thiobacillus thioeparus*. The EEM was obtained at the day of highest cell population. **Center:** An example of the SOM-derived U-Map showing separation into two big data regions. **Right:** Analysis of the sample map reveals clustering of samples and indicates self-learned identification.

Application of the SOMs made possible to differentiate between classes of substances which indicates the SOM potential to develop into a tool for detecting spectral life signatures in an autonomous manner. The SOM-output can be also used for navigation purposes, for a guidance of an underwater vehicle through unknown terrain by a method similar to chemotaxis..

ENHANCEMENT OF INORGANIC MARTIAN DUST SIMULANT WITH CARBON COMPONENT AND ITS EFFECTS ON KEY CHARACTERISTICS OF GLUTAMATERGIC NEUROTRANSMISSION

T.A. Borisova, N.G. Pozdnyakova, A.O. Pastukhov, M.V. Dudarenko, A.G. Nazarova, A.A. Borysov, N.V. Krisanova
Palladin Institute of Biochemistry NAS of Ukraine; 9 Leontovicha Street, Kiev, 01601, Ukraine
Contact: tborisov@biochem.kiev.ua

Evidence on the past existence of subsurface organic-bearing fluids on Mars was recently achieved basing on the investigation of organic carbon from the Tissint Martian meteorite (Lin et al., 2014). Tremendous amount of meteorites containing abundant carbon and carbon-enriched dust particles have reached the Earth daily (Pizzarello and Shock 2010). National Institute of Environmental Health Sciences/National Institute of Health panel of research scientists revealed recently that accumulating evidences suggest that nano-sized air pollution may have a significant impact on central nervous system in health and disease (Block et al., Neurotoxicology, 2012). During inhalation, nano-/micro-sized particles are efficiently deposited in nasal, tracheobronchial, and alveolar regions and can be transported to the central nervous system (Oberdorster et al., 2004).

Based on above facts, the aims of this study were: 1) to upgrade inorganic Martian dust stimulant derived from volcanic ash (JSC-1a/JSC, ORBITEC Orbital Technologies Corporation, Madison, Wisconsin) by the addition of carbon components, that is, nanodiamonds; 2) to analyse acute effects of upgraded stimulant on the key characteristic of synaptic neurotransmission and to compare its effects with those of inorganic dust and carbon components *per se*. Acute administration of carbon-containing Martian dust analogue resulted in a significant decrease in Na^+ -dependent uptake of L-[^{14}C]glutamate that is the major excitatory neurotransmitter in the central nervous system (CNS). The ambient level of the neurotransmitter in the preparation of isolated rat brain nerve terminals increased in the presence of carbon-contained Martian dust analogue. This fact indicated that carbon component of native Martian dust can have deleterious effects on extracellular glutamate homeostasis in the CNS, and so glutamatergic neurotransmission.

CAN THE FUNGAL COMMUNITIES OF THE EARTH DESERTS SURVIVE IN SIMULATED MARTIAN CONDITIONS?

M.O. Kruchkova¹, A.E. Ivanova¹, E.A. Vorobyova^{1,2}, V.S. Cheptsov¹, A.K. Pavlov³, V.N. Lomasov⁴

¹Lomonosov Moscow State University, GSP-1, Leninskie Gory 1-12, Moscow, 119991, Russia

²Space Research Institute of Russian Academy of Sciences, 84/32 Profsoyuznaya Str, Moscow, 117997, Russia

³Ioffe Physical-Technical Institute of the Russian Academy of Sciences, Polytechnicheskaya street, 26, Saint-Petersburg, 194021, Russia

⁴Saint-Petersburg State Polytechnical University, Polytechnicheskaya street, 29, Saint-Petersburg, 195251, Russia

Contact: margo_kruchkova@mail.ru

INTRODUCTION:

The modeling of extraterrestrial environments is one of the ways for investigating the possibility of biological life form existence on different objects of the Solar system, for studying of the potential ways of microorganism adaptation and evolution under extreme conditions. It is informative to use the models which have parameters as close as possible to the conditions of astrobiological target objects. In this case the natural microbial communities of extreme habitats of the Earth, similar in a number of physical and chemical parameters with some of the planets and bodies of the Solar system can be the objects of study. Microbial communities of such habitats have the widest set of mechanisms of protection from the effects of stress factors.

The aim of this study was the analysis of impact of simulated Martian conditions viz. ionizing radiation with low temperature and pressure on the structure of culturable microfungi communities and fungal biomass in desert soils.

MATERIALS AND METHODS:

Samples from the upper humic horizons of grey soil (Negev desert, Israel) and grey-brown soil (Moroccan mountain desert) were the objects of research.

Samples were irradiated by K-120000 gamma-ray facility with ⁶⁰Co sources in the climatic chamber allowing to maintaining pressure of 1 Torr and temperature of -50°C during the whole time of irradiation. The samples of gray and gray-brown soils had obtained 100 kGy and 1 MGy total doses respectively. Before irradiation the samples were activated by wetting and were incubated during 10 days at temperature 28°C, and then they were dried to air-dry state. After irradiation the samples were stored at -18°C.

For culturing of fungi the method of soil suspensions inoculation was applied using solid Czapek medium [3] and alkaline agar [1]. Soil suspensions were warmed before inoculation (52°C, 2 min) [2]. The amount of fungal biomass in situ and its morphological structure were evaluated by method of direct fluorescent microscopy with calcofluor white and acridine orange dyes [3].

RESULTS AND DISCUSSION:

The quantity of fungal propagules in control samples was 1-10×10⁴ colony forming units (CFU) per gram of soil. Gray-brown soil from Morocco mountain desert was characterized by larger quantity and species diversity in comparison with gray soil from Negev desert.

The irradiation by 100 kGy dose in simulated Martian conditions had activating effect on gray soil mycobiota: the quantity of viable fungal CFU and culturable species diversity increased twice, the number of fungal spores and biomass of mycelium exceeded the control level. Higher radiation dose (1 MGy) conversely led to reduction of fungal biomass content, decreasing of diversity of fungal communities, growth inhibition of many species.

Influence of simulated conditions led to significant changes in structure of soil fungal communities: only a few fungi species, which were rare or typical in control samples, usually had sharp increasing of CFU number after irradiation and they were dominants in irradiated samples. *Aspergillus fumigatus* and *A. niger* were the most resistant species which dominated after impact of extreme conditions. It is interesting to note that some species which were not observed in control

samples appeared after irradiation. They are *Emericella nidulans*, *Geomyces pannorum*, *Phialophora fastigiata*, *Rhodotorula mucilaginosa*, some species of genera *Acremonium*, *Aspergillus*, *Cladosporium*, *Fusarium*, *Penicillium*.

CONCLUSION:

It was shown that the influence of high doses of ionizing radiation at low temperature and pressure didn't lead to death of soil fungal communities formed in extreme conditions of terrestrial desert soils. The structure of these fungal communities significantly changed after impact of simulated Martian conditions. The most resistant species of micromycetes survived, some rare or not cultivated in control samples fungal species were activated.

ACKNOWLEDGEMENTS:

This work was supported by RFBR grant No. 13-04-01982 and by RSF grant No. 14-50-00029 (in part of culturing and identification of fungi).

REFERENCES:

- [1] Bilanenko E.N., Georgieva M.L. Micromycetes of saline in South Siberia (Kulunda steppe) // Mycology and Phytopathology. 2005. P.39, № 4, pp. 6-13.
- [2] Kochkina G.A., Ivanushkina N.E., Karasev S.G. et al. The survival of micromycetes and actinobacteria under conditions of long natural cryoconservation // Microbiology. 2001. P.70, № 3, pp. 412-420.
- [3] The methods of soil microbiology and biochemistry.: Schoolbook/ Edited by D.G. Zvyagintsev. M.: MSU, 1991. 304 p.

SURFACE DECONTAMINATION OF “EXOMARS-2020” MARTIAN LANDING MODULE ELEMENTS BY PULSED UV IRRADIATION

S.G. Shashkovskiy¹, E.A. Deshevaya², S.G. Kireev¹, I.A. Zhelaev¹,
A.A. Guridov², N.M. Khamidullina³, D.V. Zakharenko³, N.D. Novikova²
¹ SIE “Melitta”, Ltd., Moscow, 16/10 Miklukho-Maklaya street, 117437 GSP,
Russia

² Russian State Research Centre Institute of Biomedical Problems
of the Russian Academy of Sciences, Moscow, Khoroshevskoe Highway 76A,
123007, Russia

³ Federal State Unitary Enterprise “Scientific-Production Association
named after S.A. Lavochkin”, ROSKOSMOS, Khimki, Moscow Region,
Leningradskaya street, 24, Russia

Contact: kireevsg.melitta@gmail.com

Planetary protection is one of the key issues for heavenly bodies' exploration. The danger of transferring earth living organisms to explored planets and their satellites calls for minimizing the microbiological contamination risk for the landing modules as well as their drop and landing subsystems. As the ExoMars-2020 project includes biological experiments by means of the mars rover equipment, which is part of the landing module, the said equipment belongs to IVb type as per COSPAR classification. This places rather rigid restrictions on the allowed biological contamination level of the landing module. To comply to the planetary protection requirements a wide range of antimicrobial measures as well as a number of steps for successful mission completion are elaborated.

It is known that exposure to ultraviolet (UV) irradiation is one of efficient surfaces disinfection methods. The purpose of this study is researching the possibility of “cold” sterilization of the ExoMars-2020 landing module open surfaces by high-intensity UV irradiation of continuous spectrum.

The efficiency study of test-objects surfaces decontamination was conducted on an experimental model. A pulsed xenon lamp, placed at 20-cm' distance from the test-object, served as a continuous spectrum UV irradiation source. The average UV flow on the decontamination surface (for 200-300 nm range) was 22 W/m² at the pulsed bactericidal flow of 300 kW/m².

As test microorganisms were chosen the most UV-resistant bacteria and fungi strains, isolated from the Baikonur facilities. The initial contamination on test-objects of different materials (plastic, metal, glass, rubber and others) was from 10⁷ CFU/cm² to 10³ CFU/cm². Decontamination efficiency was assessed as per standard procedures. The exposure time to 3.3 Hz light pulses differed in the range from 0.5 to 10 minutes. The test-objects temperature after their irradiation did not exceed 45°C.

The possibility of decontaminating test-objects, previously vacuum-packed in UV transparent materials, was also studied.

It has been shown by experiments that:

- pulsed UV irradiation of continuous spectrum has a high biocidal efficiency – from 99.999% up to 100%;
- disinfection efficiency for polyethylene film packed test-objects exceeds 99.99%;
- test-object material has no effect on decontamination efficiency;
- joint impact of hydrogen peroxide vapor and pulsed UV has the most pronounced antimicrobial effect on resistant microorganism strains.

A MODEL OF SHORT-LIVED OUTBURSTS ON THE 67P/CHURYUMOV-GERASIMENKO FROM FRACTURED TERRAINS IN THE ANUKHET REGION

Yu.V. Skorov¹, L. Rezac¹, P. Hartogh¹, A.T. Bazilevsky^{1,2}, H.U. Keller³

¹Max-Planck-Institut für Sonnensystemforschung, Justus-von-Liebig-Weg 3, 37077 Göttingen, Germany

²Vernadsky Institute of Geochemistry and Analytical Chemistry, Russian Academy of Sciences, 119991 Moscow, Russia

³Institute for Geophysics and Extraterrestrial Physics, TU Braunschweig, 38106 Braunschweig, Germany

Contact: skorov@mps.mpg.de

The comet 67P experienced numerous strong and very short-lived outbursts around perihelion passage (August 13, 2015) as documented by the Rosetta NAVCAM and OSIRIS cameras (A'Hearn et al. 2016). In this paper we propose and model a new mechanism for these short-lived outbursts of cometary activity. The presented model explains the unique outburst characteristics, and actually predicts that these events are even shorter, \approx 20-30 min, which is also now supported by observations (A'Hearn et al. 2016). We also reviewed other proposed mechanisms for cometary outbursts available in the literature; however, basic physical considerations show that they fail to explain this particular outburst.

The new model is built around the geomorphological features of fractures and cracks observed on this particular cometary nucleus, which are argued to extend into the deeper interior where super-volatile ices (e.g., CO) can be preserved for a long time in steady-state conditions. We speculate as the nucleus experiences growing gravitational and non-gravitational stresses during the perihelion approach, these cracks widen and deepen (Scheeres et al. 2016). The deepening crack leads to a sudden opening and subsequent dis-equilibration of the volatile-ice laden region resulting in a violent release of gas and dust. The sublimation process induces a rapid decrease in temperature, effectively shutting itself down, at which point the medium slowly returns to its equilibrium (i.e., very weak diffusive sublimation).

The new features of the model which are pertinent to the explanation of the observed outburst are

- the independence of external heat flux induced by solar irradiation;
- natural self-induced quenching of the outburst activity after a short time;
- In addition, the model does not require presence of large isolated cavities in the nucleus,
- and/or crystallization of amorphous ice and trapped supervolatiles release.

In the current stage, our model can be used to evaluate the expected gas and dust mass production during the outburst induced by the deepening crack. It also provides a unique opportunity to evaluate physical properties of the deep region because the freed dust and gas are evacuated from the nucleus deeper regions. Nevertheless, there are no quantitative data yet available regarding the amount of extra gas and dust released from the other instruments on board Rosetta. We plan to continue this work as the needed data are published in the future. Other important future work is to build a physical model of the cracks and their deepening mechanism, and analyze more of these outbursts that have been observed (A'Hearn et al. 2016) (at least 25 of similar nature (priv. comm. J. B. Vincent, Sep. 2015)). We believe that, at least, for this particular nucleus, the outbursts induced by the geomorphological activity of nucleus fractures can be a common mechanism.

REFERENCES:

- A'Hearn, M. F., Vincent, J.-B., & Team, O. 2016, in 47th Lunar and Planetary Science Conference (Houston: Lunar and Planetary Institute), Abstract #2678.
- Scheeres, D. J., Hirabayashi, T., Chesley, S., et al. 2016, in Lunar and Planetary Science Conference, Vol. 47, 1615.

HIGH-SENSITIVITY THREE-AXIS SEISMIC ACCELEROMETER FOR MEASUREMENTS AT THE SPACECRAFT AND THE PLANETS OF THE SOLAR SYSTEM

A.B. Manukin, I.I. Kalinnikov, A.V. Kalyuzhny, O.N. Andreev

Space Research Institute of Russian Academy of Sciences (IKI RAS), 117997, 84/32 Profsoyuznaya str., Moscow, Russia

Contact: amanukin@yandex.ru

In the development of a triaxial seismometer (at the same time performing the functions of a gravimeter and tiltmeter) for measurements of seismic activity on solar system planets it is necessary to solve a number of tasks that can be summarized as follows:

1. Development of a uniaxial sensor for measuring seismic acceleration in each of 3 mutually perpendicular directions;
2. Ensuring a high sensitivity of the sensor for each measuring axis of the device;
3. Development of the geometry of the arrangement of identical sensors in the device, providing the measurement in 3 orthogonal axes;
4. Stability of the sensor to shock and vibration loads encountered during launch of the spacecraft and its landing on the planet.

As an alternative to many sensitive mechanical system can be considered the system, characterized in that the sensitivity of the sensor for only one axis is provided by the elements of its mechanical stiffness. For this test body in the form of a cylinder with stretch marks (three stretching at an angle of 120 degrees at each end of the cylinder) suspended inside the hollow cylinder - housing. Small mechanical vibrations of the test masses along its axis are measured using a capacitive differential transducer. The small gaps between the side surface of the test mass and the housing (about 10 – 30 microns), as well as in the measuring capacitor capacitive transducer provides stability sensors to shock and vibration loads in the derivation of the SPACECRAFT and landing on the planet until the overloads up to 100g and more. The use of fibers of small diameter allows to reduce the natural frequency of the mechanical oscillator and to increase the sensor sensitivity to the level of $4 \cdot 10^{-9} \text{ m/s}^2$. Used diameter stretch marks of $\sim 0.1 \text{ mm}$ is possible to reduce, for example, up to 30 μm and to increase the sensitivity determined by the equilibrium thermal noise up to $5 \cdot 10^{-10} \text{ m/s}^2$.

A variant geometry of the device. In order to allow an opportunity to measure the seismic excitation along three mutually orthogonal directions using the same single-axis sensors, each of the three sensors is mounted along one of the three edges of the cube. The cube while mounted on the top so that the main diagonal line drawn from the vertex, directed along the vector of local gravitational vertical. Experiments with the physical model of single-axis sensor confirmed key expected features.

SCIENTIFIC ASPECTS AND OPPORTUNITIES OF THE “ROBOTIC SPACE MISSION TO EUROPE”: SPACE SYSTEMS APPLICATION AND TECHNOLOGY FOR SPACE MISSION TO EUROPA (ENCELADUS) – JUPITER’S AND SATURN’S ICE MOONS

Y. Ozorovich¹, A. Kosov¹, D. Skulachev¹, S. Klimov¹, S. Gorbatov¹, S. Potemkin¹, A. Lukomsky¹, F.S. Alain², A. Ivanov³, V. Mogilatov⁴

¹Space Research Institute of Russian Academy of Sciences (IKI RAS), 117997, 84/32 Profsoyuznaya str., Moscow, Russia

²IAAA International Group (France)

³Swiss Space Center

Contact: interecos@gmail.com

This paper presents a new conceptual and methodological approach for geophysical survey of the planetary geoelectrical markers and oreols of the subsurface liquid ocean on the surface ice moons on the base “conceptual design phase” of the future space missions on the ice moons. At the design stage of such projects is considered the use of various space instruments and tools for the full the complex geophysical studies of the manifestations and planetary processes of the subsurface liquid ocean on the surface ice moons. The existence of various forms of the ryolithozone on terrestrial planets and their moons: advanced Martian permafrost zone in the form of existing of the frozen polar caps, subsurface frozen horizons, geological markers and oreols of the martian ancient (relict) ocean, subsurface oceans of Jupiter’s and Saturn’s moons-Europa and Enceladus, with the advanced form of permafrost freezes planetary caps, it allows to develop a common methodological basis and operational geophysical instruments (tools) for the future space program and planning space missions on these unique objects of the solar system, specialized for specific scientific problems of planetary missions. Geophysical practices and methodological principles, used in 1985-2015 by authors [1-5], respectively, as an example of the comprehensive geophysical experiment MARSES to study of the Martian permafrost zone and the martian ancient (relict) ocean, creating the preconditions for complex experimental setting and geo-physical monitoring of operational satellites of Jupiter and Saturn- Europa and Enceladus. This range of different planetary (like) planets with its geological history and prehistory of the common planetology formation processes of the planets formation and to define the role of a liquid ocean under the ice as a climate indicator of such planets, which is extremely important for the future construction of the geological and climatic history of the Earth.

REFERENCES

1. https://www.researchgate.net/publication/304743560_Scientific_aspects_and_opportunities_of_the_ROBOTIC_SPACE_MISSION_TO_EUROPE_Space_systems_application_and_technology_for_space_mission_to_Europa_Enceladus_-_Jupiter%27s_and_Saturn%27s_ice_moons
2. https://www.researchgate.net/publication/298326582_Scientific_aspects_and_opportunities_of_the_ROBOTIC_SPACE_MISSION_TO_EUROPE
3. https://www.researchgate.net/publication/294406932_Space_systems_application_and_technology_for_space_mission_to_Europa_Enceladus_-_Jupiter%27s_and_Saturn%27s_ice_moons?ev=prf_pub
4. https://www.researchgate.net/publication/275638508_Cryolithozone_of_Mars_-_as_the_climatic_indicator_of_the_Martian_relict_ocean

THE RANGING ACCURACY OF THE RADIOSCIENCE EXPERIMENT WITH THE RADIO-BEACON TRANSPONDER IN COMPARISON WITH LASER RANGING

V.D. Gromov, A.S. Kosov,

Space Research Institute of Russian Academy of Sciences (IKI RAS), 117997, 84/32 Profsoyuznaya str., Moscow, Russia

Contact: vgromov@iki.rssi.ru

INTRODUCTION:

High accuracy ranging techniques demonstrated his efficiency for a wide variety of tasks including orbit parameter determinations and investigations of fine details of the rotation of solar system planets and their satellites. These details give information about interior structure and its dynamics, ranging from seasonal variations of a surface layer to mass flows in a liquid core.

Direct range measurements use a time delay of an electromagnetic signal proportional to a distance. The most accurate measurements of a time-delay are possible in radio-diapason of electromagnetic spectrum (radio-science techniques) and in optical region (laser ranging). For Solar System ranging, an important role plays a compromise between power budget of distant emitter or reflector/transponder and demands for high signal to noise ratio at a receiver end. An advantage of laser ranging is use of passive reflectors (no power consumption). The radio-science ranging (RSR) systems have advantages of use of existing telecommunication systems of space vehicles and ground-based space communication networks.

The Lunar Laser Ranging (LLR) was a most successful application of the long distant laser ranging technique. During a last decade RSR measurements become more accurate and useful.

THE RADIOSCIENCE EXPERIMENT IN LUNA-RESOURCE AND LUNA-GLOB SPACE PROJECTS.

Two different radio science instruments have been included into Russian Luna-Glob and Luna-Resource projects: the lander's radio beacon and the orbiter's receiver [1].

The radio beacon has three modes of operation: the autonomic mode (with an internal frequency standard), the mode of coherent transponder (with a transmitter phase locked to a received signal) and the mode of scientific data transmitter.

The instrument can be used for precise measurements of distance like LLR, using phase modulation of ranging signal by the Tausworthe Pseudo-Noise code. The accuracy of such measurements is compatible with that of LLR.

Table 1. The main parameters of the Lunar Radio Beacon.

Transmitter frequencies:	8.4 GHz (X band) and 32 GHz (Ka band, coherent)
Frequency stability:	$1 \cdot 10^{-13}$ (coherent transponder mode)
Transmitting power:	0.3 W (for each channel)
Receiver frequency:	7.2 GHz (X band)
Receiver noise temperature:	200 K
Power consumption:	7 W (each channel)
Scientific data transfer speed:	up to 0.1 Mbit/s

The orbiter's receiver is intended for receiving the signal from Luna's radio beacon or from Earth for the precise measurements of Doppler shift and therefore velocity and acceleration.

Table 2. The main parameters of the Lunar Orbiter Receiver.

Central frequency:	32 GHz (Ka band)
Bandwidth:	0.5 MHz
Transmitting power:	0.3 W (for each channel)
Receiver frequency:	7.2 GHz (X band)

Noise temperature:	≤ 150 K
Accuracy of the dV/dt measurements:	$3 \cdot 10^{-3}$ cm/s ²

These two instruments along with ground-based stations are included in radio-science experiments for the lunar ranging [2]. A phase measurements during the experiments are the source of data for the range determination ($\Delta R = \lambda \Delta \varphi / 2\pi$). The high frequency stability and low phase noises of the instruments permit to reach a ranging accuracy about 0.1 mm.

LASER RANGING.

A first on detection of laser signal reflected from the Moon have been obtained in 1962 during the MIT experiment [3]. First useful ranging data have been obtained in 1965 [4]. The ranging accuracy of 200 m was sufficient to refine parameters of Moon-Earth system. An instrumental accuracy was 7.5 m, but the resulting accuracy was defined by inhomogenties of the lunar relief in the region of a laser spot [4, 5]. This accuracy discrepancy was overpassed by use of retroreflectors, which was placed on the Moon's surface by Apollo 11 (1969), Lunokhod 1 (1970), Apollo 14, and 15 (1971), and Lunokhod 2 (1973).

During the following four decades, a progress in laser measurement technology provided an accuracy 1-2 cm, which was realized in two LLR station - MLRS (USA) and CEGRA (France). LLR stations in USSR, Japan and Australia was less successful. A further progress in LLR accuracy is possible with use of active laser transponders [6]. But an advantage of no power supply on the space end of the measurement link, it eliminates, unfortunately.

An interpretation of high accuracy ranging data is a specific problem. To reveal the tiny effects, like deviation from general relativity [7] or lunar liquid core signs [8], you should first subtract all other effects calculated with adequate accuracy. A few teams exist now, working in this field - in USA (JPL) [7, 8], in EU (ESA) [6], and in RF [9, 10].

A complex, interscience nature of a ranging data interpretation need detailed digital simulation and modeling of experiments. It is necessary to realize fully the instrumental accuracy as it was done in [9, 10] and in following works. A recent radio-science experiment was made with the Chinese "ChangE-3" [11], functioning since 2013 on the Moon surface with ranging accuracy 0.3 mm. After a one year of RSR measurements, a volume and accuracy of scientific data exceeds a mass of data collected during 44 years of LLR measurements [10].

CONCLUSION.

The existing instrumentation for radio-science lunar ranging provide 1-2 order of magnitude better accuracy than laser ranging. A future progress in laser ranging is possible after a development of active laser transponders with low power consumption, and after finding long-living sources of energy for them, in order to replace passive retroreflectors.

REFERENCES:

1. Kosov, A. S. (2015) 6M-S³ Symposium Abstract Book, pp. 201-203 (6MS3-PS-15).
2. Gromov, V. D. , Kosov, A. S. (2015) 6M-S³ Symposium Abstract Book, pp. 43-44 (6MS3-MN-20).
3. Smullin, L. D.; Fiocco, G. (1962) Nature 194, p. 1267.
4. Kokurin, Yu. L., et al. (1966) JETP Lett. 3, p.139.
5. Kokurin, Yu. L. (2003) Quantum Electronics 33, pp. 45-47.
6. Dehant, V., et al. (2012) Planetary and Space Science 68, pp. 94-104.
7. Williams, J.G., Newhall, X.X., Dickey, J.O. (1996) Phys. Rev. D 53, pp. 6730-6739.
8. Williams, J.G., et al. (2001) JGR 106 E11, pp. 27933-27968.
9. Gusev, A., Hanada, H., Kosov, A., et al. (2015) 6M-S³ Symposium Abstract Book, pp. 35-36 (6MS3MN-17).
10. Gusev, F., Hanada, H., Petrova, N. (2015) Rotation, physical libration, internal structure of the active and multi-layer Moon. Kazan, ISBN 978-5-00019-437-9.
11. Ip, W.; Yan, J.; Li, C.; Ouyang, Z. (2014) Research in Astronomy and Astrophysics 14, pp. 1511-1513.

DEVELOPMENT OF COMPLEX METHODS FOR REGIONAL ATMOSPHERIC MONITORING BASED ON SPACE-BORNE AND GROUND-BASED REGISTRATION OF NAVIGATIONAL SIGNALS

Ya.A. Ilyushin¹, V.I. Zakharov¹, A.L. Gavrik², A.M. Vorontsov¹,
N.Yu. Borisova¹

¹Moscow State University, Leninskie Gory, Moscow, 119992, Russia

²Fryazino Branch of the Kotelnikov Institute of Radiotechnics and Electronics, Vvedenskogo 1, Fryazino, Moscow region, 141120, Russia.

Contact: ilyushin@phys.msu.ru

INTRODUCTION:

Central industrial region of Russia, as one of the most populated and industrialized region of the whole Russian Federation, is characterized by complicated ecological situation. In the Moscow city urban agglomeration a huge human population and industrial power is concentrated on a relatively small area. Moscow with its suburbs, therefore, is a notable source of anthropogenic perturbations of the natural environment. Due to its high consumption of heat and electrical energy, motor fuel, and relatively low albedo of urban landscape in visible solar spectrum, the city in fact is a strong and compact source of heat, deposited in the surrounding atmosphere. In addition, there are strong emissions of water vapor, carbon dioxide, soot, dust, aerosols etc., influencing local heat and radiation balance in the atmosphere. All the mentioned impacts cause strong perturbations of natural fields of the atmospheric parameters, e.g. temperature, pressure and relative humidity. As a consequence, there can be generated acoustical gravity waves, propagating upward and reaching ionospheric heights. These perturbations largely determine regional atmospheric dynamics, local climate and air mass transport in the city and the region.

The complexity of the problem increases additionally due to huge variety of the sources of the acoustical gravity waves, like thermal and orographic inhomogeneities of the underlying surface. Thus, influence of the urban environment on the air mass transport has been repeatedly proved in the experiments. Studies show that the acoustical gravity waves, excited by the wave source at the source of the Earth, can indeed reach the ionosphere, provided their destruction due to the non-linear effects and further extinction take place at the heights above the main ionospheric maximum of the F2 plasma layer [1]

During the propagation in the atmosphere, the most stable are the waves with periods close to the buoyancy (Brunt-Vaisala) frequency of the free vertical oscillations of stratified atmosphere. Typical frequencies of the acoustical gravity waves are lower than buoyancy frequencies at the ionospheric heights, while the velocities do not exceed the sound speed at these heights, which are from hundreds of meters up to 2 kilometers per second. [2].

For this reason, techniques of regional monitoring of the atmosphere, including both precision local in situ measurements and remote sensing of various atmospheric parameters, providing average estimates in areas, not covered by contact measurements, are of especial importance. Complexity of this problem is caused primarily by lack of various observation data, both satellite and meteorological. Due to that, development of combined techniques, capable for assimilation and integration of heterogeneous data, is now extremely important.

The objective of the present study is development of complex approach to analysis of multi-instrumental data of regional atmospheric monitoring, including in situ airborne measurements together with remote sensing data, including radio occultation and interferometric experiments with radio navigational satellite systems.

RADIO OCCULTATION TECHNIQUE FOR REGIONAL MONITORING OF THE ATMOSPHERE:

Radio occultation technique, as a powerful and promising remote sensing technique, has been widely applied for satellite observations of the planetary atmospheres and ionospheres during more than 40 years. In the last 15 years this technique is actively used for the satellite monitoring of the terrestrial environment. Since 2001, formation of an international global system

of radio occultation monitoring of terrestrial atmosphere has been started. The system includes several low Earth orbiters, capable of receiving of radio signals of 24 navigational GPS satellites, thus performing more than three thousands radio occultation events every day. The system uses space-borne receivers GRACE, COSMIC and other types, orbiting nearly circular orbits with inclination of 75-85 degrees and height about 500 - 700 kilometers. Development of these techniques significantly improved the quality of assimilated data, partly removing the limitations of traditionally applied techniques and mitigating the impact of the noise on the process and result of the experimental research, to obtain more comprehensive information about the structure of environment being sounded.

In the practice of radio occultation sounding, starting from the pioneering works [3] until the end of the twentieth century, theoretical basis of the method was the geometrical optics approximation. One of the most important disadvantages of the method is its poor horizontal resolution, largely caused by small curvature of the atmosphere and long propagation distance of the sounding signal in it. Vertical resolution of the technique is also limited, in particular, by the diffraction scale. Detection and assessment of the parameters of the atmospheric structures, not exceeding and comparable to the Fresnel zone size, requires application of the proper methods, accounting for the wave effects (radio holography, diffractive tomography) and a priori information usage. For the validation of the geometrical optics (GO) approximation in the particular wave propagation situation, and detection of violation of ray approximation, we apply the approach based on the adiabatic invariant [4]. The approach allows reveal the connections between the observed wave field quantities, functional dependence between which otherwise cannot be established. Revealing the features of re-distribution of the radiation energy, connected with the variations of the Doppler wave frequency shift in the monochromatic RO experiment caused by the refraction in the spherically symmetrical gaseous envelope of the planet, allows detection of thin atmospheric layers, typically masked by the measurements noise and atmospheric turbulence. Conditions of conservation of the adiabatic invariant, which in fact is an indicator of validity of the geometrical optics approximation, were investigated by the authors in the series of direct simulations of the wave field in the inhomogeneous atmosphere with the numerical solution of the parabolic diffraction equation. Computer simulations of the wave fields in large domains with sizes, greatly exceeding the wavelength, is a separate challenging computing task, consuming much time and computational resources.

COMBINED DATA PROCESSING APPROACH:

We not only apply new methods of the adiabatic invariant for the complex vertical profile analysis, but we assimilate additional information, obtained from radio interference measurements of the navigational satellite signals on the ground based regional GPS receivers network.

Essentials of the GPS interferometry technique for separation of ionospheric wave perturbations, applied in this work, based on simultaneous phase processing at two GPS operational frequencies L1 and L2 and further filtration of the signals for selection of waves with typical periods exceeding three minutes. [5]

For detection of wave structures, the groups of three stations each, providing minimal data set for the processing, were specially organized. Ionospheric perturbations, initially retrieved from correlation measurements, are further classified by cluster analysis. The structure is supposed to be reliably detected if the correlation measurements of the given number of groups retrieve similar parameters.

In the study we pay a special attention to specific atmospheric situations, taking place during last years, such as anomalously hot summer in 2010, accompanied by the blocking cyclone, causing dramatic consequences in Canada, Europe and Russian Federation. In this study, radio interferometric data for Moscow, Russia and Fairbanks, Alaska, USA have been processed and analyzed. Ionospheric wave structure parameters, retrieved with this approach, were in turn analyzed together with the vertical profiles of atmospheric parameters measured in situ with radiosondes.

ACKNOWLEDGEMENTS:

The present study is supported by the Russian Fundamental Research Fund (project 15-45-03266). Authors thank the Moscow State University computational facility for granting access to the high performance parallel computing systems "Lomonosov" and "Tchebyusheff".

REFERENCES

1. Gavrilov, N.M., Kshevetskii, S.P. Numerical modeling of the propagation of nonlinear acoustic-gravity waves in the middle and upper atmosphere (2014) *Izvestiya - Atmospheric and Ocean Physics*, 50 (1), pp. 66-72.
2. Gossard, E. E. and Hooke, W. H. *Waves in the Atmosphere*, 456 pp., 1975. Elsevier.
3. Phinney, R.A. and Anderson, D.L. (1968). On the radio occultation method for studying planetary atmospheres. *Journal of Geophysical Research* 73: doi: 10.1029/JA073i005p01819. issn: 0148-0227.
4. Gavrik A.L., Ilyushin Ya.A. Structure of the multi-ray radio wave field in the Venusian ionosphere: numerical simulations with parabolic diffraction equation. Abstracts of the Fourth Moscow Solar System Symposium 4ms³-PS-44
5. Zakharov, V.I., Kunitsyn, V.E. Regional features of atmospheric manifestations of tropical cyclones according to ground-based GPS network data (2012) *Geomagnetism and Aeronomy*, 52 (4), pp. 533-545.

WAVE MODULATION IN PLANETOLOGY: A NEW WAY OF PLANETARY THINKING

G.G. Kochemasov

*IGEM of the Russian Academy of Sciences, 119017 Moscow, Staromonetny 35
Contact: kochem.36@mail.ru*

"Orbits make structures". As all cosmic bodies in Universe rotate and move in several orbits with very different orbiting frequencies they are affected by modulated waves. They appear as predicted by the radio wave physics. The modulation is division and multiplication of the higher frequency by the lower one. As a result along with main frequencies appear two side frequencies with corresponding them tectonic granules. The wave born tectonic granules normally are evenly sized, shoulder-to-shoulder disposed in lines, crossing lines, grids and lattices. Examples are below (Fig. 1-11).

At the beginning of applying wave modulation procedure for explaining numerous ring structures on surfaces of cosmic bodies was used very simple (not perfect) **Titan** image made by the Hubble space telescope (HST). Titan as a satellite has two orbital periods: around Sun and Saturn. Orbiting the first makes granule size $7.5\pi R$ (the scale is Earth with one year solar period and $\pi R/4$ granule size), orbiting the second makes $\pi R/91$ (~ 90 km). Both granules were not seen at that time. But the modulation of the higher frequency by the lower one gives granule size ~670 km [$(7.5 \times 1/91)\pi R = \pi R/12$]. One observes both sizes (~90 and ~670 km) in a more perfect Cassini image (Fig. 11).

Very effective "leopard skin" structure of the **saturnian** atmosphere with regularly spaced storms about 400 km across (Fig. 5, 6) can be calculated by the modulation of rapidly rotating atmosphere (1/0.45 days, 60000 km radius) by slowly orbiting Saturn around Sun (1/30 years). To modulated side frequencies correspond smaller granules $(1/3421 \times 7.5)3.14 \times 60000 = 7.3$ km and larger granules $(1/3421 : 7.5)3.14 \times 60000 = 413.5$ km. The smaller granules are not yet observed (maybe they show themselves in kilometric radio emissions), but the larger granules are ubiquitous on the Saturn's surface as the "leopard skin" spots. Waiting for Juno detailed images we analyze the famous Voyager image with the **Red Spot** (Fig.8). This image reveals various wave forms and penetrating them weak and fine tissue made of granules ~200 to 400 km across. This size is explained by modulation by $1/12$ y. fr. of $1/10$ h. fr. giving modulated size ~191 km. Modulated granule size of **Proteus** is ~20 km (Fig. 4). It is calculated from its diameter 416 km, circumsolar granule size $41\pi R$, circumneptunian granule size $\pi R/1300$ (too small to observe with present facilities). Modulated size is $(41 \times 1/13000)\pi R = \pi R/32 = \sim 20$ km.

Pluto' rotation and orbiting with frequency $1/6.39$ days around the barycenter of the Pluto-Charon system gives granule size 16.3 km ($\pi R/228$) according to the relation between orbiting frequencies and tectonic granules sizes (Kochemasov, 1986- 2016). These granules as polygons about 20 km across are visible especially on the brightest and highest sector of Sputnik Planum (Fig. 2; Fig. 3-"lake" ~30 km across). Another widespread granule size is about 0.25 km (Fig. 1-3). It is calculated by modulation of fr. $1/6.39$ days by orbital fr. $1/248$ years = $1/90465$ days to obtain side frequency $1/14157$ and corresponding to it granule size 0.263 km.

Ceres has $1/4435$ days orbital frequency and $1/9.07$ hours rotation frequency. To both parameters correspond tectonic granules too large and too small to be observed ($3.3\pi R$ and $\pi R/3863$). The wave modulation (division and multiplication of the higher frequency by the lower one) gives two side frequencies: $1/85212$ and $1/965410$. To them correspond tectonic granules $\pi R/38.8$ and $\pi R/440.8$ ($R=475$ km), thus about 38.4 km and 3.4 km. Now both sizes are discerned: larger granules from larger distance as 'blobs' at wave intersections (HST image, Fig. 7) and small circles in strings and grids covering the whole imaged surface (not presented here).

The **Churyumov-Gerasimenko** comet 6.6 years – 2398 days, 57552 hours - orbiting period ($1/57552$ hours frequency.) gives $1.65 \pi R$ tectonic granule according to the frequency-granule size relation – too large to observe directly. But modulations by this small frequency the much higher rotation frequency of the comet ($1/12.5$ hours) gives two side frequencies: $1/4604$ and $1/719400$. To them correspond two granule sizes: $\pi R/4604$ and $\pi R/719400$ ($R \sim 2500-2000$ m) or 1.70-1.36 and 0.011-0.009 m. Rosetta' images reveal penetrating comet's body geometrically regular lattice with spacing about a few meters (fig. 9).

The **Moon** has two main and two side fr. with corresponding sizes $\pi R/4$, $\pi R/48$, and $\pi R/15$ and $\pi R/240$. Observed in the Chang'3 landing site (Fig. 10) intercrossing fine ripples with cm spacing (the scale is Yutu robot 's trace, fig. 10) most probably are modulated by the Galaxy fr. ($\sim 1/2000000000$ y.) of the above Moon's fr-s. The Galactic modulation is fixed in enigmatic meter size radio waves of Sun and decameter waves of Jupiter.

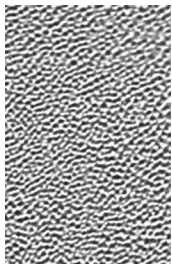


Fig. 1

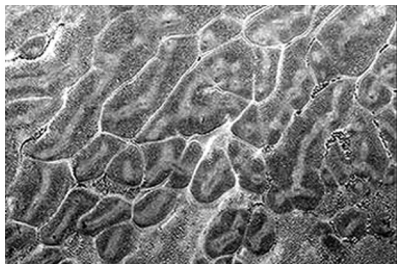


Fig. 2.

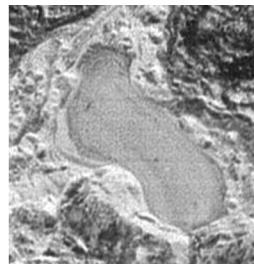


Fig. 3.

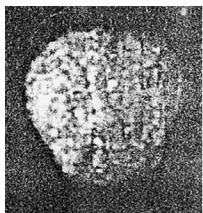


Fig. 4

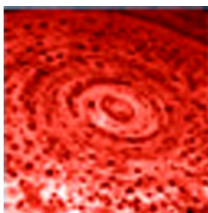


Fig. 5.

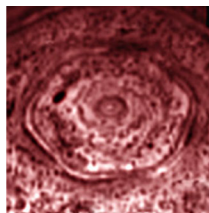


Fig. 6.

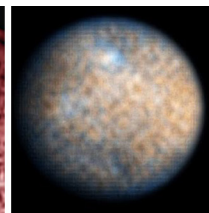


Fig. 7.



Fig. 8



Fig. 9.

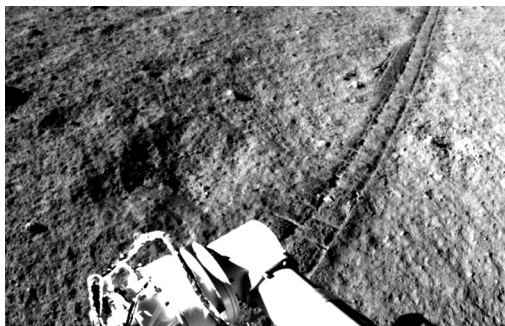


Fig. 10

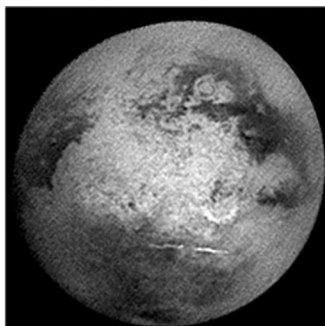


Fig. 11.

Fig. 1-3 – Pluto; **4**- Proteus; **5-6**-Saturn; **7**-Ceres; **8**-Yupiter; **9**- Churyumov-Gerasimenko; **10**-Moon; **11**-Titan.

Images **1-3**-New Horizons; **4, 8**-Voyager; **5, 6, 11**-Cassini; **9**-Rosetta; **7**-Dawn projects

ON THE MODERN STATE OF COMPARATIVE PLANETOLOGY

A.A. Barenbaum

Oil and Gas Research Institute RAS, Gubkin str. 3, Moscow, 119333, Russia.

Contact: azary@mail.ru

INTRODUCTION:

The Comparative planetology by definition K.P. Florenskiy [1] is the science that studies the Sun and planets, as the single system of natural bodies into the aggregate of all of their properties. Being closely related with cosmogony, geology, geochemistry and geophysics, Comparative planetology occupies its independent place in cosmic natural science.

Today, with the help of using space vehicles is received a large amount of new data about the processes that took place earlier in the Solar system, on its planets and their satellites. This information compels to revising earlier views on the formation and evolution the Solar system in general as well as its individual planets.

As a result, Comparative planetology today is in the state which we can justifiably be called a crisis, when this science loses the ability to address emerging challenges. According to the theory T. Kuhn [2], a way out of crisis state is possible as a result of the scientific revolution, which is accompanied by a change of the paradigm.

On author's conviction, a way out of this crisis is possible by transition in Comparative planetology to the representations of Galactocentric paradigm [3]. In this article we give a summary of Galactocentric paradigm as well as of some its provisions that lead to changes in representations of Comparative planetology.

GALACTOCENTRIC PARADIGM:

It is now established that the Sun, in process of its movement in the Galaxy, through 20-37 million years crosses the spiral arms of our stellar system. At such moments all the planets are subjected to intense bombardment by galactic comets. And one time in a billion years the Solar system interacts with dense clusters of stars, dust and gas in galactic arms, that is strongly influenced on many processes in Solar system and on its planets.

Given this influence, the author has constructed a theoretical model [4], which binds the most important events in geological history of the Earth with periods when Sun is in the spiral arms of Galaxy. This model formed the basis for the development of Galactocentric paradigm, which unlike the Kant-Laplace hypothesis considers processes in Galaxy as a major factor of the formation and evolution of Sun and planets. On the base of new paradigm the author has offered the agreed solutions of row key problems of an astronomy, geology, and planetary cosmogony that proved the adequacy of developed representations.

This article provides a summary of Galactocentric paradigm and some its provisions, which are necessary, on the author opinion, to overcome the crisis in Comparative Planetology.

NEW REPRESENTATIONS:

- Formation of the Sun and the planets this is not a one-time event, but a cyclical process, which since moment of the Solar system birth is abruptly intensified in the epochs when the Sun is in the Galaxy branches. We can distinguish two main periods of formation of the Solar system. The first – it is the era of emergence of the Sun and planets of 6.6 billion years ago. And the second – the event of 4.6 billion years ago, with which we associate the second period of planets formation. Both events occurred [5] in the spiral arm "Perceus + 1" [6], in star-forming region in the distance of corotation radius from center of the Galaxy.
- The first event is well explained by the standard model of the formation of the solar system. [7] While the second event which according to the hypothesis of O. Schmidt [8] led to the formation of gas shells and the satellites systems of giant planets, the author explains by the model [9]. This model, based on hypothesis G. Olbers of Phaeton destruction, lets also explain the origin of the asteroid bodies and the observed comets [3]. According this model, the formation of belt asteroid bodies from Phaeton's fragments, which have become objects of intense collisions with galactic comets, has initiated four processes taking place in different areas of Solar system at the one time: 1) increase of Sun's mass by about on half due to the capture a new cosmic matter; 2) evaporation and crushing of galactic comets at colliding with bodies of belt as well as mixing of substance of those and others; 3) ejection from asteroid belt large fragments of Phaeton which bombarded

the planets; 4) emission out the zone belt of huge mass of gas and dust, resulting in epochs of cometary bombardments on the outside of asteroid belt has been formed the "secondary" gas-dust disk of Sun, part substance of which has been invaded by modern giant planets.

Here are some of our findings [3]:

- Prior to the Phaeton destruction the masses of all planets are followed of general power dependence [7]. However after Phaeton destruction, many of planets have changed, that led to their separation into "internal" and "external". The outer planets: Jupiter, Saturn and Uranus, which turned inside the secondary disk of Sun, captured a new substance, which has become their gas shell and provided themselves by system of satellites. While the inner planets: Mars and Earth lost their own masses.
- At destruction moment Phaethon represented terrestrial planet with mass in 2.5 Earthly masses. As and modern Earth, the Phaeton already had possessed five differentiated silicate shells and the inner Fe-Ni nucleus. The main difference in the structure of both planets is in that now Earth has a more massive metallic nucleus and contains in mantle silicates less Fe than the Phaeton, the evolution of which was interrupted at an earlier stage.
- Phaeton's death also has led to appearance of satellite Earth – the Moon. Calculations show [10] that as a result of the falling large fragments of the Phaeton our planet is probably lost 245 ± 10 km of surface layer rocks, consisted on 1/3 of the primary crust and on 2/3 of the mantle rocks. About 20% of lost material has formed a ring on the near-Earth orbit and entered into composition of Moon, and the rest was lost. Thereby origin of Moon could be result fallings onto Earth a plurality of smaller bodies, not collision Earth with another planet. What is better satisfies to geochemical data for Earth and Moon by opinion A. Ringwood [11].
- The comets that we observe are products collisions of galactic comets and asteroids that have been captured by the Sun on near-solar orbits. The vast majority of such comets born and were thrown out from belt of $1 \div 5$ million years ago during the last bombardment the Solar system by galactic comets. At that the "secondary" comets having very large periods currently finished only the first its turn-over around the Sun. Therefore the aphelion their orbits are located from the Sun at distance of $(2 \div 50) \times 10^3$ au, which determines the position of the cloud of comets according hypothesis of Oort. Thus, the "Oort's cloud" is the concentration area of aphelion orbits of secondary comets, which previously left the belt and are now returning to the Sun. Of course, this "cloud of extreme points of cometary orbits" has nothing to do with the formation of Solar system [12].

CONCLUSION:

The presented materials give a fairly clear idea about major changes that are a result of the scientific revolution in the Comparative Planetary caused by Galactocentric paradigm.

REFERENCES:

- [1] Florensky K.P., Bazilevsky A.T., Burba G.A. et al. (1981) Essays on Comparative Planetology. (Moscow: Nauka).
- [2] Kuhn T.S. (1962) The Structure of Scientific Revolutions (Chicago: University of Chicago Press).
- [3] Barenbaum A.A. (2010) Galactocentric Paradigm in Geology and Astronomy (Moscow: LIBROKOM).
- [4] Barenbaum A.A. (2002) The Galaxy, Solar System, Earth: Coordinated Processes and Evolution (Moscow: GEOS).
- [5] Barenbaum A.A. (2015) The Sun position in Galaxy in era of Phaeton destruction, Proceedings of XVI Intl. Conf.: Physic-chemical and petrophysical studies in Earth Sciences. (Moscow: IGM RAS) pp. 39-42.
- [6] Vallee J.P. (2002) Metastudy of the spiral structure of our home Galaxy, *Astrophys. J.*, V. 566, №1, pp. 261-266.
- [7] Vityazev A.B., Pechernikova G.V., Safronov V.S. (1990) Terrestrial Planets. Origin and Early Evolution (Moscow: Nauka).
- [8] Schmidt O.Yu. (1957) Four Lectures on Theory of Earth Origin (Moscow: USSR Academy of Sciences).
- [9] Barenbaum A.A. (1992) The origin of asteroids and meteorites (a new concept of cosmogony), Conceptual bases of geology (St. Petersburg: Sankt Petersburg Mining institute) pp. 9-27.
- [10] Barenbaum A.A. (1992) Solar system in the Phaeton explosion era. Origin of the Moon, Conceptual bases of geology (St. Petersburg: Sankt Petersburg Mining institute) pp. 95-106.
- [11] Ringwood A.E. (1988) Lunar origin: single giant impact or multiple large impacts?, Abstract Paper 19-th Lunar and Planets Sci. Conf., Pt. 3, Houston. pp. 982-983.
- [12] Barenbaum A.A. (1990) New ideas about the origin of comets and their interactions with the objects of Solar system, *Kometnyy tsirkulyar*. № 418. Kiev. pp.11-12.

GEOGRAPHICAL DISTRIBUTIONS OF AN INTERNAL GRAVITY WAVE ACTIVITY IN THE EARTH'S POLAR ATMOSPHERE FOR DIFFERENT SEASONS REVEALED BY RADIO OCCULTATION FORMOSAT-3/COSMIC DATA

V.N. Gubenko¹, I.A. Kirillovich¹, Y.-A. Liou²

¹Kotelnikov Institute of Radio Engineering and Electronics of the RAS, Vvedenskogo square 1, 141190 Fryazino, Moscow region, Russia

²Center for Space and Remote Sensing Research, National Central University, Chung-Li 320, Taiwan

Contact: vngubenko@gmail.com

INTRODUCTION:

The satellite mission FORMOSAT-3/COSMIC (Constellation Observing System for Meteorology, Ionosphere and Climate) consists of six micro-satellites, and each of them has four GPS-antennas. It was launched in April 2006, orbiting around the Earth at approximately 800 km. The primary scientific goal of the mission is to demonstrate the value of near-real-time radio occultation (RO) observations in improving operational numerical weather predictions (NWP). The goal is readily shown by assimilating the measurements of atmospheric parameters into used NWP-models. These parameters include density, temperature, pressure and relative humidity fields in the atmosphere. An analysis of their geographic and seasonal distributions is necessary to the understanding of the energy and momentum transfer and the reaction of the polar atmosphere in response to global warming. This task is especially important as the polar regions are very sensitive to the change in global temperature and it may be a major cause of global sea level rising. In this work, a statistical analysis of the internal gravity wave (IGW) activity in polar atmospheric regions (latitudes $> 60^\circ$) using FORMOSAT-3/COSMIC RO temperature data collected from July 2006 to March 2009 has been performed. Geographic and seasonal distributions of the IGW potential energy per unit mass \bar{E}_p (wave activity indicator) in the altitude interval from 15 to 35 km have been determined and analyzed. The obtained results show that the wave activity in the polar atmosphere is strong in winter and spring. The potential energy of IGWs in spring is largest in Antarctic atmospheric region, while it is largest in winter in Arctic region. The wave potential energy increases with altitude up to 35 km in the atmosphere of both Earth's hemispheres. In Antarctic region, internal waves with high potential energy occur in the atmosphere over the Antarctic Peninsula. In Arctic region, a high wave activity is mainly observed over North Atlantic Ocean (Iceland) and Scandinavian Peninsula. The aim of this work is:

1. Statistical analysis of the IGW activity in polar regions (latitudes $> 60^\circ$) of the Earth's atmosphere using FORMOSAT-3/COSMIC RO temperature data collected from July 2006 to March 2009.
2. Determination and analysis of geographic and seasonal distributions of the wave potential energy per unit mass in the altitude interval from 15 to 35 km.

CALCULATIONS OF IGW POTENTIAL ENERGY PER UNIT MASS \bar{E}_p IN POLAR REGIONS FROM FORMOSAT-3/COSMIC RO TEMPERATURE DATA COLLECTED IN 2006–2009

The Level 2 products of FORMOSAT-3/COSMIC RO data from TACC (<http://tacc.cwb.gov.tw>) are used in this study. These data having a very good altitude resolution provide a unique opportunity to study a global morphology of IGWs in the Earth's polar stratosphere. The precision of FORMOSAT-3/COSMIC RO refractivity is $< 0.2\%$ between 10 and 20 km degrading to 0.7% at 30 km, and the accuracy of the derived temperature is better than 0.5 K [Alexander *et al.*, 2009].

In this study, the altitude range between 15 and 35 km is considered. Temperature profiles from DOY 194 in 2006 to DOY 90 in 2009 with latitudes greater than 60° are collected and split into the background part and temperature residuals. Then, band-pass filtering with cutoffs at 2 and 10 km is applied to this

temperature residuals to separate the fluctuations with vertical wavelengths λ , ranging from 2 to 10 km. We obtained E_p data in the cells with $2.5^\circ \times 2.5^\circ$ in longitude and latitude, and the monthly mean E_p magnitudes are calculated at 15–20 km, 20–25 km, 25–30 km and 30–35 km from the following expression [Gubenko *et al.*, 2008, 2011, 2012, 2015]:

$$E_p = \frac{1}{2} \frac{g^2}{N_b^2} \left(\frac{T'}{T_b} \right)^2 = \frac{1}{4} \frac{g^2}{N_b^2} \left| \frac{T'}{T_b} \right|^2 = \frac{N_b^2}{4m^2} \cdot \frac{g^2 m^2}{N_b^4} \cdot \left| \frac{T'}{T_b} \right|^2 = \frac{N_b^2}{4m^2} \cdot a_b^2 < \frac{N_b^2}{4m^2}.$$

The value $N_b^2/(4m^2)$ is the threshold magnitude of potential energy for saturated IGWs ($a_b < 1$) with any intrinsic frequency. Thus, we concluded that the observed temperature fluctuations in the stratosphere are generally related to IGWs when the E_p value obeys the inequality $E_p < N_b^2/(4m^2)$.

Figure 1 show geographical distributions of the monthly mean E_p values for different seasons in 2006–2009 averaged at 20–25 km in the Arctic and Antarctic regions. An analysis of FORMOSAT-3/COSMIC RO data shows that the wave activity in the stratosphere of polar regions is strong in winter and spring. In the Arctic region, the wave potential energy E_p shows clear annual variation with a maximum in winter (Figure 1, left). In the Antarctic region the values of E_p gradually increases from July and reaches maximum in spring before decreasing rapidly (Figure 1, right).

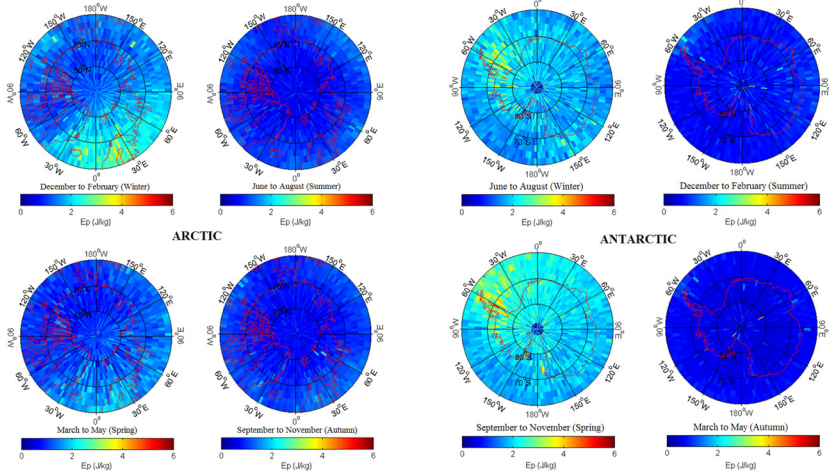


Fig. 1. Geographical distributions of the monthly mean E_p values for different seasons in 2006–2009 averaged at 20–25 km in the Arctic (left) and Antarctic (right) atmosphere.

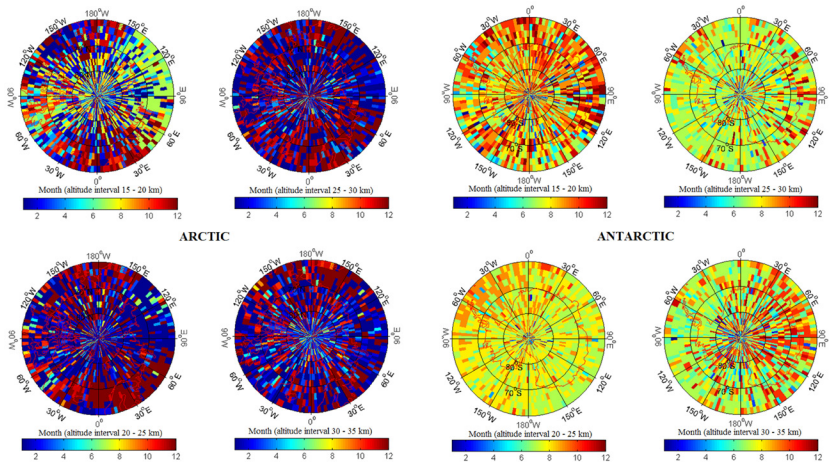


Fig. 2. Geographical distributions of the strongest wave activity months in 2006–2009 for different altitude intervals in the Arctic (left) and Antarctic (right) atmosphere.

Figure 2 demonstrate geographical distributions of the strongest wave activity months in 2006–2009 for different altitude intervals in the Arctic and Ant-

arctic atmosphere. Figure 2 (left) shows the strongest months of the mean potential energy with different altitude intervals in the atmosphere over Arctic. The strongest wave activity month for the 15–20 km interval is less regular. Some occur in July and most occur from November to February. Above 20 km, almost of the strongest wave activity months occur from November to February. In Antarctic (Figure 2, right) the strongest months for 15–20 km interval is less regular. The strongest wave activity months from 20 to 25 km are concentrated in July, August and September, but August occupies the largest part. In the altitude interval of 25 to 30 km, July and August dominate the strongest months, but July rather than August become the largest part.

CONCLUSION:

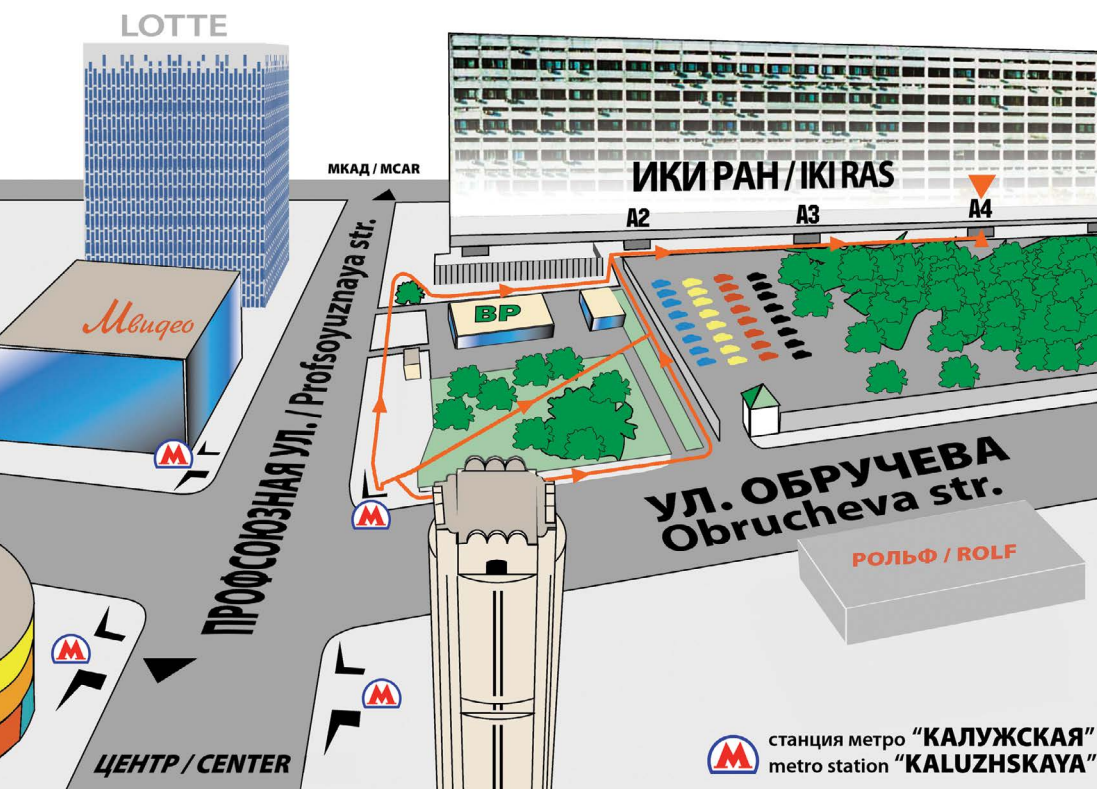
We studied the behavior of the atmospheric IGWs in the stratosphere at 15–35 km in both the Arctic and Antarctic regions (latitudes $> 60^\circ$) by using FORMOSAT-3/COSMIC RO data from July 2006 to March 2009. From the temperature profiles, we calculated the background mean temperature, Brunt-Vaisala frequency squared and the temperature fluctuations with vertical wavelengths from 2 to 10 km. Then we determined the wave potential energy E_p at 15–20 km, 20–25 km, 25–30 km and 30–35 km. The E_p values were averaged every one month and season in a cells $2.5^\circ \times 2.5^\circ$ in longitude and latitude. The wave potential energy increases with altitude up to 35 km in both the Northern and Southern Hemispheres. A significant localized enhancement of E_p in winter and spring is recognized over a few specific mountainous areas such as Scandinavia, Iceland, Greenland, Antarctic Peninsula and Trans-Antarctic Mountains (Figure 1). Therefore orographic effects seem to be one of the main mechanisms for generating IGWs in the polar regions. However, the line of sight of the FORMOSAT-3/COSMIC observations in all regions are preferentially oriented close to the north-south axis, making mountain waves more likely to be observed [Alexander *et al.*, 2009]. This suggests an overestimate of orographic activity of IGWs when compared to isotropic wave sources.

ACKNOWLEDGMENTS:

This work was partially supported by the Program No. 7 of the RAS Presidium. Y.-A. Liou acknowledge the National Science Council (NSC) of Taiwan for the support of grant NSC 95-2111-M-008-011-MY3.

REFERENCES:

- Alexander S. P., Klekociuk A. R., and Tsuda T. (2009). Gravity wave and orographic wave activity observed around the Antarctic and Arctic stratospheric vortices by the COSMIC GPS-RO satellite constellation. *J. Geophys. Res.*, V. 114, No. D17103, DOI: 10.1029/2009JD011851.
- Gubenko V.N., Pavelyev A.G., Andreev V.E. (2008). Determination of the intrinsic frequency and other wave parameters from a single vertical temperature or density profile measurement. *J. Geophys. Res.*, V. 113, No. D08109, DOI:10.1029/2007JD008920.
- Gubenko V.N., Pavelyev A.G., Salimzyanov R.R., Pavelyev A.A. (2011). Reconstruction of internal gravity wave parameters from radio occultation retrievals of vertical temperature profiles in the Earth's atmosphere. *Atmos. Meas. Tech.*, V. 4, No. 10, P. 2153–2162, DOI:10.5194/amt-4-2153-2011.
- Gubenko V.N., Pavelyev A.G., Salimzyanov R.R., Andreev V.E. (2012). A method for determination of internal gravity wave parameters from a vertical temperature or density profile measurement in the Earth's atmosphere. *Cosm. Res.*, V. 50, No. 1, P. 21–31, DOI: 10.1134/S0010952512010029.
- Gubenko V.N., Kirillovich I.A., Pavelyev A.G. (2015). Characteristics of internal waves in the Martian atmosphere obtained on the basis of an analysis of vertical temperature profiles of the Mars Global Surveyor mission. *Cosm. Res.*, V. 53, No. 2, P. 133–142, DOI: 10.1134/S0010952515020021.



ИКИ РАН,

площадь академика Келдыша

Метро "Калужская", первый вагон из центра, по тоннелю — прямо, по второму поперечному тоннелю- направо, выход на площадь, далее по стрелкам на схеме

IKI RAS

You should get off at "Kalyzhskaya" metro station using the southern exit. After leaving a station lobby through glass doors you should go straight to the end of the tunnel, then take right and use the stairs to get to the surface. From this point you may follow either arrow on this map

MOSCOW METRO SCHEME



СХЕМА МОСКОВСКОГО МЕТРОПОЛИТЕНА



REGISTRATION AND INFORMATION DESK

location:
IKI,
entrance A-4

time:
10 october, 8:30–18:00
11 -14 october, 9.00-18.00

SCIENTIFIC SESSIONS

location:
IKI conference hall,
second floor

POSTER SESSIONS

location:
IKI exhibition hall,
ground floor

time:
10 october, 18.00-19.00
12 october, 18.00-19.00

SOCIAL PROGRAM

10 october	11 october	12 october	13 october	14 october	15 october
10.00-18.00 IVAN AIVAZOVSKY. FOR THE 200TH ANNIVERSARY <i>Exhibition</i> The Tretyakov Gallery on Krymsky Val					10.00 EXCURSION TO ASTRO-NAUTICS MEMORIAL MUSEUM VDNH Subway
18.00 WELCOME PARTY Space Research Institute (IKI) Exhibition hall	19.00 GISELLE <i>Ballet</i> State Kremlin Palace	19.00 LA BOHÈME <i>Opera</i> Stanislavsky and Nemirovich-Danchenko Moscow Music Theatre	18.00 CONCERT Space Research Institute (IKI) Conference hall	19.00 MAYERLING <i>Ballet</i> Stanislavsky and Nemirovich-Danchenko Moscow Music Theatre	
		19.00 MOSCOW REGION ACADEMIC CHOIR Moscow International House of Music	19.00 RECEPTION Space Research Institute (IKI) Exhibition hall	19.00 IL TROVATORE <i>Opera</i> Novaya Opera	

for additional information and registration for the events please contact

Mrs Julia Brekhovskikh

E-mail: Social.program2016@gmail.com

INTERNET ACCESS AND WIFI

there is Internet access in and near the conference hall

lunch points nearest to IKI / точки питания вблизи ИКИ



- 1. SPACE RESEARCH INSTITUTE OF THE RAS, Food center, Ground Floor, Section A3**
ИНСТИТУТ КОСМИЧЕСКИХ ИССЛЕДОВАНИЙ РАН, столовая, 1 этаж, секция А3
- 2. INSTITUTE OF APPLIED MATHEMATICS OF THE RAS, Food center, Ground Floor**
ИНСТИТУТ ПРИКЛАДНОЙ МАТЕМАТИКИ РАН, столовая, 1 этаж
- 3. “KALUZHSKIY” Market Center, Profsoyuznaya Street, 61A, 2 Floor**
ТЦ “КАЛУЖСКИЙ”, ул. Профсоюзная, д. 61А, зона ресторанов, 2 этаж
- 4. Bar СПБ, Obrucheva Street 34/63, Building 1**
Бар “СПБ”, ул. Обручева, 34/63, строение 1
- 5. “Colibri” restaurant in Bussiness Center Gas Field, Obrucheva street 23**
Ресторан “Колибри” в Бизнес-центре Газпром, ул. Обручева, 23
- 6. Café “AnderSon”, Obrucheva Street 30/1**
Кафе “АндерСон” на ул. Обручева, д. 30/1

